

Trinity College Dublin
Coláiste na Tríonóide, Baile Átha Cliath
The University of Dublin

Investigation of Static & Active Structural Colouration in Ultrathin Film Lossy Fabry-Perot Resonator Stack Structures

Evan Roy

A thesis presented in partial fulfilment of the requirements

for the degree of

Doctor of Philosophy

School of Physics

Faculty of Engineering, Mathematics and Science

Trinity College

University of Dublin

Academic Supervisor: Professor David McCloskey

2025

Declaration

I declare that this thesis has not been submitted as an exercise for a degree at this or any other university and it is entirely my own work.

I agree to deposit this thesis in the University's open access institutional repository or allow the Library to do so on my behalf, subject to Irish Copyright Legislation and Trinity College Library conditions of use and acknowledgement.

I consent to the examiner retaining a copy of the thesis beyond the examining period, should they so wish (EU GDPR May 2018).

Signed: 

Date: 31/01/2025

ID No: 16316413

Abstract

The main aim of the research laid out in this work is to characterise the optical response of high index lossy absorbers like MoS_2, Si, Ge, VO_2, and Nio in various all-thin-film Fabry-Perot wave interference nanocavity stack structures. More specifically I wish to ascertain how strong absorption, light-matter interaction, and colouration, can be explained in these multilayer assemblies when ultrathin lossy layers are used in conjunction with either opaque or semi-transparent back reflective metals like Ag, Au, Al, W, Cr, and Ni, which are sometimes also paired with lossless transparent dielectric spacers and anti-reflection coating films.

An all-thin-film (ATF) approach in this context refers to a thin film device that requires no lithography in the manufacturing process, also known as a lithography-free process. By focusing on an ATF stack structure, many of the drawbacks that are traditionally associated with nanofabrication, such as increased design cost and complexity, can be circumvented. Thus, the research presented will focus mainly on using thin film interference as the primary strategy to create structural colour over other patterned metasurface methods. Simple two-layer stacks that access the normally forbidden zeroth order Fabry-Perot mode will be discussed at length for the lossy materials mentioned in both passive and active settings. Additionally, other phenomena like broadband near perfect absorption in the ultrathin regime will also be explored in the context of a lithography free approach, demonstrating how careful thin film design can concentrate most of the incoming light across the visible into extremely thin high index absorbing layers less than 10 nm in thickness. Furthermore, the same concept of focusing light into an ultrathin absorbing film will also be shown to produce steep and bright structural colour when coupled with a higher order Fabry-Perot mode associated with the narrower metal-insulator-metal (MIM) resonator, in a design known as a Fano-resonant cavity. Using this stack configuration, it will be evident that the performance of active index change devices, based on electrochromic and phase change active materials like NiO and VO_2, are greatly enhanced in terms of their on/off state contrast in reflection. Moreover, it will be shown that the colour gamut and resonant peak brightness performance of these Fano-resonant devices supersedes the two-layer zeroth order Fabry-Perot mode stack structures.

Publications

Papers

[I] A. L. Lynch, C. P. Murray, **E. Roy**, C. Downing, and D. McCloskey, "Extreme Dewetting Resistance and Improved Visible Transmission of Ag Layers Using Sub-Nanometer Ti Capping Layers," *ACS Omega*, vol. 9, no. 8, pp. 9714–9719, 2024, doi: 10.1021/acsomega.3c09774

[II] N. Shelly, **E. Roy** *et al.*, "Strong Absorption and Modulation in Deeply Subwavelength Transition Metal Dichalcogenide Thin Films." *In prep,* 2024

[III] N. Shelly, C. P. Murray, **E. Roy**, D. McCloskey, "Enhanced Photoconductivity in Ultrathin MoS_2 Films Using Lithography Free Structural Colour", *In prep, 2024*

[IV] D. Khicher, **E. Roy**, C. Murray, D. McCloskey, "Investigation of Metal Backed Electrochromic NiO in the Ultrathin Film Regime", *In Prep, 2024*

[V] **E. Roy**, D. Khicher, C. Murray, D. McCloskey, "Design of Zeroth Fabry-Perot Mode Broadband Absorbers Using Ultrathin Lossy Dielectric films ", *In prep, 2024*

Posters

[I] **E. Roy**, N. Shelly, C. Murray, D. McCloskey, "Investigation of Strong Optical Absorption in Thin Film Transition Metal Dichalcogenides." *9th instalment of the Biennial Photonics Ireland Conference, Virtual, 2021*

[II] **E. Roy**, N. Shelly, C. Murray, D. McCloskey, "Investigation of Reflection and Strong Optical Absorption in Thin Film Transition Metal Dichalcogenides," *SFI Science Summit 2021, Virtual,* 2021

[III] N. Shelly, **E. Roy**, C. Murray, D. McCloskey, "Field Effect Modulation using Transparent Conductive Oxides and Multilayer Transition Metal Dichalcogenides", 43rd Conference of *CLEO. San Jose California USA, 2023*

[IV] **E. Roy**, N. Shelly, C. Murray, D, McCloskey, "Investigation of Field Effect Tuning of Refractive Index in Transparent Conducting Oxide Thin Film Fabry-Perot Cavity Structures", *META The 13th International Conference. Paris, 2023*

[V] D. Khicher, **E. Roy**, C. Murray, D. McCloskey, " Enhancing Electrochromism of Transition Metal Oxides Using Fabry-Perot Interference", *AMBER Conference. Dublin, 2024*

Acknowledgements

First and foremost, I would like to convey my deepest thanks to my supervisor Prof. David McCloskey for allowing me to be a part of this project. He has provided expert advice, guidance, and knowledge thoughout the course of this work on a huge range of topics. Thank you for providing me with this irreplaceable opportunity to learn, grow, and teach others.

I'm extremely greatful to Chris Murray for his extensive and unparrallel knowledge of the operation of various tools that can be found in CRANN and AMBER. I'm also very appreciative of his sage advice and observations, not only in regards to carrying out science but also on life in general. I will always hold his role as a mentor in very high regard. The completetion of this thesis would not have been possible without the invaluable help of Dilkhush Khicher. I'm forever greatful for her kindness and help in understanding and carrying out measurements and sample synthesis in electrochromics. She has gone above and beyond board in her work and I wish her the best of luck going forward

I would like to extend my deepest gratitude to Kenny Yu for his kindness, being a role model, and his wealth of knowledge. Particularly in optics and thermal physics. I greatly appreciate the many discussions and laughs we've had over the years working together as well. Huge thanks to current and previous group members Erik Soderholm, Eoin Cotter, Nishtha Shelly, Anandhi Parthiban, and Sayuj Sasidharan for their help and company over the past four years as well. Many a great conversation has been had on science and all different matters of life. I will cherish these moments always.

I'd like to recognise the amity I've had with many others in the CRANN and SNIAM over the course of the project. Escpecially to those that were and are in Prof. Micheal Coey's Magnetism and Spin Electronics Group, such as Dr. Jean Besbas and Prof. Plamen Stamenov among many others, whom I first interned with many many years ago in my undergrad. My decision to continue my education was firmly rooted in the positive experience I had working in their research group and seeing first hand how science in academia is done.

I'm forever indebted to my father Colm Roy, my mother Emer Roy, and my younger brother Eoin Roy, for their unwavering support over the last 4 years. Without their love and assistance I would not have been able to complete my work. They've stood by me every step of the way. Finally, I would also like to acknowledge the Science Foundation Ireland for providing the funding which enabled me to take part in this research project.

List of Acronyms & Abbreviations

Acronymns

1D	One Dimensional
2D	Two Dimensional
3D	Three Dimensional
4PP	Four-point-probe
AC	Alternating Current
AFM	Atomic Force Microscopy
ALD	Atomic Layer Deposition
AOI	Angle of Incidence
AR	Anti-Reflection
ATF	All-Thin-Film
atm	Atmosphere (unit of pressure)
BSF	Beam Splitter Filter
CA	Chronoamperometry
CCD	Charge-Coupled Device
CCDTR	Charge-Coupled Device Based Thermoreflectance
CIE	Commission Internationale de l'Éclairage
CV	Cyclic Voltammetry
CVD	Chemical Vapour Deposition
DC	Direct Current
EC	Electrochromic
ECD	Electrochromic Display
ECM	Electrochromic Material
EM	Electromagnetic
EMA	Effective Mean Approximation
ENZ	Epsilon Near Zero
EQE	External Quantum Efficiency
fcc	Face-Centered Cubic
FDTD	Finite Difference Time Domain
FEM	Finite Element Method
FP	Fabry-Perot
FROC	Fano-Resonant Optical Coating
FWHM	Full Width Half Maximum
HOMO	Highest Occupied Molecular Orbital
IR	Infrared
KHz	Kilohertz
KK	Kramers-Kronig
LCD	Liquid Crystal Disaplay
LED	Light Emitting Diode
LIGO	Laser Interferometry Gravitational Observatory
LUMO	Lowest Unoccupied Molecular Orbital
MHz	Megahertz
MIM	Metal-Insulator-Metal
MSE	Mean Square Error
NA	Numerical Aperature

NIR	Near-Infrared
NPVD	Nano Physical Vapour Deposition
OPL	Optical Path Length
PEC	Perfect Electric Conductor
PSD	Polarisation State Detector
PSG	Polarisation State Generator
PSU	Power Supply Unit
PV	Photovoltaics
PVD	Physical Vapour Deposition
RF	Radio Frequnecy
RMS	Root mean Square
sccm	Standard Cubic Centimeter Per Minute
SE	Spectroscopic Ellipsometry
SEL	Solid Electrolyte Layer
SEM	Scanning Electron Microscopy
SFI	Science Foundation Ireland
STM	Scanning Tunnnleing Microscopy
TAC	Thermal Assisted Conversion
TCM	Thermochromic Material
TE	Transverse Electric
THz	Terahertz
TM	Transverse Magnetic
TMD	Transition Metal Dichalcogenides
TMM	Transfer Matrix Method
TMO	Transition Metal Oxide
UV	Ultraviolet
UV-Vis	Ultraviolet-Visible
VdW	Van Der Waals
w.r.t	With Respect To
XRD	X-Ray Diffraction

Chemical Abbreviations

$[Co(Cp^*)_2]$	Cobaltocene
$[Fe(Cp)_2]^+$	Ferrocenium
Ag	Silver
Al	Aluminium
Al_2O_3	Alumina
Au	Gold
Cl	Chlorine
Cr	Chromium
CuO_2	Copper Oxide
DNA	Deoxyribonucleic Acid
Fe	Iron
FTO	Fluorine Doped Tin Oxide
GaAs	Gallium Arsenide

Ge	Germanium
H_2SO_4	Sulphuric Acid
HfO_2	Hafnia
InGaAs	Indium Gallium Arsenide
ITO	Indium Tin Oxide
KOH	Potassium Hydroxide
$LiClO_4$	Lithium Perchlorate
MgF_2	Magnesium Fluoride
MoS_2	Molybdenum Disulphide
Ni	Nickle
NiO	Nickle Oxide
Pt	Platinum
Se	Selenium
Si	Silicon
Si_3N3	Silicon Nitride
SiO_2	Silica
Ta_2O_5	Tantalum Pentoxide
Te	Tellurium
Ti	Titanium
TiN	Titanium Nitride
TiO_2	Titanium Dioxide
V	Vanadium
V_2O_5	Vanadium Pentoxide
VO_2	Vanadium Dioxide
WO_3	Tungsten Trioxide
WS_2	Tungsten Disulphide
ZnS	Zinc Sulphide
α-Ge	Amorphous Germanium
α-Si	Amorphous Silicon

Table of Contents

Declaration ..... **ii**

Abstract ..... **iii**

Publications ..... **iv**

Papers iv

Posters iv

Acknowledgements ..... **v**

List of Acronyms & Abbreviations ..... **vi**

Acronyms vi

Chemical Abbreviations vii

Chapter 1. Introduction **1**

1.1 Thesis Aims & Objectives 1

1.2 Origin & Overview of Colour 3

1.2.1 Quantifying Colour 3

1.2.2 Colour in Nature 8

1.2.3 Active Colour Change in Nature 12

1.2.4 Artificial Active Colour Change 13

1.2.5 Active Colour Change with Electrochromics & Thermochromics 15

1.3 Vibrant Colouration & Strong Absorption Using Fabry-Perot Cavity Resonators Paired with Ultrathin Lossy Dielectric Absorbers 21

1.3.1 Introduction to Fabry-Perot Resonator Interference 21

1.3.2 Accessing the Zeroth Mode Using an Ultrathin Lossy Fabry-Perot Cavity 24

1.3.3 Omnidirectionality of the Zeroth Order Fabry-Perot Mode 29

1.3.4 Enhanced Colour Gamut Using Additional Oxide Capping Layers 32

1.3.5 Central Lossy Higher Order Fabry-Perot Cavity Colour Filters 34

1.3.6 Fano-Resonant Fabry-Perot Cavity Colour Filters 35

1.4 Summary 36

1.5 References 40

Chapter 2. Theories of Light-Matter Interaction 50

2.1 Introduction to the Theory of Electromagnetic Waves.....50

2.1.1 Describing Light as an Electromagnetic Wave.....50

2.2 Quantum Nature of Light & Matter.....52

2.2.1 Light Particle-Wave Duality.....52

2.2.2 Matter Particle-Wave Duality 55

2.2.3 The Continuum Limit & Electronic Band Formation.....58

2.3 Explanation of Conductors, Semiconductors, & Insulators.....59

2.3.1 The Free Electron Drude-Lorentz Model of Conductors 59

2.3.2 The Direct Interband Transition Model of Semiconductors 61

2.3.3 The Indirect Interband Transition Model of Semiconductors.....67

2.3.4 Description of Free Excitons in Semiconductors 69

2.3.5 Normal Dispersion Models of Transparent Dielectric Insulators.....73

2.4 Thin Film Wave Interference.....77

2.4.1 Electromagnetic Wave Interference & the Principal of Superposition.....77

2.4.2 Electromagnetic Wave Interference in Multilayer Stack Structures.....79

2.5 Transfer Matrix Method Theory.....81

2.5.1 Ellipsometry Analysis & Interference Depending on Light's Polarisation.....81

2.5.2 Complex Refractive Index & Dielectric Function of Thin Film Materials.....84

2.5.3 Kramers-Kronig Relations.....86

2.5.4 Fresnel Equations & the Matrix Generalization to Multilayer Thin Film Stacks 88

2.5.5 Corrections & Additions to the Transfer Matrix Formulation.....92

2.6 Summary.....96

2.7 References.....97

Chapter 3. Sample Creation & Characterisation Methods 101

3.1 Introduction to Methods Used for Sample Synthesis & Measurement.101

3.2 Overview of Magnetron Sputtering.....102

3.2.1 Physics of Magnetron Sputtering Using a Direct Current & Radio Frequency Gun 102

3.2.2 NPVD Magnetron Sputtering System & Sample Preparation 112

3.2.3 Auxiliary Sample Synthesis Methods 118

3.3 Spectroscopic Ellipsometry 123

3.3.1 Physics of Spectroscopic Ellipsometry 123
3.3.2 Accuracy of the Ellipsometer Optical Model 128
3.3.3 Refractive Index Dispersion Expressions 133
3.3.4 J.A. Woollam Alpha Spectroscopic Ellipsometer System 135
3.4 Spectroscopy 136
3.4.1 Overview of Spectroscopy 136
3.4.2 Perkin Elmer UV-Vis Spectrometer System 138
3.4.3 Processing of UV-Vis Data 140
3.4.4 Physics of X-Ray Spectroscopy 142
3.4.5 CRANN X-Ray Reflectometer System 149
3.4.6 Physics of Raman Spectroscopy 149
3.4.7 Raman Spectrometer Characterisation of MoS_2 153
3.5 Optical Microscopy, Scanning Electron Microscopy, & Atomic Force Microscopy for Characterising Surface Morphology 154
3.5.1 Optical Microscopy 154
3.5.2 Scanning Electron Microscopy 155
3.5.3 Scanning Tunnelling & Atomic Force Microscopy 158
3.6 Electrical Characterisation 164
3.6.1 Four-Point-Probe 164
3.6.2 CRANN Four-Point-Probe System 168
3.7 Summary 169
3.8 References 170

Chapter 4. Zeroth Order Fabry-Perot Resonant Enhanced Absorption & Structural Colouration in High Index Lossy Dielectric Ultrathin Films 176
4.1 Fabry-Perot Resonance Enhancement of the Light-Matter Interaction & How to Access the Zeroth Mode 176
4.1.1 Enhancement of the Light-Matter Interaction Using Fabry-Perot Resonance 176
4.1.2 Lossy ATF Design to Access the Zeroth Mode 178
4.2 State of the Art Work Accessing the Ultrathin Zeroth Mode 182
4.2.1 The Zeroth Mode in Ultrathin Si 182
4.2.2 The Zeroth Mode in Ultrathin Ge 186
4.2.3 Recap of the Literature Review 190

4.3 Characteristics of TAC Grown TMDs 191
4.3.1 Large Dielectric Function of TMD Thin Films 191
4.3.2 Surface & Active Reflection Change Properties of the TAC Grown TMDs 194
4.3.3 Spectroscopic Ellipsometry of the TAC Grown TMDs 199
4.4 Results of our Lossy Dielectrics in the Zeroth Order Fabry-Perot Resonator Stack Layout 205
4.4.1 Vivid Colouration of Lossy Zeroth Mode Resonators 205
4.4.2 Strong Absorption of Lossy Zeroth Mode Resonators 210
4.4.3 Layer Resolved Absorption of Lossy Zeroth Mode Resonators 218
4.4.4 Angle & Polarisation Response of Lossy Zeroth Mode Resonators 221
4.4.5 Enhanced Colouration of Oxide Capped Lossy Zeroth Mode Resonators 223
4.5 Summary 226
4.6 References 227

Chapter 5. Zeroth Order Fabry-Perot Resonant Enhanced Absorption & Structural Colouration in Active Electrochromic Transition Metal Oxides 236
5.1 Introduction to Electrochromic Materials 236
5.1.1 Applications of Electrochromism 236
5.1.2 Enhancing Colouration of ECMs Using Fabry-Perot Resonance 238
5.2 Electrochromic Response of Cathodic TMO WO_3 240
5.2.1 WO_3 in the Literature 240
5.2.2 Results for the Electrochromic Response of Protonated WO_3 242
5.3 Electrochromic Response of Anodic TMO NiO 245
5.3.1 NiO in the Literature 245
5.3.2 Comparing the Preliminary Results Gathered for our NiO & WO_3 250
5.4 Absorption & Contrast of the Zeroth, & Higher, Fabry-Perot Mode in NiO 255
5.4.1 Strong Absorption & Dynamic Contrast for NiO on Metal Backing 255
5.4.2 Understanding Discrepancies between the TMM & UV-Vis Data of the Zeroth, & Higher, Fabry-Perot Mode in NiO 261
5.4.3 Dynamic Colouration of the Zeroth, & Higher, Fabry-Perot Mode in NiO 269
5.4.4 Layer Resolved Absorption & Angle Response of the Zeroth, & Higher, Fabry-Perot Mode in NiO 271

5.5 Explanation of CV & CA to Characterise the EC Parameters 276
5.5.1 Description of the Electrochemical Reduction Chemistry 276
5.5.2 Cyclic Voltammetry Cell Setup & Chronoamperometry 280
5.6 Comprehensive Study of the EC Response & Parameters of NiO on Ag 285
5.6.1 Electrochromic Parameter Results of Sputtered NiO on Ag 285
5.6.2 Colourimetry Results of Sputtered NiO on Ag 289
5.7 Summary 293
5.8 References 294

Chapter 6. Enhanced Structural Colouration & Broadband Absorption Using Ultrathin Lossy Dielectrics in Higher Order Fabry-Perot Resonators 304

6.1 Introduction to Higher MIM Fabry-Perot Modes Modified by Strategically Placed Ultrathin Lossy Films 304
6.2 Centrally Placed Lossy MIM Colour Filters 305
6.2.1 Lossy Ultrathin Absorber MIM Transmission Filters in Literature 305
6.2.2 Lossy Ultrathin Absorber MIM Transmission Filters Based on MoS_2 & Cr 308
6.2.3 Lossy Ultrathin EMA Bilayer Absorber MIM Reflection Filters in Literature 314
6.2.4 Lossy Ultrathin Cr/VO_2 EMA Bilayer Absorber MIM Reflection Filters 318
6.3 Centrally Placed Lossy Ultrathin Broadband Absorber 324
6.3.1 Overview of Ultrathin Broadband Absorption Optics & the Ideal Stack Structure 324
6.3.2 Centrally Placed Ultrathin Cr Absorber in Dielectric Sandwich Backed with Ag 332
6.3.3 Centrally Placed Ultrathin Ge Absorber in Dielectric Sandwich Backed with Ge 336
6.4 Active Colour Change MIMs Using a Thermochromic VO_2 Spacer 339
6.5 Fano-Resonant MIM Reflection Filters 342
6.5.1 Explanation & Properties of Fano-Resonance in a Compact ATF Device 342
6.5.2 Fano-Resonant MIM Reflection Filters Based on MoS_2 & Ge 350
6.5.3 Fano-Resonant MIM Reflection Filters Based on NiO & VO_2 354
6.6 Summary 359
6.7 References 360

Chapter 7. Conclusions & Future Work 367
7.1 Conclusions 367
7.2 Future Work 374
7.2.1 Future Work with Fano-Resonant Devices 374
7.2.2 Future Work with EMA Lossy MIM FP Devices 380
7.2.3 Future Work with Solid-State Electrolyte Electrochromic Devices 380
7.3 References 383

Appendix – Material Recipes 386

Chapter 1. Introduction

1.1 Thesis Aims & Objectives

At the beginning of the project the main aim was to investigate further into reports of large field effect unity order change in the refractive index of transition metal dichalcogenides (TMDs) MoS_2 and WS_2 seen in the literature [1], specifically in the context of fast modulating devices [2]. As this process can only operate in the ultrathin regime due to geometric confinement effects [3], enhancement of the light matter interaction was necessary in order to manifest large measurable changes in the optics.

To facilitate this using only an all-thin-film approach (ATF) to the device design, as opposed to a patterned metasurface with dielectric/metallic ring resonators or plasmonic nanostructures, to simplify modelling and manufacturing, an asymmetric Fabry-Perot (FP) optical resonator structure was employed based on the work carried out by Seyed Sadreddin Mirshafieyan and Mikhail A. Kats [4], [5], wherein a lossy dielectric is placed on top of a reflective opaque back mirror like Ag, Al, or Au. The resonator structure they investigated can access the normally forbidden deeply subwavelength zeroth FP resonance mode due to the non-trivial complex phase shifts of the partial reflections at the boundaries of the top lossy dielectric thin film. In so doing many advantageous benefits can be gained such as strong absorption and/or structural colouration, reduced iridescence w.r.t Angle of incidence (AOI), and isomorphism in the polarisation specific response.

Though this setup was initially taken for the purpose of enhancing the modulation capabilities of MoS_2 and WS_2, due to issues arising in reliably manifesting the gate tuneable response beyond the micron scale, only the passive colouration and absorption results obtained could be compared with literature. Chapter 4 looks at both TMDs, alongside Si and Ge, in this context to see how they improve upon what has been reported previously [6]–[8].

From there, the scope of the thesis evolved further towards the objective of characterising passive structural colouration and active electrochromic change using

ultrathin film NiO in the same asymmetric thin film Fabry-Perot stack configuration as before. NiO was chosen for investigation due to its large broadband index change between a lossy dielectric state and a transparent dielectric state when intercalated (bleached for the anodic NiO) with different ions like H^+, Li^+, Na^+, etc [9]–[11]. Moreover, reports in the literature indicated that the colouration efficiency was quiet high despite the small amount of ion intercalation occurring into the bulk [10]. The properties and performance of NiO in the ultrathin regime are also not well explored in comparison to bulkier films with thickness on the order of the wavelength of light or greater.

Transfer matrix simulation indicated that accessing the zeroth mode with NiO on Au or Ag would enable strong contrast between the bleached and coloured state of the FP device, while operating in reflection, that is comparable in magnitude to the contrast in transmission seen with traditionally bulkier ITO/Glass backed electrochromic stack structures used in dimmable smart windows applications [9]. The details of the results gathered are given in ch.5.

Finally, to further improve upon the purity (purer colours are comprised of fewer colour peaks like RGB, while purple requires red and blue), saturation, brightness, and gamut of the structural colours achievable with the simpler two-layer asymmetric device designs, the possibility of combining the zeroth FP mode stacks with other higher order Fabry-Perot device structures in both the theoretical and experimental sense for use as a more angle robust compact colour filter in reflection and transmission was also investigated. In simulation, the inclusion of a lossy ultrathin absorbing layers in various arrangements such as central and capping placement positions were shown to markedly improve upon the colourimetry performance [12], [13]. Furthermore, the highly spectrally dispersive Fano-resonant colour filters investigated showed promising results in all colour metrics as compared to many of the other ATF colour filter designs found in the literature with reflection/transmission peaks that are often too broad when not enough lossy material is included to narrow the resonance, and too dim when said lossy films become too thick and decouple the incoming light from the resonator cavity.

1.2 Origin & Overview of Colour

1.2.1 Quantifying Colour

Colour is the subjective interpretation of EM radiation by our brain in the 400-800 nm bandwidth. The human eye detects colour across this wavelength range over a huge range of intensities using rods and three photoreceptor cones called S, M, and L-cones which have different spectral sensitivities outlined in Fig.1.1(a) [14]. There are 7 million of these cones highly concentrated around the eye's fovea region which is adjacent to the optic nerve and the rest of the retina is scattered with rods, numbering 120 million, specialized in detecting motion instead of colour (Fig.1.1(b)). In this way the eye efficiently detects wavelength resolved data on incoming EM radiation directly in the line of sight/focus while also remaining sensitive to sudden changes in the background and periphery of human vision. Both have obvious evolutionary advantages such as rapid detection of motion and distinguishing between ripe and unripe fruit. The latter is likely the driving force behind why primates have trichromatic vision (red, green, and blue hues are perceived) [15].

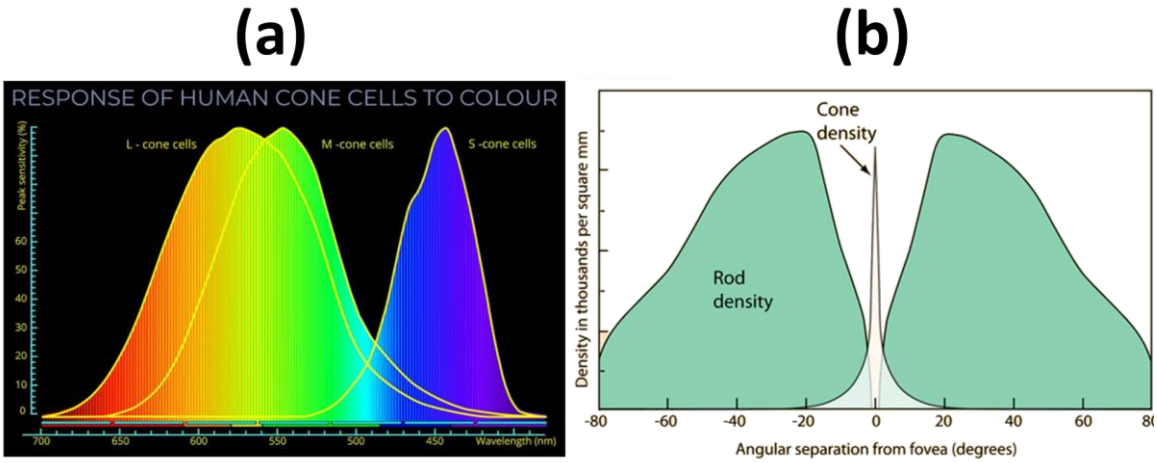


Figure 1.1. (a) The sensitivities are normalised but the L and M cones are less sensitive than S [16]. *(b) Cones are densely packed in the fovea across a 0.3 mm diameter region. Rods are spread across almost all the retina and light from very glancing angles can be absorbed for motion detection and environmental threat awareness purposes* [14].

The cones are optimised for bright sunlit conditions while the rods dominate night vision response due to their higher light sensitivity [14]. This distinction leads to interesting phenomenon such as the case where stars are visible in the peripheral vision, but not when looked at directly. Furthermore, since rods do not have a strong red response, night vision

can be preserved using a red light source [14]. A fact that many astronomers would be familiar with.

The discovery of the three different cone photoreceptors eventually lead to the creation of the famous CIE (Commission Internationale de l'Éclairage) 1931 XYZ colour chart in Fig.1.2(a). This was a French standardisation of colour perception for a human being under arbitrary lighting conditions controlled by tristimulus curve weighting functions (Fig.1.2(b)). D65 illumination is used to replicate sunlight as a source, with a correlated colour temperature of 6500 K [17]. The source light will bounce off an object and the resultant reflection spectra will produce a colour in terms of the objective parameters of hue, saturation, and brightness.

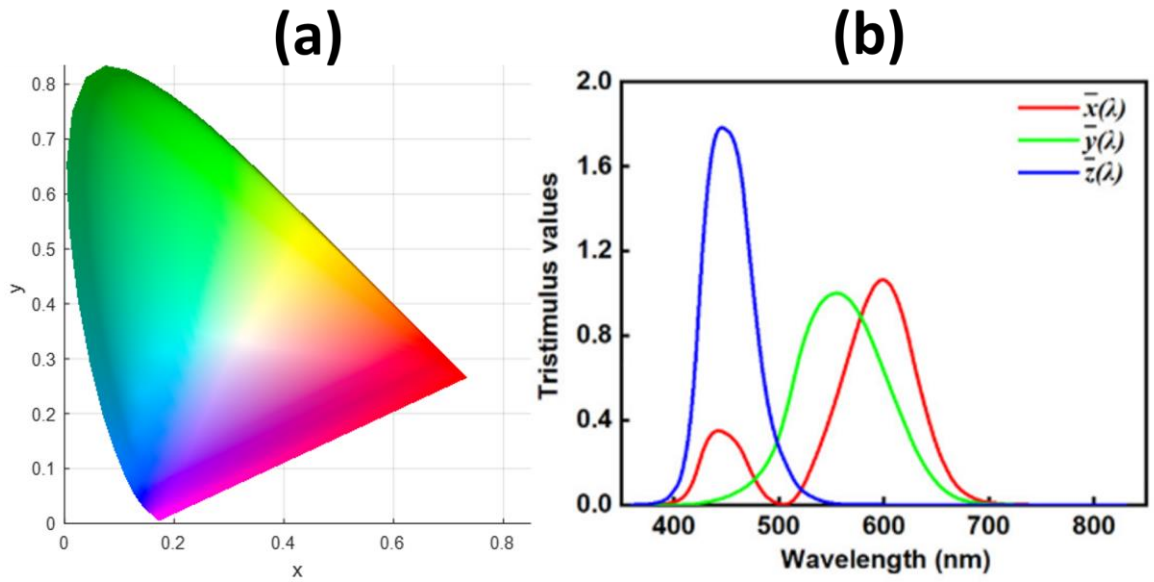


Figure 1.2. (a) The CIE 1931 colour chart. The xy coordinate position in the triangle represents the hue and saturation of an object very well but this 2D representation does not easily distinguish different brightnesses. (b) The tristimulus colour matching curves for the three different cones. Blue is clearly more sensitive while red and green are comparable. These weighting curves represent that human eyes are preferentially more sensitive to some colours such as green, while deep blues and reds are dim [18].

The following equations are used to obtain the xy coordinates on the chart with source spectral power distribution, reflection spectrum, and eye response being the most important experimental parameters [18].

$$X = \frac{1}{k}\int_{\lambda_1}^{\lambda_2} \bar{x}(\lambda)I(\lambda)R(\lambda)d\lambda\,,\; x = \frac{X}{X+Y+Z}$$

(1 . 1)

$$Y = \frac{1}{k}\int_{\lambda_1}^{\lambda_2} \bar{y}(\lambda)I(\lambda)R(\lambda)d\lambda\,,\; y = \frac{Y}{X+Y+Z}$$

(1 . 2)

$$Z = \frac{1}{k}\int_{\lambda_1}^{\lambda_2} \bar{z}(\lambda)I(\lambda)R(\lambda)d\lambda\,,\; z = \frac{Z}{X+Y+Z}$$

(1 . 3)

$$k = \int_{\lambda_1}^{\lambda_2} \bar{y}(\lambda)I(\lambda)d\lambda$$

(1 . 4)

The value k is normalisation factor, $I(\lambda)$ is spectral power distribution of source such as solar blackbody spectrum, $R(\lambda)$ is the reflection spectrum, and $\bar{x}(\lambda)$, $\bar{y}(\lambda)$, and $\bar{z}(\lambda)$ are the tristimulus colour matching factors. Not all colours are created equal, the human eye clearly perceives a large amount of unique green hues while the range of blue and red hues are more limited. The hue of an object is defined as the dominant wavelength present, saturation as the monochromaticity of the colour (narrow or broad in the spectral domain), and brightness as intensity, respectively. The XYZ chart cannot accurately distinguish samples of different brightnesses as clearly seen in Fig.1.3 below.

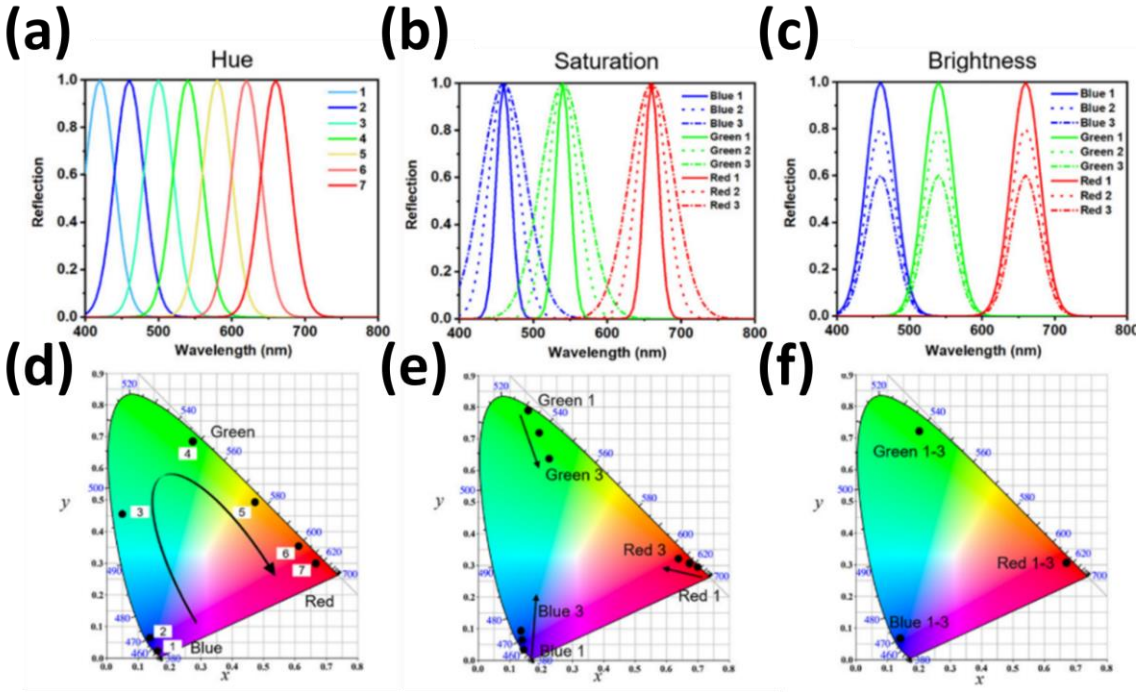


Figure 1.3. (a), (d) Using a gaussian profile for simplicity's sake, the hue will be the spectral peak position. The chart is quite sensitive to change in spectral peak position as one move towards the centre of the visible spectrum, which is to say that more hues are perceived in that region. (b), (e) By changing the line width $\Delta\lambda$, one can vary the saturation of the hue. Higher saturation produces more vibrant colour at the edge of the chart. (c), (f) Different brightness cannot be distinguished from one another. Despite this drawback the XYZ chart is still a useful tool and simpler to use than more complicated 3D colour charts [18].

This shortcoming led to the development of the CIE 1976 L*a*b colour space chart which utilises a more complex opponent model spherical chart in 3 dimensions to accurately gauge the true colour (see Fig.1.4). Brightness is given by z-axis parameter *L* between 0 and 100. Parameters *a* and *b* on the xy plane describe chromaticity and both have a range of -128 to 127 (8-bit system) [18]. The a-axis moves from green to red while the b-axis moves from blue to yellow. Like with the XYZ chart, coordinates closer to the edge are more saturated. Along the z-axis, the closer one gets to the south pole the darker the overall appearance will be. Towards the north pole the opposite is true, and the colour will be brighter. Unlike the XYZ chart, this chart is non-linear, matching the photopic response of human eyes, wherein perceptual changes in hue corresponds to uniform straight-line distance between two points in the L*a*b chart. The equations to determine L*a*b chart positions are shown below [18].

$$L^* = 116f\left(\frac{Y}{Y_n}\right) - 16\,, \qquad f(t) = \begin{cases} t^{\frac{1}{3}} & t > \left(\frac{6}{29}\right)^3 \\ 7.787t + 0.138 & t \leq \left(\frac{6}{29}\right)^3 \end{cases}$$

(1 . 5)

$$a^* = 500\left[f\left(\frac{X}{X_n}\right) - f\left(\frac{Y}{Y_n}\right)\right], \qquad b^* = 200\left[f\left(\frac{Y}{Y_n}\right) - f\left(\frac{Z}{Z_n}\right)\right]$$

(1 . 6)

$X, Y,$ and Z have their same definitions from the XYZ chart above while $X_n, Y_n,$ and Z_n represent a white achromatic source reference, e.g., illuminant D65. The function $f(t)$ is divided into two domains to prevent infinite slope at t = 0. To match $f(t)$ in both domains the slope in the linear regime is taken to be 7.787. Illuminant D65 has parameters $X_n = 95.0489, Y_n = 100, and\ Z_n = 108.884$. Fig.1.4 showcases this spherical chart [18].

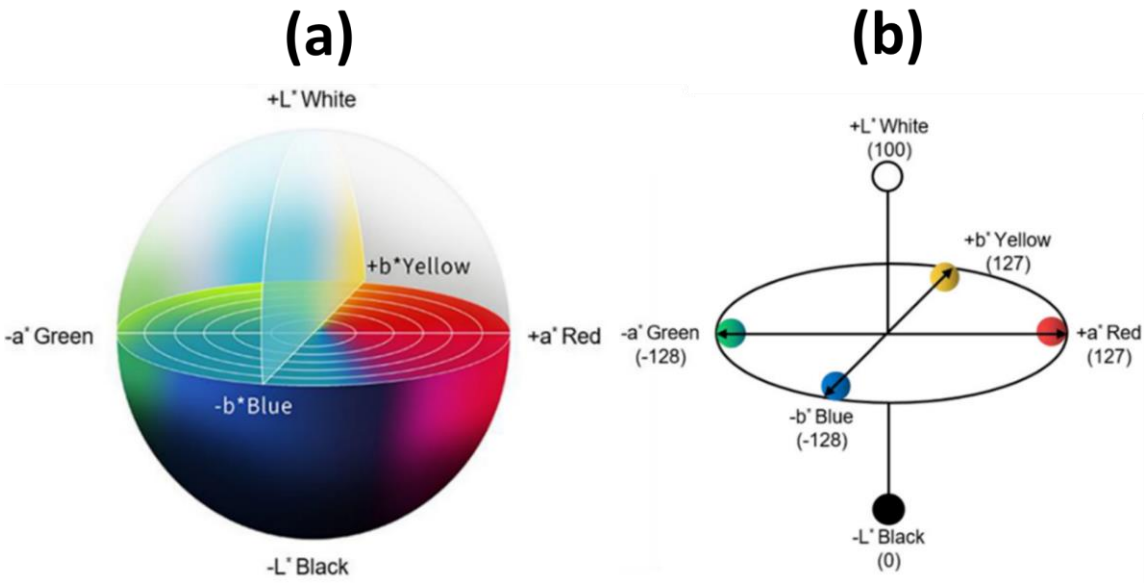


*Figure 1.4. (a) the CIE 1976 L*a*b chromaticity diagram with opposing colours across the xy plane and brightness along the vertical z axis. (b) this setup delineates a and b into floating point numbers between -128 and 127* [18].

Throughout the rest of this study, the CIE 1931 XYZ will be used chart to denote sample colour mainly due to the model's simplicity and the ease of visualising 2D charts when writing up documents. The XYZ chart is also widely used in the relevant fields of study

looked at in this work, such as structural colour and electrochromics. Therefore, comparison can be made when using the same colour chart for the spectra results obtained in this thesis.

1.2.2 Colour in Nature

In nature there exists a wonderful diversity of vibrant, sometimes iridescent, hues. Materials will often make use of spectrally selective absorption to confer colour upon themselves. This is called chemical pigment colouration, and many real examples exist such as organic dyes, plant chlorophyll, human skin/hair melanin, and paint among many others [19]. By absorbing certain frequencies of white light, the reflected light off an object will take on a distinct hue, saturation, and brightness as seen below in Fig.1.5.



Figure 1.5. (a) Chlorophyll is an organic pigment that plants evolved to absorb light from the sun. Blue and red light is absorbed while green light is reflected away. (b) Organic dyes can take on a huge variety of vibrant hues based on the structure of the organic molecule that is absorbing the incoming light. The ferrous compound Prussian blue is a famous example and was the first synthetic pigment invented by humans back in the early 1700's [20] .

Unfortunately, this form of colouration can be plagued by several disadvantages such as UV damage from the sun and heat damage from the environment due to chemical instability. There is also limited spatial resolution and time response as well, making this intrinsic colouration scheme less attractive as colour display technology enters the micron/nano scale regime.

Due in part to these limitations, scientific research has shifted more towards the development and use of structural colour, i.e., colour created by the interaction of light with matter's structure at subwavelength distances. This colouration scheme can also be found in nature

[21]. Some famous examples include the beautifully vibrant wings of a butterfly, the iridescent sheen of a soap bubble, and the rainbow colours seen on bismuth crystals; see Fig.1.6 below. Compared to chemical colouration structural colour is more robust, being resistant to UV and heat damage [22]. However, manufacturing them can also be more costly due to difficulties that can arise in the scaling and/or complexity.

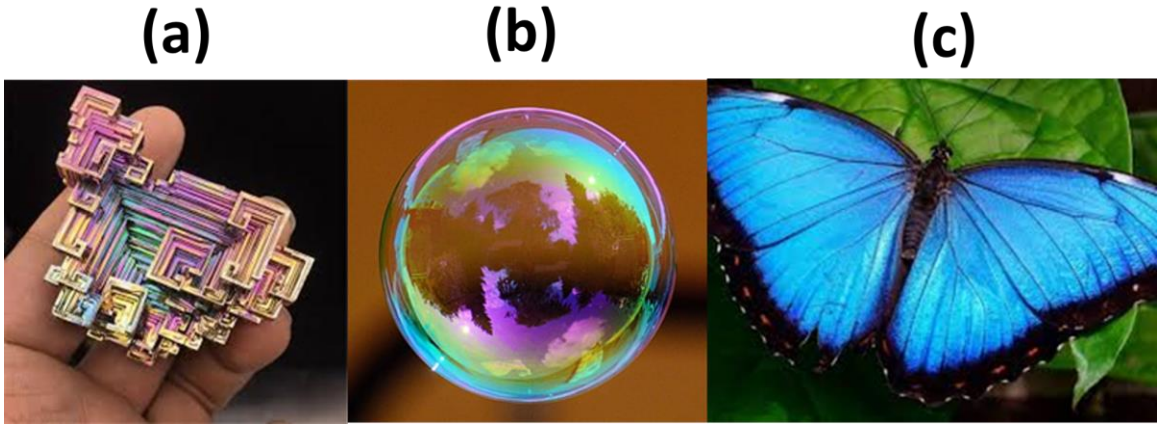


Figure 1.6. (a) The thickness of the bismuth oxide layer that forms on the surface of bismuth crystals is variable. Depending on thickness the resonant peak position of the reflected light is blue or red shifted. (b) light travelling in and reflecting off opposing soap layers interfere with one another to produce a distinct hue. As the angle of incidence increases the colour will change due to the changing path length of light. (c) Patterning on the surface of the butterfly's wing scatters light in such a way that blue dominates over the other colours present in white light.

The origin of structural colouring can be divided into two main categories. The first is subwavelength patterning. Sir Issac Newton first suggested that the vivid colours of birds and insects could be explained by the patterning of thin film structures on their feathers/chitin [23]. The idea was that subwavelength structures on their bodies could manipulate incoming light to create strong colouration and iridescence through purely physical means such as diffraction, interference, and scattering. A similar phenomenon happens with atoms in the atmosphere causing blue light to be preferentially scattered, also known as Rayleigh scattering [21]. This is imaged in Fig.1.7 below.



Figure 1.7. (a) Rayleigh scattering of indirect sunlight off oxygen and nitrogen atoms give the daylit atmosphere its blue hue. (b) At sunset the red and orange hues dominate as they travel further through the air than blue, filtering the latter out (image taken from the air of Mount Teide on the island of Tenerife in 2023).

Although Newton lacked the technology at the time to prove this, it was later in the 20th/21st century that imaging became advanced enough to look at these biological micro/nano structures directly. Peacock feathers and butterfly wings were looked at in close detail and the physical origin of their beautiful appearance was found to be periodic array barb structures that would scatter light of certain wavelengths [21]. The brilliance of colour produced is further enhanced by other mechanisms such as light interference, more complex resonant structures like 2D photonic crystals, complementary vibrant pigments, and optical gratings [22], [24]. Fig.1.8 below shows the geometry of this sub-micron patterning.

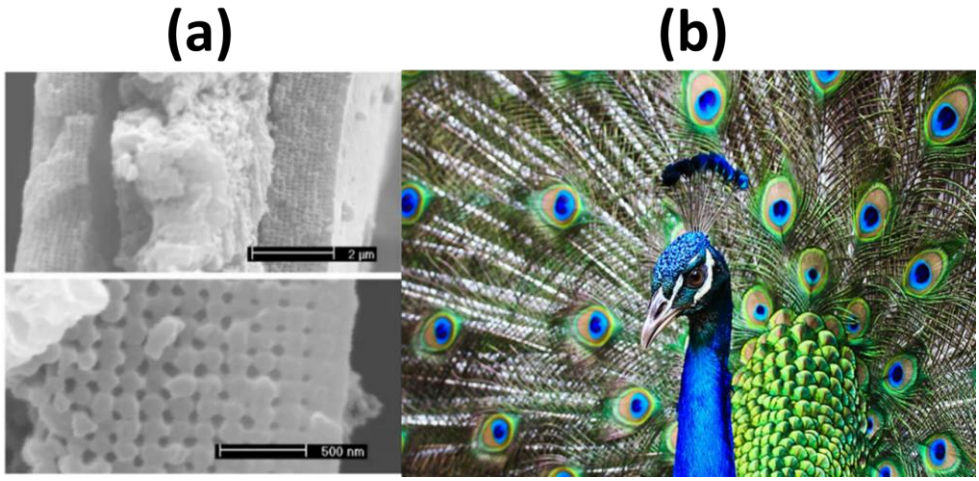


Figure 1.8. (a) The sub-micron barbs on the cortex of peacock feathers strongly reflect light of specific wavelengths. These barbs are on the order of the size of optical wavelengths. (b) The result is the beautiful colours of the male peacock. Vibrant blues, greens, and yellows are used to attract mates and for intimidating predators [24].

The existence of subwavelength patterning in nature further inspired scientific research in the pursuit of greater understanding and creation of superior artificial structural colour using various approaches such as plasmonics, periodic resonator arrays, guided mode resonance, and photonic crystals to name a few [25]–[28]. This work also heavily overlaps with the study of optical metasurfaces, both passive and active, with the Capasso group and Atwater group being two major giants in the field [29], [30].

The second category of structural colour has its origin in the simpler planar thin film wave interference. The emerald/gold sheen of beetle wings, the diverse array of hues on oxidised bismuth, and the variety of colours in soap bubbles find their origins here. See Fig.1.9 below.

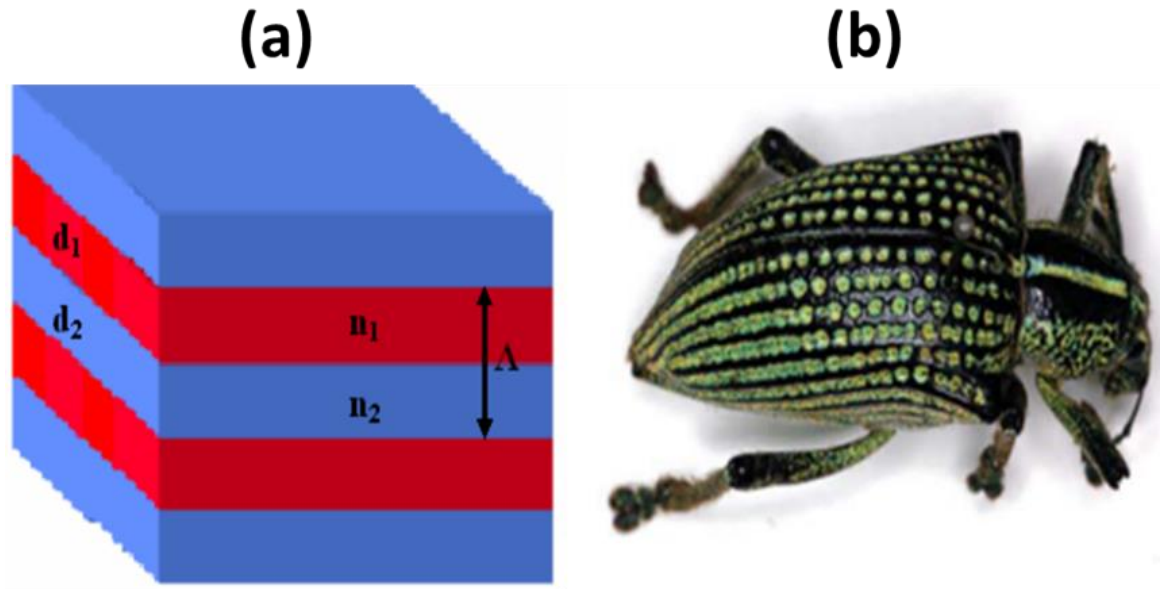


Figure 1.9. (a) The thin film multilayer design of a 1D photonic crystal. Refractive index n_1 and n_2 are not equal, thus this stack is a graded device. The spectral position of the reflection peak is determined by layer thickness, count, and refractive index difference [31]. *(b) Beetles can use this phenomenon to produce the emerald/gold hues in their wings* [32].

The basic concept is that light passes through multiple thin film layers with different refractive indices. Depending on the arrangement and thicknesses of these layers, different colours can be produced. This situation can be simulated quiet well using the general transfer matrix method formalism for electromagnetic media [33]. Moreover, it is often easier to work with thin film multi-layer structures than patterned surfaces for a host of reasons. Namely factors such as design simplicity, ease of modelling, cost, and scalability. The latter two points are of particular interest to any company that wishes to produce a product that is ultimately profitable.

Although the nano-structural patterning approach has more design freedom, owing to periodic condition in the xy plane, the design and modelling of such devices is more complex and will often need industry standard computational tools like COMSOL or Lumerical to model them effectively. These programs use the finite difference time domain (FDTD) or finite element method (FEM) to compute the complex 3D electromagnetic profile, using the Maxwell equations. It is also often the case that machine learning is necessary to find optimum geometric configurations given how vast the parameter space can be.

1.2.3 Active Colour Change in Nature

Many examples have been given above for structural colouration but perhaps the most fascinating case of nature's use of this phenomenon is the ability of certain organism to actively modify their colour profile. The reader may be somewhat familiar with the chameleon's famous ability to change the hue of its scales [34]. This process works via the dispersing and concentration of special cells known as chromatophore pigment and iridocyte cells that are connected by a networks of protein elastomers that can vary their length and therefore the spacing between themselves, as seen below in Fig.1.10 [35].

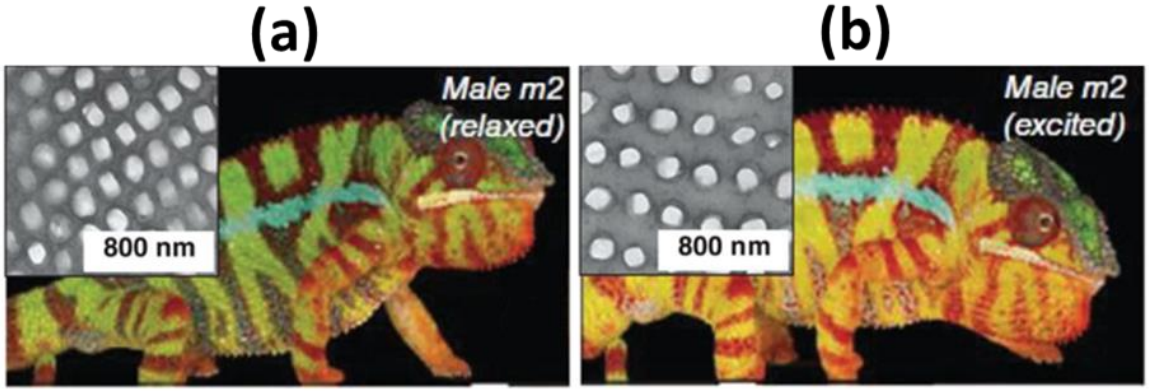


Figure 1.10. (a) A bluer-greener colour is seen for closer spacing while a redder-yellower colour in (b) is seen for farther spacing between the pigment cells. The spacing is subwavelength in scale and controlled by the contraction and relaxation of an elastomer protein network that these cells are superimposed on top of. [35]

Other animals also display this ability such as the cephalopods like squids and cuttlefish. Like chameleons the response time of their colour change is on the order of 100's of milliseconds and can appear near instantaneous to the human eye [36]. Also, like chameleons, their ability has evolved for the purpose of camouflage and mate selection. The way in which the incoming light scatters and the change in peak hue position is consistent with how one would design an active metasurface. Of course, nature can engineer things

from the bottom-up approach so high spatial resolution and quality are achieved in biological systems through the gradual process of natural selection. Artificially replicating this colour changing feat has been a challenge that has led to productive research looking into synthetic analogues of the components making up the biological metasurface such as elastomers [35], [36]. This philosophy of using nature as an inspiration for the design is known as biomimicry; see Fig.1.11 below.

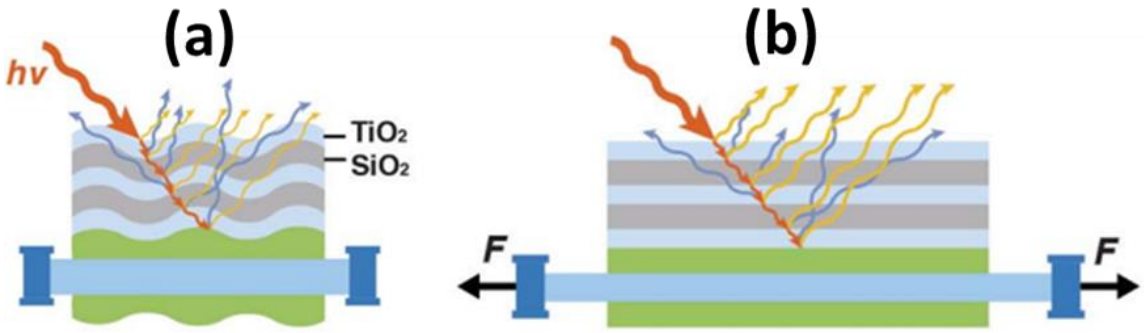


Figure 1.11. (a) An inorganic analogue of how squid skin can preferentially scatter light of certain frequencies. (b) The relaxation of the skin cells, controlled by muscle, red shifts the peak wavelength of the scattered light. [36].

The examples given thus far use a patterned surface to achieve their strong colouration as well as a mechanically active substrate to control the spacing of the elements. Such a design approach is intuitive for living organisms to evolve as all the individual elements of the colour change system can, and have, evolved separately many times due to powerful environmental pressures: For example, all animals require muscles for movement and control, skin is needed for protection and maintaining homeostasis, and mate selection has often spurred on the evolution of new colour patterns as well as eyes that can perceive them, so called sexual selection [37].

1.2.4 Artificial Active Colour Change

Active colouration can also occur by changing the intrinsic refractive index of an inorganic material. In so doing its reflection profile can be altered. Different stimuli can induce this change such as applying electric fields, magnetic fields, temperature, light, absorption, or desorption of gases/liquids, etc. Just like in nature these different stimuli can be used on active materials in various optical resonator configurations to achieve large colour gamut and other useful results such as strong tuneable absorption. Figure 1.12(a) below shows different resonators that are utilised along with a complementary technological application

[38]. Of particular interest is the Fabry-Perot (FP) cavity resonance which is simple in form and can be readily integrated into a thin film stack design. The simplest and most well-known type of FP cavity is a metal-insulator-metal (MIM) stack structure such as $Ag/SiO_2/Ag$. The specific detail of how a FP cavity works to achieve vivid colouration and strong absorption will be discussed in more detail in section 1.3.

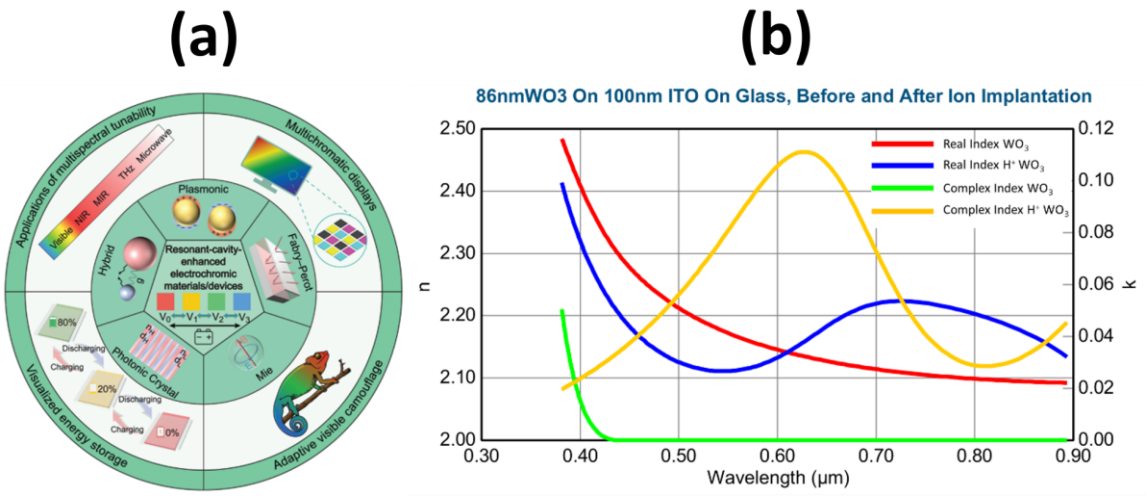


Figure 1.12. (a) Different active resonant structures such as field effect gated plasmonics and FP cavities. Different application of these tuneable optical resonators include multichromatic displays and adaptive camouflage [38]. *(b) the refractive index changes of thin film 86 nm WO_3 after implantation of hydrogen ions in solution via an applied electric field. Data measured using spectroscopic ellipsometry.*

Using nature as inspiration, research over the last half century has led to tremendous progress in using active nanomaterials in resonant structures to achieve unique technological goals, as strong optical field enhancement is the building block for a large number of modern photonic devices such as, but not limited to, compact semiconducting lasers [39], vibrant active colour displays [40], and ultrasensitive chemo and bio sensors using spectrally narrow sharp resonances [26]. Indeed, using optical resonator structures to enhance the performance of active nanomaterials is one of the key ideas being explored in this work, as outlined previously in section 1.1. Data will be outlined in chapters 4-6 for both inorganic passive and active index change materials with different resonator stack layouts such as the compact zeroth-order FP cavities, lossy central absorber MIMs, and ATF Fano-resonant devices to name a few. Lithography free design is crucial as it benefits scalability which is especially relevant to products that are large in size such as smart windows and display colour filters, see Fig.1.13 below [13], [41].

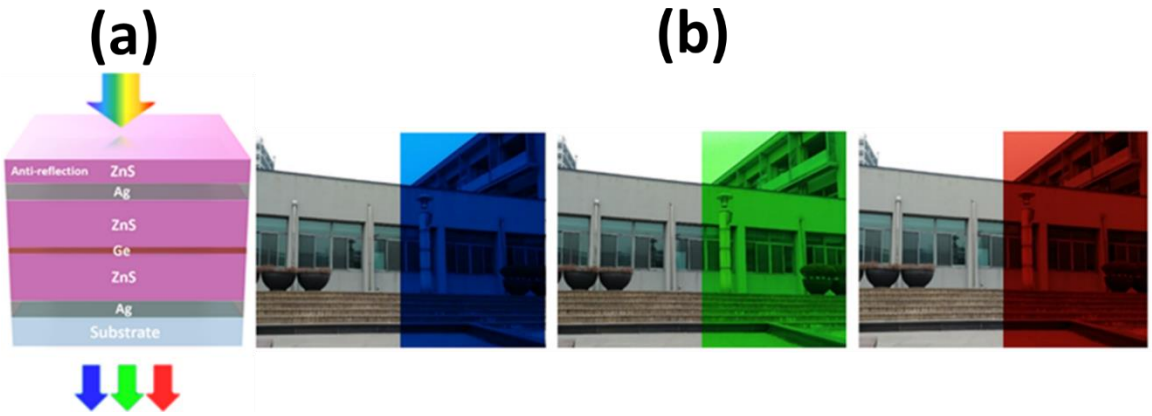


Figure 1.13. (a) the stack structure of an ATF transmission colour display filter with lossy Ge in the middle supressing high order FP modes in the spectra. (b) Changing ZnS spacer thickness shifts the filter spectral peak, capturing the RGB colours. [13]

1.2.5 Active Colour Change with Electrochromics & Thermochromics

Smart windows and active colour displays have seen particular interest in the field of electrochromics (ECs). They can be classified as organic or inorganic based and there are advantages and disadvantage therein associated which either one [42]. Electrochromic materials (ECMs) that are organic based are known to have greater inherent vibrancy than their inorganic counterparts but they suffer from serious durability issues related to cycling lifetime and resistance against environmental damage [42]. Viologens are an organic ECM that have been extensively studied in the literature owing to their low driving voltage which is advantageous for low energy displays and fast response devices. The exact physics on how organic polymer ECMs work will not be looked at in high detail in this work but suffice to say they, like most other organics, suffer from stability issues making its use in smart windows and displays potentially problematic [43]. Figure 1.14 below shows the chemical structure of viologen and how this gel can be integrated into a display unit.

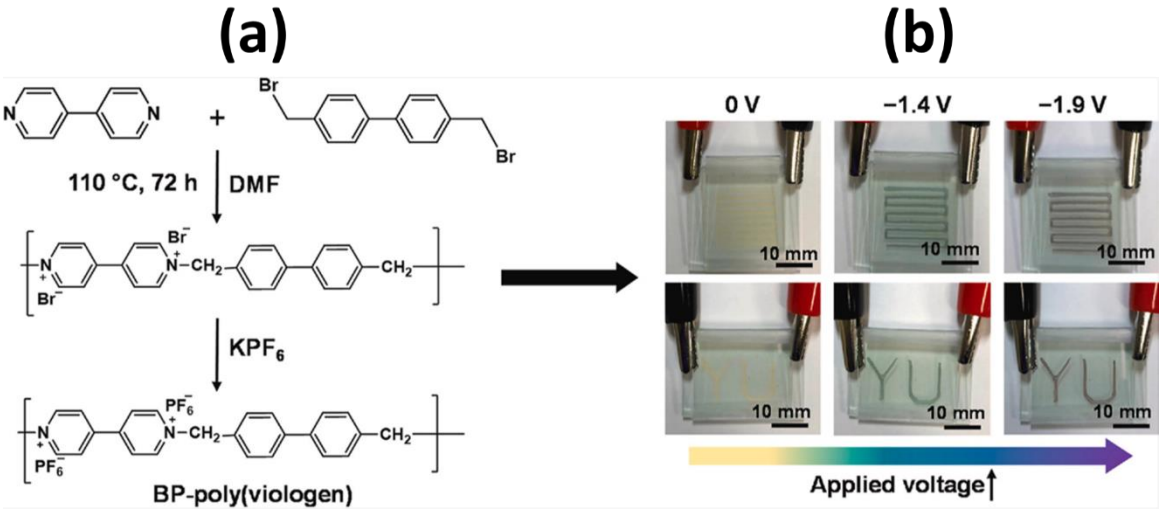


Figure 1.14. (a) Chemical synthesis steps to make a viologen organic EC polymer. (b) with low driving voltages a conductive transparent display can be biased to show letters. The viologen is isolated between two conducting layers to prevent ion loss. [44]

Inorganic ECMs in contrast are more durable than organics against environmental damage, and cycle stability is also generally superior [42]. The chemical structure of inorganics is also less complex than organic polymer chains. Certain transition metal oxides (TMOs), like WO_3 and NiO can absorb ions into their lattice structure and undergo a colour change. The physical process of intercalating ions into and out of their lattice modifies the refractive index considerably from an absorbing to near transparent state or vice versa over the course of several seconds each way. A comprehensive description will be given in chapter 5 where the EC mechanism is explored in further detail [40], [45], [46]. This work will heavily focus on using the inorganic ECMs WO_3 and NiO, particularly the latter, within different optical resonator structures such as asymmetric zeroth order FP cavities. The results obtained will be compared with literature to showcase the novelty and improved EC performance of the materials studied as well. Figure 1.15 below shows one of the first samples of NiO made as part of this thesis work on a magnetron sputtering tool with an Ni target. The EC response will always fade with w.r.t the number of cycles.

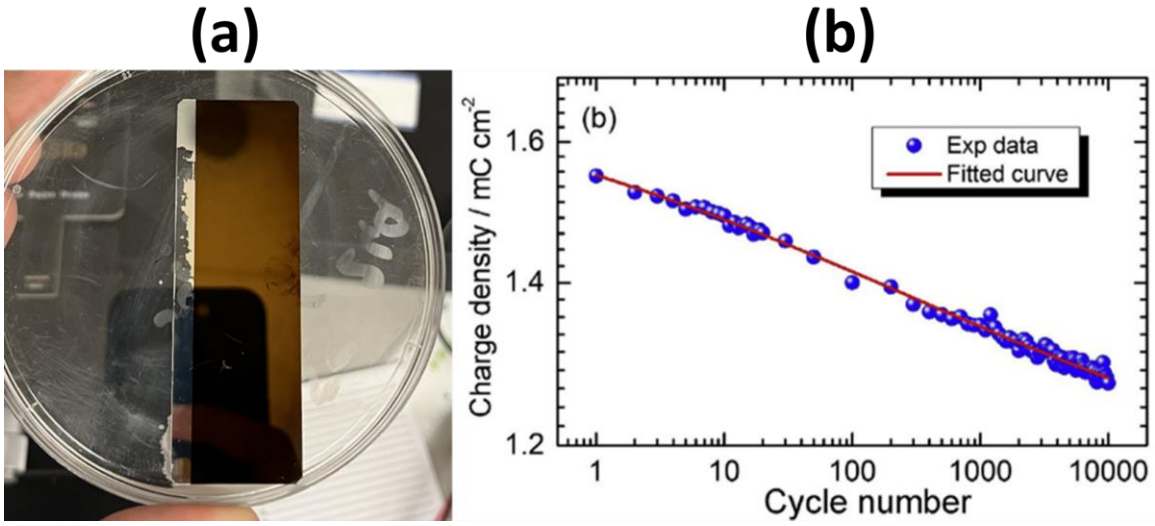


Figure 1.15. (a) Image of NiO deposited on Ag using a magnetron sputtering device. The side silver strip is exposed Ag for electrical contact when the sample is place in liquid electrolyte solution. (b) An example of the cycle degradation seen in NiO dipped in a Li electrolyte solution from literature. Overtime less ions can be held, and the EC response weakens. The response in linear w.r.t to logarithmic cycle number meaning there is a quick drop off followed by a slow gradual decline. [42]

Both inorganic TMOs and organic polymer ECMs have seen some use commercially already at large scales such as in airplane dimmable windows to replace the slide down blinds, smart regular and sunroof windows on cars, smart glass on buildings for energy saving and glare reduction, and dimmable side and rear view car mirrors [47]. At one point in time ECs were also somewhat competitive against other mature display technologies on the market, such as liquid crystal displays (LCDs). An electrochromic display (ECD) was used for an Apple nanochromic screen on the iPod at one point due to the low energy requirements required for a mobile device [48] (see Fig.1.16(a)). LCDs appeared as a superior replacement to Cathode ray tube (CRT) displays, ultimately replacing the latter from 2007 onwards [49]. Like with ECs, electric fields are used to change the state of the active material which in this case is a solid/liquid phase change crystal. Modulating this crystal with field effects can change the passage of back light through it, modifying any resultant image formed on the screen [50]. LCDs currently dominate the display market having replaced CRTs, but alternatives exist in the form of more efficient LED display technology. Miniaturising the ECM film further in all dimensions could help to make ECDs a more competitive technology against LCDs and possibly the more energy efficient LED displays in low power niches.

The active layer in ECDs is typically many 100's of nanometres in thickness, and this slows down the response time and makes it harder for ions to diffuse deep into the bulk. The

contemporary technologies shown in Fig.1.16 below operate in this regime. Using thick layers is considered necessary to see large on/off state contrast but using the appropriate optical resonator one can circumnavigate this issue by drastically increasing the light matter interaction, i.e., an FP cavity. This is the main strategy used in this work to investigate the viability of EC dimmable windows/mirrors and displays in the ultrathin regime.

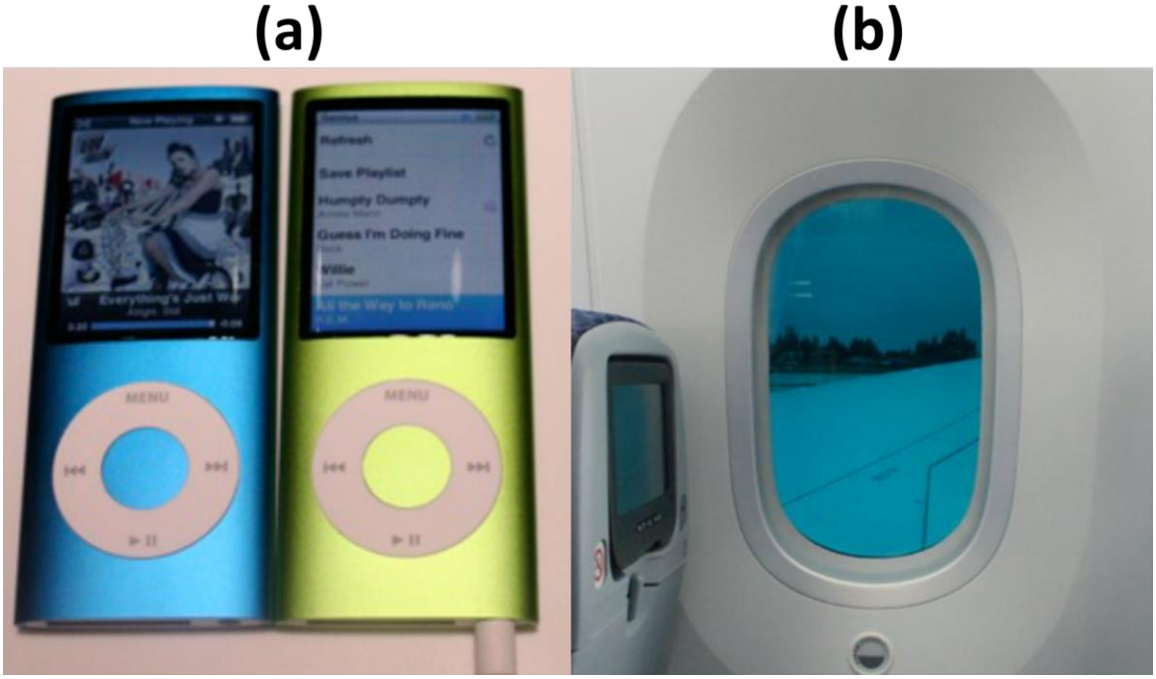


Figure 1.16. (a) A nanochromic EC display on a nano-iPod of the mid to late 2000's. The screen dims over time but its low energy use and thus suitable for the tiny portable music device [48] *(b) A smart dimmable window on an airplane that drastically reduces the daytime glare that would illuminate the cabin.* [51]

Active thermochromic materials like VO_2 are also looked at in the literature as well such as the state of the art research results of Jianjun Zhao *et al.* (2021) [52]. They were able to show dynamic strong colouration in a compact Fabry-Perot device using an Al back mirror, an Ag top mirror to increase colour saturation, and a tuneable VO_2 spacer to modify the peak colour position. By changing the temperature of VO_2 above and below 68°C the crystallographic form could change, lowering the index of VO_2 by as much as unity in certain parts of the visible spectrum [53], [54]. This phase transition is from monoclinic to rutile conformation as seen in Fig.1.17 below. The transition can be measured by monitoring the resistivity of the VO_2 thin film when heated (most likely with some kind of heater array) using the 4-point probe method. A sudden increase in conductivity signifies the rutile lattice shape arrangement has been taken. The change can also be seen using the spectroscopic ellipsometry techniques to determine the index dispersion.

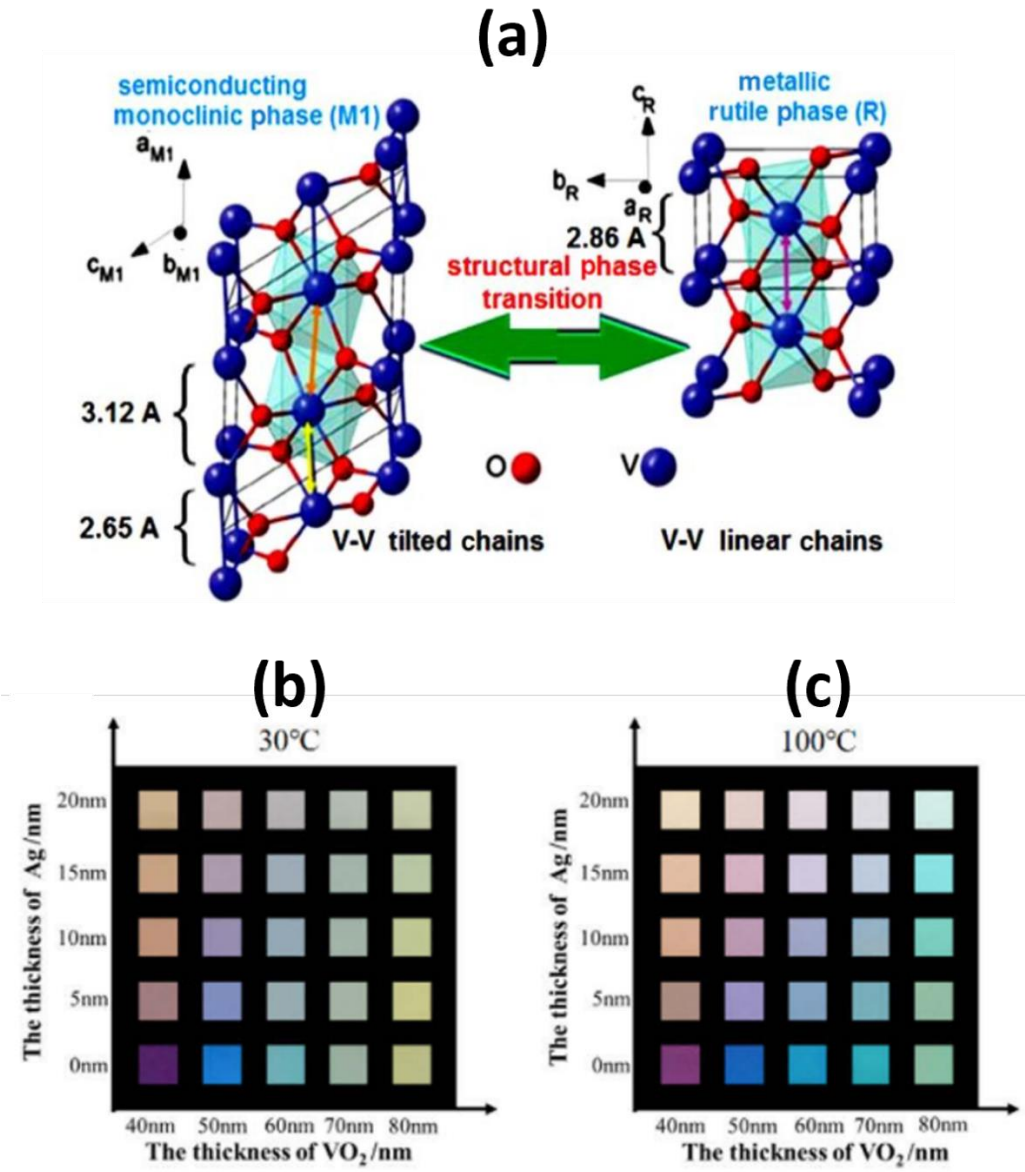


Figure 1.17. (a) At 68°C the monoclinic semiconducting crystal lattice of thin films VO_2 will transition to a rutile conformation in a matter of microseconds, much faster than the active electrochromic response which takes place over seconds due to the slow nature of the diffusion limited reaction. [55] *(b)-(c) The colour map of the sample produced depending on top Ag thickness and VO_2 later thickness. The colour gamut is not that great and most of the hues generated are pastel in appearance with the exception of the vibrant blue and violet colours created when no Ag is present.* [52]

Some vivid structural colours are shown but the dynamic colouration change they achieved is not as strong as it could be given the data that will be presented in chapter 6 when VO_2 is paired with a Fano-resonant stack configuration. The index change of VO_2 is not as transformative as the results that will be presented for coloured/bleached NiO either due to both the semiconducting and metallic phases being highly absorbing in the visible as a result of the low band gap of VO_2 around 0.5 eV [56] . The biggest optical change for VO_2 is in the real refractive index n above 600 nm wavelength. Indeed, VO_2 is most strongly affected

in the NIR region when converting from monoclinic to rutile lattice form, becoming much more reflective when conforming to the arrangement of the latter. A result in-line with a Drude-Lorentz model use to describe most metals and explain their highly reflective nature due to their free electron gas acting as a broadband mirror below the plasma frequency [53]. See Fig.1.18 below showing the phase transitions effect on VO_2/sapphire reflectivity.

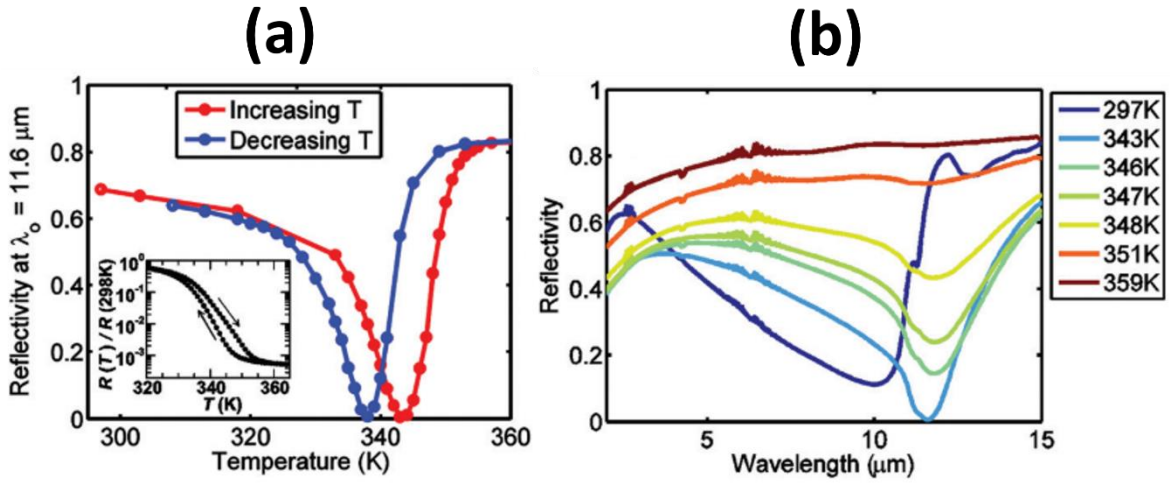


Figure 1.18. (a) The change in reflection of a VO_2 on sapphire substrate sample in the NIR region located at 11.6 μm wavelength. A micro heating array element has fine control over the thin film temperature. VO_2 is monoclinic below 340 K and converts to rutile above. The hysteresis of this crystallographic phase transition transformation forwards and backwards is also shown (b) When in the metallic phase the reflectivity sharply increases in-line with what one would expect of a Drude-like material. In the semiconducting phase the absorption will also increase above the band gap around 0.5 eV which is similar to Ge [53]

Results in chapter 5 and 6 will showcase how accessing the zeroth order FP mode can enable large on/off contrast for sub 100 nm of ECM and thermochromic material (TCM). Size effects can come into play at this scale as well since the thin films will begin to deviate from their bulk behaviour and geometric confinement effects will start to manifest in the optical response. This behaviour applies to many materials in the ultrathin regime such as metals and the lossy dielectrics like ECMs, TCMs, Si, Ge, and transition metal dichalcogenides (TMDs) MoS_2 and WS_2 [3], [57]. By backing these lossy films with opaque metal, the zeroth mode can be availed of in the ultrathin film regime, typically less than 50 nm in thickness. The optical characteristics of this zeroth mode is unique in that its generally spectrally and angularly flat and in some instances, there is little difference in how p or s polarisations of light respond. In contrast higher FP modes are more dispersive in all domains which is often very useful for colouration but with the caveat that other closely spaced modes can interfere with the colouration (more hues present). Light becomes trapped between the metal and top absorber-air interface driving up the attenuation of certain frequencies of light, and in some

cases reflectivity for most if not all frequencies across the visible are heavily suppressed. A similar situation can happen when additional dielectric layers focus light onto the top/central absorber [58].

1.3 Vibrant Colouration & Strong Absorption Using Fabry-Perot Cavity Resonators Paired with Ultrathin Lossy Dielectric Absorbers

1.3.1 Introduction to Fabry-Perot Resonator Interference

A large part of this thesis study will be focusing on the optical properties and advantages of a particular type of ultrathin film FP resonator structure designed to access the normally forbidden zeroth order FP mode that thicker lossless assemblies cannot. This resonance mode, given by the condition of m = 0, is inaccessible when using transparent dielectric materials such as SiO_2 or TiO_2 as a standalone spacer film layer (see Fig.1.19(b)). When one thinks of an FP cavity structure, they may imagine a symmetric system where a transparent dielectric spacer is sandwiched between two metallic reflectors. Indeed, this kind of setup is also the basis for creating a simple laser device [18]. This is because gain requires strong optical field enhancement for stimulated emission to lase efficiently. Figure 1.19 below demonstrates this symmetric resonator set up.

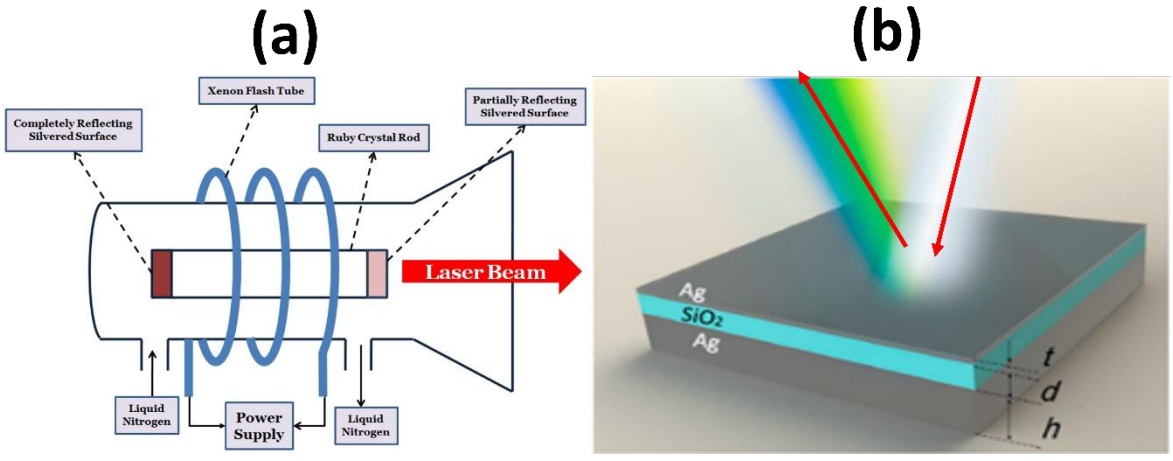


Figure 1.19. (a) The first solid state laser developed in 1960 by Theodore Harold Maiman based on the gain medium ruby. The system was quite bulky and using a liquid nitrogen coolant. The lasing was triggered by a xenon flash tube and a symmetric FP cavity acted as the optical resonator to produce the necessary gain [59]. *(b) A spectrally selective absorber based on the same FP cavity design as the laser. An SiO_2 spacer is used instead of ruby. Tuning its thickness changes the peak absorption wavelength* [18].

Starting from the simplest symmetric FP cavity, like in Fig.1.19(b), SiO_2 is sandwiched between two Ag thin film mirrors. Ag is used as it is the closest material to being a perfect conductor (PEC) and thus reflects almost all the light in the visible [60]. When light enters the cavity through the semi-transparent Ag layer it will become temporarily trapped. At certain frequencies the light will be strongly trapped and the electric field inside the structure is greatly enhanced [61]. Some of the resonant conditions of this system are given in the equations below [61].

$$d = \left(\frac{\lambda_m}{2n}\right) \cdot m \ , \quad \lambda_m = 2nd \cdot \frac{1}{m} = nL \cdot \frac{1}{m}$$

(1 . 7)

Where d is the dielectric spacer thickness, n is the refractive index of the dielectric spacer, m is the order of the FP mode and is a positive integer, L is the light path loop distance, and λ_m is the resonance wavelength. The light that is trapped loops around and depending on the thickness of the back Ag mirror, a strong reflection or transmission peak will be generated. The analytical equation for total Transmission and Reflection Intensity of an MIM is given by the equations below [18].

$$R_{FP} = \frac{2R \cdot (1 - \cos(\delta))}{1 + R^2 - 2Rcos(\delta)}$$

(1 . 8)

$$T_{FP} = \frac{(1 - R)^2}{1 + R^2 - 2Rcos(\delta)}$$

(1 . 9)

Where R is the reflection coefficient, δ is the total phase shift accumulation in the FP stack. δ can be further broken down into phase shift at the boundary and phase shift on propagation [18]. The boundary factor is mostly small and constant w.r.t angle of incidence, so by far

the most relevant parameter is the propagation contribution, δ_{prop} given by the expression that follows.

$$\delta_{prop} = \left(\frac{2\pi}{\lambda}\right) \cdot 2nd \cdot cos(\Theta_2)$$

(1 . 10)

Where n and d are again the spacer index and thickness respectively, and Θ_2 is angle of propagation through the spacer [18]. The above equation is very important because it demonstrates the importance of high index in the dielectric spacer. For display technology it is intuitive that one would want as little angle dependence as possible in the optical response. In other words, the ideal device should have an omnidirectional light response. By increasing n, Θ_2 is decreased which reduces the path length of the light. The approximate equivalence below demonstrates this even more clearly [18].

$$\left|\frac{\Delta\lambda_r}{\Delta\Theta_1}\right| \approx \frac{2d \cdot sin(\Theta_1) \cdot cos(\Theta_1)}{\sqrt{n^2 - sin^2(\Theta_1)}}$$

(1 . 11)

Shown on the left-hand side is the rate of change of resonant wavelength λ_r w.r.t the angle of incidence (AOI) into the FP stack, labelled Θ_1. On the right-hand side, the variables have the same previously stated meanings. It can be seen that increasing *n* reduces the rate of change of resonant peak position, thus conferring omnidirectionality to the MIM [18]. Examples of high index transparent spacers include TiO_2, Ta_2O_5, and Si_3N_4 [12], [62], [63]. In the case of the magnetron deposition tool that was used during the project, the TiO_2 sputtered was quite consistent in quality with a high index of 2.2-2.3, hence this spacer material was used extensively for work presented in the sixth chapter of the thesis focusing on higher order MIM stack structure colour filters. A more detailed description of the physics of magnetron sputtering will be given in chapter 3. Figure 1.20 below displays state of the art literature results for the purity and omnidirectionality of structural colour of a Ta_2O_5 FP cavity with an asymmetric layout using an Al back reflector and a lossy absorber filter [12].

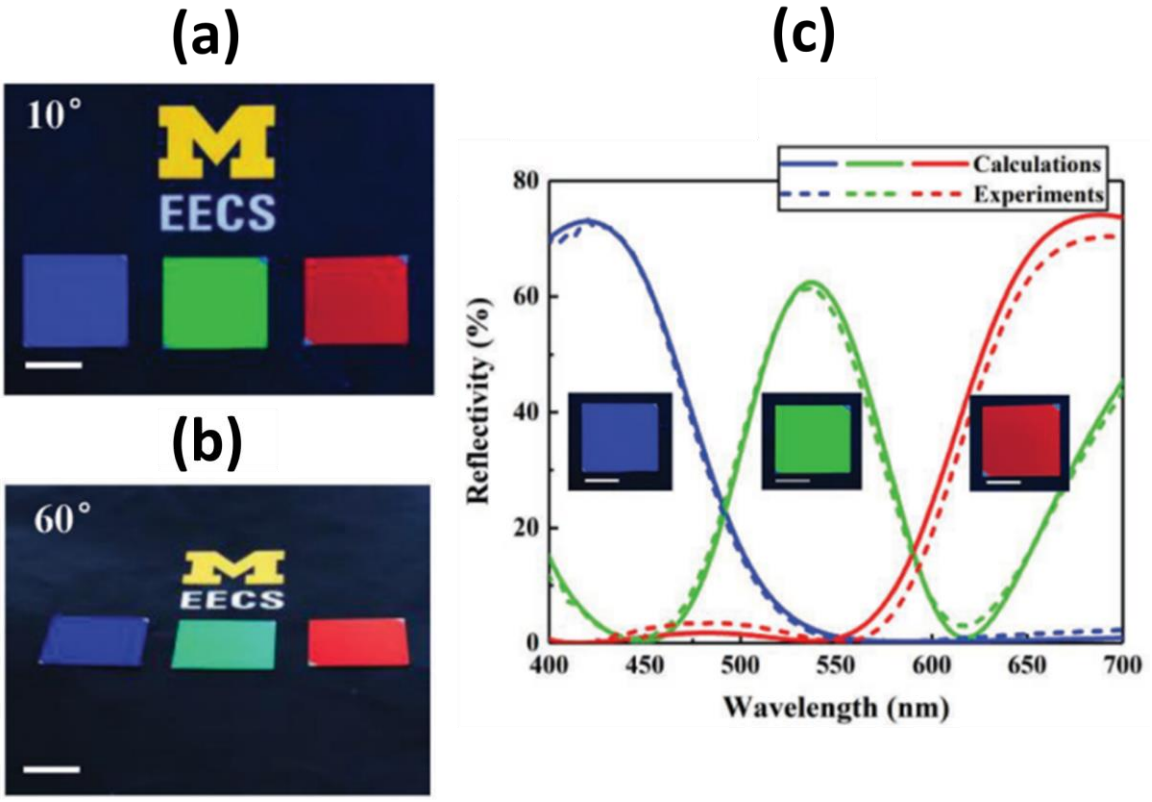


Figure 1.20. (a)-(b) The difference in colour between 10˚ and 60˚ is small. At high angle the colour becomes slightly more pastel, further from the edge of the CIE colour chart. (c) the spectral colour purity is high especially for the blue and red samples while for the green, other colour appear. The addition of lossy effective mean approximation (EMA) bilayer central absorbing layer in the stack structure is the reason for this. [12]

To increase the design freedom in their work, a lossy effective mean approximation (EMA) absorbing bilayer was introduced for the purpose of index matching to improve suppression of MIM off-peak resonance in reflection mode by Zhengmei Yang *et al.* (2019) [12]. It also was noted that the performance of such devices could be improved further with additional anti-reflection (AR) layers to supress off peak resonance in multiple different spectral regions. More details on this will be shown in chapter 6 focusing on the union between ultrathin absorbers and bright MIM FP peaks. In practice asymmetric FP cavity structures are almost always more useful for generating vibrant colours and strong absorption when confined to compact devices geometry. There is also a greater parameter space to work with and optimise since additional lossy materials are being added into the design.

1.3.2 Accessing the Zeroth Mode Using an Ultrathin Lossy Fabry-Perot Cavity

The way this kind of lossy FP resonator is approached is similar to the lossless symmetric FP case but this time the phase pickup on interface reflection cannot be ignored and non-

trivial solutions that access forbidden states become a possibility due to the reflection coefficient over multiple passes utilising the complex plane instead of the restrictive 1D number line, as shown below in Fig.1.21 [4].

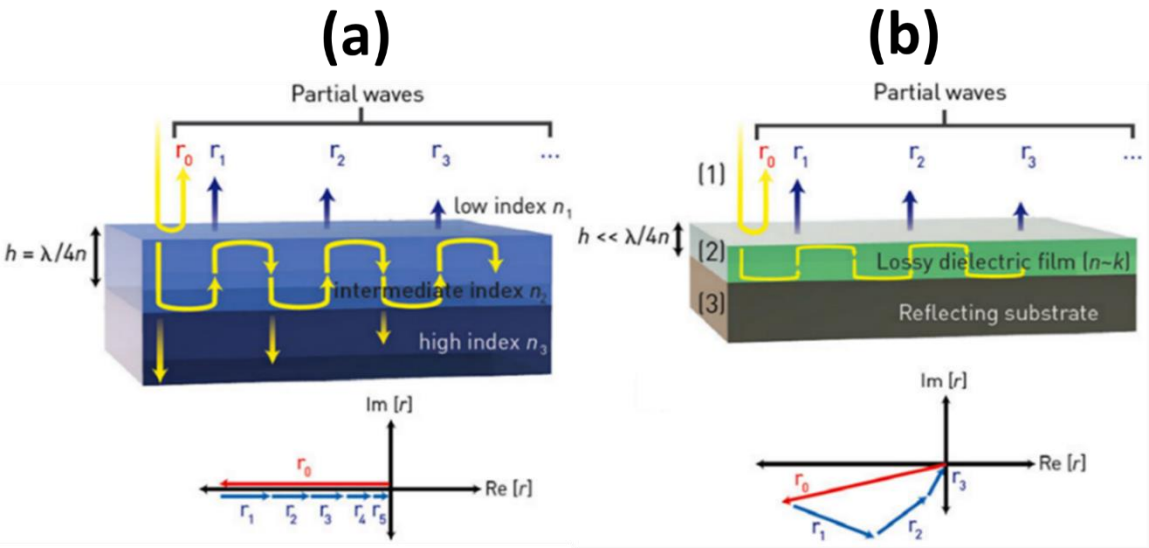


Figure 1.21. (a) An AR coating which couples light strongly and suppresses back reflections at the air interface. However, since lossy materials are not used only trivial solutions are possible such as the quarter-wavelength and index matching condition. (b) The simplest lossy dielectric FP cavity reflector. As the reflection coefficient phasor is now complex, non-trivial solutions in refractive index and film thickness are possible for strong absorption and colouration. [4]

An anti-reflection (AR) coating on a transparent substrate has a fundamental FP resonance of $m = 1$ where the π phase shift on reflection of r_0 destructively interfere with successive back and forth reflections of light tapped inside to eliminate all outgoing light and maximise transmission straight through. This is the simplest kind of FP cavity to understand because no lossy layers have been used. AR coatings are incredibly useful especially in the field of photovoltaics (PVs) where maximizing the coupling of light into a PV cell can make all the difference in competing against polluting fossil fuel [64]. Extensive research has gone toward incorporating these coatings onto commercial PV cells, and it is now a standard in the industry to employ some kind of AR capping film. This may be done using the ATF approach or with a designed patterned glass surface [65], increasing light transmission into the PV cell across a wider range of angles for greater absorption. AR layers can also help with protecting the active layers of the PV device against environmental damage, potentially increasing the lifetime of solar panels which are currently only warrantied for 25 years on average [66]. Figure 1.22 below is of a commercial multilayer AR coating using silica and zirconia. Multilayer coatings have a broader working wavelength range. Theoretically you

could keep adding layers but then the design would become too expensive and troublesome to integrate onto a working panel.

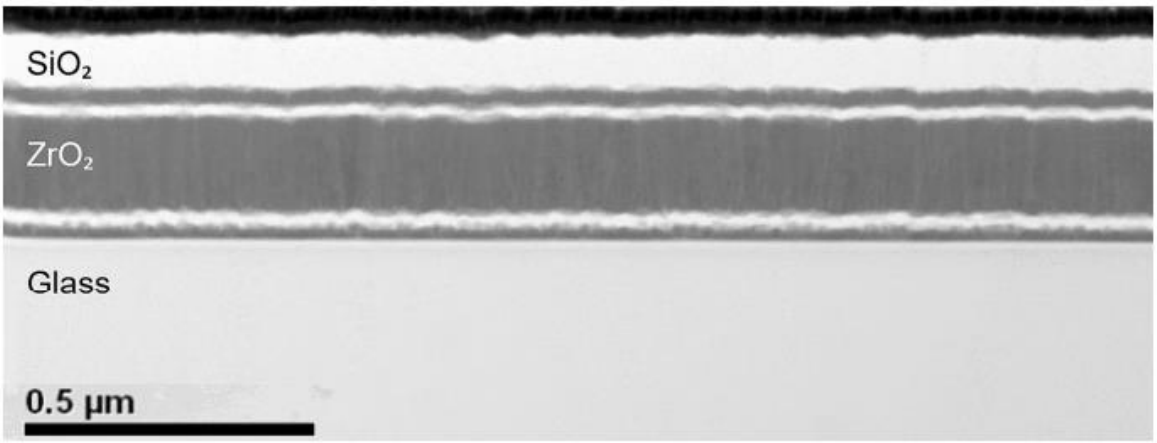


Figure 1.22. (a) An AR coating that could be sputtered over a PV cell. The zirconia adds physical durability and lengthens the lifetime of the coating as compared to silica on its own which is porous. More transparent dielectric layers broaden the minimisation of reflectivity. Commercially 2-3 layers work quiet well. [64]

The equations below can be used to optimise for single AR capping film ideal index and thickness in relation to the substrate underneath and the surrounding semi-infinite dielectric (air in most cases). For sputtered porous AR films like SiO_2, the EMA can be applied to determine what the effective index will actually be as a function of volumetric fractions and intrinsic material index [64]. Increased porosity will decrease the index further towards that of the surrounding medium at $n = 1$.

$$n_2 = \sqrt{n_1 n_3}\,, n_{eff} = V_{AR} n_{AR} + V_{air} n_{air}\,, h = \frac{\lambda_0}{4 n_2} \qquad (1.12)$$

Where n_2 is the ideal index of the AR layer while n_1 and n_3 denote the index of the layers above and beneath the coating film. The value of n_2 will fall in between n_1 and n_3 . n_{eff} is the effective index of the AR film, n_{AR} is the intrinsic AR index, V_{AR} and V_{air} are the volumetric species fractions constituting the porous layer, and h is the ideal thickness of the AR coating. n_{eff} will be close to n_{AR} in the bulky limit while for very thin subwavelength films the porosity of sputtered coatings will certainly measurably decrease the index of the medium. More on the EMA will be explained in chapter 3 focusing on spectroscopic ellipsometry (SE) in the context of modelling microscopic surface roughness [57].

So far, there has been discussion on lossless and lossy thin film FP resonators and how the mathematics describing them can also lead to an understanding of how to design the simplest ATF AR coatings. In Fig.1.21(b) it was demonstrated that a metal backed lossy FP resonator has an ultrathin film thickness solution for the top lossy layer. Lossy dielectrics like Si, Ge, MoS_2, WS_2, and VO_2 can be used for this purpose along with a whole host of complementary back metals [4]. The result therein will be shown in the result chapters of the thesis. When optimising for strong and broadband absorption in this two-layer FP configuration, lossy back metals such as Ni and Cr are preferable due to another index matching condition that will be mentioned in chapter 4 [4]. While optimising for colouration, more conductive metals like Ag, Al, and Au are the ideal as the zeroth mode band is narrower and more dispersive in the spectral and thickness domain (sharper colour peaks).

State of the art zeroth order FP resonators based on Si have been looked at and characterised in detail for some time in the literature. Particularly this comprehensive study on ultrathin Si in colour filters by Seyed Sadreddin Mirshafieyan, Hong Guo, and Junpeng Guo, published in 2016 [5]. In their study ultrathin sub 50 nm Si was deposited on various backing metals such as Ti, Cr, Ag, and Au. By controlling both the thickness of the Si and the specific backing metal used, strong colouration was produced with hues ranging from blue and violet to pink and beige. Figure 1.23 showcases some of the collected data.

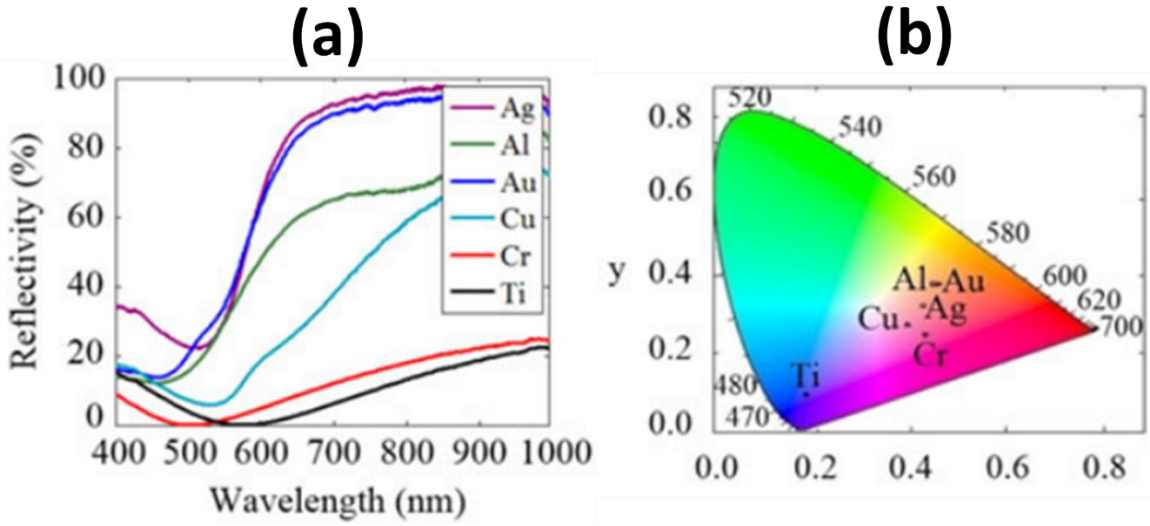


Figure 1.23. (a) The reflectivity spectra of 25 nm Si/Metal samples. Cr and Ti absorb quiet broadly as they are metals with a high n and k. Ag and Au are more spectrally selective. (b) The colours associated with the spectra shown mapped out on a CIE chart diagram. It is a common theme with these zeroth order FP samples to have vibrant hues of blue, violet, orange, and perhaps red. However green remains somewhat elusive to produce as the spectral peaks are too broad.

The explanation behind how ultrathin Si on an opaque back metal can produce such vibrant hues ultimately circles back to how strong absorption can occur in such a subwavelength thin film. Following a similar train of thought to the mathematics describing the behaviour of symmetric FP cavities one can consider the phase shift accumulation of the light at interface boundaries and by propagation. This system has two boundaries consisting of Air-Si and Si-Metal, and a propagation through the Si. Thus, the total phase condition is expressed like so [4].

$$\delta_{total} = \delta_{prop} - \delta_{21} + \delta_{23}$$

(1 . 13)

Where δ_{21} is the phase delay at the Si-Air interface, δ_{23} is the phase delay at the Si-Metal interface, and δ_{prop} is the propagation phase delay in the Si film (see p.23). When the total round trip phase delay picked up is a multiple of 2π, the FP resonance condition is satisfied and since these samples are backed with opaque metal, strong absorption of the trapped light will occur. By setting the above equation to 0, for $m = 0$, the zeroth order mode solutions can be found as shown visually in the simulated maps of Fig.1.24 below.

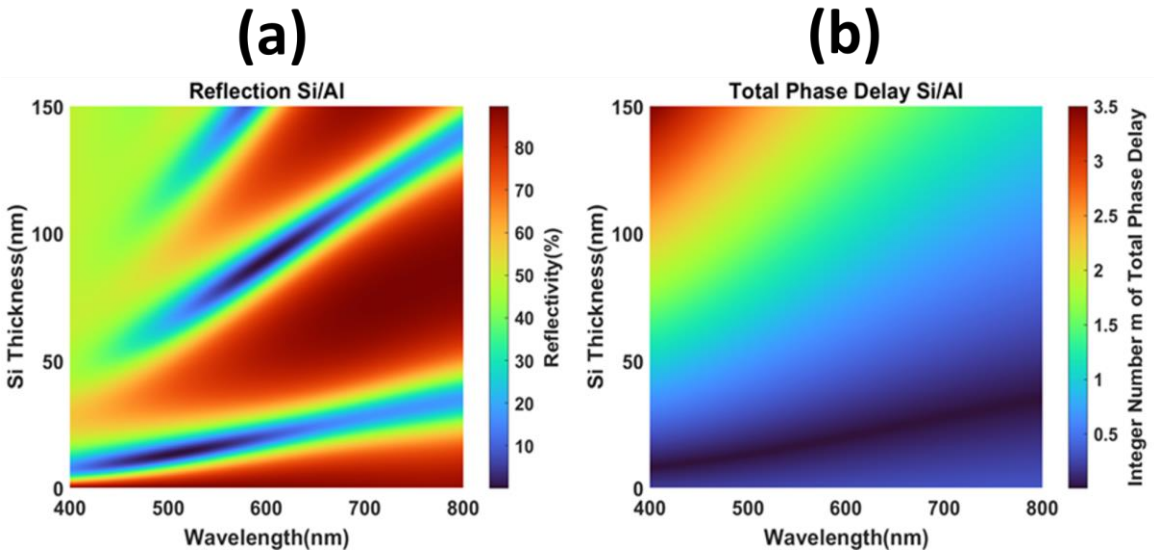


Figure 1.24. (a) The reflectivity surface map of a Si/Al FP cavity. Narrow absorption bands can be seen, each one corresponding to the resonance condition of the stack. The lowest in the ultrathin regime is the zeroth FP mode, while the higher up steeper bands are associated with the first and second FP mode. (b) This is a surface map of the total phase delay as calculated by eq.1.13, the dark blue band is the m = 0 solution, and it overlaps perfectly with the strong absorption spectral region.

The absorption band is quite narrow, and by shifting the thickness between 15-35 nm colours from blue to the orange can be generated. This explanation is true for all lossy dielectric layers on metal backings.

1.3.3 Omnidirectionality of the Zeroth Order Fabry-Perot Mode

By looking a little closer at the fundamental physics of the situation, one can appreciate even more how unique the zeroth mode is to enhancing colouration. Not just in the spectral flatness but also the omnidirectionality, a property this kind of sample has in common with the high index lossy MIMs in Fig.1.20 [5], [12]. Though impressively this is done with fewer layers in the stack. The iridescence that often plagues physically thicker thin film structures can be overcome by the near zero rate of change in phase pickup w.r.t to angle of incidence as shown in Fig.1.25 below [67].

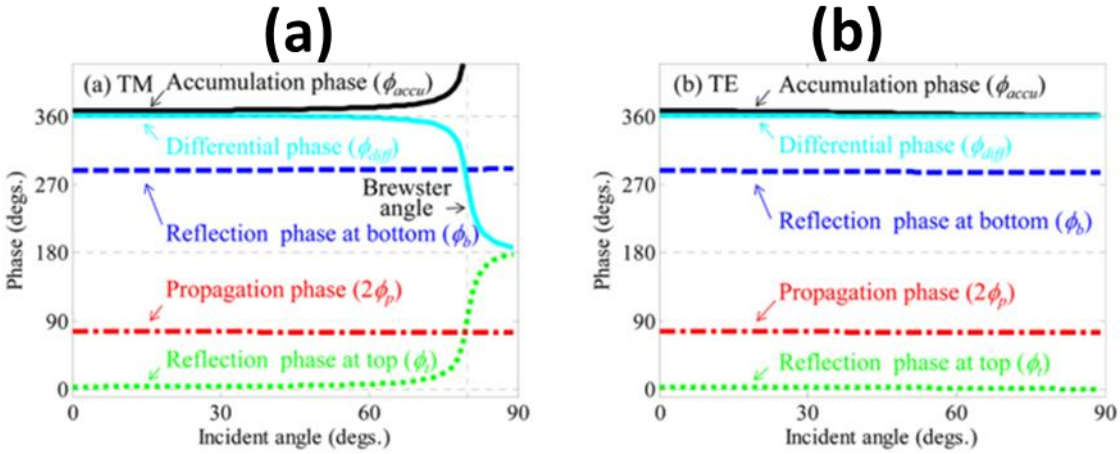


Figure 1.25. (a) The phase pickup components for TM light polarisation. The response is incredibly flat and only at very high incident angles above 75˚ does the Brewster phenomenon begin to dominate the way light couples into the stack. (b) The same as before but for TE light polarisation. As the Brewster angle normally only pertains to TM light, the TE angular dependence remains flat in this instance. [67]

The omnidirectionality of the optical response in this case is not exclusively due to the high index of the lossy dielectric, as in the case of a high index lossy MIM, but also due to the way in which the phase propagation delay and phase interface delay terms closely compensate one another. A similar phenomenon is seen in the spectral domain as well, see Fig.1.26(a) and Fig.1.26(b), and this manifests as a flat band in both the absorption and phase delay which was shown in Fig.1.24 (a) and Fig.1.24(b). A welcome surprise is the similarity between the TM and TE light polarisation response. Typically, the light matter interaction

of these two states will differ significantly for higher angle of incidence. However, for these ultrathin samples there exists a sort of polarisation independence in the light response alongside omnidirectionality [67]. Having both traits make the zeroth resonance mode very attractive for use in solar absorption and structural colouration in general, as one would not want an object coated with this thin film stack to look completely different depending on where the Sun's position is in the sky, or the perspective viewing angle of the observer. It also stands to reason that the reduction of absorption towards specific orientations of light (polarisation states) is disadvantageous unless more niche applications are being considered where alternate artificial light sources are employed, such as in laser communications [68].

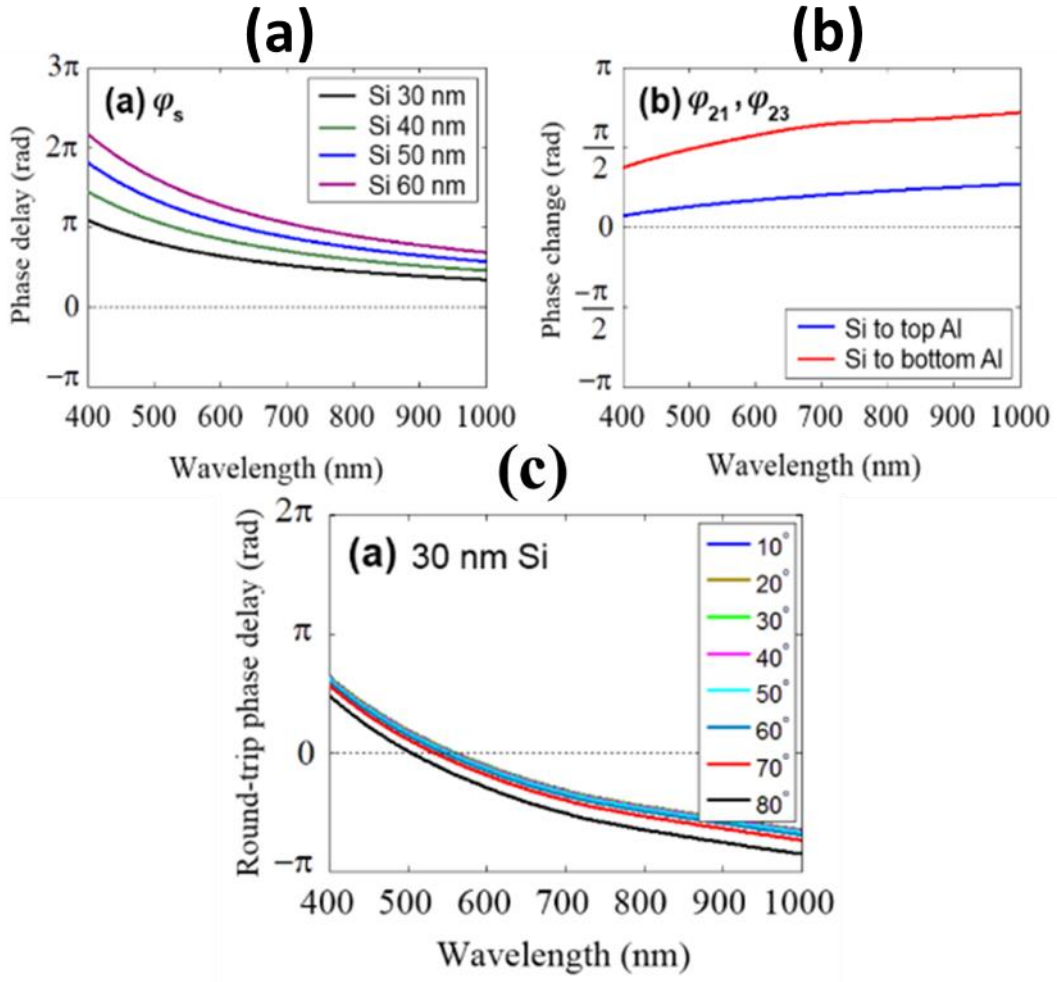


Figure 1.26. (a) The phase delay on propagation for Al/Si/Al. Thicker Si increases phase delay. (b) The phase delay at the top and bottom interface of Si with Al. A very thin Al is placed above Si in this study to increase the saturation of the colour produced, but the fundamental principles of the zeroth mode solutions remain unchanged. (c) The omnidirectionality of the phase delay is seen by most of the lines overlapping one another. Very little change occurs until 80˚ AOI. [7]

One can see that there are limits to the range of colours that can be generated. A review of the literature brings back results showing many blues, violets, oranges, and reds, but vibrant greens with lossy dielectric top layers remain a challenge [4], [69]. The reason behind this harkens back to the flatness and broadness of the zeroth mode band in the spectral domain. It is difficult to get pure green reflections from this flat broad response. In most cases the gamut of this two-layer asymmetric FP system is elliptical and restricted to the lower regions of the CIE colour chart seen below in Fig.1.27(b). WO_3 shows an impressive range of colouration as seen in Fig.1.27(a) but the principle behind this is not the same as the strong absorption in lossy dielectric FP resonator samples. However, from this comes the idea that one could enhance the colouration of the lossy samples further by adding an additional transparent layer onto the stack [40].

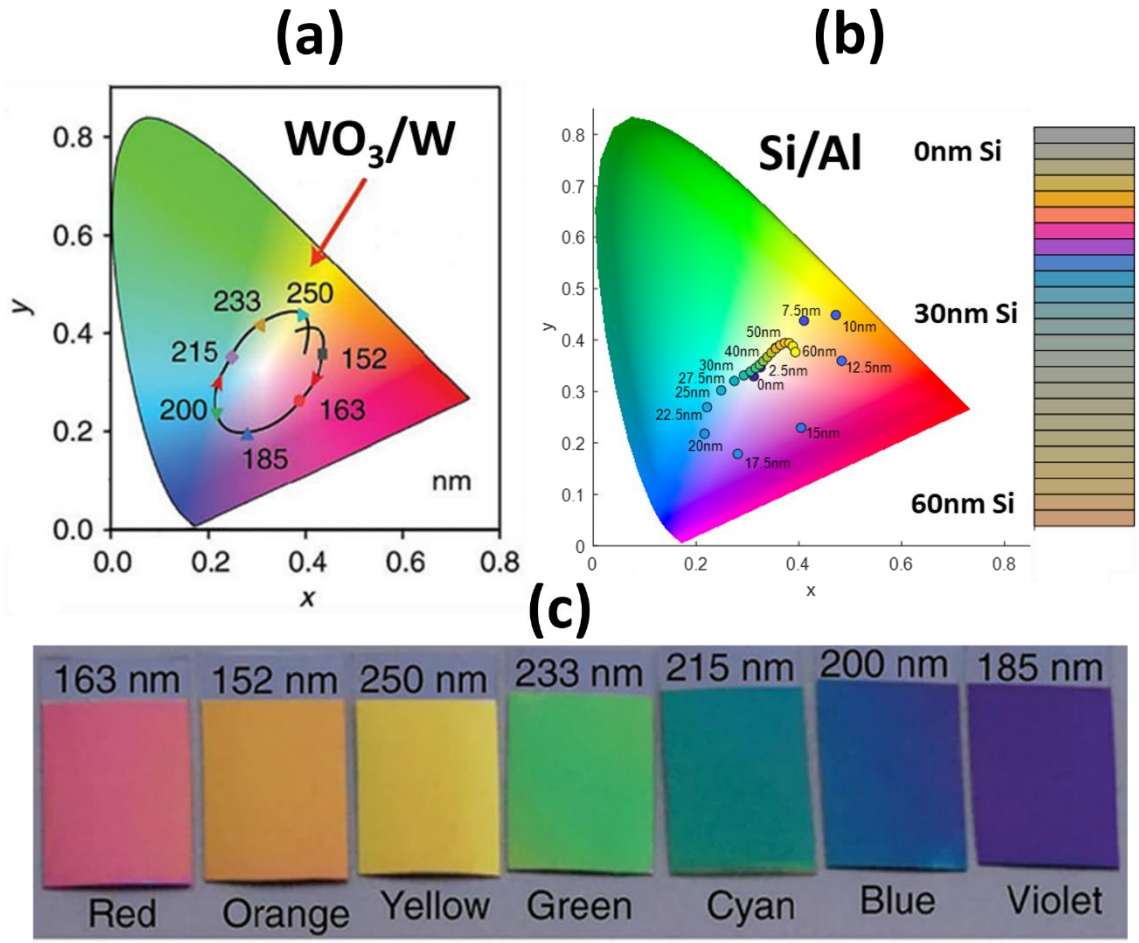


Figure 1.27. (a) Cie colour gamut of WO_3/W which shows a more circular varied colouration of the CIE chart than many zeroth FP resonator stacks [40]. *(b) The simulated colour gamut of a Si/Al stack based on index data gathered during this thesis. Most of the variation in colour is between 7 nm and 30 nm Si. The literature also indicates that redder hues can be created. However given the indices of the metals and Si that were created, this result could not be reproduced* [4]. *(c) An image of the samples charted in (a).*

1.3.4 Enhanced Colour Gamut Using Additional Oxide Capping Layers

As shown above, transparent capping oxide layers can enhance the colouration of the lossy metal backed devices. They can also serve to protect the lossy dielectric film and metal underneath from mechanical and chemical damage. Metals like Au are easily scratched and MoS_2 or WS_2 are known to be used as lubricants in their bulk form due to the weak van der Waals interlayer interaction [70]. For this reason, thin adhesive layers and oxide capping layers are often used to keep these kinds of easily damaged materials attached to the stack structure, so that they do not disintegrate during handling, additional deposition, or annealing steps. Extensive research in group has been done regarding how sub-nanometer Ti layers can help adhere these more fragile films onto glass or Ag/Au substrate, greatly increasing their resistance to dewetting by an order of magnitude over standard thicker 5 nm Ti adhesion layers. Additional oxide capping layers like conducting oxide ZnO can also improve stability further [71]. Figure 1.28 below lays out how this looks.

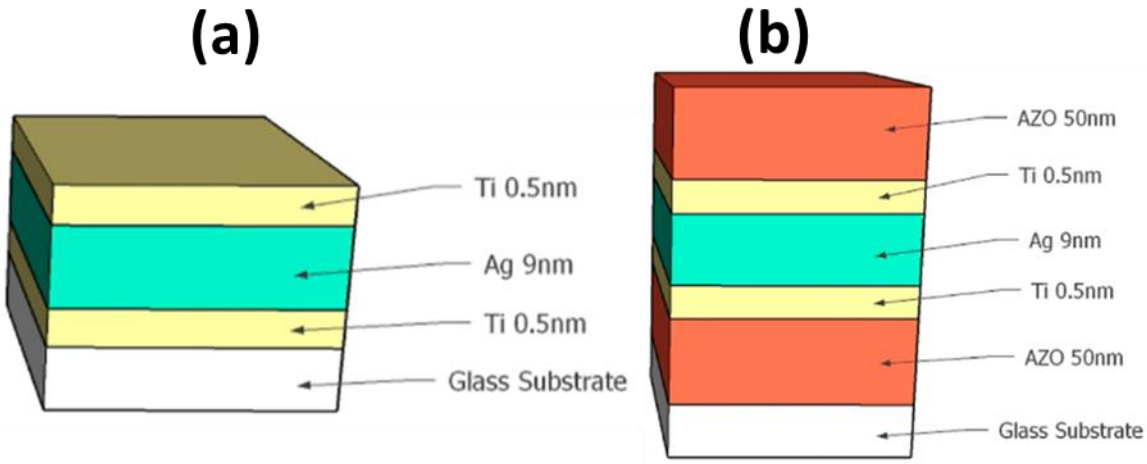


Figure 1.28. (a) Ultrathin Ag sputtered onto glass substrate. It was found that 0.5 nm of Ti is the ideal adhesion and capping layer thickness while also maximising the transmission and eliminating solid state dewetting of the Ag. (b) The addition of oxide capping layers, such as high index ZnO, confers AR coating benefits and protection of the Ag against atmospheric degradation. [71]

By using Ti adhesive, dewetting and back sputtering of Ag during deposition can be greatly mitigated. Back sputtering is the re-deposition of the sample onto the magnetron sputtering targets. This can be mitigated by reducing the power used in the DC and RF gun, as well as using adhesive layer steps in the creation process. The experience gained from depositing AR oxide coatings beforehand helped with the creation of high-quality reproducible FP resonator samples combining both metals and oxides layers together.

For lossy Ge on Opaque Ag, the addition of Ta_2O_5 drastically widens the colour gamut, see Fig.1.29. Not only is the vibrancy on the blue and orange regions of the CIE chart improved, greener turquoise hues also become accessible. Furthermore, the range of hues that can be accessed is superior to thin film oxide samples like SiO_2/Si which are far thicker with SiO_2 measuring in the many 100's of nanometres and Si being cut at 500 µm in most situations. The capped FP ultrathin resonators that were simulated have more colourimetric variance and are far more compact. They are also less sensitive to surface degradation issues such as porosity, which is known to affect oxides like SiO_2 in AR coatings [66], since the strong colouration ultimately originates from the zeroth order FP resonance condition in the protected lossy layer. Thin film oxide interference on its own will also be affected by iridescence more which is nowhere near as big an issue for the compact FP resonators.

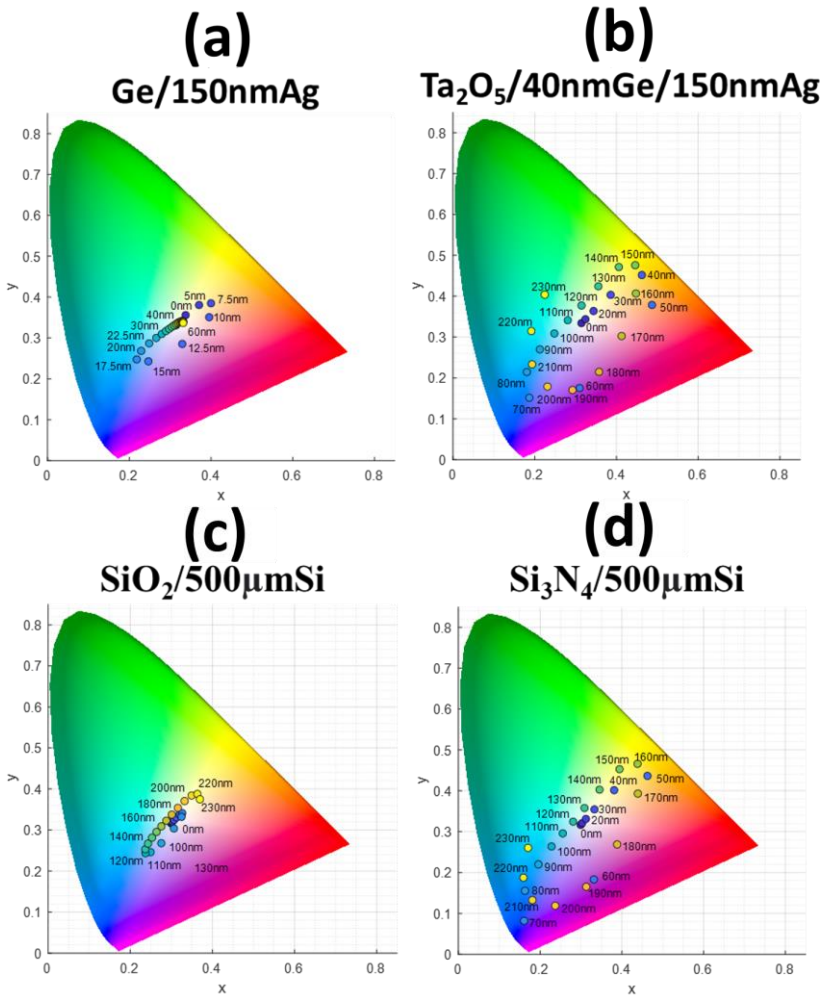


Figure 1.29. (a) CIE chart of Ge/Ag. The colours produced are quite dull. (b) The addition of Ta_2O_5, and the variations of its thickness, drastically widens the colour gamut while keeping the stack compact. (c)-(d) the CIE chart for SiO_2 and Si_3N_4 on a thick Si wafer. In comparison to the ultrathin FP resonator these samples are very thick and less robust to angle change.

1.3.5 Central Lossy Higher Order Fabry-Perot Cavity Colour Filters

The central lossy absorber stack in reflection mode, shown earlier when reviewing the mathematics of the FP thin film interference, can produce more vibrant colours, especially greener hues, than the oxide capped zeroth mode stacks. This increase in gamut also applies to transmission mode samples as well like the work of Kyu-Tae Lee *et al.* (2019) [13]. The lossy central ultrathin absorber MIM structure targets a resonant wavelength around the 3rd FP mode and the central absorber supresses off-peak reflection just as it did for the reflector configuration. With this approach a compact device was shown to be capable of producing high brightness saturated green peaks in transmission, see Fig.1.30.

The use of an ultrathin absorbers in an MIM to enhance the resonant colour peak is a common theme shared among all the higher order FP stack designs that were investigated for the purpose of structural colouration in the thesis. Indeed, with more clever design and lower index dielectric materials these colouration samples can be turned into a very strong broadband absorber [72]. More details will be given on these topics in chapter 6.

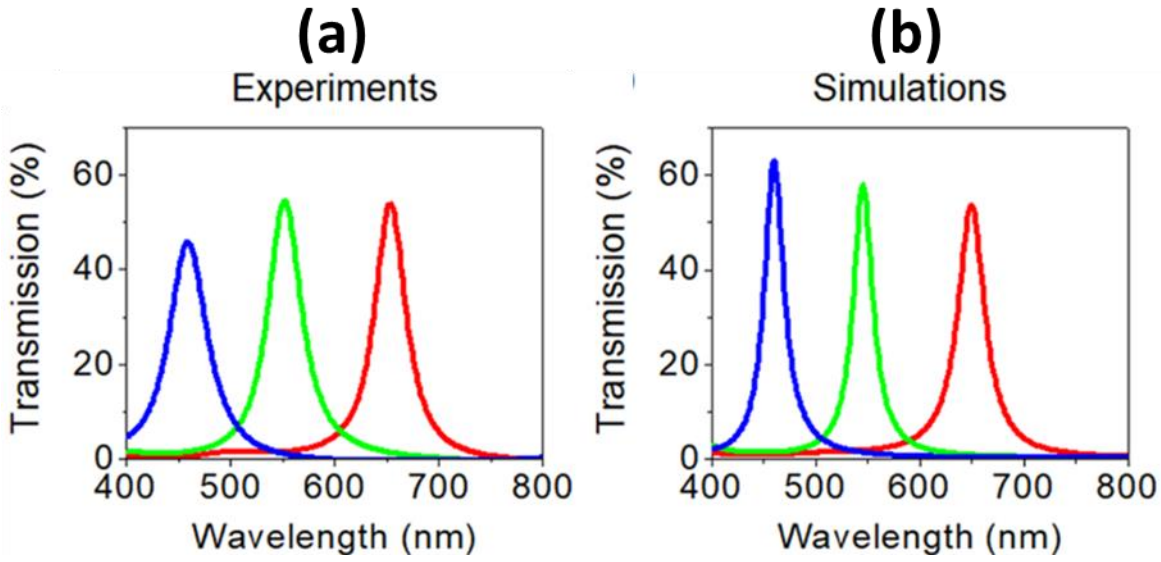


Figure 1.30. (a)-(b) comparison of the simulated and transmission spectra of three samples constituting the RGB peaks. Agreement between simulation and experiment is quite good and the colours are more saturated than the zeroth order FP peaks, especially in the green region. These are third order FP peaks with supressed higher order. [13]

1.3.6 Fano-Resonant Fabry-Perot Cavity Colour Filters

The final major FP resonator type looked at, and by far the most promising for both passive and active colouration, is the ATF Fano resonator. This device was analysed to solve the issue of dull colouration, elliptically narrow colour gamut, and low saturation seen in most of the ultrathin absorber FP cavity stack structures reviewed, particularly the zeroth order FP resonance mode two-layer stacks which were generally too flat to create vibrant hues in the middle of the visible spectrum. By coupling a weakly damped oscillator to a broad oscillator, a very sharp asymmetric line peak can be formed with brightness and saturation rivalling what can be achieved with much more complex metasurface design such as the split ring resonators all dielectric stack; though the latter is still unmatched when it comes to its extremely narrow bandwidth $\delta\lambda$ on the order of 2 nm [26].

Based on the work of Mohamed El Kabbash *et al.* (2021) [73], the ATF Fano-resonant optical coatings (FROCs) can be broken into a two-resonator structure scheme. One composed of the top broad lossy layer, and another composed of the internal MIM structure beneath it. Using the mechanical oscillator theory, the characteristics of the Fano resonance colouration peak can be shown to be controlled by the MIM unit spacer thickness and the top reflective metal being in a state of adequate semi-transparency which allows enough light to enter and subsequently drive the superstrate electric field. These FROC stacks were not only illustrated to be capable of very strong colouration with brightness as high as 80 % as seen in Fig.1.31(c). They were also demonstrated to be of great benefit in unique tasks such as efficiently selectively splitting the solar spectrum into above band gap and below band gap energy channels. This spectrally selective capability improved power output of a solar α-Si PV test cells by 50 % for high optical concentration values. They also reduced the working temperature of the panels by 20˚C, which drastically increased panel lifetime [73].

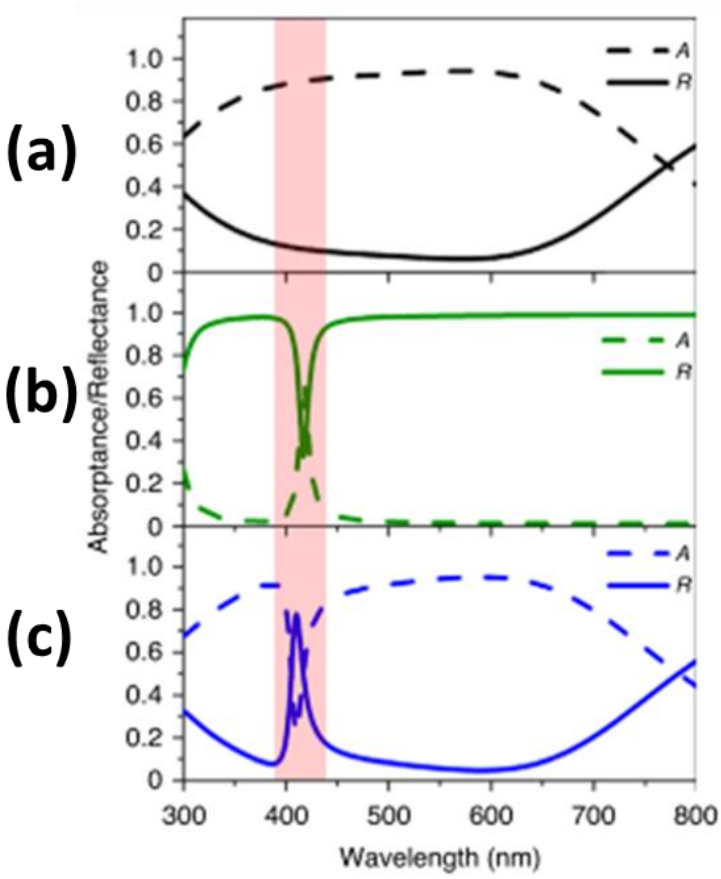


Figure 1.31. (a)-(c) A comparison of the absorption and reflection between a broadband light absorber, a narrow band light absorber MIM, and a FROC device. The steep dispersion and narrow bandwidth gives reflection filter FROCs vibrant strong colouration compared to a broadband absorber or a MIM. [73]

In general, the FROC Fano resonant peak sharpness, omnidirectionality, and bandwidth, can be tightly controlled directly by the spacer layer index and thickness. Higher index equates with steeper spectral dispersion and narrower peak line bandwidth while lower index causes the opposite to occur, with increased iridescence to contend with as a result. More detail will be given on FROC device characteristics and results in chapter 6, wherein the unparalleled omnidirectional colour gamut and on/off state contrast response of ECM and TCM based FROCs are investigated alongside side the attempted Ge FROC devices as a point of reference.

1.4 Summary

In summary, quiet a few topics have been covered thus far. Initially, an overview of the main aims/objectives of the thesis was given, followed by the history and quantification of colour both in nature and artificially made by humans using the CIE colour chart. Using that tool, based on the human eye response, colour could be broken down into its hue, saturation, and

brightness which are objectively defined parameters. The intrinsic colouration of pigments and dyes was compared to structural colour and the advantages and disadvantages of both were listed. Structural colour was shown to be more robust than chemical pigmentation as a method of conferring colours and furthermore it was acknowledged that nature had keenly been making use of this for eons in a large variety of animal species in the reptile, bird, and fish groups.

The subject of structural colour was split into two different groups; one based on patterned and textured materials and another on the ATF approach. Many examples of either could be found throughout nature, with peacock feathers, beetle wings, and chameleon scales all attributing the origin of their colouration to subwavelength surface texturing of structures on the surface of their bodies. The presence of certain phenomenon was attributed to these micro/nano structures such a Mie, plasmonic, and guided mode resonances which manipulated the light to produce vibrant hue. Examples of thin film interference in nature were shown such as the outer surface of bismuth oxide crystals, the 1D photonic crystal layer structure of opal, and the iridescent sheen of soap bubbles.

In the context of artificially created structural colour, colouration derived from thin film interference and surface structural texturing were compared with one another in terms of the cost to manufacture, design complexity, scalability, and ease of modelling. The lithography-free or ATF approach to creating colour became the focus of study since planar samples avoided many of the pitfalls that patterned meta surfaces possessed. Furthermore, the process of simulating and optimising simple flat optical coatings is much simpler using the transfer matrix method than with the more complex simulation tools like COMSOL and Lumerical that utilise FDTD and FEM to compute the 3D EM profile.

Active colouration in nature was touched on briefly to showcase how structural colour could be dynamically tuned by animals for several different purposes such as optical camouflage, mate selection, and communication. The variation of colour in chameleons, cuttlefish, and squids, were shown to be fundamentally derived from modifying the spacing of resonant pigment cells on their skin, controlled by muscles connected to an elastomer substrate. In this way the colouring is controlled by dynamically changing thickness and therefore optical path length and phase delay. Interestingly, examples do exist of artificial colourimetric geometric variation devices. For example, hydrogel MIMs which expand with changing

humidity levels [18]. However, this work will not focus on these thermal expansion materials.

The active colour change ATF approach with inorganic electrochromic and thermochromic materials like WO_3, NiO and VO_2 was explored. Electrochromic technologies are already present on the market in some forms such as dimmable airplane window technology, but the configuration and amount of active material used is quite bulky. To improve the thin film contrast and colouration change response of ECMS and TCMs lots of research can be found utilising them in optical resonator structures though not many delve into the capabilities of such a union in the ultrathin film regime, with some notable exceptions like the work of Mikhail A. Kats *et al.* (2012) [53] (which is a part of Federico Capasso's research group [29]) on zeroth order FP thin film VO_2, making this an appealing avenue of research to focus on and investigate further into for the thesis.

Following on from that a quick introduction was given to the mathematical description of a symmetric FP resonator and its uses in modifying the light matter interaction to achieve a desired optical result in the ATF configuration. Specifically, different kinds of novel FP cavity designs were discussed, such as central lossy MIMs and Fano devices, when combined with certain passive or active materials, could have different unique applications such as chemical/bio sensing and vibrant colour display filters that are compact and easily scalable. The active electrochromic materials were singled out due to their capability and versatility in dynamic strong structural colouration or on/off contrast. Organic gel ECMs were compared to inorganic ECM Transition metal oxides (TMOs) to justify the upcoming potential of ultracompact inorganic EC devices using FP resonance to enhance their colour and state contrast; see Fig.1.32 below of the work done by Su Jae Kim *et al.* (2021) on the electrochromic material CuO_2 [74]. Marked attention was given to the possible implementation of ultrathin ECMs, TCMS, and TMDs into the zeroth order FP resonator cavity device structure. This avenue of study forms a huge part of the results reported on in this thesis, detailing findings on characterising and simulating the simplest 2-layer asymmetric FP resonator stack in the ultrathin film regime, as well as trying to extend the benefits of operating at this scale to thicker more complex MIM devices that can perform better at generating structural colour or attenuating light very efficiently.

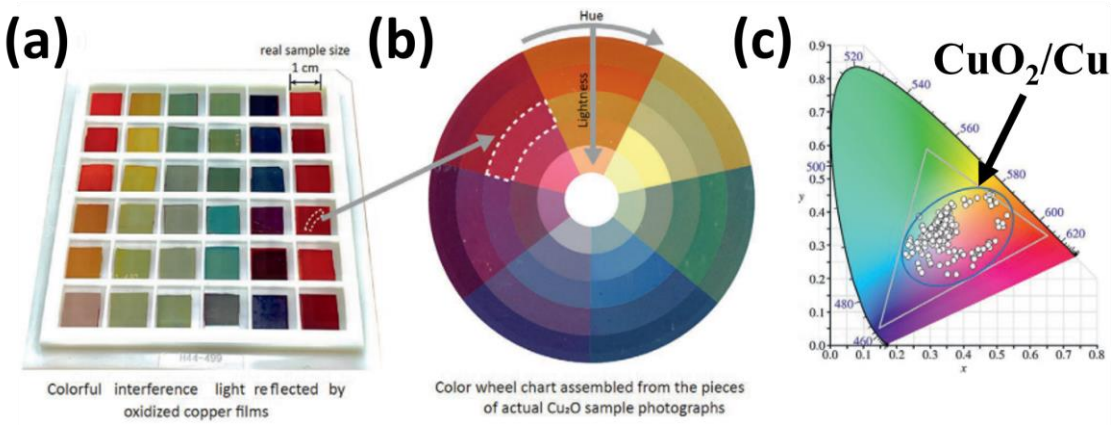


Figure 1.32. (a)-(b) A photographic image and colour wheel of the colour gamut for CuO_2/Cu samples. (c) The CIE chromaticity diagram displaying the range of colour in the blue elliptical region. Like most other zeroth order FP stacks, the colours range from blue to orange/red. [74]

The strong colouration of these zeroth order FP samples was recognised but there was also room for improvement in the colour gamut due to the lack of vibrant green hues generated. To address this the idea of adding transparent oxide capping layers was briefly explored and preliminary study suggests that the range of colouration in some instances can be enhanced considerably while also keeping the device structure sub-wavelength and compact compared to much thicker oxide thin film coatings like SiO_2/Si. Ultimately the structural colouration capabilities of the higher order lossy MIMs like central lossy transmission/reflection filters and FROCs is considered superior to what can be achieved with oxide layer capping alone in terms of peak brightness, saturation, purity, and gamut. Furthermore, the latter lends itself much better to active index change dynamic colouration due to the accessibility of the top lossy absorber layer for processes like wet electrochemistry that oxide capping layers would interfere with. The on/off state contrast is also greater for lossy active MIMs and FROCs due to the way in which light off-resonance is efficiently attenuated by the ultrathin absorber layer.

Going forward, chapters 2-3 will detail a description of the theory of light-matter interaction, the transfer matrix method, and the operation and use of measurement tools/techniques such as magnetron sputtering, spectroscopic ellipsometry, and UV-VIS spectroscopy. Chapter 4 will then focus on the data gathered characterising lossy dielectric thin film materials like Si, Ge, and the TMDs on opaque metal backing. In Chapter 5 the dynamic refractive index change material NiO, an inorganic ECM, will be looked at closely in the same opaque metal backing ultracompact stack configuration as before. Alongside this many different electrochromic properties will be highlighted such as colouration efficiency and lattice

filling ratio. For chapter 6, the application of higher order FP resonator designs like the central lossy ultrathin absorber stacks and ATF FROCs will be investigated for their use in achieving strong absorption and vivid colouration. As an addendum a quick overview of potential future work will also be discussed after the fact, mainly focusing on solid state electrochromics, micro heater array samples of VO_2, and fine tuning of the FROC device synthesis.

1.5 References

[1] Y. Yu, Y. Yu, L. Huang, H. Peng, L. Xiong, and L. Cao, "Giant Gating Tunability of Optical Refractive Index in Transition Metal Dichalcogenide Monolayers," *Nano Lett.*, vol. 17, no. 6, pp. 3613–3618, 2017, doi: 10.1021/acs.nanolett.7b00768.

[2] Z. Sun, A. Martinez, and F. Wang, "Optical modulators with 2D layered materials," *Nat. Photonics*, vol. 10, no. 4, pp. 227–238, 2016, doi: 10.1038/nphoton.2016.15.

[3] Y. Yu *et al.*, "Exciton-dominated Dielectric Function of Atomically Thin MoS2 Films," *Sci. Rep.*, vol. 5, p. 16996, 2015, doi: 10.1038/srep16996.

[4] M. A. Kats and F. Capasso, "Optical absorbers based on strong interference in ultra-thin films," *Laser Photonics Rev.*, vol. 10, no. 5, pp. 735–749, 2016, doi: 10.1002/lpor.201600098.

[5] S. S. Mirshafieyan, H. Guo, and J. Guo, "Zeroth Order Fabry – Perot Resonance Enabled Strong Light Absorption in Ultrathin Silicon Films on Different Metals and Its Application for Color Filters," *IEEE Photonics J.*, vol. 8, no. 5, pp. 1–12, 2016, doi: 10.1109/JPHOT.2016.2609143.

[6] F. Schlich and R. Spolenak, "Strong interference in ultrathin semiconducting layers on a wide variety of substrate materials," *Appl. Phys. Lett.*, vol. 103, no. 213112,

2013, doi: 10.1063/1.4833537.

[7] S. S. Mirshfieyan, T. S. Luk, and J. Guo, “Zeroth order Fabry-Perot resonance enabled ultra-thin perfect light absorber using percolation aluminum and silicon nanofilms,” *Opt. Mater. Express*, vol. 6, no. 4, pp. 1032–1042, 2016, doi: 10.1364/OME.6.001032.

[8] J. Park, S. J. Kim, and M. L. Brongersma, “Condition for unity absorption in an ultrathin and highly lossy film in a Gires – Tournois interferometer configuration,” *Opt. Lett.*, vol. 40, no. 9, pp. 1960–1963, 2015, doi: 10.1364/OL.40.001960.

[9] W. Wu, M. Wang, J. Ma, Y. Cao, and Y. Deng, “Electrochromic Metal Oxides: Recent Progress and Prospect,” *Adv. Electron. Mater.*, vol. 4, no. 8, p. 1800185, 2018, doi: 10.1002/aelm.201800185.

[10] D. Dong *et al.*, “Electrochromic and colorimetric properties of anodic NiO thin films: Uncovering electrochromic mechanism of NiO,” *Electrochim. Acta*, vol. 335, p. 135648, 2020, doi: 10.1016/j.electacta.2020.135648.

[11] D. T. Gillaspie, R. C. Tenent, and A. C. Dillon, “Metal-oxide films for electrochromic applications : present technology and future directions,” *J. Mater. Chem.*, vol. 20, no. 43, pp. 9585–9592, 2010, doi: 10.1039/c0jm00604a.

[12] Z. Yang, C. Ji, D. Liu, and L. J. Guo, “Enhancing the Purity of Reflective Structural Colors with Ultrathin Bilayer Media as Effective Ideal Absorbers,” *Adv. Opt. Mater.*, vol. 7, no. 21, p. 1900739, 2019, doi: 10.1002/adom.201900739.

[13] K. Lee, S. Y. Han, Z. Li, H. W. Baac, and H. J. Park, “Flexible High-Color-Purity Structural Color Filters Based on a Higher-Order Optical Resonance Suppression,”

Sci. Rep., vol. 9, no. 14917, 2019, doi: 10.1038/s41598-019-51165-1.

[14] S. J. Williamson and H. Z. Cummins, *Light and Color in Nature and Art*. New York: Wiley 1983, 1983.

[15] E. J. Gerl and M. R. Morris, "The Causes and Consequences of Color Vision," *Evol. Educ. Outreach*, vol. 1, no. 4, pp. 476–486, 2008, doi: 10.1007/s12052-008-0088-x.

[16] "Response of Human Cone Cells to Colour," 2024. https://lightcolourvision.org/diagrams/response-of-human-cone-cells-to-colour/%0A.

[17] Commission Internationale de l'Éclairage, "Colorimetry - Part 3: CIE Tristimulus Values." https://cie.co.at/publications/colorimetry-part-3-cie-tristimulus-values-0.

[18] D. Wang, Z. Liu, H. Wang, M. Li, L. J. Guo, and C. Zhang, "Structural color generation: From layered thin films to optical metasurfaces," *Nanophotonics*, vol. 12, no. 6, pp. 1019–1081, 2023, doi: 10.1515/nanoph-2022-0063.

[19] A. Gürses, M. Açıkyıldız, K. Güneş, and M. S. Gürses, "Dyes and Pigments: Their Structure and Properties," pp. 13–29, 2016, doi: 10.1007/978-3-319-33892-7_2.

[20] J. Bartoll, "The early use of Prussian blue in paintings," *9th Int. Conf. NDT Art*, no. May, pp. 25–30, 2008.

[21] H. D. Young and R. A. Freedman, *University Physics with Modern Physics*, 14th ed. Pearson, 2016.

[22] Z. Xuan, J. Li, Q. Liu, F. Yi, S. Wang, and W. Lu, "Artificial Structural Colors and Applications," *Innovation*, vol. 2, no. 1, 2021, doi: 10.1016/j.xinn.2021.100081.

[23] M. Srinivasarao and D. B. Feathers, “Nano-Optics in the Biological World Beetles: Butterflies, Birds, and Moths,” *Chem. Rev.*, vol. 99, no. 7, pp. 1935–1962, 1999, [Online]. Available: https://pubs.acs.org/doi/10.1021/cr970080y.

[24] J. Zi *et al.*, “Coloration strategies in peacock feathers,” *Proc. Natl. Acad. Sci. U. S. A.*, vol. 100, no. 22, pp. 12576–12578, 2003, doi: 10.1073/pnas.2133313100.

[25] B. Zeng, Y. Gao, and F. J. Bartoli, “Ultrathin nanostructured metals for highly transmissive plasmonic subtractive color filters,” *Sci. Rep.*, vol. 3, no. 2840, pp. 1–9, 2013, doi: 10.1038/srep02840.

[26] M. Samadi, F. Abshari, J. F. Algorri, P. Rold, and F. D. Olio, “All-Dielectric Metasurface Based on Complementary Split-Ring Resonators for Refractive Index Sensing,” *Photonics*, vol. 9, no. 3, 2022, doi: 10.3390/photonics9030130.

[27] I. Koirala, V. R. Shrestha, C. S. Park, S. S. Lee, and D. Y. Choi, “Polarization-Controlled Broad Color Palette Based on an Ultrathin One-Dimensional Resonant Grating Structure,” *Sci. Rep.*, vol. 7, no. 40073, pp. 1–8, 2017, doi: 10.1038/srep40073.

[28] S. L. Kuai, G. Bader, and P. V. Ashrit, “Tunable electrochromic photonic crystals,” *Appl. Phys. Lett.*, vol. 86, no. 22, p. 221110, 2005, doi: 10.1063/1.1929079.

[29] “Capasso Group.” https://capasso.seas.harvard.edu/.

[30] “Atwater Research Group.” https://daedalus.caltech.edu/.

[31] S. Saravanan, R. S. Dubey, and K. S., “MATLAB Design & Analysis of 1D Photonic Band Structures Using Transfer Matrix Method,” *Int. J. Electr. Electron.*

Data Commun., vol. 1, no. 8, pp. 72–74, 2013.

[32] J. Sun, B. Bhushan, and J. Tong, "Structural coloration in nature," *RSC Adv.*, vol. 3, no. 35, pp. 14862–14889, 2013, doi: 10.1039/c3ra41096j.

[33] C. C. Katsidis and D. I. Siapkas, "General transfer-matrix method for optical multilayer systems with coherent, partially coherent, and incoherent interference," *Appl. Opt.*, vol. 41, no. 19, pp. 3978–3987, 2002.

[34] G. Cai *et al.*, "Diphylleia grayi-Inspired Stretchable Hydrochromics with Large Optical Modulation in the Visible-Near-Infrared Region," *ACS Appl. Mater. Interfaces*, vol. 10, no. 43, pp. 37685–37693, 2018, doi: 10.1021/acsami.8b12490.

[35] M. Vatankhah-Varnosfaderani *et al.*, "Chameleon-like elastomers with molecularly encoded strain-adaptive stiffening and coloration," *Science (80-.).*, vol. 359, no. 6383, pp. 1509–1513, 2018, doi: 10.1126/science.aar5308.

[36] C. Xu, G. T. Stiubianu, and A. A. Gorodetsky, "Adaptive infrared-reflecting systems inspired by cephalopods," *Science (80-.).*, vol. 359, no. 6383, pp. 1495–1500, 2018, doi: 10.1126/science.aar5191.

[37] I. P. Chen, D. Stuart-Fox, A. F. Hugall, and M. R. E. Symonds, "Sexual Selection And The Evolution Of Complex Color Patterns In Dragon Lizards," *Evolution (N. Y).*, vol. 66, no. 11, pp. 3605–3614, 2012, doi: 10.1111/j.1558-5646.2012.01698.x.

[38] J. Chen, G. Song, S. Cong, and Z. Zhao, "Resonant-Cavity-Enhanced Electrochromic Materials and Devices," *Adv. Mater.*, vol. 35, no. 47, p. 2300179, 2023, doi: 10.1002/adma.202300179.

[39] S. T. Ha *et al.*, “Directional lasing in resonant semiconductor nanoantenna arrays,” *Nat. Nanotechnol.*, vol. 13, no. 11, pp. 1042–1047, 2018, doi: 10.1038/s41565-018-0245-5.

[40] Z. Wang *et al.*, “Towards full-colour tunability of inorganic electrochromic devices using ultracompact fabry-perot nanocavities,” *Nat. Commun.*, vol. 11, no. 1, p. 302, 2020, doi: 10.1038/s41467-019-14194-y.

[41] X. Zhang *et al.*, “Inorganic all-solid-state electrochromic devices with reversible color change between yellow-green and emerald green,” *Chem. Commun.*, vol. 56, no. 69, pp. 10062–10065, 2020, doi: 10.1039/d0cc04129g.

[42] C. G. Granqvist, M. A. Arvizu, Bayrak Pehlivan, H. Y. Qu, R. T. Wen, and G. A. Niklasson, “Electrochromic materials and devices for energy efficiency and human comfort in buildings: A critical review,” *Electrochim. Acta*, vol. 259, pp. 1170–1182, 2018, doi: 10.1016/j.electacta.2017.11.169.

[43] K. Madasamy, D. Velayutham, V. S. M. Kathiresan, and Kuo-Chuan Ho, “Viologen based Electrochromic Materials and Devices,” *J. Mater. Chem. C*, vol. 7, no. 16, pp. 4622–4637, 2019, doi: 10.1039/C9TC00416E.

[44] V. H. V. Quy *et al.*, “Tunable electrochromic behavior of biphenyl poly(viologen)-based ion gels in all-in-one devices,” *Org. Electron.*, vol. 100, p. 106395, 2022, doi: 10.1016/j.orgel.2021.106395.

[45] G. Cai *et al.*, “Ultra-large optical modulation of electrochromic porous WO3 film and the local monitoring of redox activity,” *Chem. Sci.*, vol. 7, no. 2, pp. 1373–1382, 2016, doi: 10.1039/c5sc03727a.

[46] Y. Tang *et al.*, “Lattice Proton Intercalation to Regulate WO3-Based Solid-Contact Wearable pH Sensor for Sweat Analysis,” *Adv. Funct. Mater.*, vol. 32, no. 4, p. 2107653, 2022, doi: 10.1002/adfm.202107653.

[47] M. P, M. R, and R. D, *Electrochromism and Electrochromic Devices*. Cambridge University Press, 2007.

[48] J. CHENG, “Nano-chromatic: photos of the new 4th-gen iPod nanos (Updated with orange),” *ars Technica*, 2008. https://arstechnica.com/gadgets/2008/09/nano-chromatic-photos-of-the-new-4th-gen-ipod-nanos/.

[49] W. Gruener, “LCD TVs outship CRT TVs for the first time,” 2008. https://web.archive.org/web/20080226094529/http://www.tgdaily.com/content/view/36119/118/.

[50] Z. Cabading, “LED vs LCD Monitors: Key Differences Explained,” 2024. https://www.hp.com/us-en/shop/tech-takes/differences-between-led-display-and-lcd-monitor.

[51] “Dimmable Glass: What You Need To Know,” *Smart Glass VIP*, 2021. https://smartglassvip.com/working-of-electronic-dimmable-glass-for-aircraft-windows/.

[52] J. Zhao, Y. Zhou, Y. Huo, B. Gao, Y. Ma, and Y. Yu, “Flexible dynamic structural color based on an ultrathin asymmetric Fabry-Perot cavity with phase-change material for temperature perception,” *Opt. Express*, vol. 29, no. 15, p. 23273, 2021, doi: 10.1364/oe.431906.

[53] M. A. Kats *et al.*, “Ultra-thin perfect absorber employing a tunable phase change

material," *Appl. Phys. Lett.*, vol. 101, p. 221101, 2012, doi: 10.1063/1.4767646.

[54] J. H. Ko, Y. J. Yoo, Y. Lee, H. Jeong, and Y. M. Song, "A review of tunable photonics : Optically active materials and applications from visible to terahertz," *ISCIENCE*, vol. 25, no. 8, 2022, doi: 10.1016/j.isci.2022.104727.

[55] G. R. Khan, "Impact of ion irradiation , elemental doping and coating cycles on structural characteristic parameters of nanocrystalline VO2 thin films," *Micro Nano Lett.*, vol. 15, no. 3, pp. 196–200, 2020, doi: 10.1049/mnl.2019.0186.

[56] M. Jiang *et al.*, "Room Temperature Optical Constants and Band Gap Evolutionof Phase Pure M1-VO2 Thin Films Deposited at Different OxygenPartial Pressures by Reactive Magnetron Sputtering," *J. Nanomater.*, vol. 2014, no. 1, pp. 1–6, 2014, doi: 10.1155/2014/183954.

[57] M. Sakurai, "Spectroscopic ellipsometry," *Toraibarojisuto/Journal Japanese Soc. Tribol.*, vol. 57, no. 7, 2012.

[58] H. Deng, Z. Li, L. Stan, D. Rosenmann, and D. Czaplewski, "Broadband perfect absorber based on one ultrathin layer of refractory metal," *Opt. Lett.*, vol. 40, no. 11, pp. 2592–2595, 2015, doi: 10.1364/OL.40.002592.

[59] "Principle, Construction, and Working of the Ruby Laser," *Physics Vidyapith*. https://www.physicsvidyapith.com/2022/03/principle-construction-and-working-of-the-ruby-laser.html.

[60] M. Fox, *Optical Properties of Solids*. 2010.

[61] A. Atvars, "Analytical description of resonances in Fabry – Perot and whispering

gallery mode resonators," *J. Opt. Soc. Am. B*, vol. 38, no. 10, pp. 3116–3129, 2021, doi: 10.1364/JOSAB.419993.

[62] L. Ee and J. I. Y. O. B. Yun, "Realization of Structural Colors via Capped Cu-based F − P Cavity Structure," *Opt. Express*, vol. 29, no. 18, pp. 29466–29480, 2021, doi: 10.1364/OE.435768.

[63] C. Park, V. R. Shrestha, S. Lee, E. Kim, and D. Choi, "Omnidirectional color filters capitalizing on a nano-resonator of Ag-TiO2-Ag integrated with a phase compensating dielectric overlay," *Sci. Rep.*, no. 8467, pp. 24–27, 2015, doi: 10.1038/srep08467.

[64] A. M. Law, L. O. Jones, and J. M. Walls, "The performance and durability of Anti-reflection coatings for solar module cover glass – a review," *Sol. Energy*, vol. 261, pp. 85–95, 2023, doi: 10.1016/j.solener.2023.06.009.

[65] S. D. Rezaei, S. Shannigrahi, and S. Ramakrishna, "A review of conventional, advanced, and smart glazing technologies and materials for improving indoor environment," *Sol. Energy Mater. Sol. Cells*, vol. 159, pp. 26–51, 2017, doi: 10.1016/j.solmat.2016.08.026.

[66] S. Toth *et al.*, "Soiling and cleaning: Initial observations from 5-year photovoltaic glass coating durability study," *Sol. Energy Mater. Sol. Cells*, vol. 185, pp. 375–384, 2018, doi: 10.1016/j.solmat.2018.05.039.

[67] J. Park *et al.*, "Omnidirectional Near-Unity Absorption in an Ultrathin Planar Semiconductor Layer on a Metal Substrate," *ACS Photonics*, vol. 1, no. 9, pp. 812–821, 2014, doi: 10.1021/ph500093d.

[68] P. Poirier and B. Neuner, “Undersea laser communication using polarization and wavelength modulation,” *Appl. Opt.*, vol. 53, no. 11, pp. 2283–2289, 2014, doi: 10.1364/ao.53.002283.

[69] R. Gatensby *et al.*, “Controlled synthesis of transition metal dichalcogenide thin films for electronic applications,” *Appl. Surf. Sci.*, vol. 297, pp. 139–146, 2014, doi: 10.1016/j.apsusc.2014.01.103.

[70] A. K. Geim and I. V. Grigorieva, “Van der Waals heterostructures,” *Nature*, vol. 499, no. 7459, pp. 419–425, 2013, doi: 10.1038/nature12385.

[71] A. L. Lynch, C. P. Murray, E. Roy, C. Downing, and D. Mccloskey, “Extreme Dewetting Resistance and Improved Visible Transmission of Ag Layers Using Sub-Nanometer Ti Capping Layers,” *ACS Omega*, vol. 9, no. 8, pp. 9714–9719, 2024, doi: 10.1021/acsomega.3c09774.

[72] H. Deng, Z. Li, L. Stan, D. Rosenmann, and D. Czaplewski, “Broadband perfect absorber based on one ultrathin layer of refractory metal,” vol. 40, no. 11, pp. 2592–2595, 2015.

[73] M. Elkabbash *et al.*, “Fano-resonant ultrathin film optical coatings,” *Nat. Nanotechnol.*, vol. 16, pp. 440–446, 2021, doi: 10.1038/s41565-020-00841-9.

[74] S. J. Kim *et al.*, “Color of Copper / Copper Oxide,” *Adv. Mater.*, vol. 33, no. 15, p. 2007345, 2021, doi: 10.1002/adma.202007345.

Chapter 2. Theories of Light-Matter Interaction

2.1 Introduction to the Theory of Electromagnetic Waves

2.1.1 Describing Light as an Electromagnetic Wave

In 1864, the famous Mathematician James Clerk Maxwell published his groundbreaking work unifying the concepts of electricity and magnetism to form his theory of electromagnetism, and in so doing he also proved that light was an electromagnetic (EM) wave composed of alternating electric and magnetic fields. His theory can be expressed in four famous Maxwell equations, given in differential form below [1].

$$\nabla \cdot \vec{E} = \frac{\rho}{\varepsilon_0} \tag{2.1}$$

$$\nabla \times \vec{E} = -\frac{\partial \vec{B}}{\partial t} \tag{2.2}$$

$$\nabla \cdot \vec{B} = 0 \tag{2.3}$$

$$\nabla \times \vec{B} = \mu_0 \times \vec{J} + \mu_0 \varepsilon_0 \times \frac{\partial \vec{E}}{\partial t} \tag{2.4}$$

Where $\vec{E}$ is the electric vector field, $\vec{B}$ is the magnetic vector field, ρ is the volumetric charge density, ε_0 is the permittivity of free-space, μ_0 is the permeability of free-space, $\vec{J}$ is the current density across an enclosed area loop, and $\frac{\partial}{\partial t}$ is the partial derivative w.r.t time.

The divergence of $\vec{B}$ is given as $\vec{0}$ to denote the apparent absence of magnetic monopoles in nature. These equations can also be written in the integral form; however, the differential form is easier to work with in the context of light. The plane wave solution is the most commonly used model for light waves that are far from their source (sun or lab light), see Fig.2.1. They will have successive crests parallel to one another in the far-field limit. Only the electric field will be considered in this work as it is this component of light that is most relevant when describing the light-matter interaction of various non-magnetic thin film materials. Moreover, light's magnetism is also weak compared to its oscillating electric field due to the $\frac{1}{c}$ relation between them, where c is the speed of light in vacuum [2].

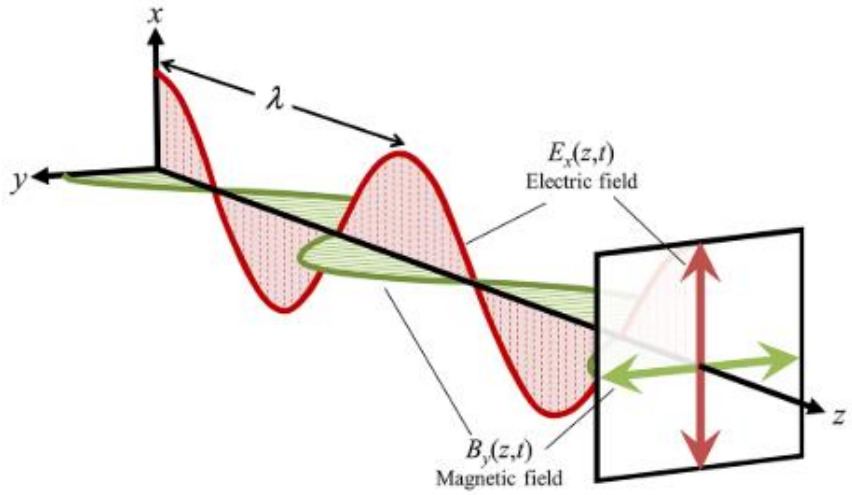


Figure 2.1. Light is an electromagnetic wave composed of alternating electric and magnetic fields that are orthogonal to one another. The cross product between the two indicates that light propagates perpendicular to the oscillation x-y plane. The size of the electric field is much larger than the magnetic component, but both are normalised relative to each other for clarity in this case. [3]

If the electric field component oscillates in the x-plane, and the wave propagates along the z-axis, then the following plane wave equation can be written to represent light.

$$\vec{E}_x(z,t) = \vec{E}_0 \cdot \sin\left(-\frac{2\pi}{\lambda}(z - vt) + \varphi\right) \qquad (2.5)$$

Where $\vec{E}_0$ is the amplitude of the wave, z is the distance along the direction of travel, v is the phase velocity of the wave which in free space is equal to the speed of light c, λ is the wavelength, and φ is the phase angle offset which is relevant when considering how two or

more plane waves interfere with one another. When following through the mathematics, an analytical expression can be obtained for the phase velocity v of the EM wave which in this instance is the speed of light given below.

$$v = c = \frac{1}{\sqrt{\mu_0 \varepsilon_0}} \tag{2.6}$$

Unlike a corpuscle/particle model, wave-like light is capable of diffraction and interference with itself, alongside the usual phenomenon of reflection and refraction [1]. Light's ability to interfere with itself is of paramount importance to the thesis work given that this behaviour is the primary mechanism behind the structural colouration and strong absorption of the ATF FP cavity resonators that are presented in the results chapters. Given the significance of light's wave nature, a closer look at the topic in the context of quantum mechanics is given in the next section, alongside a discussion on particle-wave duality for both light and matter. Furthermore, this will segway into the theory used to mathematically model the light-matter interaction of different solids such as metals and semiconductors.

2.2 Quantum Nature of Light & Matter

2.2.1 Light Particle-Wave Duality

Before discussing the theory of the light-matter interaction and thin film interference more closely, the quantum nature of light as both a particle and a wave must first be considered. It is important to note that light is also a quantum phenomenon and not purely a classical wave. Which is to say an EM wave or photons have a particle-wave duality existence [1]. This was demonstrated conclusively by Einstein in his 1905 paper on the photo-electric effect where he proved that light came in discreet packets of energy, he called photons [3]. The concept of photon particles aligned well with Max Plank's earlier work on solving the infamous ultra-violet catastrophe using a quantized model of light emission from a hot radiating blackbody. He called the emitted particle a quanta [4]. See Fig.2.2 below. The wave theory approach of EM classical physics predicted the erroneous result that infinite energy must be emitted in the UV spectrum by a blackbody. The emission spectrum drops

off extremely rapidly towards zero just after the peak spectral position, given by the experimental derived Wien's displacement law shown below, is reached [1].

$$\lambda_{peak} = \frac{b}{T}$$

(2.7)

Where T is the temperature of matter, λ_{peak} is the peak EM emission wavelength of the blackbody object, and b is the Wien's displacement constant 2898 μm·K. With the success of both the Maxwell equations and the concept of quantisation in describing experimental results, it became clear that light was both simultaneously a particle and an EM wave, especially when considering its interaction with matter.

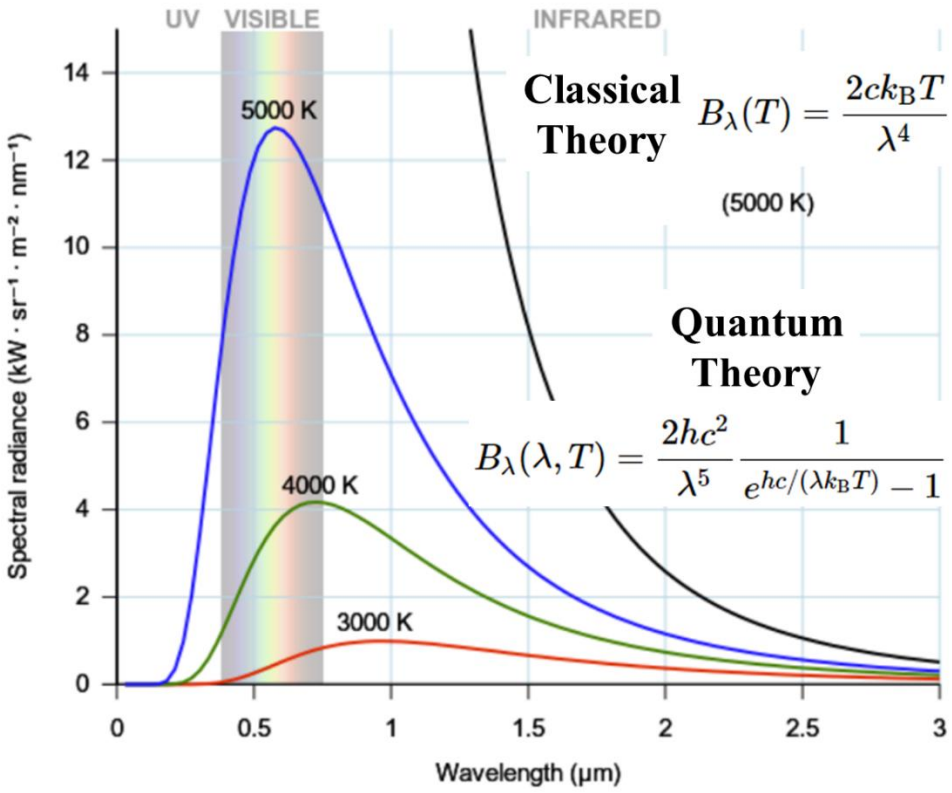


Figure 2.2. The Rayleigh-Jeans Law from classic EM physics predicted an inverse quartic dependence of the spectral radiance of a blackbody w.r.t the wavelength of light. The curve fit well for large wavelengths in the IR, but at short wavelengths the prediction of infinite energy being emitted in the UV was made. This was the first major sign that classic wave EM physics was fundamentally incorrect on its description of electrodynamic bodies. Max Planck later derived an expression based on the quantisation of photon energy. The new curve matched observation exactly and even provided an analytical definition of the Wien's displacement law in terms of fundamental constants. [5]

Einstein's and Plank's work proved the validity of the quantum postulate in solving previously insurmountable problems in classical physics, unlocking the door toward a better understanding of the light-mater interaction. The equation below is the quantisation of EM energy in the form of a photon, used by Einstein to describe the photoelectric effect [1], [4].

$$E_{Photon} = hf \tag{2.8}$$

Where E = Energy of a photon, h is the Planck Constant, and f is the frequency of the light. From this one can see that higher frequency photons contain more energy than those with lower frequency, regardless of how bright the light source is; classical intensity is directly proportional to the square of its total electric field intensity [1]. The classical EM wave can therefore be thought of as a stream of these energetic photons in the continuum limit, where the addition or subtraction of energy to the field happens in discrete steps. In free space the wave description alone is apt for explaining light's behaviour, but once light interacts directly with matter (particularly through absorption) its true quantum nature becomes very apparent. Specifically, when interacting with matter (typically an electron) that is bound or trapped in some way, requiring an exact amount of energy to change its state. These bound states can be natural resonant frequencies associated with matter's molecular structure such as vibrational modes and rotational modes. They can also be linked to the electronic interband transition states between the valance and conduction bands [2]. The formation of this electronic band structure occurs in all solids and is simply the continuum limit of the overlap of the individual atomic and molecular orbital discrete electron energy levels strongly interacting due to their close spatial association. In this way the band is de-localised but contains some of the same traits as the atomic absorbing oscillator components making it up. See Fig.2.3 below.

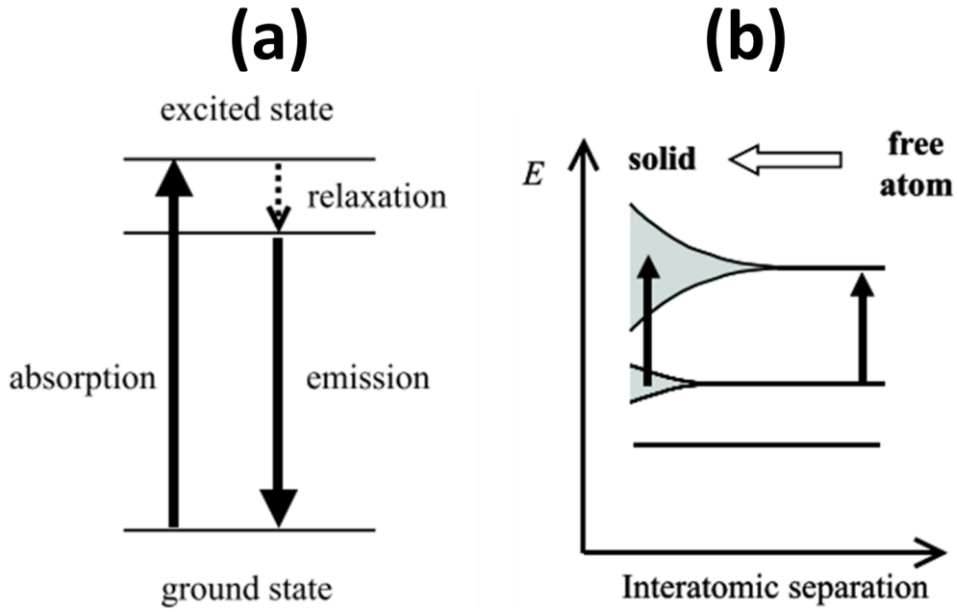


Figure 2.3. (a) An interatomic electron transition between the ground and excited state when absorbing a photon of the right frequency. After a relaxation step, a photon is emitted to lower the electron back down to the ground level. (b) When more atoms are brough together these sharp lines become delocalised, creating a distinct band structure in reciprocal space (energy versus momentum). [2]

2.2.2 Matter Particle-Wave Duality

Like light, matter is also quantised as is given by the famous De Broglie matter wave equations below [1].

$$\lambda_{matter} = \frac{h}{\vec{p}}$$

(2 . 9)

Where λ_{matter} is the de Broglie wavelength of the mater particle, h is Planck's Constant, and $\vec{p}$ is the momentum of the particle. Furthermore, the uncertainty principal which governs the fundamental limit to how precisely one can measure two different physical properties of matter in quantum mechanics is as shown [1].

$$\Delta x \Delta \vec{p} \geq \frac{h}{4\pi}$$

(2 . 10)

Where Δx is position uncertainty and $\Delta \vec{p}$ is momentum uncertainty. These famous relations demonstrate that matter particles, which is to say fermions, behave as waves on the smallest of scales just like bosonic light. Their existence can be spread out across a volume of space and over a range of different momenta. Trying to pin down the exact value of either will drastically increases the spread of the other. This understanding led to an accurate picture of the true structure of the atomic system, which was once thought to be indivisible hence the name deriving from the Greek word Atomos [6].

Instead of a plum pudding ball with electrons sitting on the positive nucleus core, a real atom is a quantum mechanical system in which electrons occupy atomic orbital shells/clouds with discrete energy levels. This quantised system can also be thought of as a standing wave that surrounds the nucleus [7]. This standing wave takes on different shapes depending on its energy level and the lowest levels are always filled first. See Fig.2.4 below. Unlike with photons, the Pauli-exclusion principal ensures that electrons will fill up higher and higher states if the levels below are occupied. Electrons of the exact same quantum state cannot occupy the same region of space. Given that all electrons are identical as fundamental particles, the only way to distinguish them is through their quantum numbers. Namely, the principal quantum number n and quantum mechanical intrinsic spin up and spin down [7].

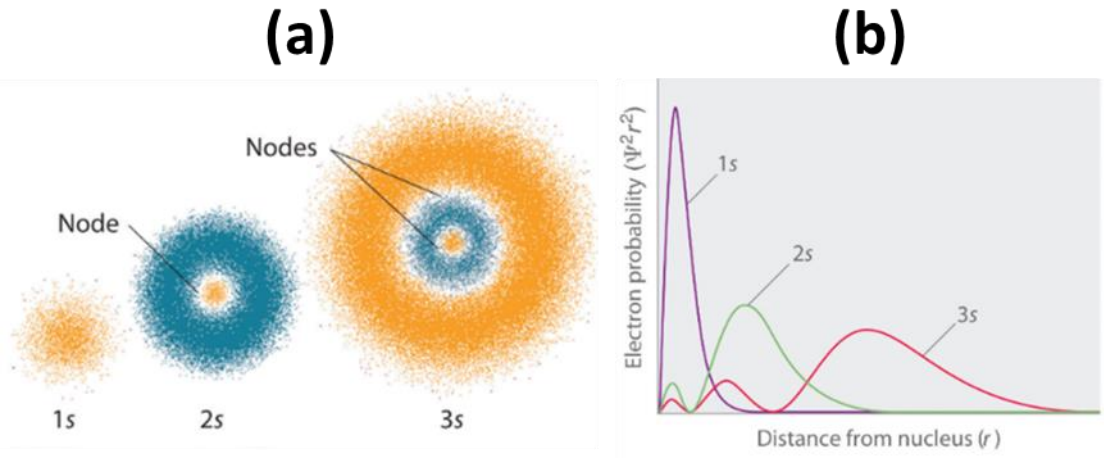


Figure 2.4. (a) The 3D probability density of the electron orbiting the hydrogen nucleus at 3 different energy levels. Orange corresponds to a positive wavefunction and blue to a negative. The white space in between are regions with a very low chance to find an electron while the antinodes are the opposite. (b) The maximum probability radius for each shell corresponding to n = 1, 2, and 3 agrees exactly with the Bohr model of the hydrogen atom. By treating the electron as a wave, one can also see that the electron of the 3S can be found in the same region as the 1S shell. The probability of finding an electron far away tends to zero and likewise it is difficult for the electron to make a close approach of the nucleus. Electron-electron repulsion effects are ignored in this instance. [7]

The potential holding the electron and proton atomic system together is the coulomb force between them. The shape of the quantum mechanically confined orbiting electron clouds is worked out it with the general form of the Schrödinger wave equation shown below. It can be noted that the probability of a collision between the proton and electron is unlikely. Furthermore, the mass-energy density state of the separated electron-proton system is measurably lower than the electron captured system which generates a neutron and neutrino as the output. Without going beyond the scope of the thesis, the process of electron capture is supressed by proton-neutron mass difference (twice the rest mass of the electron) and the low probability of a weak interaction using a $W^{\pm}$ boson (The W boson is very massive) [8].

$$\widehat{H}(r,\Theta,\phi)\Psi(r,\Theta,\phi) \;=\; E\Psi(r,\Theta,\phi)$$

(2 . 11)

Where r is the radial distance from the nucleus, Θ and ϕ are angular parameters from spherical polar coordinates geometry, Ψ is the electron wavefunction, $\widehat{H}$ is the Hamiltonian of the system, and E is the energy level. Contained within the Hamiltonian is the coulomb potential between the electron and proton, and the electron kinetic energy. The analytical solutions are somewhat complicated so for simplicity the atomic energy levels E_n of the S spherical electron shell is given w.r.t principal quantum number n [1].

$$E_n \;=\; -\frac{m_e e^4}{8\varepsilon_0^2 h^2 n^2}$$

(2 . 12)

Where m_e is the electron mass, e is the fundamental electric charge, and ε_0 is the permittivity of free space. To excite electrons from the ground level to one of the higher shell orbitals, light of the correct frequency must interact with the electron through absorption. If there's too little energy, then the atom will be transparent to the light. This is why atomic emission lines are so sharp and incredible useful in identifying the elemental composition of rarefied materials such as excited gas/plasma [1]. Telescopic analysis of the sharp emission spectra received from the sun, or the atmosphere of distant planets, can therefore be used to catalogue the chemical makeup of those extraterrestrial worlds and

indeed profile the elemental buildings blocks present anywhere in the universe [9]. This technique is known as atomic emission spectroscopy and the basic premise can be applied to other spectral regimes like the IR to access vibrational mode transitions, or the x-ray region to excite deep core electrons.

2.2.3 The Continuum Limit & Electronic Band Formation

Moving back to the light-matter interaction in solids, when bands start to form as the number of atoms increase, these quantised atomic shells will first become molecular orbitals and the molecular orbitals will then begin to smear out into a continuum where the LUMO level becomes the conduction band and the HOMO becomes the valence band [2]. See Fig.2.5 below. The valence band is so named because it is occupied by the outermost electrons of the materials that participate in chemical reactivity, like the covalent bonding that holds together many solid materials like Si, Ge, and carbon. The conduction band is nearly always unoccupied at standard ambient conditions. It is described as conductive because the majority of the energy levels in the band are unfilled, which is to say that the electron population capable of inhibiting conduction is extremely low. Any electron that can be promoted to the conduction band, typically with light, can now flow freely under the bias of an external electric field. The elevation of an electron from the valence to the conduction band by absorption of a photon is called an interband transition [2].

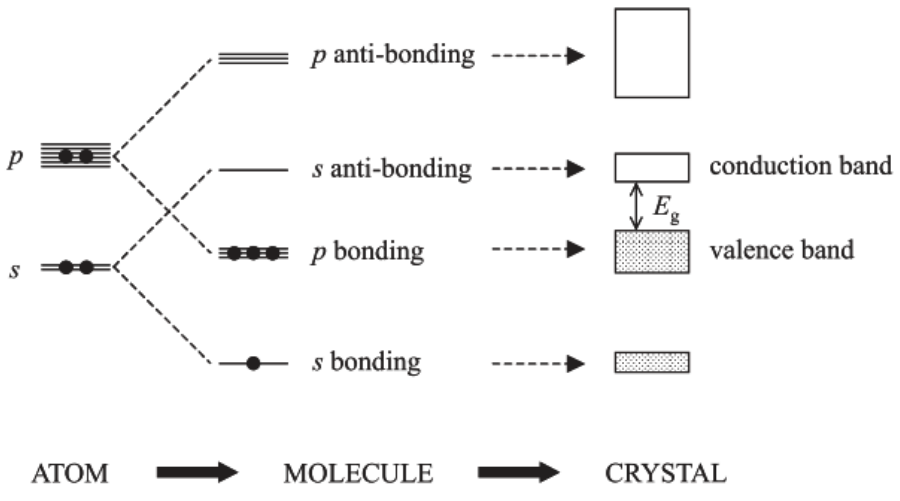


Figure 2.5. As the number of atoms increases the atomic orbitals and their energy levels become more and more closely spaced together, both in terms of energy and spatial position, until the continuum limit is reached, and a band forms. Depending on the electronic structure of the band and its fermi level, the resulting solid can be conducting, semiconducting or insulating. Transitioning between the valence and conduction band is known as interband transition, and this absorption is particularly important to understanding the light matter interaction in semiconductors.[2]

2.3 Explanation of Conductors, Semiconductors, & Insulators

2.3.1 The Free Electron Drude-Lorentz Model of Conductors

At this point it would be good to clarify the three major classes of solid material. The first is conductors, the second is semiconductors, and the third is insulators [1]. Generally speaking, conductors do not have fully occupied valence bands which means, with a little resistance, electrons can flow freely under an applied electric voltage. Conductors are best modelled as a free electron gas, as the optically active valance electrons are not bound as tightly compared to other more insulating solids [2]. The freedom of the electrons is also why a classical approach to describing the metal light-matter interaction works well, e.g., the Drude model based on the EM theory concept of the dipole oscillator without a restoring force; developed by Paul Drude in 1900 to explain the properties of conductive transition metals like Cu, Au, and Ag [2]. The Drude equation for the optical dielectric function, ε(ω) of a free electron plasma is given below in its modified form [2].

$$\varepsilon(\omega) = \varepsilon(\infty) - \frac{\omega_p^2}{\omega^2 + i\gamma\omega}, \qquad \omega_p^2 = \frac{ne^2}{m_e\varepsilon_0}$$

(2 . 13)

Where $\varepsilon(\infty)$ is the infinite energy offset contribution related to the bound electron interband structure, ω_p is the plasma frequency of the metal, ω is the angular frequency, n is the free carrier concentration of the metal (almost always electrons in metals), and γ is the collision frequency of the free electrons with the positive ion cores of the metal lattice. The energy offset term is constant in the visible spectral range for most metals [2]. A Lorentz dipole oscillator model with driving force resonant frequency can be used to express its quantity analytically. The plasma frequency can best be thought of as the resonant frequency of the entire free electron gas in contrast to the background polarisability bound electrons which are subject to restoring forces located at some other resonant frequency ω_0 [2]. At the plasma frequency the reflectivity of light from a conductor will tend to unity as shown in Fig.2.6.

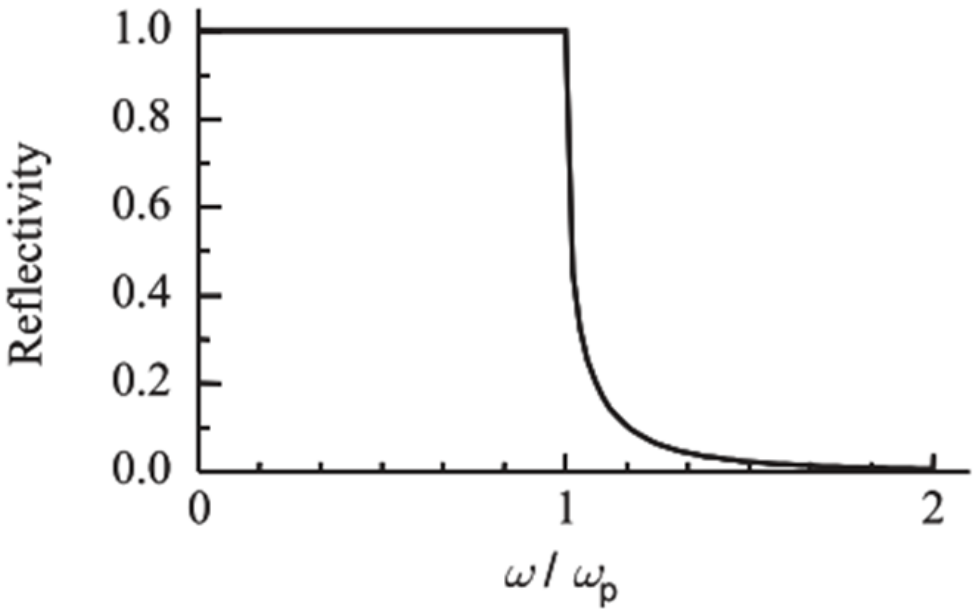


*Figure 2.6. Conducting solids are highly opaque below the plasma frequency due to the free electron gas compensating against the driving oscillating electric field of incident light with their own **D** field. Above this frequency the metals starts to become more transparent provided there are no additional interband transition deeper into the UV that anomalously interfere with the light-matter response.* [2]

Below the plasma frequency the conductor is very reflective as the free electrons will compensate for the oscillating electric field of incoming light, greatly attenuating its penetration depth into the metal. This is known as the skin effect and its implications are important to understanding how thin a metal film must be made for it to act as a semi-transparent layer in a multilayer stack FP resonator. Metals generally become opaque when their thickness is 100 nm or more. The window for semi-transparency is around 30 nm, depending on the metal used. The skin penetration depth, δ_{depth}, is given below [2].

$$\delta_{depth} = \sqrt{\frac{2}{\sigma_{DC}\omega\mu_0}}$$

(2 . 14)

Where σ_{DC} is the DC electrical conductivity of the conductor, and μ_0 is the magnetic permeability (normally taken to be the free space value, but in magnetic materials the relative parameter would be used) [2]. Above the plasma frequency many metals will start to become transparent since their resonant frequencies are centred well above the visible,

causing them to appear opaque to the human eye. Since the phenomenon of the plasma resonant frequency occurs for all materials governed by free electron gas behaviour, its manifestation can be seen across many spectrums. For example, in the Earth's upper atmosphere, UV and x-ray radiation form the sun ionises the gas molecules forming a very rarefied plasma known as the ionosphere with a resonant frequency in the MHz range (radio frequencies). Due to this plasma sheet layer, AM Radio with KHz frequencies can be reflected and travel over greater distances [10]. Transparent conducting oxides (TCOs) have a plasma frequency located in the NIR making them as "see-through" as glass is to the eye, while also carrying electrical current [11]. This enables the detection of touch on mobile LED display technology in smart phones, which routinely use ITO for their capacitive touch screens to function correctly without affecting the monitor brightness. See Fig.2.7 below.

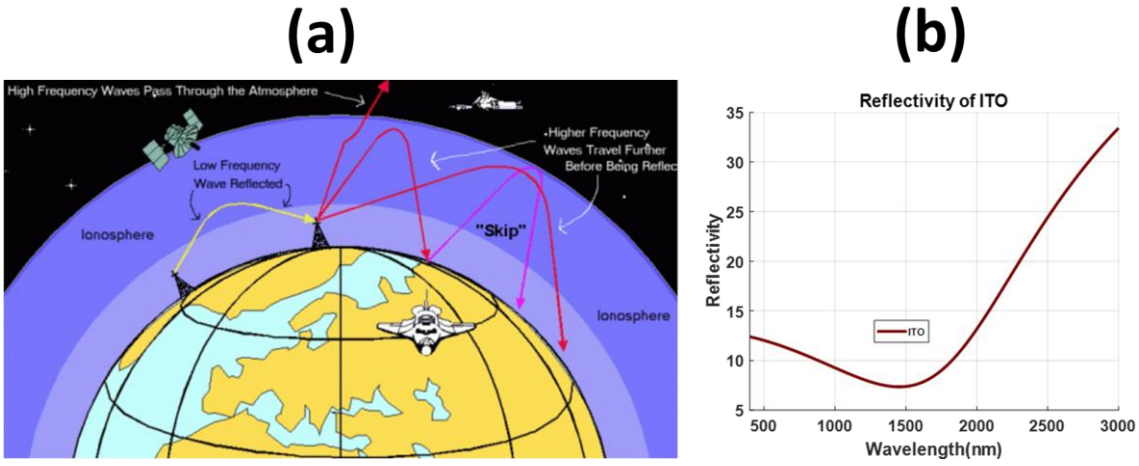


Figure 2.7. (a) Ionization of gas molecules in the upper atmosphere extends the range of radio communication towers due to the near perfect reflection at and below the plasma frequency [10]. *(b) The same process happens in solids like the TCOs where a plasma resonant frequency in the near to mid IR leads to total transparency in the visible spectrum. The free electrons cannot respond to optical light.* [10]

2.3.2 The Direct Interband Transition Model of Semiconductors

Semiconductors are very nuanced and the topic of much discussion and research in the literature. The story of the 20th century is the story of how humanity came to master it is understanding of these types of material for use in modern optics, electronics, and computing. The valence electrons of semiconductors are normally bound, but can be promoted to the conduction band if given enough energy to jump the gap bandgap, typically on the order of 0.5-4 eV [2]. This absorption is purely quantum mechanical and therefore no matter how bright a light is shone on a semiconductor; it will remain transparent unless the

individual photons themselves have enough energy to push an electron up hill. Absorption in the semiconductor will continue to increase as the energy of the incident photon increases above the band gap, with the main reason being that the electrons deeper within the valence can now be elevated up into the vacant conduction band [2]. This is why absorption in solid semiconductors is spectrally broadband and not extremely narrow like the response seen for the individual atoms constituting its makeup.

Semiconductors fall into two categories distinguished by their band structure: One, the direct bandgap semiconductors, and two the indirect gap. The former is easier to conceptually understand as it does not require the addition of quantised lattice vibrational modes, known as phonons, to help assist the interband transition process while simultaneously conserving momentum. See Fig.2.8 below.

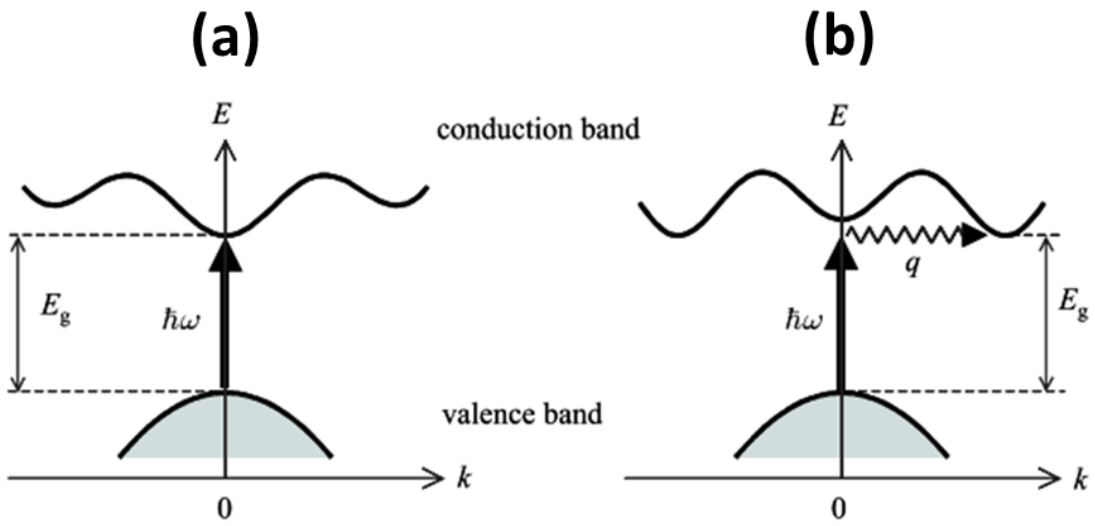


Figure 2.8. (a) A direct band gap transition occurs almost entirely in the energy domain given the negligible momentum $\vec{k}$ of the photon in comparison to the electron. (b) The minima of the conduction and the maxima of the valence band are separated in the momentum position of the Brillouin zone of the crystal lattice. For the Interbrand transition to proceed, additional momentum is needed from a lattice phonon vibrational mode, which have significantly higher $\vec{k}$ than the photon. [2]

The rate of direct transition, and therefore absorption of the incoming photon, is described quantum mechanically by Fermi's golden rule given below [2].

$$W_{i\to f} = \frac{2\pi}{\hbar}|M|^2 g(\omega)$$

(2 . 15)

Where $W_{i\to f}$ is the transition rate for the electron starting in the ground state and ending in the final state, $\hbar$ is the reduced Planck's constant, M is the matrix element which contains information on the effect of EM perturbation on the electron caused by the incoming plane wave light, and $g(\omega)$ is the density of states w.r.t angular frequency. In the semi classical approach, the matrix element M is governed using the Dirac notation, meaning the expectation value of the perturbed electron wavefunction is evaluated. Furthermore, the time dependence can be waived aside as it is included within the formulation of Fermi's golden rule [2]. M and the perturbation of the electron dipole H is given by the expressions below.

$$M = \langle f|H|i\rangle = \int \Psi_f^*(\vec{r})H(\vec{r})\Psi_i(\vec{r})\, d^3\vec{r}$$

(2 . 16)

$$H(\vec{r}) = eE_0\vec{r}\cdot exp(i\vec{k}\cdot\vec{r})$$

(2 . 17)

Where *i* is the initial state, *f* is the final state, Ψ_i is the electron wavefunction in the valence band, Ψ_f^* is the complex conjugate of the electron wavefunction in the conduction band, $\vec{r}$ is the position vector of the electron in the lattice, $\vec{k}$ is the momentum vector of the electron, E_0 is the intensity of the oscillating electric field perturbation, and e is the electron charge. Given the regular periodicity of the solid crystal, the wavefunction of the electron is a product of plane waves that fit discretely inside the crystal lattice and the envelope functions that relate back to Bloch functions [2]. The wave function is then normalised relative to the volume of the lattice unit cell V_{unit} to set the overall size of the physical system at play (unique to each material's lattice parameter and crystal structure). The electron wavefunction of the initial and final state is generalised below.

$$\Psi_{i/f}(\vec{r}) = \frac{1}{\sqrt{V_{unit}}} u_{i/f}(\vec{r}) \cdot exp(i\vec{k}_{i/f} \cdot \vec{r})$$

(2 . 18)

Where $u_{i/f}(\vec{r})$ is the initial or final envelope function with periodicity identical to the lattice periodicity. With algebraic substitution the M of the entire crystal can be computed and further simplified into a summation of all the individual unit cell contributions. Therefore, the value of M will differ considerably depending on the identity of the solid bring analysed. Moreover, assumptions can be made about crystal symmetry that simplify the description. Anisotropic semiconducting crystals would need additional considerations that would manifest in chiral behaviour w.r.t lights polarisation for example. For direct transitions $\vec{k}_{\mathrm{i}} = \vec{k}_{\mathrm{f}}$, simplifying the mathematics further [2]. This approximation can be made for optical light because $\vec{k}_{\mathrm{photon}} = \frac{2\pi}{\lambda}$, which is on the order of $10^7\ \mathrm{m}^{-1}$, while $\vec{k}_{\mathrm{electron}} \propto \frac{\pi}{\mathrm{a}}$, which is on the order of $10^{10}\ \mathrm{m}^{-1}$ for lattice constant a = 10^{-10} m. To fully evaluate $W_{i\to f}$ one must also determine $g(\omega)$. This factor accounts for the fact that there are not just two levels but a continuum of available states in either band. The use of the density of states can be found all throughout physics and is extremely useful for defining certain behaviour in condensed matter. It can even be used to describe the behaviour of electrons in exotic high energy environments like electron degenerate fermi gas holding the structure of a white dwarf together against its own self gravitational energy [12]. The equation for the density of states of an electron in a semiconductor in the momentum and energy domain are given below [2].

$$g(\vec{k}) = \frac{\vec{k}^2}{2\pi^2}, g(E) = \frac{1}{2\pi^2}\left(\frac{2m_{eff}}{2}\right)^{\frac{3}{2}} E^{\frac{1}{2}}$$

(2 . 19)

Where E is energy and m_{eff} is the electron effective mass. The effective mass is used to account for the difference in the motion of the electron in its confined lattice environment compared to being situated in the vacuum. It is essentially a correction factor constant to simplify the band structure description [2]. The final density of states can be found by

evaluating $g(E)$ at the initial and final state. From these relations it can be seen that the electrons will sit in a parabolic band. Moreover, when one works diligently through all the necessary maths, they will find that the density of states within the band is also very large, greatly increasing the absorption strength. This is also just another way of saying that the light-matter interaction is stronger in solids than in a rarefied medium like gas [2].

GaAs is the chief example of a direct band gap semiconductor with its band structure shown in Fig.2.9 below. The letters seen in the band-diagram are associated with points of high symmetry in the crystal lattice of GaAs. GaAs has a zinc blende crystal structure with two overlapping fcc sublattices [13]. Points X and L are at the Brillouin zone edges and all valence bands exist below the fermi level, meaning they are completely filled with electrons. Multiple bands will often exist because each band is associated with the continuum limit of the molecular HOMO bonding orbitals and the LUMO orbitals. The three valence bands for GaAs therefore correspond to the 4p shells involved in the covalent bonding of the compound while the single unoccupied conduction band originates from the 4s shell antibonding state. All interband transitions are direct given that the maxima all align at the Γ point of the Brillouin zone. The band gap is the distance from the highest maxima to the lowest minima which is directly overhead. In this case its value is 1.424 eV [2].

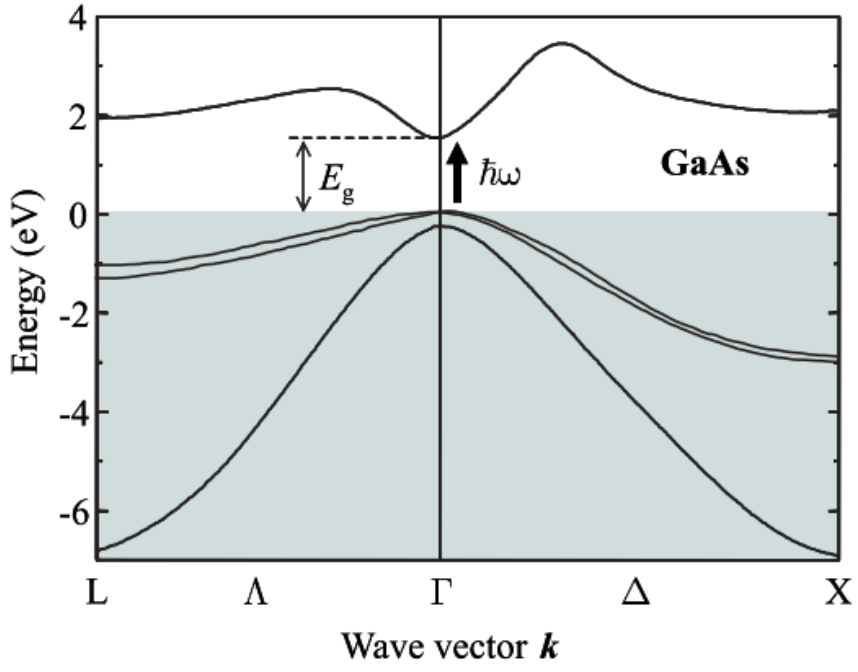


Figure 2.9. The shaded region is occupied with electrons under the Fermi level. All three valence band maxima are centred at the Γ point underneath the conduction band minima. Direct transitions are thus highly probable compared to indirect transition to distant minima at the band edges. [2]

Each one of the valence bands has its own associated effective hole mass. Holes will be discussed soon when covering excitons and their effects on the light matter interaction but suffice to say the heavier the effective mass the broader the parabolic dispersion is in momentum space. The transition rate can now be linked to a much more useful and experimentally observable parameter known as the absorption coefficient $\alpha(\omega)$. Naturally, this will vary w.r.t frequency as well, hence its dispersion. When the reduced mass of the electron and hole pair system, μ_{mass}, is considered in a semiconductor it can be shown that $g(\omega) \propto (\omega - E_g)^{\frac{1}{2}}$ [2]. Thus, it can be inferred that at, and above, the bandgap the absorption coefficient will also be proportional to the same factor [2]. To experimentally confirm this a direct bandgap semiconductor can be measured using the UV-Vis spectroscopy technique in and around the spectral vicinity of its bandgap [14]. With Beer-Lamberts law the coefficient can be linked to wavelength resolved intensity data and if the semiconducting transition model holds true the square of $\alpha(\omega)$ will increase linearly w.r.t incident photon energy. Figure 2.10 below show a graph of what this data looks like. A linear regression fit in the region above the band gap can then be used to determine the exact value of the band gap E_g [2].

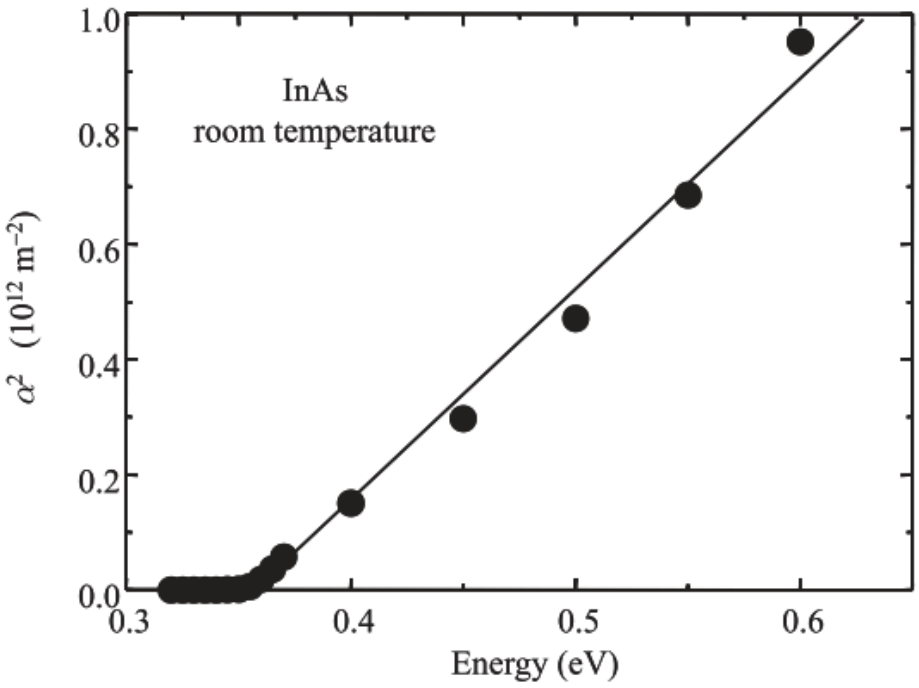


Figure 2.10. Using Beer-Lamberts law the absorption coefficient can be inferred form absorption intensity data gathered with UV-Vis spectroscopy. A linear region fit of spectral data can determine the value of the bandgap, which in this case in 0.35 eV for InAs. If the semiconductor being measured is thin film and semi-transparent, an ellipsometer is a more effective tool to infer α directly from the extinction coefficient of refractive index κ. [2].

2.3.3 The Indirect Interband Transition Model of Semiconductors

Grasping the physics of indirect band gap semiconductors is vital as some of the most important semiconducting materials to the industry fall into this category, notably Si and Ge which were made use of in thesis. The defining difference between the Optical bandgap of a direct bandgap material like GaAs and an indirect band gap material like Ge/Si is the shift of the conduction band minima away from the Brillouin zone centre in momentum space [2]. Thus, the only way to excite an interband transition is to use a second order indirect process like a photon-phonon absorption or a photon absorption and phonon emission event. The momentum and energy conservation equations for such a process is given below.

$$E_f = E_i + \hbar\omega \pm \hbar\Omega \,,\, \overrightarrow{k_f} = \overrightarrow{k_i} \pm \vec{q} \qquad (2.20)$$

Where E_i and E_f are the initial and finial energy state, $\hbar\Omega$ is the phonon energy, Ω is the phonon angular frequency, and $\vec{q}$ is the phonon momentum given by the crystal momentum that is on the order of about 10^{10} m^{-1}. Figure 2.11 demonstrates this through a comparison of the dispersion of the absorption coefficient of GaAs and Si [2].

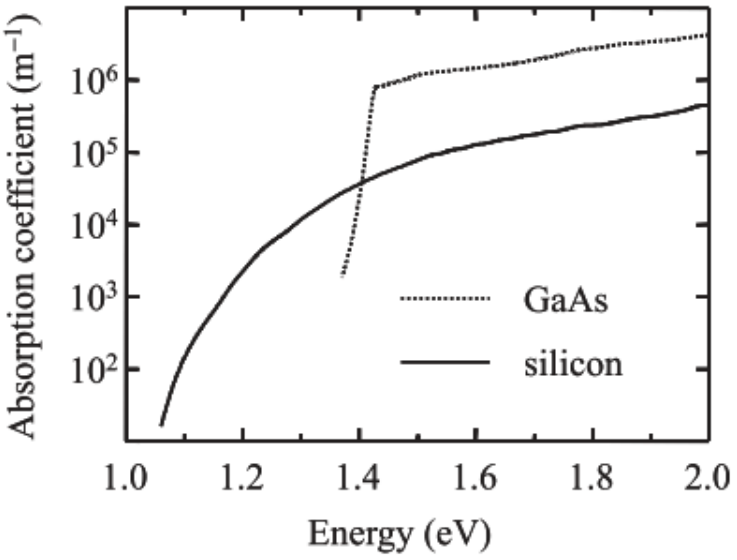


Figure 2.11. Even though the band edge of GaAs is higher than Si, the absorption quickly increases due to its high probability of direct transition just above the bandgap energy. Si can only access direct transition when photon energy is well above the bandgap. So before that point its absorption is rate limited by the indirect nature of the interband transition around the band edge. [2]

Fermi's golden rule can also be applied to the transition rates of indirect semiconductors to obtain the following absorption relation $\alpha(\omega) \propto (\hbar\omega - E_g \mp \hbar\Omega)^2$ [2]. At room temperature there are many vibrational modes within a solid crystal lattice meaning that phonon absorption and emission both contribute to the interband transition. The phonon emission channel will be the only available way to transition at very low temperature while at ambient room temperature the absorption channel will make an additional contribution. This temperature dependence manifests due to the underlying statistical mechanics governing the population of available thermally excited phonons in the lattice. The phonon population is proportional to the Bose-Einstein formula given below [2].

$$f_{BE}(\hbar\Omega) = \frac{1}{exp\left(\frac{\hbar\Omega}{k_B T}\right) - 1}$$

(2 . 21)

Where f_{BE} is the probability distribution of phonons at different energies at thermal equilibrium, k_B is the Boltzmann constant, and T is the temperature of the lattice. The indirect band gap lowers as the system gets hotter and more thermally excited phonons can participate to compensate for the low probability of the second order transition processes. This gives a characteristic tail around the band edge on α vs $\hbar\omega$ plots. Once the photon energy is high enough direct transitions can start to occur that will completely overshadow the indirect channel, creating absorption peaks in the spectral domain. See Fig.2.12 below [2].

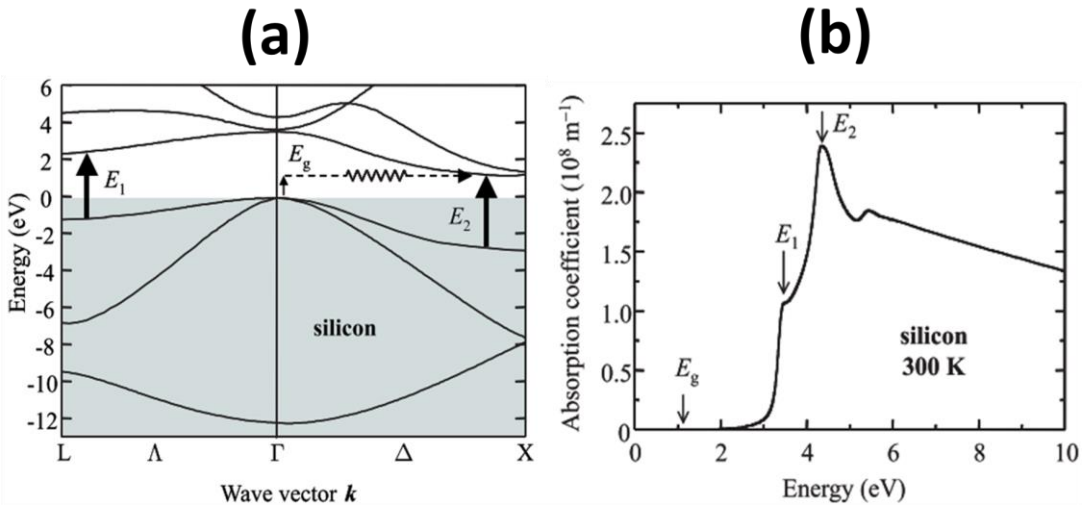


Figure 2.12. (a) The band structure of indirect bandgap material Si. Si begins to absorb using a second order photon-phonon mediated transition. Once the energy increase into the blue and then UV spectrum, the electrons deeper within the highest valence band can be promote directly to conduction band with no phonon needed. The parallel valence and conduction bands also enable electrons of many different momenta to directly transfer up, greatly increasing the density of states around energies E_1 and E_2. These points are called van Hove singularity critical points (b) As a result of this strong absorption peaks are seen to emerge above the bandgap at E_1 and E_2. Due to the strong light-matter interaction, the refractive index of Si is large. [2]

2.3.4 Description of Free Excitons in Semiconductors

Before moving on its important to note that these models for direct and indirect band gap semiconductors are somewhat idealised compared with a real-world material. Most discrepancies from the theory will only become more pronounced for a wide band gap, and small dielectric constant, materials. Wide band gap semiconductors must contend with the influence of strong coulomb attraction between electron-hole pairs on the absorption, specifically certain excited states known as Frenkel excitons with very tight binding radii on the same order of the lattice constant parameter [2]. Doped semiconductors, which are extremely important in the creation of modern transistors are also not closely looked at either, though in short, their absorption characteristics can contain features consistent with the free electron gas model. The dispersion of the interband transitions will begin to deviate for energies high above the bandgap as well due to the parabolic band approximation no longer holding true for the density of states parameter [2].

The coulomb attraction between the excited electrons in the conduction band and the associated hole in the valence band can form a bound neutral 2 particle system that is analogous to the hydrogen or positronium atom. The orbit of the electron around the hole is known as an exciton, and they are found in most crystals when excited above the band gap

[2]. Wannier-Mott excitons have large radius compared to the lattice constant parameter allowing them to act freely as they are very delocalised. Frenkel excitons on the other hand are tightly bound with binding energies on the order of 1 eV or more. They are commonly found in insulators or wide band gap semiconductors. These excitons are so localised that they can be thought of as excited states of individual atoms in the solid crystal lattice and are difficult to model theoretically [2]. See Fig.2.13 below.

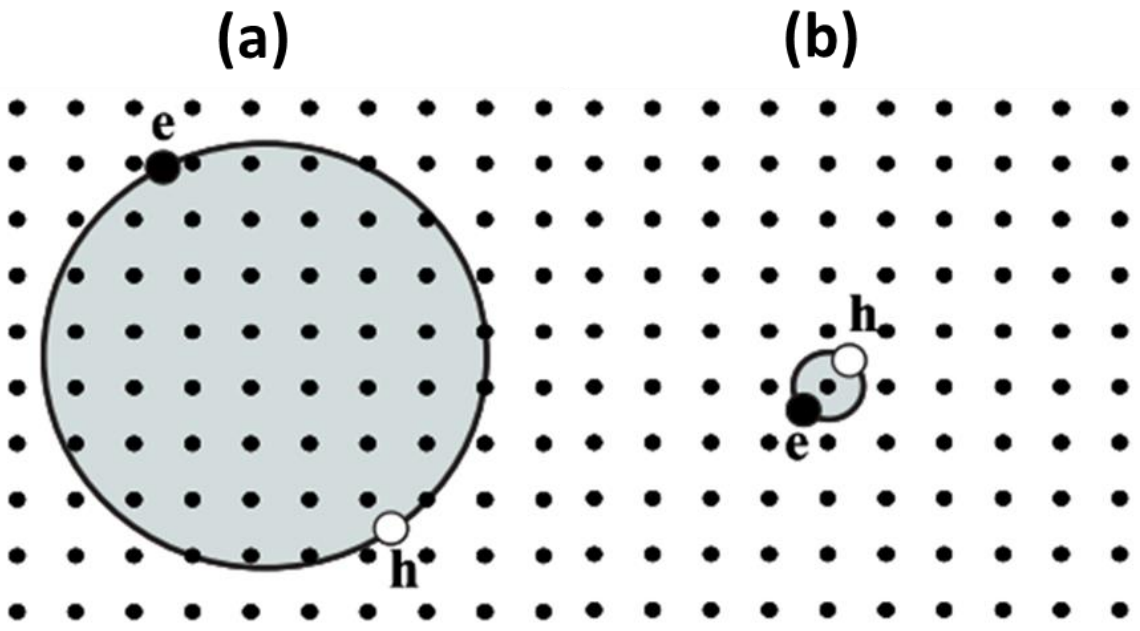


Figure 2.13. (a) A Wannier-Mott exciton delocalised across many different atoms in the crystal lattice. Binding energy is less than 0.1 eV, and they are not very stable at room temperature due to phonon interactions. (b) tightly bound Frenkel excitons with large binding energy more than 1 eV. They are momentarily stable at room temperature until they recombine in accordance with their coulomb attraction. Frenkel excitons are more akin to molecular excitations than the semi classical condensed matter approach used so far. [2]

Excitons are considered to be stable if their binding energy is larger than the maximum energy of the thermally excited phonon modes of the lattice, a value that is proportional to the Boltzmann factor $k_B T$. Therefore, most free excitons have little to no impact on the optical behaviours of semiconductors under standard laboratory conditions [2]. At cryogenic temperatures they can be stable for long enough to have a large measurable impact on the absorption spectrum. The Bohr hydrogen model is the simplest and most accurate way to model a free exciton as a weakly coupled electron-hole pair. See the expression below for the energy levels, $E(n)$, and size scale, r_n, of such as system [2].

$$E(n) = -\frac{\mu_{mass}}{\varepsilon_r^2 m_e} \cdot \frac{R_H}{n^2} = -\frac{R_X}{n^2}, \frac{1}{\mu_{mass}} = \frac{1}{m_e^*} + \frac{1}{m_h^*}$$

(2 . 22)

$$r_n = \frac{m_e}{\mu_{mass}} \varepsilon_r n^2 r_{Bohr}$$

(2 . 23)

Where m_e^* and m_h^* are the effective masses of the electron and hole respectively associated with the conduction and valence band, ε_r is the averaged static electric permittivity of the crystal medium between the electron and hole, R_H is the Rydberg energy of hydrogen equal to 13.6 eV, R_X is the Rydberg energy of the exciton, n is the principal quantum number, and r_{Bohr} is the fundamental hydrogen atom radius of 0.53 Angstroms. Unlike a hydrogen atom in the vacuum of space, the exciton is immersed in a high permittivity environment, with a reduced mass much smaller than the electron mass. For most semiconductors the radius of the fundamental exciton at state *n = 1* is on the order of 1-10 nm, encompassing many tens of thousands of atoms in the lattice [2]. Higher energy levels are more dispersed and incredibly weak.

Excitons are almost always seen in direct bandgap semiconductor transitions as its ideally the case that the excited electron have the same momentum as the hole it leaves behind [2]. Excitons associated with different electron and hole $\vec{k}$ are called dark excitons and phonon scattering is needed to drive their forbidden transition [15]. A more stringent requirement is that the electron and hole must have the same group velocity, v_g, given by the gradient of the band structure [2]. Since the gradient of the valence and conduction band is identical at the centre of the Brillouin zone for direct gap semiconductors, excitonic effects should be observable around the band gap. Excitons enhance broadband semiconductor absorption through elevating the interband transition rate $W_{i \to f}$ due to greater spatial overlap of the electron and hole wavefunctions [2]. Narrow lines associated with each energy level n also appear in the absorption spectra.

Free excitons are normally very weak at room temperature but in certain cases they can be greatly enhanced by different effects such as geometric confinement and weak dielectric screening of the medium between the electron and hole [16]. Both of these points hold true for ultrathin film TMDs like MoS_2 and WS_2 which exhibit very strong excitonic behaviour at room temperature and pressure [15]. The strong binding energy of the excitons in these 2D semiconducting materials, is on the order of 500 meV, enabling many kinds of excitonic transitions to possibly occur as revealed in Fig.2.14.

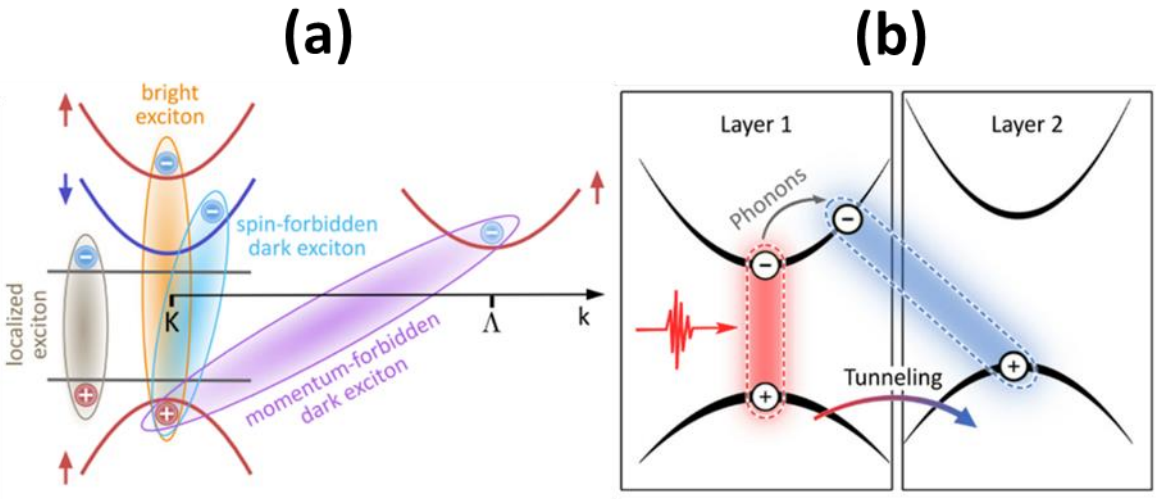


Figure 2.14 (a) The many different types of excitonic transitions that can occur in 2D thin film heterostructures. Localized excitons behave with atomic character while spin forbidden excitons require certain orientations of incoming light to be accessed. (b) Van der Waals heterostructures with strong coulomb interaction between electron-hole pairs enables tunnelling between adjacent layers, forming interlayer excitons. [15]

Light normally does not respond strongly to an applied external electric or magnetic fields. Only within matter can its properties be considerably changed towards some useful result. In the context of normal undoped bulk semiconductors, there is little that an external field can do to change the light-matter interaction as such fields will only make minor distortions to the crystal lattice structure. If however the excitons dominate the optical response then this opens up the possibility of large light-matter interaction change using field effects [2], [17]–[19]. DC electric fields can supress or enhance excitonic absorption peaks by pushing the electron-hole pair away from or closer to each other, depending on the bias direction. If the field is strong enough the exciton will be eliminated completely, which is an effect known as field ionisation where the electron and hole no longer find it energetically favourable to exist in bound state [2]. Figure 2.15 below shows the effect of field gating on

the real and imaginary components of the refractive index of direct bandgap semiconducting CVD grown monolayer MoS_2.

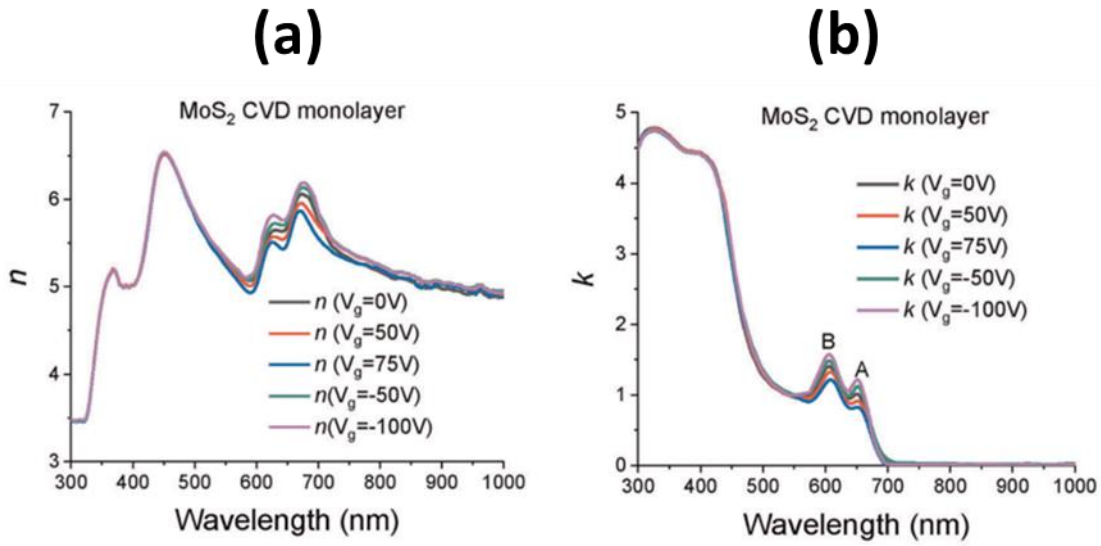


Figure 2.15. (a) The Real refractive index n of MoS_2. In this sample orientation the index is lowered for positive bias and increased for negative in agreement with the Kramers-Kronig relations. The C exciton peak can also be seen at just above 450 nm wavelength but external electric fields do not modify this excitonic transition (b) The absorption of the spin split bright exciton A and B is supressed with positive bias and enhanced with negative. [20]

2.3.5 Normal Dispersion Models of Transparent Dielectric Insulators

In insulating materials, the bandgap is so large that no electron can make it to the conduction band, even with thermal or optical excitation. Furthermore, since many insulators are also held together with ionic bonding, this means that the reflection capability of the bonding electrons are greatly reduced in comparison to metals that can be modelled with a dampened Lorentzian oscillator function with no restoring force [2]. However, the insulator medium, like almost all other solids, are still polarised by the incoming oscillating electric field of light meaning that the electric dipole image can be used to establish an understanding of the light-mater interaction.

No anomalous dispersion in the dielectric function will exists within the optical regime for most electrically insulating solids that are pure. Glass is the most famous example of a bulky insulating transparent dielectric. In the visible spectrum the complex permittivity coefficient ε_2 is taken to be 0 meaning no losses occur while light propagates through. Owing to the long history of using glass in prisms and lenses, there are many normal dispersion relations

which model the gentle increase in refractive index of transparent insulators w.r.t decreasing wavelength [3]. Relations, like the Cauchy equation, attempt to reproduce the dispersion curve of the insulator's optical response using the linear addition of higher order wavelength terms with Taylor series like character. See the expression below.

$$\varepsilon_1(\lambda) = \left(\frac{A}{\lambda^0} + \frac{B}{\lambda^2} + \frac{C}{\lambda^4}\right)^2$$

(2 . 24)

Where ε_1 is the real component of the optical dielectric function, A, B, and C are all experimentally derived parameters determined though a best fit. It is usually sufficient to fit without the C coefficient. Both the B and C parameters describe the curvature of the dispersion; larger values mean greater dispersion. A is analogous to the real component of the refractive index. Although this relation was derived experimentally through trial and error, one can use the electric dipole Lorentzian oscillator model to obtain the same result as shown below starting with the expression for an undamped dipole oscillator with restoring force resonant frequency ω_0 [2].

$$\varepsilon_1(\lambda) = 1 + \frac{\omega_p^2}{\omega_0^2 - \omega^2}$$

(2 . 25)

To establish a Taylor expansion approximation to this , two new terms a and b are defined as given below. Then with algebraic summation one can obtain a new definition for $\varepsilon_1(\lambda)$.

$$a = \frac{\omega}{\omega_0} \approx \frac{\lambda_0}{\lambda}, b = \frac{\omega_p}{\omega_0}$$

(2 . 26)

$$\varepsilon_1(\lambda) = 1 + \frac{b^2}{1 - a^2} \propto (\beta_1 a^0 + \beta_2 a^2 + \beta_3 a^4 + \cdots)^2$$

(2 . 27)

Where the beta coefficients are the Taylor expansion coefficient terms. Only the even power terms are considered because $\varepsilon_1(\lambda)$ is an even function of parameter a. Finally, this can be expanded upon, as shown below, to the λ^4 term in the region where $\omega << \omega_0$. That is the spectral region where no absorption exists (the normal dispersion condition).

$$\varepsilon_1(\lambda) = \left(\overbrace{\sqrt{b^2 + 1}}^{A} + \overbrace{\frac{b^2\lambda_0^2}{2\sqrt{b^2 + 1}}}^{B} \frac{1}{\lambda^2} + \overbrace{\frac{b^2(3b^2 + 4)\lambda_0^4}{8(b^2 + 1)^{\frac{3}{2}}}}^{C} \frac{1}{\lambda^4} + \cdots \right)^2$$

(2 . 28)

Transparent dielectric thin films are used some cases in this work to establish FP cavity resonance modes when placed between two mirrors to act as an optical spacer. Dielectric layers are also used as antireflection coatings to help couple light more easily into a device structure. Although SiO_2 (glass) is a very common insulator used in industry for applications like AR [21], the most useful dielectrics are the high index materials like TiO_2, Si_3N_4, HfO_2, Ta_2O_5, and ZnS which can all be modelled with the Cauchy equation relation. These high index thin films can confer FP devices with a superior angle independent optical response compared to lower index materials like silica, alumina, and MgF_2, as will be shown in chapter 6. Figure 2.16 below displays spectroscopic ellipsometry measurements of some of the thin film dielectrics deposited in this study with the magnetron sputtering system RF guns available.

A substrate material known to have significantly different refractive indices to the unknown dielectric film is usually chosen to make accurate measurement easier, due to the contrast between adjacent layers [3]. For that reason, Au or Ag metal backings are ideal. Higer index dielectrics can also stand out well against other transparent dielectric substrates like glass. Higher porosity in the sputtered dielectric thin films will have the effect of lowering their index closer towards that of air at $n = 1$. If the porosity is significant enough then the Cauchy model, which assumes homogeneity, cannot be used and alternative inhomogeneous

approaches such as graded index films and EMA layer mixtures, must be used [22]. It may also be the case that impurities or defects in the insulating solid could lead to some anomalous dispersion, requiring a hybrid approach (low-loss Lorentz oscillator) to describing the true dispersion.

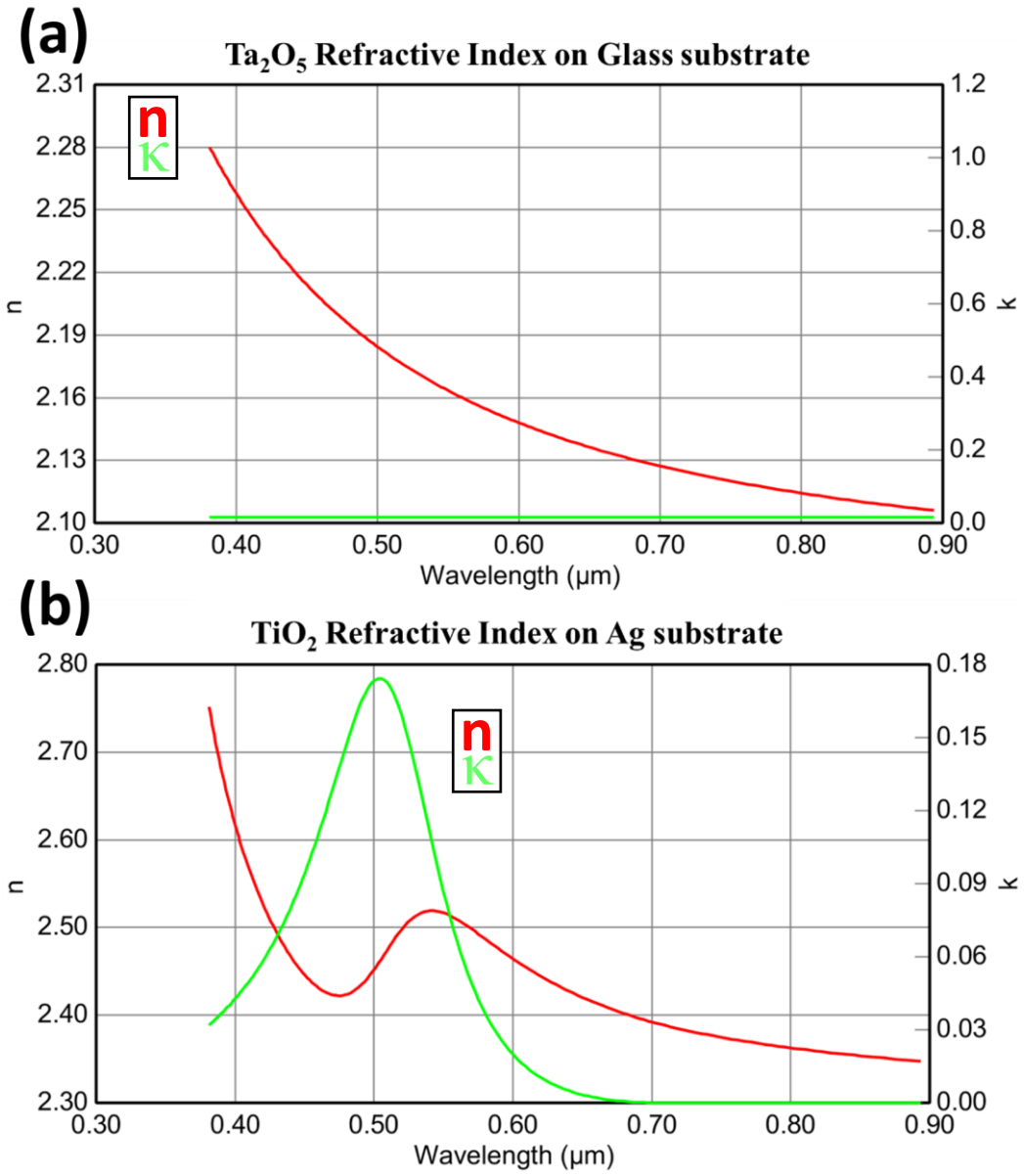


Figure 2.16. (a) The refractive index of Ta_2O_5 on Glass as measured by SE. There is no anomalous dispersion that modifies the real index n via the Kramers-Kronig relations. (b) The refractive index of TiO_2 on Ag as measured by SE. The band gap of TiO_2 is closer to around 400 nm yet nonzero absorption is seen below 700 nm wavelength due to potential impurities in the thin film. In this case a Tauc-Lorentz fit was used to model the dispersion. If the ellipsometer had a greater range with UV capability the rapid increase in absorption at the interband transition would cause the real refractive index to drop off toward unity.

With a firm grasp on understanding how to optically model conductors, semiconductors, and insulating materials, the physics of the light-matter interaction, which can now be

appreciated in the classical and quantum mechanical perspectives, will be covered in the context of wave interference in the planar ATF FP resonator stack structures created throughout the course of this thesis work.

2.4 Thin Film Wave Interference

2.4.1 Electromagnetic Wave Interference & the Principal of Superposition

In the introduction chapter it was shown that interference of optical waves inside a thin film FP resonator can create a strongly enhanced light-matter interaction. When generalised the interference principal can be applied across many different wave phenomena in the acoustic regime for sound and the ripples and waves seen across the surface of the ocean [1]. Why do waves interfere with each other in this manner? The answer is that waves can overlap one another in space and time, with the net result being equal to the linear vector addition of the different waves present in the system depending on their phase (position in their wave cycle). This is also known as the principal of superposition and it is an extremely important concept when trying to understand the behaviour light in thin film multilayer structures.

Through the principle of superposition, which drives wave interference, two or more waves of the same frequency can influence each other if they are in the same spatial region. This interaction can change the net amplitude of the wave at any given point depending on how the crests and troughs of the different individual waves line up. Using a two-wave system as the simplest model; when the crests of either wave line up in the time domain there will be constructive interference, and the total wave amplitude will increase with the linear vector addition of the individual wave amplitudes. When the troughs and crests overlap there is destructive interference [1]. The offset between the toughs and crests of opposing waves is given by a phase difference parameter. Thus, the most important factors for interference to appear are spatial overlap of at least two different waves, phase coherence of the waves that are superimposed, and frequency matching of the waves (high frequency waves do not interfere with low frequency waves) [1]. Figure 2.17 below illustrates how constructive interference occurs when two standing oscillating electric field waves are superimposed on one another in a cavity.

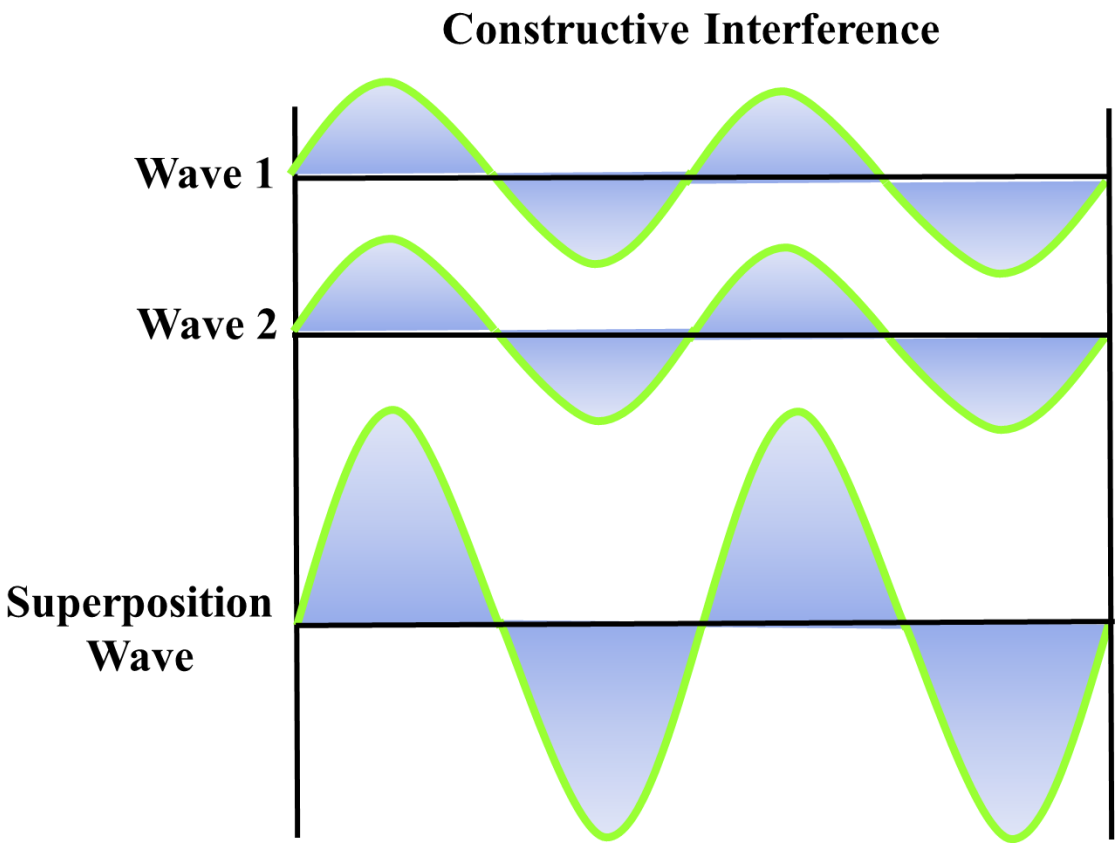


Figure 2.17. Constructive interference of two coherent standing oscillating electric field waves. They are both in phase meaning the final wave is twice as tall in amplitude as the initial two waves. Standing waves are meaningful to thin film optics as the electric field inside a stack structure will be a superposition of many optical fields that have reflected and refracted off the layer boundaries inside.

When considering thin film optics, the overlap of waves only becomes a relevant consideration to light's behaviour at thicknesses of around the coherence length *L* of the light-matter system. An expression for this coherence length is given below [23].

$$L = \frac{2ln(2)}{\pi} \cdot \frac{\lambda^2}{n_g \Delta\lambda}$$

(2 . 29)

Where $\Delta\lambda$ is the spectral width of the light source and n_g is the group refractive index of the medium the light has entered. This equation is very useful for understanding the size scale of the coherent regime of an optical device. In the thin film regime, the phenomenon of interference, which often manifests as fringes in the reflection and transmission intensity profiles, will typically only happen for stack structures that are below 1-10 µm in thickness

or less when white light is used [24]. For the thin film coatings looked at in the thesis, the stack thickness will typically never exceed 300-400 nm overall, making them subwavelength in scale. To increase the coherence length far beyond this size scale a very narrow bandwidth laser can be used to extend the coherence into the range of kilometres. Creating devices that utilise wave interference is also an effective way at increasing the sensitivity of optical measurements. This is because interferometers are very sensitive to the phase difference between two light waves. Even a minute shift in the optical path length of one of the waves can cause a large increase in detected signal strength if both waves are configured to initially be in a state of destructive inference. The gravitational observatory LIGO uses that sensitivity to detect neutron star and black hole mergers through the change in the laser optical path length of a kilometre long Michelson interferometer arm when a gravitational wave distorts and contracts space-time its vicinity [25]. See Fig.2.18 below.

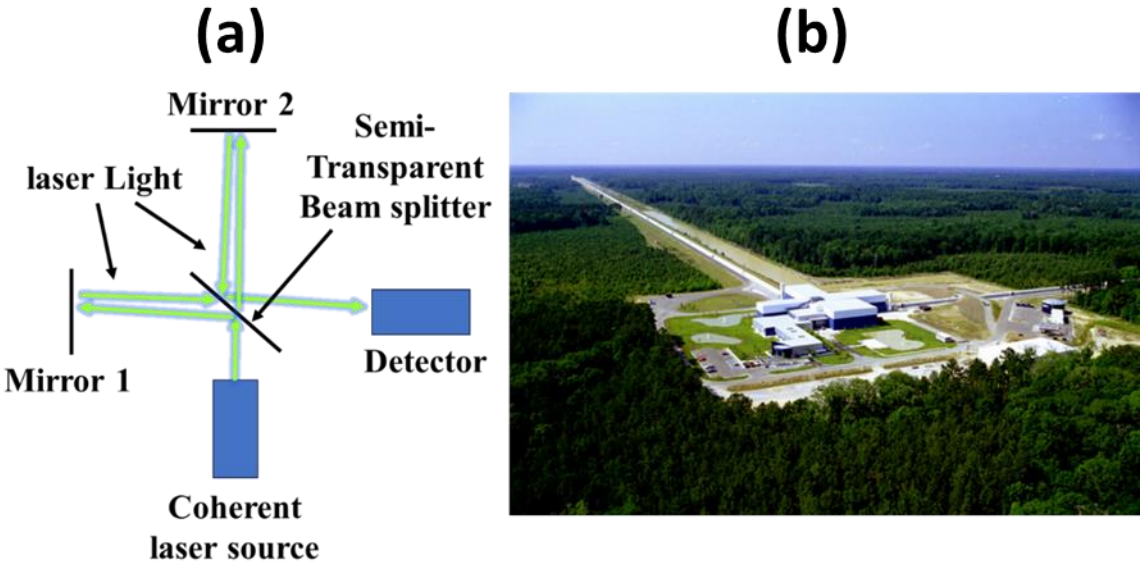


Figure 2.18. (a) A Michelson interferometer setup with slight angle offset between the travelling beams. When destructive interference occurs, there is no signal at the detector. A slight change in the optical path length of one of the arms causes the phase difference to change and thus a signal emerges. (b) An aerial image of LIGO Livingston in Louisiana. This detector uses interferometry on the scale of kilometres to detect gravitational waves generated by stellar collisions of massive objects. [25].

2.4.2 Electromagnetic Wave Interference in Multilayer Stack Structures

Gravitational wave detection is not the only way to take advantage of light's interference behaviour to enhance experimental measurement. It can also be availed of when seeking to accurately determine the optical characteristics of planar thin film layers with the spectroscopic ellipsometry technique [3], [22]. Specifically, by measuring the change in the

s-p polarisation state of the final reflected beam due to wave interference, boundary reflections, and internal refractions. Within these thin multilayer coating assemblies, the light will interfere with itself, and a unique spectrum will be produced once it re-emerges or passes all the way through. This is the basic concept of the thin film interference phenomenon that forms the back backbone of the FP resonator device physics. This process creates structural colour and can also potentially greatly increase the absorption of ultrathin film stacks with the right layer configuration geometry [26].

Put in in terms of light's electric field, the normal component of the oscillating electric field traveling in and out of the stack experiences constructive and destructive interference that is likened to the diagram shown in Fig.2.17. The innumerable back and forth reflections and refractions at internal layer boundaries will result in a superposition of internal optical waves that will act as standing waves in the steady state (constant illumination with no time dependence) [27]. These standing waves in each layer also interact and couple to one another (since they are physically connected and driving each other). The dispersion of the optical field of the illuminated sample reflected or transmitted into the human eye is therefore the result of this complex interplay of standing wave layer interference, and the ease at which light of any frequency can enter the thin film stack structure initially. See Fig.2.19.

The description of the multilayer coating system just given can be accurately modelled as the linear multiplication of back-and-forth standing waves associated with each layer and is called the general transfer matrix method (TMM) representation of electromagnetic media [27]. In a sense this matrix formalism is just an efficient way of calculating the countless applications of the Fresnel equations that are needed to chronicle light's entire journey through a multilayer construct. With the TMM, the predicted reflection, transmission, and absorption intensity of the total stack and each of its individual planar layers can be resolved if the layer thicknesses and refractive indices are also specified. These necessary input parameters are often defined by SE measurement [3]. Hence the order of operation for sample analysis is SE evaluation, TMM simulation in MATLAB, and UV-Vis spectroscopy of real fabricated multilayer builds. More details on the mathematics of the TMM will be given after covering thin film refractive index and some of the introductory concepts behind the TMM formalism.

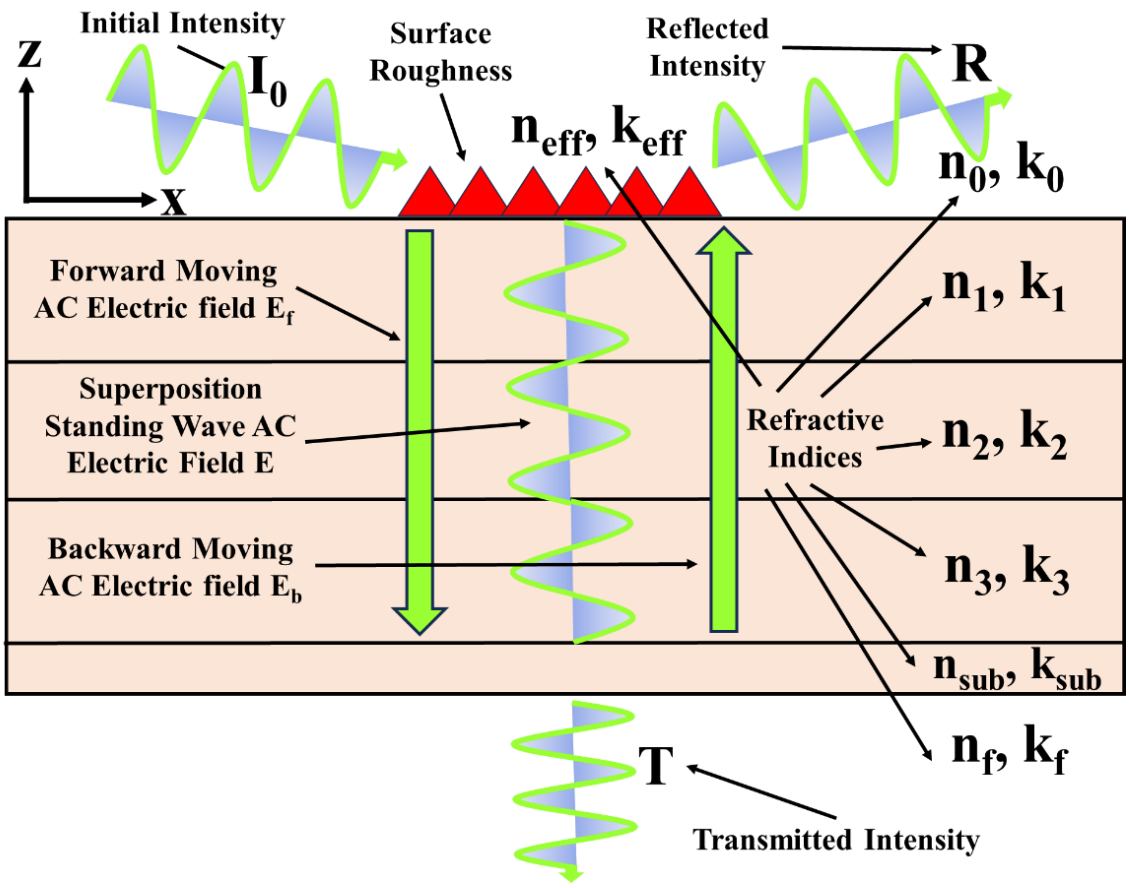


Figure 2.19. When light enters a multilayer stack structure a standing wave of forward and backward moving oscillating electric fields will be created in every layer by the principal of superposition. The interaction of the resultant standing wave for each layer in the steady state decides the ultimate optical response of the entire stack assembly. Ignoring scattering effects, the layer thicknesses and refractive indices, as determined by SE, can be used to predict the dispersion of the stack reflectivity, transmission, and absorption intensity. The effect of microscopic surface roughness can also be added as an additional EMA layer in the TMM optical model.

2.5 Transfer Matrix Method Theory

2.5.1 Ellipsometry Analysis & Interference Depending on Light's Polarisation

When carrying out SE analysis to begin characterising the light-matter interaction of a new sample, X-ray reflectometry (XRR) or Raman spectroscopy will often be pre-emptively used to determine thin film thickness by first principles. That allows the user to decouple the optical model correlations that may exist between the thickness t, real refractive index n, and extinction coefficient κ of one or more thin layers in the stack structure being viewed [3], [22]. SE is a powerful non-destructive method to quickly evaluate optical coatings that are 10's to 100's of nanometres thick, perfect for ATF devices deposited with magnetron sputtering. See Fig.2.20 below. Generally speaking, SE considers light to be an EM wave and the thin film solid to be described with any number of the matter-optical response

theories given in the description of conductors, semiconductors, and insulators further above. This methodology is known as the semiclassical approach, combining classical and quantum physics together in a sensible fashion to solve problems in physics.

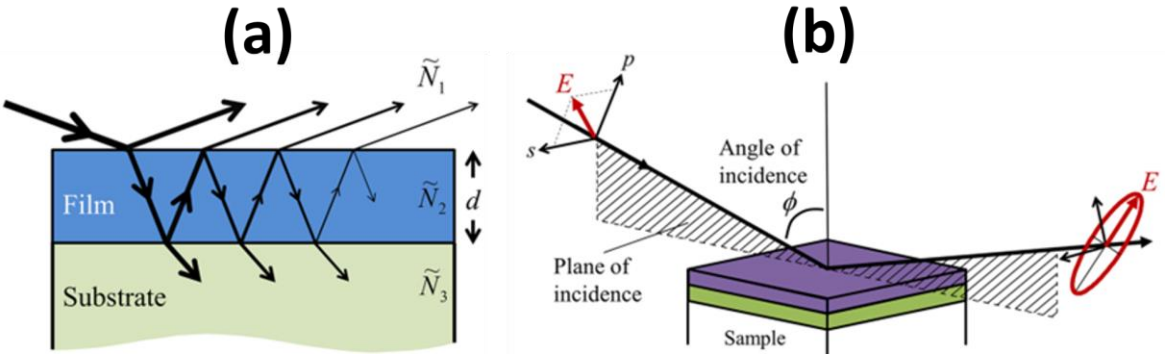


Figure 2.20. (a) A simplified view of the light matter interaction seen in Fig.2.19. The refractive index and thickness of the layers are unknown, but the data collected during SE can resolve those details based on the influence of wave interference. (b) SE specifically measures the change in the polarisation state of the reflected beam as compared to the incident beam. This change is very sensitive to optical field interference inside the stack being analysed, meaning fluctuations in incident intensity do not influence the output anywhere near as much as the accumulated phase delay of the light. In this regard SE is superior to light intensity-based experimental methods to measure the optical constants, especially in regards to thin films. [3]

Light's polarisation state is important to understanding the workings of SE. Considering only the electric field of light, the orientation of the oscillating electric field vector around the s-p plane can vary in time or remain fixed depending on the how much s-character or p-character it contains, as well as the phase difference between them. s and p refer to coordinate directions in the reference frame of the light beam and are perpendicular to the wave vector of the light [3]. See Fig.2.20(b) above. By convention, the s-axis is perpendicular to the incident plane, formed by the incident and specularly reflected beam, and the p-axis is parallel. Following from basic principles of vector mathematics it is possible to decompose the electric field of light with any orientation on the s-p plane into two separate vectors that point orthogonally from one another. If the incoming light is completely linearly polarised in the s direction, then the light is said to be s-polarised or TE light. A similar argument is made for p-polarisation named TM light.

If there are differences in the relative amplitudes of either polarisation state's contribution, or a phase delay between them, the resultant light will be circularly or elliptically polarised. These differences are induced by thin film wave interference because the way in which TE and TM light propagate, reflect, interfere, and refractive inside thin film samples can vary considerably w.r.t AOI [3]. Therefore, to make SE more effective the measurements are run with linearly polarised incident light at steep angles, typically in the vicinity of the Brewster angle as this is when TM light reflections off the surface is suppressed and the difference between TM and TE response is at its largest. See

Fig.2.21 below. As SE is only concerned with the change in state of the incident light's orientation, it does not need to worry about long calibration runs that UV-Vis requires to normalise the amount of incoming light onto the sample and photodetector. Another huge advantage of SE is that it also contains more data than a standard optical intensity measurement w.r.t wavelength, making each measurement more unique [3].

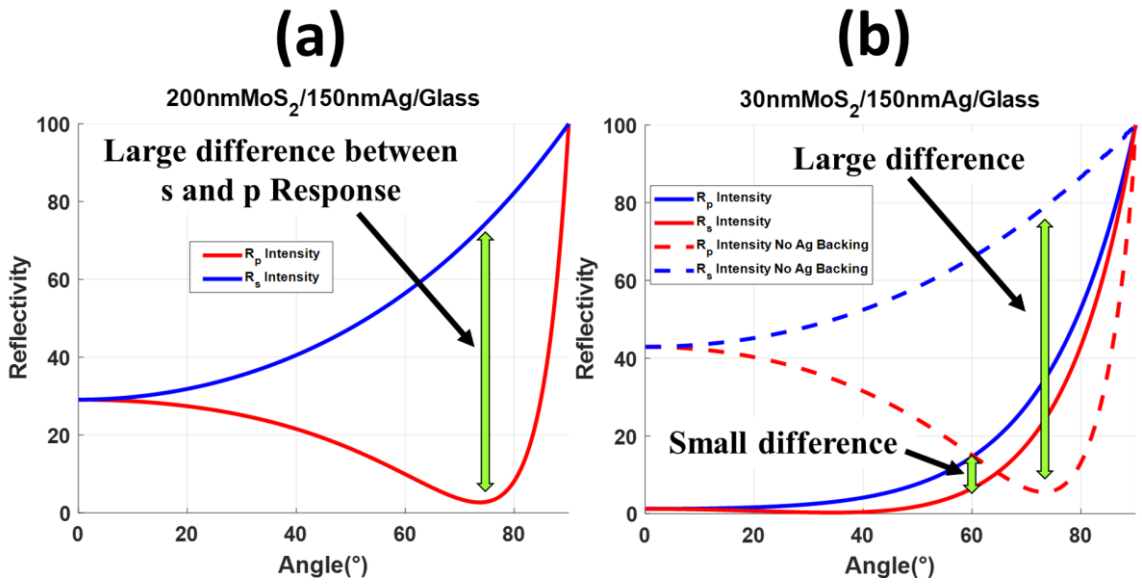


Figure 2.21. (a) For optically thick 200 nm MoS_2 there is a large difference in the reflectivity response of TE and TM polarised light at the Brewster angle minima. The pseudo ellipsometer parameters could be used in this case to easily solve for the complex refractive index of bulk MoS_2. (b) For 30 nm MoS_2 on 150 nm Ag the difference between TM and TE response is more subtle. Indeed, this says that the optical response of a zeroth-order FP resonator stack is polarisation independent (alongside its omnidirectionality). The contrast can be increased again by removing the opaque metal backing and creating an MoS_2/Glass interface instead. SE measurement of MoS_2 is preferably done on a transparent backing, which also comes with the additional benefit of normal transmission intensity weighting to help decouple thin film thickness from the indices.

The change in polarisation state is represented by two parameters $\Delta(\omega)$ and $\Psi(\omega)$. Δ is the change in the phase difference between TE and TM light before and after reflection off the multilayer sample, and Ψ is the inverse amplitude ratio of TM and TE light. These two parameters can be combined in the expression below known as the fundamental equation of ellipsometry $\rho(\omega)$ [3]. This ratio varies w.r.t the frequency of light ω.

$$\rho(\omega) = tan\big(\Psi(\omega)\big)e^{i\Delta(\omega)} = \frac{r_p(\omega)}{r_s(\omega)}$$

(2 . 30)

Where $r_p(\omega)$ and $r_s(\omega)$ are the reflection coefficients of p and s polarised light, respectively. The optical model attempts to fit the dispersion curve of this equation using a MSE best fit for inputs like layer index and thickness. SE is robust and versatile, capable of characterising both transparent and semi-transparent absorbing materials in the thin film regime. Therefore, SE allows one to derive the complex refractive index $\widetilde{N}$ of the material being looked at [3], [22]. The value of the index is very comprehensive as it completely describes the optical response of the material at a certain wavelength. By taking data across a broad wavelength range, the even more powerful dispersion relation $\widetilde{N}(\omega)$ can be found to completely describe all index values in the applicable spectral region. More in depth details and nuances on the SE technique are given in chapter 3.

2.5.2 Complex Refractive Index & Dielectric Function of Thin Film Materials

The complex refractive index of a thin film $\widetilde{N}$ is a generalisation of the normal refractive index n, that includes information on a material's absorbing capabilities as well. When light enters a denser medium some of it will undergo specular reflection (incident angle equals reflected angle) while most of the rest will refract inside of that material at an angle given by Snell's law. Some amount of light will also be lost to scattering effects that are elastic (Rayleigh) or inelastic (Raman) depending on surface and bulk conditions [3].

$$\widetilde{N_1} \cdot sin(\theta_i) = \widetilde{N_2} \cdot \sin(\theta_R)$$

(2 . 31)

Where $\widetilde{N_1}$ is the complex refractive index of the initial medium, $\widetilde{N_2}$ is the complex refractive index of the second medium, θ_i is the incident angle, θ_R is the angle of refraction. This angle shift occurs because the phase velocity of the denser medium is lower than air/vacuum [1]. The light that refracts into the denser medium can also be extinguished if said medium is absorbing. Metals are an example of a strongly absorbing material as most of them will appear opaque to the naked eye at 100 nm or more thickness in accordance with the skin depth attenuation relation. The general form of $\widetilde{N}$ is shown below.

$$\widetilde{N} = n \pm i\kappa$$

(2 . 32)

Where $i = \sqrt{-1}$ the imaginary number. For most materials, the $i\kappa$ component is given a positive sign based on standard sign convention for lossy dielectrics. A negative sign would result in optical gain which is associated with lasers. The normal refractive index n can be related to the speed of light in vacuum, c, and the speed of light in a medium, v, simply in the expression below [1].

$$n = \frac{c}{v}$$

(2 . 33)

The extinction coefficient is related to absorption and thus can be related to the absorption coefficient α that was brought up in the context of determining a semiconductor's bandgap, see sections 2.2.2 and 2.3.3 .

$$\kappa = \left(\frac{\lambda}{4\pi}\right)\alpha$$

(2 . 34)

For most situations, the amplitude of light will decrease exponentially as it propagates through a lossy material. If a material is thick enough, then all the light will be lost in a single pass through it. If it is very thin, then the dynamics are complicated by interference from back reflections within the absorbing medium, making a direct measurement of α through Beer lambert's law difficult [3], [14]. This is why SE is particularly useful as one can derive κ directly from the optical model fit, independent of α, and then use equation 2.34 to determine the best fit for α. This can be used to great effect for measuring the absorption characteristics and bandgap of ultrathin film semiconductor layers [28], [29].

A more direct way to know a materials response to light is to determine the complex dielectric function $\tilde{\varepsilon}$. This function has a real and imaginary component, ε_1 and ε_2, like the

complex refractive index. This dielectric function formulation is easier to work with then refractive index when fitting an optical model to real SE data using the Kramers-Kronig (KK) relations. A general expression for $\tilde{\varepsilon}$ is shown [3].

$$\tilde{\varepsilon} = \varepsilon_1 \pm i\varepsilon_2$$

(2 . 35)

Where ε_1 is the electric polarisability of the material which is a measure of how lights alternating electric field distorts the distribution of charge in the material, and ε_2 is a measure of how strong the absorption oscillator resonance is (larger denotes a stronger absorption). In metals absorption can be modelled with a Lorentz oscillator while in semiconductors a Tauc-Lorentz or Cody-Lorentz oscillator model are typically used to mark the rise in absorption above the band gap energy. The dielectric function and complex refractive index can be related directly to one another by the equation below.

$$\tilde{\varepsilon} = \tilde{N}^2$$

(2 . 36)

As a rule of thumb, the dielectric function parameters are more useful when discussing the light-matter interaction directly as its more closely linked to the oscillating electric field dynamics, while the refractive index parameters are useful for highlighting the optical density and material attenuation or opacity when penetrated.

2.5.3 Kramers-Kronig Relations

ε_1 and ε_2 are linked together through the all-important Kramers-Kronig (KK) relations that physically bind them together. They are bound because in complex analysis the real and imaginary elements of any complex functions are related to one another through the integral relation shown below [2], [3].

$$\varepsilon_1(\omega) = 1 + \frac{2}{\pi} \cdot P \int_0^{\infty} \frac{\omega' \varepsilon_2(\omega')}{\omega'^2 - \omega^2} \, d\omega'$$

(2 . 37)

$$\varepsilon_2(\omega) = \frac{-2\omega}{\pi} \cdot P \int_0^{\infty} \frac{[\varepsilon_1(\omega') - 1]}{\omega'^2 - \omega^2} \, d\omega'$$

(2 . 38)

Where *P* is the principal part of the integral, ω' is the oscillator pole resonant frequency, and ω is the photon frequency of the incoming light. When using the KK relation to determine the complex dielectric function of an unknown material, it is normally the case that the oscillator ε_2 is defined first and subsequently the dispersion of ε_1 is calculated from the above integral. Thus, the shape of the ε_1 curve is accurately reproduced. Eq.2.37 resolutely produces an accurate $\varepsilon_1(\omega)$ curve but the absolute magnitude of the true ε_1 may be offset due to the influence of other factors like band dispersion [3]. This is commonly the case with metals where the bound electrons can influence the behaviour of the free electron gas at the top of the valence band, as explained in the outline of how conductors interact with light above. This offset parameter is known as $\varepsilon(\infty)$ and it is commonly given as a constant over a certain wavelength range. Figure 2.22 demonstrates this response as well as the characteristic wiggles seen in ε_1 around ε_2 absorption poles. These wiggles are the anomalous dispersion and the larger the absorption is the greater the distortion. The KK relations will almost always hold true for lossy media with anomalous dispersion. In cases where dispersion is normal only the use of KK functions is overkill as no losses are occurring near the spectral domain being looked at. Other simpler models should be availed of like the Cauchy relation, which is the Taylor expansion approximation of the Lorentz oscillator electric-dipole function when located far away from its absorption pole resonant frequency.

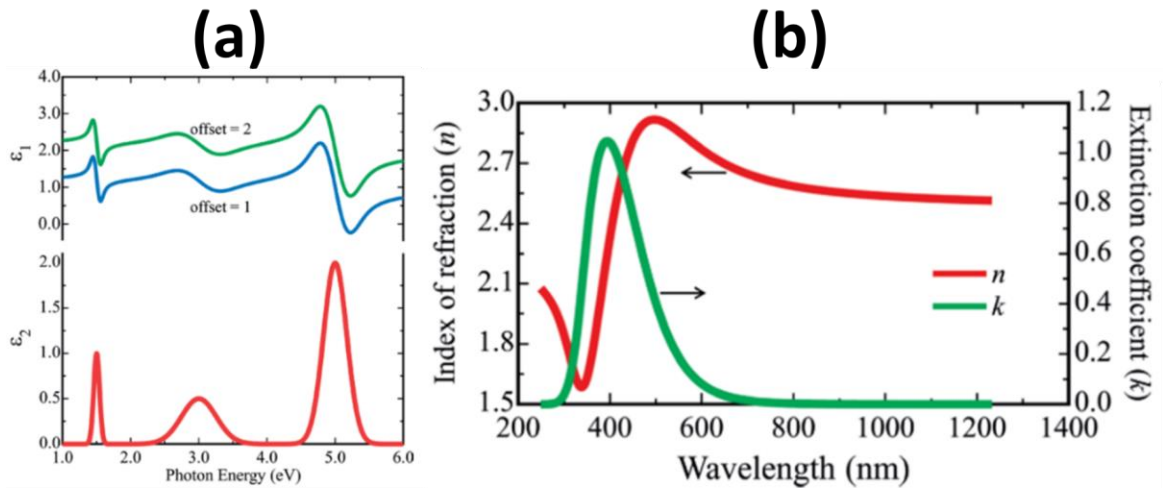


Figure 2.22. (a) The taller and narrower the absorption poles the greater the change in ε_1. Broader oscillators will produce less distortion in ε_1. The energy off-set correction factor for the influence of the electronic band structure allows the magnitude to be matched. (b) When converted into refractive indices, the presence of the absorption pole causes anomalous dispersion in n to appear making it decrease rapidly, when before it was increasing with higher photon energy. [3]

2.5.4 Fresnel Equations & the Matrix Generalization to Multilayer Thin Film Stacks

With the thin film thickness and refractive indices well understood, the multilayer stack optics can be simulated using the continual application of the Fresnel equations that detail light's reflection and transmission coefficient amplitude and phase at an interface in terms of refractive index, AOI, and light polarisation state [27]. These conditions follow directly from the Maxwell equations in which the tangential components of the $\vec{E}$ field are continuous across a dielectric material boundary. The Fresnel equations are shown below in generalised form at a boundary between medium 1 and 2 [3].

$$r_{s,12} = \frac{E_s^{refl}}{E_s^{inc}} = \frac{\widetilde{N_1}cos(\phi_1) - \widetilde{N_2}cos(\phi_2)}{\widetilde{N_1}cos(\phi_1) + \widetilde{N_2}cos(\phi_2)} \quad (2.39)$$

$$r_{p,12} = \frac{E_p^{refl}}{E_p^{inc}} = \frac{\widetilde{N_2}cos(\phi_1) - \widetilde{N_1}cos(\phi_2)}{\widetilde{N_2}cos(\phi_1) + \widetilde{N_1}cos(\phi_2)} \quad (2.40)$$

$$t_{s,12} = \frac{E_s^{tran}}{E_s^{inc}} = \frac{2\widetilde{N_1}cos(\phi_1)}{\widetilde{N_1}cos(\phi_1) + \widetilde{N_2}cos(\phi_2)}$$

(2 . 41)

$$t_{p,12} = \frac{E_p^{refl}}{E_p^{inc}} = \frac{2\widetilde{N_1}cos(\phi_1)}{\widetilde{N_1}cos(\phi_2) + \widetilde{N_2}cos(\phi_1)}$$

(2 . 42)

Where r_p and r_s are the reflection coefficients for p and s polarised light, t_p and t_s are the transmission coefficients for p and s polarised light, ϕ_1 is the incident angle, and ϕ_2 is the transmitted refracted angle. If there is only one interface such as an air-glass system, the Reflection R and transmission T intensities are evaluated by the square of the coefficients.

$$R_p = \frac{\left|E_p^{refl}\right|^2}{\left|E_p^{inc}\right|^2} = \left|r_{p,12}\right|^2 , R_s = \frac{\left|E_s^{refl}\right|^2}{\left|E_s^{inc}\right|^2} = \left|r_{s,12}\right|^2$$

(2 . 43)

$$T_p = \frac{\left|E_p^{tran}\right|^2}{\left|E_p^{inc}\right|^2} = \left|t_{p,12}\right|^2 , T_s = \frac{\left|E_s^{tran}\right|^2}{\left|E_s^{inc}\right|^2} = \left|t_{s,12}\right|^2$$

(2 . 44)

When the only considerations are one interface in the bulk regime, these analytical equations are very handy to use. Unfortunately, the innumerable back and forth reflections interfering with each other inside a multilayer assembly can only be handled quickly with a numerical approach unless the design is simple enough that a complex analytically expression can be calculated, and even in the case of the latter it is more practical to use brute force numerical

methods given how powerful modern computers are. To achieve this, the general transfer matrix method approach, written in the MATLAB development environment, is used [27].

As mentioned in Fig.2.19 on p.81, When light enters a complicated multilayer stack structure a standing wave is created in each layer by the superposition of forward and backward traveling oscillating electric fields. By considering that there are N layers in the thin film assembly, light enters as a plane wave from a semi-infinite layer (typically air) and propagate through the structure until it re-emerges back on top as a reflection and/or all the way through to the end as a transmitted beam (once again back into the same medium with semi-infinite extent). Figure 2.23 demonstrates this mathematically in terms of the tangential components of the incoming electric field.

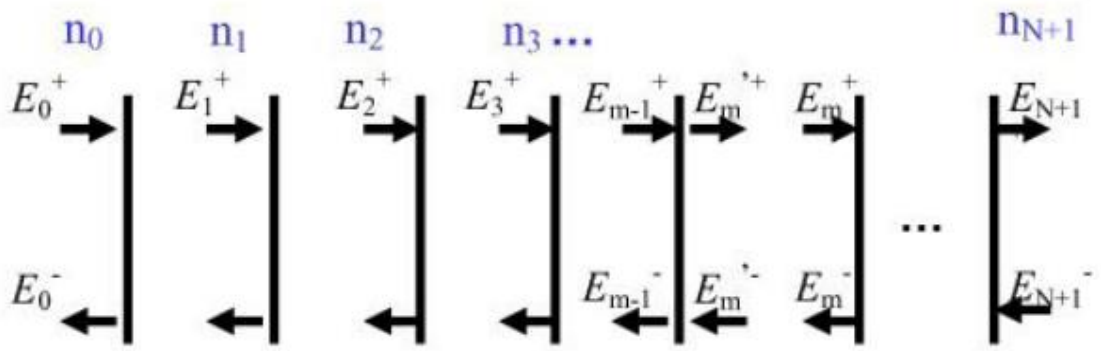


Figure 2.23. Considering only the tangential components of the oscillating electric field, light enters from air, medium zero, into a multilayer stack structure with N layers with forward '+' direction. Light will reflect backward with '-'direction and/or will transmit all the way through to layer N + 1 which is typically the same medium as the semi-infinite zeroth layer. The field amplitude and phase delay of each layer is affected by the interface on either side as well as the light's propagation through the layer. [30]

Electric fields travelling forward are labelled with the "+" symbol while backward traveling waves are given the "-" sign. Bearing in mind layer $(m-1)$ and the m^{th} layer for the purpose of algebraic generalisation, the field on either side of the interface can be related as shown below.

$$\begin{pmatrix} E_{m-1}^{+} \\ E_{m-1}^{-} \end{pmatrix} = I_{m-1,m} \begin{pmatrix} E_{m}^{+} \\ E_{m}^{-} \end{pmatrix}$$

(2 . 45)

Where $I_{m-1,m}$ is a dynamic matrix that describes how light's amplitude and phase behaves at the interface and is analogous to the bulk regime Fresnel reflection and transmission expressions, determining how light reflects back or refracts and transmits forward into the adjacent layers [27]. $I_{m-1,m}$ can be written like so in terms of the Fresnel coefficients that are calculated from equations 2.39 – 2.42.

$$I_{m-1,m} = \frac{1}{t_{m-1,m}} \begin{pmatrix} 1 & r_{m-1,m} \\ r_{m-1,m} & 1 \end{pmatrix}$$

(2 . 46)

When working with p or s polarised light the correct Fresnel equations must be used at this step to get the matrix elements of $I_{m-1,m}$ right. To include the effect of wave propagation into this matrix description, another parameter P_m is needed [27].

$$P_m = \begin{pmatrix} e^{-i\delta_m} & 0 \\ 0 & e^{i\delta_m} \end{pmatrix}, \begin{pmatrix} E_m'^{+} \\ E_m'^{-} \end{pmatrix} = P_m \begin{pmatrix} E_m^{+} \\ E_m^{-} \end{pmatrix}$$

(2 . 47)

Where δ_m is the phase shift due to propagation through layer m, the prime symbol in $E_m'^{+}$ denotes the field at the left side of the m^{th} layer, and the field at the right side has no additional prime symbol. An expression for propagation phase delay is given below.

$$\delta_m = 2\pi k \widetilde{N_m} d_m cos(\phi_m)$$

(2 . 48)

Where k is the wave number of the light, $\widetilde{N_m}$ is the complex refractive index of the m^{th} layer, d_m is the m^{th} layer thickness, and ϕ_m is the angle of refraction in the m^{th} layer. When all these matrix transformations are combined, they can be repeatedly applied from one layer to the next in sequential order, forming a large product of $N + 1$ matrices that collectively generate a 2 x 2 system matrix T_{Grand} that describes the optical response of the entire stack. The generalised form of this matrix multiplication is given below [30].

$$\begin{pmatrix} E_0^+ \\ E_0^- \end{pmatrix} = I_{0,1} P_1 I_{1,2} P_2 I_{2,3} \cdots P_N I_{N,N+1} \begin{pmatrix} E'^+_{N+1} \\ E'^-_{N+1} \end{pmatrix}$$

(2 . 49)

$$\begin{pmatrix} 1 \\ r_{stack} \end{pmatrix} = \overbrace{\begin{pmatrix} T_{Grand_{11}} & T_{Grand_{12}} \\ T_{Grand_{21}} & T_{Grand_{22}} \end{pmatrix}}^{T_{Grand}} \cdot \begin{pmatrix} t_{stack} \\ 0 \end{pmatrix}$$

(2 . 50)

Finally, the Fresnel coefficients r_{stack} and t_{stack} can be found with the following relations of the matrix elements of system transfer matrix T_{Grand} [27].

$$r_{stack} = \frac{E_0^-}{E_0^+} = \frac{T_{21}}{T_{11}}$$

(2 . 51)

$$t_{stack} = \frac{E'^+_{N+1}}{E_0^+} = \frac{1}{T_{11}}$$

(2 . 52)

The predicted reflection and transmission, R and T, intensity of the multilayer stack can be calculated trivially by squaring the coefficients. Absorption intensity is then inferred from the conservation of energy $A = 1 - R - T$. To corroborate the accuracy of the planar thin film model, and the optical indices and thickness derived from SE, the simulated spectra can be compared with UV-Vis measurement across the same spectral domain.

2.5.5 Corrections & Additions to the Transfer Matrix Formulation

The TMM approach presented so far is idealised for multilayer stack structures where light remains coherent throughout. That is the optical path length of the systems does not closely

approach the coherency length L. This is a suitable picture for ultrathin film samples with opaque metal backings as back reflections from deep within the substrate will never reach the surface to interfere with the light. If, however, the substrate backing is transparent, one must contend with the difficulty of incoherence and introduce a new strategy to the TMM model to account for its presence.

The phenomenon of incoherence will most of the time manifest as very rapid oscillation fringes in the predicted spectra of the sample. They are an artifact of the assumption of coherency in the system and will not appear when measuring the stack structure with UV-Vis spectroscopy [24]. To account for this the addition of an extra phase delay parameter, φ , to the propagation phase delay δ_m can be done as shown.

$$\delta_m = 2\pi k \widetilde{N_m} d_m cos(\phi_m) + \varphi$$

(2 . 53)

This new parameter varies randomly on time scales much smaller than the measurement time of a CCD photodetector. Thus, the UV-Vis spectra will be time averaged and smooth compared to the rapidly fluctuating steady state TMM prediction. Although there are methods to eliminate the undesirable fringes involving the use of a modified system transfer matrix that has squared elements [27], by far the simplest way to account for the effects of incoherence caused by a thick glass substrate is the averaging of many different phase offset spectra together. This is most notably done using an arbitrary randomly generated number of them. Phase averaging in this way works because a collection of sine wave with randomised phase will average out to a constant value [24]. The random averaging method is computationally expensive and converges very slowly as shown in Fig.2.24(a) below.

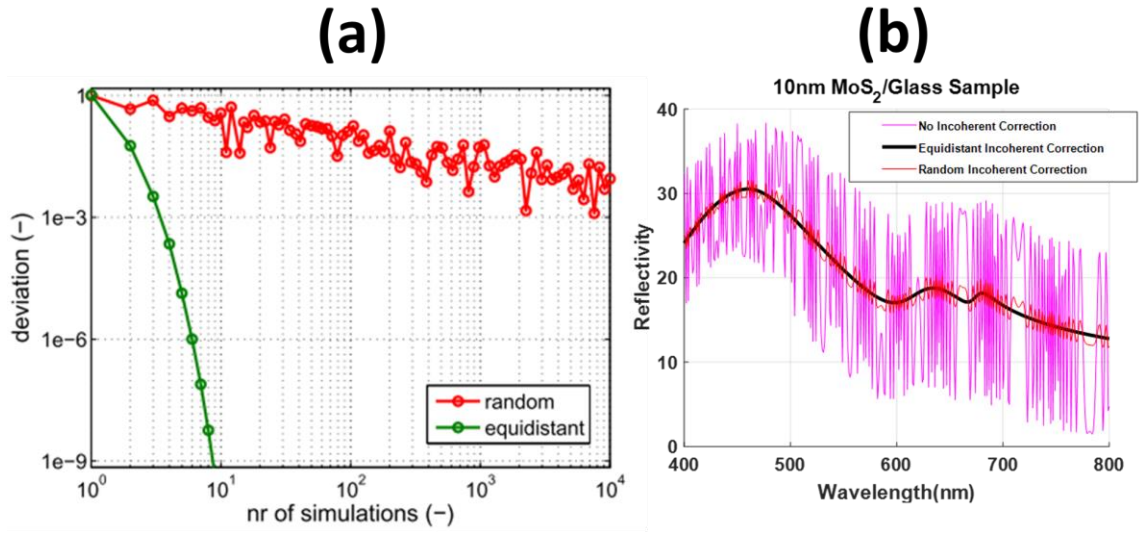


Figure 2.24. (a) Both random and equidistant phase averaging are normalised to unity by definition when N = 1. The randomised approach converges very slowly. Even above 10^3 offset inputs, the error is still on order of 1 % which is certainly visually noticeable. In contrast the equidistant approach has converged very rapidly by the 10^{th} input. [24] *(b) A comparison of the spectra predicted for 10 nm MoS_2 on bulky glass substrate when (i) no incoherence correction is used, (ii) random incoherence correction is used, and (iii) equidistant incoherence correction is used. The equidistant approach is by far the most efficient and accurate phase averaging technique for these kind of thin film samples.*

Instead of using randomised phase inputs to approximate the time averaged response, a phase vector of N elements between 0 and 2π with equidistant spacing can be used. Each element in the vector array eliminates a corresponding higher order reflection term generated by the back reflections from the bottom of the transparent incoherent layer [24]. Since successively higher order reflection terms have exponentially lower intensity contribution to the overall spectra, this equidistant phase offset method efficiently eliminates the dominant contributions of the lower order terms, rapidly converging the TMM predicted spectra towards the time averaged smooth experimentally measured result. This averaging also preserves the wave interference effects of the thin film stack section as it only applies directly to light in the bulky incoherent layer. Equidistant phase averaging converges extremely rapid as seen in Fig.2.24(a), and after only 10 phase inputs used (meaning the elimination of 10 reflection order terms) the deviation error between the true and incoherent correct value is on the order of one in a billion! Figure 2.24(b) demonstrates the power of this result for 10 nm MoS_2 on glass. Calculations that would normally require 10^2 – 10^3 random phase inputs to get a visually errorless smooth spectra now only require 10 equidistantly spaced phase inputs to achieve far superior results. Doing away with random number generation and large for-loops is a great boon for speeding up computation.

To finish off this overview of the TMM, it is also possible to calculate the layer resolved absorption of a thin film multilayer stack by making use of the change in the Poynting vector $\Delta\vec{S}$. The Poynting vector is an incredibly useful concept in physics that represents directional energy flux. When applied to light it is the directional power flow of the EM wave [1]. It follows directly from Poynting theorem which states that the difference in EM energy entering and leaving a region is equal to the energy dissipated in that region. This fact can be used to find out how much light is absorbed in the m^{th} thin film layer by calculating the difference in $\vec{S}$ upon entering the m^{th} and layer *(m + 1)* [31]. Using the tangential electric field components, the surface normal component of the Poynting vector at the *(m - 1)* boundary interface is written below, normalised to incident power for s and p polarisation.

$$\vec{S}_{m_s} \cdot \hat{z} = \frac{Re\left[\widetilde{N_m} cos(\phi_m)(E_m'^{+^*} + E_m'^{-^*})(E_m'^{+} - E_m'^{-})\right]}{Re\left[\widetilde{N_0} cos(\phi_0)\right]}$$

(2 . 54)

$$\vec{S}_{m_p} \cdot \hat{z} = \frac{Re\left[\widetilde{N_m} cos(\phi_m)^*(E_m^+ + E_m^-)\left(E_m'^{+^*} E_m'^{-^*}\right)\right]}{Re\left[\widetilde{N_0} cos(\phi_0)^*\right]}$$

(2 . 55)

Where the '*' denotes the complex conjugate. $\Delta\vec{S}$ is the absorption of light in the m^{th} layer as normalised to incident intensity, and its general form is detailed below.

$$\Delta\vec{S}_{s/p} = \vec{S}_{m_{s/p}} - \vec{S}_{m+1_{s/p}}$$

(2 . 56)

Ascertaining layer resolved absorption can be important to understanding which absorbing layers in a stack structure have the greatest impact on the light-matter interaction. For example, an ideal thin film solar absorber PV cell should preferentially want to concentrate as much of the light in the semiconducting absorbing layer to generate electron-hole pairs through interband transition. Any radiation lost in the complementary supporting layers like Ag or Au back metal reflectors is wasted as heat that raises the PV cell temperature. See

Fig.2.25 below. In chapter 6, central lossy broadband absorber device structures can use clever stack design to focus and trap the optical field into an ultrathin lossy dielectric like Cr or Ge [32]. Characterisation and optimisation of these multilayer structures require an understanding of layer resolved absorption to demonstrate that the central lossy layer performs similarly to a much thicker absorbing layer.

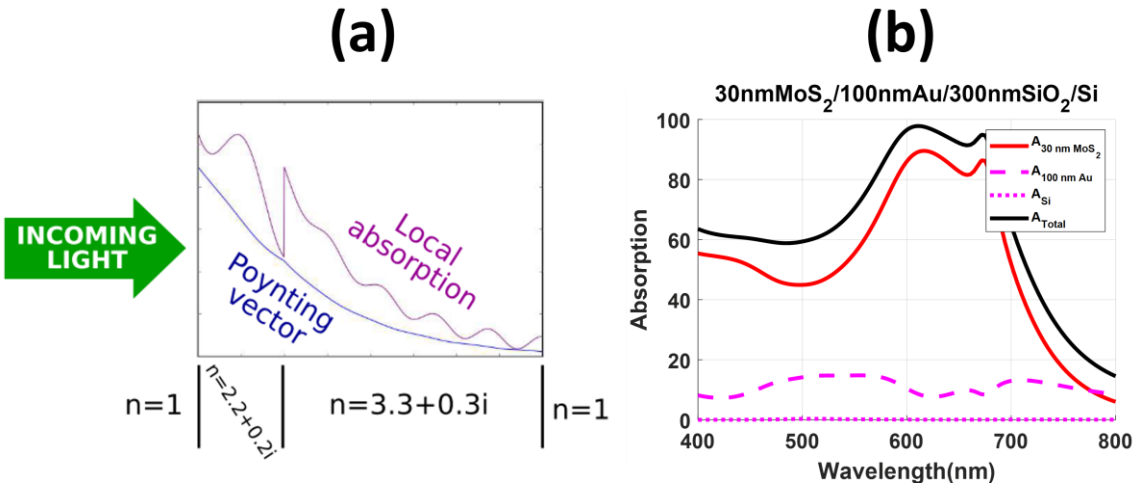


Figure 2.25. (a) The local absorption will vary with depth in a layer and is related to where the electric field preferentially concentrates. For the purposes of this thesis, knowledge of the depth profile is not that important and only the total effect of the layer is needed. This can easily be done by calculating the change in the Poynting vector across the layer of interest. [31] *(b) The layer resolved absorption of a 30 nm MoS_2 on 100 nm Au sample. The zeroth FP mode spectral band is located around 600-700 nm wavelength for 30 nm MoS_2, and one can clearly see that most of the incident light absorbed is attenuated in the top MoS_2 layer.*

2.6 Summary

In summary starting from Maxwell's equations, light is understood to be an EM wave that is most usefully modelled as an oscillating electric field. The wave characteristics of light were explored and expanded upon to take on board the implications but also the limits of the classical wave viewpoint when matching observation of light's behaviour, especially when interacting with matter in way that is clearly quantised. A dual quantum and classical wave approach was shown to be ideal for how one should outline the physics of light. Likewise, matter's response to light was looked at in detail in the context of conductors, semiconductors, and insulators. In some cases, a classical Lorentz electric-dipole description was sufficient to clarify accurate results while in other materials a semiclassical approach incorporating quantum mechanics was needed like the interband transitions of semiconducting solids. Wave interference was elaborated on in greater detail to set the stage for the explanation of the transfer matrix method as a tool for simulating the optical response

of the multilayer stack structures created during this project. The TMM model was shown to be an extension of the Fresnel equations and the principle of thin film oscillating electric field interference working in tandem. Some corrections and additions to the idealised TMM formalism were also touched on for dealing with the effects of incoherence in thick semi-infinite transparent substrate layers and resolving the layer specific absorption of lossy dielectrics with the use of the Poynting vector.

2.7 References

[1] H. D. Young and R. A. Freedman, *University Physics with Modern Physics*, 14th ed. Pearson, 2016.

[2] M. Fox, *Optical Properties of Solids*. 2010.

[3] M. Sakurai, "Spectroscopic ellipsometry," *Toraibarojisuto/Journal Japanese Soc. Tribol.*, vol. 57, no. 7, 2012.

[4] M. Planck and M. Planck, "On the Law of Distribution of Energy in the Normal Spectrum," *Ann. Phys.*, vol. 4, p. 553, 1901.

[5] R. Peverati, "The Ultraviolet Catastrophe," *Florida Institute of Technology*. https://chem.libretexts.org/Bookshelves/Physical_and_Theoretical_Chemistry_Textbook_Maps/The_Live_Textbook_of_Physical_Chemistry_(Peverati)/16%3A_The_Motivation_for_Quantum_Mechanics/16.03%3A_The_Ultraviolet_Catastrophe#:~:text=The ultraviolet (UV) catastrophe%2C,wavelength decreases (see figure 16.3.

[6] A. G. van Melsen, *From Atomos to Atom: The History of the Concept Atom*. Dover Publications, INC, 1954.

[7] "The Schrödinger Wave Equation for the Hydrogen Atom." https://chem.libretexts.org/Courses/University_of_California_Davis/Chem_107B%3A_Physical_Chemistry_for_Life_Scientists/Chapters/4%3A_Quantum_Theory/4.10%3A_The_Schrödinger_Wave_Equation_for_the_Hydrogen_Atom.

[8] A. Das, T. Ferbel, and N. Gauthier, *Introduction to Nuclear and Particle Physics*. 1994.

[9] I. Morison, *Introduction to Astronomy and Cosmology*, 1st ed. Wiley, 2013.

[10] "Ionosphere," *NOAA*. https://www.swpc.noaa.gov/phenomena/ionosphere#:~:text=The Ionosphere is part of,used for communication and navigation.

[11] E. Feigenbaum, K. Diest, and H. A. Atwater, "Unity-order index change in transparent conducting oxides at visible frequencies," *Nano Lett.*, vol. 10, no. 6, pp. 2111–2116, 2010, doi: 10.1021/nl1006307.

[12] S. Chandrasekhar, "The density of white dwarf stars," *London, Edinburgh, Dublin Philos. Mag. J. Sci.*, vol. 11, no. 70, pp. 592–596, 1931, doi: 10.1080/14786443109461710.

[13] "GaAs Crystal Structure," 2024. https://next-gen.materialsproject.org/materials/mp-2534.

[14] P. Liu, P. Longo, A. Zaslavsky, and D. Pacifici, "Optical bandgap of single- and multi-layered amorphous germanium ultra-thin films," *J. Appl. Phys.*, vol. 119, no. 1, pp. 182–184, 2016, doi: 10.1063/1.4939296.

[15] T. Mueller and E. Malic, "Exciton physics and device application of two-dimensional transition metal dichalcogenide semiconductors," *npj 2D Mater. Appl.*, vol. 2, no. 29, 2018, doi: 10.1038/s41699-018-0074-2.

[16] Y. Yu *et al.*, "Exciton-dominated Dielectric Function of Atomically Thin MoS2 Films," *Sci. Rep.*, vol. 5, p. 16996, 2015, doi: 10.1038/srep16996.

[17] Y. Yu, Y. Yu, L. Huang, H. Peng, L. Xiong, and L. Cao, "Giant Gating Tunability of Optical Refractive Index in Transition Metal Dichalcogenide Monolayers," *Nano Lett.*, vol. 17, no. 6, pp. 3613–3618, 2017, doi: 10.1021/acs.nanolett.7b00768.

[18] S. Funke, B. Miller, E. Parzinger, P. Thiesen, A. W. Holleitner, and U. Wurstbauer, "Imaging spectroscopic ellipsometry of MoS2," *J. Phys. Condens. Matter*, vol. 28, no. 38, 2016, doi: 10.1088/0953-8984/28/38/385301.

[19] S. Park *et al.*, "Direct determination of monolayer MoS2 and WSe2 exciton binding

energies on insulating and metallic substrates," *2D Mater.*, vol. 5, no. 2, Jan. 2018, doi: 10.1088/2053-1583/aaa4ca.

[20] V. G. Kravets, F. Wu, G. H. Auton, T. Yu, S. Imaizumi, and A. N. Grigorenko, "Measurements of electrically tunable refractive index of MoS2 monolayer and its usage in optical modulators," *npj 2D Mater. Appl.*, vol. 3, no. 36, 2019, doi: 10.1038/s41699-019-0119-1.

[21] A. M. Law, L. O. Jones, and J. M. Walls, "The performance and durability of Anti-reflection coatings for solar module cover glass – a review," *Sol. Energy*, vol. 261, pp. 85–95, 2023, doi: 10.1016/j.solener.2023.06.009.

[22] E. Complete, *CompleteEASE Software Manual Version 3.18*. J. A. Woollam Co., Inc., 2007.

[23] C. Akcay, P. Parrein, and J. P. Rolland, "Estimation of longitudinal resolution in optical coherence imaging," *Appl. Opt.*, vol. 41, no. 25, pp. 5256–5262, 2002, doi: 10.1364/AO.41.005256.

[24] R. Santbergen, A. H. M. Smets, and M. Zeman, "Optical model for multilayer structures with coherent , partly coherent and incoherent layers," *Opt. Express*, vol. 21, no. S2, pp. 262–267, 2013.

[25] "LIGO Livingston," *LIGO Caltech*, 2015. https://www.ligo.caltech.edu/image/ligo20150731c.

[26] M. A. Kats and F. Capasso, "Optical absorbers based on strong interference in ultra-thin films," *Laser Photonics Rev.*, vol. 10, no. 5, pp. 735–749, 2016, doi: 10.1002/lpor.201600098.

[27] C. C. Katsidis and D. I. Siapkas, "General transfer-matrix method for optical multilayer systems with coherent, partially coherent, and incoherent interference," *Appl. Opt.*, vol. 41, no. 19, pp. 3978–3987, 2002.

[28] G. A. Ermolaev *et al.*, "Broadband optical properties of monolayer and bulk MoS2," *npj 2D Mater. Appl.*, vol. 4, no. 1, pp. 1–6, 2020, doi: 10.1038/s41699-020-0155-x.

[29] C. Yim *et al.*, “Investigation of the optical properties of MoS2 thin films using spectroscopic ellipsometry,” *Appl. Phys. Lett.*, vol. 104, no. 10, pp. 9–14, 2014, doi: 10.1063/1.4868108.

[30] M. C. Troparevsky, A. S. Sabau, A. R. Lupini, and Z. Zhang, “Transfer-matrix formalism for the calculation of optical response in multilayer systems: from coherent to incoherent interference,” *Opt. Express*, vol. 18, no. 24, p. 24715, 2010, doi: 10.1364/oe.18.024715.

[31] S. J. Byrnes, “Multilayer optical calculations,” pp. 1–21, Mar. 2016, doi: 10.48550/arXiv.1603.02720.

[32] H. Deng, Z. Li, L. Stan, D. Rosenmann, and D. Czaplewski, “Broadband perfect absorber based on one ultrathin layer of refractory metal,” *Opt. Lett.*, vol. 40, no. 11, pp. 2592–2595, 2015, doi: 10.1364/OL.40.002592.

Chapter 3. Sample Creation & Characterisation Methods

3.1 Introduction to Methods Used for Sample Synthesis & Measurement

Throughout the course of this work many different experimental techniques and tools have been used to characterise the samples that were deposited. These methods fall into the optical or electronic measurement categories, with optical techniques making up the bulk of the characterisation done due in part to their inherent non-destructive nature. In particular, spectroscopic ellipsometry (SE) and UV-Vis spectroscopy were vital to quantifying the refractive index of deposited thin film layers, the refractive index change of active materials like ECMs and TCMs, and the colouration of the various different ATF FP resonator devices made, charted onto chromaticity diagrams [1]–[3].

In cases where SE could not provide a good fit for thickness or refractive index, x-ray reflectometry (XRR) was used, most commonly when first depositing a new material [4]. Raman spectroscopy was also employed on occasion to infer the chemical makeup of certain thin film layers such as with MoS_2, to confirm its quality and layer thickness [5], [6]. In cases where the materials deposited should be conductive, a 4-point probe system was availed of to determine a whole host of parameters such as, but not limited to, continuity, thickness, and thin film crystallinity (identification of amorphous or polycrystalline ITO after annealing) [7].

Given the nature of the EC ion intercalation process, there was often concern over the continuity, integrity, and cycle lifetime of the ultrathin ECM samples made. To understand the detailed topology of these surfaces both atomic force microscopy (AFM) and scanning electron microscopy (SEM) were used to scan for defects like pinholes, extreme surface roughness, and short circuiting from overlap [8]. See Fig.3.1 below for AFM data on a rough EC NiO thin film after liquid electrolyte ion implantation. The use of these techniques was also of great help towards the optimisation and reproducibility of lab deposition tool's output in this thesis work, determining how high the power of the sputtering guns could be taken

before the surface became too irregular. The data gathered on surface morphology could also be incorporated into ellipsometry to improve the accuracy of the optical model used.

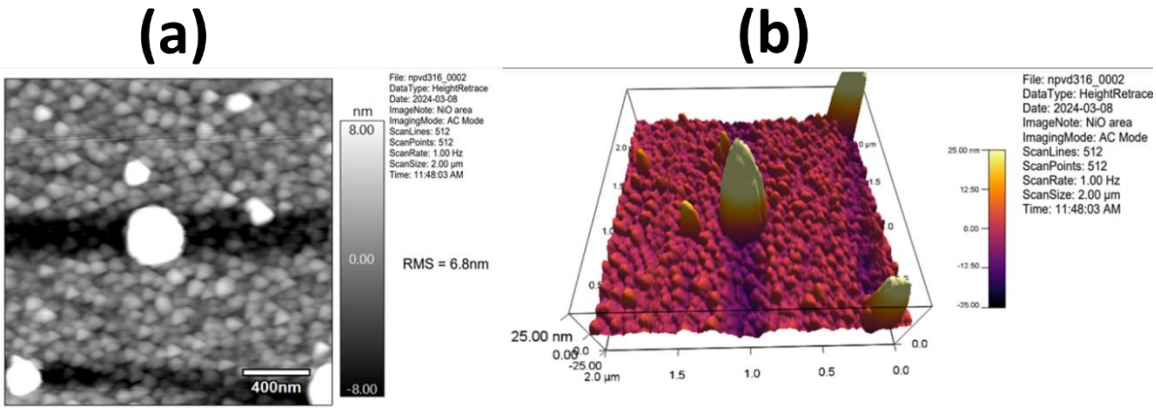


Figure 3.1. (a) Raw data gathered from AFM on a sample of NiO on Ag after being immersed in a highly concentrated liquid electrolyte KOH solution. (b) The intercalation of ions in and out exasperated existing defects in the crystal lattice leading to the peculiar tall protrusions from the surface

Many different techniques were utilised for sample creation at different stages of the project such as thermal assisted conversion (TAC) and physical vapour deposition (PVD) [9], [10]. Though, with the acquisition of a new magnetron sputtering tool, many of the samples from then on were synthesised using the RF and DC guns inside that system, which is why section 3.2 will focus on the physics of how this tool works for sample synthesis. The process of learning how to create a well-built sputtered stack structure involved a keen understanding of the inner workings of the different parts in the machine and how they all come together to produce a consistent sputter yield for all target materials involved.

3.2 Overview of Magnetron Sputtering

3.2.1 Physics of Magnetron Sputtering Using a Direct Current & Radio Frequency Gun

The phenomenon of sputtering is described as the ejection of particles, be they atoms or ions, from the surface of a target material due to bombardment by energetic ions [11]. In that sense sputtering is a form of material erosion that can be utilised for the purpose of thin film coating deposition, which is the building up of a material layer atom by atom. Sputtering can be chemical in nature of purely physical in terms of collisions and impacts. The latter is the predominant applicable viewpoint in this context. Sir William Robert Grove is accredited

with being the first to observe this effect in 1852, while experimenting with discharge tube for the purpose of measuring gas conductivity with direct-current glow discharge [12]. He described it as an undesirable “dire effect” [13], [14]. He described the build-up of metallic deposits on the inside of the tube as an undesirable “dire effect”. Under normal conditions, atoms in the atmosphere will not have the kinetic energy to bombard deeply into a material’s surface and subsequently cause a cascade of collisions and displacements. Therefore, it is only in experiments that expose gases to large electric field voltages on the order of many 10’s to 100’s of Volts that this phenomenon can manifest in earnest . Figure 3.2 below displays a diagram of how physical sputtering occurs.

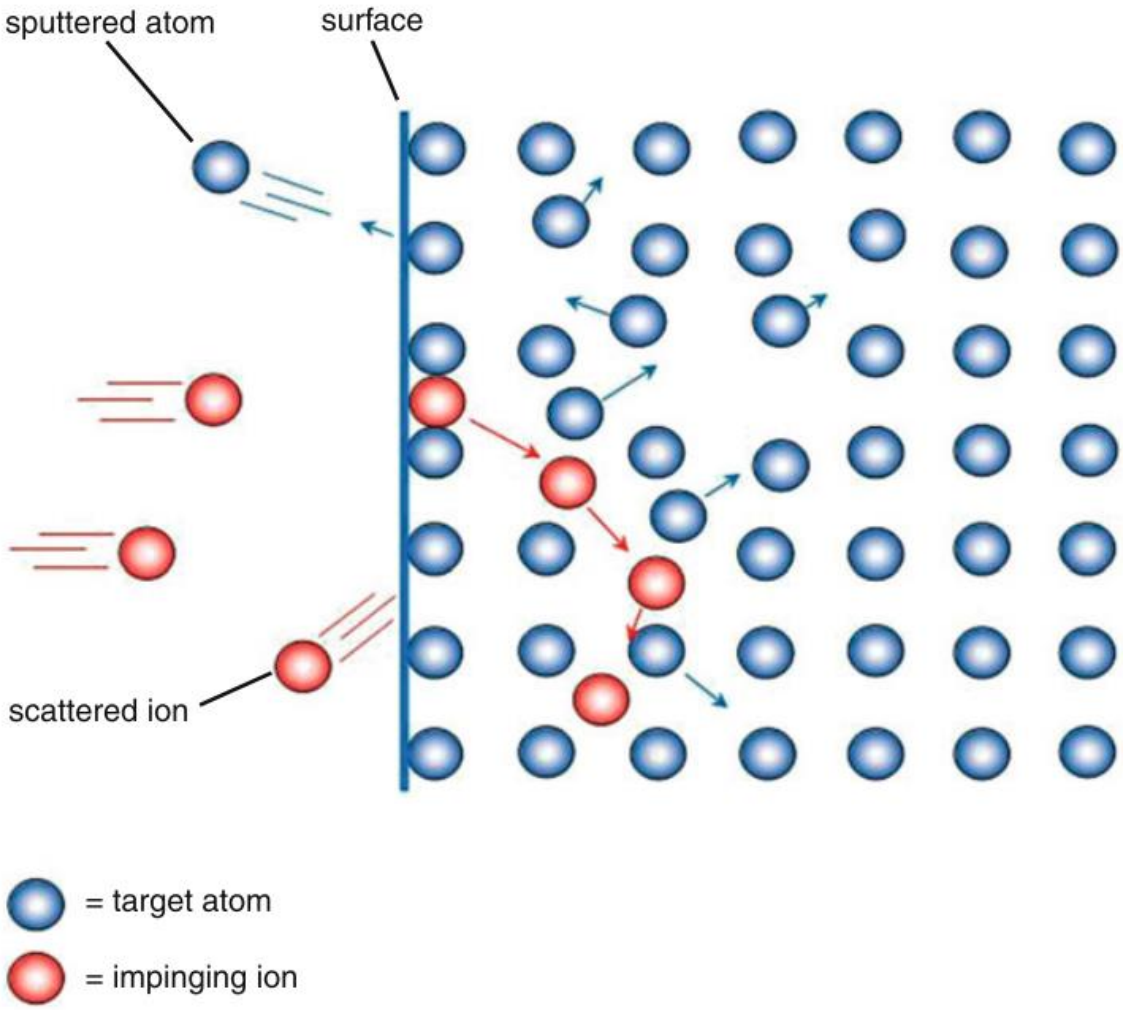


Figure 3.2. The red ions are accelerated by an electric field and impinged into a stationary substrate target. When an impact occurs a series of subsequent collision will follow that displace and bounce the blue target atoms around. This will lead to some of them escaping past the surface as sputtered atoms. This gradual irradiation by accelerated ions will erode at the target until it is all used up. [9]

Although noted to exist, the phenomenon of sputtering was of no practical use for any beneficial task due to the inadequacies of the vacuum technology in the latter half of the 19th century. High Vacuum chambers are needed for sputtering to be efficient as a method of depositing material from a target onto a substrate, as undesirable collisions will occur between target atoms and the surrounding gas molecules when the ambient atmosphere is highly rarefied (large mean free path between collisions) [15]. Furthermore, the presence of other impurities in the chamber can influence the material created by the deposition, especially in the context of reactive sputtering where certain reactive gases are added to the chamber like hydrogen or oxygen [9]. Given that the mean free path of particles in air is equal to 38.5 ± 1 nm at 300 K and 1 atm, it would not be until the 1960's and 1970's that affordable high vacuum technology became available to industry, reliably reaching chamber pressures in the region of 10^{-5} - 10^{-6} mbar before commencing deposition [16]. With high vacuum chambers on the market, the first attempt at using sputtering to deposit thin films was a DC powered diode device which glow discharged a low pressure Ar plasma on a target to deposit the sputtered atoms onto the nearby anode substrate [13]. During this period, the idea of using a radio frequency (RF) gun was introduced to deposit highly insulating oxide targets onto the substrate as well. Ultimately, glow discharge diode technology never caught on for industrial applications due to the severe drawback such as low deposition rates and high thermal load on the target. Substrates with low melting points could not be used either as the target was in very close proximity. Both issues would cost significant amounts of time, bottlenecking the production process.

DC diode guns needed 1000's of volts in some cases to produce enough collisions to maintain the struck plasma in the steady state. The steady state is simply when the electron yield from collisions supplies enough secondary electrons to maintain the ionisation of the ambient gas/plasma (typically Ar). The high voltages and ambient pressures needed to prolong the steady state were at odds with one another due to the safety concerns regarding unwanted electrical discharge in such a system [15]. Many of the issues, primarily low deposition rates, holding back sputtering technology from practical application were solved by the introduction and further optimisation of the planar magnetron sputtering device, patented by J.S. Chapin [17]. This novel tool made use of a magnetron's magnetic field lines to trap the excited electrons closer to the cathode target through a phenomenon known as the Hall effect. Incidentally, these devices can also be found in the home setting for uses

such as in microwave ovens. The hall effect is the drift in electron path due to orthogonal components of an applied $\vec{E}$ and $\vec{B}$ field, also called $\vec{E}\,x\,\vec{B}$ drift [18], see Fig.3.3 below.

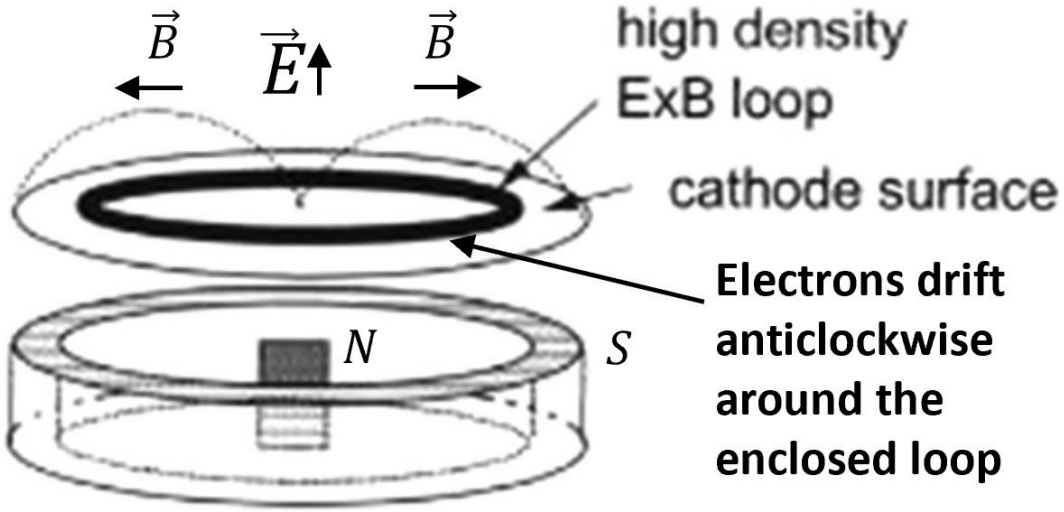


Figure 3.3. Due to the hall effect the electrons will be trapped and continually collide with the ionised gas as long as they remain trapped in the magnetic field. The stronger the field, the better the trap and the more collisions will take place, allowing gas pressure to be dropped further and increasing deposition rates. [13]

By making use of the hall effect, the efficiency in maintaining the plasma is greatly increased and this allows for a 1000 times reduction in working gas pressure during the sputtering process [15]. The operating voltage need only be in the 100's of volts compared with kV ranges in the nonmagnetic sputtering tool. The higher vacuum and lower voltage largely eliminate electrical safety concerns in such systems, preventing the need for the addition of elaborate insulation techniques that are difficult or impracticable to use outside of the lab setting [15]. The $\vec{E}\,x\,\vec{B}$ drift must be a closed loop which works for many different cathode geometries. For the nano physical vapour deposition (NPVD) magnetron sputtering system in this thesis work, small circular planar magnetrons are used, as the samples that were deposited onto are typically no bigger than a standard size microscope glass. For wide coverage applications seen in industry, larger rail like cathodes can be used, see Fig.3.4(a) below. In this way magnetron sputtering is a very clearly a versatile thin film deposition technique, explaining why there was/is so much investment into its use and operation in key industries such as semiconducting fabrication and glass coatings [15]. The latter would pave the way for the scalable addition of AR thin film coatings to PV solar panel technology [19].

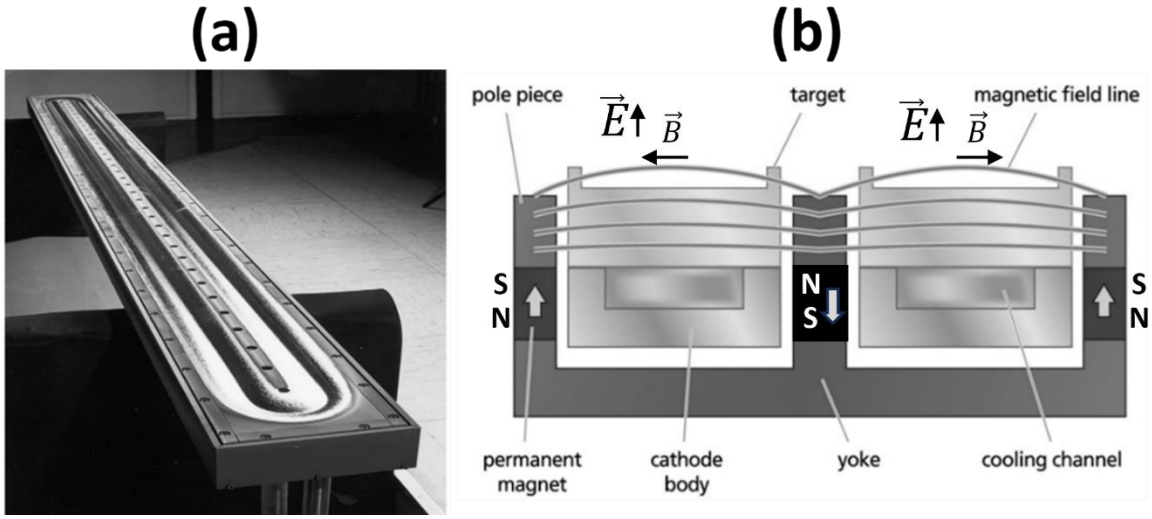


Figure 3.4. (a) A large rectangular planar magnetron sputtering cathode for architectural glass coating. The inner tube dip is the area that high density plasma is created eating away at the target. The target will fail when it is etched all the way through into the copper layer underneath. (b) a circular planar geometry setup. The trapped electrons will drift around anticlockwise in a circle perpendicular to the $\vec{E}$ and $\vec{B}$ field, though eventually they will escape. The path length is proportional to the applied magnetic field strength $\vec{B}$. [13]

Harkening back to the first principles of how the phenomenon operates as shown in Fig.3.2, a mathematical description can be given. Sputter yield $S(E)$ is determined by the fraction of recoil atoms that can escape the target surface after being irradiated by an accelerated impact ion as given below in the energetic equation for an ion exceeding 1 KeV.

$$S(E) = \frac{3}{4\pi^2} \cdot \frac{1}{C_0 U_0} \cdot \alpha \cdot S_n(E) \qquad (3.1)$$

Where C_0 is the interaction potential of the target atoms at the recoil energy, U_0 is the binding energy of the surface atoms or adatoms, α is a term denoting the efficiency of momentum transfer of impact ion to recoil atom, and $S_n(E)$ is the energy loss per unit length of the accelerated ion due to collisions. The interpretation of these parameters is quite intuitive. As much momentum as possible should be transferred to the adatoms of a target with low surface binding and high interaction cross section. For impacting ions below 1 KeV the following equations can be used [9].

$$S(E) = \frac{3}{4\pi^2} \cdot \alpha \cdot \frac{T_m}{U_0}$$

(3 . 2)

$$T_m = \cdot \frac{4M_1M_2}{(M_1 + M_2)} \cdot E$$

(3 . 3)

Where T_m is the maximum energy transfer term and E is energy. M_1 and M_2 are the mass of the ion and target particle, respectively. Sigmund derived these expression in his 1968 paper on sputtering [20]. Ar is found in the atmosphere, so it is much cheaper than other alternatives such as krypton. It is also a Nobel element meaning it will not react chemically with any material unless it is put under extreme non-terrestrial conditions. This makes it an ideal plasma gas [9]. As has been discussed previously, the sputtering yields are too low when magnetic fields are not employed to increase electron collision frequency. Deposition rates for micron scale thicknesses can be as long as days. Magnetrons fix this by applying a Lorentz force $\vec{F}$ to the excited electrons just above the cathode surface, trapping them in a loop. See the equation below.

$$\vec{F} = -q \cdot (\vec{E} + \vec{v} \times \overrightarrow{B_p})$$

Where q is the fundamental electron charge, $\vec{v}$ is the electron drift velocity, $\overrightarrow{B_p}$ is the magnetic field parallel to the target surface, and $\vec{E}$ is the applied field. The magnetic field is normally generated by a permanent magnet, but electromagnets can also be implemented. The trapped electrons follow helical paths that maximise their interaction with the Ar gas close to the cathode target. This process dramatically increases the amount of ionisation occurring and therefore the sputtering yield is enhanced [9]. The order of operation of magnetron device is as follows. In the context of a DC powered gun, the Ar plasma is stuck using a large voltage of 1-2 KV. This initial burst of ionisation will create many free electrons which are then subsequently trapped in helical loops by the Lorentz force, see Fig.3.5 below. At this point, the sputtering device can operate in the steady state at lower

voltages in the 500 V range. Other reactive gases may then be introduced to the chamber depending on the recipe being used. As an example, oxygen can be flowed into a chamber while sputtering vanadium to create Vanadium pentoxide or vanadium dioxide on the substrate. Other deposited material parameters can also be influenced in the same way like thin film porosity in oxides as well as carrier concentration in ITO and FTO to name a few [7], [21]. Finally, the power can be cut.

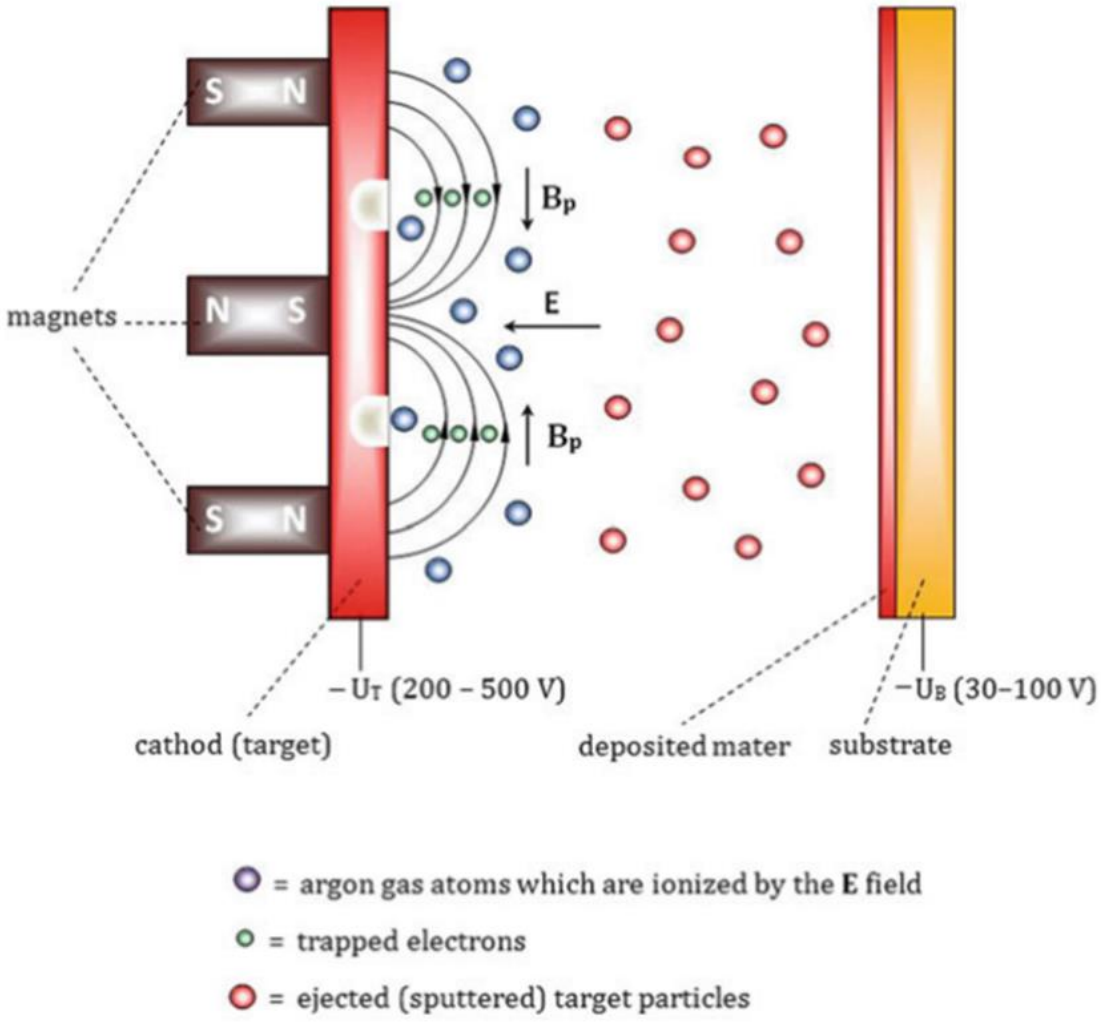


Figure 3.5. A cross-sectional diagram of a circular planar magnetron sputtering device. The permanent magnets trap the electron helical loops, driving them to maintain the ionised state of argon plasma as its used up in surface impacts. To create an electric field between the target and substrate, both ends are held at different electrical potentials. [9]

The "racetrack" marks that develop on the target as it is sputtered away indicates the working area being etched. Under ideal circumstances 100 % of the target should be used up, but unfortunately the depth profile of the racetracks is non-uniform [13]. For a circular planar

magnetron DC Gun, the target will erode with a gaussian like depth profile as shown below in Fig.3.6.

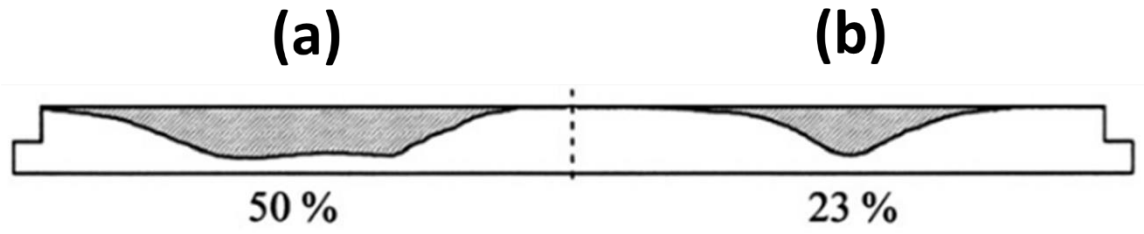


Figure 3.6. (a) The erosion profile for an interpole target-hollow magnetron that uses soft magnetic pole pieces to flatten the parallel magnetic field lines. (b) a simple circular planar magnetron target erosion profile with no field shaping. Only one quarter of the target can be used up before a short develops. [13]

Research into alleviating this issue predominantly revolved around manipulating the shape of the magnetic field using different magnetic materials around the device structure. The interpole target-hollow magnetron did this by flattening the magnetic field with soft pole pieces lateral to the target [13]. Others developed the tubular magnetron that rotates the target into the active plasma zone at a rate of 1Hz. In this way they were able to utilise 90 % of the target over the course of its lifetime though at the expensive of much greater complexity and increased number of failure points [13]. The benefit of being able to use up almost all the target material can outweigh the economic cost worries where large area coatings is concerned.

One other optimisation added over the years was to hold the substrate at a negative potential of around -50 to -100 V. This was done to reject ions with unfavourable kinetic energy that would induce back sputtering onto the target [9], named the ion mixing problem. Without this additional bias the deposited thin film layer would not be adhered well to the substrate. The initial atoms of the thin film layer would be concentrated heavily at the substrate surface instead of mingling there way deeper into the substrate to sew a tighter bond with the bulk atoms, see Fig.3.7 below [9]. Additionally, certain deleterious surface growth morphologies like island formation of the deposit were found to be mitigated by thermal heating of the substrate during deposition, which also doubled to remove gaseous impurity from materials like metals that can show quiet a considerable variability in their refractive index and conductivity depending on how they are grown (grain size, porosity, etc) [1], [22].

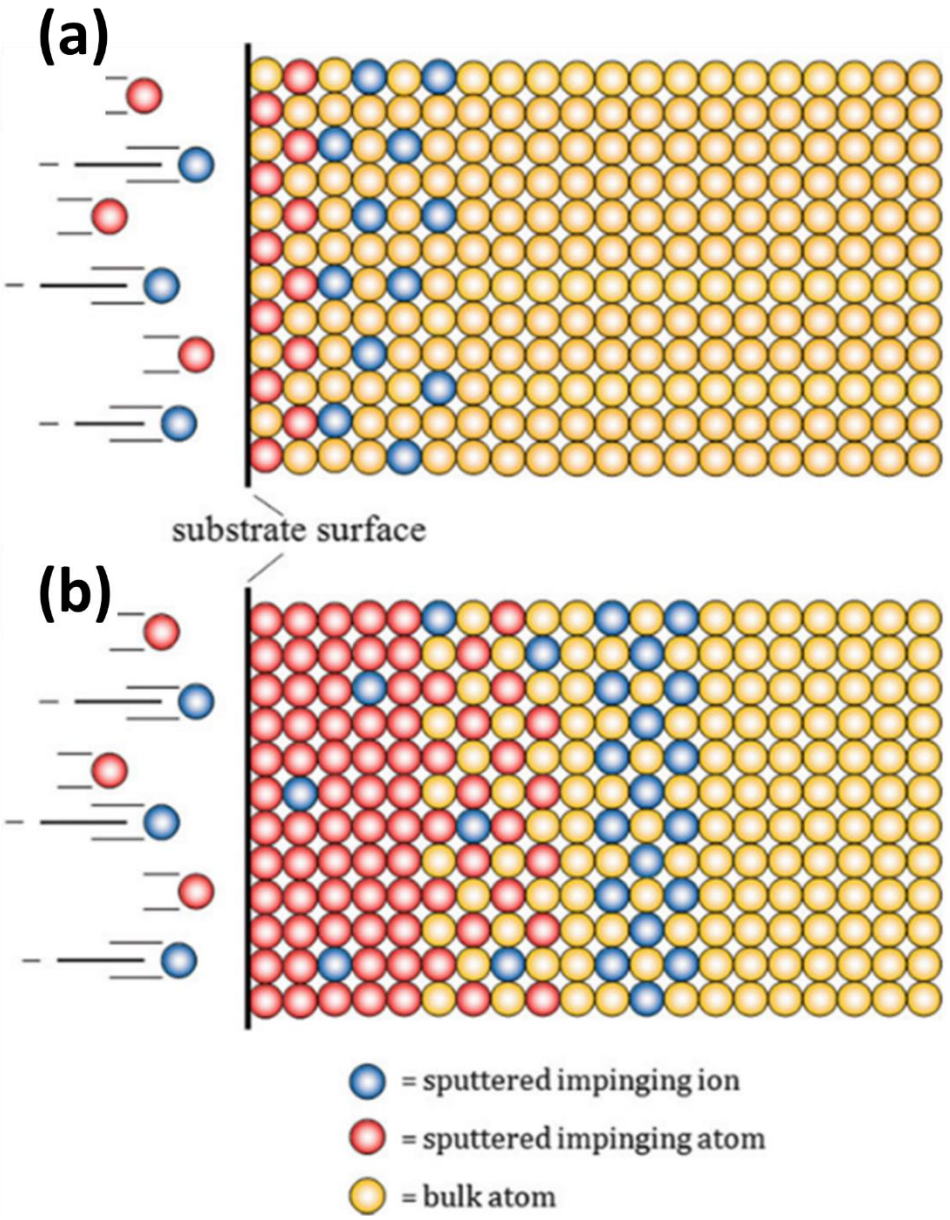


Figure 3.7. (a) Without a substrate bias the thin film deposit is adhered loosely. (b) the addition of a bias on the order of -100V prevents ion mixing of the incoming target ion onto the substrate. This creates a tighter bond between the thin film and the bulk underneath [9].

Magnetron sputtering was a tool used almost exclusively for depositing thin metal films and it saw little or poor use with insulating materials as they could not be sputtered well with a DC gun. Although insulating metal oxides could be made by co-sputtering oxygen with the base transition metal, this could often be accompanied by unacceptable issues such as target poisoning from the DC source which is of the utmost concern when creating high quality insulating dielectric optical coatings [23]. To fix this problem, the idea of using a variable power source gun or RF gun was conceived. The basic premise of the RF gun is as follows. The target is not electrically conductive, so to negatively bias it one must use an AC power

source that can be alternate between positive and negative states. Since the frequency of the source is in the range of around 13 MHz (RF frequency range) the heavy argon ions remain mostly unaffected by the fields close to the cathode and are therefore capable of impacting the target. In contrast the electrons which are a thousand times smaller are smashed into the surface very often [9]. This causes the surface to be held at a net negative potential for much longer than positive potential, facilitating the escape of the sputtered target ion towards the substrate, which themselves are also heavy and not affected too severely by the RF gun switching. See Fig.3.8 below for a cross section of an RF gun. Due to the nature of this RF cycling the charge build up is being cleaned rapidly in time and this reduces the chance of arcing, a form of discharge that disrupts the quality control of the deposition process [24].

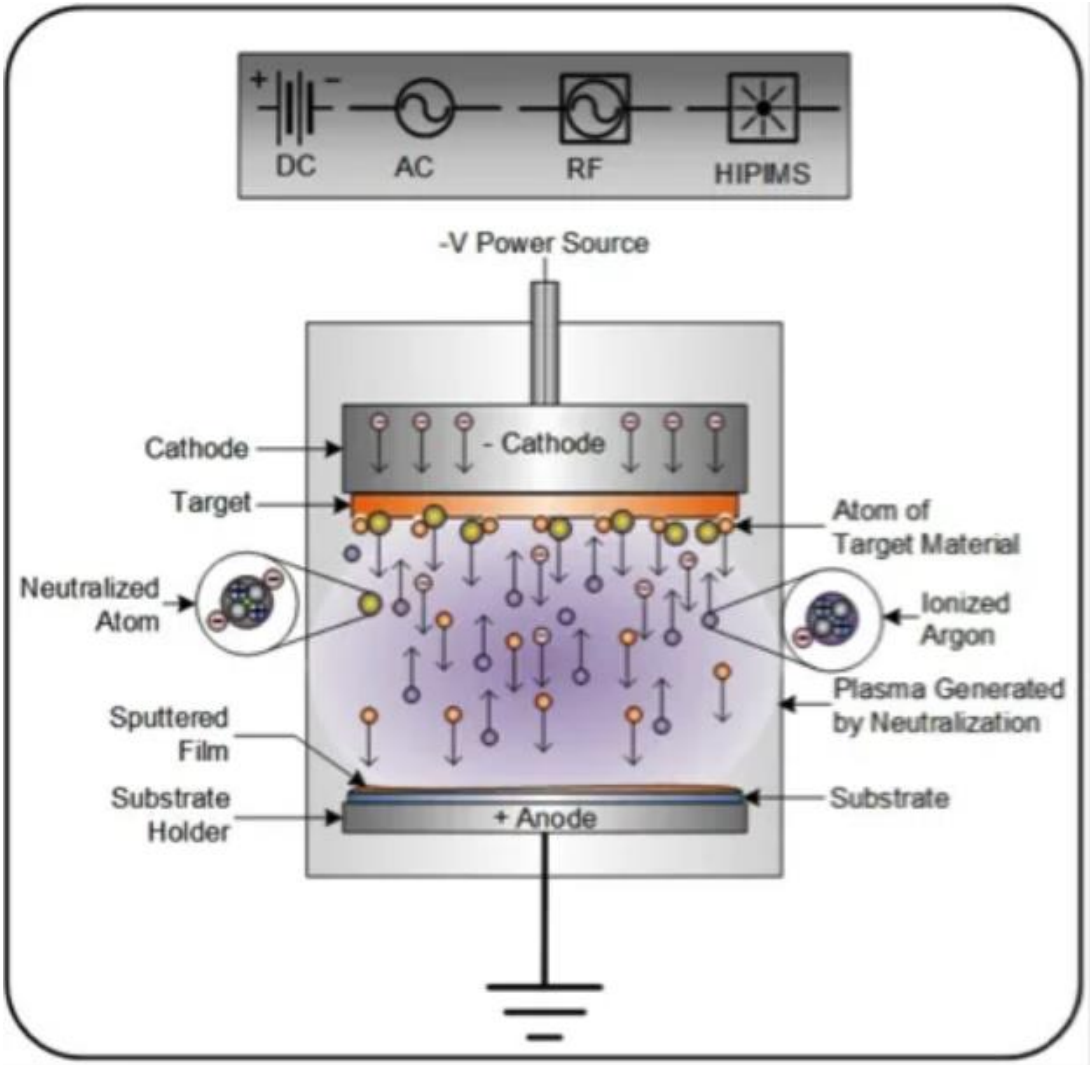


Figure 3.8. In an RF gun, operation proceeds similar to a DC gun, but the gun target will clean its build-up of positive charge using RF field induced electron collisions. If this is not done the sputter yield will drop to zero and the deposition will fail. The rate of deposition using RF gun is noticeably slower than DC guns, so in most cases RF guns are used when high quality transparent dielectric thin film coatings are desirable. [24]

RF magnetron sputtering comes with a host of advantages and disadvantages that warrants when it is appropriate to use. It can operate at lower chamber pressure while still maintaining a stable plasma. Racetrack erosion is mitigated as the electrons are less confined by the magnetic field, allowing the bombarding plasma to spread out over more of the target surface, thus material waste is reduced [24]. Unfortunately, there are big drawbacks such as the higher operating voltages to keep the plasma driven, overheating issues due to the more complex power supply and insulting materials involved, and reduced deposition rate [24]. Despite these short comings, RF magnetron sputtering has matured considerably over the last few decades and is now used routinely in the industry for dielectric thin film coatings, such as in semiconducting chip fabrication, metal surface protective coatings, and in certain medical applications that use material such as TiN to cover medical implant metals for biocompatibility purposes, see Fig.3.9 below [23], [9].

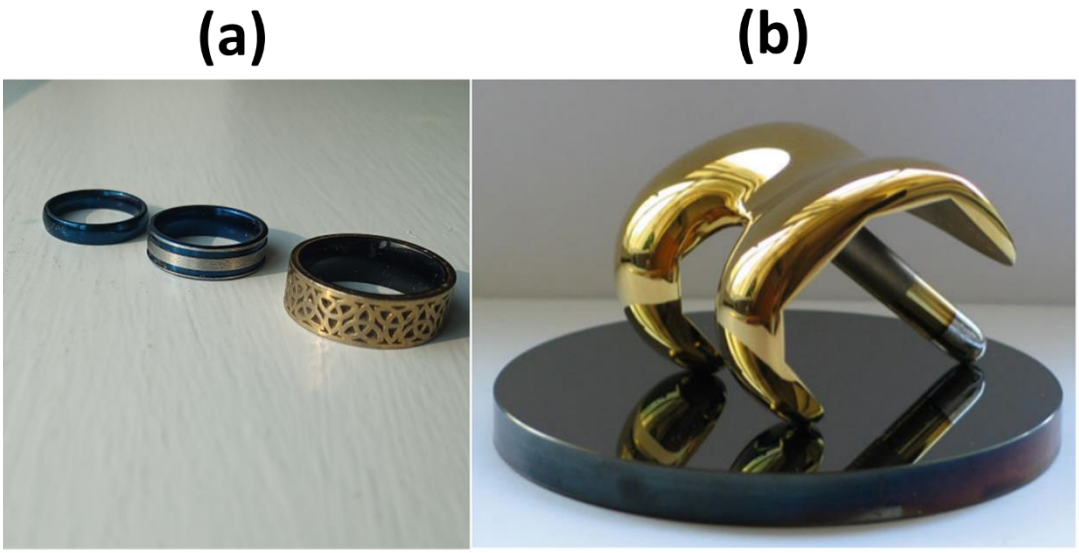


Figure 3.9. (a) A photographic image of titanium rings that have been sputtered with various metals and nitrides to produce an omnidirectional metallic lustre in their appearance. (b) An artificial knee joint that has been coated with TiN to prevent the body from mounting an immune response and rejecting the implant.

3.2.2 NPVD Magnetron Sputtering System & Sample Preparation

The magnetron sputtering system used in this thesis work is a tabletop top NPVD tool made by Moorfield nanotechnology. The system is compatible with RF and DC sputtering guns and can use up to three circular targets in the chamber [25]. The maximum permissible sample size is 10cm in diameter though in practice depositions onto standard microscope BK7 glass slides is the norm. There is substrate rotary capability, and the user interface

control panel is a 7” touchscreen. The touchscreen displays information on chamber pressure and several other safety interlock features such as the status of the coolant, door, and vacuum pump systems. When the tool was first bought halfway through the project, only one DC and RF magnetron sputtering gun were fitted into the chamber. By the conclusion of the work, a secondary RF gun was also installed making it easy to build up multilayer FP devices without breaking vacuum to change targets. Figure 3.10 below displays photographic images of the NPVD tool.

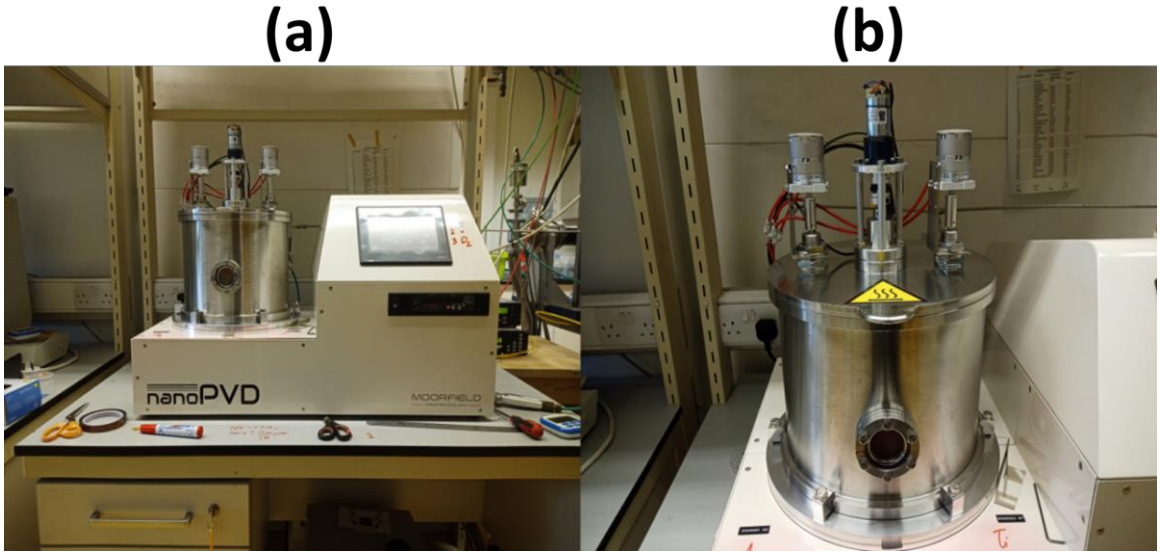


Figure 3.10. (a) The entire magnetron sputtering NPVD system can fit on a benchtop, though there are cooling, and vacuum pump auxiliary systems located underneath at ground level. (b) A close-up view of the vacuum chamber containing the sputtering system, a viewing port provides a view of the inside during operation once the argon plasma has been struck.

Two pumps are needed in series to pump down the chamber pressure to operational requisite. The first is a roughing pump which will equally reduce the pressure down by a factor of 1000 and second is a turbo molecular pump which will bring the final pressure ever closer to 10^{-7} mbar if given enough time. The chamber takes approximately 15–20-minutes to pump down to 10^{-6} mbar which is sufficient in most cases. If the NPVD does not reach a target pressure after 10–15-minutes, it will automatically vent and log the failure in the diagnostics tab of the on-board operating system. Over time the system struggles to reach this target due to a build-up of out gassing material in the chamber. To alleviate this concern, periodic cleanings every quarter are needed on the chamber components exposed directly to deposition such as the substrate shutters and target shielding. Cleaning of the equipment involves the use of sandblasting and baking to force contaminants out. Care is given to the

opening of the chamber which uses delicate rubber O-rings to form a seal when the air is evacuated. Acetone can never be used on these rings as the rubber will degrade. Therefore, IPA is used as the main solvent to clean excess dirt from any other surface that cannot be removed from the chamber.

On the main menu of the touchscreen one can access the process control tab which will bring the user to a layer editor. On this screen, recipes can be made for whatever layer may be desired, with certain variables being controllable like gun power, deposition time, reactive and inert gas flow rate in sccm, substrate heating temperature, and the rotational speed of the substrate mounted on a Z shift assembly. See Fig.3.11 for images of the process control.

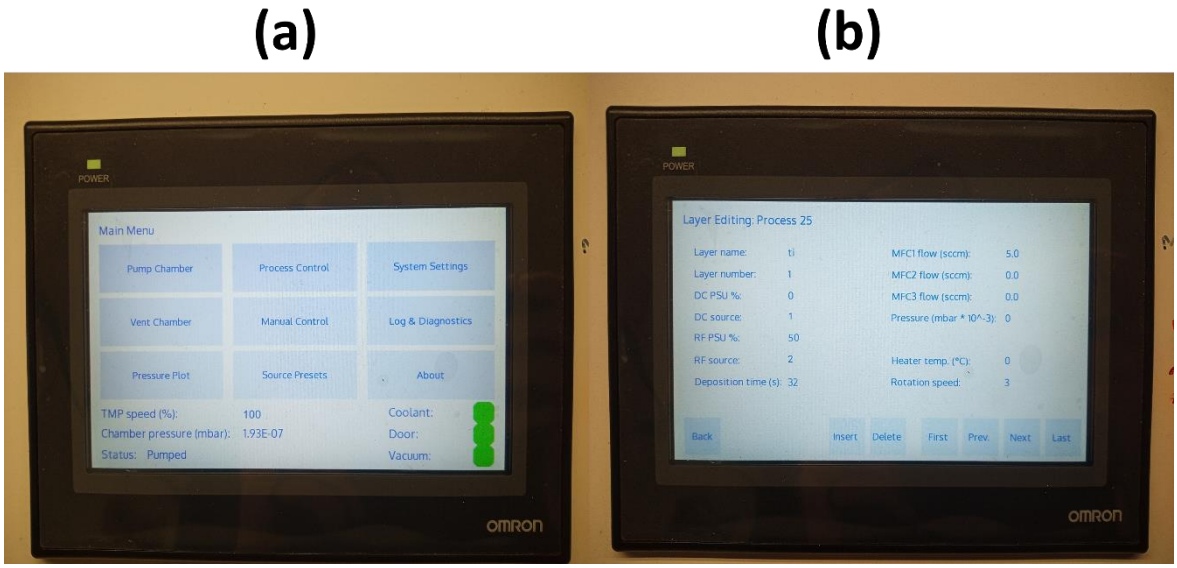


Figure 3.11. (a) The main menu of the touchscreen display. There are nine different tabs to choose from with pump and vent chamber controlling the release and intake of air into the tool system, (b) Under process control the layer editor allows one to create a recipe for a thin film using the variables displayed. Multiple processes can be stacked together to form a multilayer recipe.

For most purposes 5 sccm of Ar is used during the steady operation state. Increasing this generally increases deposition rate but also negatively effects surface roughness. After Argon, the most utilised gas that is flowed into the chamber is O_2 to make oxide thin films like NiO and WO_3 from their base transition metal atoms. In the NPVD system the DC gun power is typically set to around 10 % of the maximum 800W PSU. Through trial and error, 80W DC gun power was found to be convenient for most conducting target materials in terms of deposition rate, sample quality and homogeneity (continuity and precedence of density variations with thickness). The latter could be inferred from XRR which measures thin film thickness and density quiet well [26], [27].

To further improve upon sample homogeneity, the substrate stage is connected to an axially rotating shaft with seven different set rotation speeds. Setting 3 and 4 are most commonly used. The rotation of the samples is necessary since the magnetron guns are mounted at an angle to the substrate surface normal. It is imperative that the substrate rotate into and out of the maximum deposition region to avoid non-uniform wedge like sample formation such as the image shown below in Fig.3.12.

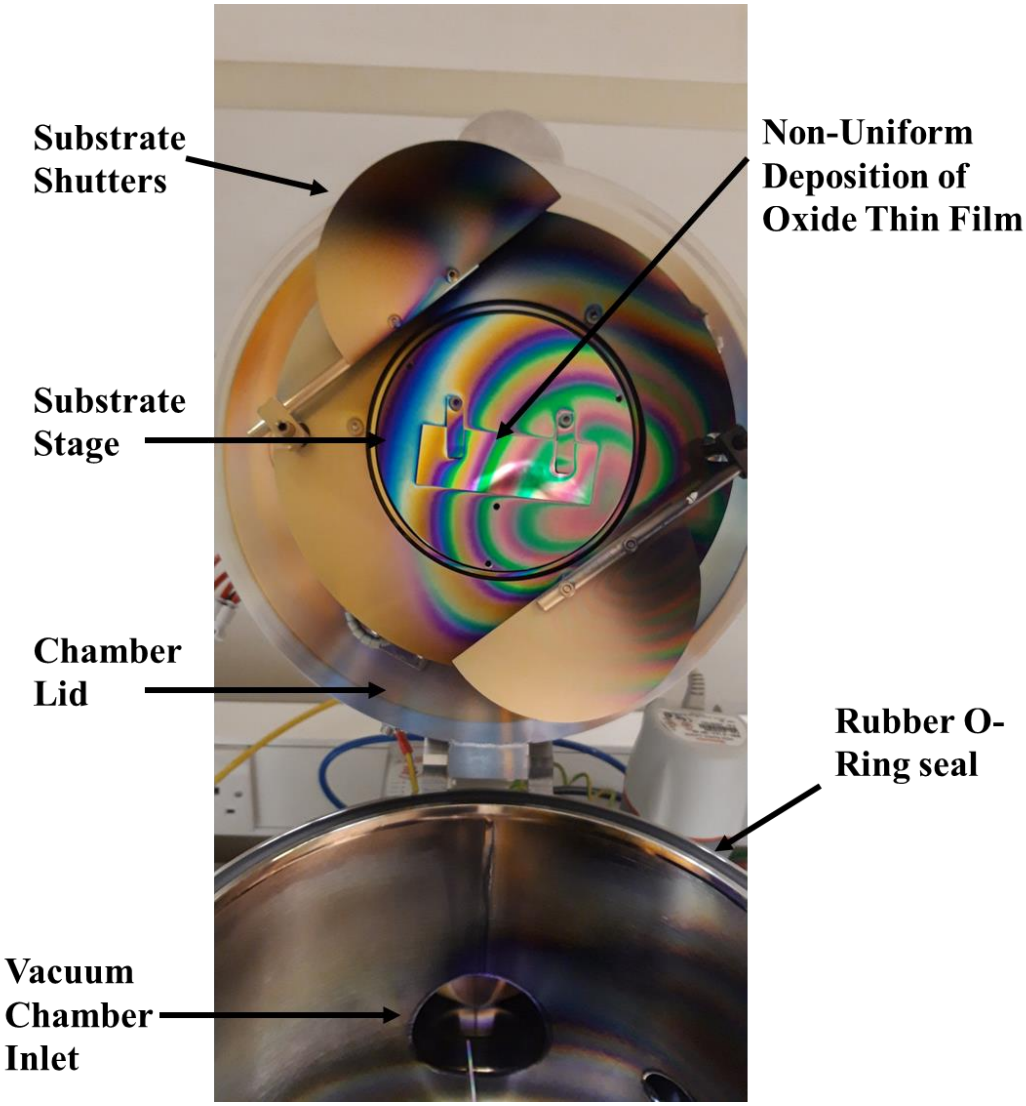


Figure 3.12. Layout of the substrate stage and other auxiliary components around it. The vacuum chamber inlet can be seen at the bottom along with the rubber O-Ring seals around the top rim. These rings will form a tight seal with the steel chamber lid under vacuum. Pneumatic controlled shutters slide in and out to control the exposure of the substrate to sputtering. In this case, failure of the rotary device, caused non-uniform deposition which is exemplified by the different colour bands present on the oxide layer.

The RF gun power under most circumstances is set at 75 % of 150 W. Through experimentation, lower values of power were found to produce very slow deposition rates that made thicker oxide layers above 100 nm very impractical to fabricate in terms of time

needed. Any higher than 75 % and problems began to arise regarding target thermal management issues and rough deposits. The former was especially troublesome as the RF gun could not operate for longer than 30 minutes before safety interlocks would shut the power off to allow time for the target to cool back to ambient. Such issues are not readily encountered with DC guns given their superior thermal conductivity and large deposition rates as high as 10 nm/min or larger in some cases. Thus, the most agreeable compromise for the RF system was to bring power as high as possible and then use multiple deposition steps to build up a thicker oxide layer. This was managed well with insulating dielectric layers like TiO_2 where thick spacer films were built up for the Fano-resonant device stack structure without needing to break vacuum. The only major cost being the added time needed to carry out the process. Figure 3.13 below displays diagrams of the magnetron sputtering guns. Both the RF and DC guns look visually identical. Inside the chamber a tall metal sheet wall is placed between all three active guns to prevent cross target deposition. A shield around the target also aids in grounding it, protecting it and collimating the sputtered adatoms.

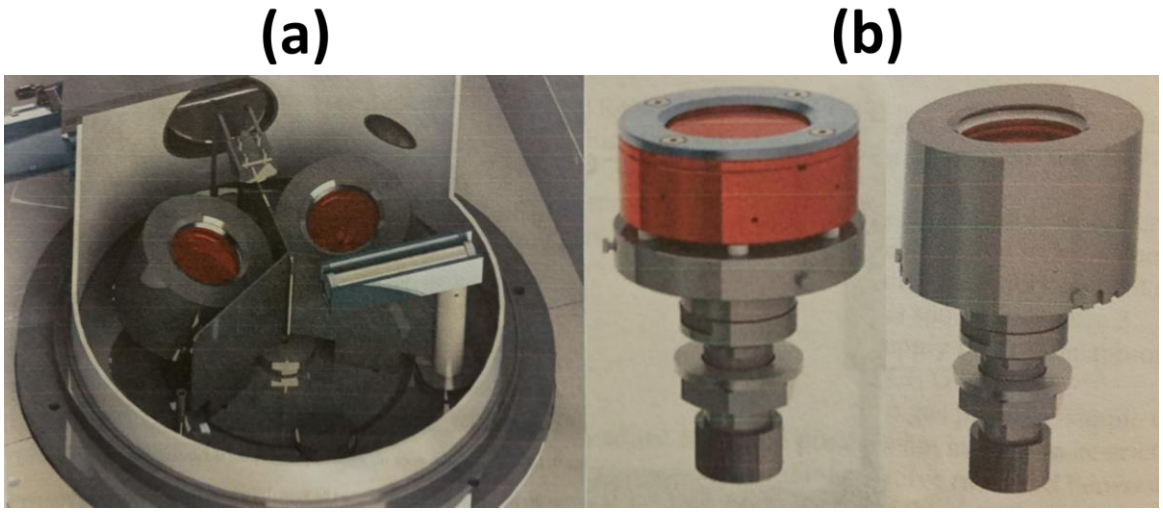


Figure 3.13. (a) The magnetron guns are angled towards the central axis of the chamber with a wall placed between them. (b) A magnetron sputtering device with and without its shielding. [28]

Targets are replaced by disassembling the shielding and unscrewing the interpole rings. Once this is done the target disks can be swapped out quickly. Most targets will use a copper backing to improve electrical and thermal conductivity. Many targets will have dirty surfaces due to exposure to air or cross contamination from other sources within the PVD chamber. To correct for this an additional step is performed before the substrate shutters are

opened called the pre-sputter deposition step. During this step, the top layer of the target is sputtered off onto the shutter shielding. If the target is a metal like W, Ni, or V, then the adatoms immediately on top are likely to be some form of native oxide or dirt that was left there from handling. Handling should therefore always be done with nitrile or latex gloves. In general, it is always good practice to be wearing laboratory gloves when working with vacuum equipment.

Samples are mounted on the substrate stage using Kapton tape rated for vacuum or by using one or more of the metal clips found around the edge. In practice, the most efficient arrangement was to place two to three 2" microscope slide samples on a standard Si wafer and then mount all of it together using the three available clips. Care must be taken when positioning and tightening the clips as the dimensional tolerances for available space are small. Over tightening can break the clips and perhaps even worse, under-tightening will result in one's sample falling onto the target setup under gravity. To maximise the quality of the deposit the substrate must be as clean as possible. To do this a glass slide is submerged in acetone and the beaker is then placed in an ultrasonic bath like in Fig.3.14(a). After a few minutes, the glass is washed off with IPA without letting the acetone evaporate as that would cause scum to form across the surface. With that step concluded the final task is to air dry the glass with an air gun connected to a nitrogen supply. It is also possible to put the substrate through a plasma asher cleaning step though for most purposes this is overkill and is normally only done when wanting to remove photoresist layers in photolithography process.

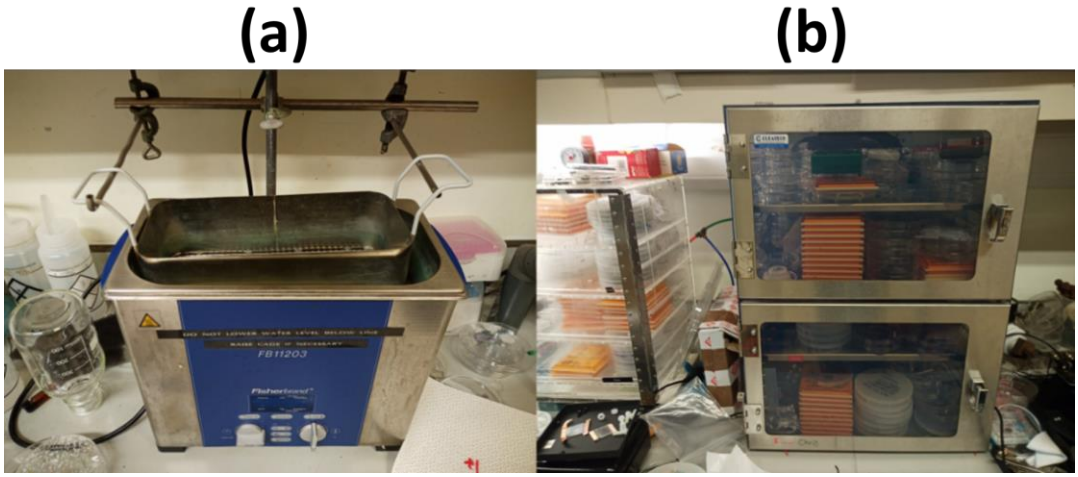


Figure 3.14. (a) Before mounting the glass slide substrate into the vacuum chamber, it is cleaned in an ultrasonic bath while immersed in acetone. After this step, the sample is rinsed with IPA to remove acetone residue and then air dried with an air gun. (b) The sample storage box has an inert nitrogen atmosphere to slow down the degradation of samples that are susceptible to being tarnished or oxidised.

After the sputtering process is complete the chamber is vented, and 10-15 minutes must elapse before it is safe to open the top lid. If the heater was used, then safety interlocks may keep the chamber closed for longer till the heat is dissipated. Once the chamber is pressurised any excess heat will quickly convect away. The samples can then be removed from the stage and placed into a holder in a nitrogen dry box as shown in Fig.3.14(b) above. The inert nitrogen atmosphere preserves the thin film stacks for longer which is very helpful in the lab as CRANN is located in Dublin city centre where pollutants such as sulphur and nitrogen dioxide can be found in the air [29].

3.2.3 Auxiliary Sample Synthesis Methods

Other sample creation and deposition tools have been used throughout the course of the project. Mentioning them briefly here there was the first benchtop PVD system that was inherited as part of the lab setup. This system was called the Gatan precision etching coating system (PECS), shown below in Fig.3.15. The Gatan had a much smaller vacuum chamber and sputter target. It was difficult to change the target as well. This system was mostly used for depositing metals like Mo and W for the eventual fabrication of transition metal dichalcogenide materials MoS_2 and WS_2. Early in the project the Gatan had reoccurring issues with maintaining vacuum until eventually it could no longer hold one. The tool was then set aside, and the Shamrock 19608 sputtering system in CRANNs cleanroom was used instead. The Shamrock was much larger an operated and owned by the Magnetism & Spin Electronics research group at Trinity college Dublin. The lack of freedom in how the device could be used led to the decision to purchase the Moorfield NPVD system, and thereafter many 100’s of samples have been made ranging from ultrathin metal sheets on glass, simple AR coatings, to complex FP resonators stacks structures using a large variety of different lossy dielectric absorbers.

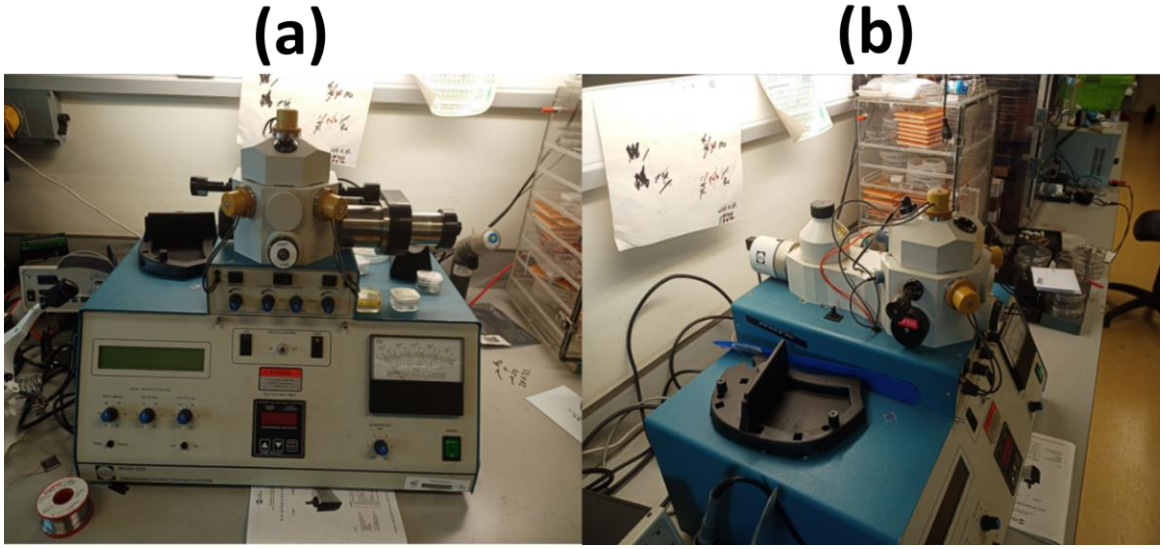


Figure 3.15 (a) A front view of the Gatan deposition system. The chamber is in the top protrusion. The large arm in the right side is the substrate stage. (b) A side view of the system containing the PSU for the gun assembly, four different targets could be mounted into the system.

Figure 3.16 below is an image of the Shamrock system in the cleanroom. There are two chambers. One that can pump and vent to allow sample mounting, and a second larger chamber that is always kept at high vacuum. Typical layer runs with this tool were Au, Ti, Al, and Mo. This system is also located beside the spectroscopic ellipsometer which will be looked at in detail in the following section. The use of this system is expensive, so most users would organise a date where many samples could be coated all at once to maximise efficiency. Having to coordinate in this manner can be problematic when the system is popular to use. Moreover, it is difficult to optimise a new sputtering process when there is a small number of deposition runs, and the materials used throughout the course of the week is limited. This ultimately slows down the rate of sample optimisation/improvement that can being done.

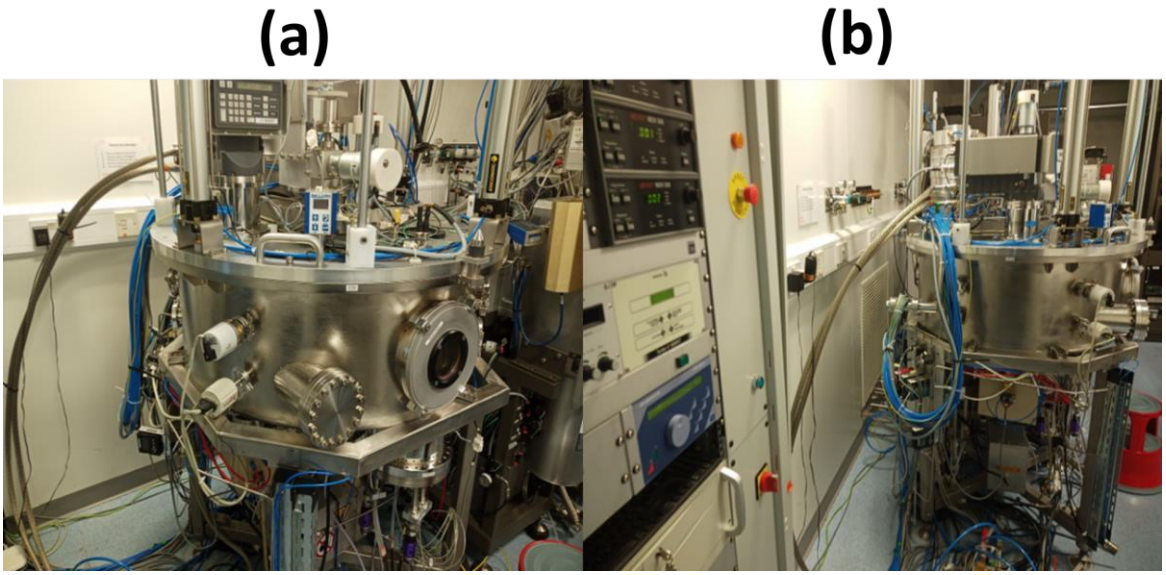


Figure 3.16. (a) A front and (b) side view of the Shamrock deposition system. A large porthole window provides a visual of the inside of the chamber while its operating. The environment of the large vacuum chamber is heavily controlled as it is not exposed to the atmosphere unless a cleaning needs to be done to remove excess build up that condenses on the bottom.

The Thermal assisted conversion (TAC) process, primarily carried out by group member Nishtha Shelly who is an expert in the technique, was used to form the majority of the TMDs looked at over the course of the thesis project; most notably the TMD MoS_2. The basic concept is derived from Chemical vapour deposition (CVD). In CVD a gas or vapour is reacted with a thin film layer on a substrate. Under the right conditions all the material will be converted. In this sense CVD is self-limiting because the amount of product produced is proportional to how much starting material one had in the thin film layer [30]. Many metals react this way with oxygen through the formation of a native oxide layer. CVD will accelerate this by modifying the gas that the sample is exposed to such as pure oxygen, sulphur, or hydrogen. In TAC, the process is thermally assisted which is to say that the new compound formed from gas solid reaction requires heat to transform [10]. In the case of MoS_2 or WS_2, Mo and W samples are placed in a quartz furnace tube that is evacuated of atmospheric air. A flash lamp then heats up a container with sulphur, vaporizing some of it. This vapour is then mixed with hydrogen/argon gas mix to drive the reduction of the surface of the metals which will likely have some native oxide present. This is done at a high temperature of 750˚C or higher [10]. Once they are completely reduced the sulphur will bond and a new compound is formed. Figure 3.17 illustrates this.

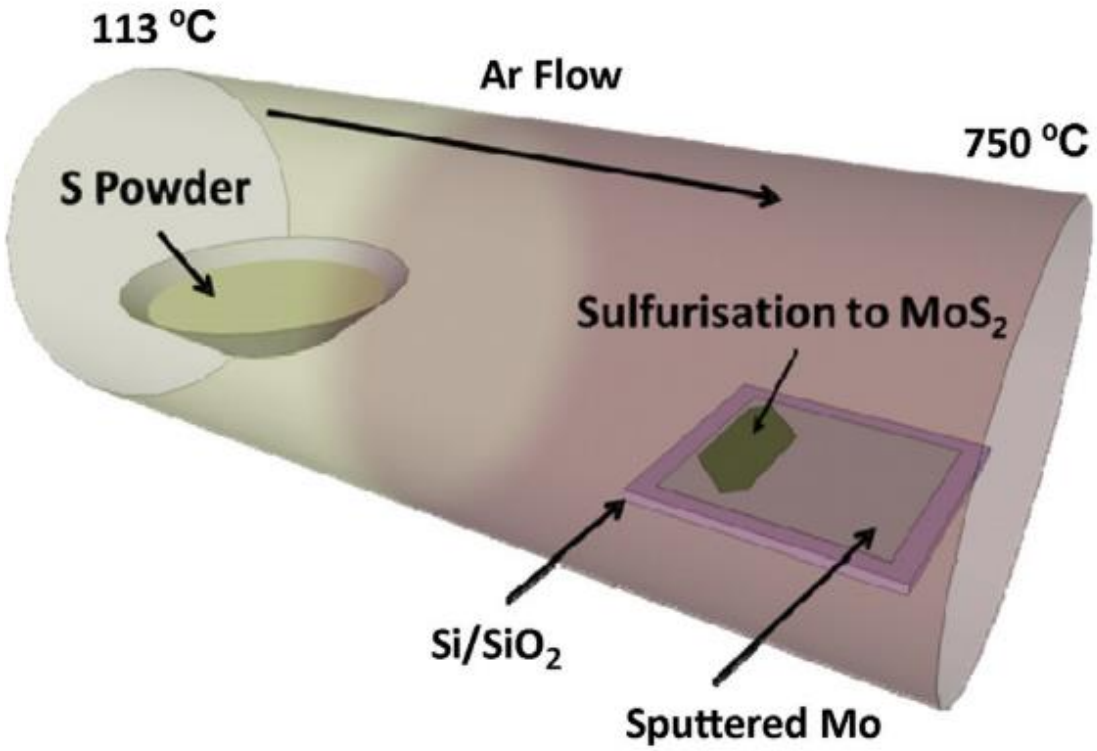


Figure 3.17. A diagram of the TAC process when applied to MoS_2. Mo on a Si wafer substrate is reduced and subsequently sulphurised by sulphur vapour at 750˚C. These temperatures are reached by placing the active section of the quartz tube inside of an oven heater. Quartz tubes are used due to their low coefficient of thermal expansion and high melting point. Glass would shatter under the same conditions.

Over the course of the project, group member Nishtha Shelly, became more and more adept at creating TAC grown TMDs with electrical and optical qualities ever closer to mechanically exfoliated layers that generally have higher quality surfaces than other growth methods like TAC and CVD (less defects) [31]. The biggest challenge was in creating continuous thin films without substantial amounts of roughness and defects like holes across their surface. High resolution electron microscopy and AFM indicated the tumultuous nature of most TAC samples produced, but despite this fact, samples of MoS_2 with smooth surfaces on the scale of microns were eventually grown, enabling their use in pixels with active gate tuning by an electric field bias. The usual processing time for TAC is 30 minutes but for thicker samples more time is needed to react with metal deeper beneath the air/surface interface. In some cases, more sulphur must be added as well as more heat to completely convert the thin metal film. Care must also be taken in what substrate is chosen given the high temperatures involved. SiO_2/Si is a common choice, while quartz is also an excellent option too for its high melting point. Figure 3.18 shows photographic imagery of the TAC furnace located across from the NPVD magnetron sputtering system.

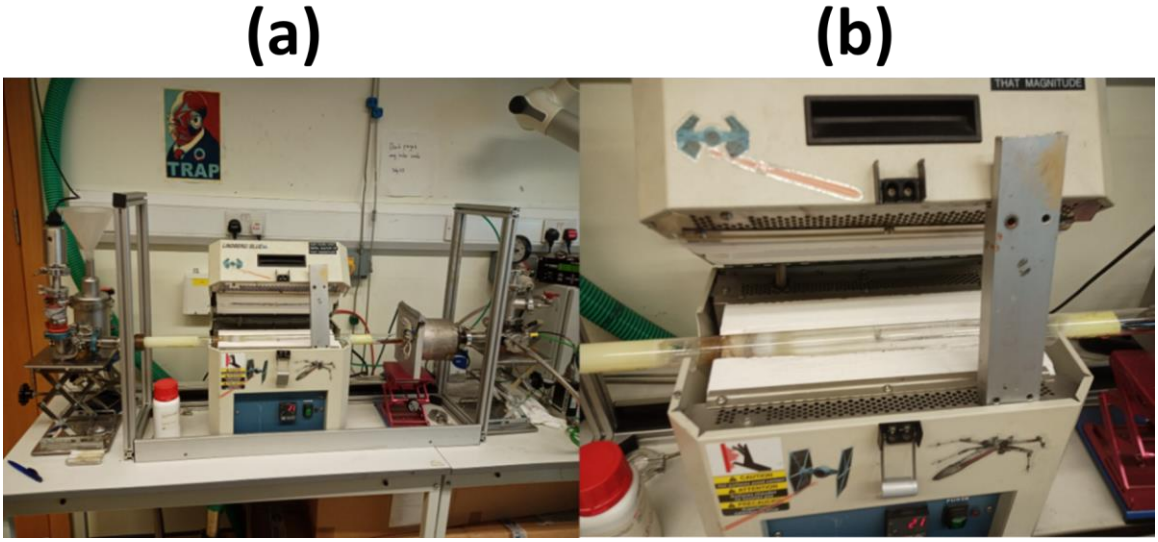


Figure 3.18. (a) An overview of the entire TAC furnace device, with the oven heater in the middle, the flash lamp to vaporise sulphur on the right, and a liquid nitrogen cold trap on the left to help evacuate the quartz tube. Samples are mounted from the left side and are placed in a boat. (b) A close-up view of the oven region. The door stopper is removed to lower the door and bring the heating elements closer together. A digital temperature gauge can be seen in the front as well.

Other dichalcogenides can be brought in for the reaction such as selenium and tellurium. At one stage selenium was also used with the TAC furnace in the lab, albeit with a separate quartz tube to create selenides like WSe_2 and $MoSe_2$. However, due to safety concerns over the exposure levels, its use was discontinued. As a matter of note the safety limit is some 400 micrograms per day and there is no known antidote to chelate excess out of the body [32]. In this way Se can quickly become an acute toxin, especially if it has been vapourised into the air where it is possible to breath it into the lungs. Sulphur in contrast is much more common in nature than Se by a factor of 100,000, and Te by a factor of a million, and is dealt with routinely by the human body[33].

So far, different techniques and equipment used to fabricate thin film samples have been focused on, most notably magnetron sputtering. The topic of discussion will now shift to the many characterisation methods that were used to quantify them, both optically and electrically. Particularly spectroscopic ellipsometry and UV-Vis spectroscopy, which together form the core of measurements done in this thesis. A background will be given to each experimental method and a description of the procedure carried out will follow.

3.3 Spectroscopic Ellipsometry

3.3.1 Physics of Spectroscopic Ellipsometry

To measure the refractive index, the process is a simple enough task where thick transparent bulky materials are concerned, such as glass prisms, windows, and water. Many principles of optics were gleamed during the scientific revolution by observing the way light behaves when interacting with these media, such as the pioneering work carried out by Sir Issac newton and Willebrord Snellius [34]. The latter whom the famous Snell's law of refraction is named after. Without knowledge of the Maxwell equations, Snell had determined through experiment that the way in which light bent as it passed from one medium to another way given by the equation below.

$$n_1 sin(\phi_1) = n_2 sin(\phi_2)$$

(3.4)

Where n_1 and n_2 are the real refractive index of the first and second medium, and ϕ_1 and ϕ_2 are the incident and refractive angle, respectively. By controlling the ϕ_1 and ϕ_2 the value of index of the unknown second medium could be determined. Air is assumed to be unity, $n_1 = 1$. The principles on how light reflected off surfaces was also characterised by French engineer and physicist Augustin-Jean Fresnel, who had the idea to describe light as a transverse wave even before it was understood that light is an EM wave [1], [34]. The electric field notation for light can be used to describe the amplitude of the optical field in a manner identical to Fresnel as shown below. In this case the s-polarised light reflection coefficient is given by the following equation also outlined in the previous chapter.

$$r_{s,12} = \frac{E_s^{refl}}{E_s^{inc}} = \frac{\widetilde{N_1} cos(\phi_1) - \widetilde{N_2} cos(\phi_2)}{\widetilde{N_1} cos(\phi_1) + \widetilde{N_2} cos(\phi_2)}$$

(3.5)

Where $\widetilde{N_1}$ and $\widetilde{N_2}$ are the generalised complex form of the refractive index, E_s^{refl} is the electric field of the reflected s-polarised light, and E_s^{inc} is the electric field of the incident

light. $r_{s,12}$ is the reflection coefficient of the interface between medium 1 and 2. For normal incidence onto a transparent material like SiO_2, this can simplify further and the index $\widetilde{N_2}$ can be determined experimentally from the equations featured below.

$$r_{s/p,12} = \frac{1 - \widetilde{N_2}}{1 + \widetilde{N_2}} \tag{3.6}$$

$$R_p = R_s = \left(\frac{\widetilde{N_2} - 1}{\widetilde{N_2} + 1}\right)^2 \tag{3.7}$$

Where all variables have their usual meaning and R_p and R_s are the reflection intensities for each polarisation state making up the incoming light. Both p and s light are equivalent for 0˚ AOI as an EM plane wave will always oscillate in-plane at that angle [1]. It can be seen from Snell's law and the Fresnel equations that the refractive index of an unknown material can be determined from measuring angle and intensity values through experiment. This works neatly for a bulky medium but if multiple different layers are stacked one on top of the other this greatly complicates matters. Furthermore, if these layers are optically thin then wave interference effects will begin to dominate the outcome of the lights behaviour as it passes though. It will also not be possible to measure the thickness of such thin films using traditional mechanical means like micrometres or callipers [1].

With the conundrum of how to decouple the different refractive indices and thicknesses of the complex stack, motivation to pursue a new technique emerges that can make this possible. Spectroscopic ellipsometry (SE) facilitates this by incorporating the change in light polarisation state before and after reflection into the measurement process. The basic setup and wavelength range of an SE instrument is shown below in Fig.3.19. In so doing the layer structure properties can be understood once an optical model is compared with the measured result. The governing equation of SE is given by the fundamental equation of ellipsometry, previously defined in chapter 2, p.83. eq.2.30; see eq.3.8 below [1].

$$\rho(\omega) = tan\big(\Psi(\omega)\big)e^{i\Delta(\omega)} = \frac{r_p(\omega)}{r_s(\omega)}$$

(3 . 8)

Where, ω is the frequency of light, $tan\big(\Psi(\omega)\big)$ is the amplitude ratio of the reflected p and s polarisation states $r_p(\omega)$ and $r_s(\omega)$, and $\Delta(\omega)$ is the change and in phase difference between p and s states before and after reflection. Δ is given by the equation below.

$$\Delta(\omega) = \delta_1(\omega) - \delta_2(\omega)$$

(3 . 9)

Where $\delta_1(\omega)$ and $\delta_2(\omega)$ are the phase difference between p and s light polarisation before and after sample reflection, respectively.

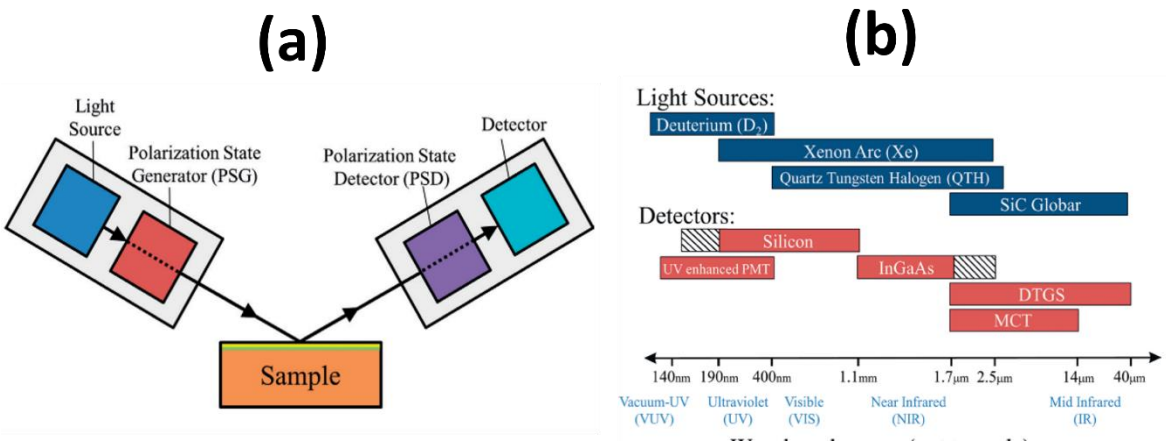


Figure 3.19. (a) A PSG controls the incident polarisation of the two arm SE system, and the PSD detects the change in polarisation state after reflection. (b) Various different light sources are used for specific wavelength ranges. Tungsten halogen is the norm for Visible frequencies while more exocytic sources like deuterium are used for far UV. [1]

The SE instrument will measure a unique combination of Ψ and Δ for each stack and an optical multilayer thin film model can then be applied to compare the observed result with simulation. This is the main drawback of using SE as one requires some prior understanding of the structure of the thin film device being analysed. When sufficient knowledge of device structure is missing, there can be difficulties in decoupling thin film thickness from refractive index, especially when there are many different layers stacked together [1]. This

is complicated even further by the introduction of semi-transparent absorbing layers which extinguish light and have complex light-matter interaction. Fortunately, most of the issues can be overcome with experience and adequate evaluation of the sample structure using other techniques like AFM, XRR, 4-point probe, and Raman [8], [27], [35]. Figure 3.20 below illustrates how light becomes elliptically polarised after entering a thin film stack structure.

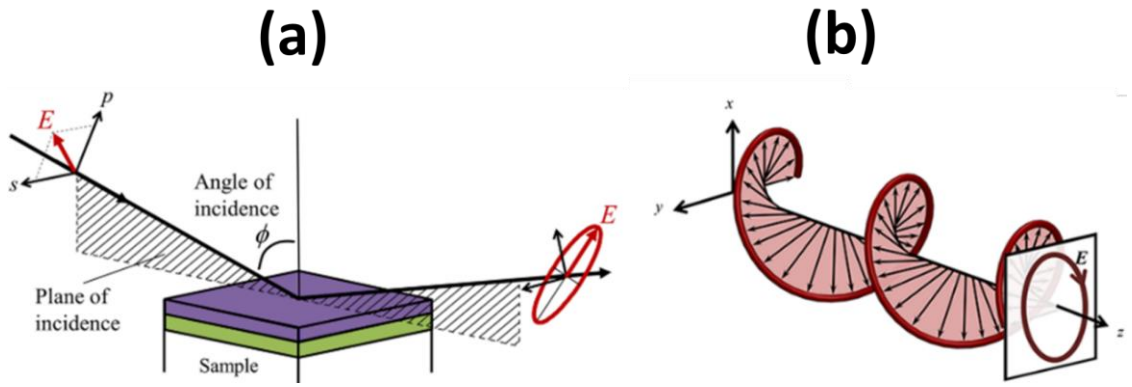


Figure 3.20. (a) Light is emitted by a source traditionally filtered to be one wavelength for the first SE instruments. The polarisation state is controlled and, in many cases, linear. After interacting with and reflecting off the thin film stack it has picked up a change in its polarisation state and the E field propagates elliptical with time as shown in (b). A sensor on the receiving end can measure this change and the ellipsometry parameters can be inferred. [1]

The specific reason for why the change in polarisation state carries information on the layer thickness and indices in the stack is related to the previously discussed thin film wave interference phenomenon that was covered in the previous chapters, needed to describe FP resonators. As a quick reminder, light that enters a multilayer stack will bounce around and refract inside the structure an innumerable amount of times. In fact, the number of times this occurs can be so large that attempting to apply the Fresnel equation directly in a sequential manner is a fool's errand.

Instead, another approach is used called the transfer matrix method (TMM) approach to simplify the problem into a steady state superposition of outbound and inbound travelling electric fields [36], [37]. More on this can be found in chapter 2. Each layer will leave an imprint on the final state of the reflected light beam given that all of the successive back and forth interface reflections/refractions, as well as layer propagation, will modify the amplitude and phase of the perpendicular electric field components that are in superposition with one another as shown below in Fig.3.21 [36].

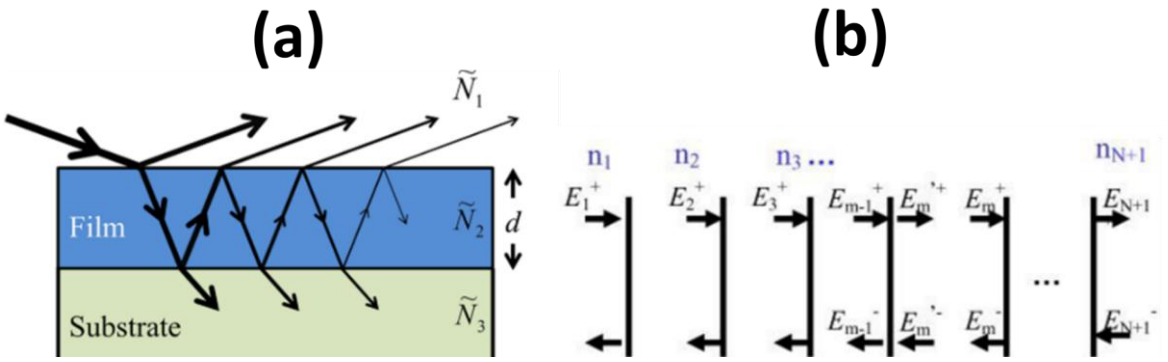


Figure 3.21. (a) Thin film interference of light propagating into a multilayer stack structure. The reflected light is made from the superposition of all light that escapes whether that be on first reflection or after the light has passed through, refracted, and remerged from the stack. (b) Superposition occurs for the perpendicular components of the lights electric field. Travelling in and out. Each of these fields subsequently represent innumerable back and forth reflections within their respective layer though high order contributions become vanishingly small in line with perturbative theory. [1], [37]

The proper practice of ellipsometry to study thin film surfaces began in the early 20th century with the use of limited wavelength measurements tools or single wavelength ellipsometry [38]. They required tedious manual operation and had none of the broad-spectrum capabilities of the post 1990 automatic modern systems that use rotatory and phase compensators, as well as vastly superior optical components that mitigate the effects of dispersion. These automatic spectroscopic ellipsometers incorporated fast charge-coupled device (CCD) detection into their design to rapidly speed up measurement time from minutes to seconds when paired with the rotary compensator [1]. These giant improvements were largely driven by demands from the industry, particularly the semiconductor fabrication sector which at that stage was creating chip nodes with features on the sub-micron scale [39].

Ellipsometers excel best at ultrathin to 1000 nm films, beyond which light is no longer coherent, presenting challenges with the optical modelling [40], [41]. The rapid refinement of SE towards the current day has enabled the creation of instruments that can completely profile the Stokes-Mueller Matrix, a 4x4 matrix representation of an optical element's transformation of lights intensity and polarisation in all 3 spatial dimensions. This matrix formulation expressed below reduces to the simpler 2x2 Jones matrix for isotropic materials in which no cross polarisation between s and p orientations occurs [1]. However, in cases where anisotropic thin films or stacks are used, the ability to quantify the entire 4x4 matrix is valuable as a method of non-destructively measuring the dimensions of sub wavelength structures like those one might find on a modern 10 nm chip process node.

$$\begin{bmatrix} S_0 \\ S_1 \\ S_2 \\ S_3 \end{bmatrix}_{out} = m_{11} \begin{bmatrix} 1 & -N & 0 & 0 \\ -N & 1 & 0 & 0 \\ 0 & 0 & C & S \\ 0 & 0 & -S & C \end{bmatrix} \cdot \begin{bmatrix} S_0 \\ S_1 \\ S_2 \\ S_3 \end{bmatrix}_{in}$$

(3 . 10)

$$N = cos(2\Psi), C = sin(2\Psi)cos(\Delta), S = sin(2\Psi)sin(\Delta)$$

(3 . 11)

Where m_{11} is the unpolarised reflection intensity, S_0, S_1, S_2, S_3 are the intensity vector elements, and the ellipsometer parameters N, C, and S are derived from Ψ and Δ [1]. For the purposes of this work N, C, S, or the Stokes-Mueller matrix are not central to understanding the thin film samples made. Most of the materials and stack structures worked with are isotropic or amorphous in their crystallographic nature and therefore cross polarisation concerns can be ignored. More complex anisotropic patterned surfaces would have need of this level of scrutiny, however [1].

3.3.2 Accuracy of the Ellipsometer Optical Model

To determine the uniqueness, sensitivity, and accuracy of the final optical model there must be a way to quantify the difference between the measurement simulation. To accomplish this simply the mean square error (MSE) or χ^2 formalism is used in the regression analysis of the fit at each wavelength data point. This form of MSE is shown below.

$$MSE^2 = \frac{1}{2P - M} \sum_{i=1}^{N} \left[\left(\frac{\Psi_i^{mod} - \Psi_i^{exp}}{\sigma_{\Psi,i}^{exp}} \right) + \left(\frac{\Delta_i^{mod} - \Delta_i^{exp}}{\sigma_{\Delta,i}^{exp}} \right) \right] = \frac{1}{2P - M} \cdot \chi^2$$

(3 . 12)

Where in this instance, P is the number of Δ and Ψ data point pairs, M is the number of fit parameters like thickness and refractive index, mod stands for model, exp stands for experimental data, and σ is the error in experimental Ψ or Δ. An MSE close to unity is ideal as this would indicate complete agreement between the model and experiment [22]. It is not possible to achieve exactly unity MSE due to inaccuracies in certain parameters like AOI or inhomogeneity in the sample that cannot be accounted for easily. An ideal MSE vs fit parameter M profile would look like Fig.3.22(a) below while the flat response in Fig.3.22(b) indicates an accurate but poor model. In other words, MSE is insensitive to film thickness in model 2 of Fig.3.22(b). Within the constraints of the available experimental data there may be correlations between the fit parameters M that create this profile. Significant correlations, particularly between index and thickness make it impossible to determine a unique solution, ultimately invalidating the regression fit [42].

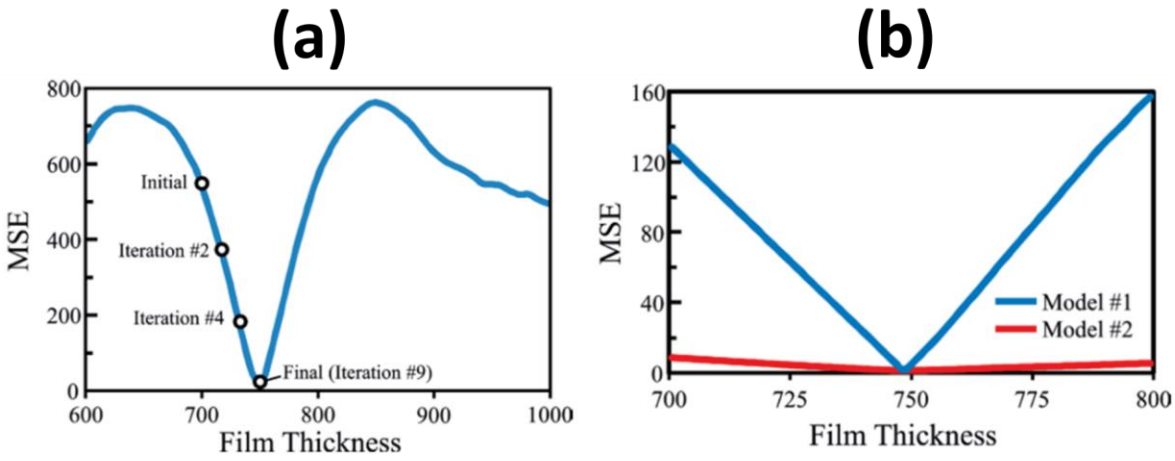


Figure 3.22. (a) A typical example of regression analysis in SE. The model used had an initial thin film thickness guess of 700 nm which after 9 iterations fell to the global minimum at 749 nm. (b) A comparison between a good model and a bad model showcasing how too much complexity in the simulations can induce high correlation. Most importantly both models have the same ideal film thickness but the second is not trustworthy at all. As a rule of thumb, the least complicated and correlated model is always the best choice. [1]

One way to see this in action is when multiple fit parameters adjust the model fit response in the same manner. The only way to rectify this would be to gain additional data using other techniques like XRR and UV-VIS spectroscopy to determine thickness and spectral intensities. This would decouple the fit parameters, and the profile would become more V-shaped than flat. There is a long list of tactics that can be carried out to help with this fit uniqueness issue and understanding them played a huge part in improving the accuracy of the results obtained from SE. One such tactic is to combine SE data with depolarisation data

acquired simultaneously during data acquisition. This is especially relevant for transparent or semi-transparent samples placed on glass substrate. Light that propagates through the optically thick glass will be depolarised [22]. When this light combines with reflection near the surface it will "muddy" the signal received by the detector. The compensator in the benchtop SE instrument can compensate for this whenever it occurs. In many instances, the inclusion of this additional data has adequately decoupled thin film thickness and index enough to make a unique solution viable. See Fig.3.23 below for SE data de-correlated by including depolarisation in the fit.

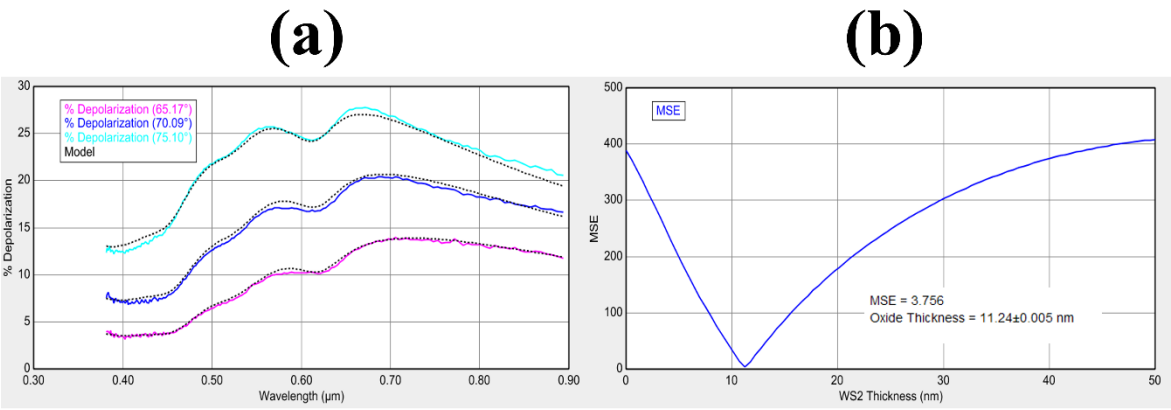


Figure 3.23. (a) The depolarisation caused by light propagating through the glass substrate and reflecting backup into the WS_2. By including depolarisation, the refractive index can be decoupled from thickness allowing the determination of the thickness of WS_2 on this glass sample to be 11.24 nm. (b) This solution in sensitive and unique given the V shape of the MSE profile.

Another commonly used tactic is to measure the sample in a transparent spectral region where $\kappa = 0$. This reduces the number of fit parameters down to thickness and index n, therefore mitigating the chance of correlation occurring. In practice this is done with transparent dielectrics, organic polymers, and semiconductors in the IR to NIR region depending on the light source available to the system. Many of these materials, especially the dielectrics, have smooth, predictable, and continuous dispersion in the same spectral region making it much easier to fit the data with a minimal number of parameters or functions depending on the model used [22]. Once the thin film has been fit in the NIR its thickness can be fixed and the existing fit can be extended to lower wavelengths by interpolation to find the index there. If the samples being looked at are known to be physically smooth, then this tactic works quiet well. If, however, there is inhomogeneities and microscopic surface roughness present, the NIR light will struggle to "see it" as easily as the shorter wavelength light and this could cause issues where an absorbing region and

transparent region model do not agree with each other. The depolarisation data from before could also be included to help with this, or to combat inhomogeneity more directly multiple different points on the sample could be measured to average out the final result. Given the limitations of the J.A. Woollam alpha SE tool used in this thesis work, the working range could not be extended further into the NIR to make use of this transparent region decoupling for some of the materials looked, like Ge and Si. Only in certain cases, like with ultrathin MoS_2, was this implementable as a strategy for decoupling as its optical bandgap fell within the working range of the ellipsometer. Figure 3.24 below displays data on this.

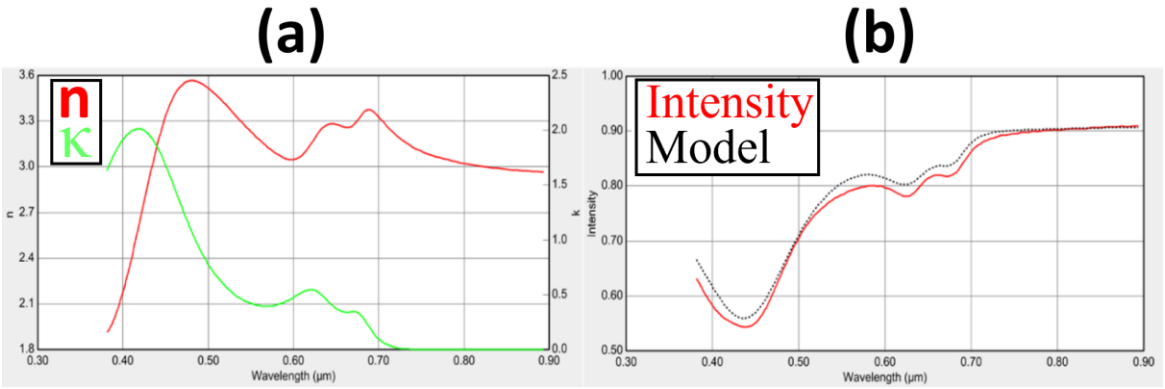


Figure 3.24. (a) The refractive index of 4.2 nm MoS_2 on an Al_2O_3/Quartz substrate. The thickness was bounded in the region of 700-900 nm wavelength, and the index for lower wavelengths was interpolated with a KK consistent Bspline function with resolution of 0.3 eV. (b) Decoupling was also assisted with the use of a transmission intensity T weighting performed after SE data acquisition. T baselines at 90 % in the NIR due to 10 % reflection at normal incidence for glass slides. The T intensity profile clearly shows the excitonic peaks of ultrathin MoS_2. The model fits reasonably well.

As seen in Fig.3.24(b), intensity weighting with reflection or transmission spectra can decouple correlated parameters. The J.A. Woollam Alpha SE Measurement instrument could perform transmission weighting after SE data acquisition by calibrating a straight through transmission with no material in the light path. Once calibrated a sample can be placed such that light enters it with a 0˚ AOI. This decoupling technique was used whenever for characterising the refractive index and thickness of ultrathin lossy dielectric absorbers, metals, and semiconductor samples like Cr, Ag, Au, W, Si, Ge, MoS_2, WS_2, and NiO, and so on. When on a glass backing only, these materials are expected to have greater absorption the thicker they are, in line with Beer lambert's law (single pass absorption) [1], [43].

To make further improvements on this one can produce several samples of the same lossy material with different deposition times and measure each one for SE and transmission intensity data. Then the results can be combined as a multi-sample analysis. This works well

for films that are not extremely thin but also not optically opaque as size effects can substantially change the refractive index of many materials [44]. Figure 3.25 makes this clear in the context of TMDs wherein ultrathin layers have very strong excitonic effects even at room temperature. The index of monolayer, bilayer, and trilayer TMDs are all measurably different from one another, and all deviate substantially from bulk. Similar size effect can occur in ultrathin metals due to dewetting, which Ag is infamous for, as well as the microstructure of the preferred grain sizes being constrained by thickness.

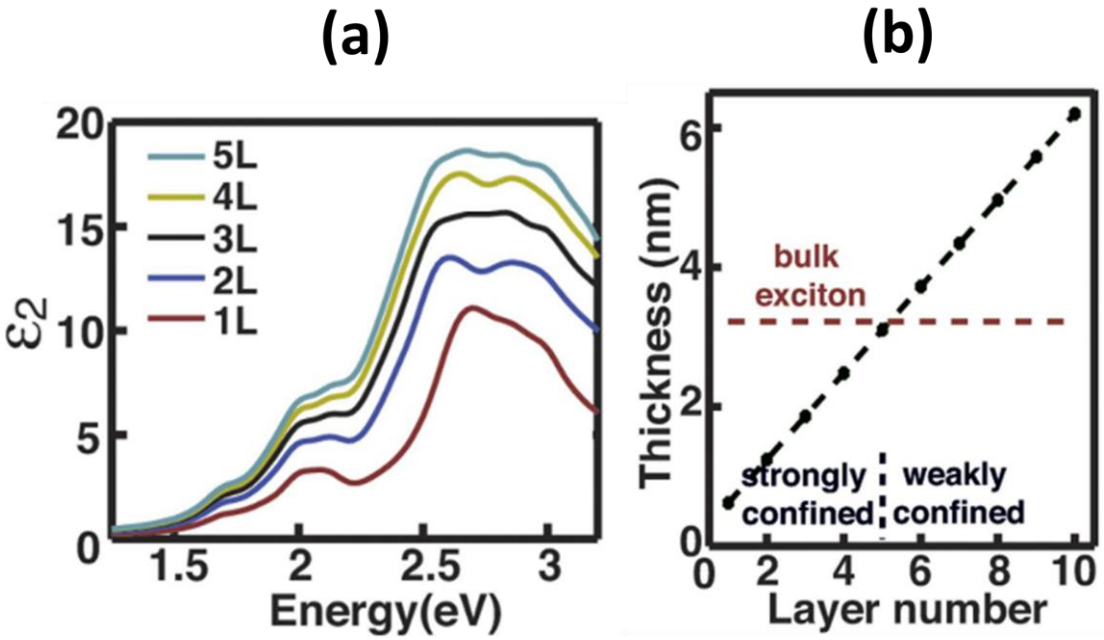


Figure 3.25. (a) There is a substantial change in the optical characteristics of MoS_2 as it shrinks in layer count in the ultrathin film regime. (b) This phenomenon is due to layer confinement of the 3.22 nm radius exciton, excitonic effects are very large in TMDs. [44]

Given the nature of SE, reflection intensity *R* can be done at the same time as ellipsometry and requires calibration using a very standardised sample. Typically, a thin SiO_2 on Si wafer. On the system used, *R* can be calibrated with a 25 nm SiO_2 on 500 µm Si 4" wafer. In practice this ends up being much less useful that Transmission weighting when it comes to decorrelation as SE data in a sense is already giving one reflection information. A straight - through reflectivity measurement may be of some benefit if used in conjunction with transmission, though this strategy has never been necessary for this thesis work.

Another way of acquiring more data on the same sample is to change the angle of incidence of the light striking it. An ellipsometer capable of this is called a variable angle ellipsometer and most modern devices have this functionality. Motorising the arms of the tool can add

quiet a lot of cost so cheaper benchtop solutions like fixed angle position are also possible alternatives. Having access to different angles is only useful if their response will vary a lot w.r.t AOI, which may not be the case with many of the omnidirectional device structures looked at like the zeroth order FP and Fano-resonators stacks [45]. Since SE characterisation of a fully developed multilayer FP resonator is not necessary to determine the refractive indices of the lossy dielectrics, this is not a big concern. If it were though, there are a few strategies to improving the angular response such as interference enhancement. If an absorbing layer with high n and k is placed on top of a thick oxide layer, then the difference in path length traversed by light for different angles can considerably change the value of Ψ and Δ enough to easily distinguish a unique fit as shown in Fig.3.26 below [22], [42].

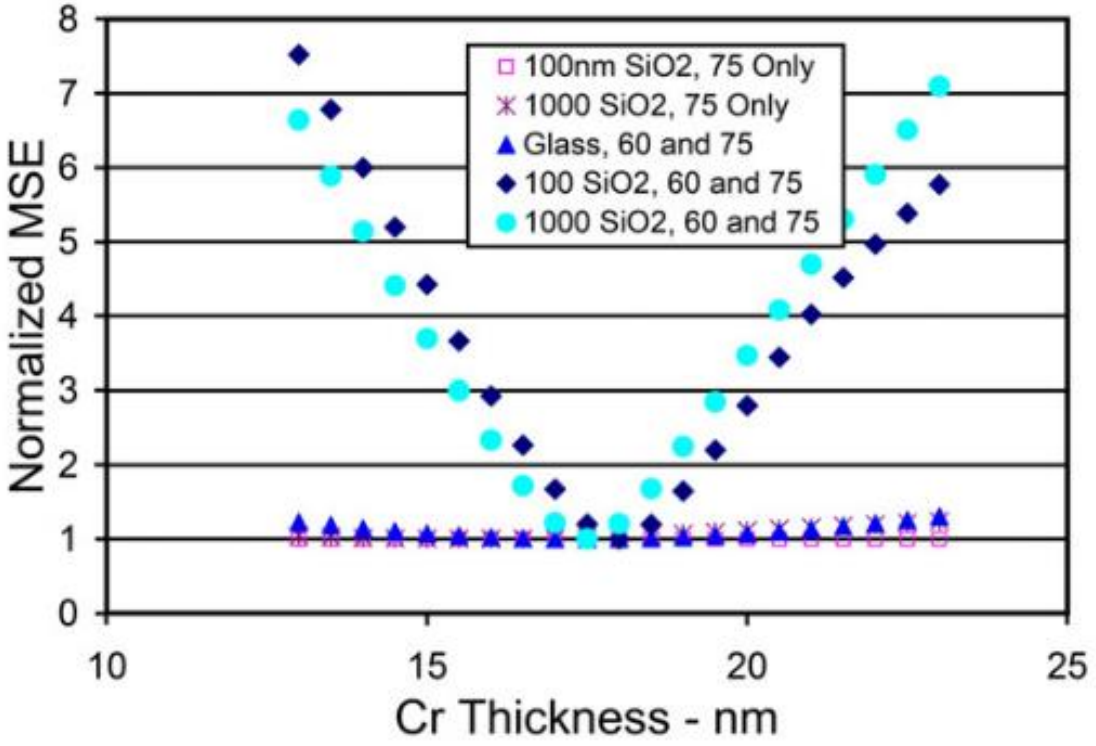


Figure 3.26. Different samples have been capped with Cr and measured at an AOI of 65˚ and 75˚. The samples with the thickest oxide spacer layer have the most unique uncorrelated solution compared to the extremely flat MSE profile of the glass only. [42]

3.3.3 Refractive Index Dispersion Expressions

Before moving on to describe the SE system used in closer detail, the topic of decorrelation will be concluded by briefly mentioning Parametrisation functions and the strategy of using intentional opacity in the thin film structure. For the former, the amount of information needed to describe the optical constants can be expressed with a dispersion equation. By

using an equation or a set of equations that are Kramers-Kronig consistent, the parameter space of possibilities can be greatly constrained [1], [42]. This strategy is one of the most effective decorrelation tools and will nearly always produce vastly superior result than a blind WVL fit that treats each wavelength data point independently. Most metals can be parametrised with one or more Lorentz oscillator functions that are linearly combined. In the case of semiconductors, the Tauc-Lorentz expression is almost always the best fit, and transparent dielectric thin films are accurately characterised by a Cauchy relation or a Sellmeier equation when there may be absorption in the NIR. Some of these expressions are listed below and originate from the J.A. Woollam Complete Ease user manual for reference [22].

$$n(\lambda) = A + \frac{B}{\lambda^2} + \frac{C}{\lambda^4}\ , Cauchy\ eq.$$

(3 . 13)

$$n(\lambda) = \left[\varepsilon(\infty) + \frac{A\lambda^2}{\lambda^2 - B^2} - E\lambda^2\right]^{\frac{1}{2}}\ , Sellmeier\ eq.$$

(3 . 14)

Where n is the refractive index, λ is the wavelength, A, B, and C are dispersion parameters, $\varepsilon(\infty)$ is index offset, and E is an NIR pole that also vertically offsets the dispersion. The optical model of an absorbing sample can be simplified through making it opaque. Under these circumstances no light from deep within the stack structure can reemerge due to the light being extinguished by absorption. This only occurs for optically thick materials like 150 nm Au and Ag or 300 nm Ge in the visible spectrum. Without the need to worry about thin film interference one can simply model the system as a simple single reflection interface described by the Fresnel equations given above. This allows one to derive an analytical expression for the optical parameters of the thick opaque absorber given by the expression below [42].

$$\langle \varepsilon \rangle = \langle \varepsilon_1 \rangle + i \cdot \langle \varepsilon_2 \rangle = sin(\phi)^2 \cdot \left[1 + tan(\phi)^2 \cdot \left(\frac{1 - \rho}{1 + \rho} \right)^2 \right]$$

(3 . 15)

Where all variables have their usual meanings and ρ is the fundamental equation of ellipsometry. The optical permittivity parameters are surrounded by bra-ket notation markers to denote that they are "pseudo parameters". In the bulk condition the pseudo parameters are equivalent to the intrinsic dielectric function [42]. Care must be taken to account for potential surface oxidation or microscopic roughness when relying on the pseudo approximation. For an inert metal like Au, this technique works very well while W will quickly form a native oxide that re-introduces wave interference back into the model.

3.3.4 J.A. Woollam Alpha Spectroscopic Ellipsometer System

The hardware specifications of the J.A. Woollam Alpha SE system used is as follows. Its capable of measuring an AOI of 65˚, 70˚, and 75˚. Straight through AOI of 90˚ is also possible. A quartz tungsten halogen lamp is used as the light source. The available wavelength range in 400-900 nm. An automated mechanical stage adjusts the sample alignment in the z direction. The detector is a CCD and typical data acquisition rates are 5-10 seconds for the entire available spectrum. It is a benchtop top system that has since been replaced by a superior alpha 2.0 with a wavelength range of 400-1000 nm. The alpha SE used works best with planar transparent and absorbing dielectric thin films, which suits the purposes of this work well. Photographic imagery of the tool can be seen below in Fig.3.27. All surfaces have been given a matt finish to prevent unwanted specular reflections. The AOI is also adjusted manually with a pulling locking mechanism attached to a spring. Both the emitting and detecting arm must be moved to the same angular position, otherwise the complete Ease software controlling the instrument will display and error message. A similar error will occur if the reflected light beam fails to enter the detector aperture due to tilted sample orientation off the horizontal. If the tool fails to acquire the beam position for erroneous reasons, a system restart or stage re-calibration will normally resolve the issue.

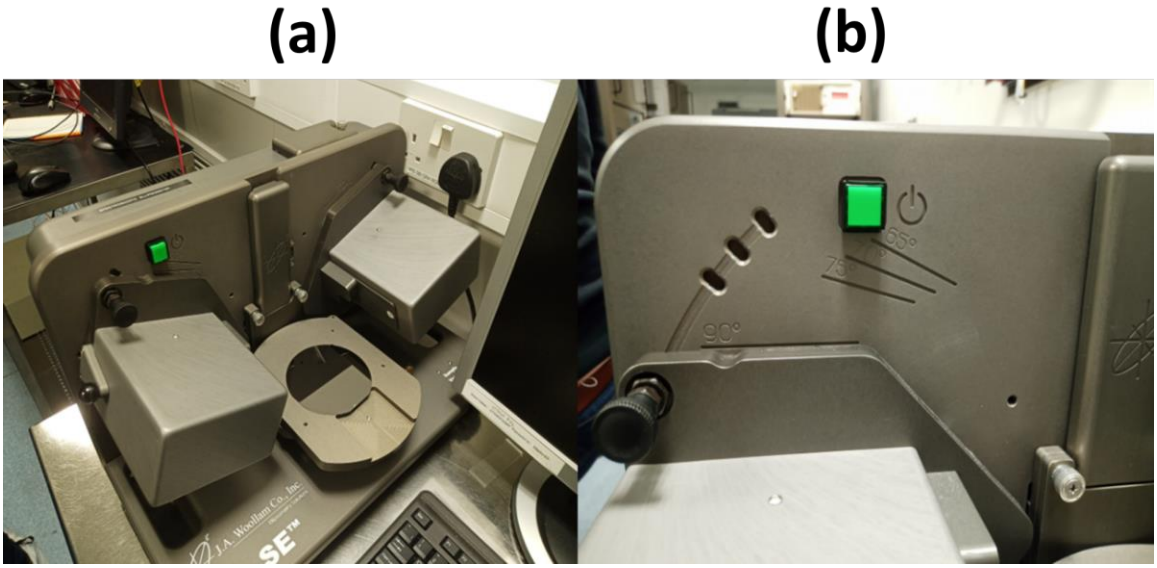


Figure 3.27. (a) A view of the entire SE measurement instrument with a SiO_2/Si wafer placed on the sample stage. (b) The range of AOI available to the system.

With this overview of SE complete, the next techniques that will be looked at in detail are spectroscopy based. Spectroscopy itself is a field of study focusing on the interpretation of EM intensity spectra in a whole host of different regimes. For the aptly named UV-Vis technique, the part of the EM spectrum that human eyes can see is the region of focus. For Raman spectroscopy the scattered terahertz frequency (10^{12} – 10^{14} Hz) vibrational mode peaks of an unknown material are looked at to determine the identity of the substance being illuminated by a laser [6]. In the case of the first principles x-ray reflectivity (XRR) technique, X-ray photons are shone onto a thin film sample at nearly 90˚ AOI near the critical angle. By careful monitoring the reflected intensity w.r.t the x-ray beam angle one can ascertain the thin film thickness ad density from fitting the resultant intensity oscillation peaks [27]. XRR is first principles as no prior knowledge of the sample is needed, making it ideal for initial estimates of the deposition rates of magnetron sputtering targets. Foregoing knowledge of the thickness also makes it possible to decouple parameter correlations in the SE technique.

3.4 Spectroscopy

3.4.1 Overview of Spectroscopy

The study of optical spectroscopy is historically associated with Newton's study of the dispersion of the Sun's light when it passes through a prism [46]. By splitting white light

into its constituent colours, it became possible to measure the wavelength resolved EM response of matter. This was used to look at the wavelength specific absorption profiles of gasses and liquids, leading to the discovery of the famous Beer Lambert law [43].

$$\mathrm{I(x)} = I_0 \exp(-\alpha x)$$

(3 . 16)

Where I_0 is initial light intensity, α is the extinction coefficient, and x is the penetration depth. This expression is readily applicable to bulk materials in which wave optic effects can be ignored. The unique absorption spectra of different isolated gases were measured in the lab setting as the scientific revolution came onto the stage. Using these absorption spectra as reference, astronomers proved that the Sun along with all stars were made from a hydrogen helium mixture [34]. They were also able to confirm the presence of many terrestrial elements in deep space nebulae.

With the arrival of thermodynamics onto the scene, scientists also began to understand the statistical mechanics behind black body spectrums for matter in equilibrium with their environment. In so doing they attempted to understand the mathematical equation underpinning the black body spectrum of heated objects and stars. A deeper comprehension of this fact would lead to a better understanding of the phenomenon of colour as experienced on the surface of the Earth. Max Planck in 1901 published a landmark paper displaying equation for the spectral energy density of a blackbody's radiation profile using the expression below [34].

$$\rho_v(v,T) = \frac{8\pi v^2}{c^3} \cdot \frac{hv}{exp\left(\frac{hv}{k_B T}\right) - 1}$$

(3 . 17)

Where ρ_v is the spectral energy density, v is frequency of light, h is Planck constant, k_B is the Boltzmann constant, T is temperature, and c is the speed of light. To arrive at this famous result Plank assumed the quantum nature of light indicating that the EM field was discretely broken up into quanta or photons of specific energy w.r.t their wavelength as explained in

chapter 2 section 2.2.1. Thus is this way the wave nature of the EM field was linked to the quantum particle nature of the photon. On the most fundamental level, absorption from then on was understood to be a quantum phenomenon leading to the quantised subtraction of energy from an incident EM field. Furthermore, this led to an avalanche of new discoveries over the course of the 20th century in the field of electrodynamics and optics which improved on the design and capabilities of spectrometers among many other experimental instrumentation. The range of available wavelengths also increased as microwaves, THz frequencies, and x-ray reflectometer tools became available to researchers for material characterisation purposes [34]. In particular, the evolution of X-ray measurement devices were greatly helped by the rapid improvement of vacuum technology in the latter half of the last century [8], [27]. Photodetector sensors drastically improved in sensitivity and wavelength range as well in the form of CCDs [1], [35].

3.4.2 Perkin Elmer UV-Vis Spectrometer System

In modern times the UV-Vis spectrometer is versatile and can measure the intensity of reflection R, absorption A, and transmission T for a whole host of different ample types depending on the set up. The spectrometer system used in this thesis work is the Perkin Elmer LAMBDA 1050 UV/VIS/NIR, funded by Science Foundation Ireland (SFI). A triple detector device system capable of accurately measuring the intensity spectra of R, T, and A across a wavelength bandwidth of 200-2500 nm. A tungsten halogen lamp and D_2 lamp generates the necessary spectrum and the monochromator filters light as a drum rotates inside the tool. A beam splitting system is used for monitoring the output alignment. There are two chambers with the first containing the aperture stand for controlling the beam size incident on the sample to be measured, and the second compartment used for the lens function and sample mounting. When operating the tool in transmission mode, the lens drums must be rotated to focus the light source beam onto the front of the sample. The PerkinElmer system is not angle resolved so all measurements are done with straight through AOI. The sample can then be mounted onto the clips as shown in the photographic image below in Fig.3.28(a). Before measurement, a null sample calibration is done to normalise the intensity of light hitting the InGaAs detector. This detector lies inside an integrating sphere which captures almost all light that transmits through or reflects off a sample used by this spectrometer. The integrating sphere is coated with barium sulphide which has very high reflectivity across the working wavelength range of the device.

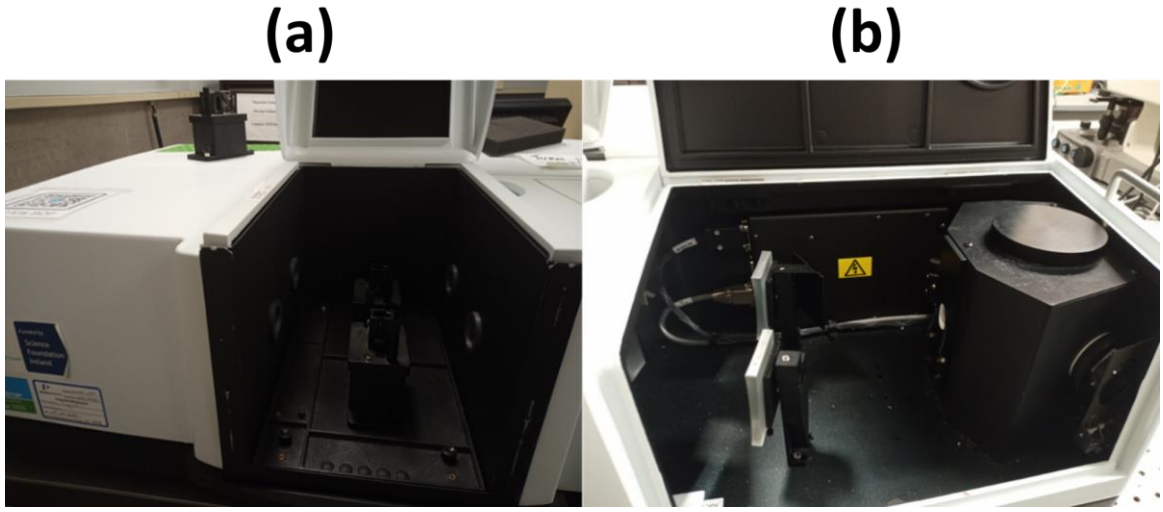


Figure 3.28. (a) The aperture compartment of the optical spectrometer system. The aperture size controls the incident beam intensity. (b) The lens drum has been removed for clarity. The sample sits on the clips at the entrance to the integrating sphere on the right with the top cap sticking out. The lens system will sit in front of this entrance during operation. The flip open door will also be drawn down to eliminate outside light from interfering.

To be more technical the integrating sphere in the steady state enhances the spatial integration of radiant flux. The more reflections that occur within the sphere, the more light can be taken in by the detector. Figure 3.29 below illustrates this point. The mathematics that describes this originates from diffuse reflection theory which can be very complex [47].

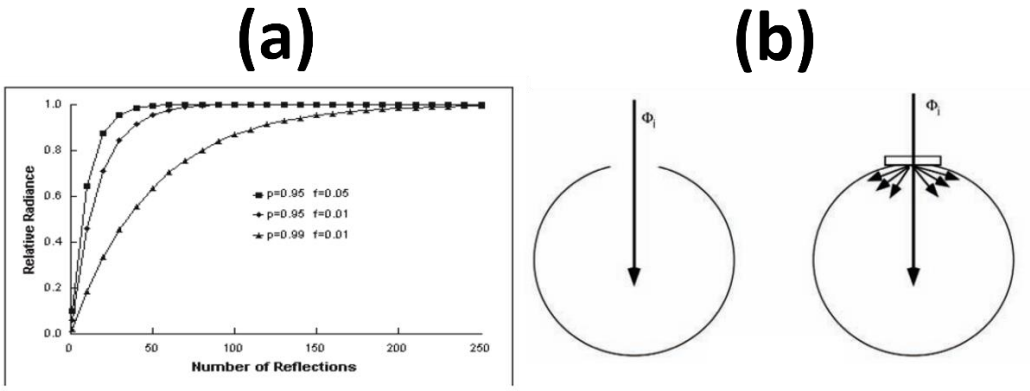


Figure 3.29. (a) As the number of reflections go up the radiance of the sphere increases which optimises the spatial integration. (b) A cross sectional diagram of the integrating sphere in the null condition and with a sample placed in front of it for a transmittance measurement. [47]

There is a 20–30-minute warm-up period for the lamp intensity to stabilise in time. Even still, the intensity will waver somewhat overtime at a relatively constant rate due to the PSU. Extremely low incident intensities should therefore be avoided as the calibrated spectrum would contain too much noise relative to signal. An initial beam diameter of around 3-4 mm

was found to be sufficient for keeping 100 % straight through calibration stable while also allowing one to measure smaller sample areas, particularly the centre of the microscope glass slide which housed the highest quality thin film deposit compared to the more irregular surface topology of the edge regions. In reflection mode the sample must be placed at the back of the integrating sphere in place of the back white cap shown below in Fig.3.30(a). The lens drum is rotated so that the light beam comes to focus on the back of the sphere. A re-alignment of the optics may be necessary to centre the beam on the back light trap exit of the sphere. Apart from sample mounting, lens choice, and aperture width, all device parameters are controlled by a UV WinLab software. The scan range and resolution, measurement mode, detector response, and monochromator slits can be adjusted digitally.

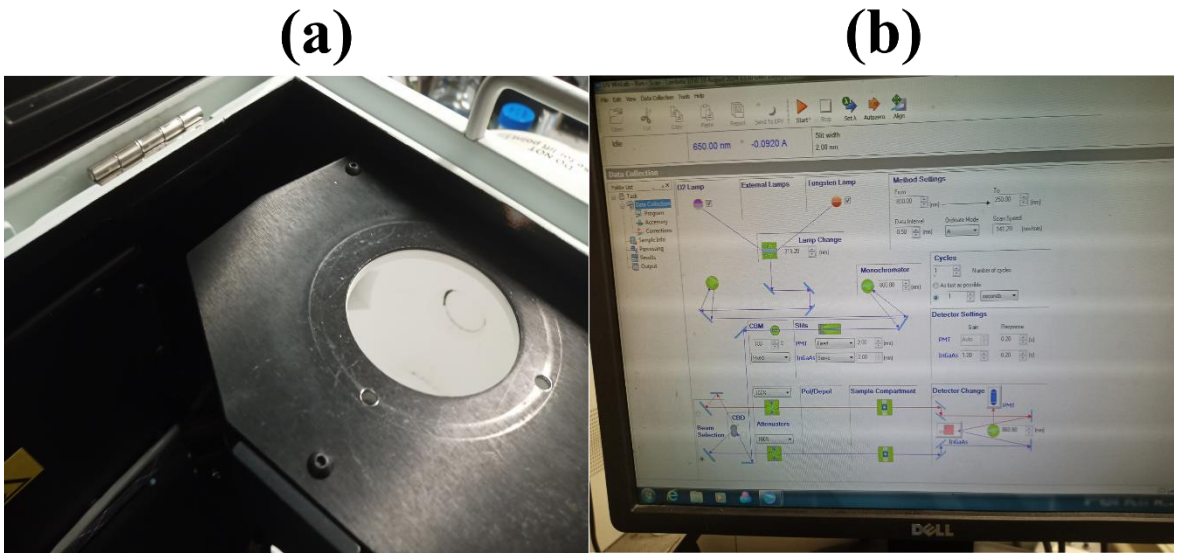


Figure 3.30. (a) A top view of the integrating sphere with the removal of the light trap back cap inside. In reflection mode the sample will sit here in place of the white reflector. (b) Aspects such as the wavelength range, resolution, and detector measurement time can all be changed virtually using the UV Winlab software interface. This software also indicates the two light source lamps as a D_2 and tungsten Halogen lamp.

3.4.3 Processing of UV-Vis Data

Once all measurements are taken, they can be exported to excel files, which can be opened in OriginLab software and used to present the data with professional clarity. The spectra can also be opened by a chromaticity diagram MATLAB program to calculate the colour coordinates on the CIE 1931 chart. This colour mapping program is based on the chromaticity code created by Tingbiao Guo at Zhejiang University China [48]. Its compatible with reflection and transmittance spectra. The transfer matrix method (TMM), also written on Matlab, can simulate the intensity spectra profile for R, T, and A using data

acquired from SE. The accuracy of the predicted spectra and colour can be compared by superimposing both on the same graph as Fig.3.31 below of a TiO_2 on Ag calibration sample illustrates. Small discrepancies that may be found between experiment and simulations are normally attributable to microscopic surface roughness. Other kinds of nonideality like macroscopic thickness inhomogeneity across the beam diameter can change the effective index of the thin film layer, altering the optical response. On a smooth planar film these effects are very minimal at best.

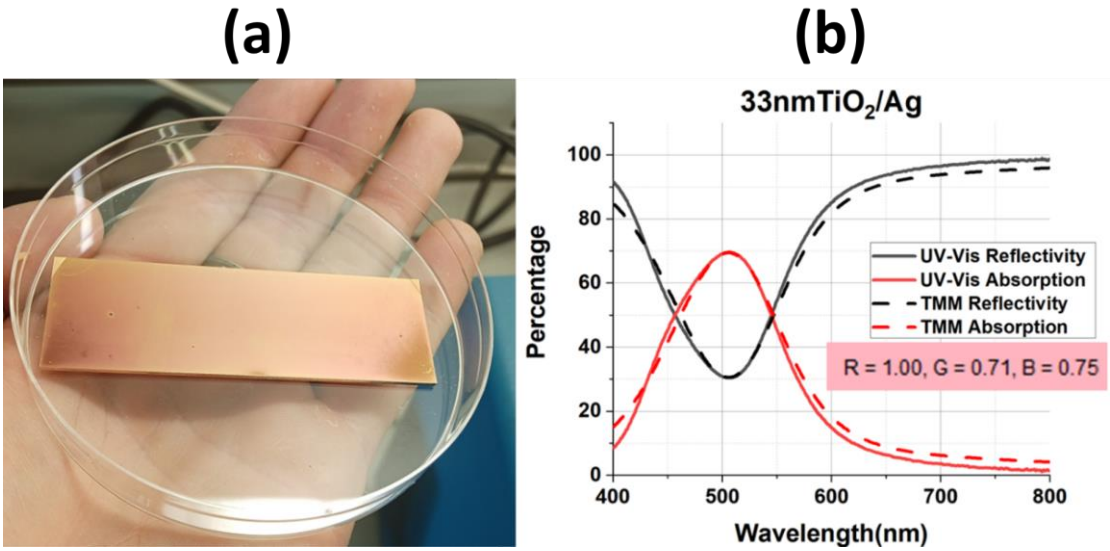


Figure 3.31. (a) A pink 33 nm TiO_2 on Ag, used for calibrating the lower MIM section of the Fano-resonant device structure. The quality of the thin film is greatest at the centre near the palm of the hand while discolouration and defects can be seen at the edges. The length of the glass substrate slide is roughly on the same order as the diameter of the magnetron sputtering target. (b) A comparison between TMM simulation and UV-Vis spectroscopy measurement of the reflection and absorption of this sample. There is very good agreement in the overlap which around the absorption peak at 510 nm is likely due to the Tauc-Lorentz oscillator that models the dispersion of the index in SE. The slight deviation in spectra at lower and higher frequencies is most likely due to microscopic surface roughness or slight differences in the index of the Ag back reflector from its reference value.

The presence or absence of surface roughness may not be readily detectable by SE for multiple reasons. The MSE fit might not improve significantly enough (> 25 %) if the EMA roughness layer is included. The effective index of the rough layer could also be very close to the thin film underneath making it difficult to sperate the contributions of each separate layer to the optics of the stack. If enough sensitivity exists towards the roughness layer, then it can be incorporated into the optical model. SE is insensitive to the roughness of low index films, especially those that are transparent due to the close impedance match between them and air like MgF_2 and SiO_2 [1], [42]. A thin film with a large index difference between itself and air will have surface roughness that is much easier to resolve. One can effectively model

it as a sperate EMA layer on top of the film underneath [1]. Bulk Au and Ag are candidate examples of this. The surface morphology of higher index lossy dielectrics such as Si and Ge can be "seen" more easily too. Figure 3.32 below showcases the near 300 % improvement in MSE fit of a bulk Au calibration sample when roughness is included.

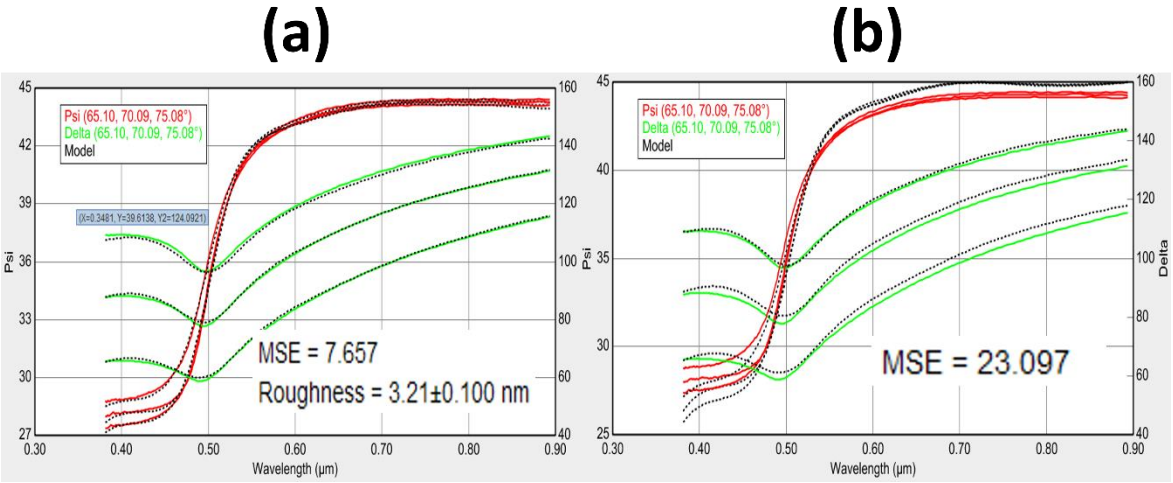


Figure 3.32. (a) An SE fit of 200 nm of Au on glass substrate using a 3.2 nm EMA roughness layer in the model. Visually the fit is quite good. (b) Without the roughness layer the fit is considerably worse and visually deviates in the near UV and red regions of the spectrum. The larger deviation in Ψ relative to Δ indicates that the model most certainly needs an additional lower index layer to be added.

It is important to note that SE and optical spectrometry cannot look at the true physical nano scale surface structure directly but are instead sensing its optical effect, if there is any. Its instead always prudent to look directly at the surface morphology using first principal techniques like AFM to image the surface with true Angstrom resolution. Features at such subwavelength size scales primarily only influence the optical response by wave inference effects, with minimal to no scattering occurring [1]. Researchers have gone through great lengths to establish models that link the more cumbersome to acquire AFM data to simpler and more rapid optical characterisation methods. This effort remains on going.

3.4.4 Physics of X-Ray Spectroscopy

Both SE and optical spectroscopy played a significant role throughout the course of the project, forming the core of measurements done to characterise the samples made. Other previously mentioned spectroscopic techniques like XRR and Raman spectroscopy found an auxiliary role, helping to conclude sample identity, quality, and dimensions. The basic physics outlining both is explained in the following. X-rays were first discovered by

Wilhelm Conrad Röntgen in 1895, where they were used to photograph the bones in his wife's hand [27]. Progress in the theoretical understanding of x-rays led scientists to use them in characterising very small structures on the order of the scale of the atom itself (Angstroms). Namely x-rays allowed chemists and condensed matter physicists to analyse the crystallographic structure of solids directly [27]. By measuring the angularly resolved intensity profile of diffracted x-ray radiation, the crystal structure of the sample being measured could be ascertained. As a result, parameters like lattice constant, uniformity and symmetry could be obtained with a high degree of accuracy. The structure of DNA was found using this approach, with the only major difficulty being the isolation of the strand given it measures 2 nm in width [27]. See Fig.3.33(b) below illustrating x-ray crystallography of the DNA molecule.

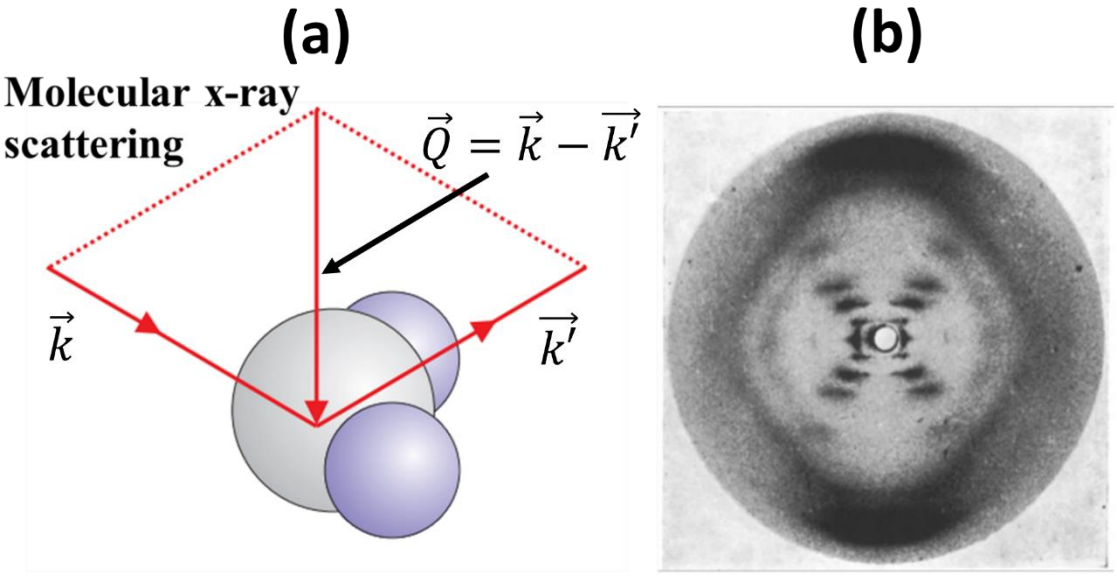


Figure 3.33. (a) The wavevector of the incident x-ray $\vec{k}$ scatters off a molecule with new wave vector $\vec{k'}$. The wave vector transfer $\vec{Q}$ is given as shown. When many molecular scatterings take place a picture of the molecule can be built up in momentum space (reciprocal space) which can then be Fourier transformed into real space for the true structure [27]. *(b) The famous Watson and Crick 1953 result showing a DNA x-ray image proving that the molecule had a double helix structure.* [49]

At the beginning of the 20th century the brilliance of x-ray sources was limited due to the inefficient x-ray tube source. This held back progress to some extent in the development of the technology, especially in the context of using x-rays to probe magnetic resonance effects in matter given how weak spin orbit interactions are for nonmagnetic materials compared to the electric response [27]. With the introduction of more powerful sources like the synchrotron electron accelerator in the 1970's, dramatic improvements were made in the

capabilities of x-ray measurement tools with nearly a trillion-fold increase in average brilliance obtained. These synchrotron devices went on to be used in particle physics to discover the so called “particle zoo” of hadrons and baryons made from the fundamental quark particles and are the basis behind the engineering design of incredible powerful TeV energy level modern colliders [27], such as the large hadron collider in Geneva Switzerland. Figure 3.34 displays a diagram of the exponential trend in x-ray beam brilliance increase over the 20th century, ultimately culminating in the development of modern free electron laser systems that can reach astoundingly high brilliance almost 20 orders of magnitude higher than the fixed tube design used by Röntgen over a 100 years ago.

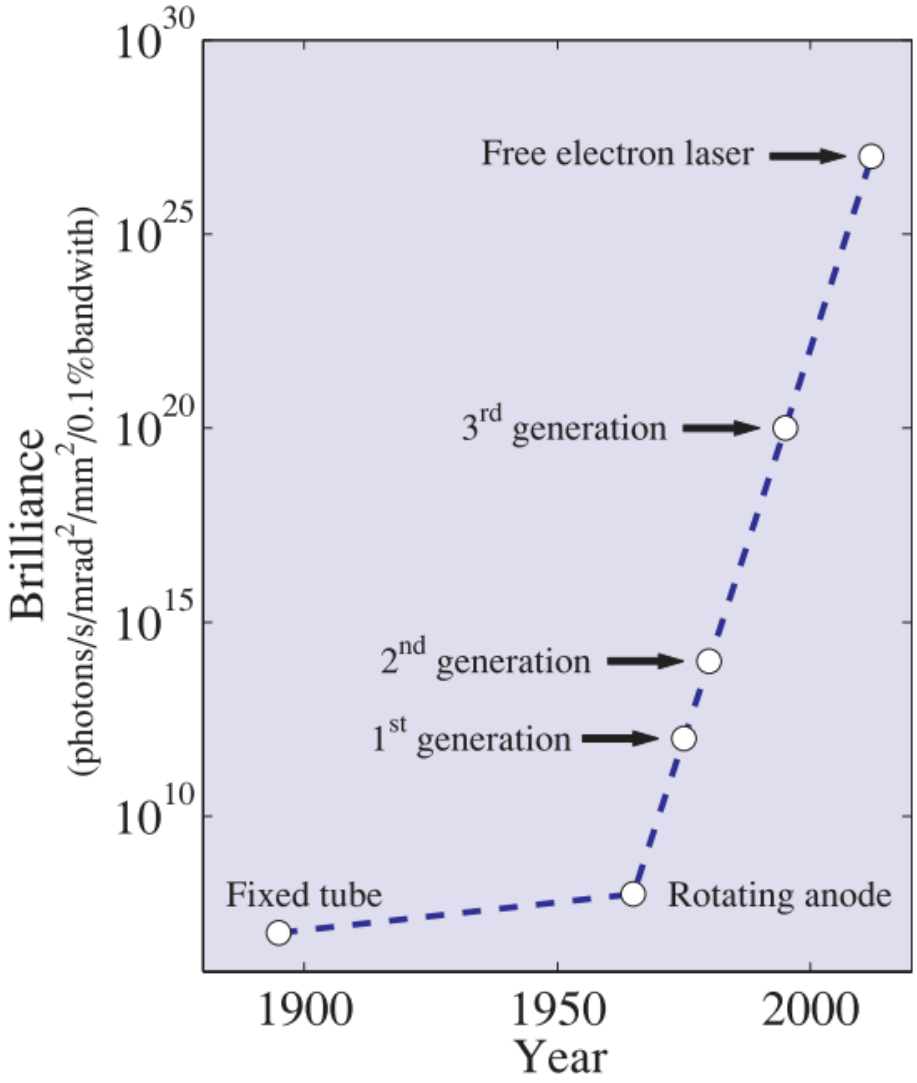


Figure 3.34. The exponential improvement in x-ray beam brilliance w.r.t time since the invention of the first x-ray tube in 1895. With the arrival of high quality affordable commercial vacuum technology onto the scene in the 60’s and 70’s, the performance has since jumped by 17-18 orders of magnitude. [27]

XRR is a reflectometry technique that illuminates a thin film target with monochromatic x-ray EM radiation. Under the condition of total external reflection x-rays will penetrate very little into an EM medium [50]. In this way the intensity of reflected light will vary sharply with grazing incident angle making this technique extremely sensitive to surface conditions. The source of x-rays on some modern instruments is a synchrotron storage ring which produces a spectrally narrow continuous beam of x-rays. Free electron lasers can produce higher intensities but at the cost of being pulsed. Pulsed light sources are useful for situation in which certain quantities need to be resolved temporarily [27]. In the case of optics, a pump probe delay laser system is designed to measure pico-second time dynamics of the light matter interaction such as the excitation and relaxation of electrons in semiconductors or the thermal physics of electron-phonon scattering [51]. For pulsed free electron laser, attosecond (10^{-18} s) time scales can be explored such as the decay of fundamental particles and motion of electrons between atoms [52]. Figure 3.35 below is a diagram of a synchrotron storage ring accelerator x-ray beam source.

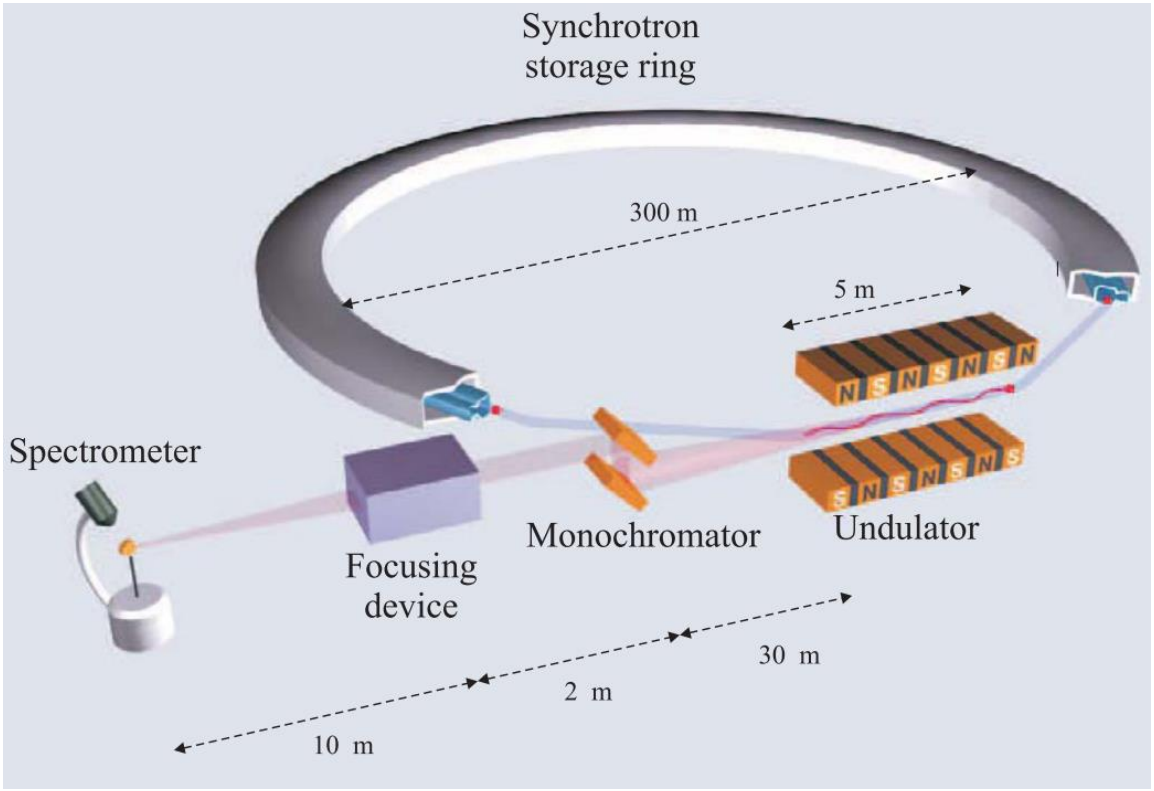


Figure 3.35. A third-generation synchrotron x-ray source. X-rays are created as accelerated electrons pass though the undulator. This generates a collimated x-ray beam that is directed towards a crystal setup called a monochromator that spectrally narrows the beam before sending it to a device that focuses the x-rays down to the target sample in the spectrometer section [27].

For benchtop compact x-ray instruments, the rotating anode can be used to generate the x-ray emission. The basic layout of the more compact XRR tool used is given by Fig.3.36 below. When considering sizes above the atomic and molecular level x-rays should fundamentally be thought of as EM waves that can interfere with one another [27]. Given their wave nature it stands to reason that under certain circumstances x-rays may be made to interfere with one another inside matter like how optical fields act in ATF stack structures [36]. The major differences are the penetration depths, and the working angles involved. With x-rays the AOI must be at an extremely grazing angle for it to undergo specular reflection, otherwise scattering behaviour will dominate which is not desirable for reflectometry purposes [27]. Due to the high angle, the penetration depth of the evanescent x-rays can practically not go beyond 100 nm, meaning XRR has no use in characterising bulky samples clearly outside of their surface roughness or morphological features within this thickness bound [4], [26].

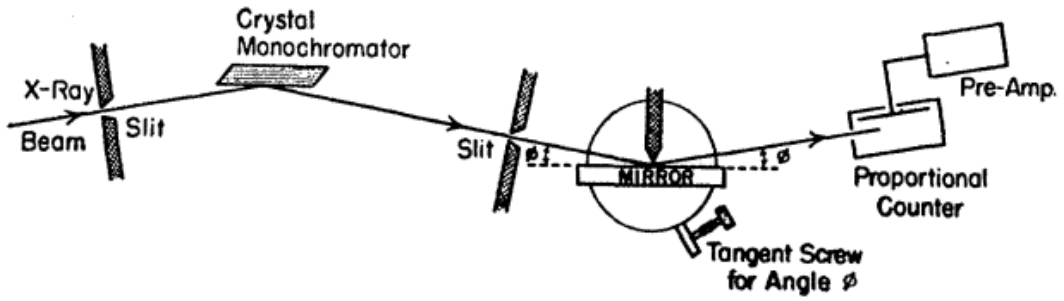


Figure 3.36. The x-rays produced by the rotating anode are collimated with a slit and spectrally narrowed with a crystal monochromator. The reflection off the crystal is collimated again with another slit before falling incident on a sample at and below the critical angle for specular x-ray reflection. The beam will then strike a proportional counter detector that absorbs x-ray light. The detection equipment is similar in principle to radiation counters that monitor EM ionising radiation from nuclear sources. Incoming radiation is scintillating into visible light where its then subsequently detected by a photodiode connected to an amplifier unit [50].

The physics of how x-ray reflections can be used to determine surface parameters harkens back to the Fresnel equations that govern the behaviour of EM waves. For planar homogenous stratified media, the Fresnel equations describe the reflection and refraction of light because of an EM wave entering the stack, in other words the light-matter interaction at the interface [34]. At x-ray energies the dispersion is determined not by the polarisability of bound valence electrons or oscillation resonances but instead by the scattering of x-rays off core electron shells bound tightly to the nucleus [27]. Materials with large refractive index in the radio and microwave regime are commonly found, but at ionising energy levels

almost all objects will have a refractive index that is very close to unity. The exact value is given by the expression below.

$$n = 1 - \delta + i\beta$$

(3 . 18)

Where δ is the decrement of the material from unity, related to how strongly the core electrons scatter the x-rays, and β is the imaginary component which is very small for most materials. δ is always positive but very small at around 10^{-5} in solids and 10^{-8} in air [27]. With this expression the critical angle α_c can be determined for total external reflection using the equations derived from Snell's law below.

$$cos(\alpha) = n \cdot cos(\alpha') \, , \alpha_c = \sqrt{2\delta}$$

(3 . 19)

Where α and α' are the incident and refractive grazing angle (relative to horizontal and not the surface normal line like is usual for this nomenclature). Below the critical angle there will be a sharp drop in penetration depth as specular behaviour takes hold and the x-rays act as an evanescent wave parallel to the surface [27]. Gathering data around α_c will therefore provide exquisitely sensitive information about the surface condition. This angle is often extremely small on the order of a milliradian. Under these circumstances a sample placed in the XRR machine can have its thickness and density determined form fitting the characteristic shape of the reciprocal space intensity count oscillations that represent the interaction of the evanescent wave with the surface layer [27]. The thinner and simpler the layer the less oscillations there will be. Thicker thin films will produce more tightly spaced oscillations. The Bragg equation from fundamental condensed matter theory can be used to relate thickness to the Kiessig oscillation fringe spacing and AOI as shown [26].

$$2D\sqrt{sin^2(\alpha) - sin^2(\alpha_c)} = m\lambda$$

(3 . 20)

Where D is film thickness, α is again the AOI, λ is wavelength, and m is the integer number of the oscillations with oscillations closer to α_c being lower in number [26]. The oscillations produced can be shown versus wave vector or AOI. AOI is the standard dimension for the x-axis as seen in Fig.3.37. Material density ρ of the thin film slab can be found from the following relation [26].

$$\alpha_c{}^2 = (5.402 \times 10^{-6}) \cdot \frac{(Z + f')\rho\lambda^2}{A} \qquad (3.21)$$

Where Z is the atomic number, f' is the real component to the anomalous dispersion correction factor which essentially accounts for x-ray absorption effects specific to the material being analysed, and A is the atomic weight of the thin film slab [26]. The entire process of setting up the sample, aligning it, and carrying out the angle sweep takes about 20–30-minutes in comparison with the 5–10-seconds to perform SE. Once the data is collected a χ^2 best polynomial fit can be done to match equations 3.20 and 3.21. This fit can then be used to directly ascertain the D and ρ material parameters.

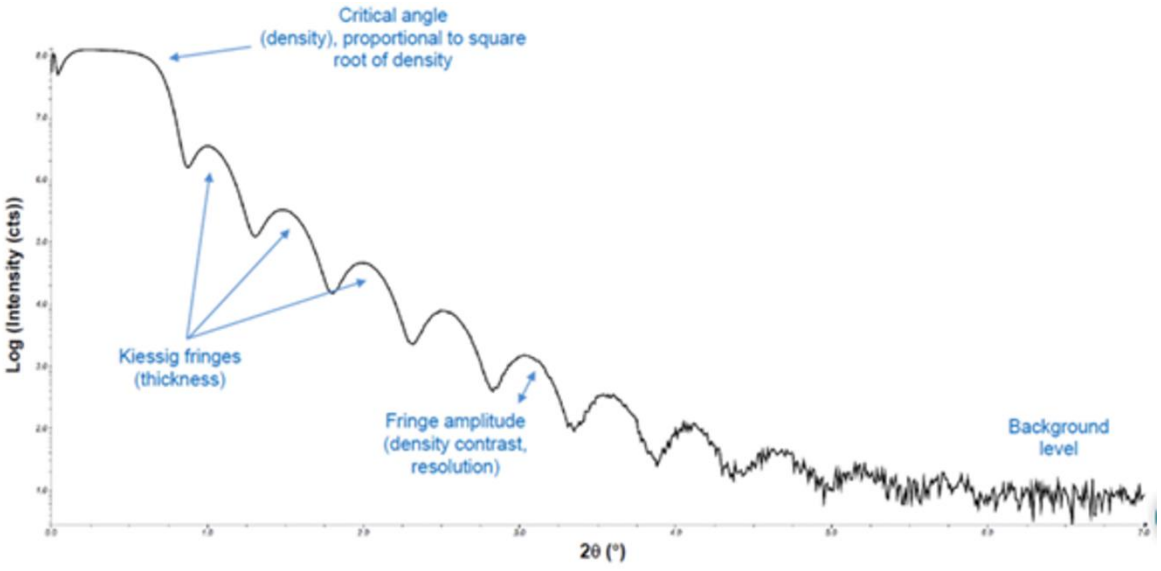


Figure 3.37. Different features of the XRR spectrum are accounted for by different material properties. The fringe spacing is highly dependent on thin film thickness while density affects the height of the fringes and the critical angle. Higher density materials often have larger atomic number which increases the interaction cross section for x-rays. This is why calcium containing bones light up bright white on x-rays while flesh is much more transparent.. [4]

3.4.5 CRANN X-Ray Reflectometer System

Shown in Fig.3.38 are photographs of the XRR tool available for use in CRANN. A lead lined glass shielding interlock door protects the user from scattered x-ray photons as they are cancer causing. This machine can carry out XRR and XRD, the latter having already been glimpsed over earlier to characterise crystallographic structure with high precision. Different armatures are needed for either run as the angle swept in each case is drastically different. The group expert on carrying out the XRR technique in both the physical measurement and polynomial fitting is Chris Murray.

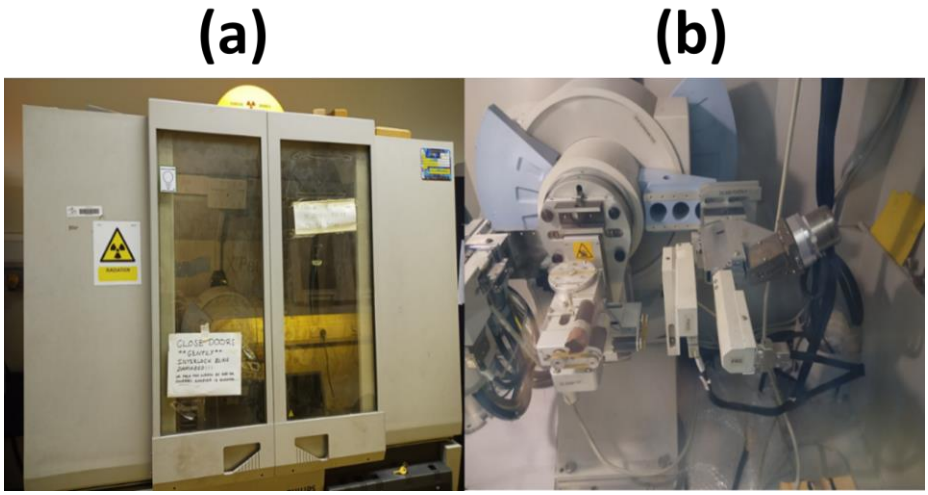


Figure 3.38. (a) The lead lining in glass doors adds a yellow brown tinge to the glass. An interlock is attached to instantly shut off power to the x-ray source if the door is opened during operation. (b) The sample can be seen sitting on the centre adjustable stage with two arms rotating around it. One arm contains the x-ray source, and the other is the scintillator photodetector.

3.4.6 Physics of Raman Spectroscopy

Raman spectroscopy was used sparingly throughout the course of this project. It was most useful for characterising the thickness of ultrathin TAC MoS_2 or confirming the presence of certain oxides through their vibrational resonance modes. Raman scattering analysis first came onto the scene in 1928 thanks to the work of Indian scientist and Nobel laureate C. V. Raman who observed the hall-mark inelastic scattering, also known as Raman scattering, of photons off organic liquids; using the data to identify the vibrational modes of the chemical bonds making up the organic compounds suspended in solution. Austrian physicist Adolf Smekal had predicted the existence of this phenomenon even further back in 1923 [53]. Raman spectroscopy relies on illuminating a sample with a light source that is

monochromatic, i.e., a laser source is ideal. A Mercury gas discharge lamp was initially used for this purpose after the technique became widespread. However, with developments in laser technology in the latter half of the 20th century the lamp design was replaced by a high-quality narrow bandwidth laser source, typically operated in continuous emission mode [35]. In most cases specular elastic reflection occurs but there is also a small probability that the light from the laser will scatter off the sample being illuminated.

Since in this instance the scattering object is on the size scale of a molecule(s), the dominant scattering mode taking place is Rayleigh scattering, shown on p.10 in chapter 1 of the thesis, which is responsible for the blue hue of the sky and the orange shades at dusk. The exact dynamics of what happens during such a scattering event is related to the distortion of the molecule's excited electron cloud by the lights electric field, but suffice to say there are some instances where the scattered light is not equal in frequency to the incident photon but instead down or up converts through accessing additional EM energy from molecular vibrational mode channels, since they are simultaneously perturbed as well [35]. In this sense Raman scattering is the interaction of optical and vibration THz oscillations [54]. Figure 3.39 further below illustrates this point.

Each peak in the Raman spectral plot (intensity versus energy) corresponds to a shift in energy away from the incident light energy $E_\gamma = hf$ where h is Planck's constant, and f is the frequency of the incident laser light illuminating the sample. When a scattering event occurs, the molecule is in a short-lived virtual energy state where any number of things can follow. Rayleigh scattering is most likely but every now and then the vibrational states can change simultaneously causing a net decrease or increase in the energy of the molecule. In the case of the former the photon gains energy and an anti-stokes shift or upshift occurs. The opposite case is called a stokes shift or downshift. Its critical to make clear that the molecule cannot be in a real excited electronic state which would involve the much more likely process of absorption to have occurred. It can only occur through inelastic scattering in the short-lived virtual state.

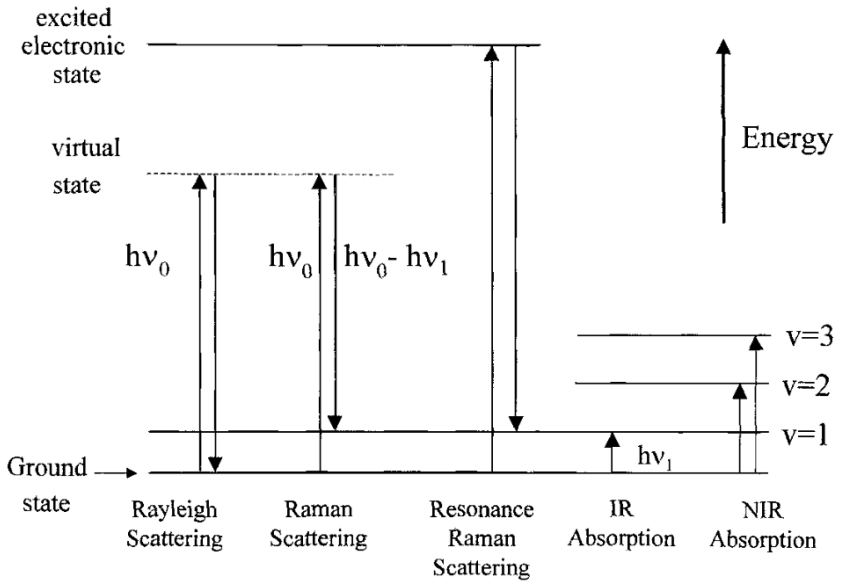


Figure 3.39. The virtual state is very short lived and occurs for light that scatters via the Rayleigh scattering phenomenon related to molecule size and incident photon size. Light can be scattered with an upshifted or downshifted frequency depending on what whether the vibrationally excited molecule takes or gives energy to change its state. Interestingly the final state of the system can correspond to the excited state of IR absorption. [35]

The interference of other more likely competitive interactions (namely IR absorption or fluorescence) competing with Raman scattering made it difficult to distinguish the Raman signal from the unwanted noise [35]. Visible light used in the technique often excites impurities in the sample producing a fluorescence emission spectrum that can compete with the Raman spectra as seen in Fig.3.40. To combat this many technological advances have been made since the 1980's to overcome the issues holding this method back.

Fourier transform Raman spectroscopy in the NIR was pioneered to eliminate the dominance of fluorescence since lower frequency light could not efficiently access that undesirable channel lowering its intensity by orders of magnitude [35]. Although the Raman signal produced was weaker, improvements in photodetectors such as CCDs helped compensate for this by massively improving the signal to noise ratio with multichannel detection, vastly outperforming the intensified photodiode arrays that were traditionally used at the time [35]. The rapid development of fibre optic cable towards the dawn of the 21st century led to a unique opportunity in enhancing the versatility of Raman spectroscopy over other vibrational mode spectroscopic techniques like FTIR. The scattered wavelength could be collected by fibre optic cables specifically designed to work well in the appropriate wavelength range of the Raman scattered light. This enabled remote sampling in-factory with inherently selective wavelength capabilities, increasing the attractiveness of Raman

spectroscopy to the chemical industry [35]. Laser light filters also assisted with cutting down the intensity of deleterious Rayleigh scattering which gave no useful information about the molecule being studied. This was conventionally done with a bulky double monochromator, but compact notch filters have since replaced this using much more advanced optical element coatings made possible by progress in the material science of dielectrics and semiconductors over the intervening decades [35].

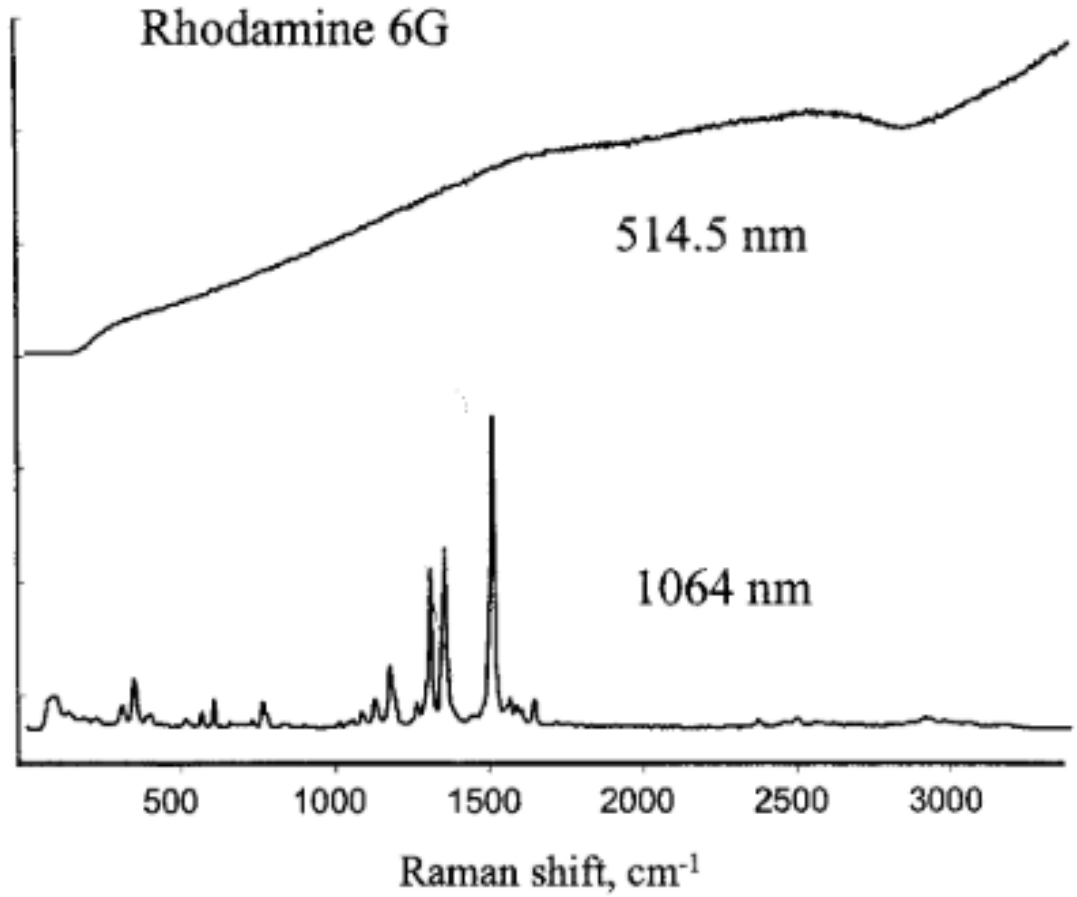


Figure 3.40. The intensity of a fluorescent dominated signal (excited with a green laser) compared with a Raman dominated signal (excited with a NIR laser) for Rhodamine 6G. Both are shown together but separate to highlight the difference in shape and magnitude The biggest challenge of developing Raman spectroscopy was isolating the Raman spectra from other inimical competitive background signals obfuscating the effect. The upper signal is many order of magnitude greater than the lower [35]

The integration of many of these advances has led to the creation of what is now seen as the standard modern Raman spectroscopy tool setup with wide ranging capability, exceptional sensitivity, and greatly decreased complexity, size, and cost.

3.4.7 Raman Spectrometer Characterisation of MoS_2

Figure 3.41(a) displays Raman spectra results, from the Raman setup in CRANN, used in this thesis work to analyse a TAC grown 3 nm MoS_2 film produced by Nishtha Shelly. The thickness of ultrathin MoS_2 (less than 4-5 layers) can be inferred directly and accurately from the value of the Raman shift between the out-of-plane and in-plane vibrational mode peaks in accordance with Fig.3.41(b) below [5]. This graph from literature is compared directly to AFM data to accurately gauge the thickness independently from the Raman signal. Although peak intensity and width can vary arbitrary across many different MoS_2 samples, depending on factors like synthesis method and surface/substrate conditions, the frequency positions of the Raman peaks and the shift between them is understood to be quiet robust and tied closely to the number of layers making up the thin film, as work by Hong li *et al. (*2012) demonstrates [6]. Hong li *et al.* attributes this decrease in the Raman shift in thinner MoS_2 films to a weakening in the coupling between the electronic transition of MoS_2 and its optical phonons due to quantum confinement effects, that also cause the excitonic transitions to dominate the dielectric function [44], or to elongated intralayer atomic bonds in the 2D limit. As can be seen in Fig.3.41(b) this reduction in coupling strength is linearly proportional to film thickness, and the change in shift flatlines in the bulk limit regime [6].

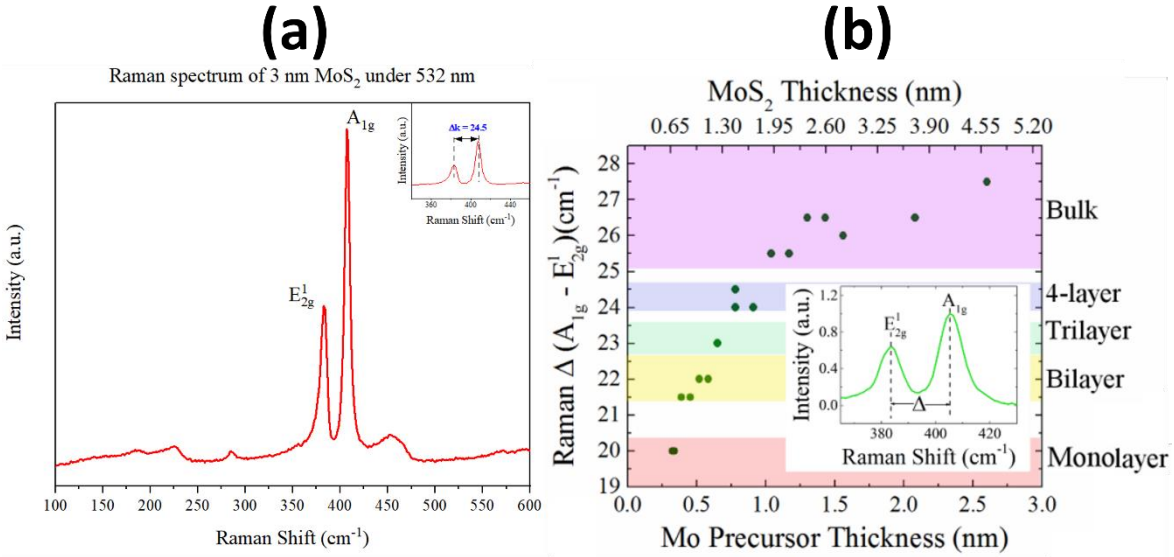


Figure 3.41. (a) The Raman spectra shift peaks of 3 nm MoS_2. The E^1_{2g} peak and the A_{1g} peak corresponds to the Raman shift associated with the planar and out of plane vibrational modes, respectively. (b) A graph of Raman peak to peak distance Δ versus sputtered precursor Mo thickness before undergoing TAC to MoS_2. From this one can infer that a value of Δ = 24.5 cm^{-1} is produced by 4–5-layer thick (3 nm) MoS_2. [5]

3.5 Optical Microscopy, Scanning Electron Microscopy, & Atomic Force Microscopy for Characterising Surface Morphology

3.5.1 Optical Microscopy

Microscopic surface roughness and the presence of sample defects can be determined through microscopy techniques like atomic force microscopy (AFM) and scanning electron microscopy (SEM) [8]. Historically these versatile atomic level tools for characterisation of surface morphology were unavailable and quality control was conducted by human eye. As the field of optics rapidly developed in the age of enlightenment, lenses were used in sequence to greatly magnify the size of the surface being looked at [34]. The all-encompassing term for this field of study is optical microscopy. Optical microscopy opened a whole new world of understanding to humanity about the true structure of matter and nature. Important discoveries regarding animal and plant anatomy, as well as the existence of microorganisms which led to germ theory, expeditiously sped up the improvements in medicine and healthcare, increasing life expectancy [55].

Optical microscopy is unfortunately limited by the wavelength of the visible light. This limit is related to the wave phenomenon of diffraction that makes subwavelength structures and features difficult or impossible to resolve. The mathematical expression for this resolution limit is given below [40].

$$d = \frac{\lambda}{2n \cdot sin(\Theta)} = \frac{\lambda}{2(NA)} \qquad (3.22)$$

Where d is the minimum resolvable distance, λ is wavelength of light, n is the refractive index of the materials being analysed, Θ is half the angle that subtends the minimum resolvable distance, and NA stands for numerical aperture and is typically on the order of 1.4-1.6 in modern optical microscopes [40]. The photographic images in Fig.3.42 below are of the advanced Olympus light microscope setup in the group lab in CRANN. Extremely high-quality images can be made with this tool all the way down to the diffraction limit.

This instrument is routinely used to quickly discern non-destructively how well the deposition went after the magnetron sputtering or TAC process. Macroscopic defects will also be quite apparent when viewed at optical frequencies as they are on the order of, or larger than, wavelength of light. Smaller features in the quarter wavelength region or below are impossible to resolve however which is why other techniques are needed to bridge the gap between this scale and all the way down to the atomic level at one Angstrom.

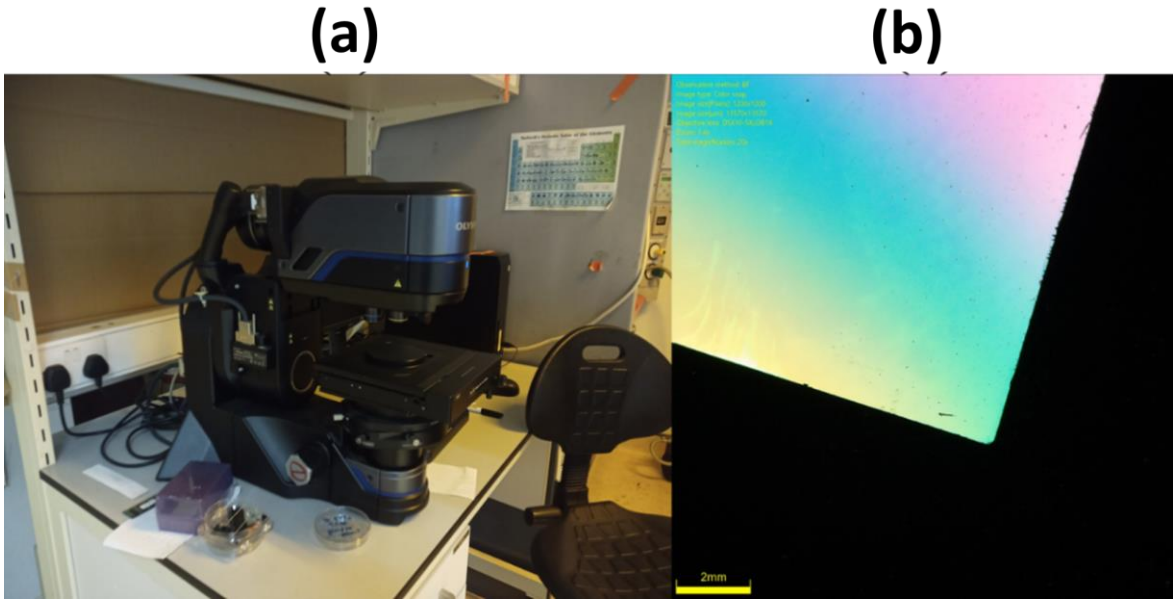


Figure 3.42. (a) A full view of the Olympus light microscope set up with adjustable mechanical sample stage and expensive refractive optics. (b) An image taken by this system of a Fano-resonant stack with the different coloured bands coming from thickness non-uniformity.

3.5.2 Scanning Electron Microscopy

For green light, d = 250 nm which is much too large to see the minute structure of microscopic surface roughness, very small organisms like viruses, or the structure of proteins inside the cell. To get around this issue scientists thought of using other particles to "sense" the surface. By the late 1920's, thanks to the work of pioneering quantum physicists like Paul Dirac and Erwin Schrödinger, it was known that matter particles like electrons were both a particle and a wave as shown by the expression below [34].

$$i\hbar\frac{\partial}{\partial t}\Psi^{(2)} \cong -\frac{\hbar^2}{2m_e}\vec{\nabla}^2\Psi^2$$

(3 . 23)

Where Ψ is the probabilistic wave equation of the electron, ħ is the reduced Planck constant, and m_e is the mass of the electron. Theoretically with this in mind one could use high energy electrons to "see" the deeply subwavelength surface features that optical microscopy cannot. In practice a tightly focused beam of electrons is created with energy in the 0.1 KeV to 40 KeV region [8], [56], [57]. This beam is made incident on the sample being analysed for various AOI. The beam is steered across the area of the sample being imaged with a television raster scan like pattern. The intensity of the back scattered electrons can then build up an image of the surface. In many cases secondary electrons produced by the energetic collisions can also be monitored for in the lower energy regime of around 100 eV. In the early 1930's serious efforts began in academic institutions such as Cambridge to fully realise the capabilities of SEM as a technique to characterise surfaces. It would not be until 1965 that many of the technical difficulties could be fully ironed out and a commercial product first entered the scene in the form of the U.K's Stereoscan 1 SEM, followed shortly thereafter by Japan's JEOL JSM-1 [57]. Figure 3.43 below is a photograph of a prototype of the Stereoscan SEM 1.

Many different signals can be created by the scattering of electrons off matter. These include the previously mentioned secondary electrons, various types of EM signals like characteristic x-rays and cathodoluminescence, and transmitted electrons if the sample is thin enough (metal foil) [56]. Naturally given the nature of these signals the sample chamber must be under high vacuum else they will be lost to absorption. The more intensity data that can be captured the more comprehensive ones understanding of the sample will be. The directly back scattered electron will have greater sensitivity deep within the sample being looked at. If sensors are available to specially capture this signal along with the characteristic x-ray intensity, a profile of the distribution of different elements can be made in the analysed region as well.

The distinctive 3D look of SEM images comes predominantly from how narrow the incident electron beam is giving a large depth of field [56]. The magnification of SEMs comes from

fine control of the electron beam width and raster size on the specimen. To further assist in obtaining high magnification, coherence, and spatial resolution, the source of electrons in modern SEM instruments is the Schottky-emitter electron gun, a type of field emission gun that is sharply pointed as shown in Fig.3.44 [57]. The thermionic emission of the sharp tungsten point is enhanced by the Schottky barrier reduction from zirconia coating the tip, lowering the work function [58]. The incredibly sharp tip also conveniently helps with both beam narrowing and stable discharge of electrons when the element is heated to near 2000 K with current.

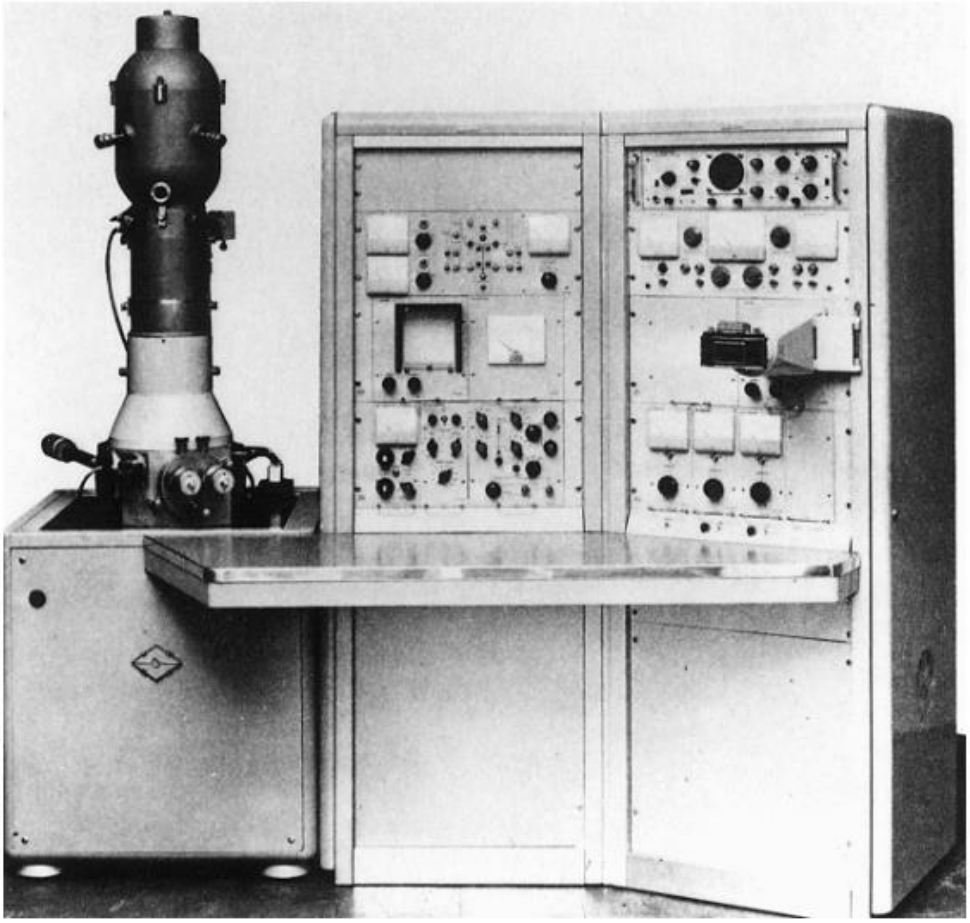


Figure 3.43.The prototype of the first commercial SEM instrument brought to market, the Stereoscan 1 SEM. In modern devices the inside of the machine has remained mostly the same due to the fundamental physics governing its operation. The biggest difference seen is in how bulky the auxiliary electronics are. Present day SEMs benefit greatly from the exponential miniaturisation and increase in compute power since its debut in the mid-1960s. Detector systems, such as those designed to record x-rays, have also improved a lot over the decades enhancing the signal to noise ratio of the images produced. [57]

SEM, and other electron-based microscopy techniques, are not without its drawbacks, however. The most limiting pitfall is the materials that can be looked at must be conductive. Nonconductive materials will collect charge as they are raster scanned leading to artifacts in

the image. To avoid this a thin film metal coating must be deposited onto the sample [8], but this in and of itself can change the surface condition one is trying to observe, especially for ultrathin films. Another issue is the damage that electrons will inflict as they bombard the surface. Over a long enough exposure degradation in the structure of the solid sample will occur as the emitted electrons are essentially equivalent to low energy beta radiation in term of the damage that can be done. SEM also requires high vacuum to function, slowing down the speed at which measurements can be carried out as well as restricting the viable samples to solids only. Contrast this with optical microscopy which is benchtop and can be done on solids and liquids in a fraction of the time needed to carry out SEM.

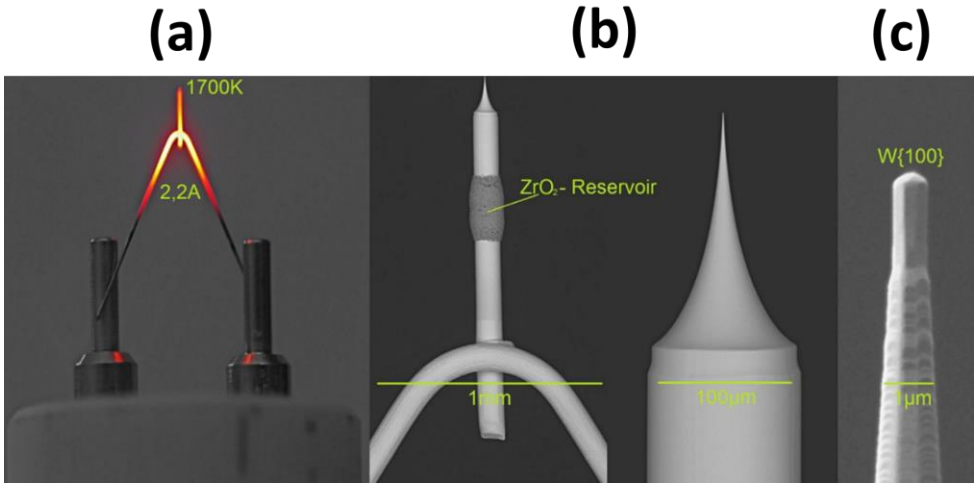


Figure 3.44. (a) The narrow beam width Schottky-emitter electron source found in many SEM instruments glowing red hot at a temperature of 1700 K. (b) When looked at closely a ZnO_2 coating can be seen that favourably lowers the work function of the emitter enhancing thermionic emission. (c) The very tip of the emitter has a diameter roughly on the order of the wavelength of visible light, making it incredibly sharp. [58]

3.5.3 Scanning Tunnelling & Atomic Force Microscopy

To address some of these problems development began on the scanning tunnelling microscope (STM) with the first being invented in 1981 by Binnig and Rohrer [8]. This technique was shown to be capable of true real space atomic resolution at the surface of a conductor. In STM a conductive tip delicately traced over the surface as shown in Fig.3.45 below. By placing the tip in close proximity (less than 1 nm) to the conductive surface a quantised current can flow between the two via quantum tunnelling [8].

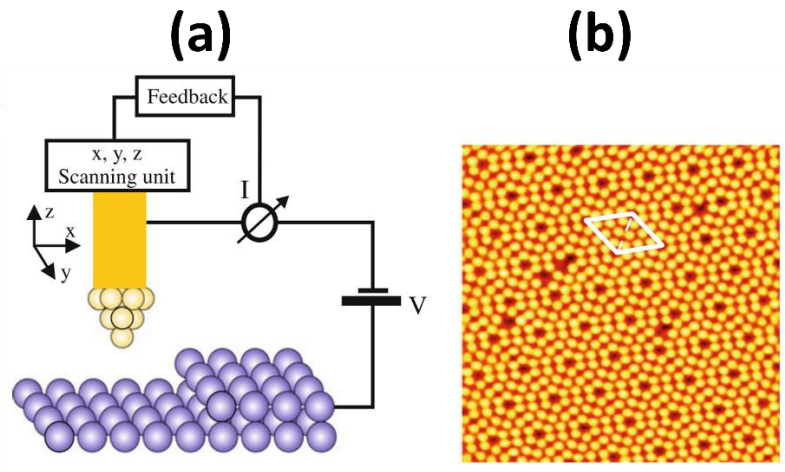


Figure 3.45. (a) The position of the STM tip is controlled by piezo electric motors with incredibly fine and smooth adjustments in position being possible. A feedback mechanism maintains the tips height by monitoring the tunnelling current with an ammeter. (b) The rhombic structure of Si(111) surface. Defects are also visible as dark spots. [8]

The generalised depth profile probabilistic formula below for a free electron quantum tunnelling through a potential barrier (the vacuum) is given alongside the transmission coefficient T for the proportion of electrons that tunnel all the way through [8].

$$|\Psi(z)|^2 = |\Psi(0)|^2 e^{-2\kappa z}, K = \sqrt{\frac{2m_e\phi}{\hbar^2}}$$

(3 . 24)

$$T = \frac{|\Psi(d)|^2}{|\Psi(0)|^2} \approx e^{-2Kd}$$

(3 . 25)

Where ϕ is the barrier height, K is the decay constant, z is the depth position, m_e is again the electron mass, and d is the tunnelling gap distance. From this it can be seen that the tip is extremely sensitive to adatoms as tunnelling will primarily occur between the tip and atoms exactly at the surface-vacuum interface (last atoms). Just like with SEM though, this technique can only work with conductive surfaces, otherwise tunnelling will not occur across the gap [8].

To address this issue AFM was brought onto the scene in the mid-1980s in a landmark paper by Gerd Binnig in the physical review letters [59]. Both AFM and STM use sharp tips to sense the surface but the biggest difference conceptually between the two is in what quantity is being measured. While conductive surfaces will tunnel their electrons into the tip, insulating dielectric surfaces will still exert a force on the tip that is in line with the well-known intermolecular Leonard-Jones 12-6 potential, V_{LJ}, formula given below [8].

$$V_{LJ}(r) = 4\varepsilon\left[\left(\frac{\sigma}{r}\right)^{12} - \left(\frac{\sigma}{r}\right)^{6}\right]$$

(3 . 26)

Where ε is the minimum depth of the potential well, σ is the value of r where $V_{LJ} = 0$, and r is the radial distance between the tip and the insulating surface adatom. The potential changes as the tip move towards the surface; the force can be extrapolated from the first derivative with respect to distance r. Figure 3.46 provides a visual of this. By taking note of the force, the AFM can work universally on any surface, provided there is grounding between the surface and the tip, with surface force sensitivity on the order of 10^{-18} N being achievable [8].

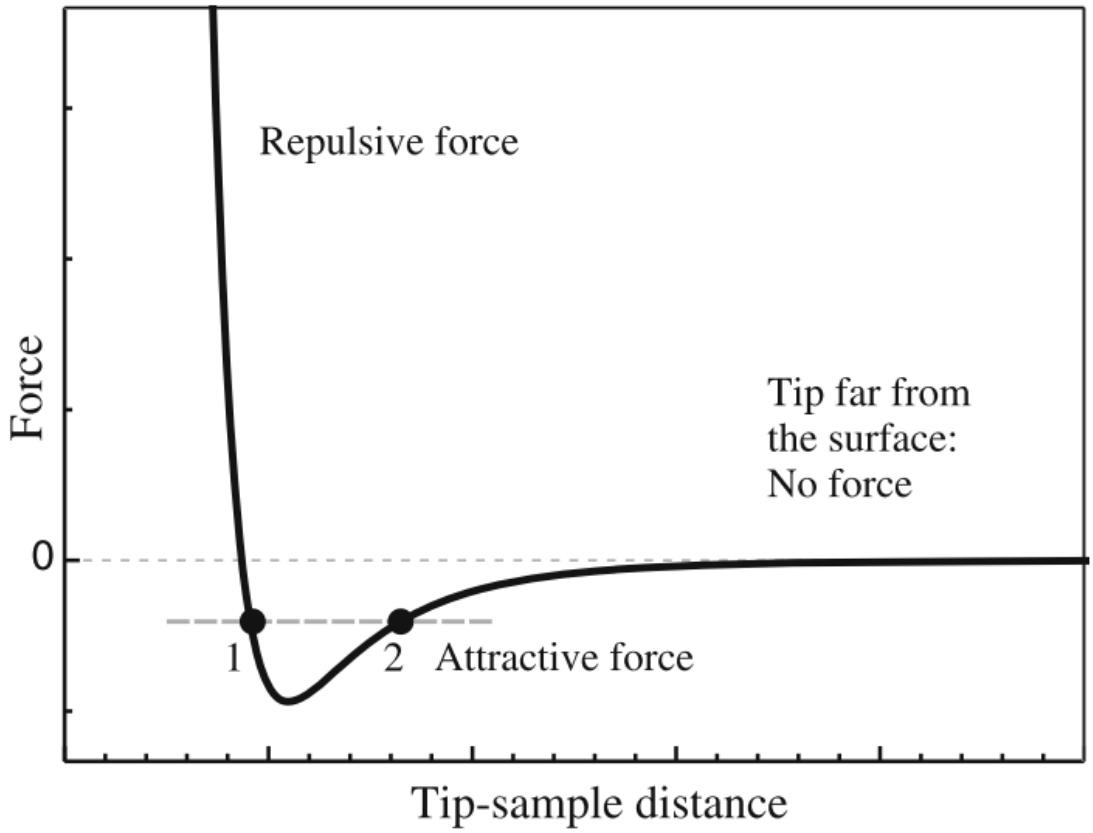


Figure 3.46. The force experienced by a cantilever AFM tip as it approaches a surface. When they are brought close enough an attractive force is felt at position 2 shown towards $r = \varepsilon$. *Any closer and the repulsion dramatically increases. My slowly scanning across the surface the tip can smoothly maintain itself at equilibrium distance above the surface allowing one to measure the true real space topography.* [8]

When imaging the surface with AFM the standard sequence of events is as follows [8]. The tip is brought close to the surface with piezoelectric elements while the user observes the potential of the tip. When the cantilever tip reaches very close to the surface the potential will change rapidly. At this point, the tip is stopped and raised ever so slightly. In so doing the tip is now in position 2 or 1 of Fig.3.46 above depending on whether some distance (no-contact) or complete contact between the probe and the surface is desired. More delicate softer materials like organic polymers should be measured in region 2, while harder surfaces can be done in region 1 [8]. Then the laser is aligned so that its incident on the tip itself, reflecting onto the split photodiode. With everything in position, the AFM tool can be instructed to begin a static raster scan where a feedback mechanism will attempt to maintain the tips height above the surface as it moves along. Care must be taken on how fast the tip moves. If it is understood that the surface is very rough or changes in height occur rapidly, the scan speed should be slowed. Otherwise, the tip equilibrium condition can be lost and in the worst case it can crash into the surface adatoms, most likely breaking it.

Following directly from Hooke's simple harmonic motion spring law [34], except applied at the atomic level, the deflection of the cantilever tip due to the intermolecular force can be inferred directly using a laser focused on the tip as the configuration diagram for a basic AFM setup illustrates below in Fig.3.47. This laser light is reflected into a split diode sensor that registers the moving reflection beam as a change in vertical tip position of the cantilever. As the surface is scanned the feedback mechanism will attempt to maintain the cantilever in the deflected state which means it keeps the force constant [8]. An image of the surface topography is then slowly built up while the tip moves up and down as it travels, always trying to keep the same relative height between itself and the surface underneath.

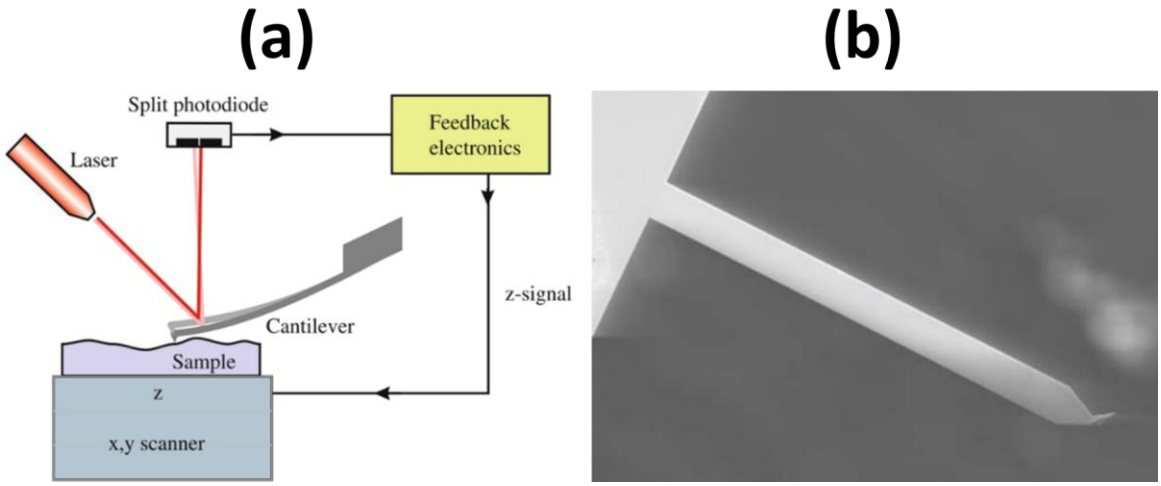


Figure 3.47. (a) A basic AFM schematic showing the electronic feedback mechanism to maintain tip height as it races across the surface. Piezoelectric elements control the positioning with Angstrom level precision. (b) An SEM image of a Si cantilever used for AFM with length 450 µm. [8]

The image that is produced from this height variation map can then be used to determine true surface roughness. If the sample is designed cleverly with an edge step, the thickness of the layer can also be determined by slowly moving the tip from the top of the cliff edge to the bottom [5]. Some of the main advantages of AFM are as follows. AFM produces a true 3D image of the surface as compared to SEM, which is still technically 2D, though some depth can be inferred from monitoring multiple signals produced (secondary electrons and elastically back scattered electrons, etc) [56]. AFM does not need a vacuum environment to function, and the theoretical resolution of AFM is also higher by an order of magnitude, or more, than SEM. Figure 3.48 compares different microscopy techniques and their physical range of use [8].

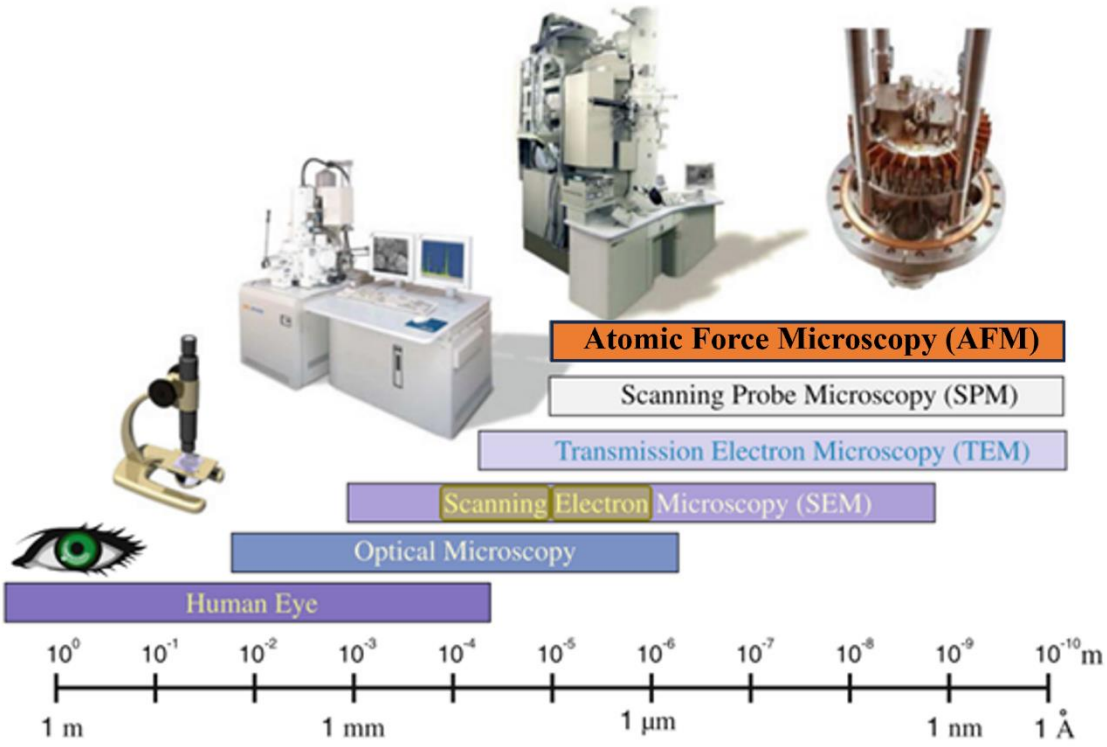


Figure 3.48. SPM and AFM have near identical limits on their spatial resolution. SEM struggles to resolve anything below 1 nm and pushing the energy higher to shorten the wavelength will ultimately just result in electrons that act like high energy MeV beta radiation. Most materials will not hold up physical against such intense irradiation. Surprisingly the human eye can see object all the way down to a tenth of a millimetre. [8]

The future of AFM looks bright but there are still some disadvantages holding it back. Namely, the scan speed is much slower than SEM and the certain features are tricky for AFM to resolve such as very steep topography and protrusion with high radius of curvature with respect to the tip and the surroundings [8]. Making the tip even sharper could alleviate some of these concerns, but this could compromise the structural integrity of an object that is already so delicate. The size of the scan area is also poor compared to spectroscopic techniques, but this is somewhat to be expected given the fact that near every adatom position is being physically measured. Moving too quickly to widen the scan area risks a collision with the surface that can ruin the probe tip. Ultimately the only way to overcome such a drawback would be to use an even faster feedback system that could change the tip position more rapidly. Perhaps an all-optical approach may speed things up further than working with electronics. Currently, such an innovation if possible is far off. Figure 3.49 below shows some images obtained from the AFM and SEM systems available in CRANN.

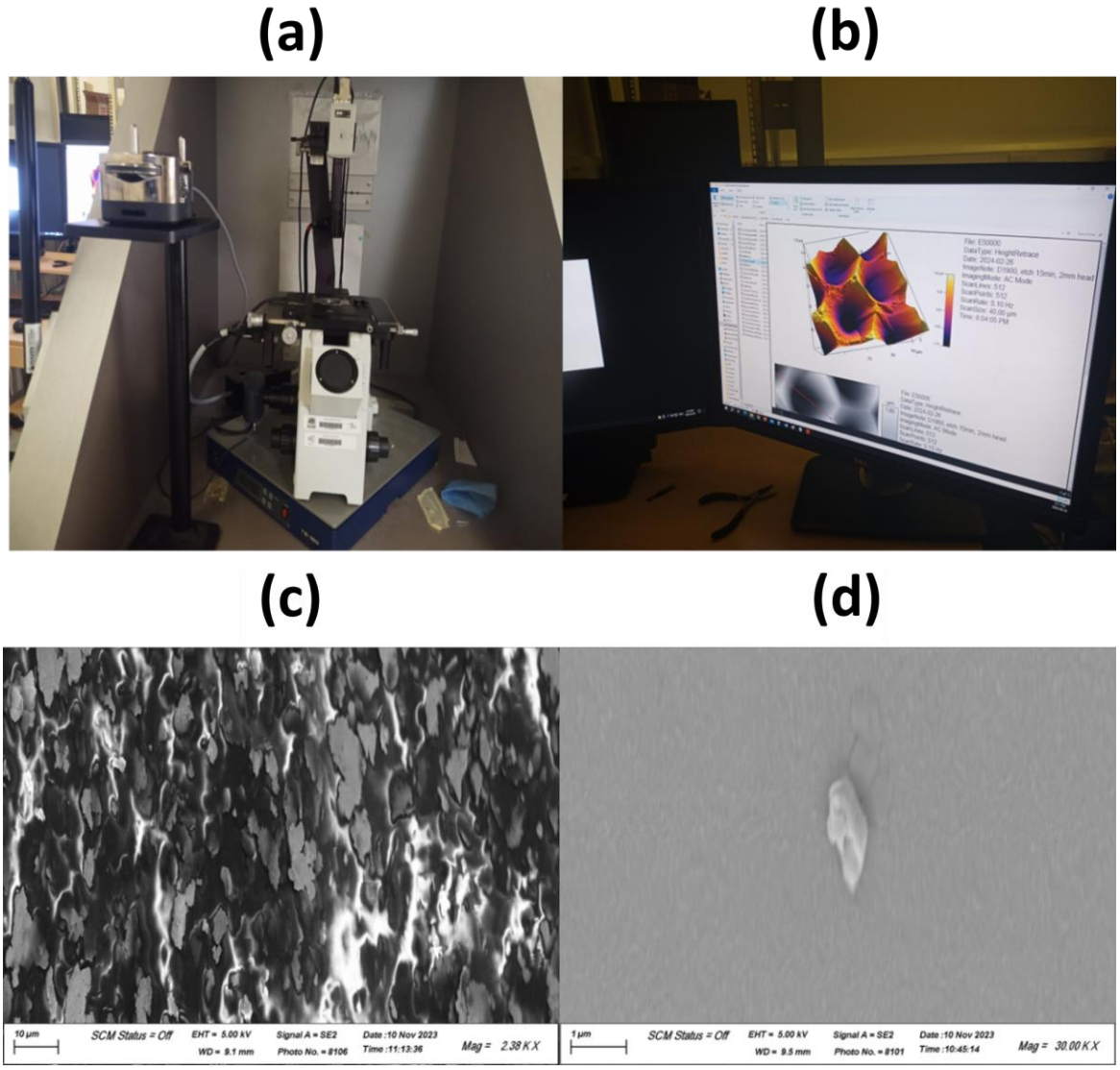


Figure 3.49. (a) A front view of the AFM system in CRANNs basement. The piezo-electric control system is on the left stage elevated above the rest of the assembly. The entire system is placed on an area of flooring isolated from the surroundings to mitigate environmental vibrations. Even still, a train passing by Trinity college can still be recorded as artefact striations in the image. (b) An AFM measurement of an antireflection coating etched glass with hemispherical surface hollows helping to couple light into the material by improving impedance matching. (c) SEM imagery of silver paint used for making thin film electrical contacts. (d) SEM imagery of a WO_3 sample with a minute dust particle on its surface a micron across.

3.6 Electrical Characterisation

3.6.1 Four-Point-Probe

While the majority of experimental methods carried out for the purpose of the project were optical or mechanical in nature as outlined above, certain electrical measurement techniques were also used to characterise the samples made. Namely the four-point-probe (4PP) method to determine thin film sheet resistance for metals or transparent conducting oxides. F. M.

Smits's1958 paper published in The Bell System Technical Journal gives a comprehensive overview of the linear probe configuration 4PP measurement technique as applied to the determining thin film sheet resistance of circular and rectangular samples [60]. This setup is most applicable to the one utilised in characterising the conductivity of sputtered metal and ITO/FTO. Sheet resistance is an important quantity that remains invariant w.r.t scaling, thereby allowing one to compare the quality of the conductive film being analysed across significantly different size scales. As the name suggests sheet resistance applies to materials that have sheet like geometry, which is to say one of the dimensions of the material is highly constrained compared to the other two. Planar thin films can be modelled as an infinite sheet with finite thickness [36]. To understand where sheet resistance originates from, one can start from the first principles of electrical conductivity [34]; the resistance R, resistivity ρ_r, thickness t, and other material dimensions can all be linked together as shown below.

$$R = \frac{\rho_r L}{tW} = R_s \frac{L}{W}$$

(3 . 27)

Where L is the length of the material, W is the width, and R_s is the sheet resistance. When considering an infinite sheet with finite thickness and the linear 4PP setup, one may approach the problem with a logarithmic solution as outline by Smits below [60].

$$R_s = \frac{V}{I} \frac{\pi}{ln(2)}$$

(3 . 28)

Where I is the current between the outer probes and V is the potential difference between the inner probes. Figure 3.50 below illustrates a diagram of the arrangement of the linear 4PP tool.

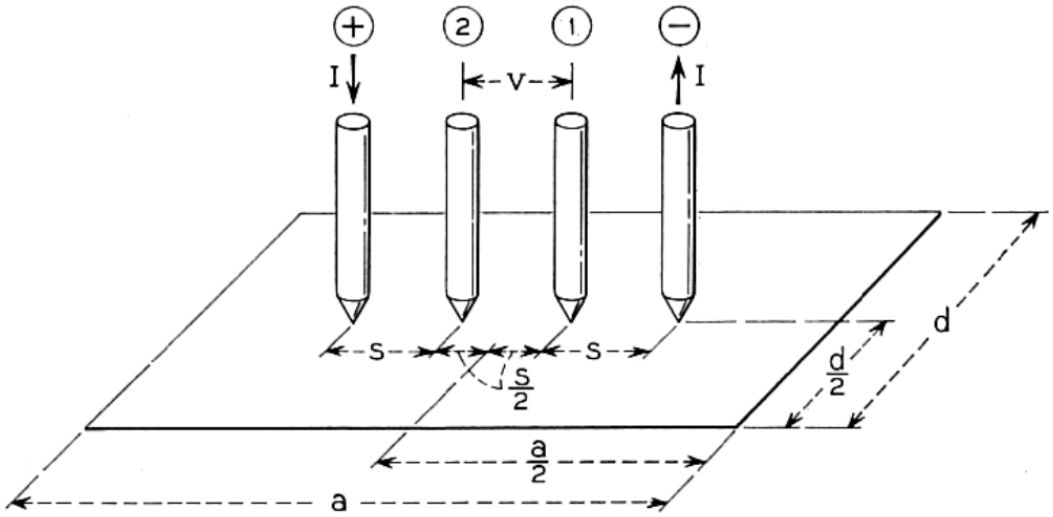


Figure 3.50. A linear four-point-probe setup arrangement on a rectangular sample surface. A dipole is created between the two outer electrodes using a current source while the potential between them is monitored by inner probes 1 and 2. The spacing between the probes relative to sample thin film thickness determines the magnitude of the correction factor applied. [60]

The 4PP setup cannot cover the entire sheet so to account for the finite limits, equation 3.28 must be multiplied by correction factors F and C. These correction factors account for the finite boundaries and thickness of the sample as well as the contributions of all other dipole arrays across the surface [61]. In general, the thickness of the individual films produced in this work are on the other of 100 nm which is very small compared with the probe spacing parameter s. Thus, F can be taken to be unity. The C factor is of greater concern and is determined by how wide the sample is relative to the spacing of the probes. An approximation of the average sample width D looked at in this thesis is 25 mm (the width of a microscope glass slide), while the spacing between the probes s on the 4PP tool in CRANN is 1 mm. This gives a ratio $\frac{D}{s} = 25$. The length of the glass slide substrates, L, are 75 mm meaning the ratio $\frac{L}{W} = 3$. Therefore, based on the table displayed in figure 3.51, correction factor C will roughly be on the order of 4.47. Figure 3.51 displays tables that outline C and F for the most common sample geometries such as rectangular, circular, and square [61]. D should be taken to be the width or diameter depending on the sample geometry and the probes are aligned parallel to the longest axis.

Correction Factor C

D / s	Circle	Square	Rectangle L/W=2	Rectangle L/W=3	Rectangle L/W=4
1				0.9988	0.9994
1.25				1.2467	1.2248
1.5			1.4788	1.4893	1.4893
1.75			1.7196	1.7238	1.7238
2			1.9475	1.9475	1.9475
2.5			2.3532	2.3541	2.3541
3	2.2662	2.4575	2.7000	2.7005	2.7005
4	2.9289	3.1127	3.2246	3.2248	3.2248
5	3.3625	3.5098	3.5749	3.5750	3.5750
7.5	3.9273	4.0095	4.0361	4.0362	4.0362
10	4.1716	4.2209	4.2357	4.2357	4.2357
15	4.3646	4.3882	4.3947	4.3947	4.3947
20	4.4364	4.4516	4.4553	4.4553	4.4553
32	4.4791	4.4878	4.4899	4.4899	4.4899
40	4.5076	4.5120	4.5129	4.5129	4.5129
Infinity	4.5324	4.5324	4.5325	4.5325	4.5324

Correction Factor F

t / s	C.F.2
< 0.4	1.000
0.400	0.9995
0.500	0.9974
0.555	0.9948
0.625	0.9896
0.714	0.9798
0.833	0.9600
1.000	0.9214
1.111	0.8907
1.250	0.8490
1.429	0.7938
1.667	0.7225
2.000	0.6336

Figure 3.51. The thin film sheet resistance correction factors w.r.t sample geometry, width, thickness, and probe spacing. Nanofilms are so thin that F can be taken to be unity, C is taken to be 0.95-0.98 depending on the overall sample width. [61]

The invariance of sheet resistance with size is seen in its units Ω/sq. Although dimensionally equivalent to Ω the strange unit is better thought of as the aspect ratio factor that allows you to predict the value of measured resistance across a sample of any geometry and size. For example, the resistance of a rectangular sample much longer than the measured reference square sample can be inferred using the sheet resistance multiplied by the dimensional difference factor. Practically speaking the most useful aspect of 4PP was in the determination of resistivity which allowed the conductivity to be calculated. Resistivity, the inverse of conductivity, can be obtained using the formula below.

$$\rho = R_s \cdot t$$

(3 . 29)

Using this method the conductivity of the magnetron sputtered metals could be compared with literature values to ascertain surface continuity. The 4PP was used a lot when working with thin film ITO as well. In this case certain properties of the ITO such as the optical frequency of its epsilon near zero (ENZ) region and its crystallinity could be determined from the conductivity. ENZ materials are promising due to the large change in refractive index observed in the frequency range where the real component of the optical dielectric function is at or near zero [62] This was quite useful when attempting to optimise ITO during

synthesis and post deposition annealing to increase the plasma frequency further towards the visible regime. The investigation of ITO followed on from the work of Dr. Stephen Adrian O'Brien [7]. This work however eventually gave way to more promising dynamic colour results in ATF Fabry-Perot devices based on sputtered electrochromic materials like WO_3 and NiO, shifting the focus of research in that direction instead [3]. Even still, the experience gained with this technique went on to be of great help in the group's study of the effect annealing had on the conductivity of ultrathin 10 nm Ag adhered with 0.5 nm Ti onto glass, with and without an AR coating layer [63]. See Fig.3.52 below.

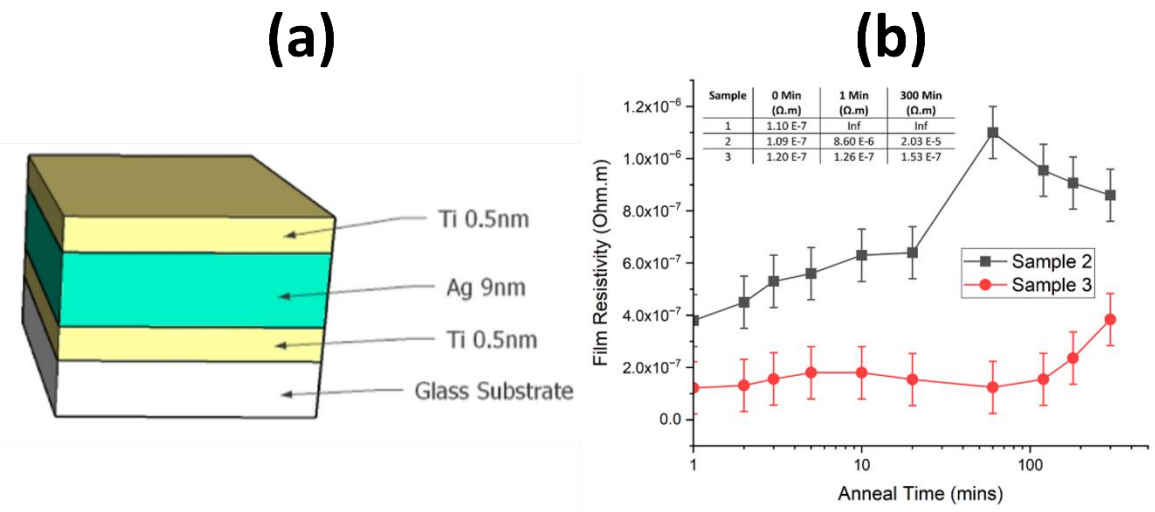


Figure 3.52. (a) The configuration of the ultrathin Ag conductive glass coating stack using Ti adhering and capping layers to greatly resist dewetting. (b) sample 1 was Ag on glass, Sample 2 adhered Ag to glass with 0.5 nm of Ti and sample 3 added another 0.5 nm Ti capping layer on top. Thermal annealing accelerated the dewetting (a process ultimately driven by thermodynamics and surface energetics), but despite this the 4PP measured resistivity did not increase substantially for sample 3, even after two hours of exposure [63].

3.6.2 CRANN Four-Point-Probe System

When operating the 4PP a Keithley DC power supply was used to apply a controlled amount of current to the outer 4PP probes. Then the probes were lowered onto the surface of the sample firmly to make good contact. After a second the potential voltage read by the same supply can be noted. This process is normally repeated 3 times for each input current, with care taken to not destroy the sample with large quantities of current. Typically, 10^{-8} to 10^{-3} A was applied depending on sample conductivity and thickness. R_S can then be found using the statistically averaged value of eq.3.29 on p.67. Figure 3.53 shows photographic images of the linear 4PP system used for the research project.

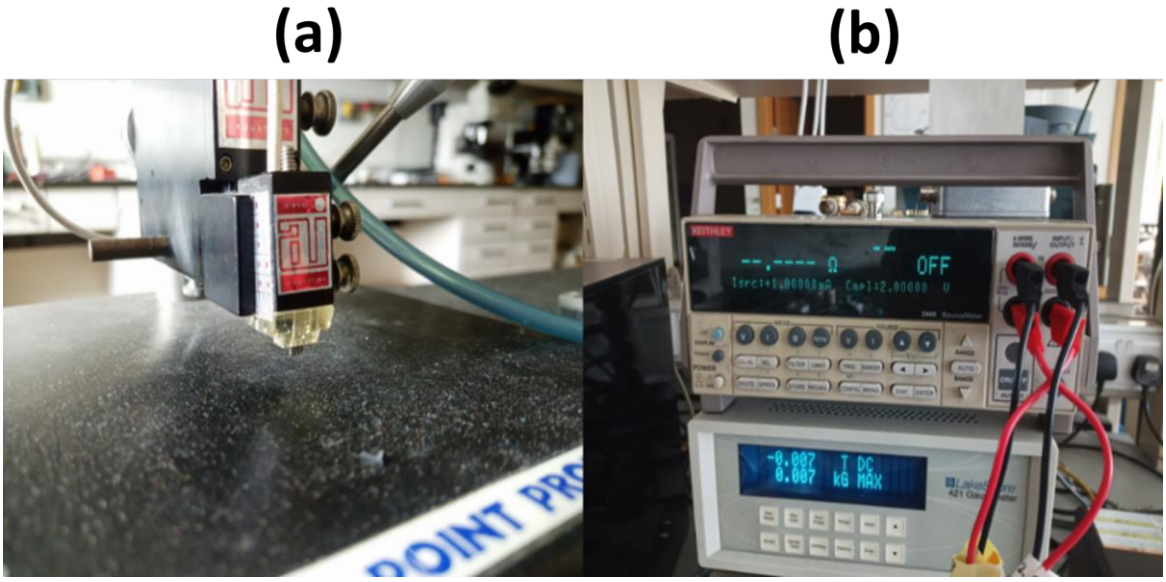


Figure 3.53. (a) A photographic image of the linear 4PP tool. The lever in the background is used to depress the probes into the sample being studied. (b) The Keithley power source used to supply current to the outer probes and measure the resultant voltage. From Ohm's law, less resistance means lower voltage. When a sample hits compliance that indicates that the material is electrically insulating.

3.7 Summary

In summary, many of the different experimental techniques and sample creation methods most relevant to the work carried out for this thesis, and used primarily by the author, have been reviewed. The magnetron sputtering process was discussed in detail, and was crucial to the creation of the FP resonators looked at in this thesis using passive and active materials in the design. Several other sample creation processes were also briefly evaluated for their merit, such as TAC, used to create TMDs, in which the expertise of colleague Nishtha Shelly was invaluable. Spectroscopic ellipsometry was analysed closely to showcase the power and versatility of the technique as it pertained to the work done in modelling multilayer ATF stack structures. Furthermore, UV-Vis spectroscopy was discussed at length, along with its use in aiding SE and determining sample colour. Supplemental spectroscopic techniques, like Raman and XRR, were succinctly covered, demonstrating their use in characterising the thickness of ultrathin films from first principles independent of SE. There was a long discussion on the surface topography characterisation methods of AFM, SEM, and optical microscopy. Their history and capabilities were explained, alongside their use in the project as the primary tool for gauging sample quality and accurately gauging true surface roughness, in the case of AFM. Finally, the electrical experimental measurement of 4PP was perused over as a tool used for ascertaining conductive thin film quality and continuity.

3.8 References

[1] M. Sakurai, “Spectroscopic ellipsometry,” *Toraibarojisuto/Journal Japanese Soc. Tribol.*, vol. 57, no. 7, 2012.

[2] J. H. Ko, Y. J. Yoo, Y. Lee, H. Jeong, and Y. M. Song, “A review of tunable photonics : Optically active materials and applications from visible to terahertz,” *ISCIENCE*, vol. 25, no. 8, 2022, doi: 10.1016/j.isci.2022.104727.

[3] J. Chen, G. Song, S. Cong, and Z. Zhao, “Resonant-Cavity-Enhanced Electrochromic Materials and Devices,” *Adv. Mater.*, vol. 35, no. 47, p. 2300179, 2023, doi: 10.1002/adma.202300179.

[4] “X-ray Reflectometry (XRR).” https://covalentmetrology.com/service/x-ray-reflectometry-xrr/.

[5] J. Robertson, X. Liu, C. Yue, M. Escarra, and J. Wei, “Wafer-Scale Synthesis of Monolayer and Few-layer MoS2 via Thermal Vapor Sulfurization,” *2D Mater.*, vol. 4, no. 4, pp. 16–20, 2017, doi: 10.1088/2053-1583/aa8678.

[6] H. Li *et al.*, “From bulk to monolayer MoS2: Evolution of Raman scattering,” *Adv. Funct. Mater.*, vol. 22, no. 7, pp. 1385–1390, 2012, doi: 10.1002/adfm.201102111.

[7] S. A. O’Brien, “The Optics and Photonics of Two-Dimensional Nanomaterials,” Trinity College Dublin, 2019.

[8] B. Voigtländer, *Scanning Probe Microscopy - Atomic Force Microscopy and Scanning Tunneling Microscopy*. Springer, 2015.

[9] M. Braun, “Magnetron Sputtering Technique,” in *Handbook of Manufacturing Engineering and Technology*, Springer, London, 2015, pp. 2929–2957.

[10] R. Gatensby *et al.*, “Controlled synthesis of transition metal dichalcogenide thin films for electronic applications,” *Appl. Surf. Sci.*, vol. 297, pp. 139–146, 2014, doi: 10.1016/j.apsusc.2014.01.103.

[11] A. Y. C. Nee, *Handbook of Manufacturing Engineering and Technology*, 1st ed.

Springer, 2015.

[12] “Magnetron Sputtering: How It Began and How VON ARDENNE Became a Technology Pioneer,” *Von Ardenne*, 2021. https://vonardenne.in/news/magnetron-sputtering-how-it-began-and-how-von-ardenne-became-a-technology-pioneer/.

[13] G. Bräuer, B. Szyszka, M. Vergöhl, and R. Bandorf, “Magnetron sputtering – Milestones of 30 years,” *Vacuum*, vol. 84, no. 12, pp. 1354–1359, 2010, doi: 10.1016/j.vacuum.2009.12.014.

[14] W.R.Grove, “On the Electro-Chemical Polarity of Gases.,” *Philos. Trans. R. Soc. London*, vol. 142, no. 142, pp. 87–101, 1852, [Online]. Available: https://royalsocietypublishing.org/doi/epdf/10.1098/rstl.1852.0008.

[15] S. M. Rossnagel, “Magnetron sputtering,” *J. Vac. Sci. Technol. A*, vol. 38, p. 060805, 2020, doi: 10.1116/6.0000594.

[16] A. You, M. Be, and I. In, “Dynamics of molecular collisions in air and its mean free path,” *Phys. Fluids*, vol. 35, p. 097131, 2023, doi: 10.1063/5.0166283.

[17] A. S. Penfold, “Early Days Of Magnetron Sputtering - An Enigma,” *Thin Solid Films*, vol. 171, pp. 99–108, 1989, doi: 10.1016/0040-6090(89)90037-0.

[18] D. Hoffman, B. Singh, and J. H. T. III, *Handbook of Vacuum Science and Technology*, 1st ed. Academic Press, 1997.

[19] A. M. Law, L. O. Jones, and J. M. Walls, “The performance and durability of Anti-reflection coatings for solar module cover glass – a review,” *Sol. Energy*, vol. 261, pp. 85–95, 2023, doi: 10.1016/j.solener.2023.06.009.

[20] P. Sigmund, “Sputtering efficiency of amorphous substances,” *Can. J. Phys.*, vol. 46, pp. 731–737, 1967, doi: 10.1139/p68-090.

[21] R. Wang, L. Pan, Q. Han, H. Zhu, M. Wan, and Y. Mai, “Reactively sputtered Ta2O5 solid electrolyte layers in all thin film electrochromic devices,” *J. Alloys Compd.*, vol. 865, no. 158931, 2021, doi: 10.1016/j.jallcom.2021.158931.

[22] E. Complete, *CompleteEASE Software Manual Version 3.18*. J. A. Woollam Co., Inc., 2007.

[23] F. Wang and J. Wu, *Modern Ion Plating Technology : Fundamentals and Applications*, 1st ed. Elsevier, 2023.

[24] M. Hughes, "What is RF Sputtering?," *Semicore*, 2016. https://www.semicore.com/news/92-what-is-rf-sputtering.

[25] "Benchtop PVD Systems," 2024. https://moorfield.co.uk/category/benchtop-pvd-systems/.

[26] T. C. Huang, R. Gilles, and G. Will, "Thin-film thickness and density determination from x-ray reflectivity data using a conventional power diffractometer," *Thin Film Soldis*, vol. 230, no. 2, pp. 99–101, 1993, doi: 10.1016/0040-6090(93)90499-F.

[27] J. Als-Nielsen and Des McMorrow, *Elements of Modern X-ray Physics*, 2nd ed. 2011.

[28] Moorfield, "Moorfield nanoPVD-S10A Manual," 2024.

[29] "Air quality - Dublin." https://www.pleanala.ie/publicaccess/EIAR-NIS/TA0001/EIAR/EIAR -Chapter 9-Air Dust and Climatic Factors.pdf?r=619407.

[30] T. Xie, W. Kao, L. Sun, J. Wang, G. Dai, and Z. Li, "Preparation and characterization of self-matting waterborne polymer – An overview," *Prog. Org. Coatings*, vol. 142, p. 105569, 2020, doi: 10.1016/j.porgcoat.2020.105569.

[31] M. S. Diware *et al.*, "Characterization of wafer-scale MoS2 and WSe2 2D films by spectroscopic ellipsometry," *Curr. Appl. Phys.*, vol. 17, no. 10, pp. 1329–1334, 2017, doi: 10.1016/j.cap.2017.07.001.

[32] D. L. Thomas, "Selenium Toxicity - News Medical," *News Medical Life Sciences*, 2023. https://www.news-medical.net/health/Selenium-Toxicity.aspx#:~:text=and copper ingestion.-,Toxic levels of selenium,pigs with selenium inhalation toxicity.

[33] "Rare Earth Elements—Critical Resources for High Technology," *U.S. Geological*

Survey. https://pubs.usgs.gov/fs/2002/fs087-02/.

[34] H. D. Young and R. A. Freedman, *University Physics with Modern Physics*, 14th ed. Pearson, 2016.

[35] R. L. McCreery, *Raman Spectroscopy for Chemical Analysis*. Wiley, 2004.

[36] C. C. Katsidis and D. I. Siapkas, "General transfer-matrix method for optical multilayer systems with coherent, partially coherent, and incoherent interference," *Appl. Opt.*, vol. 41, no. 19, pp. 3978–3987, 2002.

[37] M. C. Troparevsky, A. S. Sabau, A. R. Lupini, and Z. Zhang, "Transfer-matrix formalism for the calculation of optical response in multilayer systems: from coherent to incoherent interference," *Opt. Express*, vol. 18, no. 24, p. 24715, 2010, doi: 10.1364/oe.18.024715.

[38] U. Rossow, "A Brief History of Ellipsometry," *Ipss*, vol. 256, no. 2, p. 1800307, 2019, doi: 10.1002/pssb.201800307.

[39] S. E. Thompson and S. Parthasarathy, "Moore 's law : the future of Si microelectronics," *Mater. Today*, vol. 9, no. 6, pp. 20–25, 2006, doi: 10.1016/S1369-7021(06)71539-5.

[40] A. B. B. Max Born, Emil Wolf, *Principles of Optics: Electromagnetic Theory of Propagation, Interference and Diffraction of Light*, 7th ed. Cambridge University Press, 1999.

[41] C. Akcay, P. Parrein, and J. P. Rolland, "Estimation of longitudinal resolution in optical coherence imaging," *Appl. Opt.*, vol. 41, no. 25, pp. 5256–5262, 2002, doi: 10.1364/AO.41.005256.

[42] J. N. Hilfiker *et al.*, "Survey of methods to characterize thin absorbing films with Spectroscopic Ellipsometry," vol. 516, pp. 7979–7989, 2008, doi: 10.1016/j.tsf.2008.04.060.

[43] P. Liu, P. Longo, A. Zaslavsky, and D. Pacifici, "Optical bandgap of single- and multi-layered amorphous germanium ultra-thin films," *J. Appl. Phys.*, vol. 119, no.

1, pp. 182–184, 2016, doi: 10.1063/1.4939296.

[44] Y. Yu *et al.*, “Exciton-dominated Dielectric Function of Atomically Thin MoS2 Films,” *Sci. Rep.*, vol. 5, p. 16996, 2015, doi: 10.1038/srep16996.

[45] J. Park *et al.*, “Omnidirectional Near-Unity Absorption in an Ultrathin Planar Semiconductor Layer on a Metal Substrate,” *ACS Photonics*, vol. 1, no. 9, pp. 812–821, 2014, doi: 10.1021/ph500093d.

[46] S. A. Edwards, “Isaac Newton and the problem of color,” 2012. https://www.aaas.org/taxonomy/term/10/isaac-newton-and-problem-color.

[47] Labsphere, “Integrating Sphere Theory and Applications.” doi: https://mmrc.caltech.edu/Cary%20UV-Vis%20Int.Sphere/Literature/labsphere%20Theory%20and%20App.pdf.

[48] T. Guo, “Convert spectrum to color,” 2024. https://www.mathworks.com/matlabcentral/fileexchange/98289-convert-spectrum-to-color.

[49] M. Evagorou, S. Erduran, and T. Mäntylä, “The role of visual representations in scientific practices : from conceptual understanding and knowledge generation to ‘ seeing ’ how science works,” *Int. J. STEM Educ.*, vol. 2, no. 11, pp. 1–13, 2015, doi: 10.1186/s40594-015-0024-x.

[50] L. G. Parratt, “Surface Studies of Solids by Total Reflection of X-Rays,” *Phys. Rev.*, vol. 95, no. 2, pp. 359–369, 1954, doi: 10.1103/PhysRev.95.359.

[51] D. G. Cahill, “Analysis of heat flow in layered structures for time-domain thermoreflectance,” *Rev. Sci. Instrum.*, vol. 75, no. 12, p. 5119, 2004, doi: 10.1063/1.1819431.

[52] P. Feulner, F. Hennies, A. Fink, D. Menzel, P. M. Echenique, and W. Wurth, “Direct observation of electron dynamics in the attosecond domain,” *Nature*, vol. 436, pp. 373–376, 2005, doi: 10.1038/nature03833.

[53] A. Smekal, “Zur Quantentheorie der Dispersion,” *Naturwissenschaften*, vol. 11, pp.

873–875, 1923, doi: 10.1007/BF01576902.

[54] M. Fox, *Optical Properties of Solids*. 2010.

[55] S. Dattani, L. Rodés-Guirao, H. Ritchie, E. Ortiz-Ospina, and M. Roser, “Life Expectancy,” 2023. https://ourworldindata.org/life-expectancy.

[56] J. I. Goldstein, D. E. Newbury, J. R. Michael, N. W. M. Ritchie, J. H. J. Scott, and D. C. Joy, *Scanning Electron Microscopy and X-Ray Microanalysis*, 4th ed. Springer, 2017.

[57] D. McMullan, “Scanning Electron Microscopy 1928 – 1965,” *Scanning*, vol. 17, pp. 175–185, 1995, doi: 10.1002/sca.4950170309.

[58] J. Orloff, *Handbook of Charged Particle Optics*, 2nd ed. CRC Press, 2008.

[59] G. Binnig, C. F. Quate, and C. Gerbe, “Atomic Force Microscope,” *Phys. Rev. Lett.*, vol. 56, no. 9, pp. 930–934, 1986, doi: 10.1103/PhysRevLett.56.930.

[60] F. M. Smits, “Measurement of sheet resistivities with the four-point probe,” *Bell Syst. Tech. J.*, vol. 37, no. 3, pp. 711–718, 1958, doi: 10.1002/j.1538-7305.1958.tb03883.x.

[61] “Resistivity Theory,” *Materials Development Corp Europe*. https://www.mdc-europe.com/resistivity-theory-and-data-correction-coefficients-depending-on-sample-size/.

[62] D. Wang, Z. Liu, H. Wang, M. Li, L. J. Guo, and C. Zhang, “Structural color generation: From layered thin films to optical metasurfaces,” *Nanophotonics*, vol. 12, no. 6, pp. 1019–1081, 2023, doi: 10.1515/nanoph-2022-0063.

[63] A. L. Lynch, C. P. Murray, E. Roy, C. Downing, and D. Mccloskey, “Extreme Dewetting Resistance and Improved Visible Transmission of Ag Layers Using Sub-Nanometer Ti Capping Layers,” *ACS Omega*, vol. 9, no. 8, pp. 9714–9719, 2024, doi: 10.1021/acsomega.3c09774.

Chapter 4. Zeroth Order Fabry-Perot Resonant Enhanced Absorption & Structural Colouration in High Index Lossy Dielectric Ultrathin Films

4.1 Fabry-Perot Resonance Enhancement of the Light-Matter Interaction & How to Access the Zeroth Mode

4.1.1 Enhancement of the Light-Matter Interaction Using Fabry-Perot Resonance

As seen in chapter 1 section 1.3, FP resonance has been shown to be a simple and eloquent mechanism to generate vibrant structural colouration (in reflection and transmission) and strong absorption. When working with media much thicker than the wavelength of visible light, such as glass substrate, there is a significant amount of bulk for the light to accumulate phase delay on propagation and/or for the phenomenon of refraction to be readily seen by the naked eye (altering light's path) [1], allowing considerable variation in reflection, transmission and absorption to occur depending on sample geometry, sample index, and AOI. Bulky opaque metals also benefit from strong contrast with their surroundings due to their high extinction coefficient κ and a real refractive index n that differs considerably from materials with normal dispersion (often much lower or higher than unity) leading to an impedance mismatch that can significantly alter the optical response as compared to a conventional lossless dielectric mediums that more closely match the refractive index of air [2]. More on impedance will be discussed shortly in the next subsection.

Given how constrained the thickness dimensions of thin films are in this thesis (typically on the order of 10's to 100's of nanometres), using resonant effects, like FP wave interference, to enhance the light-matter interaction within them is a necessity, as a single pass of light though said thin films is not adequate enough to considerably alter the resultant reflection/transmission/absorption intensity as compared to the intensity profile for the bare substrate only. In the context of the ATF approach, light must be made to undergo multiple passes within a thin film layer (or stack assembly) of interest, be that for lossless materials like TiO_2 or a lossy dielectric like MoS_2, to manifest a practically useful optical response like vibrant colouration peaks on reflection and/or near-unity attenuation across the visible

(or at specific targeted wavelengths) [3], [4]. FP resonance constrains light within the stack structure, facilitating these multiple passes to occur. The ability to force light to undergo multiple passes can be very powerful when paired with opto-electronic 2D materials like MoS_2 and graphene , as this can allow one to simultaneously gain the discussed optical benefits of the bulk while also acquiring significant improvements in the electronics (gate tuneable absorption and plasmonics in graphene and giant gate tuneability of geometrically confined excitons in MoS_2 [5], [6]) that wouldn't be accessible in thicker regimes.

Work done with ultrathin graphene by Z. H. Ni *et al.* (2007) [7], showcases how multiple passes of light within the graphene film can greatly increase the contrast between itself and the surrounding substrate. Moreover, the contrast between graphene at various thicknesses is also greatly improved. This Provides a non-destructive optical method to differentiate minute difference in film thickness accurately down to the number of individual layers making up the graphene deposit. See Fig.4.1 below.

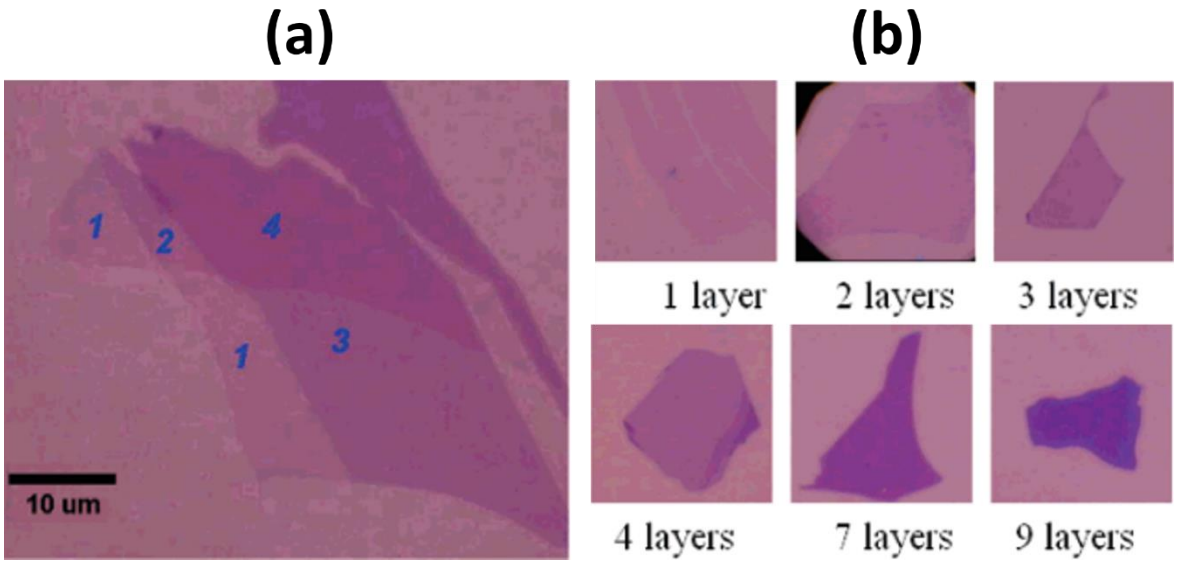


Figure 4.1. (a) Comparison image of a 1-layer, 2-layer, 3-layer, and 4-layer graphene film on a 285 nm SiO_2 on Si reflective substrate taken using optical microscopy. The contrast between each layer can be seen, with the difference between 4-layer and monolayer being readily apparent. (b) This trend continues to thicker graphene films where the structural colouration become more vibrant and violet in appearance. Although difficult to tell with the naked eye, the difference between 1-layer and 2-layer is readily apparent from UV-Vis spectroscopy [7].

In the stack design of Z. H. Ni *et al,* the structural colouration is attributable to higher order (m=1 or above) FP resonance as a transparent internal spacer of 285 nm SiO_2 is used between the lossy graphene ($n_{Monolayer-graphene} = 2.2 + 1.1i$ [7]) and the reflective opaque Si.

These higher order FP modes are well understood and reported on widely in the literature [3], [8], [9]. They are associated with thin film or multilayer thin film stacks with thickness on the order of 100-200 nm or more. More on applying higher FP modes for the purpose of structural colouration and broadband absorption will be discussed in chapter 6. The following section will once again review the details of ultrathin 2-layer asymmetric zeroth order Fabry-Perot resonators, previously discussed in chapter 1 p.24-31. Like with higher order FP modes (starting at m=1), this zeroth mode resonance can also generate colouration and strong absorption, with the key difference being the deeply subwavelength thickness solution of the resonant dielectric film required.

4.1.2 Lossy ATF Design to Access the Zeroth Mode

In this chapter, a greater overview is given on the use of ultrathin resonators to generate strong absorption and colouration using passive lossy dielectric materials, particularly Si, Ge, MoS_2, and WS_2. Transfer matrix method simulations and experimental measurements will be presented and compared, and conclusions will be drawn from the investigation of the gathered results.

To quantify the optical characteristics of thin film FP resonator stacks, the spectroscopic parameters that can be directly measured and used to determine colouration and light-matter interaction. Using the Fresnel coefficients discussed in chapter 2 p.88-89, the reflection intensity, transmission intensity, and absorption intensity of a thin film stack structure can be calculated to compare with experimental UV-Vis measurement. As lossy dielectrics are the material of interest, the attenuation of the EM wave is very consequential to the overall spectra produced. A simple strategy when trying to maximise absorption is to sweep the parameter space of all possible stack configurations to maximise for the total absorption, or the layer resolved absorption. For asymmetric FP devices using an opaque back reflector to bounce light back into the top lossy layer, it is ideal for little to no optical losses to occur in the back metal so that it can act as a perfect mirror (PEC) while the thin layer on top absorbs all the incident photons (enhanced light-matter interaction due to the ultrathin film stack wave interference) [10].

Interestingly, maximising the imaginary component κ of the top lossy absorber's refractive index will not necessarily result in larger absorption overall [11]. In the thin film regime where multiple passes within the lossy layer can be made, the optimum solution is a non-

trivial function of field penetration into the stack structure and optical losses therein [10]. The concept is very closely linked to the phenomenon of optical impedance matching. The impedance $Z(\omega)$ of a non-magnetic medium is given by the expression below [2].

$$Z(\omega) = \frac{Z_0}{\widetilde{N}(\omega)}$$

(4 . 1)

Where $\widetilde{N}(\omega) = n + i\kappa$ is the generalised complex refractive index of the medium and Z_0 is the impedance of free space with a value of 377 Ω [12]. If κ is large and n is smaller or bigger than unity, the mismatch between $Z(\omega)$ and Z_0 substantially increases and less transmission/coupling of light into the medium occurs. This is the fundamental reason why some metals like Ag, Au, and Al are generally broadband reflectors instead of broadband absorbers, given the difficulty light has in transmitting through the air-metal interface when $n << 1$ and $\kappa >> 0$.

The process of improving the 2-layer FP stack design to increase absorption is very similar to the strategy of how one would optimise an anti-reflection (AR) coating layer when operating in transmission mode with no lossy thin films. This is because the optical physics underpinning both structures can be explained using a near identical mathematical treatment based on accumulated phase delay and thin film wave interference in a resonant FP cavity [10]. Anti-reflection (AR) thin films confer many benefits, such as increasing the coupling of light into a stack (less back reflection at certain wavelengths) and the ability to physically protect and isolate a potentially more delicate layer or surface underneath [13], [14]. When considering only one lossless AR layer, no non-trivial deeply subwavelength solutions for reflection minimization exist like with the lossy 2-layer zeroth FP resonators assemblies.

An ultrathin film absorber on a reflective back metal can be thought of as a simple single layer AR coating, or an “absorbing AR coating” [10]. Therefore, to understand how to approach the problem of ideal lossy layer refractive index and thickness for strong sample absorption and colouration, a brief description of a traditional AR coating is useful in the stack configuration given in Fig.4.2 below. Chapter 1 p.26 also discusses this topic.

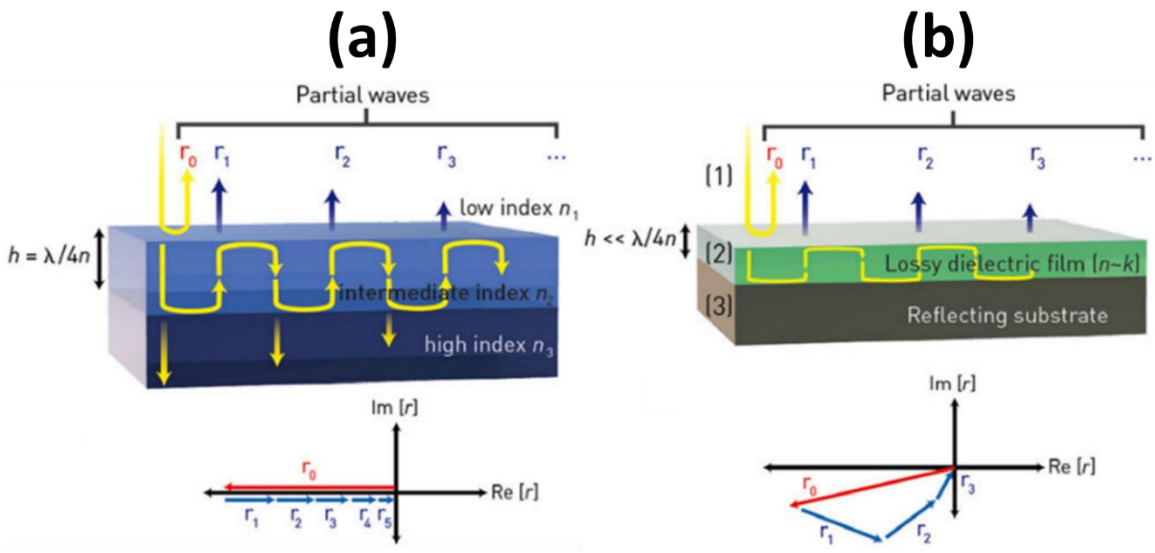


Figure 4.2. (a) A typical AR coating stack structure with partial reflection coefficients that are bound to the real number axis. At resonance the light will be transmitted through with little back reflection. (b) The same resonance condition and stack structure except the materials are opaque and lossy. Instead of transmission at resonance, strong absorption will occur as the trapped light will cycle and decay exponentially with multiple passes. The partial wave coefficients are complex allowing for deeply subwavelength thin films with near perfect absorption at certain wavelengths. [10]

A conventional AR coating, using a transparent top medium, optimises the transmission into the structure while minimizing surface back reflections, see Fig.4.2(a). Solar panels often utilise lossless dielectrics like SiO_2, MgF_2, or Al_2O_3 on their transparent protective glass faces to act as a nominal AR coating to increase transmittance into the Si absorbing PV cell element while reducing back reflection across the visible by about 4 % on average [13]. When one follows through the wave optics mathematics of the superposition of the partial wave reflections and their accumulated phase delay in the coating layer, the quarter waveplate condition of $h = \frac{\lambda_0}{4n_2}$ and the index matching condition $n_2 = \sqrt{n_1 n_3}$ solutions emerge [15]. With those conditions met the reflection is supressed by destructive interference since all partial waves but $\vec{r_0}$, which has phase delay = π, have an accumulated phase delay of 0 at the resonant frequency. As all the phasors lie on the real number line of the complex plane, there is no non-trivial zeroth order FP mode solution as that would require the thin film thickness to be 0 nm.

When the glass substrate is replaced with an opaque perfect conductor (PEC), an idealised metal [16], the ideal AR conditions cannot be met by most naturally existing transparent dielectrics. Furthermore, the combination of the PECs opacity and the large $\frac{\kappa}{n}$ ratio results

in the internal reflection being strongly enhanced instead . Put simply, since the top thin film is not lossy the total reflectivity is strongly inclined towards approaching unity across the visible, turning an AR stack into a strong reflector. This type of device structure is more broadly known as a Gires-Tournois etalon or an asymmetric Fabry-Perot cavity and is used as a phase shifter element in optical system, though with alternative materials or layer configurations used that aren't as reflective such as semi-transparent metal thin films and more lossy metals/dielectrics [15]. If the top thin film coating is made very lossy then the resultant phasor diagram will appear like the graph in Fig.4.2(b), with light being trapped circulating back-and-forth inside the cavity, resulting in enhanced near unity absorption at certain wavelengths for high n and κ MoS_2, Si, Ge, WS_2, and even other high index lossy oxides like VO_2 [2], [10], [17].

This is because the full complex plane now becomes available to the interface reflection coefficients, leading to the possibility of the non-trivial zeroth order resonance mode being accessible. Two conditions need to be satisfied, with eq.4.3 defined previously in chapter 1 p.28 eq.1.13, expressed below [10].

$$|r_{21}| = |r_{23}| \cdot e^{-4\pi\frac{h}{\lambda_0}Im[n_2]} = |r_{23}| \cdot e^{-h\alpha_2} \quad (4.2)$$

$$2\pi m = \delta_{prop} - \delta_{21} + \delta_{23} \quad (4.3)$$

Where h is the thin lossy absorber thickness, α_2 is the absorption coefficient of that thin film. $|r_{ij}| = |r_{ij}| \cdot e^{-i\delta_{ij}}$, where δ_{ij} is the interface reflection phase shift between the i^{th} and j^{th} layer, δ_{prop} is the propagation phase delay pick-up through the film, and m is an integer number starting form 0. Under the right circumstances the interface phase delay will compensate the propagation phase delay allowing for a real value of h solution for $m = 0$. For highly lossy films where $n \approx \kappa$, the reflection coefficients will trace out a phasor loop in complex space as seen in Fig.4.2(b), enabling the zeroth mode solution to be possible. If $n_3 \approx n_2$, which is to say the metal (n_3) and top lossy layer (n_2) are both very lossy (metals like Ni, W, and Ti), then absorption will tend to unity over a broad bandwidth for very

subwavelength films, $h << \frac{\lambda_0}{4n_2}$ [10]. This is not as useful for structural colouration, but it very advantageous for attenuating as much of the trapped light as possible. Though it will be shown later that the light is not highly focused in the lossy dielectric film in this case.

Most importantly the forbidden zeroth mode is now accessible due to the complex reflection coefficients extending out into the complex plane. Many lossy dielectric materials can fulfil the near unity absorption conditions in the visible spectrum such as Ge, Si, Fe_2O_3, and many TMDs. This condition can even apply more universally to material operating in the infrared spectrum region such as VO_2 and dielectrics on highly doped semiconductors substrates [18], [19]. Further analysis by Park *et al.* (2014) [17] has also demonstrated that the real component of the refractive index of the back metal n_3 must ideally be greater than 0.64 for this strong absorption effect to manifest more readily over a broader wavelength range, though this requirement is not as stringent as the others given that Ag and Au back reflectors still produce a highly absorbing zeroth FP mode band, though it is much more spectrally narrow than the response seen using Cr or Ni [4].

4.2 State of the Art Work Accessing the Ultrathin Zeroth Mode

4.2.1 The Zeroth Mode in Ultrathin Si

In the ATF approach, both strong light-trapping and the non-trivial zeroth order FP resonance occur simultaneously in the ultrathin film regime. This is fortunate given the latter cannot be of much use without the former, as light trapping is critical to making practical subwavelength optical devices, since there is so little available material to work with in the subwavelength size scale [20]–[22]. It is essential that the number of passes light makes within the stack structure is maximised as single pass absorption in accordance with the Beer Lambert law is wholly inadequate unless the absorber used has very high index values n and κ of 10 and above [11], [23], which is currently unfeasible in the optical regime. It is within this ultrathin realm that many new technologies in the fields of photonics and optoelectronics are being developed in earnest, given the advantages that miniaturisation brings to devices on the nanoscale, such as increased switching speed and enhancement of the optical response due to 2D confinement effects on materials like MoS_2 [5], [24]–[29]. Furthermore, as a near limitless source of renewable energy, efficiently capturing the sun's light remains a very active area of research [30]–[32]. The enhanced absorption in subwavelength lossy

asymmetric FP cavity structures can aid towards this goal. By accessing the zeroth order FP mode in these lossy cavity structures, strongly absorbing devices that are inherently robust to change in angle can be made as well. Such devices are called angle independent or omnidirectional strong absorbers that maintain their optical response even out to grazing angles [17], [22].

Work has been done to explore zeroth order resonance in lossy FP nanocavities regarding already well-established materials such as Si and Ge. There is great interest in utilising the zeroth order FP mode in ultrathin films for near perfect absorption. A paper by Seyed Sadreddin Mirshafieyan *et al.* (2016) describes Si in a FP nanocavity configuration acting as a spectrally selective absorber [4]. A single layer of Si in the ultrathin regime is placed over various backing metals such as Al, Ag, Cr, Au, and Ti. They had shown previously with an Al backing that the near perfect peak absorption wavelength of the FP nanocavity is due to mode-selective critical coupling in the cavity [33], [34]. Furthermore, the spectral position of the peak, and thus its structural colour, could be tuned by Si thickness as seen below for an array of different backing metals in Fig.4.3.

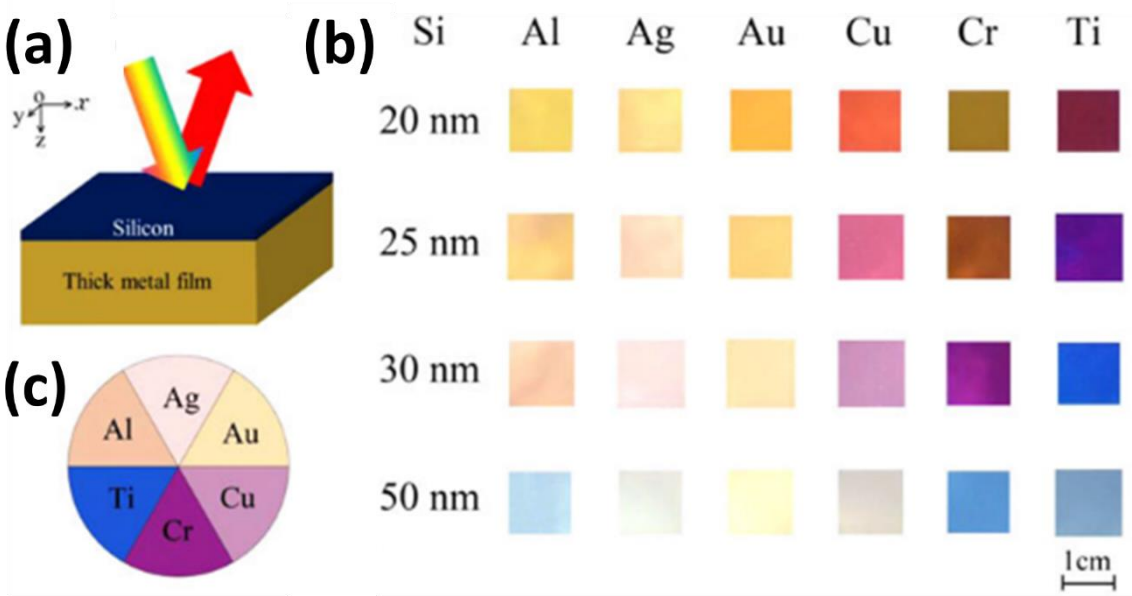


Figure 4.3. (a) The stack structure of the asymmetric FP nanocavity resonator on a α-Si top layer with metal backing. (b) Colour variation of this FP device with different Si thickness and backing metals used. (c) The colour of this device with 30 nm Si and backing metal varied showing the large colour gamut achievable [4].

The idea of using different backing metals was done to investigate if a large colour gamut distribution was possible with the stack structure shown in Fig.4.3(a) by keeping Si thickness

constant in the ultrathin film regime, meaning only one deposition step for Si is needed for different coloured pixels to be made on one complete device display. With the backing metals tested, different peak absorption positions were found for varying thicknesses of Si in the ultrathin film regime. Those colours can be seen above in Fig.4.3(b) and (c). It was found that lower-loss reflector metals such as Ag and Au produced narrower absorption spectral bandwidths while lossy metals such as Cr and Ti, both of which have much larger n values in the visible as compared to the noble metals, produced broader absorption bandwidths with flatter responses both spectrally and angularly. See Fig.4.4.

The mathematical description of the FP modes in a nanocavity requires phase analysis as this is the most important consideration after the correct lossy materials are being used. Seyed Sadreddin Mirshafieyan *et al.* indicated that the total phase delay in the cavity structure was a function of round-trip propagation phase delay in the Si and the phase delayed picked up at the Air-Si and Si-Metal interfaces as given by eq.4.3 on p.181. By setting this total round trip phase delay to $2\pi m$, where m is an integer starting from 0, a series of white lines could be overlaid on a reflection surface map as shown below in Fig.4.4 below. In so doing, they also proved that certain bands of high absorption were directly attributed to the zeroth, first, second, and higher modes beyond.

Their results, shown in Fig.4.4, also clearly demonstrated that both high n and κ are needed for the top dielectric in the zero-phase delay region as strong absorption can only occur along the bands if the dielectric material used is sufficiently lossy for the light to be efficiently attenuated over multiple passes. These conditions are maintained over a broader wavelength range, further into the red and NIR when using Si and other semiconductors with low absorption in that spectral region, when lossy metals (W, Ni, and Ti) are used as backings instead of Ag or Au which absorb strongly in the blue and green regions of the visible spectrum but poorly in the red and NIR.

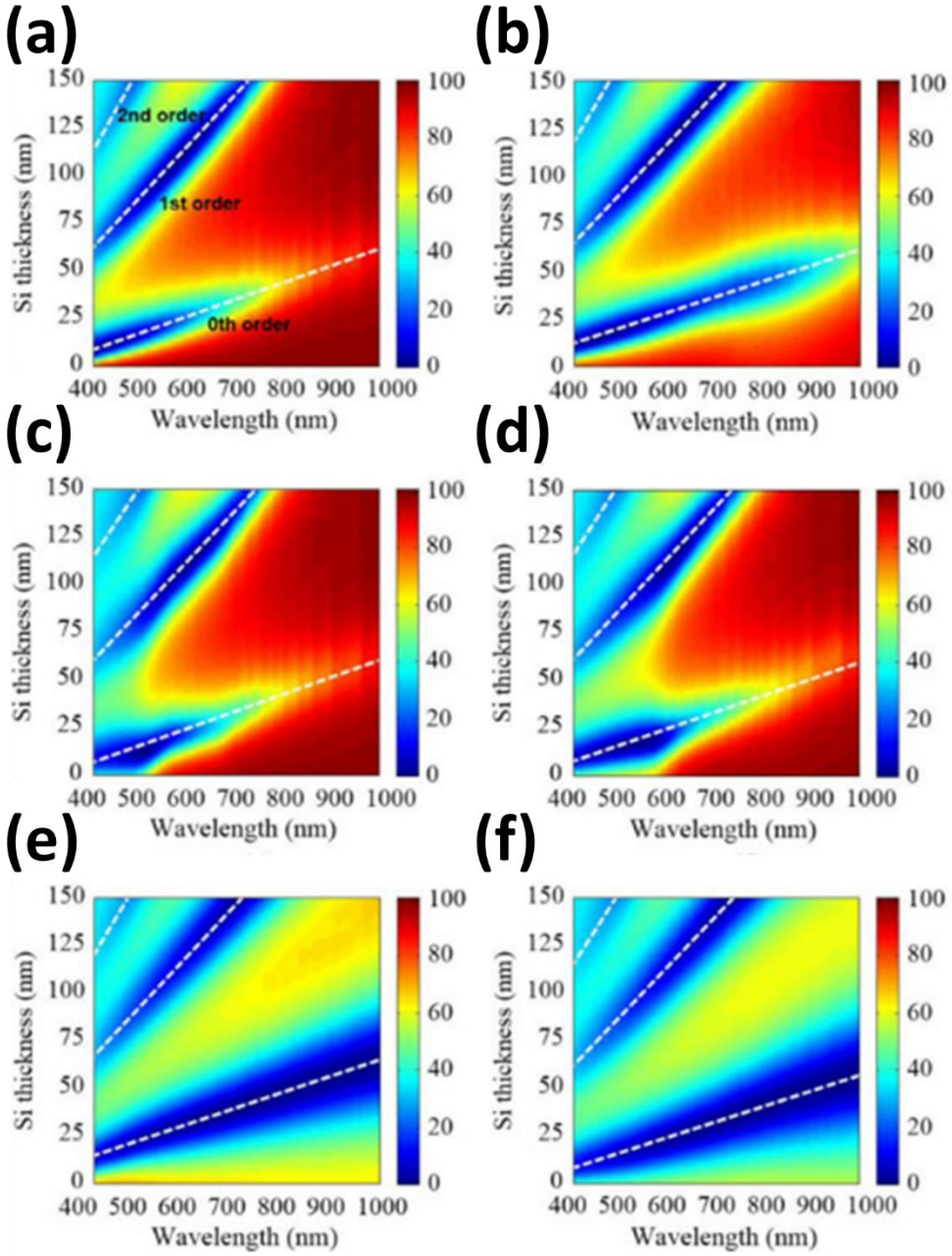


Figure 4.4. (a)-(f) The surface reflectivity map for Si Thickness versus wavelength for different backing metals. (a) Ag, (b) Al, (c) Au, (d) Cu, (e) Cr, and (f) Ti. The lowest mode is the zeroth mode, and it is also the broadest and flattest. Higher order modes are successively more vertical, and play a larger role in more complicated stack structures where spectrally selective absorption, transmission, and reflection is the goal. [4]

The above reflection surface maps also demonstrated that the zeroth order FP mode is only dominant in the ultrathin film regime below 50 nm Si thickness. Angle insensitivity or omnidirectionality for both TM and TE polarisations (polarisation independent response) was seen in all samples out to 80° AOI too as shown below in Fig.4.5 [4]. This can be evaluated by accounting for the absolute change in reflectivity w.r.t its value at 0˚ AOI. The smaller the absolute change the more omnidirectional the response is said to be, with no

change ideally being maintained out to as high and AOI as possible [17]. This omnidirectionality is directly attributable to the maintained zero total round trip phase delay condition where the reflection and propagation phase delay compensate each other [17]. The flatness of the zeroth mode is a consequence of the nanometre scale thickness of the Si layer resulting in very little phase delay accumulated on propagation.

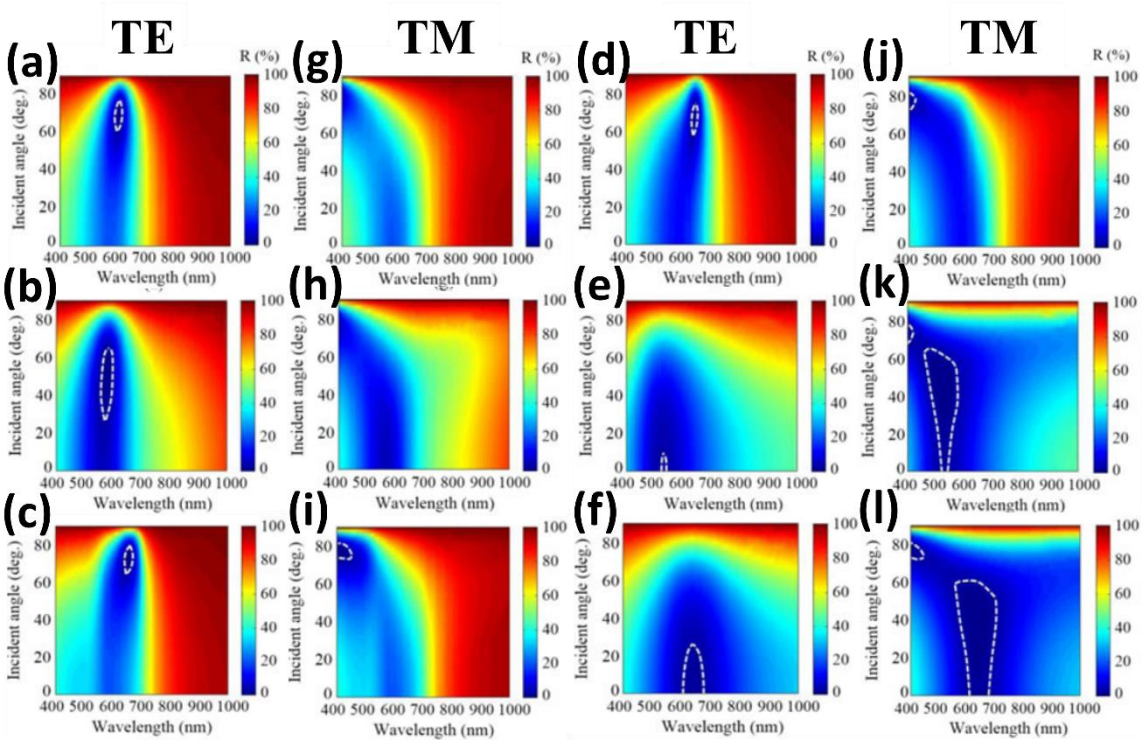


Figure 4.5. Angle resolved reflectivity versus wavelength surface maps for TE (a)-(f) and TM (g)-(l) polarisations. The same array of backing metals is used as in Fig.4.4. (a, g) Ag, (b, h) Al, (c, i) Au, (d, j) Cu, (e, k) Cr, (f, l) Ti. The contour lines shown are areas where the total absorption A is greater than 97 %. Lossy back metals like Cr and Ti have a spectrally broader omnidirectionality while Ag, Al, Au, and Cu are more spectrally selective. [4]

4.2.2 The Zeroth Mode in Ultrathin Ge

Similar state of the art pioneering work with ultracompact FP resonator stacks was done by Mikhail A. Kats and Federico Capasso using Ge in place of Si [10], Instead of structural colouration they were specifically more interested in the enhancement of electro-absorption in the ultrathin film regime due to the many advantages therein. Some of these advantages include reduced material cost, the ability to overcome the carrier recombination problem present in all optically thick semiconducting absorbers (caused by the presence of closely spaced grain boundaries and defects in the crystal structure of the material [14]), and remarkably the potential to overcome the Yablonovitch limit which is a theoretical

absorption limit in the bulky ray optics regime. When applied to conventional solar cells, this limit is primarily determined by the greatest possible enhancement of the number of total internal reflections in the many wavelengths thick semiconducting layer of interest as this maximises the propagation distance of the trapped light and therefore the absorption is greatly increased [35], [17]. Additionally, by minimising the size scale of the absorbing layer structure from above wavelength to deeply subwavelength, it is also theoretically possible to drastically increases the efficiency of single junction solar cells from 31 %, given by the Shockley-Queisser limit, to as high as 60 % under a solar concentration of 1 [36]. See Fig.4.6 below.

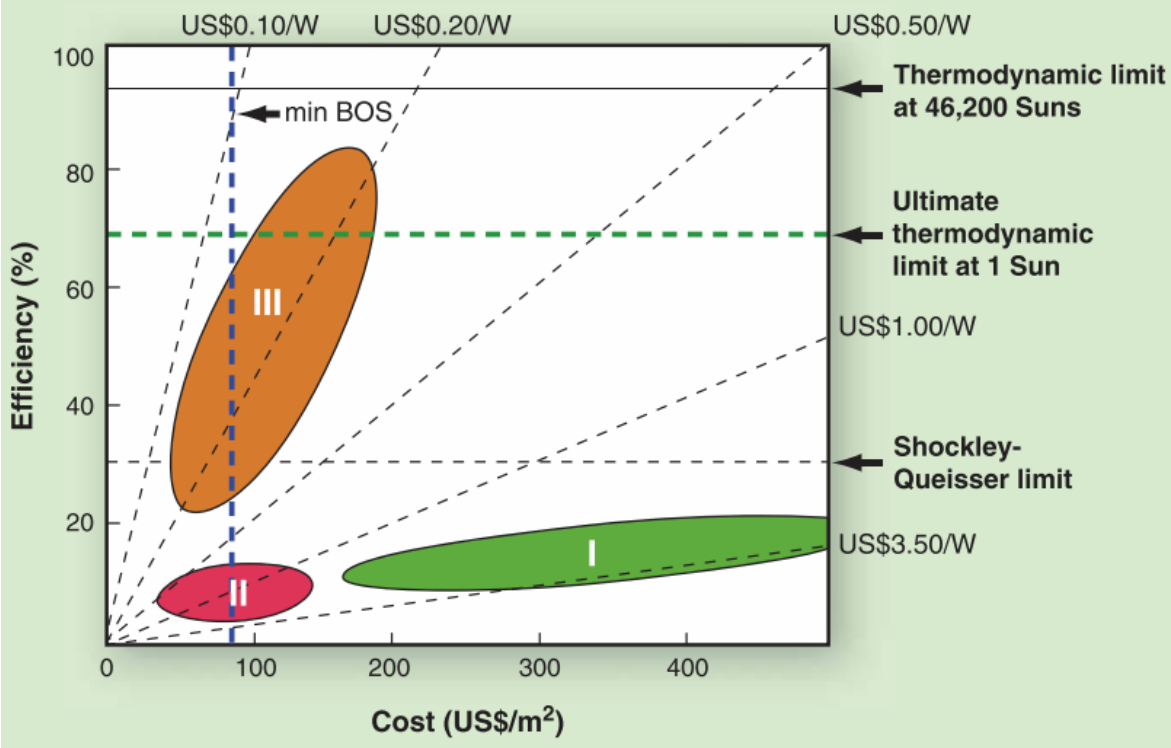


Figure 4.6. The Schockley-Queisser limit applies to all single band gap solar cells located in region 1 of the graph, with the ideal gap for the sun being in the region of 1.1-1.3 eV. A significant amount of energy in the solar spectrum exists above the bandgap however and unfortunately a lot of this energy will thermalise back to the bandgap in traditional PV cells, heating up and deteriorating them. With ultrathin absorber thin film layers or unique nanoscopic quantum absorbing devices like quantum dots, more of this excess energy can become electricity increasing the efficiency and therefore lowering the cost per Watt over the lifetime of the cell. The lifetime of a PV cell will also be increased as the high energy photons will no longer be wasted though thermal channels. If combined with a solar spectrum filter, the below band gap photons can be sent to a complementary bulkier thermal solar setup reducing the operating temperature of the cell even further. [36]

This is enabled by the short distances between the electrical junction and the absorption event in an ultrathin PV cell. Under these circumstances, the excited electrons above the bandgap can now be captured instead of primarily thermalising and deteriorating the lattice

structure [37]. These carriers are known as hot carriers and the current solution to dealing with them is to add additional materials with larger bandgaps to the solar cell device making it multi junction. This strategy is expensive though, and the increased cost is only justified in certain situations where every bit of power from the sun is needed like in space exploration.

Like with the Si/Metal samples in the Seyed Sadreddin Mirshafieyan *et al.* study [4], ultrathin Ge/Metal stacks can show large colour gamut with vibrant colours such as blue, violet, orange, and red shown below in Fig.4.7(a) [10].

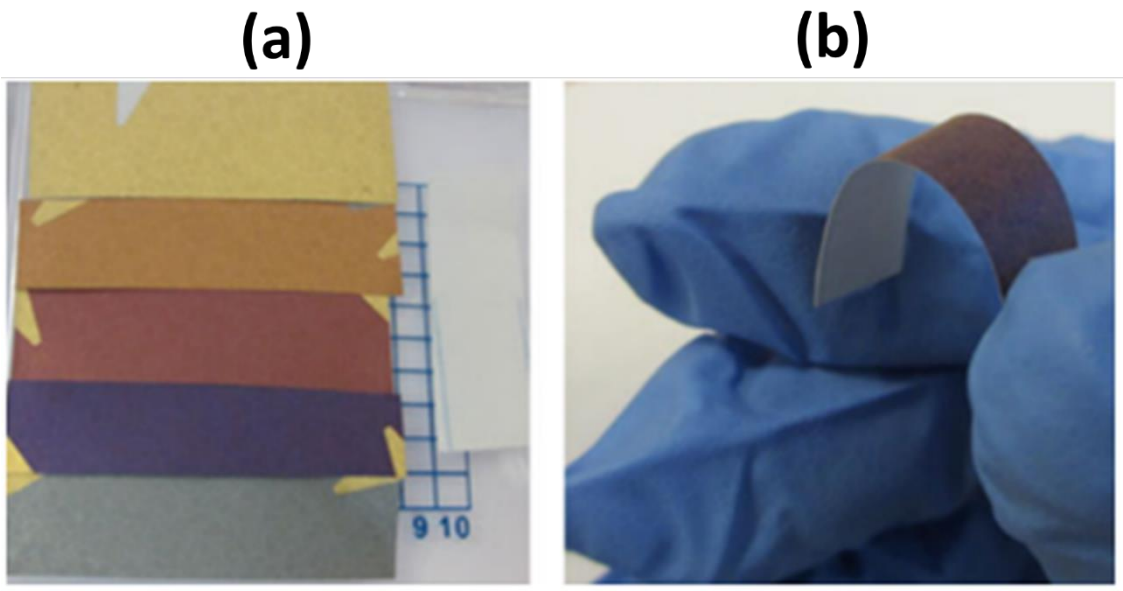


Figure 4.7. (a) Structural colour of Ge/Au film with thickness 0, 7, 10, 15, and 100 nm going top to bottom, all on a flexible rough substrate. (b) Showcasing the flexibility and omnidirectionality of the colour. [10]

With all samples using an Au backing metal, the large variety of colours seen was attributed directly to the changing Ge thickness between 0-30 nm in the ultrathin regime. Also, just as with the Si/Metal stacks, the Ge/Metal samples showed angle insensitivity to their colour. There was also insensitivity to large surface roughness as revealed in Fig.4.7(b) above where a rough paper substrate with gold backing was used. This unresponsiveness in colour change w.r.t roughness continues even to the point of the colour becoming more matte than specular [14], [38]. The previously mentioned Yablonovitch Limit is not strictly applicable to ultrathin films using high loss materials, but it is a useful indication to show how ultrathin solar cells could outperform conventional solar technology as optical FP resonators trap and greatly enhance the light matter interaction, without the need for surface roughening or a wavelength thick absorbing layer [35]. One can see the big difference between the trivial

single pass absorption Ge and light trapping ultrathin Ge/Ag stack with near perfect absorption in the zeroth FP mode around a wavelength of 620 nm in Fig.4.8 below [10]. This near-perfect absorption at 620 nm corresponds to an ATF FP resonant frequency where total phase delay accumulated is zero. Due to the extreme thinness, and the specific refractive index dispersion of Ge and Ag, the total phase delay remains close to zero outside this resonant position as well, given that the interface and propagation phase delay terms compensate each other, which is why high absorption is maintained to some extent. This is especially the case for the blue and green regions of the visible spectrum while the trend drops off in the far red and NIR regimes as Ge becomes less absorbing.

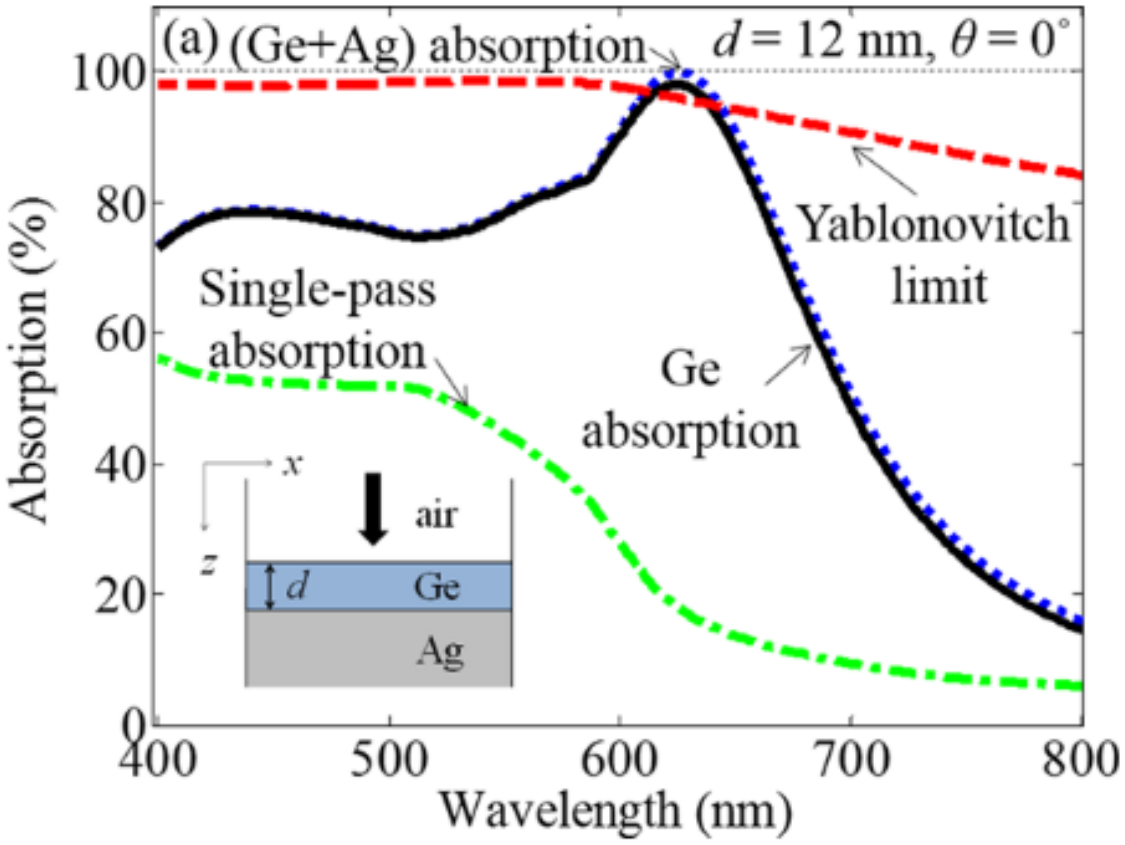


Figure 4.8. Comparison of ultrathin 12 nm Ge absorption with and without the Ag substrate, with the Yablonovitch limit showcasing the limits of light trapping in conventional solar cells. The resonant position is also robust to change in angle given the large value of index n possessed by Ge [10], [17]

This result is even more noteworthy when one considers that they used 12 nm of Ge in a configuration that is technically only a single junction. At 12 nm the Ge surface film is more than an order of magnitude thinner than the active layer in conventional single junction α-Si single junction cells with approximately 300 nm thickness [31]. Furthermore, like with the

ultrathin α-Si films, deeply subwavelength Ge layers could overcome the carrier recombination problem caused by the grain boundaries and defects present in the crystallographic structure [14], [37], [39]. By reducing layer thickness to as small as possible, compared to the carrier diffusion length, the probability they will work their way to the electrical junction is greatly increased for incident photons with energy at and above the band gap. The carrier diffusion length is a measure of how far an electron or hole can travel in a semiconductor before undergoing recombination, subsequently re-emitting the light back out. A recombination event is lost energy and therefore any such event represents an undesirable drop in external quantum efficiency (EQE) of a working solar cell device [40], [41].

Ultrathin Si has had some reports of very high quantum efficiencies but only over a narrow spectral range [42]. Ideally, where solar absorption is concerned, the EQE should be large across the visible, near UV, and NIR spectrums; closely matching the AM1.5 solar emission graph as closely as possible while also reflecting away any thermal photons into space at specific frequencies where the atmosphere is transparent, i.e., at wavelengths of around 10 μm where the largest atmospheric window is located below optical frequencies [43].

4.2.3 Recap of the Literature Review

To recap the literature overview on this subject, the zeroth order mode devices showed several key advantages over their physically thicker higher order counterparts; One, a flatter spectral response than traditionally thicker active layers, allowing for easier implementation of broadband absorption. Two, reduced sensitivity to angle of incidence, also known as omnidirectionality, as path length is proportional to $d \bullet cos(\theta)$, where d is thin film thickness and θ is AOI. This is very advantageous for solar absorption applications where sun angle changes throughout the day. Three, the ultrathin regime, d < 50 nm, has interesting implications for the extraction of energy from the thin film as nonlinear electric and optical behaviour at that scale often become apparent due to material size effects [29]. One such instance of this is the phenomenon of hot carrier injection. The hot electrons that result from this possess energy above the bandgap but normally will lose that energy thermally as phonons in the crystal lattice of the semiconductor before they can be extracted, limiting device efficiency [37]. For ultrathin film semiconductors, this weakness can become a strength and its possible for the hot electrons to escape before thermal dissipation occurs,

theoretically allowing one to surpass the conventional limits of contemporary semiconducting cells [44]. Four, the highly localised electric field within the ultrathin thin film at resonance could also potentially be used in conjunction with other physics such as plasmonics and excitonics to enhance their capabilities. For example, 2D excitonic lasers or THz lasers based on inter-excitonic transitions [45].

In section 4.3 below, the work done with TMDs MoS_2 and WS_2, along with Si and Ge regarding the zeroth FP mode stack configuration on a host of different metal backings will be shown. Specifically results for absorption and colouration will be shown alongside complementary data like AFM surface roughness, spectroscopic ellipsometry, and optical spectroscopy. Some discussion will also be had noting that large active modulation of MoS_2 through exciton tuning was difficult to reproduce and ultimately of no practical use in controlling sample colour or considerably changing the amount of absorption occurring. The dynamic optical response of the MoS_2 samples were only observed on small micron scale with lithographically patterned pixel device structures, and the change measure was very small on the order of 0.1 %. This ultimately led towards researching electrochromic materials as a better viable alternative source of active dynamic colour and absorption through index tuning. More on this can be found in Chapter 5.

4.3 Characteristics of TAC Grown TMDs

4.3.1 Large Dielectric Function of TMD Thin Films

Thin film and 2D transition metal dichalcogenides (TMDs) are a class of semiconducting material with the potential to form the basis of upcoming optoelectronic nanotechnology that operates in the ultrathin film regime [45]. The optical response of TMDs is dominated by their excitonic effects as this electron-hole bound state is tightly bound around 500 meV at room temperature ambient conditions! [46] The strongest excitons are the A, B, and C excitons located and associated with different locations in the Brillouin zone in reciprocal space. The A and the B excitons are of great interest to researchers as they are more easily manipulated by external stimulus like electric and magnetic fields [47]. Figure 4.9 below illustrates the close-packed hexagonal crystal structure of TMDs, in this case monolayer MoS_2, along with the spin-orbit split band gap centered at the K and K' Brillouin zone points.

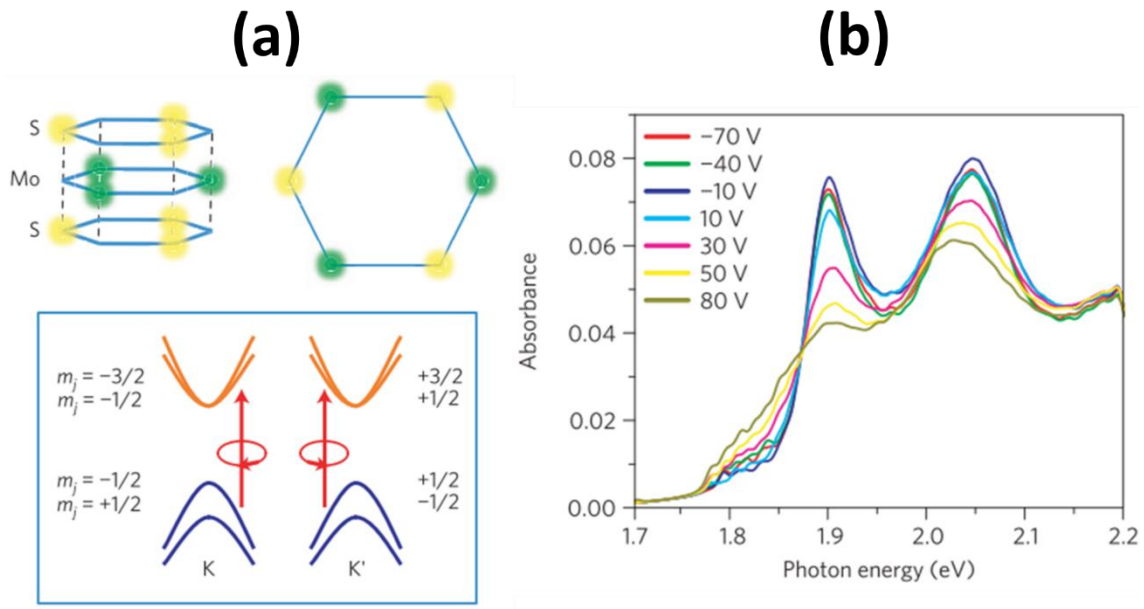


Figure 4.9. (a) A honeycomb lattice structure with an Mo plane in the middle sandwiched by two S planes. The valence band is split due to strong spin orbit coupling interactions lifting the degeneracy. The K valley and K' valley are populated when struck by left and right circularly polarised light respectively. This has profound implications for the creation of spintronic and valleytronic optoelectronic devices. (b) The A and B excitons are split by the lifting of the spin degeneracy. Both are readily tuneable by applying an electric field. With a strong enough field on the order of 100 V the excitons can be almost completely supressed relative to the contribution of the Tauc-lorentz intrinsic semiconductor absorption oscillator to the dielectric permittivity function. [47]

Electrical tuning of excitons results in strong unity order change of refractive index in these TMD thin films. This can be used to modulate the phase and amplitude of reflected and transmitted light. This unity order change in the refractive index of MoS_2 thin films, attributed to field effect suppression of the excitons, is discussed at length by Riley Gatensby and others [48]. This substantial change in n and κ is the basis for the idea of gate tunable reflectivity in ultrathin film TMD device structures [6], [45]. When paired with an asymmetric FP resonator setup, the field effect tuning of the excitons can drastically change the absorption characteristics of the TMD/metal stack if the FP resonance is centered around the same spectral position as those features.

This strong tunability, which could lead to dynamic field effect absorption and colour change, is only possible in deeply subwavelength MoS_2 films measuring at 10 nm in thickness or less. When the coating is close to being 2D the exciton, with a bulk radius of 3.22 nm, will experience significant geometric confinement increasing the spatial overlap of the electron and hole wavefunctions and subsequently increasing the binding energy [29]. This strong confinement, especially in the limit of 1-3 layers, is the primary reason why the

excitons dominate the dispersion of the dielectric function response of TMDs in this size regime. See Fig.4.10 below.

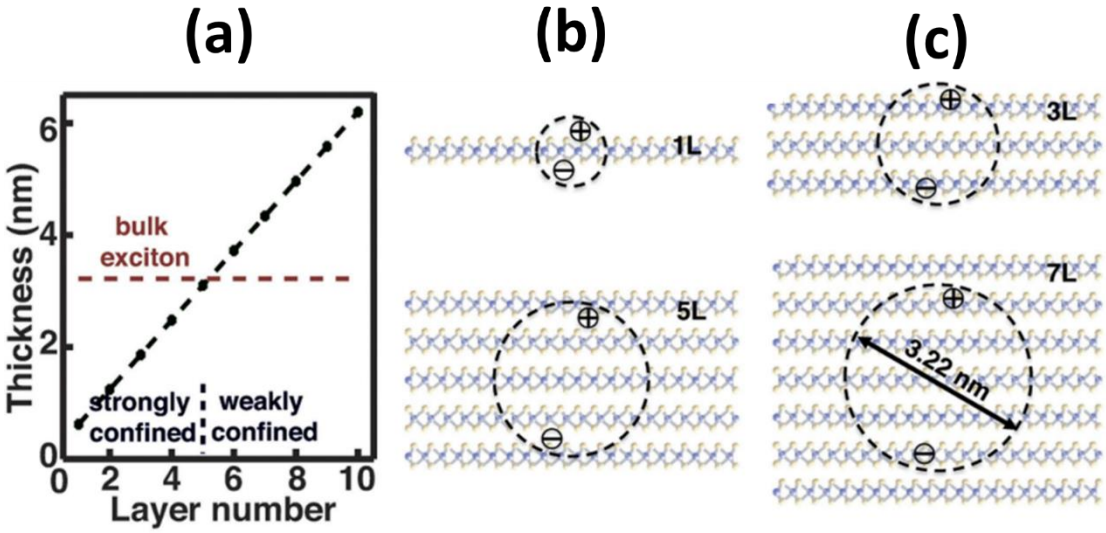


Figure 4.10. (a) Below five layers the strongly confined regime is accessed, and the bulk exciton becomes constrained in the thickness domain, increasing the binding energy of the exciton. (b) in the strongly confined regime (1L) the absorption is much more controllable by field effects compared with a standard semiconducting material like Si. (c) Once the TMD leaves the ultrathin film regime (7L) the excitonic tuning does not have as stark and impact on the optical behaviour. Their impact on the refractive index dispersion remains, albeit smaller. [29]

Since excitons are held together momentarily by coulomb forces it is sensible for one to try and manipulate it using well understood planar geometry field effect gating that is compatible with an ATF approach [49]. Literature indicates that a change in κ of 60 % and 20 % for n is possible using large field effect gate voltages on the order of 100 V [6]. The large voltages required raises some concern regarding the stability of the FP resonator devices, specifically in regard to the phenomenon of dielectric breakdown [50], which destroyed many of the TMD films made and most commonly seen occurring at surface weak points such as pinhole defects. An insulating dielectric layer is necessary to electrically isolate the gate contacts from one another, with dielectrics like Si_3N_4 , SiO_2, or HfO_2 used.

Thin film TMDs are known to have a large intrinsic refractive index n and κ, on the order of $n = 4 \sim 5$ and $\kappa = 1 \sim 2$, thus they have a stronger interaction with light compared with more conventional coatings like Al_2O_3 ($n = 1.7$) or ITO ($n = 2.1$). The large index means that even thin TMD films can have significant optical path lengths (OPL), and monolayers (0.65 nm) as thin as 3 atoms have been shown to form optical lenses and gratings [26]. It is quite fortuitous that MoS_2 or WS_2 have large refractive indices and a strong field

effect response simultaneously in the ultrathin film regime. The combination of these two elements in tandem is what makes the TMDs so promising for ultrathin passive and active device structural colour and absorption in a way that most other materials cannot match. Work carried out by Jiong Yang *et al.* (2016) showcases the ramifications of the large intrinsic indices of MoS_2 through comparison with the famous first discovered 2D material graphene, in Fig.4.11 below [26].

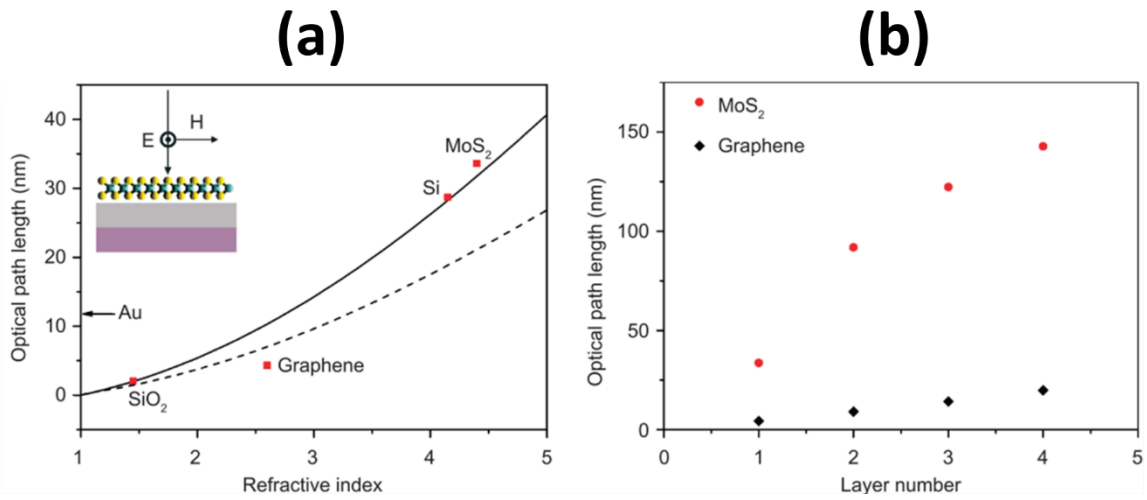


Figure 4.11. (a) The OPL of single layer Au, SiO_2, graphene, Si, and MoS_2 are all compared. The lossy dielectrics all act at least 50 time thicker than their real true physical thickness given their large index of refraction. (b) In the strongly confined excitonic regime, the OPL of MoS_2 increases linearly with each layer added, leading to the remarkable result that a 2.7 nm coating behaves as if it were 150 nm thick. Graphene in comparison struggles to interact strongly with light, with a response that is nearly an order of magnitude beneath that of MoS_2. The difference in the strength of the light matter interaction is magnified even further when one notes that graphene is not lossy enough to be able to access the ultrathin film zeroth order FP mode resonance. [26]

4.3.2 Surface & Active Reflection Change Properties of the TAC Grown TMDs

The performance of TMD devices is heavily affected by the quality of the absorbing thin film coating and overall stack. One important factor was the duration of time spent in TAC. Thirty minutes was found to be an ideal time for the ultrathin samples that were produced. Leaving the Mo precursor in too long or at too high a temperature above 750˚C led to very rough defective samples that were difficult to characterise in general using either XRR or SE. Given the high temperatures the bulky substrate used is typically quartz which is also ideal for its low thermal expansion coefficient, mitigating the possibility of lift off during the cooling process after sulphurisation. The substrate surface quality was also important as the flaky texture of TAC grown TMDs can easily fall off without adequate adhesion. The

substrate had to be as clean as possible before deposition to ensure a smooth continuous film, or at least to ensure that large enough areas of the film are connected, regarding what optical and electrical measurements can sense. This problem was specifically troublesome as many of the TMDs devices made early in the project showed no field effect response due to current leakage at defect sites and dielectric breakdown.

After much trial and error and an enormous effort on Nishtha Shelly's part, the process of sample creation was improved enough to consistently generate small changes of around 0.1 % in the reflectivity response of MoS_2/Au samples as seen by the reflectivity change data in Fig.4.12 below. The ideal recipe for ultrathin MoS_2 was therefore found to be 30 minutes of sulphurisation at 750˚C on a clean quartz substrate. It was also found that the Mo precursor film, created with a Mo target in the NPVD magnetron sputtering tool, should be pre-sputtered to ensure higher film uniformity and to avoid contamination from oxides formed on the target surface when vacuum is broken during the loading process. Due to the small changes in reflectivity, as well as the small micron size scales of the pixels, a technique known as charge couple device thermos-reflectance (CCDTR) was used to accurately gauge the observed optical changes with high spatial resolution [51]. This instrument is located in the SNIAM and is jointly used primarily by Prof. John Donegan's research group and Prof. David McCloskey's research group for studying the optical response of pixel scale devices.

With this technique, thermal stimuli are the usual trigger for optical response change but for the MoS_2/Au samples an electric field generated by a Keithly 2400 source meter was used instead. CCDTR records hundreds to thousands of images as the voltage is either swept or switched. In most cases switching between large voltages of ± 50 V was done, and after processing the images in a MATLAB program, figures like Fig.4.12 (b) could be produced highlighting regions were changes in the refection took place.

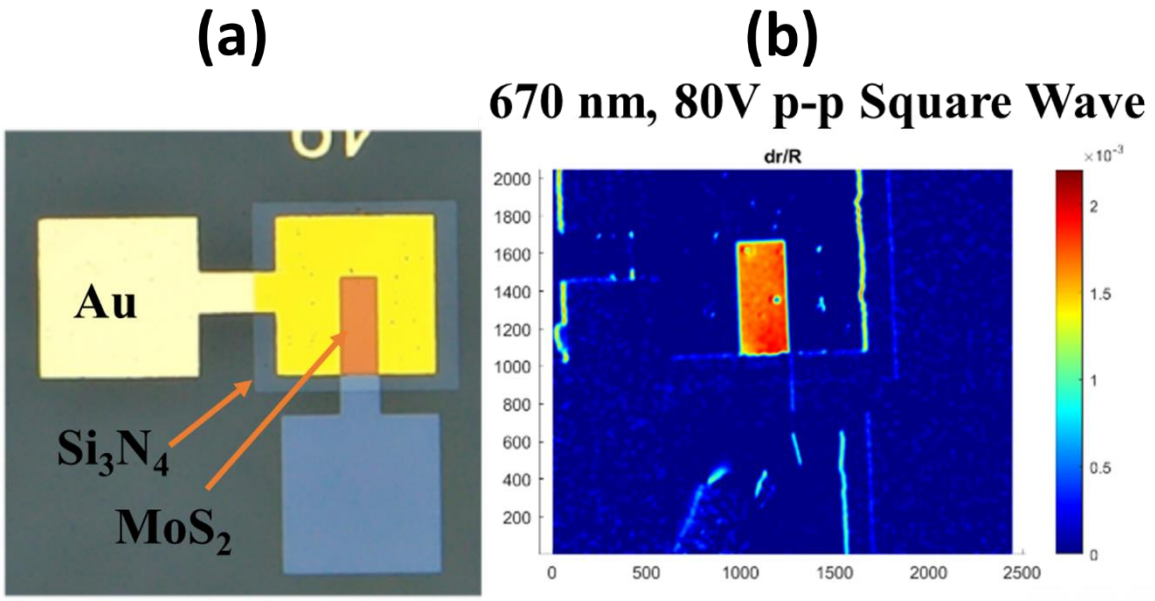


Figure 4.12. (a) Optical microscopy image, as measured by the Olympus microscope system in CRANN, of a 4 nm MoS_2 on 33 nm Si_3N_4 on Au backing. The active pixel where all planar layers overlap is the red bar in the top right quadrant. The stark difference in colour when MoS_2 is added showcases its ability to induce strong colouration when paired with Au. (b) A CCDTR measurement of the same pixel element with a 0.1 % change in reflectivity measured uniformly across the MoS_2 bar with applied voltage. The change is uniform across the MoS_2 covered bar.

The uniform response could not be seen across large macroscopic sample scales however, making further studies into active field effect TMD colour tuning a moot point for dynamic colourimetry purposes as the human eye cannot effectively perceive objects smaller than about 100 microns, or around the diameter of a strand of human hair [52]. Metal back reflectors like Ag, the most ideal mirror, cannot be used long term with TMDs in direct contact either due to sulphur and Ag reacting to form a tarnished layer [53]. Thus, Au is the preferred choice due to its inertness.

Regarding active modulation further, any defects in the TAC TMD surface can become focus points of the electric field that eventually cause dielectric breakdown to occur if one is not careful [50]. This breakdown was seen a lot during voltage switching experiments with the TAC grown MoS_2 samples measured using the CCDTR technique. See Fig.4.13 below. Based on the work done, the issue of pinholes, among other defects, is one of the major points holding back the implementation of the TAC TMDs into commercial optoelectronic technology. The TAC samples produced over the many years spent on this thesis work, have generally poor quality that is inadequate for electronic purposes at scales beyond the micron level. Furthermore, the low change in reflectivity measured w.r.t applied

voltage was a result that underperformed expectations given what has been achieved with CVD grown MoS_2 in FP resonators stack structures in the 2D optoelectronics literature, namely unity order refractive index change and reflectivity modulation an order of magnitude larger than seen in this thesis work (around 2 % in the A exciton region) [43]. Perhaps with better optimization of the sample creation process or the inclusion of additional steps to modify the surface condition after synthesis, the small change in reflectivity of around 0.1-1 % could be improved upon closer to the 2 % literature value.

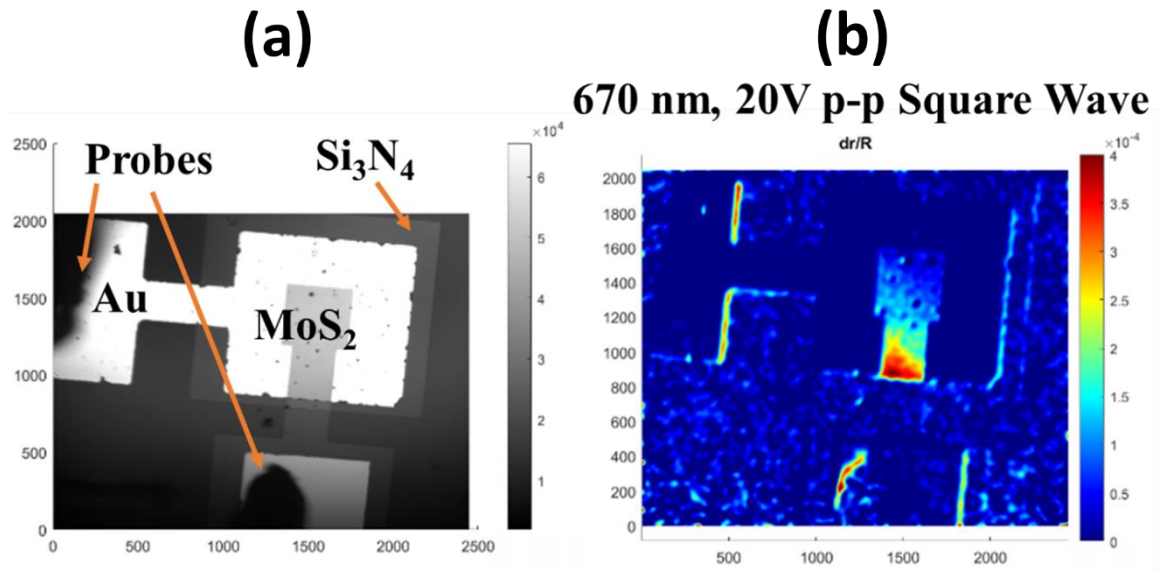


Figure 4.13. (a) A greyscale photo of a defective pixel that does not undergo field effect tuning. (b) Current leaks through near to where one of the electrode probes are in contact with the contact pads and is highly concentrated at one site coloured in dark red. The response is weaker than the uniform change in reflection seen in Fig.4.12..

The quality of these ultrathin TAC grown MoS_2 surfaces can also be quantified with AFM in contact mode. By measuring carefully between the covered bar region and the gold surrounding it, the drop off in height can be used to sense the thickness of the MoS_2 layer directly. The root mean square (RMS) roughness can also be evaluated when measuring at least 0.5 µm from the step-off point, which is to say the region close to the interface between both the MoS_2 and substrate is not included in the averaging of the surface roughness. See Fig.4.14 below detailing an AFM raster scans in a 100 µm x 100 µm region.

Due to the presence of the DART train line beside CRANN in Trinity college Dublin, there can sometimes be artifact lines/streaks in the surface image produced. Normally these lines do not ruin the image formed as the raster scan is much longer than the time taken for the

train to pass by. In any case, it was found to be good practice to avoid performing AFM measurements at rush-hours in the morning and evening when train traffic is highest.

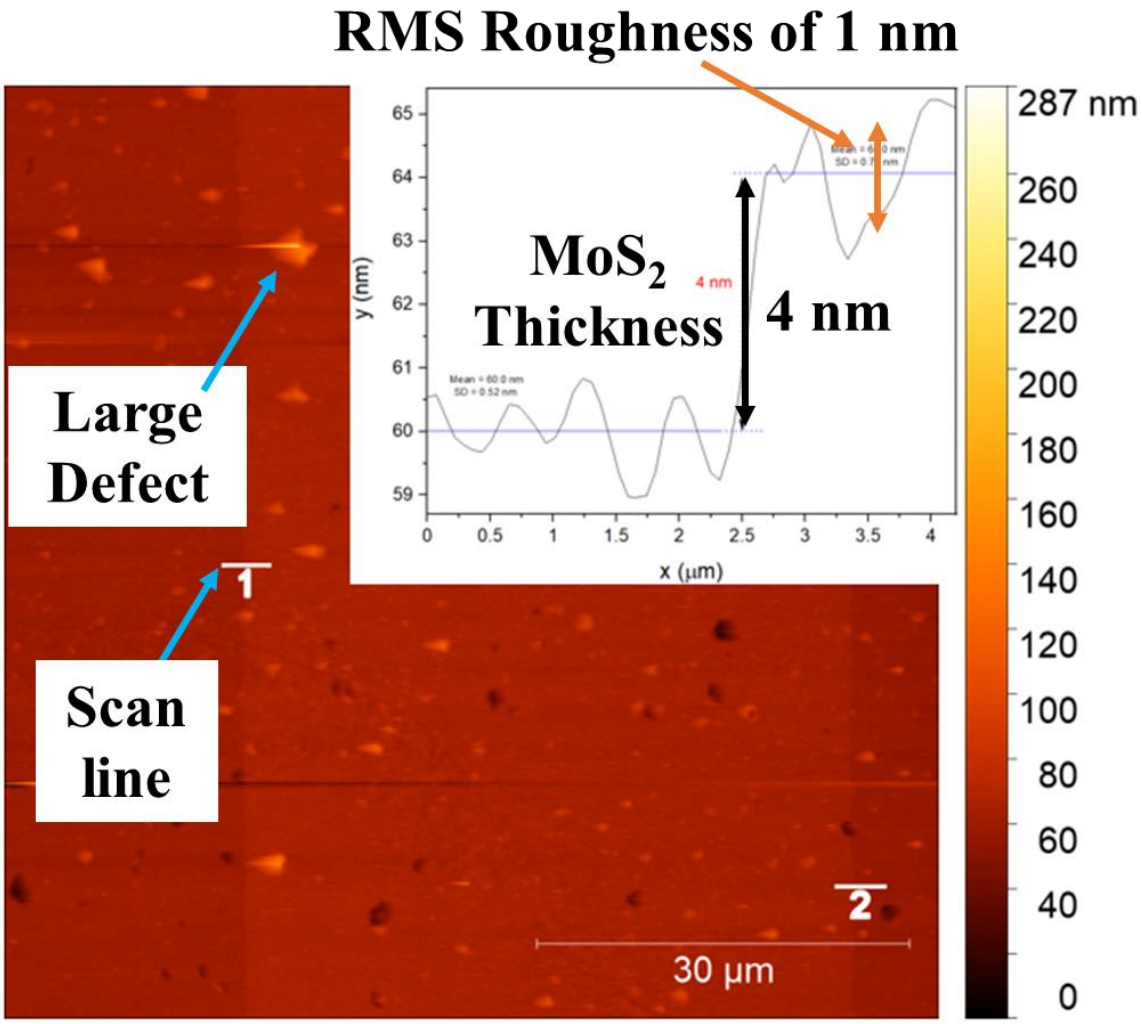


Figure 4.14. An AFM raster scan sweep of a 100 µm x 100 µm area crossing over between the top MoS_2 bar and the Au surrounding it. Large defects that dwarf the average height level can be seen in bright yellow and dark red spots. A line scan at location 1 was done to find the height of the MoS_2 bar as well as its RMS roughness which is the true physical microscopic roughness of the surface. Not to be confused with the ellipsometry roughness EMA layer value which infers the presence of the microscopic roughness from its optical effect without sensing its minute dimension directly due to the diffraction limit of visible light.

Despite efforts to clean the quartz substrate before sputtering onto them, there are large defects seen at some points much taller than the surface around them. It is defects like these that make it infeasible to scale the field effect tuning response in the TAC samples beyond the micron scale and into the macroscopic realm in which one can clearly see features with the naked eye. The film integrity and colour of large scale 1 cm x 1 cm MoS_2 deposits will still often appear smooth/homogeneous when looked at without the aid of a microscope,

indicating that these surface defects in TAC grown coatings have a minimal impact on the passive optics, instead playing a major role in limiting the opto-electronic response.

4.3.3 Spectroscopic Ellipsometry of the TAC Grown TMDs

Unless otherwise stated, the refractive index data presented in the following figures are measured using the alpha SE in CRANN. An effective way to characterise the light matter response of MoS_2 and WS_2, among other lossy dielectrics, is through the use of SE. TMDs are special in that there are large differences in the dielectric function between bulk and the 2D ultrathin film regime, exhibiting strong excitonic effects almost an order of magnitude above other conventional semiconducting materials such as Ge and Si due to geometric confinement effects that are discussed at length in the literature [24], [25], [47], [56]–[58]. They have been researched extensively in the literature due to their promising potential in future optoelectronic nanotechnology as well for that very reason [5], [6], [59]. Unlike graphene, the TMDs also boast favorable optical/electronic properties such as a favorable band gap position for PV absorption applications above just above 1.2 eV and beneath 2 eV depending on material thickness, large field effect index and carrier density tuning, and chemical stability in an oxygen ambient [24], [49], [56], [60]–[62]. In comparison, other lossy dielectrics like Si and Ge with large refractive indices have lower bandgaps in the NIR region around 1.12 eV and 0.8 eV for Si and Ge respectively, with very weak excitonic effects that can only be seen at cryogenic temperatures [63]. Therefore, field effect tuning cannot have the same magnitude of influence over the optical response as it does with TMDs in cases where no doping is used. Note that even though Ge is an indirect gap semiconductor, the direct band gap transition at 0.8 eV will dominate over the second order phonon assisted transition located lower around 0.6 eV [64] in the visible regime. This detail cannot be picked up by the alpha-SE ellipsometer however because of how large the direct transition absorption of Ge is at the lower limit of the instrument's working wavelength range at 1.38 eV compared to the indirect channel.

A multi-Lorentzian dispersion relation for the optical dielectric function is used to model the ultrathin film TMDs in this thesis work, see equation 4.4 below [65]. Figure 4.15 is also given below for passive and active field effect tuning of ultrathin MoS_2.

$$\varepsilon(E) = 1 + \sum_{k=1}^{N} \frac{f_k}{E_k^2 - E^2 - iE\gamma_k}$$

(4 . 4)

Where N is the number of Lorentz oscillators needed, f_k is the k^{th} oscillator strength, E is photon energy, E_k is pole position, and γ_k is the damping factor (how broad or narrow the resonance is). In the configuration used by Vasyl G. Kravets *et al.* (2019) [65], the positive voltage bias suppresses the excitonic pole peak strength while the negative voltage bias enhances it. Since they are working with monolayer, the difference in f_k between both biases is large at around 100 % change relative to the suppressed state. By using this dispersion relation, also known as a general oscillator parametrization, the number of parameters in the linear regression fit is drastically reduced and at the same time the dispersion is inherently KK consistent due to the model's use of KK integrals to calculate the polarisability response of the medium, $\varepsilon_1(\omega)$, based on the absorbing pole dispersion curve best fit guess $\varepsilon_2(\omega)$. KK consistency is needed for all naturally occurring materials to ensure a physically sound dispersion relationship between n and k, else it is possible that the ellipsometer may predict a negative value of refractive index n or extinction coefficient κ as the best fit [66].

Table 1. Fitting parameters for the complex refractive index of the CVD MoS_2 monolayer as a function of gate voltage

k	MoS_2 monolayer					
	$V_g = 0$ V			$V_g = 75$ V (−100 V)		
	E_k (eV)	f_k(eV^2)	γ_k(eV)	E_k (eV)	f_k(eV^2)	γ_k(eV)
1(A)	1.89	0.4	0.059	1.89	0.15 (0.57)	0.068 (0.073)
2(B)	2.03	1.75	0.12	2.03	1.15 (2.03)	0.17 (0.15)
3	2.877	42.5	0.37	2.87	42.5	0.37
4	2.275	5.0	1.2	2.275	5.0	1.2
5	3.745	160	1.3	3.77	160	1.3

The refractive index is given by the multi-Lorentzian dispersion relation defined by Eq. (1). The oscillator strength f_k, the spectral resonance energy E_k, and the spectral width γ_k of the k-th oscillator are given in eV^2, eV, and eV, respectively

Figure 4.15. The oscillator parameters of CVD monolayer MoS_2 measured through ellipsometry and modelled using several Lorentzian functions to account for the excitons and other semiconducting absorption features. Results are shown for different gate voltages applied to the MoS_2. Static 0 V and the two biased states of +75 V and -100 V. [65]

If the indices of the layers underneath the top TMD coating are also known as well then fitting becomes a one-layer problem and mathematical correlations between the contributions of different absorbing poles can be eliminated fully. A standard of practice is to measure the SE response of each layer in the stack structure as it is added. Thus, in this way each layer can be characterised for thickness and index, making the final measurement of the TMD layer a much less cumbersome task. This would ideally be done in-situ during deposition without breaking vacuum, but such a setup is expensive to install and potentially unfeasible depending on the nature of how the multilayer stack structure is created. The most affordable commercially available ellipsometers are benchtop and operate at room temperature and ambient atmospheric pressure.

Transmission weighting is used in conjunctions with SE data when measuring the index of all TMD samples on transparent backings, as the exciton dominated dielectric function will create strong Reflection and Transmission peaks and troughs around those resonant states,

reducing correlation in the fit index and thickness, and making a unique solution easier to find as the index varies more rapidly around regions of anomalous dispersion. Figure 4.16 below displays refractive index data of TAC grown WS_2 and MoS_2 on glass and Au backing respectively. Both films are a little thicker than the strong geometric confinement region for enhanced exciton binding energy, thus the associated peaks are more subtle but none the less still exist and modify the optical dielectric function.

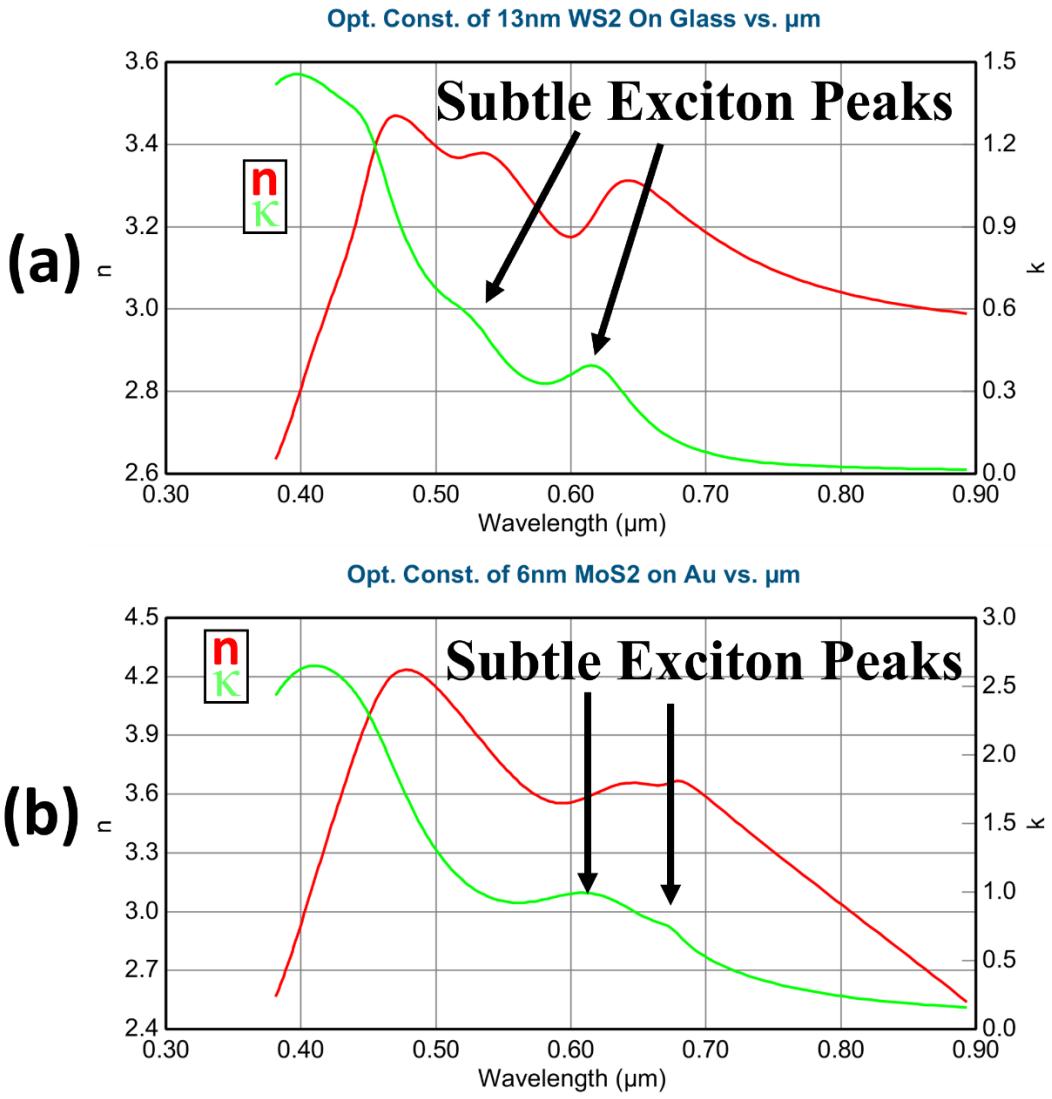


Figure 4.16. (a) The complex refractive index dispersion curve of thin film WS_2 on a glass substrate. The excitons are higher energy in WS_2 when compared to MoS_2 and the energy split is larger in magnitude due to increased spin orbit coupling. (b) At 6 nm the A and B excitons peaks located between 600-700 nm wavelength are somewhat subtle, but their presence still distorts the dispersion curve of the real refractive index in-line with the KK relation.

The transmission UV-Vis data is shown below in figure 4.17 for the 13 nm WS_2 sample on glass from figure 4.16(a) above. The enhanced absorption around the exciton peak positions causes an additional corresponding narrowband drop in transmission.

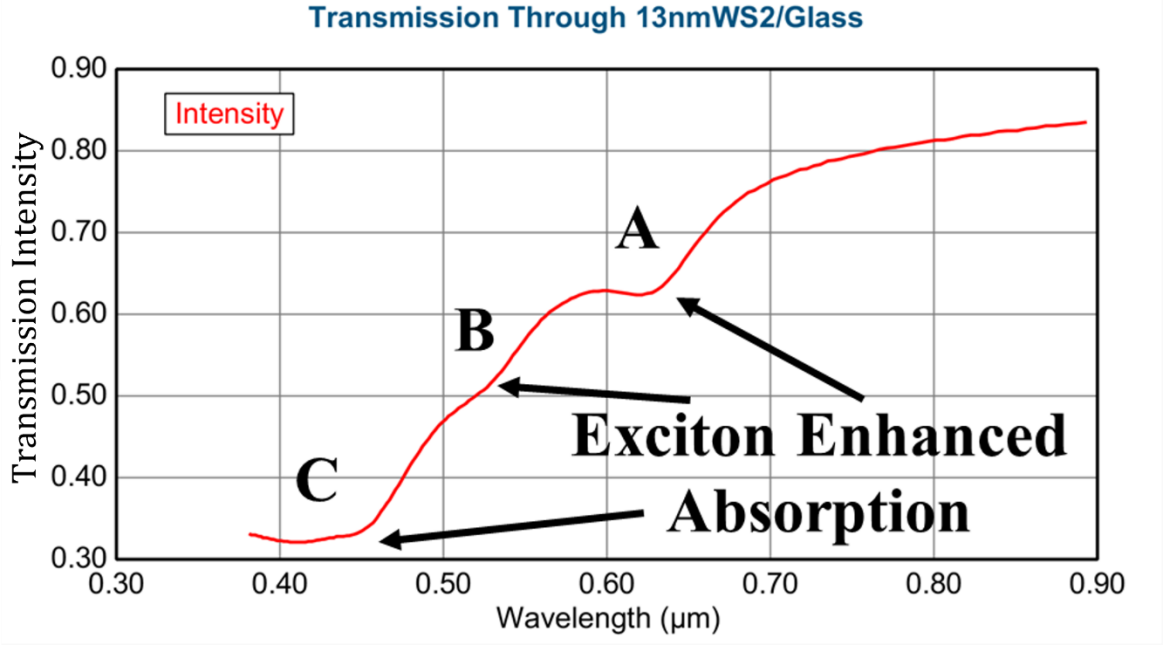


Figure 4.17. The general trend as wavelength decreases is for the transmission to drop in line with increase in absorption in the WS_2 layer. The presence of excitons at point A, B, and C enhance this absorption further.

The impact of the exciton states on the optical dielectric functions do indeed get larger in thinner 2D TMD films and this effect rapidly begins to dominate the optical response around a layer thickness of 4 nm or less as revealed for MoS_2 in Fig.4.18 below. Though the index is slightly lower than for 6 nm MoS_2, the exciton peaks are more striking in appearance relative to the broader interband transition response. With the complex refractive index dispersion of the TMDs, simulations can be done using the TMM in MATLAB to find ATF planar FP stack structures that can enhance whichever optical response is of interest, i.e. reflection change, total absorption, strong omnidirectional colouration, etc. The active reflection change capabilities of MoS_2 left much to be desired due to the issues regarding surface defects created or amplified during the TAC synthesis. My research group did not have access to an M2000 J.A Woollam ellipsometer with the correct higher power focusing lens to miniaturize the working ellipsometer beam spot diameter down to the micron scale. Thus, the field effect TMD refractive index change used in simulations was inferred from literature data like the table shown in Fig.4.15 [65]. It was had initially hoped to refine the TAC process enough to reliably create large

homogenous TMD sample areas. Unfortunately, the defect problem could not be resolved, effectively curtailing the working area of the active MoS_2 devices to the scale of 10's to 100's of microns, which was much too small a zone compared to the millimeter scale needed for the alpha SE system, to make unfeigned measurements. Therefore, focus was taken away from working on the dynamic TMD measurements, and instead towards index tuning in electrochromic materials which chapter 5 will cover.

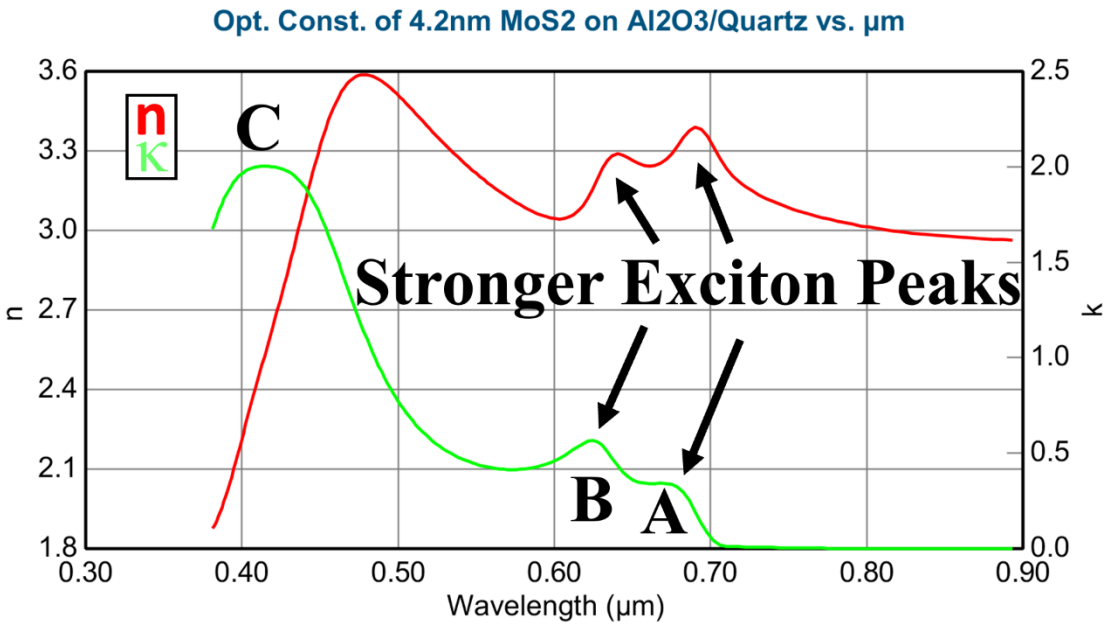


Figure 4.18. The complex refractive index dispersion curve of thin film 4.2 nm MoS_2 on a Al_2O_3/Quartz Substrate. The excitonic peaks are a more striking feature in the absorption response compared to 6 nm MoS_2 in Fig.4.16(b).

In Fig.4.19 below the bulk indices are displayed for many metals and other lossy dielectrics produced by the NPVD magnetron sputtering tool and measured with SE. Bulk in this case refers to a thickness at or greater than 100 nm where the ellipsometer will no longer register back reflections from the internal substrate interface, simplifying the MSE fitting to only reflections originating from the air interface on top [67]. In the case of Germanium, the thickness of material used is 112 nm making it somewhat semi-transparent compared to a metal like Ag that has high reflectivity in the visible regime, as a direct result of its UV plasma frequency at 138 nm. In this single reflection limit, the pseudo ellipsometry parameters can be used to calculate n and κ without a wave interference optical model needed [67].

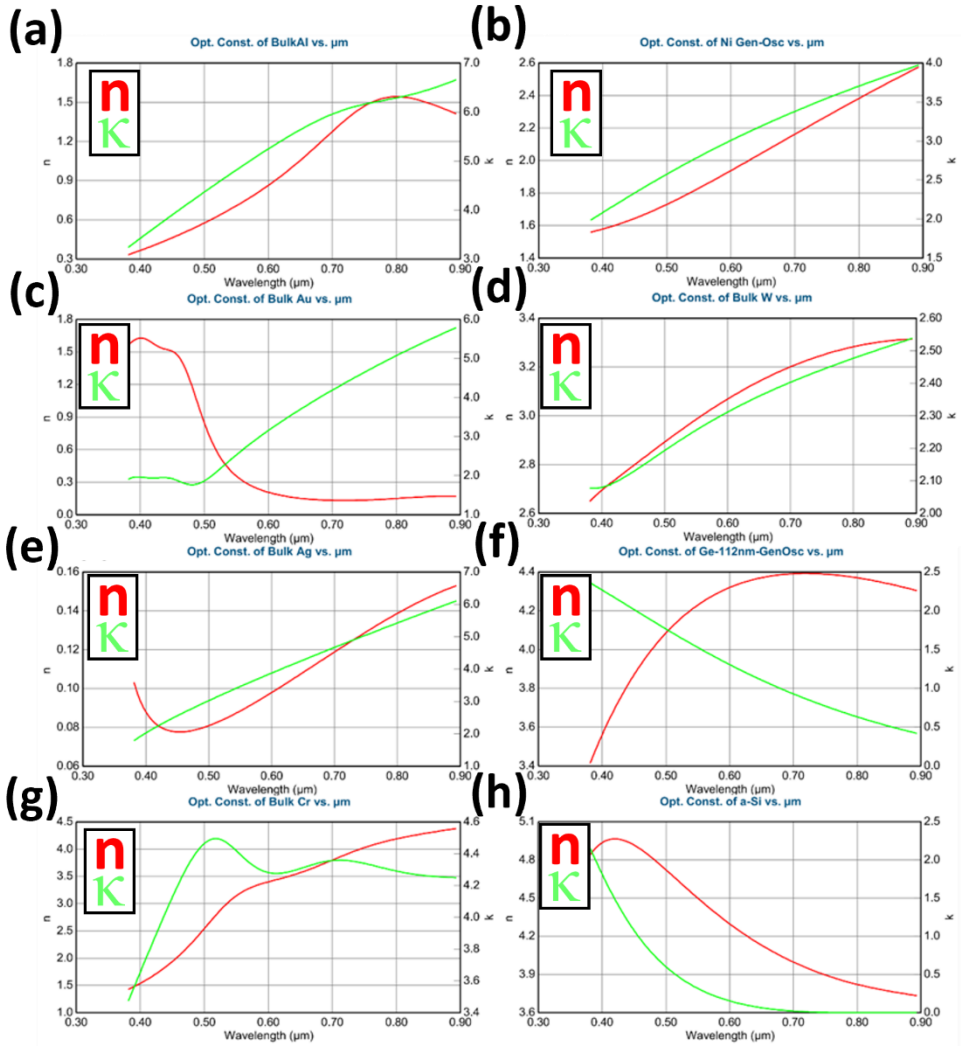


Figure 4.19. The complex refractive index of bulk metals and some lossy dielectrics deposited by the NPVD magnetron sputtering deposition tool; (a) Al, (b) Ni, (c) Au, (d) W, (e) Ag, (f) α-Ge, (g) Cr, and (h) α-Si all on glass substrate.

4.4 Results of the Lossy Dielectrics in the Zeroth Order Fabry-Perot Resonator Stack Layout

4.4.1 Vivid Colouration of Lossy Zeroth Mode Resonators

In the following pages, strong passive colouration and absorption will be investigated for several different lossy dielectrics on various opaque metal backings, using an ultracompact bi-layer zeroth-order Fabry Perot mode resonator configuration. See Fig.4.20-4.23. In some instances, the addition of a lossless dielectric on top is employed to widen the colour gamut, increasing the availability of greener hues as seen. Layer resolved absorption will also be looked at within the zeroth FP band to garner a finer sense of just how efficiently

the lossy dielectric layers attenuate the light in comparison to the opaque metal back-reflector films.

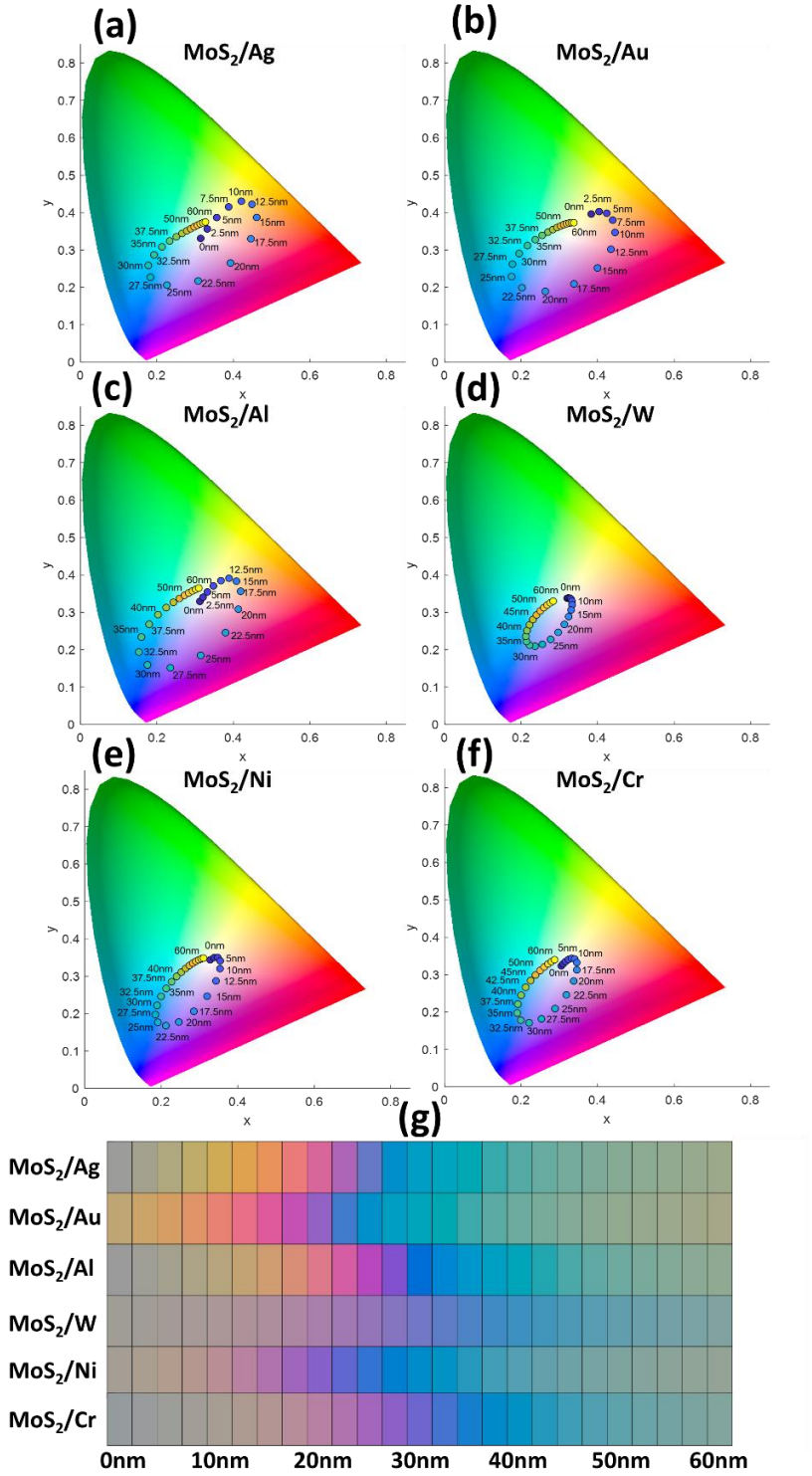


Figure 4.20. Simulated colour chromaticity diagram of MoS_2 on different backing metals. (a) Ag, (b) Au, (c) Al, (d) W, (e) Ni, and (f) Cr. (g) Lossy metal backings like Cr and Ni show less vibrant colours which is attributable to the broader absorption that occurs. Nobel metals like Ag and Au shows vibrant yellows, purples, and blues.

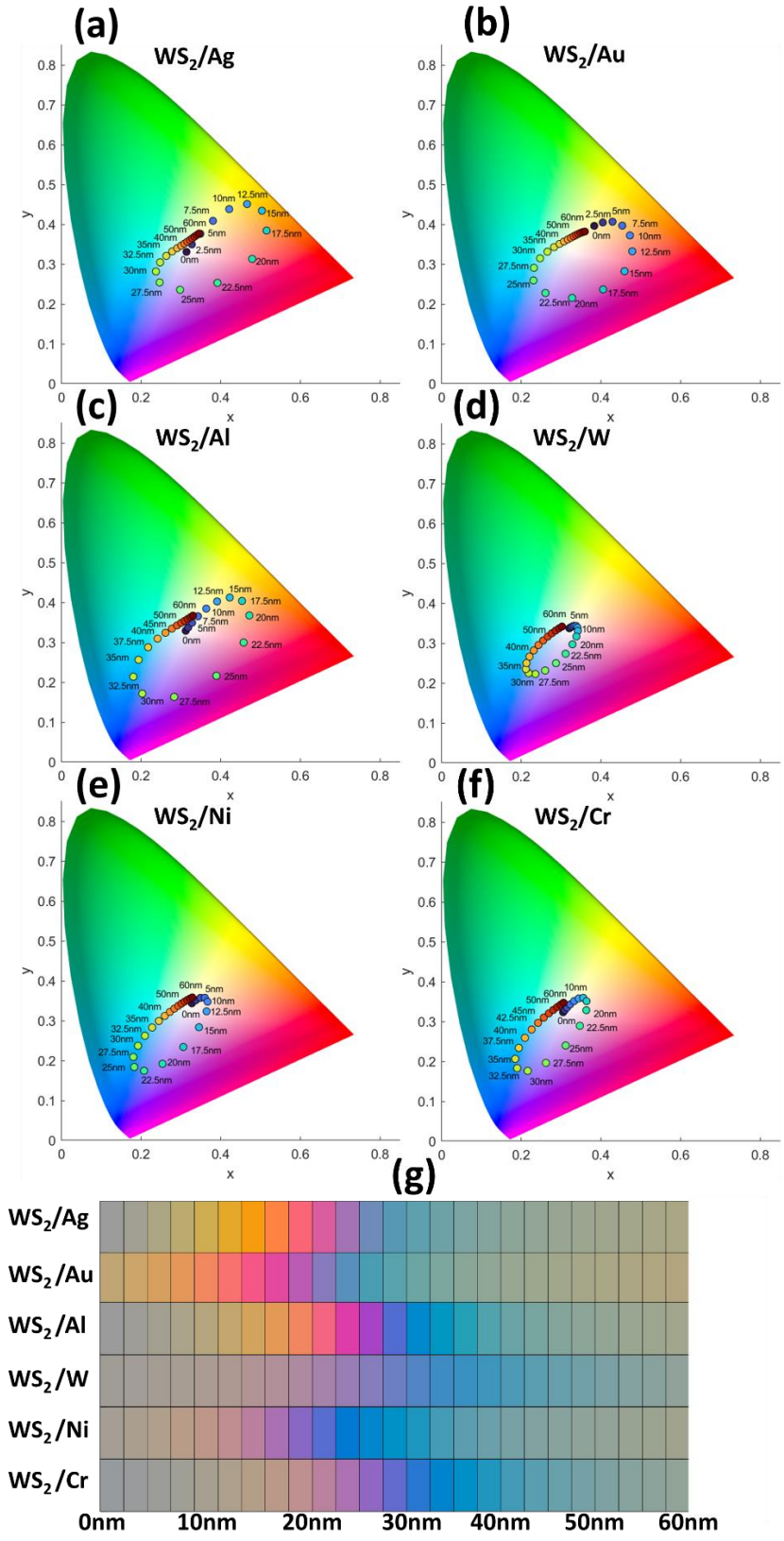


Figure 4.21. Simulated colour chromaticity diagram of WS_2 on different backing metals. (a) Ag, (b) Au, (c) Al, (d) W, (e) Ni, and (f) Cr. (g) The vibrancy of samples using low index metals like Ag and Au is slightly better than the result obtained with MoS_2, though they are both quite close in performance. Lossy backing metals W, Ni, and Cr broaden the absorption but dull colour.

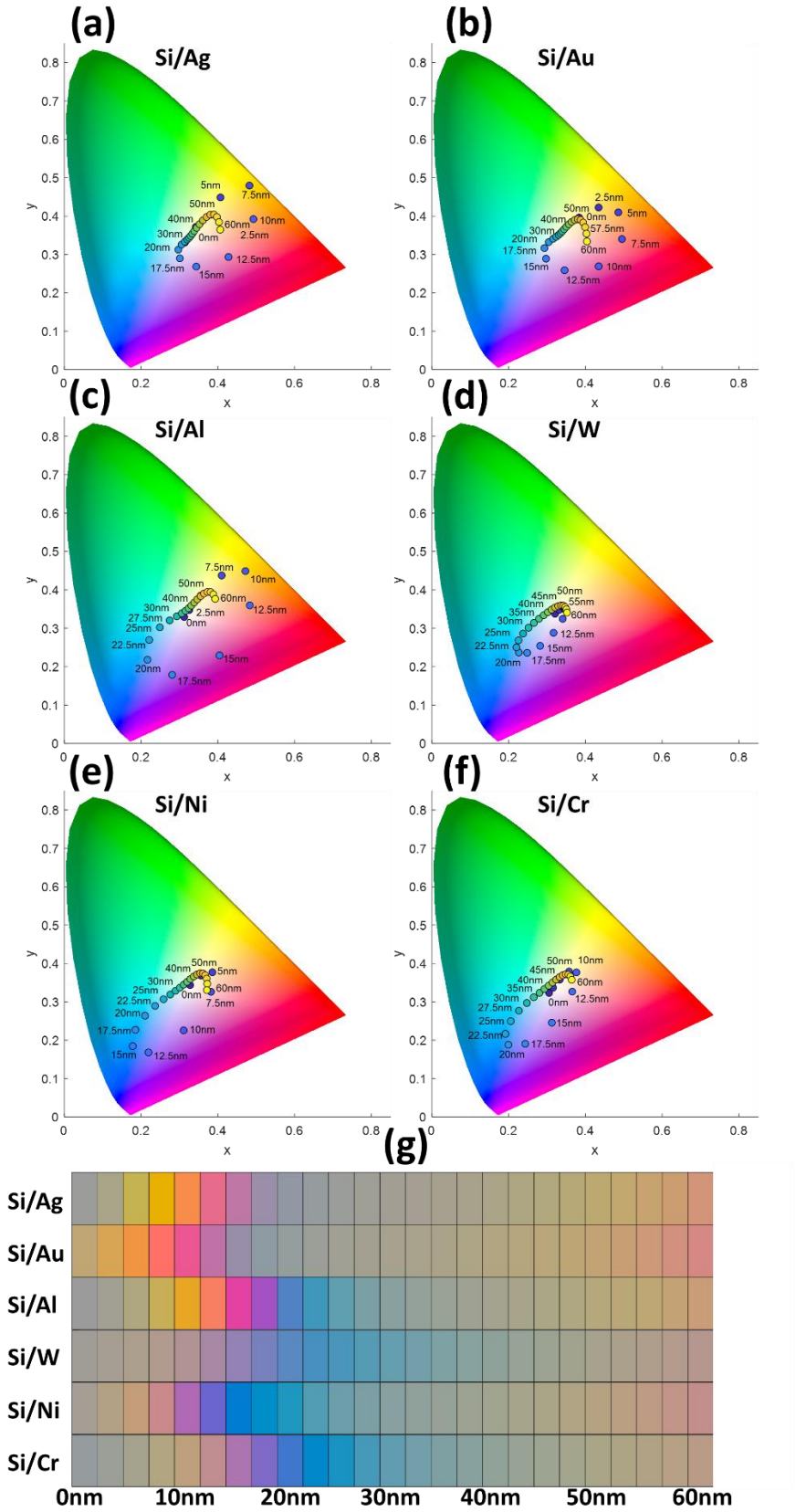


Figure 4.22. Simulated colour gamut of Si on different backing metals. (a) Ag, (b) Au, (c) Al, (d) W, (e) Ni, and (f) Cr. (g) Like with the TMDs a lossy metal backings like Cr and Ni show less vibrant colours. Nobel metals like Ag and Au shows vibrant yellows, purples, and red/orange as well.

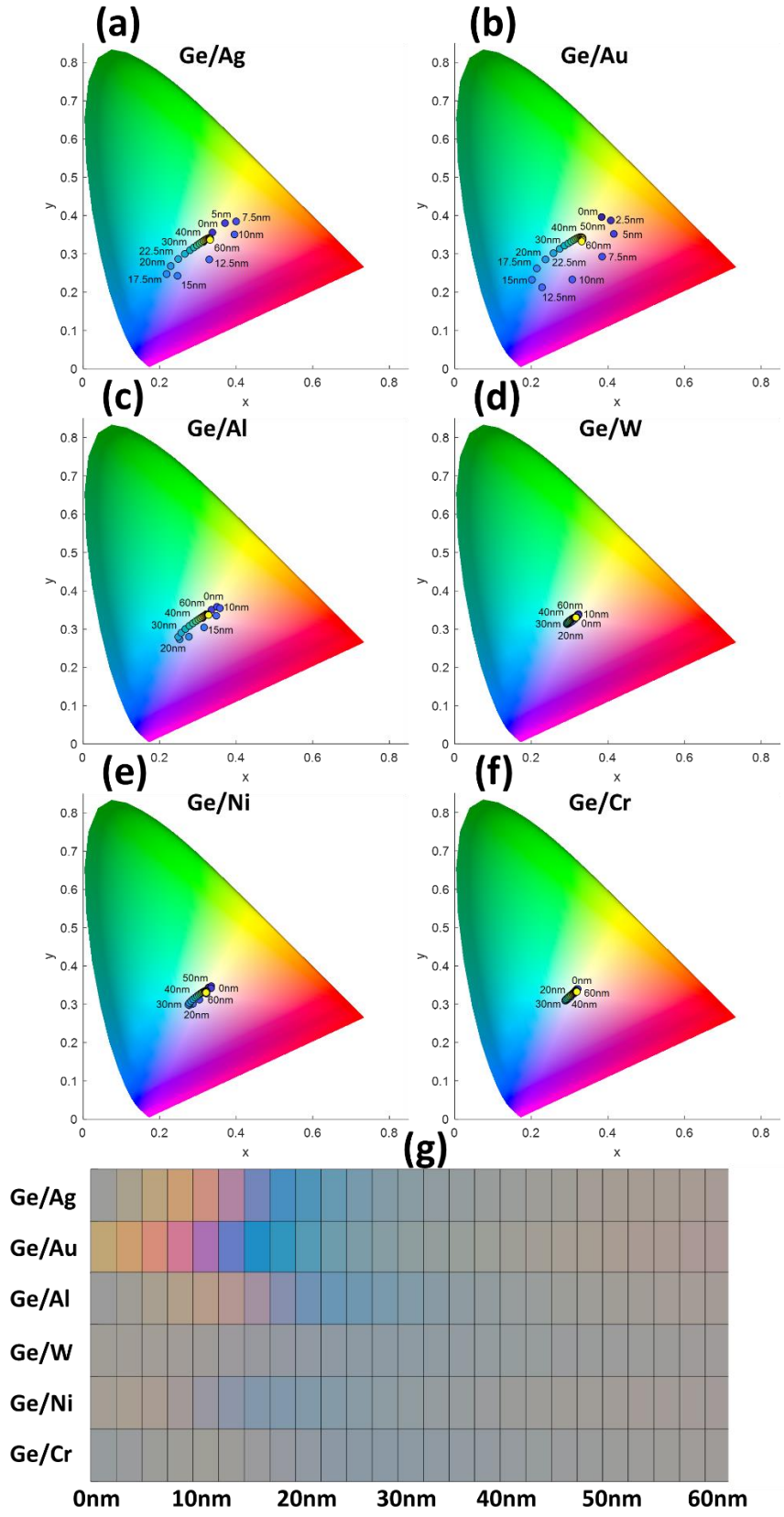


Figure 4.23. Simulated colour gamut of Ge on different backing metals. (a) Ag, (b) Au, (c) Al, (d) W, (e) Ni, and (f) Cr. (g) Almost all backing metals show dull colours except Au which is still markedly visually inferior to many of the Si/Metal colouration variation. Most samples are a dull grey in appearance.

It is clear from these simulated thickness sweep colourimetry results that the TAC MoS_2 and WS_2 sample can display vibrant passive colouration in the ultrathin film regime like that seen for Si or Ge on opaque metal backings in the literature review, section 4.2 . Indeed, the TMDs performed better than the latter two in this regard, especially compared to the colouration response of Ge. The strong colouration of Si was limited to the thin films between 5 and 20 nm while the TMDs showed vivid hues up to the 40 nm thickness mark where blue was the dominant colour generated. This wider thickness range for colouration can be attributed to the larger refractive index of Si and Ge compared to MoS_2 and WS_2 in the visible regime. Figure 4.24 below displays imagery of the structural colour produced by different TMDs of various thicknesses, backed by Au.

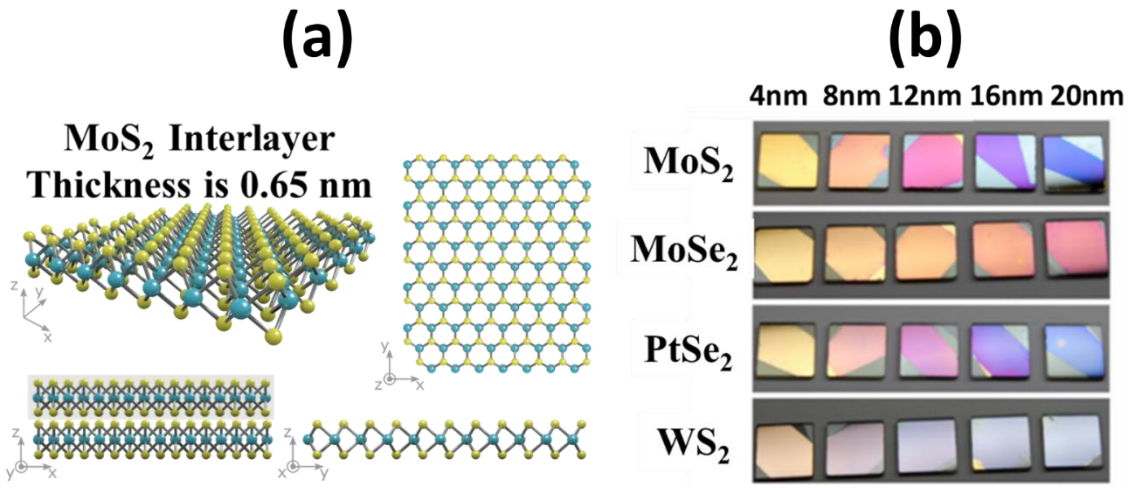


Figure 4.24. (a) The crystal structure of TMDs like MoS_2. Transition metals coatings are sulphurised to form a dichalcogenide with sulphur atoms on either side of the metal atoms, expanding the initial precursor films. Adjacent layers feel weak van der Waals force interactions [68]. *(b) Photographic imagery of some of the TMDs that were created with the TAC process on an Au backing. The vivid colours seen for MoS_2 match well with the chromaticity diagram Fig.4.20(b). The colouration of WS_2 is much duller than predicted though the change in colour from yellow/orange to blue with increasing thickness is still noticeable.*

4.4.2 Strong Absorption of Lossy Zeroth Mode Resonators

Strong colouration on reflection is generated in ultrathin absorber-metal stacks if the zeroth-order FP mode absorbs light at certain wavelengths while others are reflected back. Furthermore, the zeroth mode absorption band must not be completely flat wr.t wavelength as this would produce a colourless sample. To prove that there is a link between this forbidden band and strong enhanced absorption in the stack assembly, the phase delay and reflectivity surface maps displayed below are created to demonstrate that both phenomena overlap exactly in the spectral and thickness domain. Focusing in on MoS_2, to describe the

general TMD response, the zeroth order FP mode can be seen as a dark blue band in the phase delay space occupying the ultrathin regime below 50 nm for all the different kinds of metal backings. In Fig.4.25 MoS_2 on Ag, Au, and Al are focused on to highlight their increased spectral absorption selectivity compared to MoS_2 on Cr, W, and Ni in Fig.4.26.

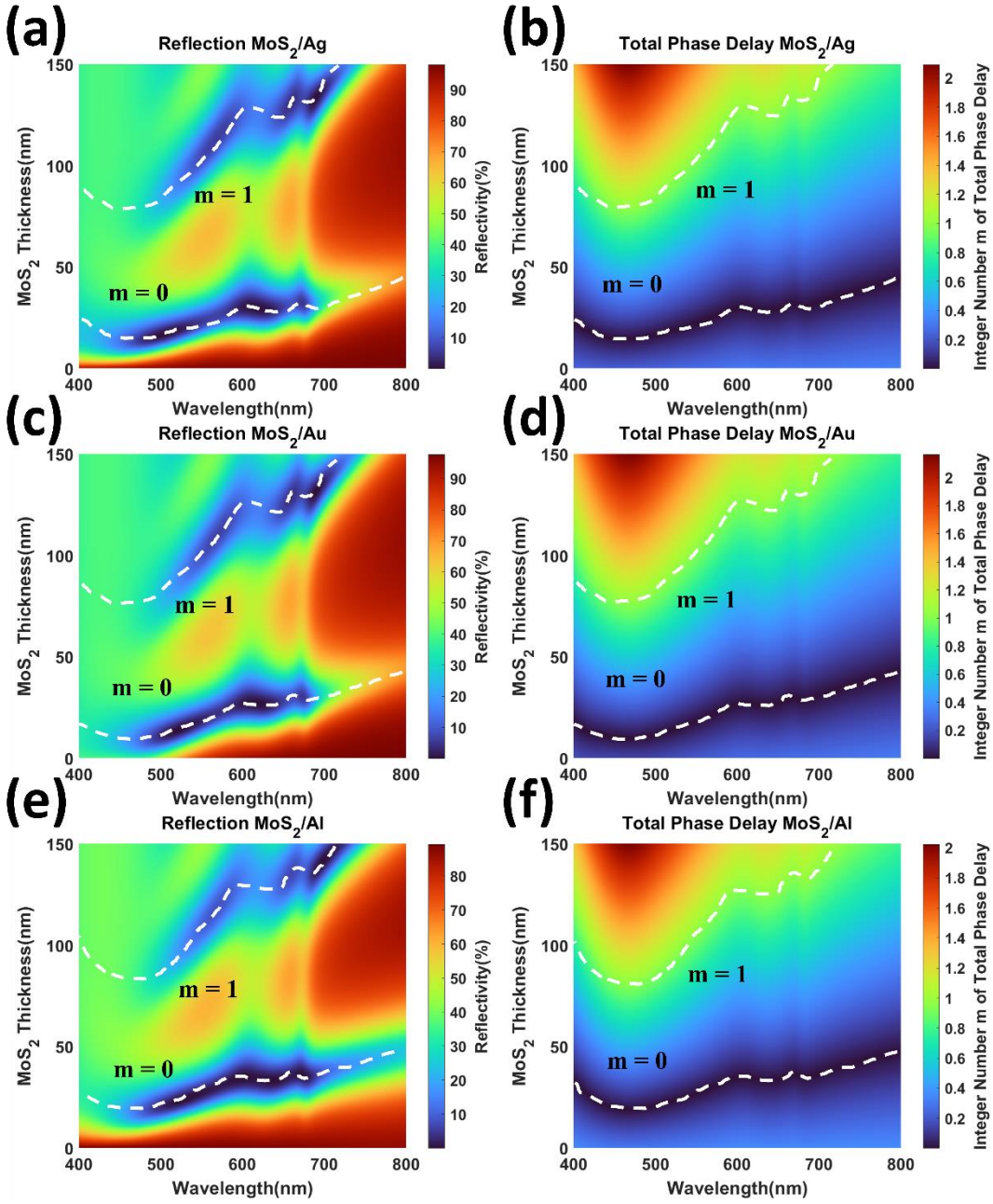


Figure 4.25. Simulated MoS_2 thickness vs wavelength surface maps showing total stack reflectivity and phase delay (a)-(b) Ag, (c)-(d) Au, and (e)-(f) Al. Dark blue bands highlighted with white dashed lines are visible in the reflectivity and the phase delay surface maps, indicating that these strong absorption regions are zeroth-order FP mode bands due to their spectral overlap. The flattest band is the zeroth order mode and higher bands in thicker MoS_2 correspond to higher integer number resonance states m = 1, 2, 3, etc...

The zeroth FP band is shown to be spectrally flatter compared to the steeper higher order FP modes of $m = 1$ and $m = 2$ which are closer to a 45˚ angle on the reflection intensity surface maps. For an ideal broadband near-perfect black absorber this minima band would be completely flat in the spectral domain (broadband near-unity absorption at one ultrathin absorber thickness). A concept that will be looked at in more detail in chapter 6.

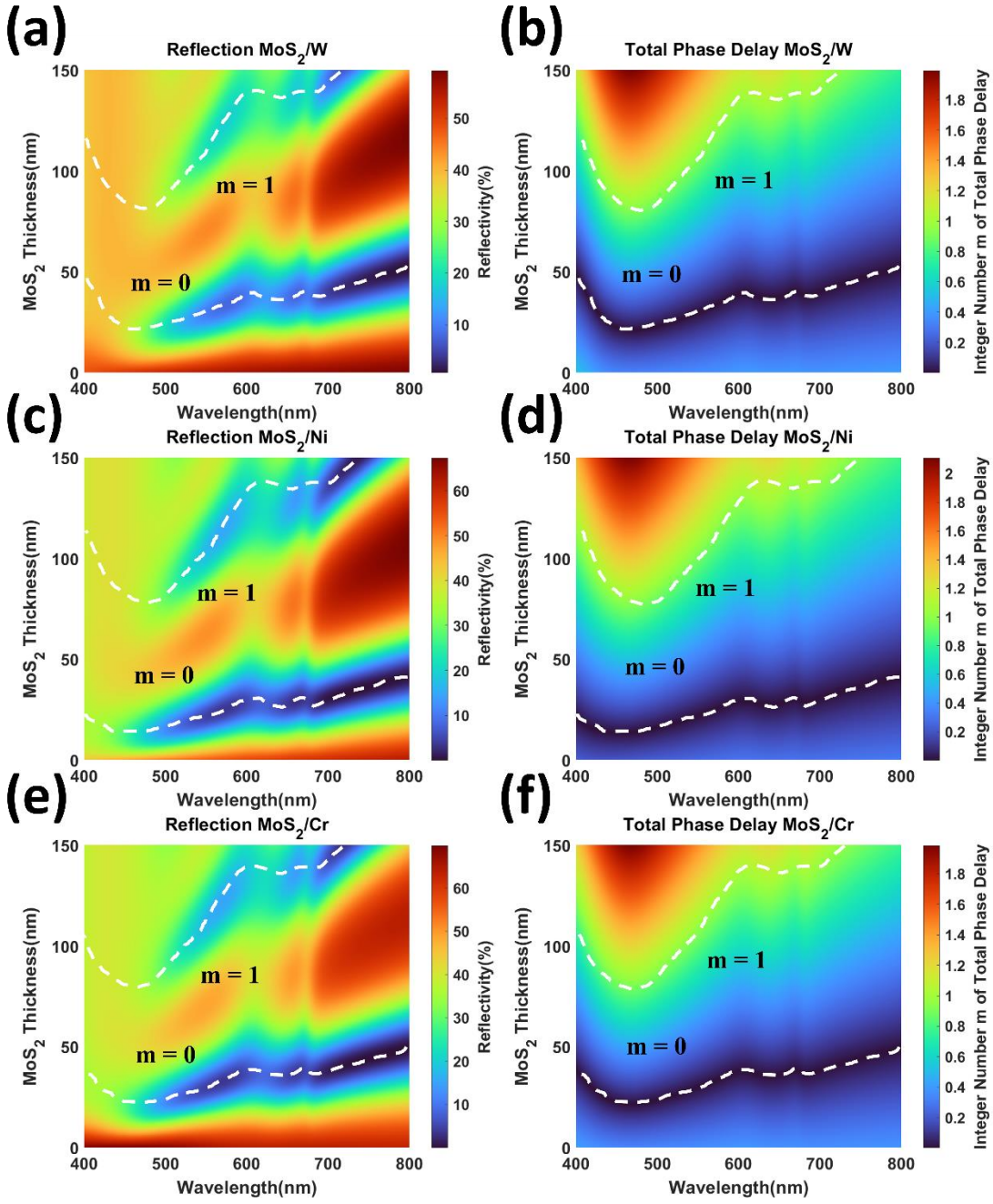


Figure 4.26. Simulated MoS_2 thickness vs wavelength surface maps showing total stack reflectivity and phase delay (a)-(b) W, (c)-(d) Ni, and (e)-(f) Cr. Using the lossy metal backing the absorption region in the zeroth mode band has become broader and more efficient in the red. As a result, the colouration capabilities are inferior to the Ag, Au, and Al backed samples.

These zeroth FP mode dark bands generally correspond to where the global minimum of stack reflectivity occurs indicating the materialization of strong optical field destructive interference in these bands. The strong absorption and zero phase delay regions are not perfectly correlated across the entire spectrum however, a fact which can also be considered a blessing in disguise for producing purer colours at certain wavelengths, like deeper blue or orange/red; wavelengths which are not affected by the light trapping effects of the zeroth mode as much when using backing metals like Ag, Au, and Al. This of course comes with the caveat that their ability to generate vibrant greens hues is diminished; an issue that manifests as the appearance of an elliptical colour gamut on the chromaticity diagrams in Fig.4.20-4.23. Ideally the gamut would reach out to all the corners of the CIE diagram or at the very least be more circular in shape (wider gamut). This ellipticity can be mitigated to some degree with the introduction of a transparent capping layer on top, as will be shown later for Ge/metal samples.

As seen in Fig.4.26 Ni, W, and Ti backed MoS_2 absorbs across more of the visible spectrum compared to when it is backed with Ag, Au, and Al. This is because the attenuation of red and green frequencies is stronger when backing the top absorber with a lossy metal. As explained on p.181, this is attributable to the approximate equivalence of the metal and dielectric refractive index $n_3 \approx n_2$, a condition which maximises overall stack absorption. The loss of this equivalence decreases attenuation of light at and below 450 nm. This is the predominant reason as to why blue hues are observed to be preferentially generated by lossy metal backed samples like Si/Cr in Fig.4.22(f) and MoS2/Cr in Fig.4.20(f).

More data below displays reflectivity and phase delay surface map results with Si and Ge for the same backing metals as with TMD stacks. The results seen with Si validate its colouration response in Fig.4.22, on p. 208. Si is shown to take on a large variety of hues ranging from blue to orange across a narrow thickness range of 10-20 nm. Due to the very high refractive index of Si, extremely thin solutions exist for strong absorption beneath 10 nm as seen in Fig.4.27(a) for an Ag backed stack in the blue part of the visible spectrum. The larger the real index n is the greater the optical density and therefore path length of light as it propagates through it (see eq.2.48 on p.91). Higer index dielectrics can act like much thicker lower index dielectrics (the zeroth mode band solution has much smaller thickness for high index Si compared to other lower index lossy materials like NiO that will be looked at in detail in chapter 5).

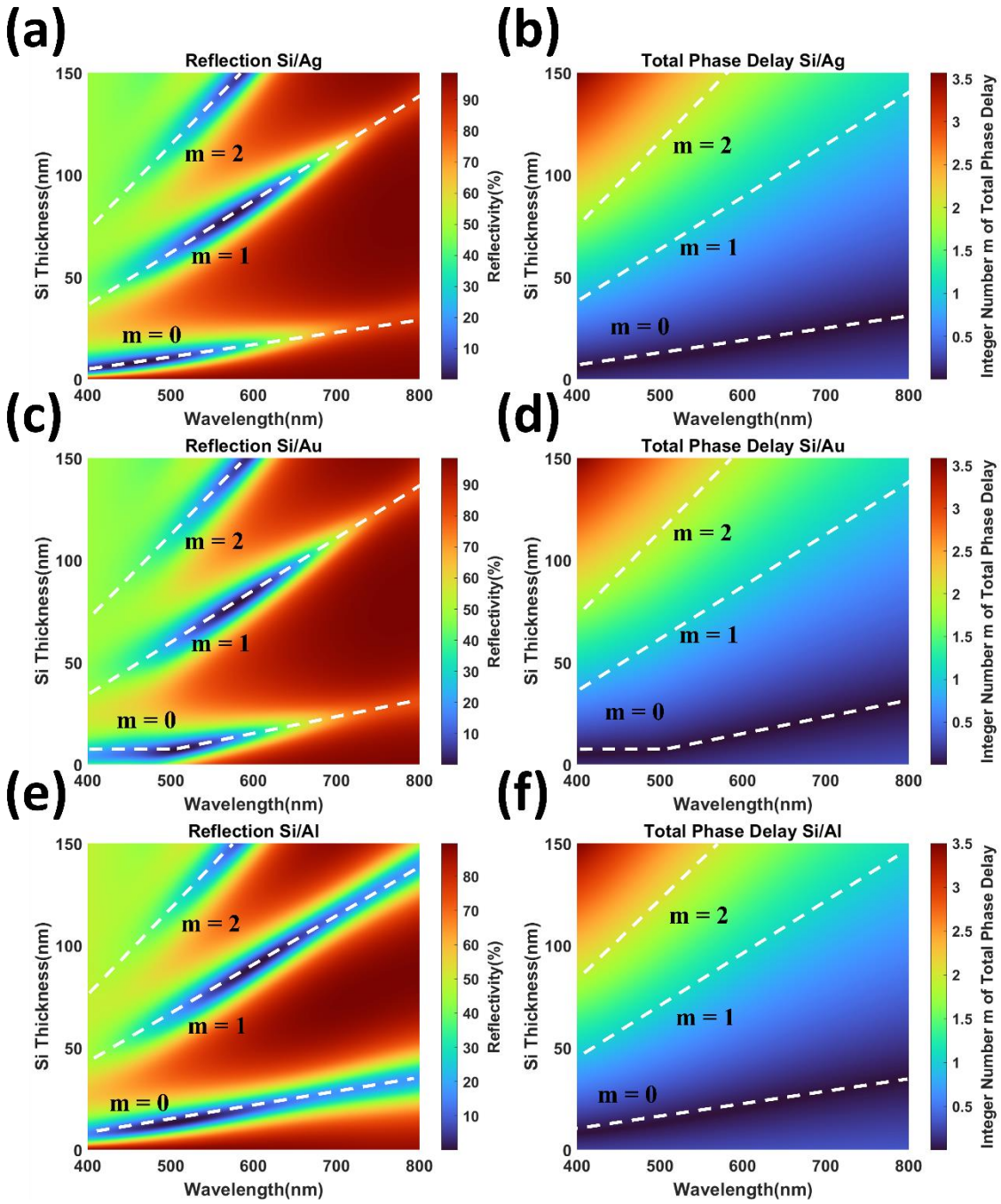


Figure 4.27. Simulated Si thickness vs wavelength surface maps showing total stack reflectivity and phase delay (a)-(b) Ag, (c)-(d) Au, and (e)-(f) Al. The high index of Si facilitates extremely subwavelength solutions to strong absorption in the blue spectral region for all metals shown. Furthermore, the reflection minima band is maintained across the visible for Al backed Si allowing for a greater variation in colour with thickness compared to Au or Ag backed samples. Like with MoS_2 vivid green hues are not a possibility.

The absorption bands widen across the visible considerably when pairing Si with the lossy back metals Ni and Cr (Fig.4.28 below). The increase in the breadth of the band washes out the colours produced, leaving only a slight blue hue, commensurate with the chromaticity results obtained with MoS_2 and Si (blue colouration in Fig.4.20(g) and Fig.4.22(g)).

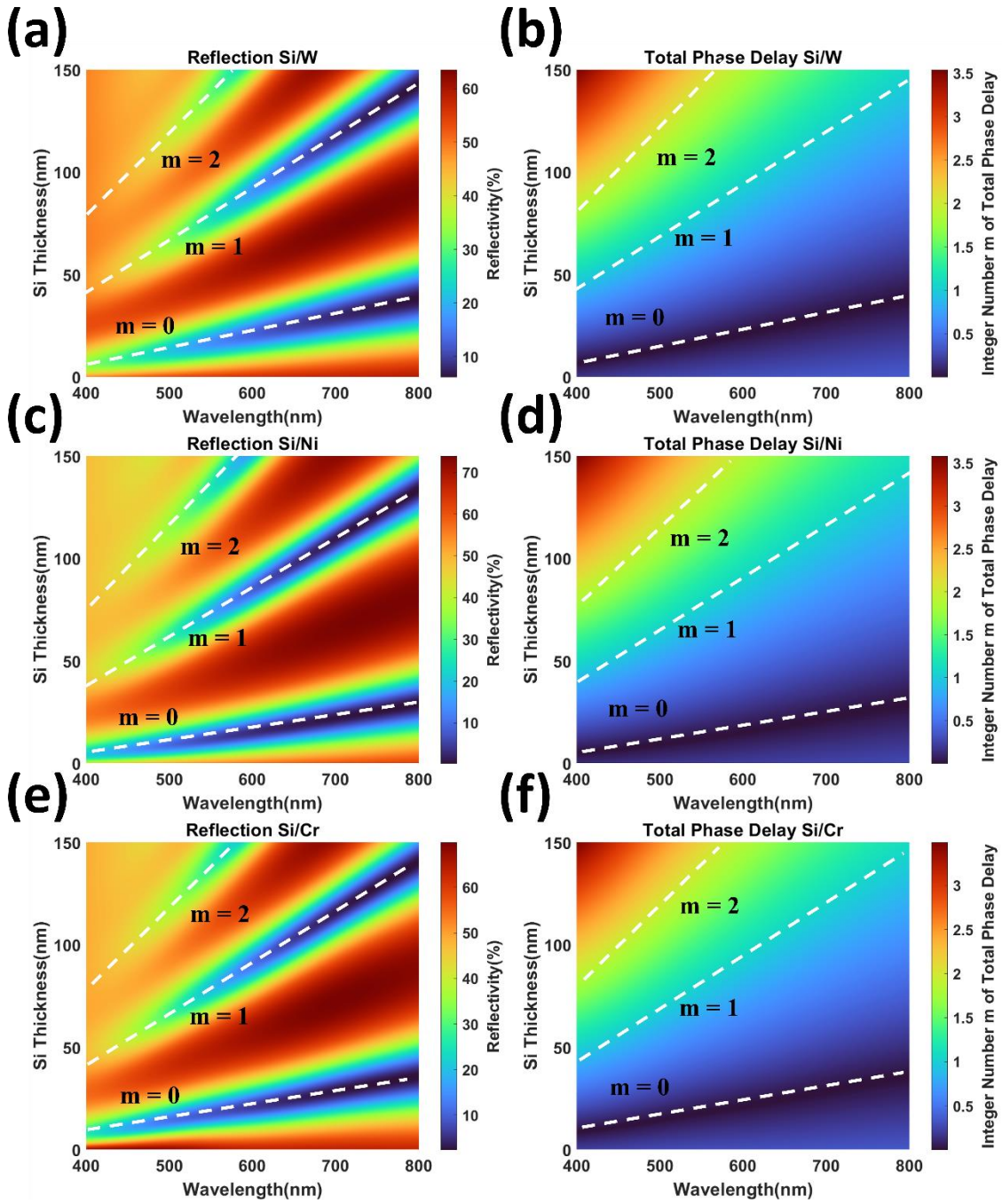


Figure 4.28. Simulated Si thickness vs wavelength surface reflectivity maps showing total stack reflectivity and phase delay (a)-(b) W, (c)-(d) Ni, and (e)-(f) Cr. All the reflection minima bands have been broadened with the addition of the lossy metal backings.

One could also try to target the higher order modes for colouration, but this would require the thin film to be 4-5 times thicker, displacing the lossy dielectric layer of the FP resonator from the ultrathin film regime. This ascension into a bulkier domain would come at the additional cost of a reduced omnidirectional and polarisation independent optical response as will be shown shortly. The colouration range of Ge is lustreless in comparison to the other

materials looked at. The colouration is negatively affected by the inferior contrast between the zeroth mode bands and the off-resonant reflecting regions in between the different FP modes. See Fig.4.29 and Fig.4.30.

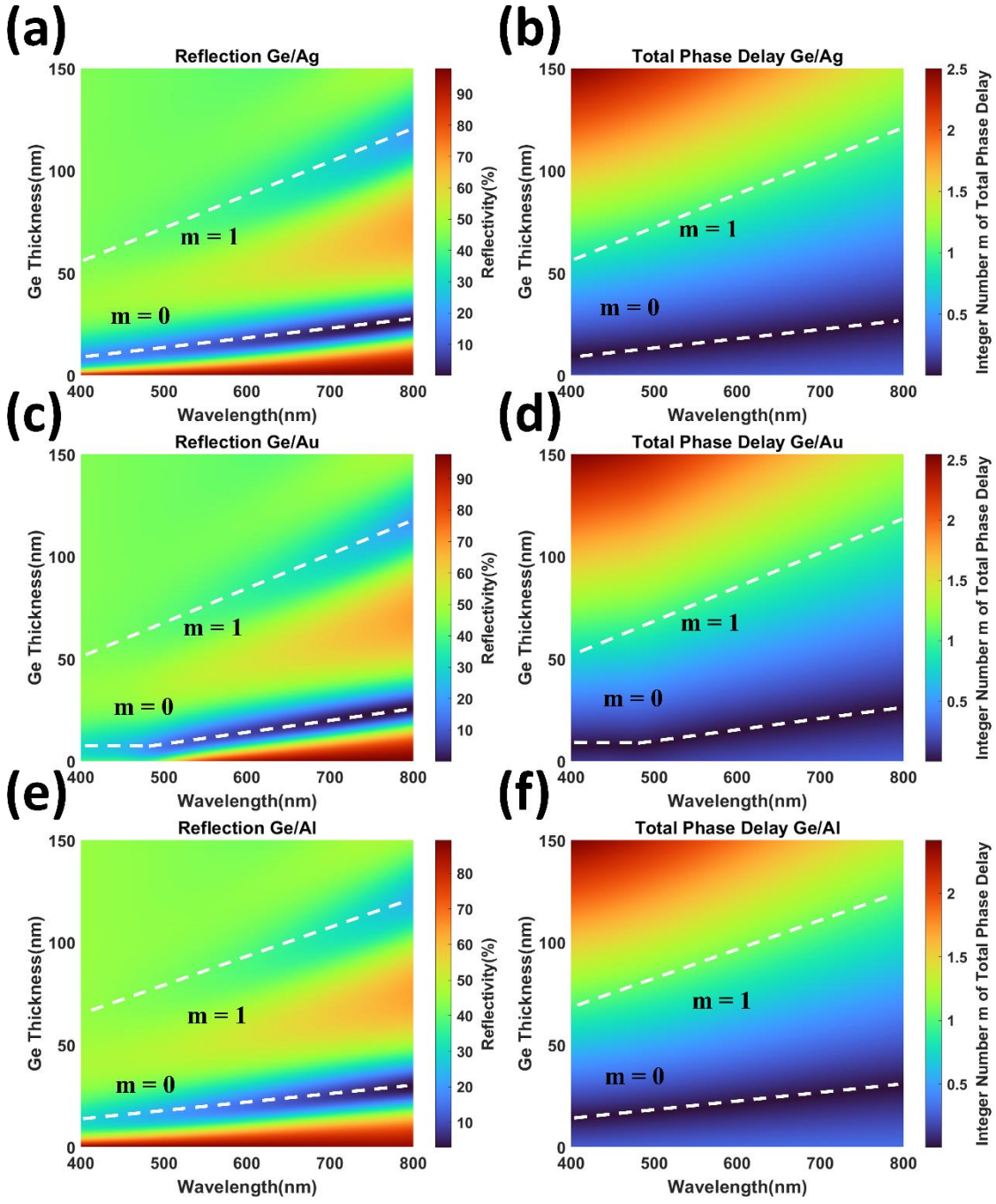


Figure 4.29. Simulated Ge thickness vs wavelength surface maps showing total stack reflectivity and phase delay (a)-(b) Ag, (c)-(d) Au, and (e)-(f) Al. The contrast between the zeroth order band absorption region and its surroundings is lower, creating a flatter spectral response with poorer colour gamut. This situation extends to the higher modes, the influence of which is non-existent in the R intensity surface plots, most likely only manifesting as increased absorption at a higher NIR wavelength beyond the range of the ellipsometer and regime of interest.

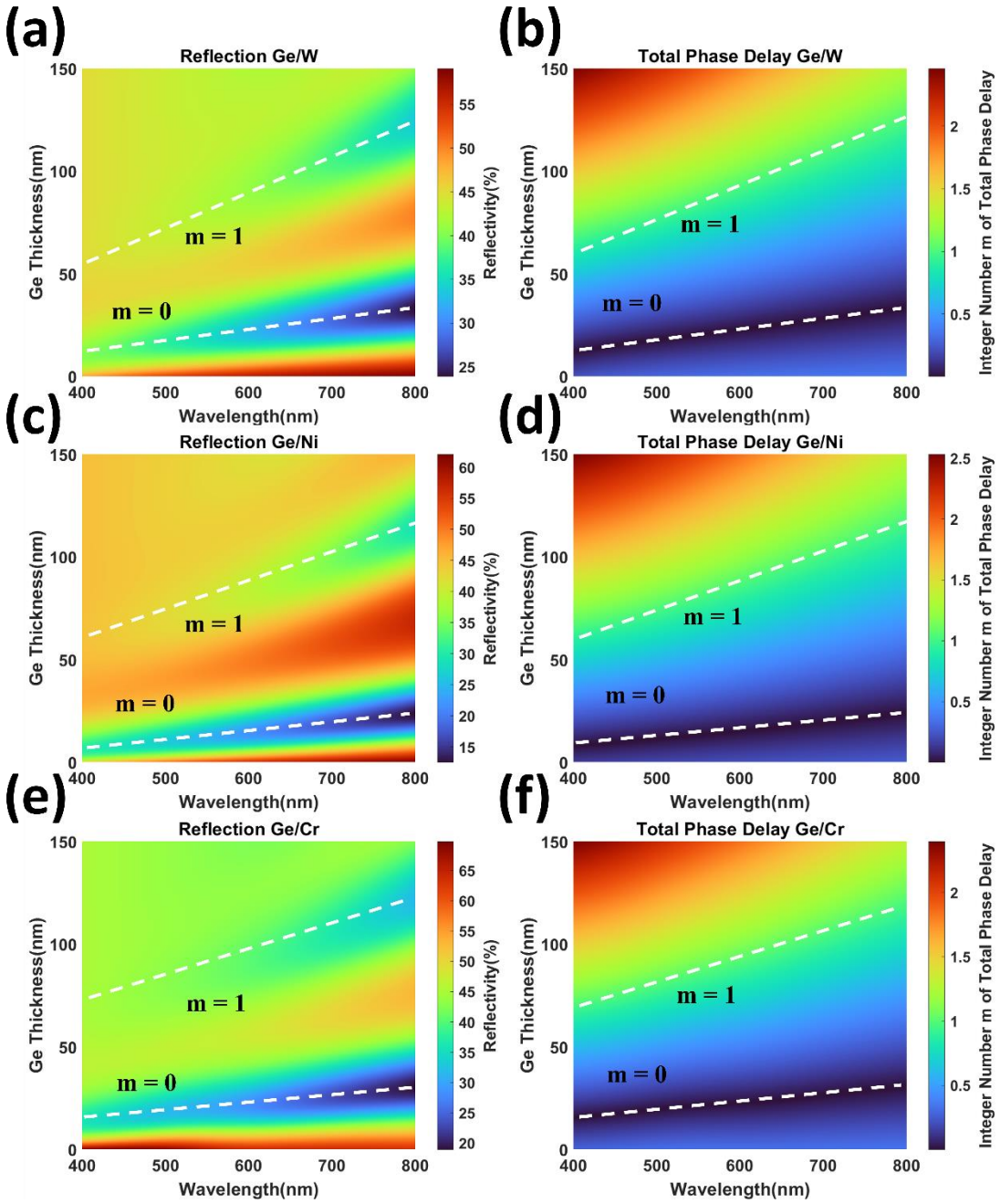


Figure 4.30. Simulated Ge thickness vs wavelength surface maps showing total stack reflectivity and phase delay (a)-(b) W, (c)-(d) Ni, and (e)-(f) Cr. The use of the lossy metals does little to improve the absorption characteristics. The only major difference is the breath of the absorption in the zeroth mode in the red part of the spectrum.

The only somewhat bright coloured hues produced by Ge are the gold backed samples with dull drab pinks and blues in the 5 – 15 nm thickness range. Thus, based on the results presented of the materials deposited/created with sputtering and TAC, TMDs and Si are more suitable for use in thin film structural colour generation due to strong spectrally selective absorption in the ultrathin film regime when using low index metal backings like

Ag and Au. Moreover, the strong absorption of the zeroth mode is extended across more of the visible (especially in the red region) when paired with lossy metal back reflectors like W, Ti, and Ni. This broader bandwidth absorption is to the detriment of colouration with only dull bluer-violet hues being producible at best.

4.4.3 Layer Resolved Absorption of Lossy Zeroth Mode Resonators

The efficiency at which the lossy dielectric and metal film attenuates light is found by calculating the local layer resolved absorption based on the change in the Poynting vector method detailed previously in chapter 2 p.95. Results comparing Si and MoS_2 on Au and Ni are shown in Fig.4.31 and Fig.4.32 respectively.

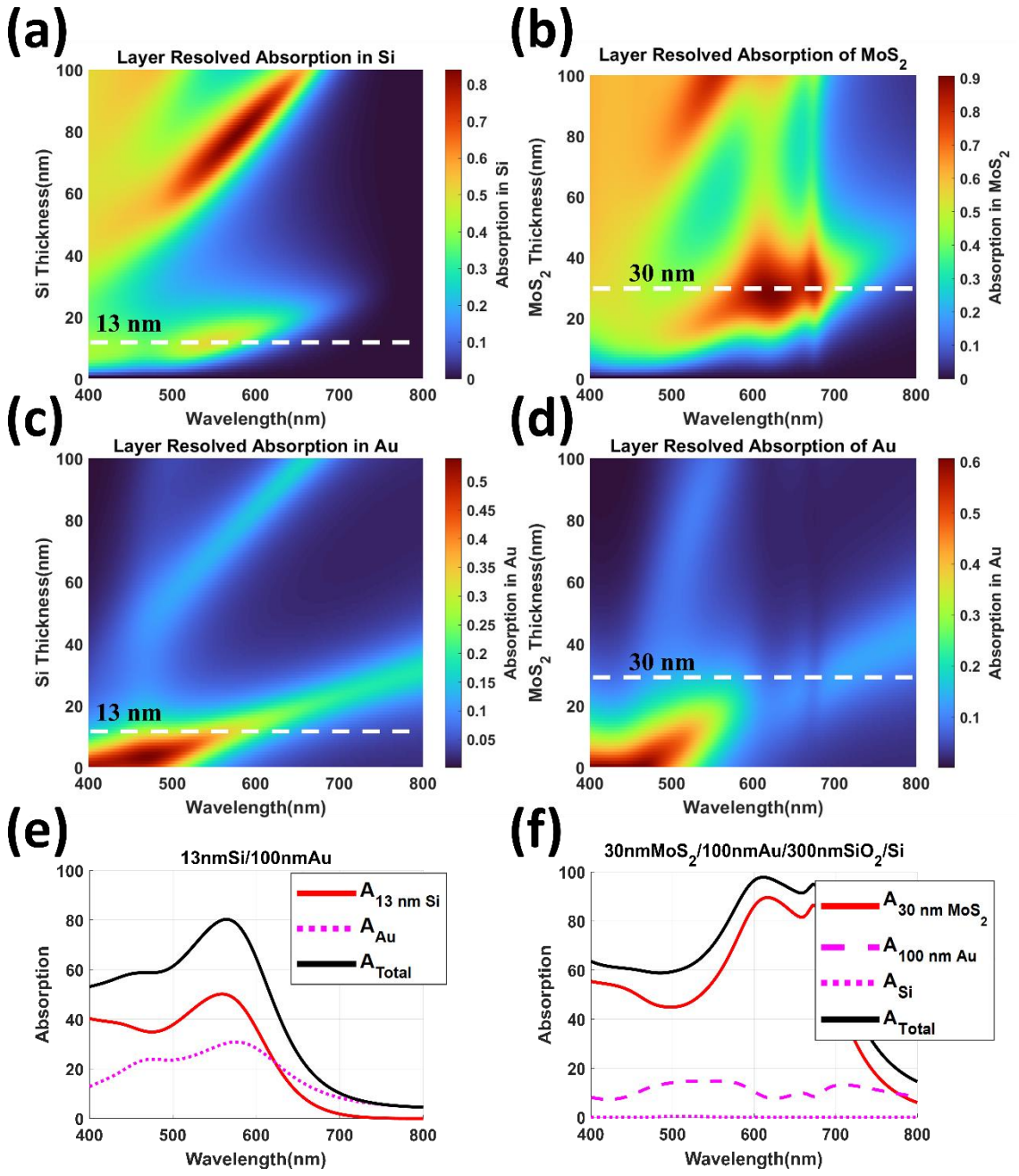


Figure 4.31. (a), (c) The layer resolved absorption in Si and Au of the Si/Au stack. (b), (d) The layer resolved absorption in the MoS_2 and Au of the MoS_2/Au stack. (e), (f) The line profile of the region where layer resolved absorption is maximised for Si and MoS_2 in the zeroth FP mode band. In the Si/Au zeroth mode both materials contribute relatively equally to the light matter interaction. The MoS_2 layer dominates its stack absorption characteristics, dwarfing the contributions Au makes to the reflection minima in the zeroth band.

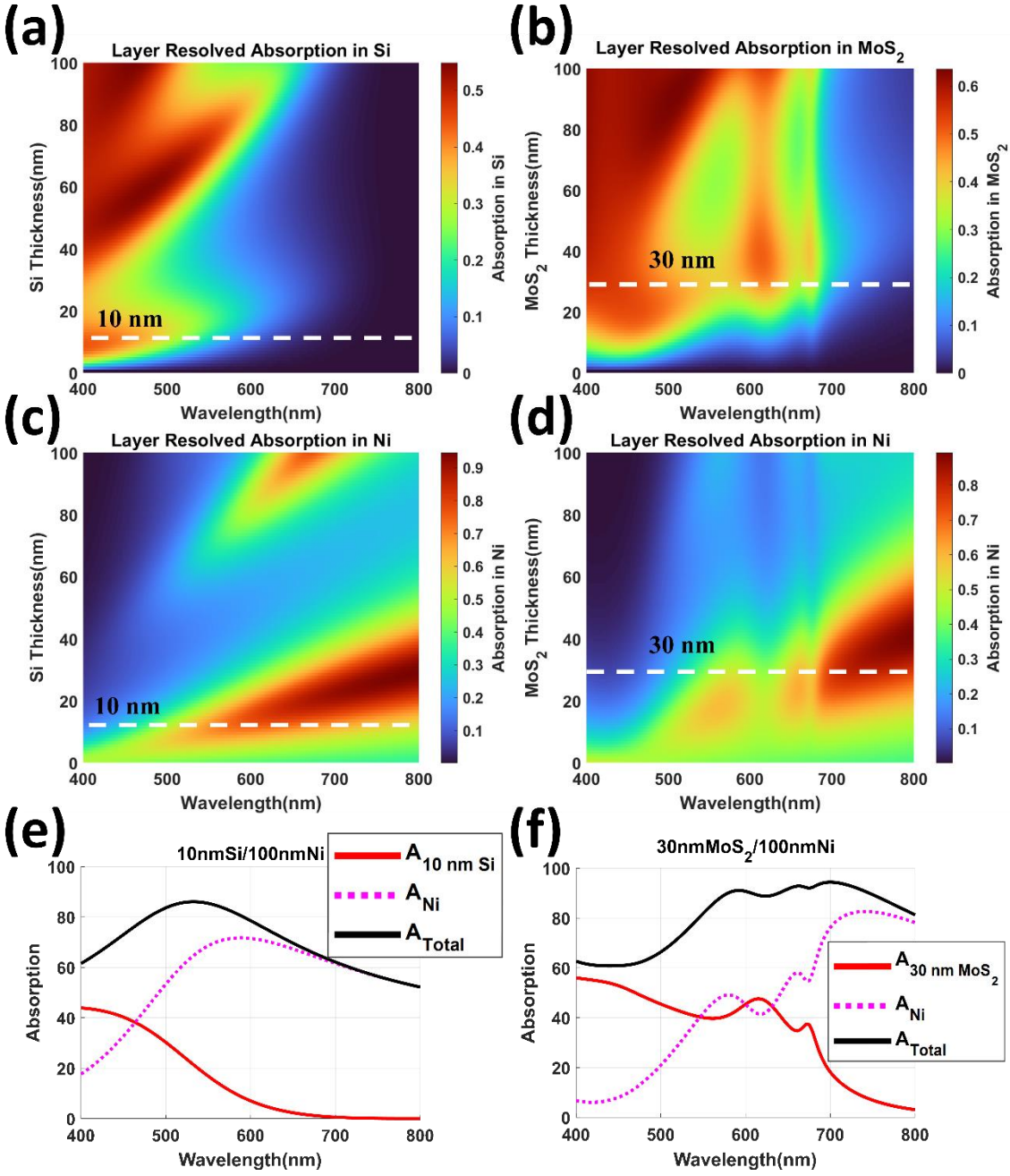


Figure 4.32. (a), (c) The layer resolved absorption in Si and Ni of the Si/Ni stack. (b), (d) The layer resolved absorption in the MoS_2 and Ni of the MoS_2/Ni stack. (e), (f) The line profile of the region where layer resolved absorption is maximised for Si and MoS_2 in the zeroth FP mode band. In the Si/Ni zeroth mode both materials contribute relatively equally to the light-matter interaction in the blue while the Ni dominates in the green and red wavelengths. The MoS_2 also follows the same trend though its contribution to the attenuation of light is equal in the green and yellow wavelengths around the excitons. Though the overall absorption across the visible is larger than for Au backing, the strong light-matter interaction is more evenly spread between the lossy dielectric and lossy metal.

It is clear from Fig.4.31 that compared to Si, the MoS_2 more effectively traps and subsequently attenuates the light within its zeroth-order FP mode band. Thus, in the TMD stack, the MoS_2 is shown to be responsible for the origin of the strong colouration produced.

This is doubly so when considering the Au absorption response is also flat across the visible, providing no dispersion to induce colouration. Figure 4.32 above displays results for Si and MoS_2 on Ni backing. Unlike with the Au backed sample, the attenuation of light is spread more evenly between the Ni back metal and top lossy dielectric layer. The Si absorbs the most amount of light at 400 nm in its zeroth mode band, at a thickness of 10 nm, before quickly dropping off as the Ni extinguishes the brunt of the EM wave at redder wavelengths. In comparison to this, MoS_2 maintains a large amount of absorption within its zeroth mode band from the blue to green wavelengths, after which Ni dominates the attenuation response. The overall absorption for Ni backing is broader and higher than Au backed samples, at the cost of increased absorption in the metal substrate. For PV purposes this is obviously not ideal, as energy lost to the Ni would be wasted as heat that diminishes the quantum efficiency and reduces device lifespan [31], [30]. There is some merit to be had for its use in solar thermal applications though where solar energy is used to directly to heat a system without conversion loses (light to electricity to heat) that a PV powered heater would have to contend with [69].

4.4.4 Angle & Polarisation Response of Lossy Zeroth Mode Resonators

As discussed on p.185-186, lossy dielectric zeroth-order FP resonators also have an omnidirectional and polarisation independent response as the results in Fig.4.33 reveal for MoS_2, Ge, and Si on Au and Ni backing.

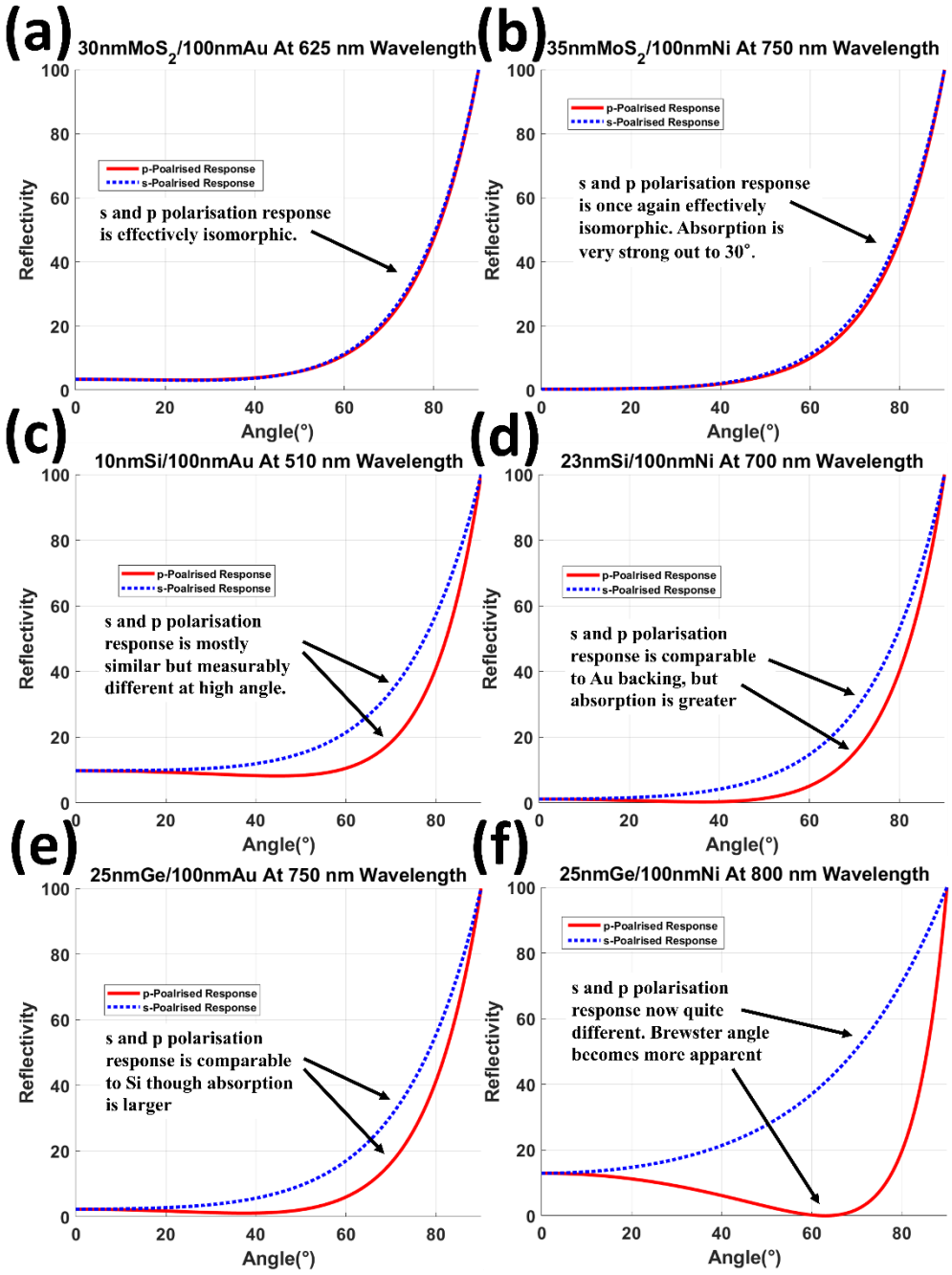


Figure 4.33. Angle and polarisation resolved data within the maximum absorption wavelength regions of the zeroth FP mode bands (a)-(b) MoS_2 on Au and Ni, (c)-(d) Si on Au and Ni, and (e)-(f) Ge on Au and Ni. The omnidirectional and polarisation independent response is superior in MoS_2 as compared with Si or the much more reflective Ge.

Strong absorption regions in the zeroth FP mode band are targeted to monitor the effect of changing AOI on the resultant angle resolved spectra. In most cases the reflectivity intensity remains quite flat out to 45°. MoS_2 in particular has an exceptional polarisation independent response for both Au and Ni backing, making it unique compared to Si and Ge which show more variation in this regard. Ge specifically has significant iridescence when backed with

the lossy metal Ni, as the Brewster angle phenomena can clearly be seen with similar character to the reflection at an air-glass interface [63]. Si also performs similarly with Au and Ni with the only marked difference being the overall total absorption. These results affirm that MoS_2 has a superior omnidirectional and polarisation independent optical response as compared to the conventional high index lossy dielectric electro-absorbing materials, like Si and Ge, in in the zeroth order FP bi-layer stack configuration. Thus, it can be said that for structural colouration and solar absorption applications, where iridescence and polarisation dependent responses are most often undesirable, MoS_2 outperforms Si and Ge. Further study could investigate whether this fact holds true on flexible substrates as well (though given the heat requirements of TAC, TMDs would have to be deposited with other techniques like CVD, where the substrate will not deform/melt during sample synthesis).

4.4.5 Enhanced Colouration of Oxide Capped Lossy Zeroth Mode Resonators

To improve upon the absorption and structural colouration gamut of the zeroth mode the idea of incorporating an insulating transparent dielectric capping layer to the stack assembly was also investigated. The inclusion of this third transparent capping layer to the zeroth order FP stack enhances either broadband strong absorption or colouration depending on the material used as well as its thickness. See Fig.4.34 below shows absorption enhancement.

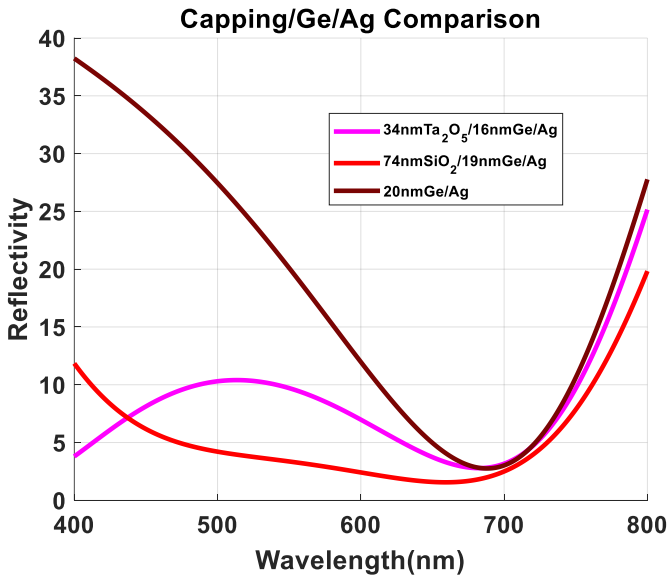


Figure 4.34. The Ge/Ag stack was shown to be quite reflective in the blue region of the zeroth mode band. The addition of a low and high index AR coatings for comparison showcases the enhancement in absorption when capping layers are deployed. The lower index 74 nm SiO_2 coating performs better due to the ideal index matching at quarter wavelength condition being met in the blue around 400 nm. 34 nm Ta_2O_5 has a similar but more dispersive response.

When Ge is paired with very thin low index silica or high index Ta_2O_5, the AR condition broadens the absorption band of the zeroth mode. The stack with the ultrathin Ta_2O_5 can attenuate similarly to a stack with a silica capping layer that is twice as thick. This demonstrates that thinner optimum absorption solutions are possible with higher index dielectrics due to the greater optical density. Similarly, this is why Si and Ge have more deeply subwavelength zeroth order mode solutions as seen in Fig.4.27 and Fig.4.29. When the top transparent Ta_2O_5 is made thicker into the region of 100 nm and above, The AR behaviour gives way to an enhancement of the colouration gamut, see Fig.4.35 below. The improvement is most noticeable with Ge which now displays vibrant violet, blues and oranges.

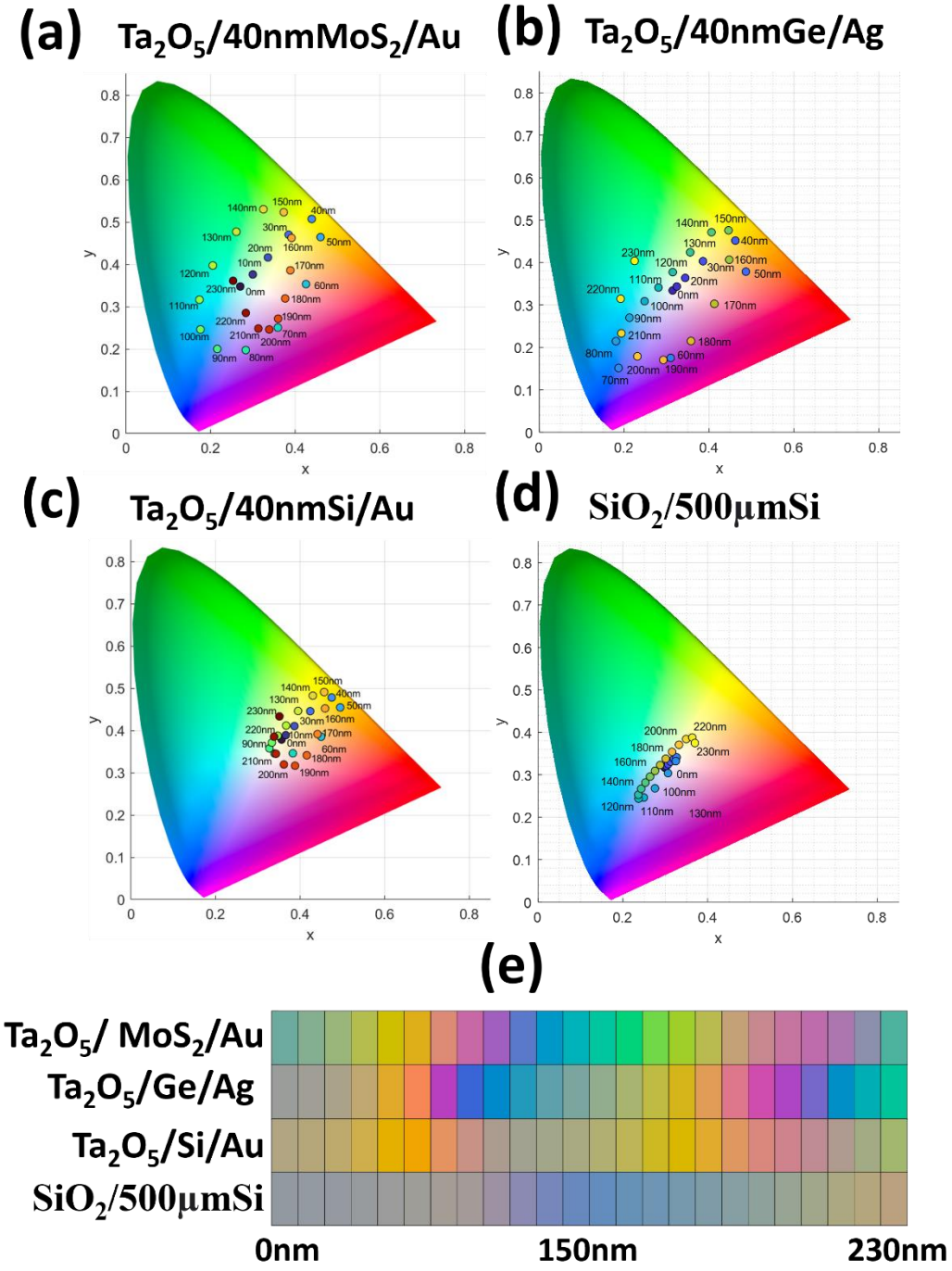


Figure 4.35. Chromaticity diagram results for variable Ta_2O_5 thickness using lossy dielectric (a) MoS_2 (b) Ge, and (c) Si as the ultrathin absorber layer. (d) The narrow colour gamut of SiO_2 on Si is listed for comparison. (e) MoS_2 and Ge display a wide variety of vibrant hues ranging from orange, to purple, to green, and to blue.

Both MoS_2 and Ge have a significant increase in the range of colours they produce while still maintaining the subwavelength dimensions of the overall stack structure (See Fig.4.20 and Fig.4.23 for comparison without the capping layer). Unlike the bi-layer configuration, greener hues are now generated and the ellipticity of the gamut has decreased to a certain

extent. These results are contrasted against a silica on Si planar film setup in Fig.4.35(d) which is much thicker than the ultra-compact zeroth order FP devices detailed so far. The colouration produced by the silica/Si is narrow and drab underscoring how weak the light-matter interaction is in this bulkier construct relative to the ultrathin lossy film stacks.

4.5 Summary

In summary, at the beginning of the chapter the necessity of using optical resonance effects like FP interference, when working with thin films, to modify the optical response of a multilayer stack structure toward a useful result like vivid structural colouration and/or strong absorption was highlighted. Regarding FP interference, light at resonance will become trapped in thin film structures, drastically increasing the light-matter interaction. In so doing very thin layers of material can have a huge effect on the overall reflectivity, transmission, and absorption profile depending on whether the stack structure uses an opaque reflective backing or a semi-transparent backing. As an example, the use of FP resonance was shown to greatly increase the contrast between the thickness of different 2D graphene films on SiO_2/Si substrate, as well as between graphene and its surroundings. This made it possible to gauge the layer number of the graphene films quickly, accurately, and non-destructively.

The enhancement of the light-matter interaction using FP resonance led to the discussion of the existence of the non-trivial zeroth order FP mode in the ultrathin regime. This FP mode solution is only accessible when using an asymmetric stack configuration with high index lossy materials such as MoS_2, WS_2, Si, and Ge. The mathematics underpinning the explanation of this normally forbidden FP resonance mode is nearly identical to the physical description of AR coatings. In both cases a phase delay condition and index matching condition must be met simultaneously for resonant behaviour to manifest strongly. While the ideal thickness and index solutions to AR coatings are trivial in nature, the zeroth order FP mode solutions for lossy dielectric stacks are deeply subwavelength conferring certain advantageous such as omnidirectionality, polarisation independence, and increased layer specific light trapping within the top lossy dielectric film, due also in part to their high refractive index (greater optical density). In all cases the strong absorption in the zeroth mode band was linked to the zero-phase delay accumulation band in phase space, with the spectral overlap helping to prove their association.

For the purposes of vibrant ATF structural colouration, lossy films backed with more reflective metals like Ag, Au, and Al were preferable for a narrower zeroth order mode absorption band with some level of dispersion across the visible spectrum, widening the colour gamut on the CIE chart in an elliptical fashion. The colouration predicted for MoS_2 matched experimental observation. Furthermore, the Si and Ge on Au simulations, based on SE data, were in line with the results presented in the literature review. TMDs were shown to produce vibrant hues over a wider number of thickness ranges in the ultrathin film regime as compared to Si or Ge. Films backed with lossy metals like Cr, Ni, and W had greater overall absorption due to close match in refractive index between substrate and absorber. However, due to this fact their optical response was also flatter limiting their colouration to drab shades, leaning preferentially blue. Moreover, the attenuation of light in these samples was also more evenly distributed between the metal backing substrate and lossy dielectric films above them, which is not ideal for PV applications. MoS_2 was also revealed to have a superior omnidirectional and polarisation independent response compared to Si and Ge with both a reflective Au backing and a more lossy Ni backing, indicating it to be the more favourable option when designing multilayer stacks for ultracompact colouration or solar absorption applications. For the latter, the bandgap of MoS_2 is also more favourably placed nearer to the peak energy of the Sun's emission spectrum in the green [70] (MoS_2 has an indirect band gap of 1.2 eV while Si has an indirect bandgap of 1.12 eV and Ge has a direct transition at 0.8 eV that dominates over the indirect transition at around 0.6 eV [49], [64]).

The addition of a third high index insulating transparent capping layer like Ta_2O_5 or TiO_2 to the compact zeroth order FP stack structure also aided in widening the colour response, giving greater access to greener hues by mitigating the ellipticity of the colour gamut seen in the chromaticity diagrams. Naturally, a capping layer of this kind would also serve to protect the ultrathin lossy dielectric film underneath which may be susceptible to degradation from reactive species in the atmosphere or physical impact.

4.6 References

[1] H. D. Young and R. A. Freedman, *University Physics with Modern Physics*, 14th ed. Pearson, 2016.

[2] J. Park, S. J. Kim, and M. L. Brongersma, "Condition for unity absorption in an

ultrathin and highly lossy film in a Gires – Tournois interferometer configuration," *Opt. Lett.*, vol. 40, no. 9, pp. 1960–1963, 2015, doi: 10.1364/OL.40.001960.

[3] D. Wang, Z. Liu, H. Wang, M. Li, L. J. Guo, and C. Zhang, "Structural color generation: From layered thin films to optical metasurfaces," *Nanophotonics*, vol. 12, no. 6, pp. 1019–1081, 2023, doi: 10.1515/nanoph-2022-0063.

[4] S. S. Mirshafieyan, H. Guo, and J. Guo, "Zeroth Order Fabry – Perot Resonance Enabled Strong Light Absorption in Ultrathin Silicon Films on Different Metals and Its Application for Color Filters," *IEEE Photonics J.*, vol. 8, no. 5, pp. 1–12, 2016, doi: 10.1109/JPHOT.2016.2609143.

[5] Z. Sun, A. Martinez, and F. Wang, "Optical modulators with 2D layered materials," *Nat. Photonics*, vol. 10, no. 4, pp. 227–238, 2016, doi: 10.1038/nphoton.2016.15.

[6] Y. Yu, Y. Yu, L. Huang, H. Peng, L. Xiong, and L. Cao, "Giant Gating Tunability of Optical Refractive Index in Transition Metal Dichalcogenide Monolayers," *Nano Lett.*, vol. 17, no. 6, pp. 3613–3618, 2017, doi: 10.1021/acs.nanolett.7b00768.

[7] Z. H. Ni *et al.*, "Graphene Thickness Determination Using Reflection and Contrast Spectroscopy," *Nano Lett.*, vol. 7, no. 9, pp. 2758–2763, 2007, doi: 10.1021/nl071254m.

[8] K. Lee, S. Y. Han, Z. Li, H. W. Baac, and H. J. Park, "Flexible High-Color-Purity Structural Color Filters Based on a Higher-Order Optical Resonance Suppression," *Sci. Rep.*, vol. 9, no. 14917, 2019, doi: 10.1038/s41598-019-51165-1.

[9] L. Zheng *et al.*, "High reflectance tunable multi-color electrochromic films based on Fabry–Perot cavity," *Ceram. Int.*, vol. 49, no. 9, pp. 13355–13362, 2023, doi: 10.1016/j.ceramint.2022.12.210.

[10] M. A. Kats and F. Capasso, "Optical absorbers based on strong interference in ultra-thin films," *Laser Photonics Rev.*, vol. 10, no. 5, pp. 735–749, 2016, doi: 10.1002/lpor.201600098.

[11] P. Liu, P. Longo, A. Zaslavsky, and D. Pacifici, "Optical bandgap of single- and

multi-layered amorphous germanium ultra-thin films," *J. Appl. Phys.*, vol. 119, no. 1, pp. 182–184, 2016, doi: 10.1063/1.4939296.

[12] Umran S. Inan, *Engineering Electromagnetics and Waves*, 2nd ed. Pearson, 2015.

[13] A. M. Law, L. O. Jones, and J. M. Walls, "The performance and durability of Anti-reflection coatings for solar module cover glass – a review," *Sol. Energy*, vol. 261, pp. 85–95, 2023, doi: 10.1016/j.solener.2023.06.009.

[14] M. A. Kats, R. Blanchard, P. Genevet, and F. Capasso, "Nanometre optical coatings based on strong interference effects in highly absorbing media," *Nat. Mater.*, vol. 12, no. 1, pp. 20–24, 2012, doi: 10.1038/nmat3443.

[15] P. Y. Amnon Yariv, *Photonics: Optical Electronics in Modern Communications (THE OXFORD SERIES IN ELECTRICAL AND COMPUTER ENGINEERING)*, 6th ed. Oxford University Press Inc, 2006.

[16] A. B. B. Max Born, Emil Wolf, *Principles of Optics: Electromagnetic Theory of Propagation, Interference and Diffraction of Light*, 7th ed. Cambridge University Press, 1999.

[17] J. Park *et al.*, "Omnidirectional Near-Unity Absorption in an Ultrathin Planar Semiconductor Layer on a Metal Substrate," *ACS Photonics*, vol. 1, no. 9, pp. 812–821, 2014, doi: 10.1021/ph500093d.

[18] M. A. Kats *et al.*, "Ultra-thin perfect absorber employing a tunable phase change material," *Appl. Phys. Lett.*, vol. 101, p. 221101, 2012, doi: 10.1063/1.4767646.

[19] W. Streyer, S. Law, G. Rooney, T. Jacobs, and D. Wasserman, "Strong absorption and selective emission from engineered metals with dielectric coatings," *Opt. Express*, vol. 21, no. 7, pp. 9113–9122, 2013, doi: 10.1364/OE.21.009113.

[20] Z. Yang, C. Ji, D. Liu, and L. J. Guo, "Enhancing the Purity of Reflective Structural Colors with Ultrathin Bilayer Media as Effective Ideal Absorbers," *Adv. Opt. Mater.*, vol. 7, no. 21, p. 1900739, 2019, doi: 10.1002/adom.201900739.

[21] H. Deng, Z. Li, L. Stan, D. Rosenmann, and D. Czaplewski, “Broadband perfect absorber based on one ultrathin layer of refractory metal,” vol. 40, no. 11, pp. 2592–2595, 2015.

[22] Z. Li, E. Palacios, S. Butun, H. Kocer, and K. Aydin, “Omnidirectional , broadband light absorption using large- area , ultrathin lossy metallic film coatings,” *Sci. Rep.*, vol. 5, no. 15137, 2015, doi: 10.1038/srep15137.

[23] H. Deng, Z. Li, L. Stan, D. Rosenmann, and D. Czaplewski, “Broadband perfect absorber based on one ultrathin layer of refractory metal,” *Opt. Lett.*, vol. 40, no. 11, pp. 2592–2595, 2015, doi: 10.1364/OL.40.002592.

[24] Q. H. Wang, K. Kalantar-Zadeh, A. Kis, J. N. Coleman, and M. S. Strano, “Electronics and optoelectronics of two-dimensional transition metal dichalcogenides,” *Nat. Nanotechnol.*, vol. 7, no. 11, pp. 699–712, 2012, doi: 10.1038/nnano.2012.193.

[25] L. Cao, “Two-dimensional transition-metal dichalcogenide materials: Toward an age of atomic-scale photonics,” *MRS Bull.*, vol. 40, no. 7, pp. 592–599, 2015, doi: 10.1557/mrs.2015.144.

[26] J. Yang *et al.*, “Atomically thin optical lenses and gratings,” *Light Sci. Appl.*, vol. 5, p. e16046, Mar. 2016, doi: 10.1038/lsa.2016.46.

[27] T. Mueller and E. Malic, “Exciton physics and device application of two-dimensional transition metal dichalcogenide semiconductors,” *npj 2D Mater. Appl.*, vol. 2, no. 29, 2018, doi: 10.1038/s41699-018-0074-2.

[28] H. Wang, H. Yuan, S. Sae Hong, Y. Li, and Y. Cui, “Physical and chemical tuning of two-dimensional transition metal dichalcogenides,” *Chem. Soc. Rev.*, vol. 44, no. 9, pp. 2664–2680, 2015, doi: 10.1039/c4cs00287c.

[29] Y. Yu *et al.*, “Exciton-dominated Dielectric Function of Atomically Thin MoS2 Films,” *Sci. Rep.*, vol. 5, p. 16996, 2015, doi: 10.1038/srep16996.

[30] M. Elkabbash *et al.*, “Fano-resonant ultrathin film optical coatings,” *Nat.*

Nanotechnol., vol. 16, pp. 440–446, 2021, doi: 10.1038/s41565-020-00841-9.

[31] T. Matsui, H. Sai, K. Saito, and M. Kondo, "High-efficiency thin-film silicon solar cells with improved light-soaking stability," *Prog. Photovoltaics Res. Appl.*, vol. 21, no. 6, pp. 1363–1369, 2013, doi: 10.1002/pip.2300.

[32] K. Lee, C. Ji, L. J. Guo, K. Lee, C. Ji, and L. J. Guo, "Wide-angle, polarization-independent ultrathin broadband visible absorbers," *Appl. Phys. Lett.*, vol. 108, no. 031107, 2016, doi: 10.1063/1.4939969.

[33] S. S. Mirshfieyan, T. S. Luk, and J. Guo, "Zeroth order Fabry-Perot resonance enabled ultra-thin perfect light absorber using percolation aluminum and silicon nanofilms," *Opt. Mater. Express*, vol. 6, no. 4, pp. 1032–1042, 2016, doi: 10.1364/OME.6.001032.

[34] S. S. Mirshafieyan and J. Guo, "Silicon colors : spectral selective perfect light absorption in single layer silicon films on aluminum surface and its thermal tunability," *Opt. Express*, vol. 22, no. 25, pp. 31545–31554, 2014, doi: 10.1364/OE.22.031545.

[35] Z. Yu, A. Raman, and S. Fan, "Fundamental limit of nanophotonic light trapping in solar cells," *PNAS*, vol. 107, no. 41, pp. 17491–17496, 2010, doi: 10.1073/pnas.1008296107.

[36] N. S. Lewis, "Toward Cost-Effective Solar Energy Use," *Science (80-.).*, vol. 798, no. 5813, pp. 798–802, 2007, doi: 10.1126/science.1137014.

[37] W. A. Tisdale, K. J. Williams, B. A. Timp, D. J. Norris, E. S. Aydil, and X.-Y. Zhu, "Hot-electron transfer from semiconductor nanocrystals," *Science (80-.).*, vol. 328, no. 5985, pp. 1543–1547, 2010, doi: 10.1126/science.1185509.

[38] F. Schlich and R. Spolenak, "Strong interference in ultrathin semiconducting layers on a wide variety of substrate materials," *Appl. Phys. Lett.*, vol. 103, no. 213112, 2013, doi: 10.1063/1.4833537.

[39] K.-K. Kam, "Electrical properties of WSe2, WS2, MoSe2, MoS2, and their use as

photoanodes in a semiconductor liquid junction solar cell," p. 119, 1982, [Online]. Available: https://lib.dr.iastate.edu/rtd/8356%0Ahttps://lib.dr.iastate.edu/rtd/8356/.

[40] T. Akama, W. Okita, R. Nagai, C. Li, T. Kaneko, and T. Kato, "Schottky solar cell using few-layered transition metal dichalcogenides toward large-scale fabrication of semitransparent and flexible power generator," *Sci. Rep.*, vol. 7, no. 1, pp. 1–10, 2017, doi: 10.1038/s41598-017-12287-6.

[41] H. Dotan *et al.*, "Resonant light trapping in ultrathin films for water splitting," *Nat. Mater.*, vol. 12, no. 2, pp. 158–164, 2013, doi: 10.1038/nmat3477.

[42] K. Lee, J. Y. Lee, S. Seo, and L. J. Guo, "Colored ultrathin hybrid photovoltaics with high quantum efficiency," *Light Sci. Appl.*, vol. 3, p. e215, 2014, doi: 10.1038/lsa.2014.96.

[43] "The Atmospheric Window," *NOAA*, 2023. https://www.noaa.gov/jetstream/satellites/absorb#:~:text=The places with limited or,the atmosphere at various wavelengths.

[44] R. Sundaram, M. Engel, A. Lombardo, A. C. Ferrari, P. Avouris, and M. Steiner, "Electroluminescence In Single Layer MoS2," *Nano Lett.*, vol. 13, no. 4, pp. 1416–1421, 2013, doi: 10.1021/nl400516a.

[45] J. Xiao, M. Zhao, Y. Wang, and X. Zhang, "Excitons in atomically thin 2D semiconductors and their applications," *Nanophotonics*, vol. 6, no. 6. Walter de Gruyter GmbH, pp. 1309–1328, 2017, doi: 10.1515/nanoph-2016-0160.

[46] G. A. Ermolaev *et al.*, "Broadband optical properties of monolayer and bulk MoS2," *npj 2D Mater. Appl.*, vol. 4, no. 1, pp. 1–6, 2020, doi: 10.1038/s41699-020-0155-x.

[47] K. F. Mak *et al.*, "Tightly bound trions in monolayer MoS2," *Nat. Mater.*, vol. 12, no. 3, pp. 207–211, 2013, doi: 10.1038/nmat3505.

[48] R. Gatensby *et al.*, "Controlled synthesis of transition metal dichalcogenide thin films for electronic applications," *Appl. Surf. Sci.*, vol. 297, pp. 139–146, 2014, doi: 10.1016/j.apsusc.2014.01.103.

[49] B. Radisavljevic, A. Radenovic, J. Brivio, V. Giacometti, and A. Kis, “Single-layer MoS2 transistors,” *Nat. Nanotechnol.*, vol. 6, no. 3, pp. 147–150, 2011, doi: 10.1038/nnano.2010.279.

[50] Q. He, K. Sun, Z. Shi, Y. Liu, and R. Fan, “Polymer dielectrics for capacitive energy storage: From theories, materials to industrial capacitors,” *Mater. Today*, vol. 68, pp. 298–333, 2023, doi: 10.1016/j.mattod.2023.07.023.

[51] M. Farzaneh *et al.*, “CCD-based thermoreflectance microscopy: Principles and applications,” *J. Phys. D. Appl. Phys.*, vol. 42, no. 14, p. 143001, 2009, doi: 10.1088/0022-3727/42/14/143001.

[52] “Diameter of human hair.” https://bionumbers.hms.harvard.edu/bionumber.aspx?id=106856&ver=2.

[53] K. R. Williams, K. Gupta, and M. Wasilik, “Etch Rates for Micromachining Processing—Part II,” *J. Micromechanics Microengineering*, vol. 12, no. 6, pp. 761–778, 2003, doi: 10.1088/0960-1317/20/5/055033.

[54] V. G. Kravets, F. Wu, G. H. Auton, T. Yu, S. Imaizumi, and A. N. Grigorenko, “Measurements of electrically tunable refractive index of MoS2 monolayer and its usage in optical modulators - Supplementary Information,” *npj 2D Mater. Appl.*, vol. 3, no. 1, pp. 1–13, 2019, doi: 10.1038/s41699-019-0119-1.

[55] M. B. M. P. Maciej R. Molas, Karol Nogajewski, Artur O. Slobodeniuk, Johannes Binder, “Optical response of monolayer, few-layer and bulk tungsten disulfide,” *J. Mater. Chem. C*, vol. 3, pp. 10715–10722, 2015, doi: 10.1039/b000000x.

[56] K. F. Mak, C. Lee, J. Hone, J. Shan, and T. F. Heinz, “Atomically thin MoS2: A new direct-gap semiconductor,” *Phys. Rev. Lett.*, vol. 105, no. 13, p. 136805, 2010, doi: 10.1103/PhysRevLett.105.136805.

[57] A. Splendiani *et al.*, “Emerging photoluminescence in monolayer MoS2,” *Nano Lett.*, vol. 10, no. 4, pp. 1271–1275, 2010, doi: 10.1021/nl903868w.

[58] X. Xu, W. Yao, D. Xiao, and T. F. Heinz, “Spin and pseudospins in layered

transition metal dichalcogenides," *Nat. Phys.*, vol. 10, no. 5, pp. 343–350, 2014, doi: 10.1038/nphys2942.

[59] D. Vella *et al.*, "Unconventional electroabsorption in monolayer MoS2," *2D Mater.*, vol. 4, no. 2, p. 021005, 2017, doi: 10.1088/2053-1583/aa5784.

[60] X. Cui *et al.*, "Multi-terminal transport measurements of MoS2 using a van der Waals heterostructure device platform," *Nat. Nanotechnol.*, vol. 10, no. 6, pp. 534–540, 2015, doi: 10.1038/nnano.2015.70.

[61] F. Liu, J. Zhou, C. Zhu, and Z. Liu, "Electric Field Effect in Two-Dimensional Transition Metal Dichalcogenides," *Adv. Funct. Mater.*, vol. 27, no. 19, p. 1602404, 2017, doi: 10.1002/adfm.201602404.

[62] A. K. Geim and I. V. Grigorieva, "Van der Waals heterostructures," *Nature*, vol. 499, no. 7459, pp. 419–425, 2013, doi: 10.1038/nature12385.

[63] M. Sakurai, "Spectroscopic ellipsometry," *Toraibarojisuto/Journal Japanese Soc. Tribol.*, vol. 57, no. 7, 2012.

[64] M. Fox, *Optical Properties of Solids*. 2010.

[65] V. G. Kravets, F. Wu, G. H. Auton, T. Yu, S. Imaizumi, and A. N. Grigorenko, "Measurements of electrically tunable refractive index of MoS2 monolayer and its usage in optical modulators," *npj 2D Mater. Appl.*, vol. 3, no. 36, 2019, doi: 10.1038/s41699-019-0119-1.

[66] E. Complete, *CompleteEASE Software Manual Version 3.18*. J. A. Woollam Co., Inc., 2007.

[67] J. N. Hilfiker *et al.*, "Survey of methods to characterize thin absorbing films with Spectroscopic Ellipsometry," vol. 516, pp. 7979–7989, 2008, doi: 10.1016/j.tsf.2008.04.060.

[68] "Molybdenum Disulfide (MoS2): Theory & Applications," *Osilla*. https://www.ossila.com/pages/molybdenum-disulfide-mos2.

[69] W. Wang *et al.*, “Single layer WOx films for efficient solar selective absorber,” *Mater. Des.*, vol. 186, 2020, doi: 10.1016/j.matdes.2019.108351.

[70] “The Solar Spectrum,” 2024. https://www.ossila.com/pages/the-solar-spectrum.

Chapter 5. Zeroth Order Fabry-Perot Resonant Enhanced Absorption & Structural Colouration in Active Electrochromic Transition Metal Oxides

5.1 Introduction to Electrochromic Materials

5.1.1 Applications of Electrochromism

In chapter 4, many results were presented for lossy dielectrics like Si, Ge and TMDs MoS_2 and WS_2. These materials were shown to be well suited to generating vivid colouration in the ultrathin thin film regime due to their high real and complex refractive indices. To realise dynamic ATF structural colour generation and strong absorption, electrochromic materials (ECMs) were brought into the project for study due to their electrically tunable large broadband change in refractive index [1]. Indeed, the ability to tune the refractive indices of ECMs across the visible, gives it a huge advantage over materials like TMDs that are restricted to the narrower exitonic absorption pole positions, namely the A and B excitons in the red visible region [2]. Electrochromism is a field that has been well studied since the 1970s, pioneered by Deb [3], in which certain materials such as TiO_2, WO_3, NiO, and some organic polymers, reversibly change their optical properties through the application of an electric field bias to drive ions into their lattices [1], [4]. Unlike TMDs which may require a large voltage bias on the order of 50-100 V or more to appreciably modulate their exitonic states [5], electrochromic thin film ion intercalation typically operates on less than ± 2 V, and the end state is also metastable, making its power consumption much lower as energy is only required to change the state [1].

Figure 5.1 below is a diagram of the periodic table highlighting the elements with inorganic EC properties and distinguishing them by their cathodic or anodic EC response to the field effect electrochemical ion intercalation process [6]. Anodic ECMs enter their absorbing state when ions are extracted from them while cathodic ECMs enter their absorbing state when ions are intercalated into them [6]. The former is an oxidative process while the latter is reduction. Bleached anodic materials have been inserted with ions while in the cathodic case the ions have been extracted.

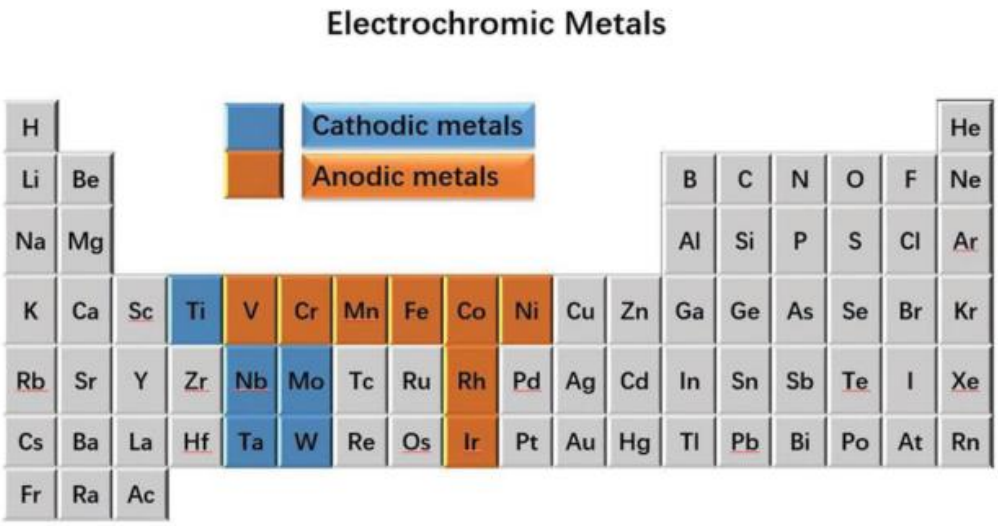


Figure 5.1. Elements with less filled d orbitals behave more cathodically while the opposite is true for elements higher up the elemental period. Nickle readily forms an oxide, which is a chief example of an anodic materials that will be studied in this chapter. Cathodic tungsten trioxide is also analysed given the ease at forming it and large amount of literature focusing on its use. [6]

The number of ions moved by the applied low voltage into the active ECM depends on electrolyte used and how thick it is as well as the electrolyte used. In regards to size scale effects, the timescale of the process of ion diffusion (τ) into the lattice of the ECM is directly proportional to the square of its thickness *L* and inversely proportional to the diffusivity *D* [7], [8] , [9]. Primarily as a result of the low voltages and power draw needed for reduction/oxidation to take place, ECMs are potentially useful for display technologies and other wearable electronic applications which greatly benefit from miniaturization and reduced energy consumption [10]–[16]. Moreover, in this thesis the ultrathin ECM films produced are considerably thinner than the bulkier films that are normally reported on in the literature (EC layers usually many 100's of nanometers in thickness [17], [18]). Hence, multilayer thin film pixel displays based on ultrathin ECMs could potentially be more competitive with well-established LCD and LED display technology that currently dominate the market (See discussion in chapter 1 p.17). LCDs and LED displays operate at higher switching speeds in the range of milliseconds [19] as compared to the tens of milliseconds that have been demonstrated in an organic polymer based multilayer EC devices [7]. Switching speeds in this context refers to the time taken for the colour of the pixel to change. For ECMs, the switching speed is the time taken for the ions to insert into the lattice and for the ions to be extracted. Results shown later in this chapter will demonstrate that the former takes longer than the latter, though the difference reduces as the thin film becomes thinner. In addition to applications in display technology, ECMs on transparent glass have seen real

world implementation on larger macroscopic scales in smart window technology, such as on airplanes [20]. In this setting, the switching speed or response time is not as much of a practical concern as it is with a fast monitor, given that the basic objective with electrochromic smart windows is to simply change them from a transparent to near opaque state in a reasonable amount of time (on the order of seconds [7]). The more important parameter to be optimised for in this case is contrast between the transparent and opaque state of the ECM, as well as the energy needed to change the state. The latter point relates directly to the EC parameter of colouration efficiency which will be discussed later in this chapter [21]. For the EC samples that were made in this thesis, the scale of smart windows is more applicable than the pixel level of displays. This is especially the case considering the ATF approach taken with the samples made. Thus, when considering the dynamic EC response in the results, particular emphasis will be put on the improvement in reflection contrast achievable in the ultrathin regime using the zeroth Fabry-Perot mode as compared to accessing higher order FP modes with typically thicker films measured in the hundreds of nanometers. Electrochromic dimmable mirrors could benefit from improvements in contrast and response time (seconds) that the ultrathin film regime may enable [22], [23], [24]. The colouration response of the zeroth FP mode or higher will be looked as well.

5.1.2 Enhancing Colouration of ECMs Using Fabry-Perot Resonance

ECMs are divided into organic and inorganic classed materials. The former has traditionally shown superior colour vibrancy and gamut as compared to their inorganic transition metal oxide (TMO) counterparts [25]–[29]. Some examples include viologens, discussed in chapter 1 p.15-16, as well as other organic polymers like polyaniline (PANI) and poly(2,2-dimethyl-3,4 propylenedioxythiophene) (PolyProDOT-Me_2) which have been used in fast switching high-contrast plasmonically enhanced displays with vibrant structural colouration and a response time of 6-18 ms [7]. These polymer ECMs are however not without their drawbacks. They are known to have issues with stability that negatively affects their cycle lifetime, and given their organic nature they are also more susceptible to environmental sources of damage (such as prolonged exposure to UV light and high temperatures degrading the material quality) that would be problematic for devices that are placed outside [30], [31]. Though the inorganic ECMs have better mechanical, thermal, and chemical stability [32], [33] than the organics, their more drab colours have been a large factor in holding them back from seeing wider spread commercial application [1]. To solve this problem the use of

various optical resonators with ECMs have been proposed to increase the light-matter interaction and overcome the narrow passive/dynamic colour gamut. Electrochromic optical resonators come in many forms such as those based on plasmonic [7], [34], Mie [9], [35], photonic crystal [36], [37], and for the interests of this thesis a FP nano-cavity resonance [38], [39]. With an FP optical resonators even ultrathin electrochromic materials can display large colour variability due to the various FP modes within the cavity structure that increase the light-matter interaction substantially, as discussed in chapter 1 p.21-24. Figure 5.2 below demonstrates this with thin film ECM Cu_2O grown on a Cu substrate [40].

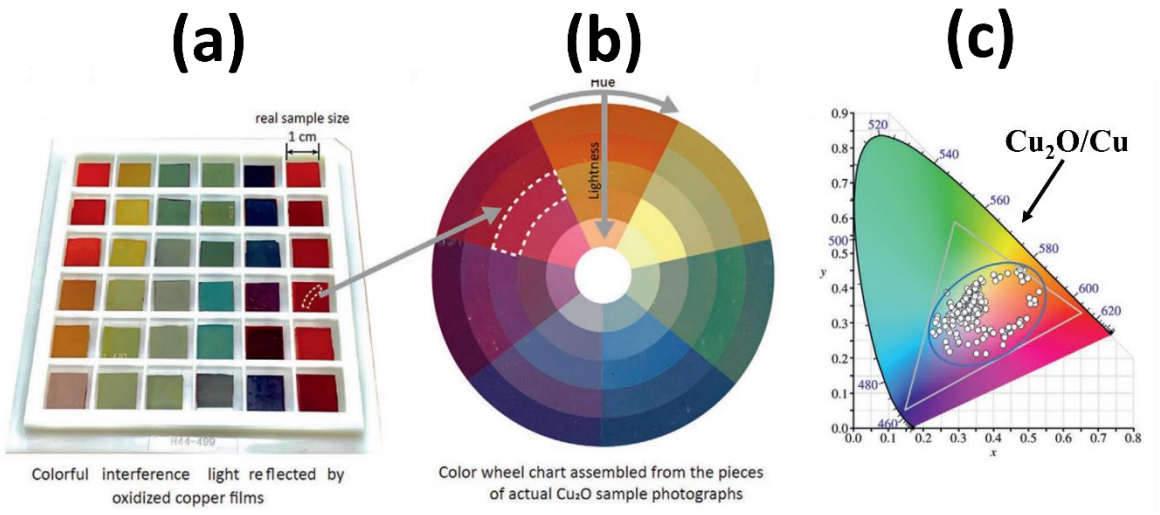


Figure 5.2. (a) The range of colours produced by the Cu_2O/Cu samples of thickness ranging from 0-60 nm. (b) A colour wheel representing the dominant hue moving clockwise and brightness moving inwards. (c) The samples from (a) represented in the CIE chromaticity diagram. The gamut is elliptical, similar to other asymmetric FP resonators [40].

Though there was clear motivation to produce Cu_2O/Cu stacks given the wide array of colours generated with such thin oxide layers in Fig.5.2(a) above, group member Mr. Chris Murray warned against this, as the presence of copper within the NPVD sputtering tool would act as a contaminant that poisons subsequent depositions. Thus, to make a colourful dynamic FP optical resonator, using electrolytes like H_2SO_4 and KOH, the cathodic ECM WO_3 was chosen as the ideal candidate, not only because there are many reports on its properties in the EC literature for reference [26], [37], [38], [41], but also because it was simple and quick to make 100-300 nm thick layers using magnetrons sputtering by co-depositing tungsten with reactive oxygen gas. Likewise with anodic Nickle oxide [21], [42], [43], a similar procedure was used to create films of various thicknesses to explore contrast and coloration in both the ultrathin film and thicker film regime.

5.2 Electrochromic Response of Cathodic TMO WO_3

5.2.1 WO_3 in the Literature

As previously mentioned, inorganic electrochromic materials often suffer from drab colours and poor colour-tuneability [44]–[46]. For the well-studied near lossless transparent ECM WO_3, the colour change between bleached and absorbing state is from a transparent dielectric to blue in appearance [17], [47]–[51]. To enhance and expand the colour variability of WO_3 an optical resonator of some kind must be employed to help trap the light inside the stack assembly. Towards this end other groups in the literature have reported on achieving this with Photonic crystals, Bragg mirrors, and Mie scatterers [6], [36], [37], [52]–[56]. However, a study done by Zhen Wang *et al.* (2020) [38] shows the capability and simplicity of the asymmetric FP nanocavity resonance approach to accomplish this too. They demonstrated a dynamic FP electrochromic (EC) device by simultaneously using a lossy W metal backing as the current collector and the back mirror reflector. The addition of W behind the WO_3 in place of FTO/glass drastically changes the reflection intensity profile from a flat response w.r.t thickness and wavelength, to a highly dispersive spectrum with strong peaks and deep troughs, seen below in Fig.5.3(e).

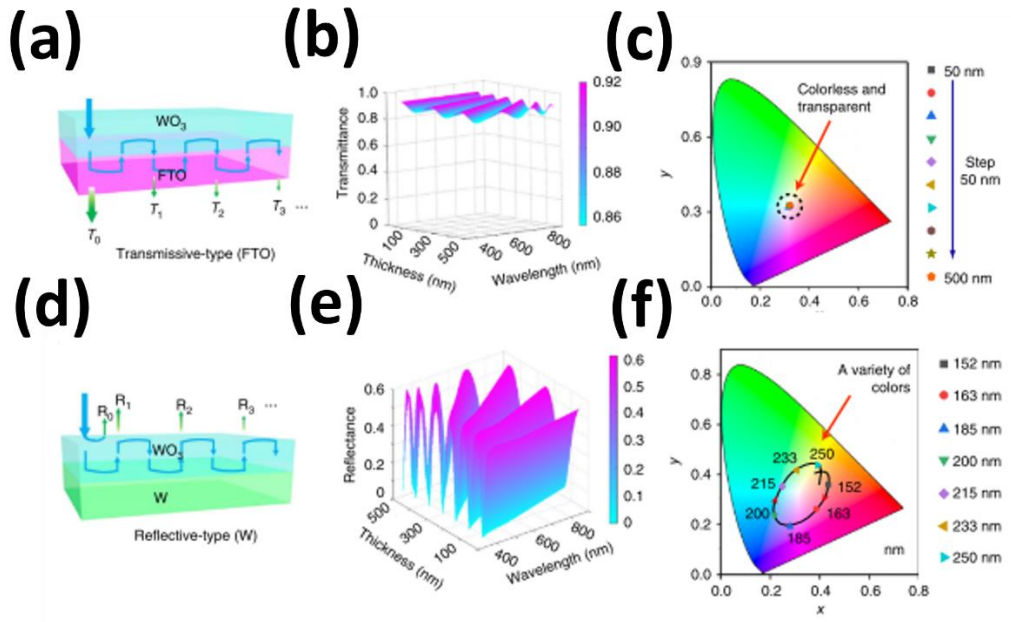


Figure 5.3. A comparison between (a) FTO and (d) W backed WO_3. In this case the zeroth mode is not targeted as the thickness is too great. The FP modes responsible for colouration in this WO_3/W sample are therefore of the 1st and 2nd order. (b), (c) Without a back reflector the spectral response is very flat and colourless. (e), (f) With W backing the colour gamut is greatly expanded upon. [38]

A clear difference in the structural colours accessible is seen between a typical transparent current collector like ITO or FTO and the metallic W back reflector. Rich yellows, reds, blues, and violets are now available from simply tuning the thickness of the WO_3 [38]. Thickness and field effect index tuning make it feasible to envision a device with very wide colour gamut distribution extending further towards the edges and corners of the CIE colour chart. See Fig.5.4 below.

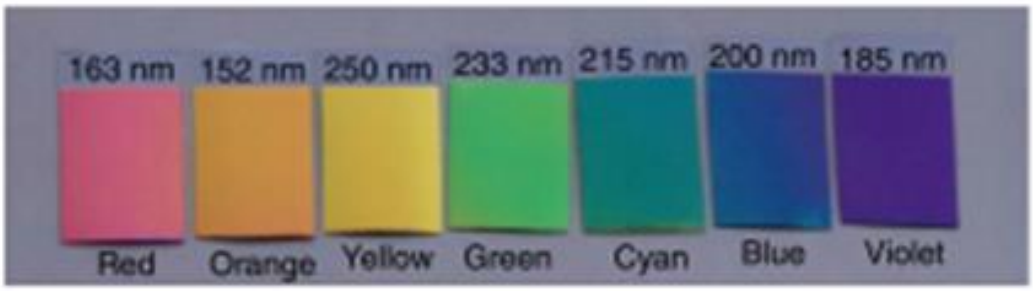


Figure 5.4. Optical microscope imagery of the WO_3/W sample fabricated by Zhen Wang et al. which targets the higher order FP modes above the ultrathin regime. The colouration range is seen to be better than the uncapped TMDs in chapter 4 p.210 [38].

The addition of a top ultrathin metal layer of Ag was also found to benefit the contrast of the resulting colours by narrowing and sharpening the FP mode peaks [38]. This translated the resultant colour coordinates on the CIE chart closer to the edges, indicating higher saturation of colour, which is a desirable result. Moreover Zhen Wang *et al.* reported that the use of W as the back current collector enables a high colouration efficiency (CE) of 48.6 $cm^2 \cdot C^{-1}$, which is slightly higher than FTO and ITO [38]. The EC switching speed is also superior with the W backing as compared to traditionally used ITO and FTO, and given that W is a refractory metal its durability is obviously greater than the conducting oxides in almost all avenues such as mechanical, thermal, electrical, etc. This is corroborated by cyclic voltammetry (CV) cycling bistability which showed that 81 % of initial charge capacity remained after 1000 cycles [38]. The lithium intercalation induced dynamic colouration from the work of Zhen Wang *et al.* is shown in Fig.5.5 below. As the voltage graduates in steps of 100 mV, the index of WO_3 changes, becoming more absorbing with negative bias and more reflective with positive bias.

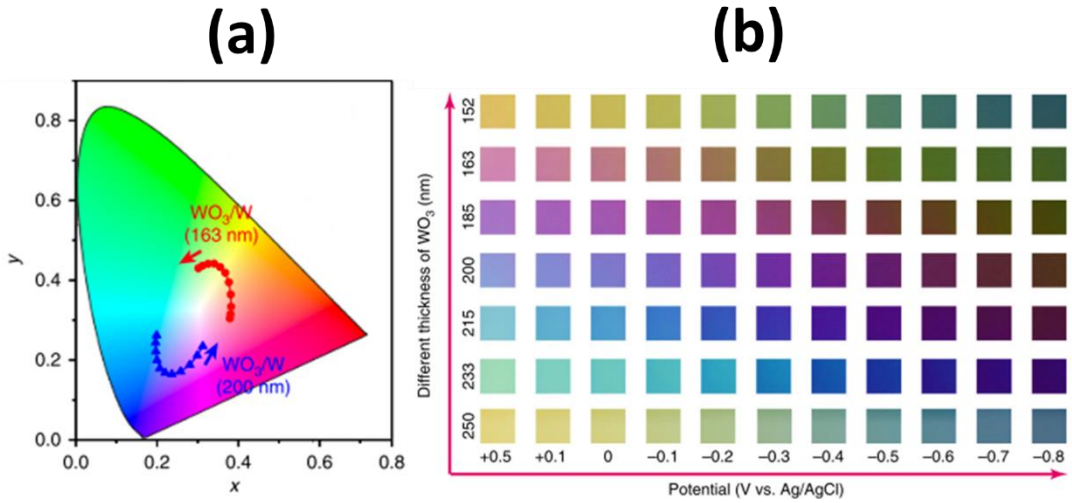


Figure 5.5. (a) Colour change sweep with voltage for 163 nm and 200 nm WO_3 on W. (b) Across many different thicknesses the intercalation of Li into the crystal lattice of WO_3 darkens the samples as they become more lossy [38].

5.2.2 Results for the Electrochromic Response of Protonated WO_3

The NPVD magnetron sputtering DC gun and W target were used to create the WO_3/W devices shown in Fig.5.6 below. Vivid colouration was seen readily without any patterning or lithography steps needed. Implantation of hydrogen ions, facilitated by using liquid electrolyte H_2SO_4 in water solution, showed colour change that was more muted compared to the results presented by Zhen Wang *et al*. This is possibly because Li has a greater colouration efficiency than H in the WO_3 lattice, which may be due in part to the huge filling ratio γ of 0.65 for Li_xWO_3 when fully reduced at negative bias. [21]. Simulated chromaticity diagrams of WO_3/W are shown in Fig.5.7.

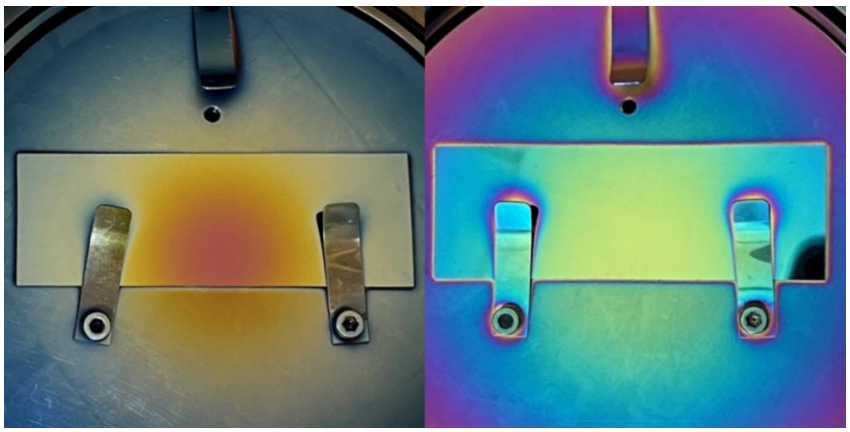


Figure 5.6. Imagery of WO_3/W created by co-sputtering a DC powered gun W target with flowing oxygen. In this way very thick oxides can be made much faster than using the RF gun. WO_3 on the Left is 163 nm while on the right is 237 nm thick.

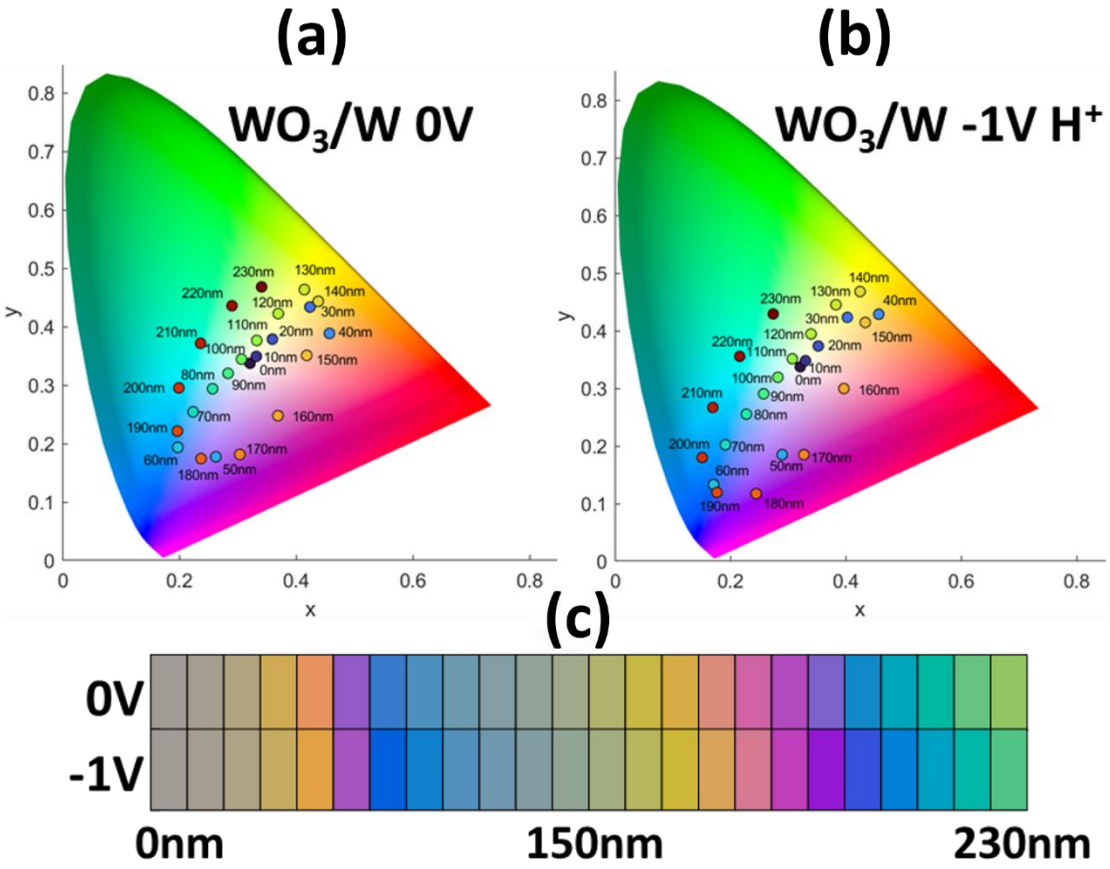


Figure 5.7. (a)-(b) Simulated structural colouration change is small when negatively biased. (c) Colouration in the negative biased state is slightly more saturated (brought closer to the edge of the CIE chart). Strong orange colours are generated at 40 nm thickness, but the colouration of the ultrathin regime is generally poor compared to the results seen for Si and MoS_2. WO_3 is not absorbing enough to unitize the zeroth FP mode effectively.

The crystal structure of WO_3 is shown in Fig.5.8 below, displaying how ion intercalation of H^+ physical changes the crystal lattice structure [57]. Ions will fill into the interstitial spaces in between the WO_6 octahedra distorting the lattice and modifying the polarisability of the medium; and changing the refractive index. When deposited at ambient temperature WO_3 will tend to form an amorphous-like thin film coating [58], but this underlying unit cell structure will remain for the ions to diffuse into when a field bias is applied to commence the electrochemical reduction process. Overtime the intercalation response will weaken the integrity of the lattice structure. This degradation will reduce the magnitude of the EC response with the most readily apparent consequence being a decrease in the cyclical bistability of the material, inferred from the reduction in the enclosed area of the CV curve trace w.r.t cycle number [32]. More details will be given later, after an overview of anodic ECM NiO is given, on how CV and chronoamperometry (CA) are needed to perform

measurements necessary to characterise the various EC parameters like cycle bistability, switching speed (response time), colouration efficiency, and filling factor.

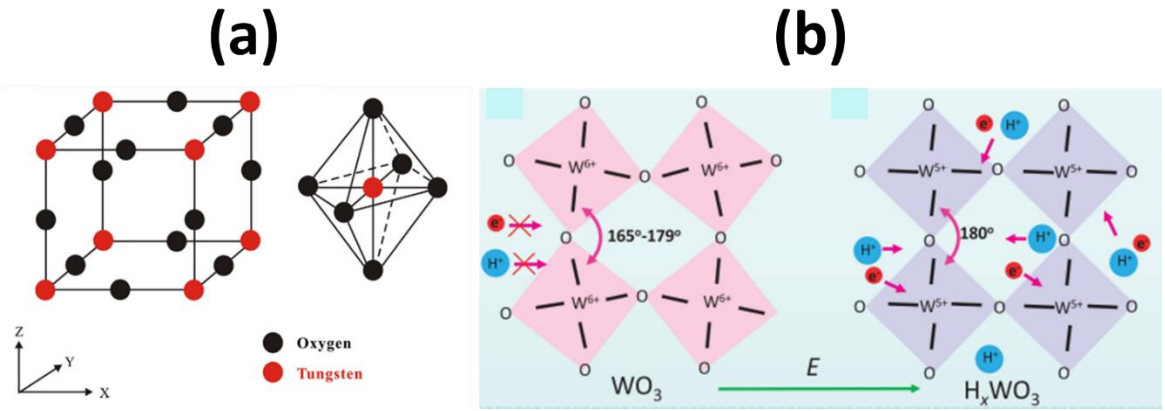


Figure 5.8. (a) The monoclinic lattice of WO_3 at ambient. The W atom cations are coordinated by 6 oxygen atoms creating an octahedral arrangement. These octahedrons sit corner to corner in the lattice with slight distortion from 180˚ as shown in (b). When an ion intercalates into the space in between these octahedrons they will straighten the off-axis distortion. For hydrogen intercalation, the once monoclinic WO_3 has now become cubic hydrogen tungsten bronze (H_xWO_3). The polarisability and conductivity of the medium is now modified. [57], [58].

Compared to the hydrogen intercalation large broadband change in refractive index (change in real index n of around 0.4 across the visible) seen by Lili Xiao *et al.* (2017) [37], the hydrogen intercalation with H_2SO_4 in this work only increases the extinction coefficient of the refractive index from 0 to 0.05, with a commensurate KK consistent tiny change in the real index component too as measured by Spectroscopic ellipsometry in CRANN. See Fig.5.9 below. This poor index modification result refocused the direction of research towards work with the ECM NiO, not only because its colouration efficiency is reported to be higher in the literature than WO_3 [21], but also because inherently high index lossy films can make use of the zeroth FP mode, discussed at length in chapter 4, to achieve angle independent strong absorption and colouration in an ultracompact multilayer assembly. Combining the zeroth order FP mode with the dynamic EC response could allow for the realisation of novel ATF dynamic colouration and large on/off state contrast (highly absorbing state to highly reflective state) solutions that are deeply subwavelength in scale, a situation which is not widely reported on in the field as bulkier transparent ECM films on the order of many hundreds of nanometers are used instead to adequately adjust the optical path length for colouration purposes using more trivial higher order FP resonance modes of the first, second, third, etc. order [38], [39], [59]. As one might expect this comes with certain

draw backs like increased sensitivity to AOI (iridescence) due to greater phase delay accumulation on propagation.

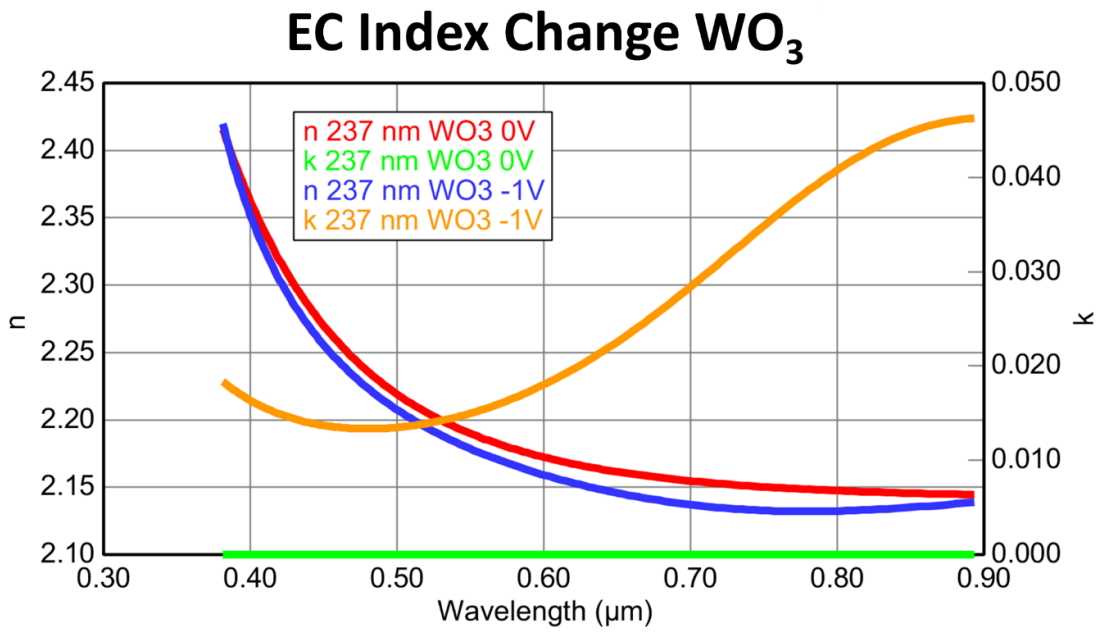


Figure 5.9. The change in refractive index of 237 nm WO_3 because of H^+ ion intercalation using a liquid electrolyte solution of H_2SO_4 in deionised water. The change is measured using spectroscopic ellipsometry. Before intercalation, WO_3 is completely transparent as it is a wide band gap material, E_g = 3 eV, described by a Cauchy relation. When H^+ enter the lattice the polarisability of the material changes and absorption appears. Two Lorentz oscillators are used to model the response.

5.3 Electrochromic Response of Anodic TMO NiO

5.3.1 NiO in the Literature

As seen from the literature, Anodic NiO is generally somewhat lossier than WO_3, as deposited, with a high real refractive index n in the region of 2 and above [60], [61]. NiO transitions from an absorbing colourful state to a nearly transparent state upon the introduction of ions such as H^+ and Li^+ into its crystal lattice structure [62]. Its EC response is the complete opposite to WO_3. Dongmei Dong *et al.* (2020) gives a comprehensive overview of the EC properties of NiO using Li^+ intercalation (lithiation), which is not as well studied as protonation (done with H_2SO_4 or KOH). They demonstrate that the EC response of NiO is not only a surface effect affected by the grain sizes, as Mathias Da Rocha conjectures [43], but also a bulk driven process where the dominant active sites are the unit cells of the ECM, similar to WO_3 [21]. They deposited very thick 400 nm NiO using a DC gun Ni target with reactive oxygen gas being flowed into the vacuum chamber.

The optical characteristics of ECMs can be dependent on the surface as well such as grain size and roughness [58]. Dongmei Dong *et al.* produced a sample brown in appearance on a transparent substrate. Figure 5.10 below displays their dynamic normal incidence transmission results as the voltage applied to NiO, immersed in the $LiClO_4$ liquid electrolyte, is scanned between ± 3 V using a CV three electrode cell set up and a UV-Vis spectrometer.

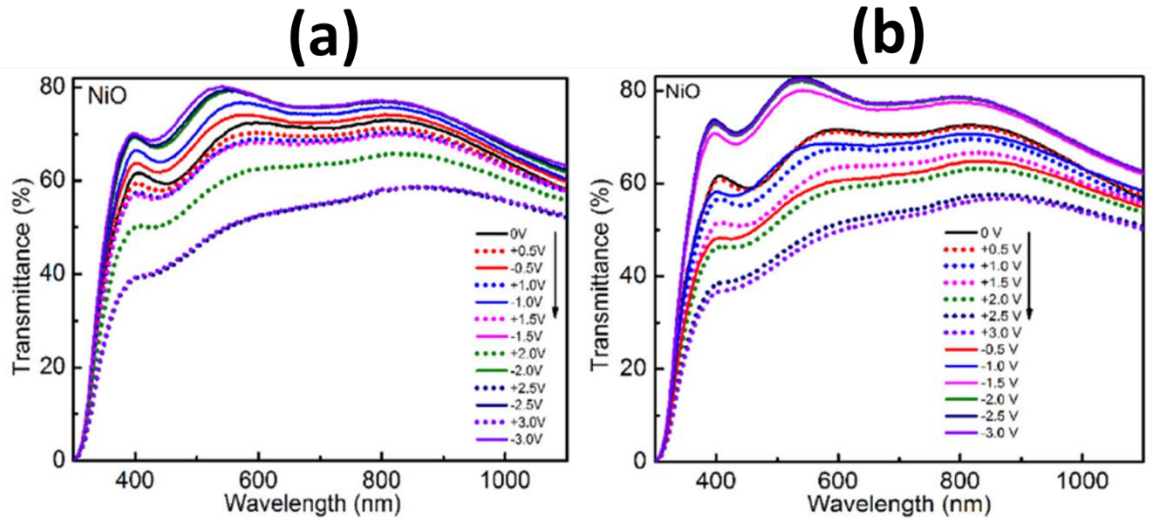


Figure 5.10. (a) A switching polarity sweep while (b) is a comprehensive modulation sweep. There is little difference in the absorption between +2.5 V and +3 V indicating no more Li can move into the lattice through redox reactions. Similarly, large negative voltages converge their response quickly, not extending beyond 80 % transmission at -2 V.[21]

Large changes in the optical response can be seen across the visible regime, indicating the broadband effect of ion intercalation on NiO indices. Furthermore, this change in transmission intensity is quite large when one considers that no light trapping mechanisms are used to help enhance the light-matter interaction in this instance. SEM imagery of NiO film surfaces before ion intercalation stipulate that the samples are quite porous which is a result that is also seen for many other oxide thin films produced by magnetron sputtering such as SiO_2 coatings that are almost always nonstoichiometric to a certain degree just after deposition. See Fig.5.11 below for SEM images taken by Dongmei Dong *et al.* before and after device switching and modulation are done [21]. In both cases the surface morphology remains relatively unchanged, highlighting the initial stability of the NiO thin films. Annealing in-situ or after the fact can be done to complete oxidation by thermally exciting the TMO into a whole number stoichiometric chemical configuration. Crystallinity and grain size can also be manipulated in this way [60].

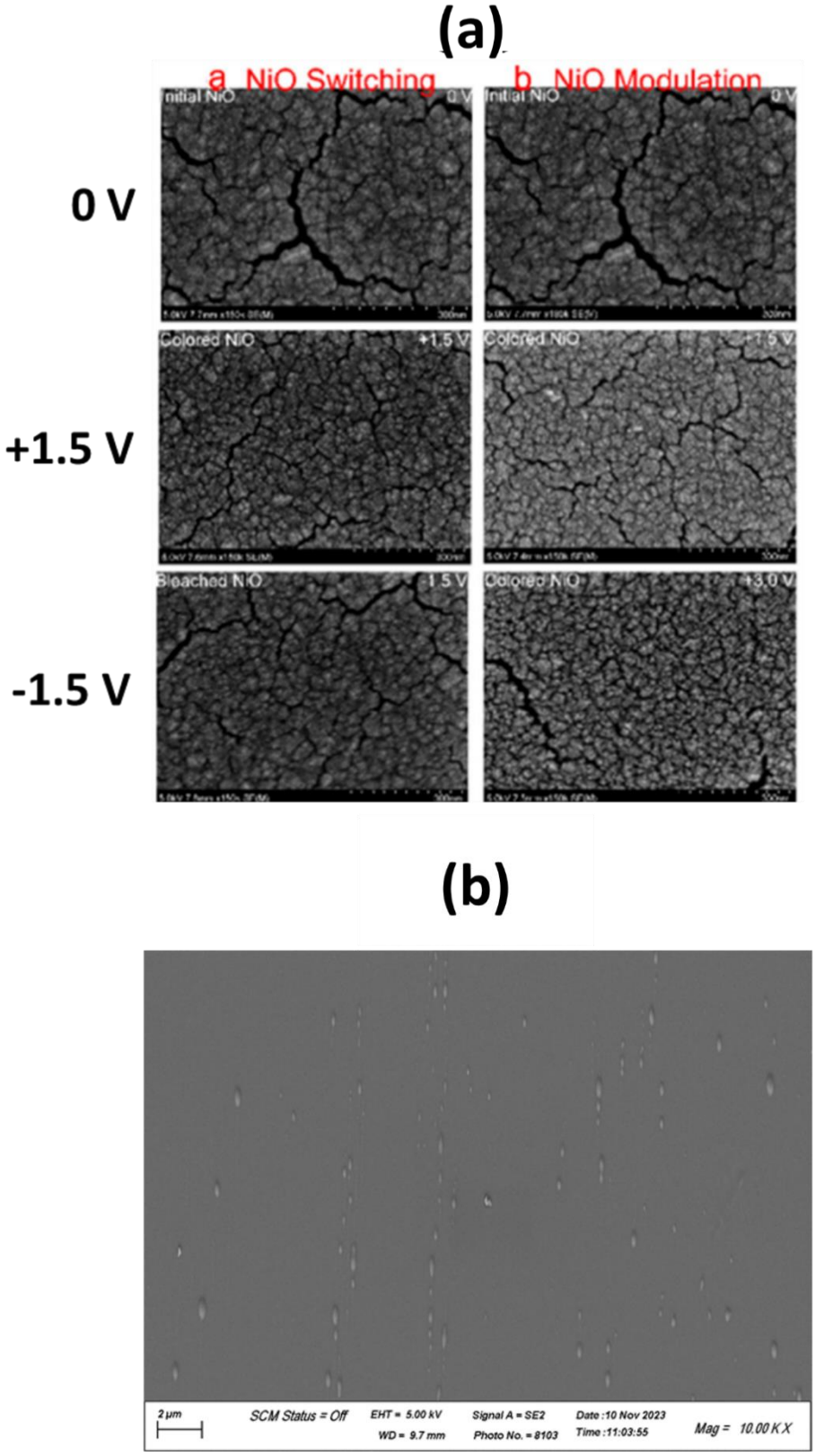


Figure 5.11. (a) SEM imagery of the NiO before and after ion implantation with switching and modulating voltage. The surface morphology remains porous throughout voltage cycling. [21] *(b) SEM imagery of NPVD magnetron sputtered WO_3 with rough protrusions jutting out of the surface. These protrusions are seen in AFM imagery as well which will be shown later. Based on the experience gathered throughout the project, AFM is more revealing than SEM in this context given the finer spatial resolution possible with the AFM probe.*

To characterise the change in the lattice structure with the introduction of Li^+, electrochromic measurements like CA and spectroscopic measurements like XRD and Raman analysis in liquid were performed by Dongemi Dong *et al*. CA was carried out to ascertain the charge capacity Q of the NiO films when bleached too. This value was found to be 15.9 C/m^2 for biases of -2.5 – -3 V. See Fig.5.12 below. With this EC parameter in hand, it is possible to directly calculate the ratio of Li atoms to Ni atoms in the NiO lattice using the equation below.

$$\gamma = \frac{MQ}{\rho h F}$$

(5 . 1)

Where M is the molar mass of NiO (7.47 x 10^{-2} Kg/mol), ρ is the NiO density (6670 Kg/m^3), h is the NiO film thickness, and F is the faraday constant (9.65 x 10^4 C/mol). γ was found to be 0.0046 which is much lower than the 0.65 value associated with protonated WO_3 films.

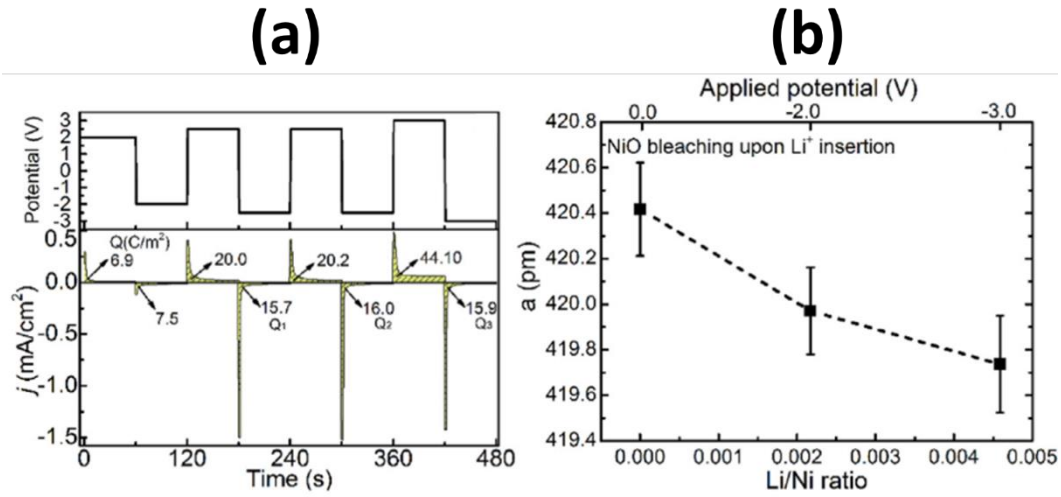


Figure 5.12. (a) Chronoamperometry measurements of NiO films between the absorbing and bleached states. The average area under the curve of the bleached current decay curve is used to determine the charge capacity Q. (b) As the ratio of Li to Ni atoms increases during intercalation the lattice constant of NiO will shrink by a small amount. This minor shrinkage can be seen from XRD and Raman analysis in-situ. [21]

Considering the fcc unit cell structure of NiO in Fig.5.13 below, Li^+ has eight different spaces to intercalate into, though in reality only a small percentage of these interstitial spots will be filled (around 0.23 % of the possible sites in this literature work) [21]. Like WO_3, Ni atoms are also coordinated by 6 oxygen atoms in an octahedral conformation.

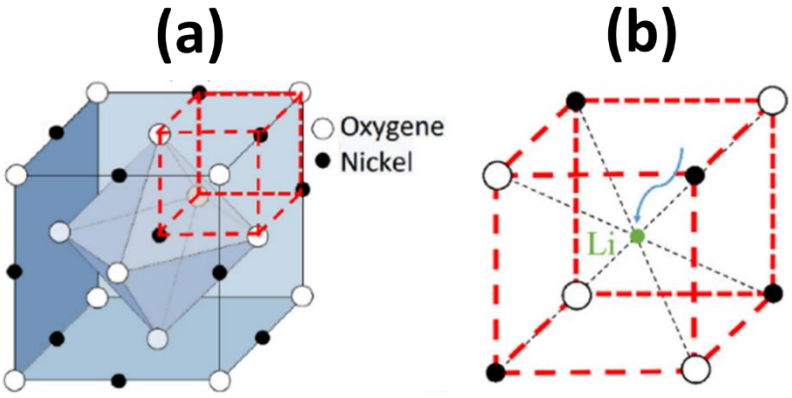


Figure 5.13. (a) fcc NiO lattice structure. There are 8 cubic cells surrounding the Ni-O octahedron where Li can intercalate into. (b) A closer view of this sub-cell with Li surrounded by 4 oxygen and Nickle atoms. [21]

X-ray diffraction (XRD) and Raman spectroscopy peak results also confirm that the EC response in NiO is a bulk phenomenon because the lattice constant is modified slightly by 0.6 pm as Fig.5.12(b) reveals above [21]. This is very advantageous for the light-matter interaction compared to a surface or interface only effect like the charge carrier accumulation layer in ITO/insulator stacks discussed by Atwater's group from Caltech [63]. Surface only index change can be large, even on the order of unity, but also simultaneously may have little impact on the resultant optical response due to how spatially concentrated it is. See Fig.5.14.

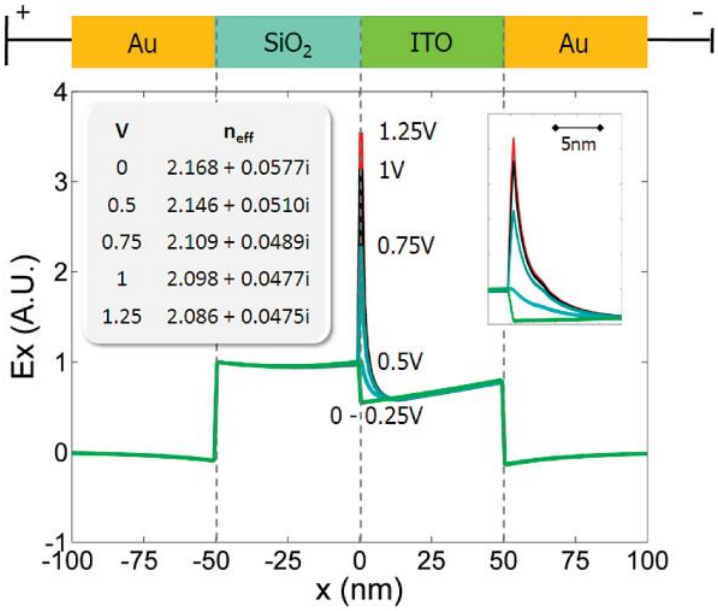


Figure 5.14. The local index change at the ITO-SiO_2 interface is on the order of unity while the effective modal index change is 0.1, indicating how small a shift the light-matter interaction will undergo. If carrier accumulation was a bulk process, then the entire ITO changing would massively impact the optics to a point that is comparable with the electrochromic results. [63]

Other means must often be incorporated into these local index change devices to remedy the minute optical path length change like gold diffraction grating metasurface elements [64]. As these patterned approaches are beyond the scope of the ATF approach taken in this thesis, it is imperative that the field effect index change be applicable to the entire bulk to maximise the small amount of planar thin film available to manipulate light. This is also plays into why high index lossy materials have become very attractive in recent years in nanophotonic research, as they allow for the further miniaturisation of optoelectronic devices when paired with optical resonant enhancement methods [65], [66].

5.3.2 Comparing the Preliminary Results Gathered for Sputtered NiO & WO_3

With the work of Dongmei Dong *et al.* in mind, NiO films were made on the NPVD system using the same method of DC gun sputtering the metal target with reactive oxygen gas flowing into the chamber. This was done on glass substrate microscope slides in preparation for ellipsometry measurements. Some optical microscope imagery of the initial samples made are shown below in Fig.5.15 with the same brownish colour as the samples produced by Dongmei Dong *et al*.

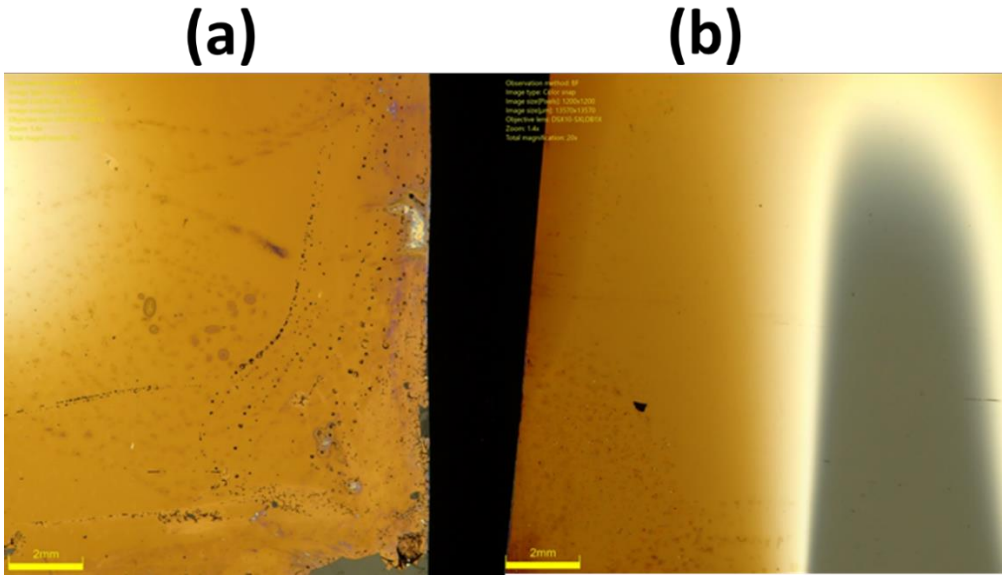


Figure 5.15. (a)-(b) Optical microscope imagery of some of the first NiO calibration sample deposited on glass slides. There are considerable surface variations near the sample edge in (a), while towards the centre the NiO film is smoother and homogenous in (b). Therefore, the most effective area to measure the EC and SE response is this central region.

To determine the refractive indices of NiO the SE technique was used. Calibration TMO samples were nearly always sputtered onto simple glass slides to avail of transmission

weighting to de-correlate thickness and index parameters in the optical fit. Contrast between the glass and TMO indices make this fitting a simple task even for ultrathin films below 10 nm in thickness due to the large index above n = 2 [67]. For NiO the real index n varies between 1.8 - 2.4 in the visible and it trends downward with decreasing wavelength, opposing the normal dispersion response of WO_3 [61]. Figure 5.16 displays results for ultrathin film and bulkier thin film NiO and WO_3 together for comparison as measured by SE.

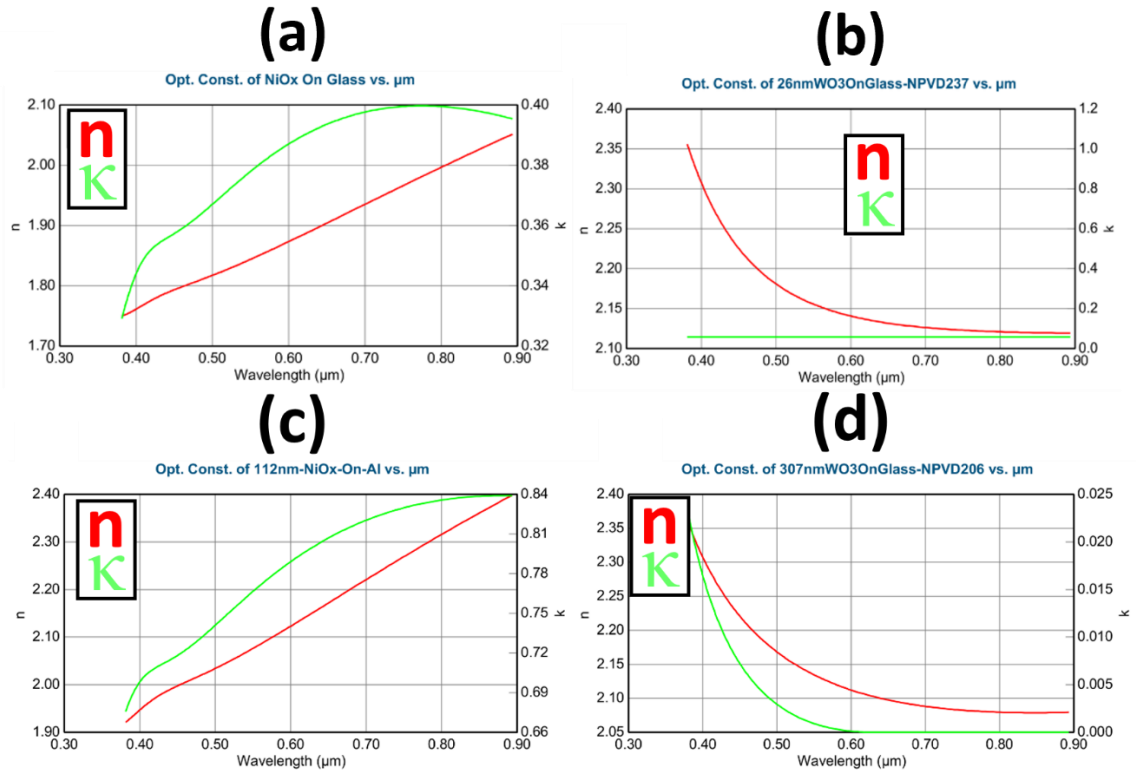


Figure 5.16. (a) The index dispersion for 6 nm NiO modelled with a KK consistent Lorentz oscillator. There is significant loss compared to literature values likely indicating incomplete oxidation as the presence of lossy metal Ni increases absorption (b) The index dispersion for 26 nm WO_3 modelled with a Cauchy relation. Most ultrathin film DC sputtered NiO and WO_3 samples had the characteristic trend and magnitude of the data shown. (c) The index dispersion for 112 nm NiO modelled with a KK consistent Lorentz oscillator. (d) The index dispersion for 307 nm WO_3 modelled with a Cauchy relation. There is a significant difference in the absorption of NiO in (c) compared to its 6 nm ultrathin counterpart in (a). Furthermore, the overall index is much higher and lossy in thick NiO. WO_3 has not changed as drastically in magnitude but there is now measurable absorption in the blue likely due to a slight downshift in the band gap energy.

The effect of thickness on the refractive index can sometimes be significant. A good example of this has already been seen in TMD materials like WS_2 and MoS_2 where geometric layer confinement of the excitons is exceptionally strong in the monolayer limit, enhancing the absorption transition rate [68]. TMD interband transition will also increase and change from indirect to direct due to an alteration in the electronic band structure [69]. As TMDs get

bulkier these excitonic features become more muted but do not completely disappear from the optical response [68]. In many materials the film grain size can greatly affect the optical constants. This is seen a lot in metals which is part of the reason why ultrathin metals have different indices than their thicker counterparts as is seen routinely with SE [67], [70], [71]. Furthermore, ultrathin film may not be completely continuous or could be very porous in nature. In both cases the effective refractive index that best models the material would be lower than the intrinsic constants in the bulk regime [67]. Comparing Fig.5.16(a) to (c), ultrathin 6 nm NiO has lower index n than for bulkier 112 nm NiO. Again, NiO in both regimes is also much more lossy than seen in literature data, strongly indicating that there is incomplete oxidation of the NiO film (residual Ni metal). This additional Ni increases absorption across the visible. On the other hand in Fig.5.16(b) and (d), WO_3 matches the normal dispersion of the optical constants seen in literature, meaning the tungsten was fully oxidised.

Although most of the TMOs created in this thesis were made with co-sputtering oxygen with a DC gun target metal, TMOs can also be deposited directly with the RF magnetron sputtering of a NiO target, at the cost of significantly increased deposition time in most cases. For the thicker films above 100 nm this is untenable as too many cooling steps are needed to prevent the RF gun from overheating during operation. See Fig.5.17 below photographs the failure of a Ge target by overheating.

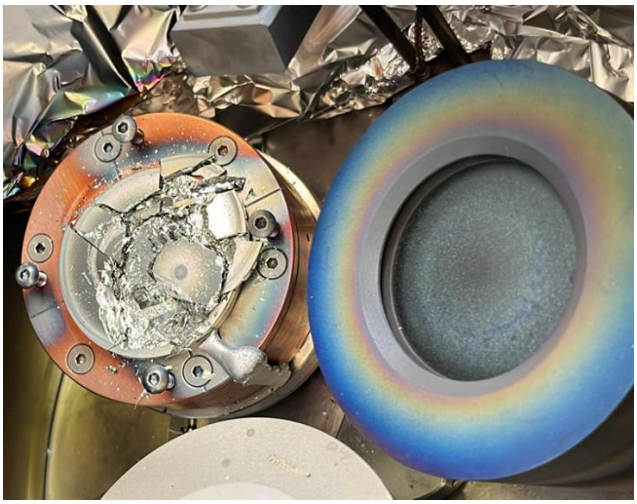


Figure 5.17. The Ge target on the left-hand side has melted and cracked after repeated overuse. Typically, this is more likely to occur with the magnetron RF gun targets as its extra difficult for heat to be removed from insulating dielectric materials. Melted solidified slag can be seen on the side of the gun frame which is normally underneath the shielding.

The DC gun with reactive oxygen flow method is therefore preferable not just for its much faster deposition rate, between 5-10 nm a minute for WO_3 in the NPVD system, but also for increased film porosity and to a certain degree, finer control over film porosity w.r.t. to O_2 flow rate. There have been studies done to evaluate this surface control of the porosity using more complex solid state protonation redox EC setups as well [72]. Porosity is ideal as a quick review of the literature reveals that more porous ECMs can help alleviate or overcome many concerns associated with the physical process of EC change such as difficulties in the charge transferring/penetrating into the thin film, large diffusion paths, and repeated mechanical stresses in the lattice due to recurrent expansion and contraction during ion insertion and extraction [47]. Figure 5.18 below indicates the improvement in a transparent EC device when porous WO_3 is used as opposed to compact WO_3. The optical density and CV electrochemical activity are both higher when porous active material is used.

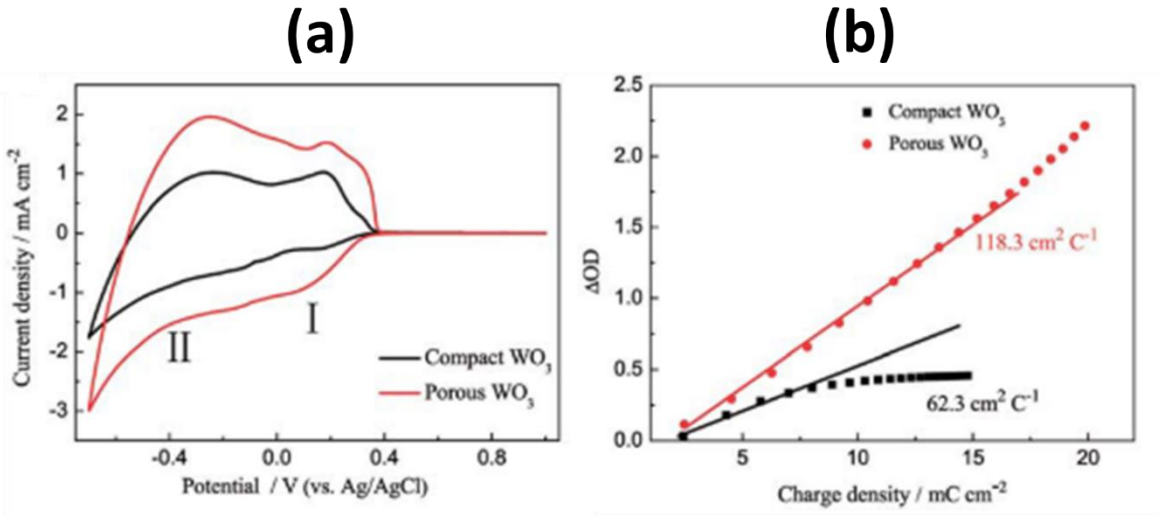


Figure 5.18. (a) The cyclic voltammetry graph of porous and compact WO_3 on ITO/Glass. The electrochemical activity is significantly increased in the porous compared to compacted thin film. Optical density OD is much higher with porous morphology as well signifying that the contrast between the EC bleached and colour state is greater. [47]

With the measured SE data at hand, the simulated colourimetric transmission response on a CIE chart for as deposited NiO and WO_3 are shown below in Fig.5.19 on a transparent glass substrate with 100 nm ITO backing. TMO thickness is varied between 0 and 230 nm, as before with the WO_3/W samples. ITO is used as the back anode to complete the electrical circuit, otherwise the ions could not gather to reduce the ECM. Microscopic surface roughness is not included in the optical model though a small amount may be present, especially after the electrochemical reduction process has taken place, as will be seen shortly

for the NiO/Al samples. Microscopic surface roughness only become very significant to the optics of most materials above 10-15 % of overall thin film thickness [67], [70]. Higer index materials are more affected by a microscopic surface roughness layer as the difference between high index layer and the air is large. See chapter 3 p.141-142 for more details.

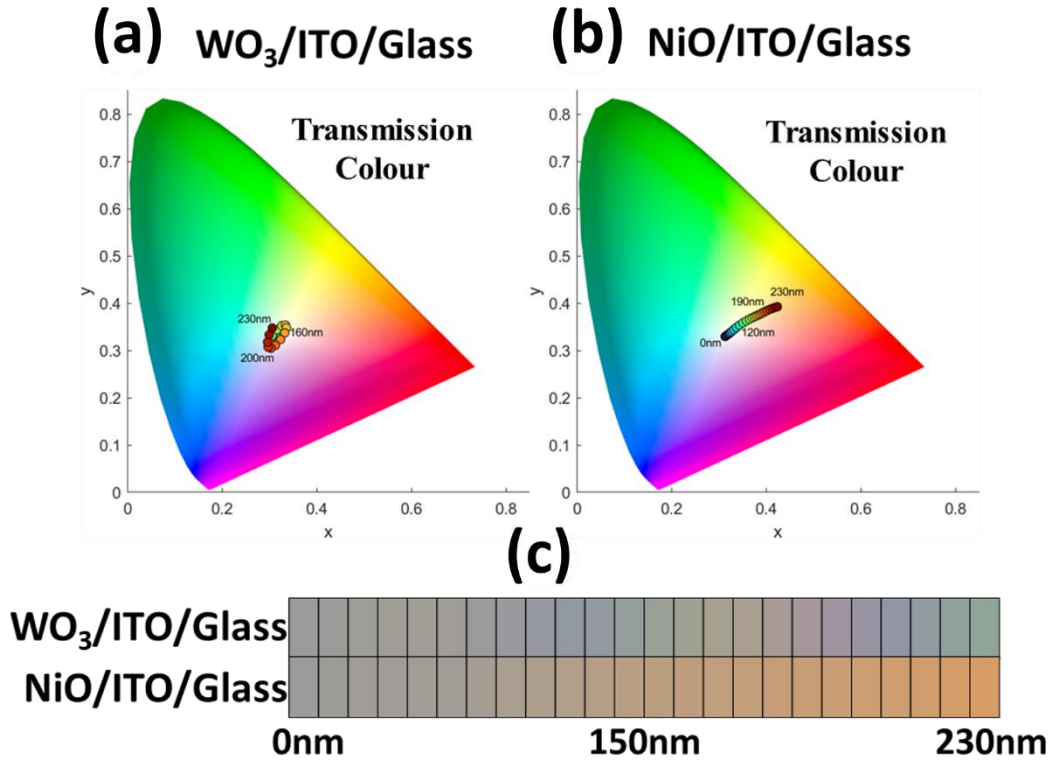


Figure 5.19 (a) Simulated transmission colour gamut of WO_3 on ITO/Glass substrate. (b) Transmission colour gamut of NiO on ITO/Glass substrate. In both cases the colour response is poor and narrow in range. NiO becomes more orange. Bleaching of NiO would return it to a white flat colour. (c) There is little variation in colour from 0 – 230 nm TMO thickness.

As expected, the transmission colour response is very narrow and drab for both ECMs in the as deposited state. This result really exemplifies how much the light-matter interaction is increased when metal backings are used. Even if the reflection colours are looked at instead the gamut is still much worse than the WO_3/W stack shown earlier on p.241-242. The spectral dispersion is also very flat as seen in Fig.5.20 below detailing the simulated transmission and reflection intensity surface plots w.r.t NiO thickness on ITO/Glass substrate. For the purposes of achieving large on/off state EC contrast a much thicker ECM layer in this configuration, many hundreds of nanometres thick, could make a reasonably functional smart window with a see-through and opaque operating modes. However, this solution is too bulky and defeats the spirit of the ultrathin film ATF approach taken in this work. It is clear that transmission based devices will not achieve the ATF dynamic optical

response goals, outlined at the beginning of the chapter on p.238-239, in the ultrathin regime. Just as was done with Si, Ge, TMDs, and the WO_3, NiO can also be backed with a range of different reflective or lossy metals to widen the colour gamut and increase light trapping at different resonant wavelengths depending on overall TMO thickness [73], [74]. The following explores the optical response of TMOs in this compact bilayer setup in the ultrathin regime and at thicker layers above 100 nm where the 1st FP mode can also start to be accessed.

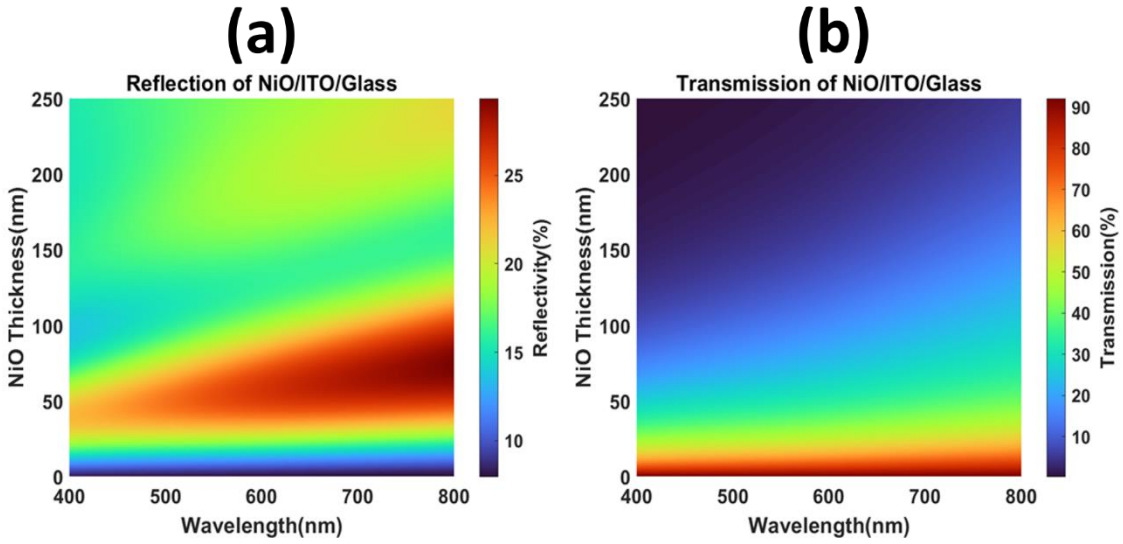


Figure 5.20. The intensity spectra (a) reflectivity and (b) Transmission for NiO on ITO/Glass. The response is very flat with higher reflection in the red at 800 nm wavelength.

5.4 Absorption & Contrast of the Zeroth, & Higher, Fabry-Perot Mode in NiO

5.4.1 Strong Absorption & Dynamic Contrast for NiO on Metal Backing

The colour, reflection intensity, and magnitude of change possible for both, when intercalating these zeroth order NiO FP stack structures with H+ ions from the electrolyte KOH, were all investigated. Tungsten is the first backing metal considered due to its durability as a refractory metal when testing the EC behaviour of the NPVD produced WO_3. This metal also adheres quiet well to glass unlike thin film Au or Ag which require an adhesion layer to improve stability on glass and guard against dewetting [75], [76]. Figure 5.21 below illustrates the reflection intensity and phase delay surface maps of NiO on tungsten as a start. Only the first and zeroth FP mode can be seen as highlighted by the white

dashed lines. The stack is absorbing for all wavelengths across the visible and the spectral dispersion is flat. At 150 nm NiO thickness the colouration leans slightly towards the red. Like with the other lossy dielectrics the zeroth order FP mode overlaps exactly with the lowest broadest absorption band in the reflection intensity surface plot. Interestingly the thickness regime is no longer between 10-30 nm as it was with Si, Ge, and MoS_2, but instead ranges between 50 nm in the blue to around 75 nm in the red. This is due to the lower real index n of NiO which curtails how ultrathin the zeroth band solution can be.

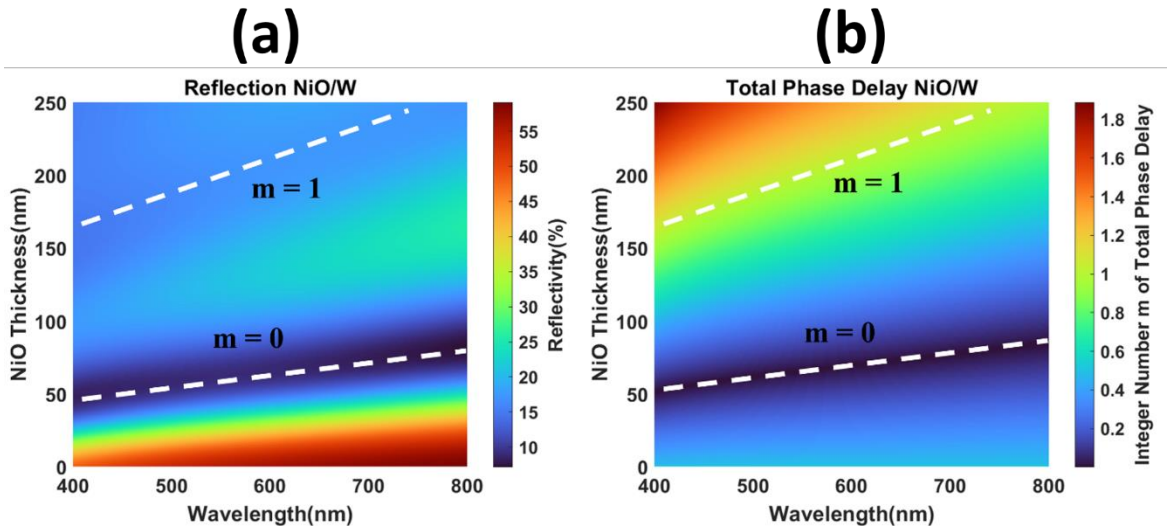


Figure 5.21. (a) The simulated zeroth FP mode absorption band is clearly visible while the 1st order FP absorption band does not stand out relative to off-resonance. (b) the phase delay response of NiO/W. In this instance, the zeroth mode is no longer completely below 50 nm as was the case with the TMDs, SI, and Ge. It instead ranges between 50-75 nm in a straight band.

If the NiO is bleached and the thickness sweep is widened even further to 0-500 nm, one can start to see dispersion in the spectral response due to the presence of the higher order FP modes that could aid in structural colour generation. See Fig.5.22 below. This colouration can only be accessed outside the ultrathin film regime, because even the lowest higher order FP mode at $m = 1$ does not exist below a thickness of 100 nm for NiO in the visible region.

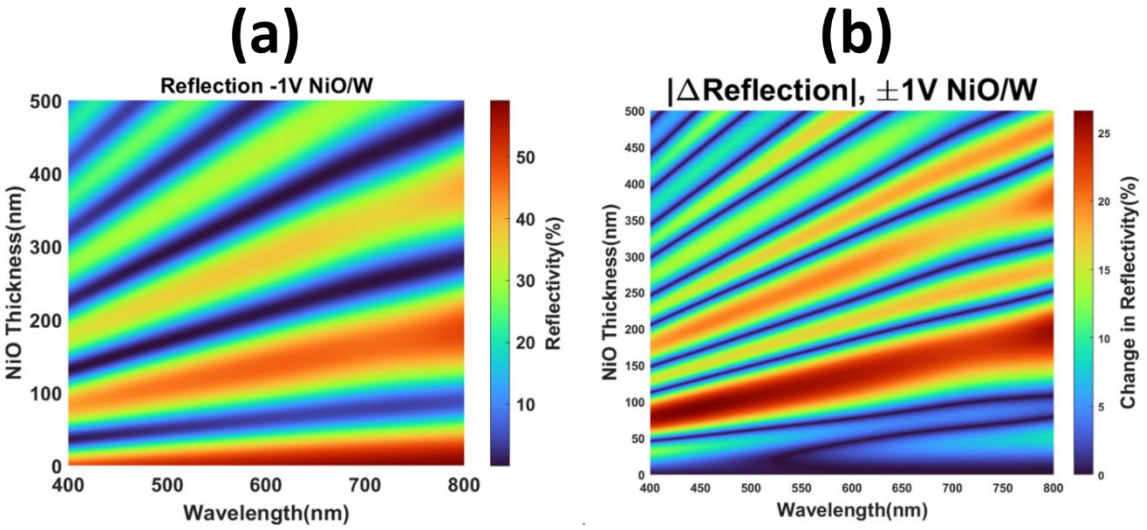


Figure 5.22. (a) When bleached the simulated NiO/W stacks will become more reflective along certain bands associated with the FP modes as the NiO now acts as a slightly lossy AR coating. Since it is lossy there is still a zeroth mode solution though not as strong as the first second and third mode at attenuating light. (b) The simulated change in reflectivity when bleached and absorbing is greatest within the region of 100 nm NiO thickness. It will be seen that more reflective metal back mirrors push this ideal zone lower into the depths of the ultrathin film regime around 50 nm and lower.

Interestingly it can also be seen that the change in reflectivity or on/off state contrast is greatest near the ultrathin film regime in Fig.5.22(b) for NiO/W, indicating that the EC response may also be well suited to changing a 2D broadband absorber into a broadband reflector for lossy TMO coatings. One application for this is smart mirror technology that can turn off and on at the behest of the user, and given how ultrathin the TMO layer is, the switching speed could be rapid below a second compared to conventionally slower bulkier EC devices that take many seconds to change their state [7]. The more reflective the backing metal is in a TMO based device , the greater this contrast will be. Thus, backing metals like Ag, Al, and Au are good candidates to work with. Furthermore, as a reminder the colouration range of TMD films backed with these metals was also more varied w.r.t film thickness (see chapter 4 p.206-207, so it is reasonable to think that the same trend may continue in lossy TMO stacks as well. The NiO EC response contrast reflection intensity graphs are plotted below in Fig.5.23 for the above-mentioned metals as well as the lossy metal Ni to act as a point of comparison to compare the low index metals to the higher index metals at a moment's glance.

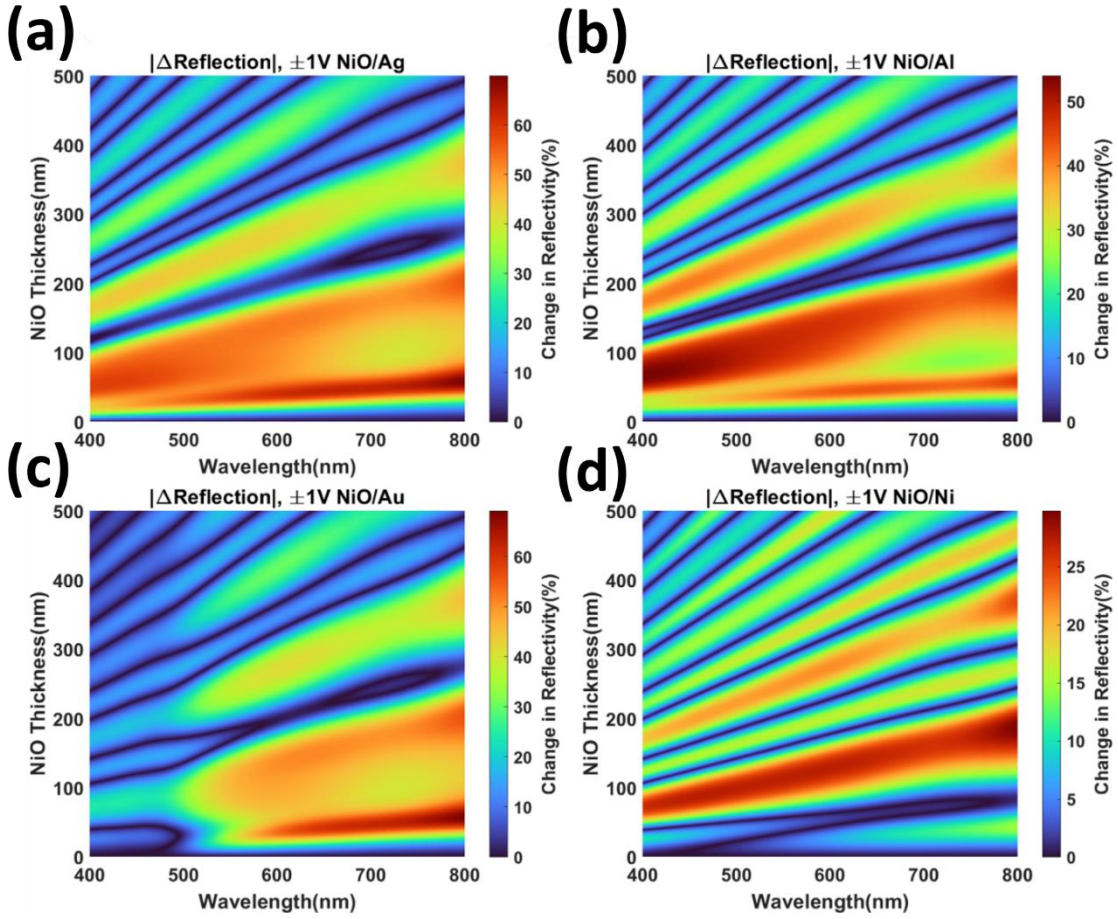


Figure 5.23. The simulated contrast between bleached and absorbing state for NiO on (a) Ag, (b) Al, (c) Au, and (d) Ni. Ag and Al give a similar response while Au has a drop-off in contrast below 500 nm wavelength. The strongest band in Ni is like the W backing response and is narrower than the noble metals. Dynamic red colouration may be feasible with films under 100 nm for Au.

Both Al and Ag backed NiO perform similarly with strong broadband contrast around and below 100 nm thickness. Strong contrast bands can also be seen in the 150 - 300 nm NiO thickness region that could enable dynamic switching of blue, green, and red hues into a colourless state. This dynamic colouration is enabled by the higher order bands being narrower and not as flat as the lowest and broadest high contrast region below 100 nm. Interestingly with Au the zeroth order strong contrast region does not extend below 500 nm wavelength allowing for ultrathin dynamic colouration solutions that would not be possible with the broader homogeneous response seen for Ag and Al in the same thickness regime. This is because of the interband transition that occurs for gold at around that wavelength [77]. The increase in absorption rapidly alters the normal refractive index of gold from far below to above unity, eliminating the reflective back mirror conditions needed for the light to remain trapped over multiple passes in the zeroth FP mode. The results with Ni backing are in line with the lossy metal W where overall reflectivity intensity magnitude is

significantly reduced, limiting whatever on/off contrast is achievable to begin with. Furthermore, the maximum change in reflectivity ΔR is less than half of what the noble metal FP stacks can achieve like NiO/Ag and NiO/Al.

Converting the contrast surface plot of NiO/Ag (see Fig.5.23(a)), the stack structure with the best dynamic contrast performance in terms of the absolute value of the reflection change, into a broad spectrum averaging of ΔR line plot gives a more easily interpreted and intuitive result accentuating just how influential the lossy nature of NiO is in enabling an ultrathin film zeroth order FP mode solution for large active contrast far beyond what is seen for other bulkier thin films while operating in reflection. See Fig.5.24 below.

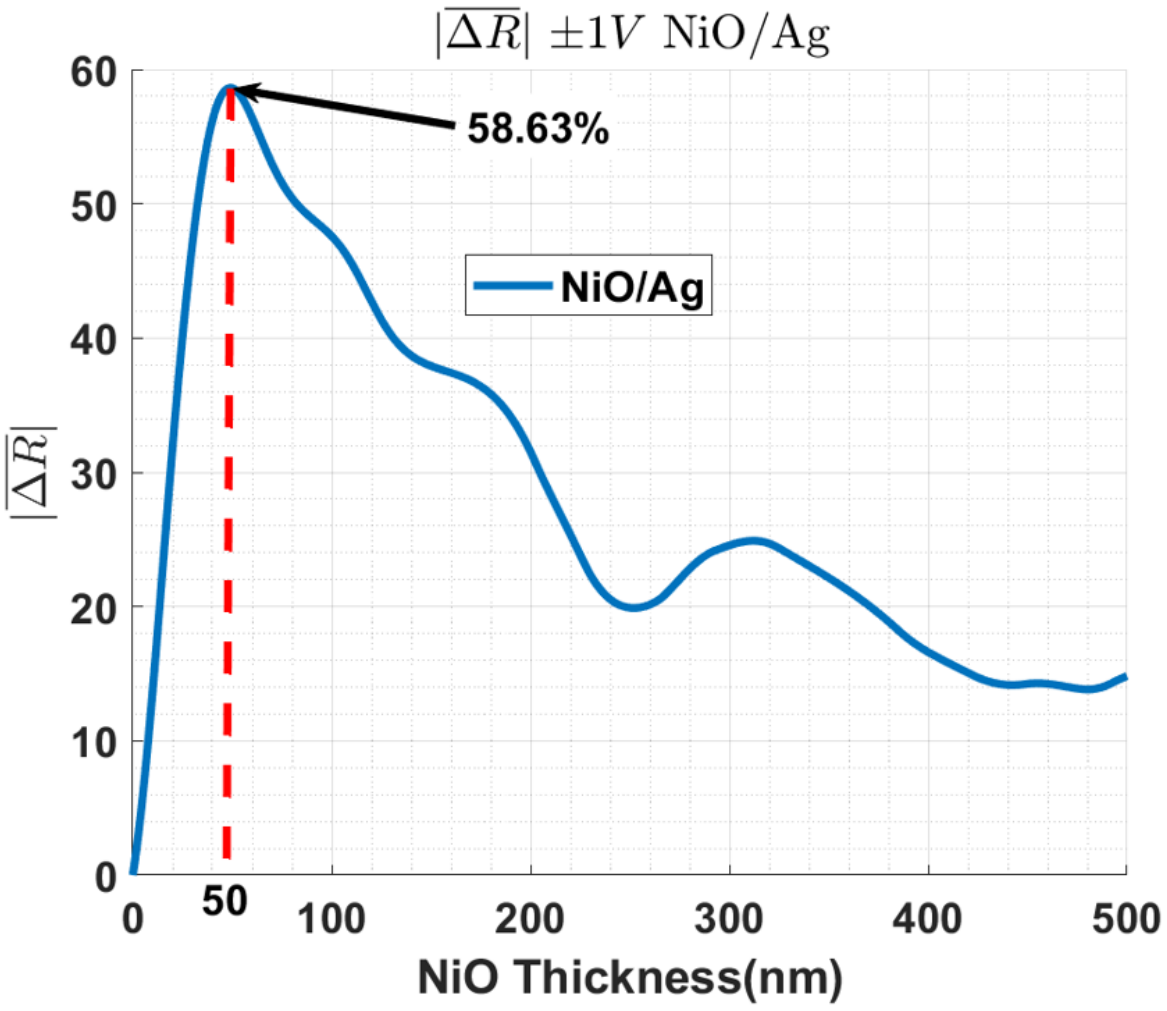


Figure 5.24. The simulated change in reflectivity response between the bleached and absorbing state of NiO on Ag, averaged across the visible spectrum. The average change is maximised at 58.63 % for a NiO thickness of 50 nm. The change is large as the NiO is acting as a thin film AR coating when bleached and a lossy absorber in the same vein as Si or MoS_2 when the ions are extracted.

In a real device operating outside of an electrochemical cell, the dynamic contrast would be reduced to some extent by the addition of bulky complementary layers needed to encapsulate and hold the KOH liquid electrolyte solution in place without leakage. Figure 5.25(a) below is a cross-sectional model of how such an EC device would look alongside the simulated ΔR line plot in Fig.5.25(b). The refractive index of KOH in the visible is taken to be 1.41 [78].

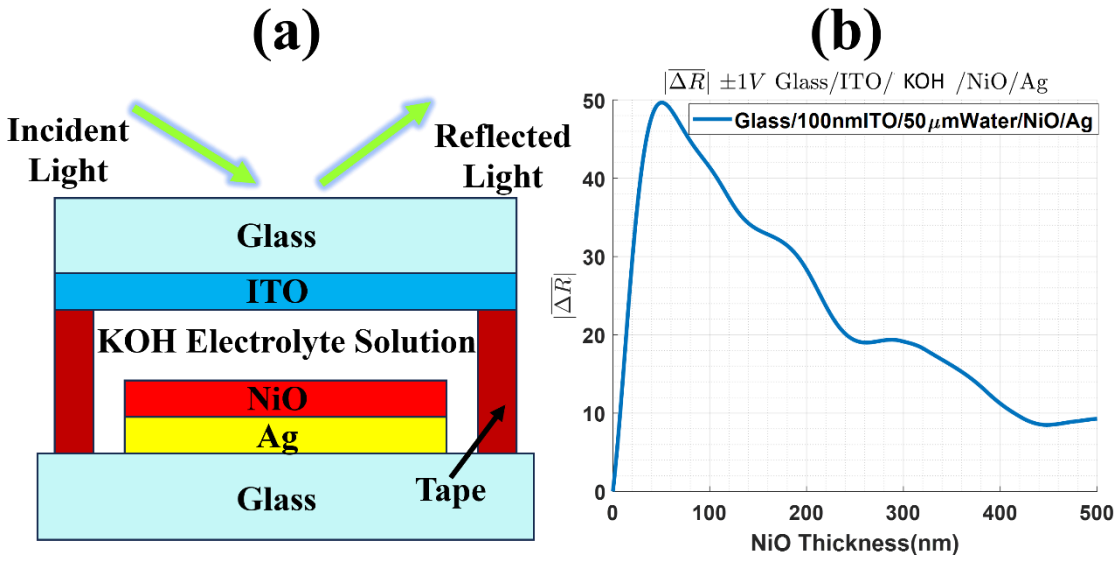


Figure 5.25. Sticky copper tape surrounds the EC stack, and a dropper is used to place a small amount of KOH on the NiO. Then the bulky ITO/Glass is placed on top to encapsulate the sample. The broadband contrast between on and off state is still large going as high as 50 % around a NiO thickness of 50 nm, which is 5 times larger than the average change at 500 nm thickness.

So far, it has become clear that there are two distinct regions for the EC response of NiO. The first is the ultrathin thin film regime where NiO on a reflective metal backing produces a broad and flat spectral response in both the bleached and as deposited (absorbing) state. The difference in reflectivity between both these states can be as large as 60 % on average across the visible for 50 nm of NiO on Ag. The second regime is for bulkier thin films above 100 nm where higher order FP modes can be accessed. Due to the greater dispersion inherent in their spectral response the colouration generated in the bleached state is more vivid that films in the ultrathin regime. Before the chromaticity diagrams for Al, Au, and Ag are shown, lets first look at how differences between UV-Vis spectroscopy measurements and SE data based TMM simulations were reconciled by incorporating the optical effect of consequential microscopic surface roughness as well as some other measures taken in the experimental methodology to help mitigate it. Namely, by reducing the electrolyte concentration and utilising materials more resistant to etching by said electrolyte.

5.4.2 Understanding Discrepancies Between the TMM & UV-Vis Data of the Zeroth, & Higher, Fabry-Perot Mode in NiO

Starting with the initial NiO/W sample made, the overall reflectivity and optical response curve is in line with a 60 nm NiO deposit shown in Fig.5.26 below. There is good agreement between TMM and spectral analysis for unbiased and positively biased NiO. However, the overlap between the simulated and experimentally measured bleached (negatively biased) NiO state spectra is low.

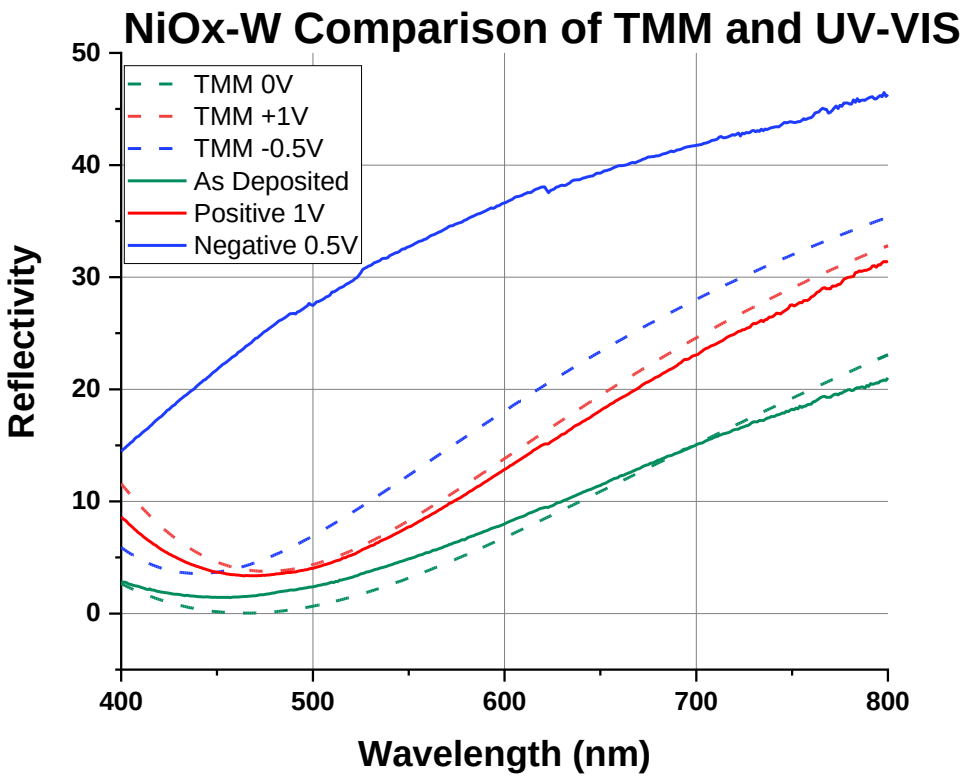


Figure 5.26. TMM matches observation relatively well, but the model fails for the bleached ion intercalated state. Clearly there is another feature that has not been accounted for. Microscopic surface roughness is the most likely culprit and given the porous nature of NiO it stands to reason that the surface may not as planarized as one would hope. Etching of the NiO could also be a factor as well.

A negative bias is expected to increase reflection as hydrogen ions from the KOH travel into the NiO crystal lattice making it more transparent. As the TMM results above contradicts this, it calls into question what is really occurring to the sample during the EC bias change. The inconsistency in predictive accuracy also brought into question the validity of the SE data/models, and a closer look at the surface reveals considerable microscopic roughening or surface damage had occurred during the EC process, as seen in Fig.5.27 below using

AFM. The likely reason for the morphological change is either the degradation of the surface quality with repeated EC cycling (most likely not an issue with NiO given the low number of cycles performed before surface deterioration was noticeable [21]), and/or the etching of the metal-substrate or NiO. Etching of the NiO layer can also have a drastic effect as this changes the optical path length of the stack assembly by modifying the thickness, see chapter 1 p.22 eq.1.7. Both a combination of sample degradation and extreme microscopic roughening (which if indicated by SE is also likely just a sign of large deterioration in the thin film quality, wherein the normal assumptions made for layer homogeneity in TMM optical models no longer hold true [70]) likely explains the contradiction in the results. There was a realisation at this point that fixing the reproducibility issue was of paramount importance as characterising the EC effect would be difficult if many samples were being destroyed considerably in the process.

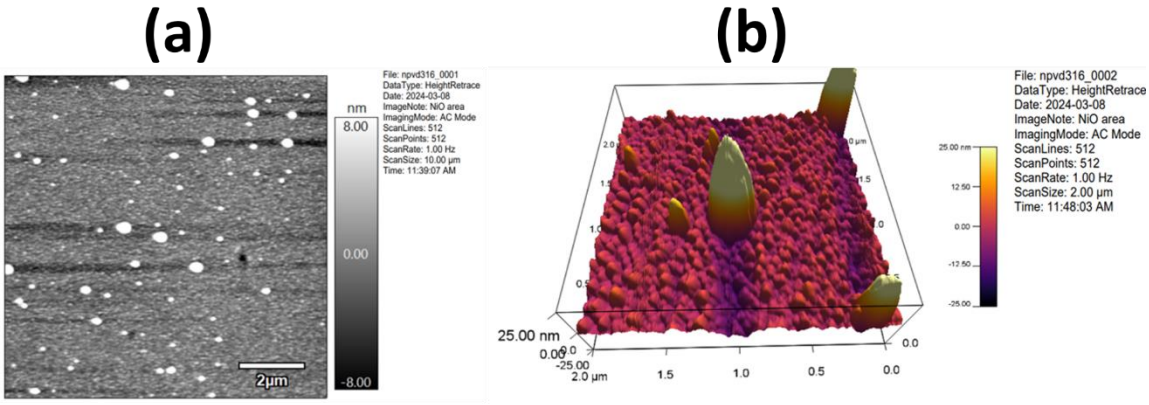


Figure 5.27. (a) AFM measurement of the microscopic surface roughness of NiO. The defects are widely dispersed on the micron scale and collectively push the RMS roughness to 7 nm. (b) A close-up view of the surface defects which themselves protrude as much as 25 nm. The porosity of the surface can also be seen in the striations across its plane.

Another difficulty to contend with when the surface quality drops so substantially the inability of the SE technique to ascertain a unique un-correlated fit that can accurately gauge NiO film thickness and the microscopic roughness layer thickness (which is modelled as an EMA mixture) together. If the best fit roughness is large compared to the true film thickness, then being off the mark in this respect can lead to erroneous simulated spectra results. Figure 5.28 instantiates this point with the SE data collected for the NiO/W seen in Fig.5.26. There is no consistency present in the thickness for any state of the NiO, and the roughness values predicted are large and vary wildly. XRR will have trouble with measuring such films as well, as the extreme surface roughness, or damaged low-quality surface (not smooth and

flat), can make a first principles analysis of the thickness quite challenging when trying to fit the XRR oscillation peaks. This is due to the assumptions of smooth isotropic planar layering of the stack no longer holding true.



Figure 5.28. SE data collected from NiO/W showcasing the difficulty in fitting each state of the NiO with the same thickness. The appearance of large surface roughness substantiates the AFM results. Roughness can also affect the best fit index of the NiO. The optical model is fitting the ellipsometer data well but with incorrect correlated results.

To solve this issue a strategy was developed to identify what was causing the most harm to the NiO surface during the ion intercalation process. It was believed that a good place to start was to reduce the concentration of the KOH electrolyte solution. Once it was established which concentration was acceptable to work with, one could then think further about adjusting the applied voltage and materials in use. Four electrolyte solutions were prepared and ordered by logarithmically increasing electrolyte concentrations 0.0005 M, 0.005 M, 0.05M, and 0.5 M. It was ultimately found that the concentration of the electrolyte solution in the range given was not the most relevant factor in NiO film surface stability. Indeed, for lower concentration, the EC response was decreased due to the reduced concentration gradient in the electrochemical cell. More on the electrochemistry is discussed in a later section of this chapter. In this case using NiO/Al, where Al was chosen due to its superior reflectivity and electrical conductivity compared to tungsten backing, SE and UV-VIS data were acquired before commencing the experiment to act as a static bias control. See Fig.5.29.

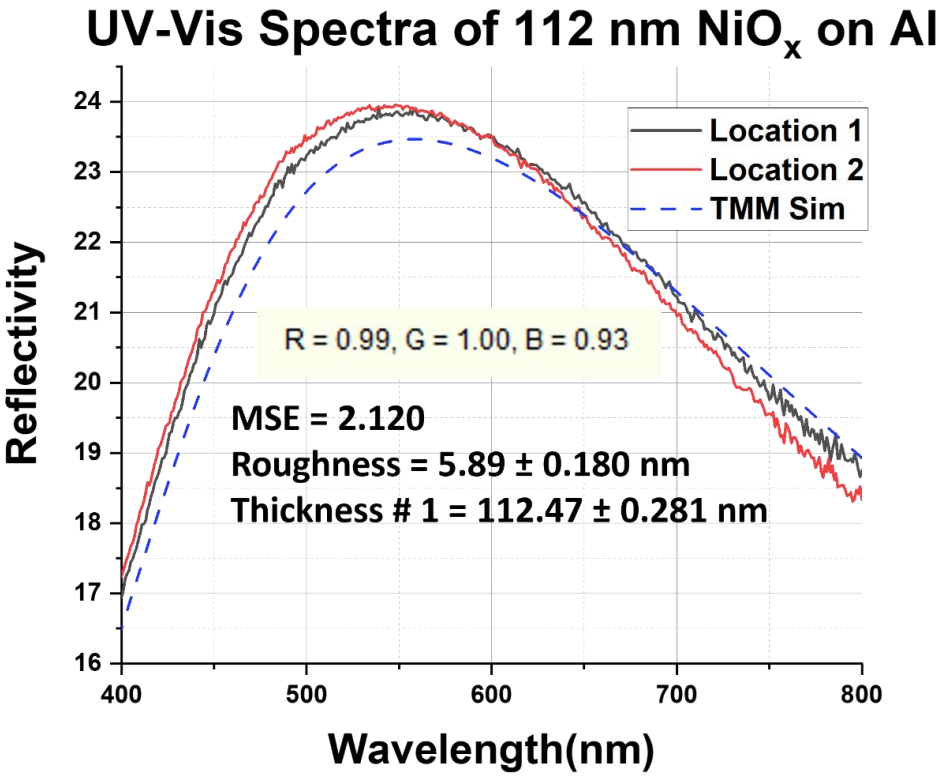


Figure 5.29. Another comparison of UV-Vis data and SE data at two different sample locations on 112.5 nm NiO, this time on Al. The agreement between simulation and experiment is quite good. The colour of the sample is a white beige.

Compared to overall NiO layer thickness, 6 nm roughness is quite small being just round 5 %. With this control set, both NiO/Al devices were split into separate samples and prepared for EC bias. Eight samples were used, and the SE data of the most relevant ones are shown below in Fig.5.30. There was no considerable improvement in sample integrity for lower ion concentrations like 0.005 M and 0.05 M compared to 0.5 M. The deciding factor then for sample destruction when biased seemed to be linked to immersion time and applied voltage magnitude. For sample A, the NiO became completely delaminated when biased at high voltages. During the delamination bubbles could be seen forming as the NiO detached away from the Al beneath. This led further towards researching the reactivity of different electrolytes with various materials and it became clear that when paired with KOH, Al was etched significantly if any part of its bulk was exposed to the electrolyte solution, see Fig.5.31 [79].

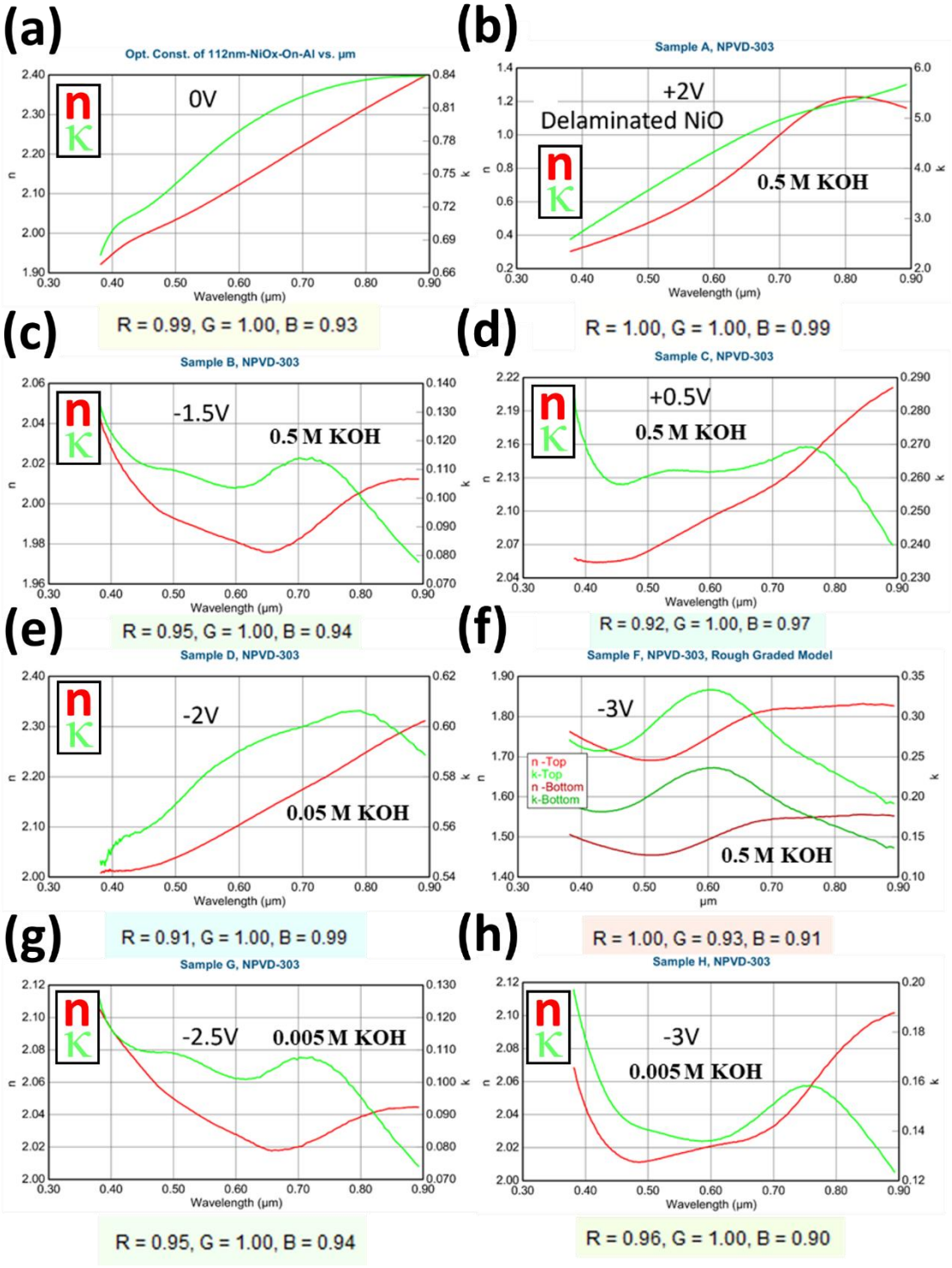


Figure 5.30. (a) Al is etched away rapidly by KOH. (b) Metals like Ag, Au, Ni, and W are unaffected so delamination of the NiO thin film is unlikely to occur. [79] *(a) SE data of the as-deposited 112 nm NiO on Al sample. The Final voltage applied and KOH concentration for each sample (b)-(h) is shown in black text on each graph. (f) sample F had a high voltage of 3V applied to it and a graded index behaviour with large roughness. It is likely to have been in the process of delaminating, and was removed before the etching process could destroy it. Sample G and B showed similar index change despite the different KOH concentrations.*

In contrast with this Ag or Au does not experience etching in this manner and is stable in KOH solution [79]. Likewise, W is also stable which leaves one with the conundrum of why the surface quality was poor enough for the ellipsometer to have difficulty in accurately modelling NiO/W as seen back in Fig.5.28. One possible answer is that the surface morphology may also be strongly affected by DC gun power supplied, which itself sets the rate of thin film deposition as well, alongside the surface evolving when exposed to KOH and EC intercalation of ions.

(a)

TABLE V
ETCH RATES OF AL, Ti, V, Nb, Ta, AND Cr (nm/min)

Etch	Aluminum Evap	Al + 2% Si Sputtered	Titanium Sputtered	Vanadium Evap	Niobium Ion-Mill	Tantalum Evap	Tantalum Ion-Mill	Chromium Evap	Chromium Ion-Mill	Patterned Cr on Au Evap
Si Iso Etch	60	400	300	9600	79	5.8	5.3	R 8.8	-	< 2.3
KOH	12,900	F	soft	< 12	3.2	S	2.8	4.2	-	0
10:1 HF	W	250	1100	S	S	S	S	S	S	-
5:1 BHF	11	140	W	< 2	0	S	R 0	0	< 0.3	P
Pad Etch 4	1.9	R < 15	< 2	S	S	S	S	S	S	-
Phosphoric	> 500	980	-	-	0	-	0	100	-	-

(b)

TABLE VI
ETCH RATES OF Mo, W, Ni, Pd, Pt, Cu, Ag, Au, TiW, NiCr, AND TiN (nm/min)

Etch	Molybdenum Evap	Tungsten Sputtered	Nickel Evap	Palladium Evap	Platinum Evap	Copper Evap	Silver Evap	Gold Evap	10Ti/90W Ion-Mill	80Ni/20Cr Evap	TiN Sputtered
Si Iso Etch	11,000	13	21	0	0	37	49	0	23	-	soft
KOH	0	0	0	0	0	T 0	T 0	0	> 300	-	-
10:1 HF	S	0	S	S	S	S	S	S	S	S	S
5:1 BHF	< 0.3	<2	< 1.1	0	0	R < 5	R < 5	0	R < 0.2	R < 1.5	2.5
Pad Etch 4	S	S	-	-	-	-	-	-	-	-	-
Phosphoric	-	-	-	-	-	-	-	0	2.5	-	-
Al Etch A	-	-	29	-	-	> 2900	-	-	-	-	-

Figure 5.31. (a) Al is etched away rapidly by KOH. (b) Metals like Ag, Au, Ni, and W are unaffected so delamination of the NiO thin film is unlikely to occur. [79]

If the DC gun is being used to create W and NiO at high power, then it is possible for the sample to become very rough on this fact alone. Furthermore, the increased microscopic roughness would likely be independent of thickness to a certain degree, as its occurrence is mostly coinciding with the higher collision frequency of liberated target adatoms onto the substrate surface, which explains why 6 nm roughness on a 112 nm NiO on Al could be considered quiet smooth compared to an equally rough but thinner 60 nm NiO film on W. 6 nm roughness would be proportionately different in each case.

A comparison between TMM simulations and UV-VIS data of the 112 nm NiO on Al samples A-H is given below in Fig.5.32, exhibiting mostly good agreement between model and measurement. NiO becomes much more dielectric in character when bleached. Indeed, the dispersion relation almost becomes normal, in-line with a Cauchy fit with a slight deviation present from the small amount of absorption still occurring. Sample H and G deviate due to damage done to their surfaces because of the KOH etching into the Al underneath. The small size of the remaining active material made it difficult to align exactly with the large ellipsometer beam spot, creating data with mixed NiO and glass features.

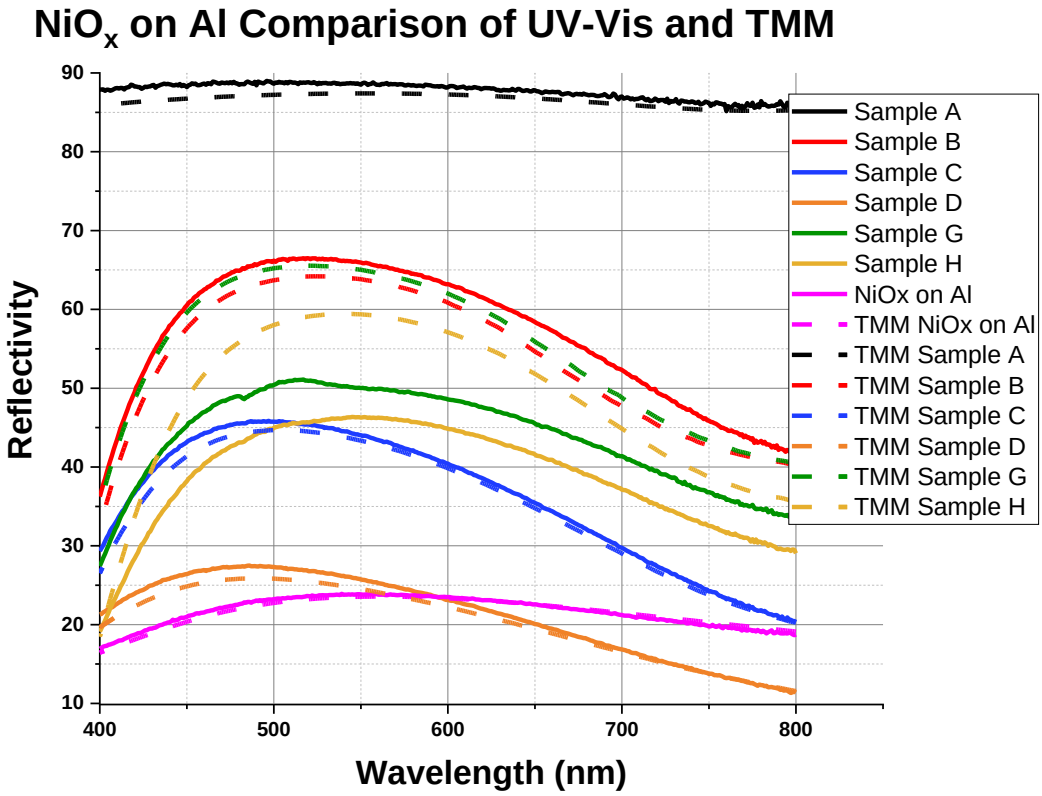


Figure 5.32. A comparison between UV-Vis data and TMM simulations based on SE data for samples A-H. Good agreement is seen except for sample G and H where significant damage was accrued due to the KOH etching into the Al metal underneath the NiO.

By abandoning the use of Al and lowering the power of the magnetron sputtering DC gun to between 5-10 %, and in some cases availing of the RF gun to make NiO, excellent agreement was obtained between TMM and UV-Vis results as revealed in Fig.5.33 for ultrathin 44 nm NiO on Ag backing metal.

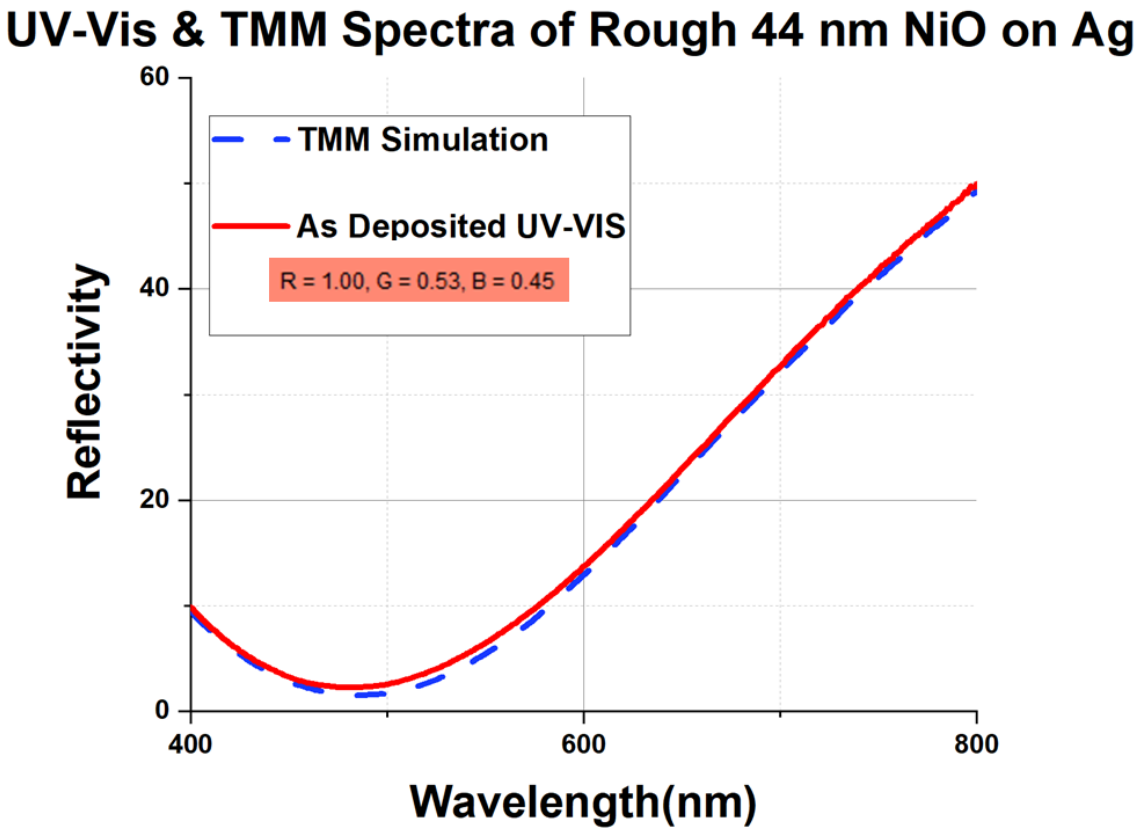


Figure 5.33. Lowering the DC gun power and O_2 flow rate, the NiO on Ag ellipsometer data fit very well to the optical model with the inclusion of a 4 nm roughness layer. UV-Vis spectral data and TMM simulation results almost perfectly overlap underscoring the improvement in the fitting accuracy.

The change in index between bleached and absorbing state for H^+ intercalated NiO on Ag using KOH is graphed below in Fig.5.34. The change in index is much more substantial than the results seen with H_2SO_4 protonated WO_3. The voltage for the absorbing state is 0 V as this is the default state of NiO. When cycling from the bleached to the non-bleached state, a voltage of + 1-2 V is done to be able to extract the ions that have diffused their way into the lattice.

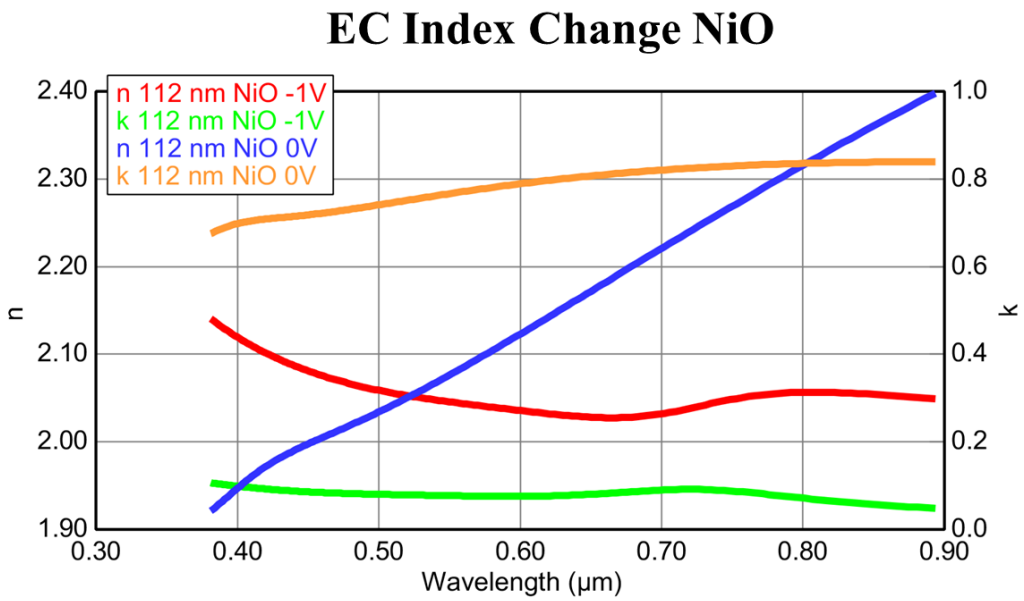


Figure 5.34. Refractive index change of KOH protonated 112 nm NiO on Ag. In the absorbing state the $n \approx 2\kappa$ while in the transparent bleached state the optical response of NiO is like a normal transparent insulating dielectric solid. The magnitude of this change is much higher than the result seen for H_2SO_4 protonated WO_3.

5.4.3 Dynamic Colouration of the Zeroth, & Higher, Fabry-Perot Mode in NiO

On p. 258 it was indicated that the more vivid and dynamic colourations of NiO are found in the thicker film regime using Ag, Au, and Al. Al is also shown for comparison though in fact KOH should not be used with Al for the reasons discussed above regarding chemical etching on p.264. Its optical response is very similar to Ag. See Fig.5.35-5.37 below. Ag will not be chemically etched by KOH either like Al and is the best back reflector in terms of colour brightness compared to the spectra produced by lossy back metal FP stacks with W or Ni. Ag is also both the most reflective and conductive pure metal, thus at first glance one may think it the ideal candidate for creating dynamic colourimetric EC devices.

Although the colour gamut seen for Ag backed NiO is greater than Au, the EC dynamic colour contrast is significantly better for Au backing across all NiO thicknesses with a similar level of brightness produced, as Au is also a good conductor with a plasma frequency located deep in the UV [77]. This increased colouration contrast is directly attributable to the interband transition in gold below 500 nm wavelength as discussed on p.258, causing greater spectral selectivity in the optical response. NiO/Au stacks also display vibrant green hues for very thick films at 340 nm and above, though this is not as impressive as one might think given that the strong colouration seen in the oxide capped ultrathin Ge film (sub 50 nm) lossy resonators on p.225 can do the same with markedly less material and device

thickness. As a rule of thumb, higher order FP modes almost always have greater spectral dispersion and therefore a better capability to generate more unique hues.

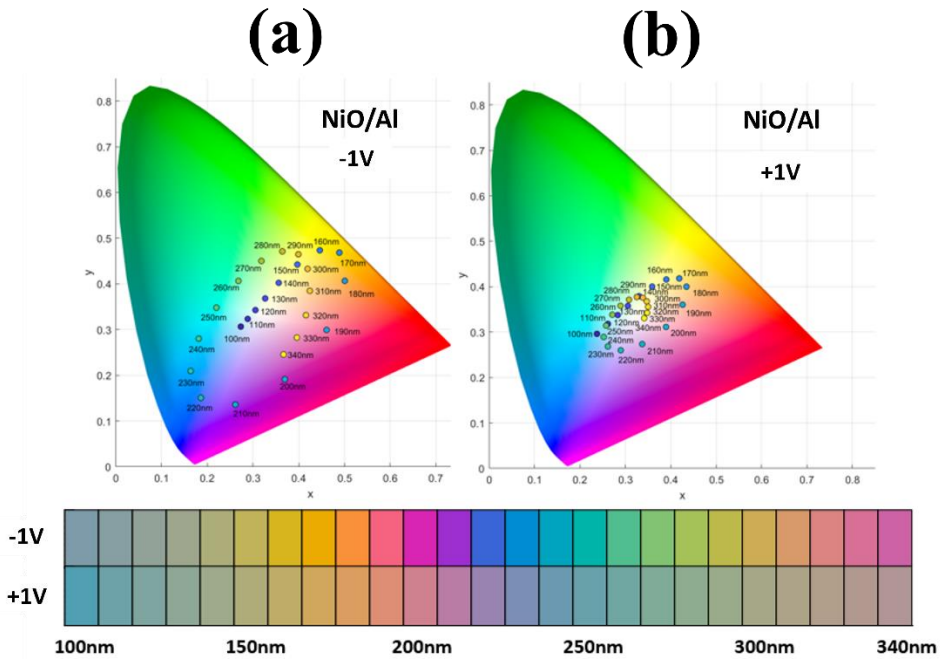


Figure 5.35. (a)-(b) The simulated colour gamut for ± 1 V KOH NiO on Al. In truth the Al would be etched away. When backed with Al, bleached NiO does shows many vivid colours between 150 nm and 340 nm.

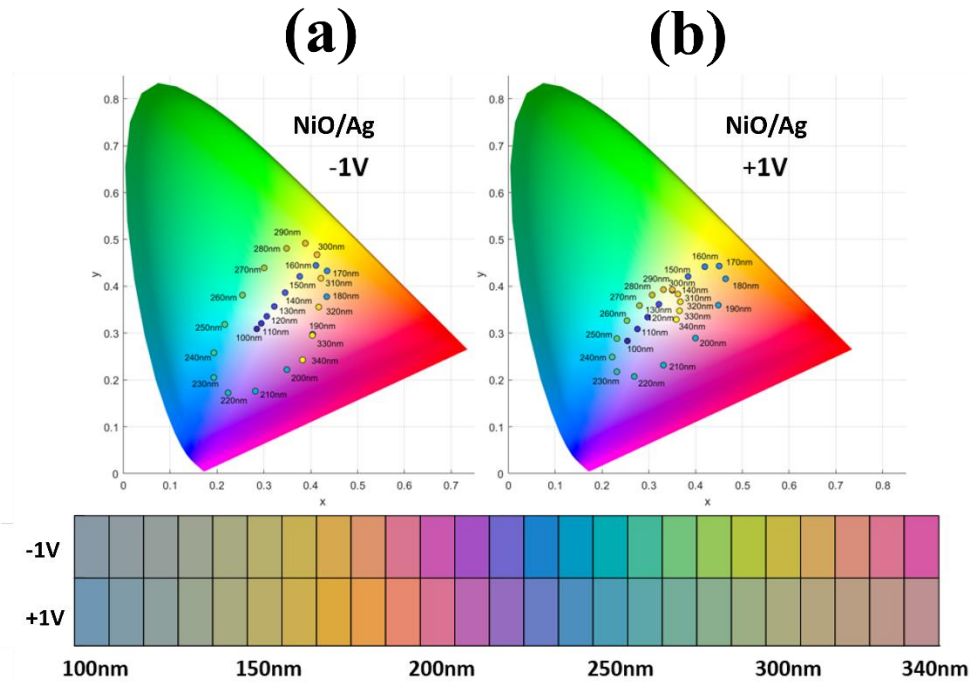


Figure 5.36. (a)-(b) The simulated colour gamut for ± 1 V KOH NiO on Ag. The colour response is like Al with slightly less ellipticity in the gamut. The change is colouration is not particularly large even for thicker films above 200 nm.

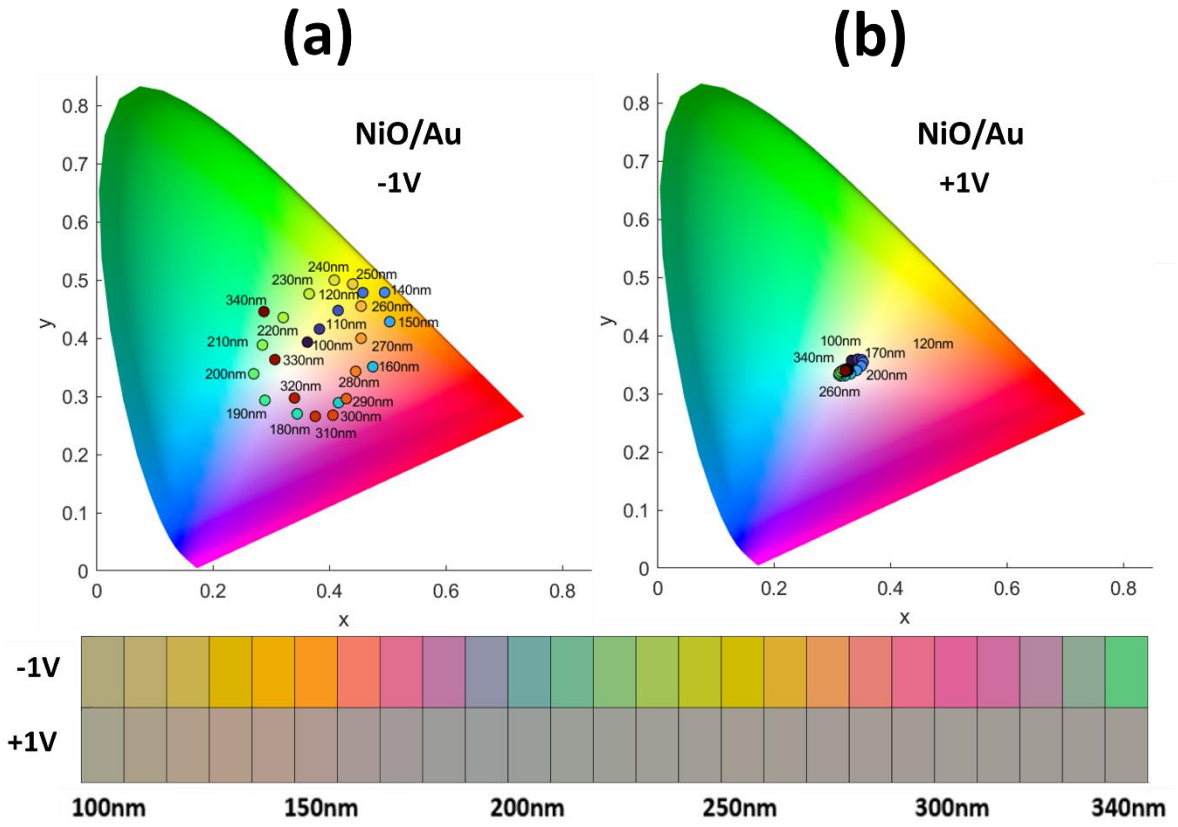


Figure 5.37. (a)-(b) The simulated colour gamut for ± 1 V KOH NiO on Au. The colour response is quiet a departure from the other two metals. The lack of reflection change below 500 nm causes the colouration to heavily favour orange hues when NiO is bleached. Therefore, even though the colour gamut is smaller, the colouration change is substantial going from drab greys to vivid tangerine hues between 100-340 nm. Some green hues can also be found in the thickest NiO stacks.

It can be concluded that the colouration properties of NiO/metals stacks are certainly superior in the bulkier thin film regime than the ultrathin film regime, where instead large broadband contrast in reflection is the dominant phenomena observed. Thus, where the ultrathin film regime is concerned, metal backed lossy TMOs are not the most effective way at generating a wide gamut of structural colour as seen with TMDs, Si, and Ge. Of course, this only pertains to the absorber/metal zeroth order FP cavity structure. Other FP resonator devices like ATF Fano-resonant stacks can in principle make vibrant, saturated, and bright structural colour using sub 50 nm NiO. More on this will be looked at in chapter 6.

5.4.4 Layer Resolved Absorption & Angle Response of the Zeroth, & Higher, Fabry-Perot Mode in NiO

Before moving onto a description of the methodology of the electrochemistry underlying liquid electrolyte electrochromics, the layer resolved absorption and angular dependence of the reflection spectrum is analsyed for NiO on Ag and Au metal backing in the as deposited

and ion bleached state. Starting with the former state, within the zeroth order FP band effectively all the incoming light is attentuated in the top NiO coating as shown below in Fig.5.38. This elimination is more efficient than in ultrathin MoS_2 or WS_2, with the added bonus of it being a broadband effect not just localsied to an excitonic resonance state.

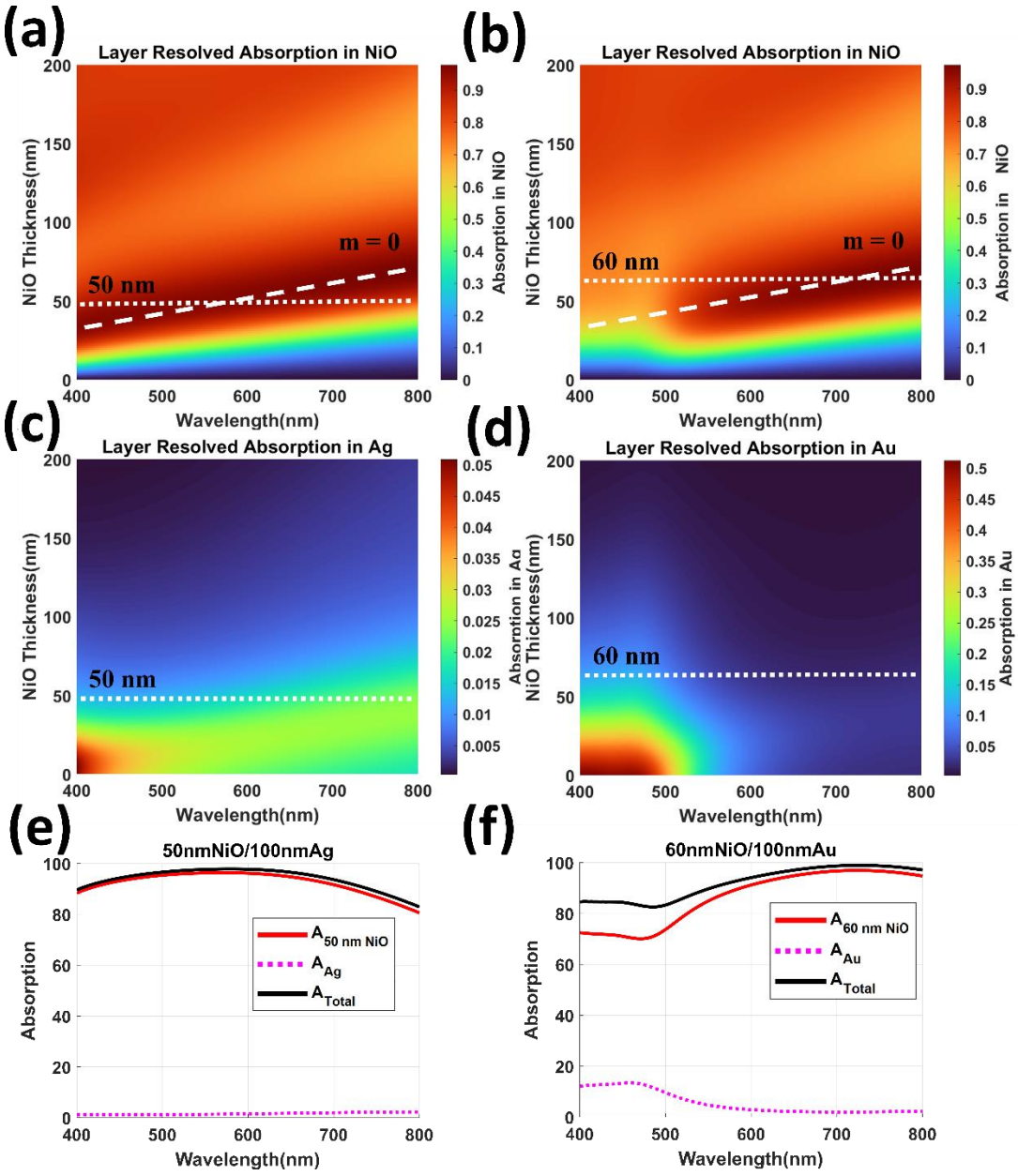


Figure 5.38. Absorbing state (a)-(c) The layer resolved absorption in a NiO/Ag stack, (b)-(d) The layer resolved absorption in a NiO/Au stack. (e)-(f) line plot of the visible spectrum attenuation of light in the NiO and back metal. Light trapping in the NiO is very strong for Ag backing. A similar trend exists for Au with the caveat that the intense trapping drops off below 500 nm wavelength.

A line plot is given for the attentuation of light for 50 nm of NiO on Ag and 60 nm of NiO on Au. These locations are chosen for their strong local absorption, and in the case of Ag,

the NiO thickness with greatest on/off contrast is also 50 nm. The spectral position of the broad absorption peak (when NiO is bleached) at this thickness coincides approximately with where the normal refractive index of NiO in the absorbing and bleached state is the same as well. The light-matter trapping in the NiO film for NiO/Au is reduced to a certain extent below 500 nm wavelength as well, due to Au itself becoming absorbing, see Fig.5.39(f).

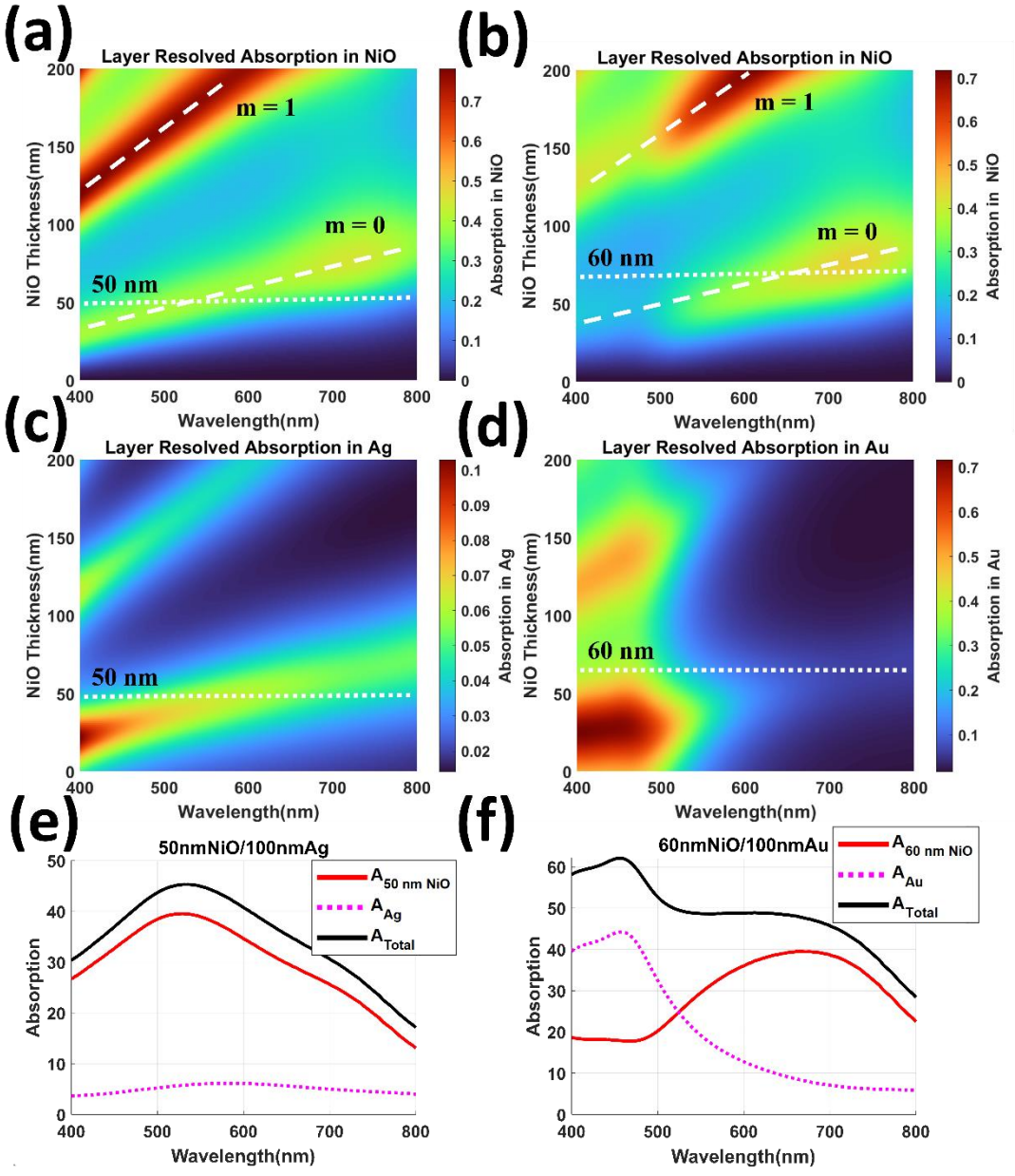


Figure 5.39. Bleached state (a)-(c) The layer resolved absorption in a NiO/Ag stack, (b)-(d) The layer resolved absorption in a NiO/Au stack. (e)-(f) line plot of the visible spectrum attenuation of light in the NiO and back metal. Light trapping in the NiO remains strong, though overall absorption has dropped substantially. Au now absorbs significantly more of the incoming light than NiO below 500 nm wavelength in the zeroth FP band.

When NiO is transitioned into its bleached state, the light matter interaction changes as Fig.5.39 reveals. For the NiO/Ag stack a zeroth mode band is still apparent but diminshed compared with the more absorbing as depsoited NiO state with larger κ. The same is true for Au backing. For both metals the light is now more strongly confined in the higher 1st order FP mode than in the zeroth FP mode, once again highlighting the importance of having both large n and κ for the zeroth FP mode to be accessible. The overall absorption within the top NiO layer has substantial dropped for NiO/Au and the flatness of the optical repsonse has been reduced as well. This coroborates the bleached state colouration gamut in the chromatcity diagram in Fig.5.37 which is much wider than the as depsoited NiO state.

The omnidirectionality and polarisation reponse of the zeroth FP mode band is investigated in Fig.5.40 below for p and s orientation on Ag and Au backing.

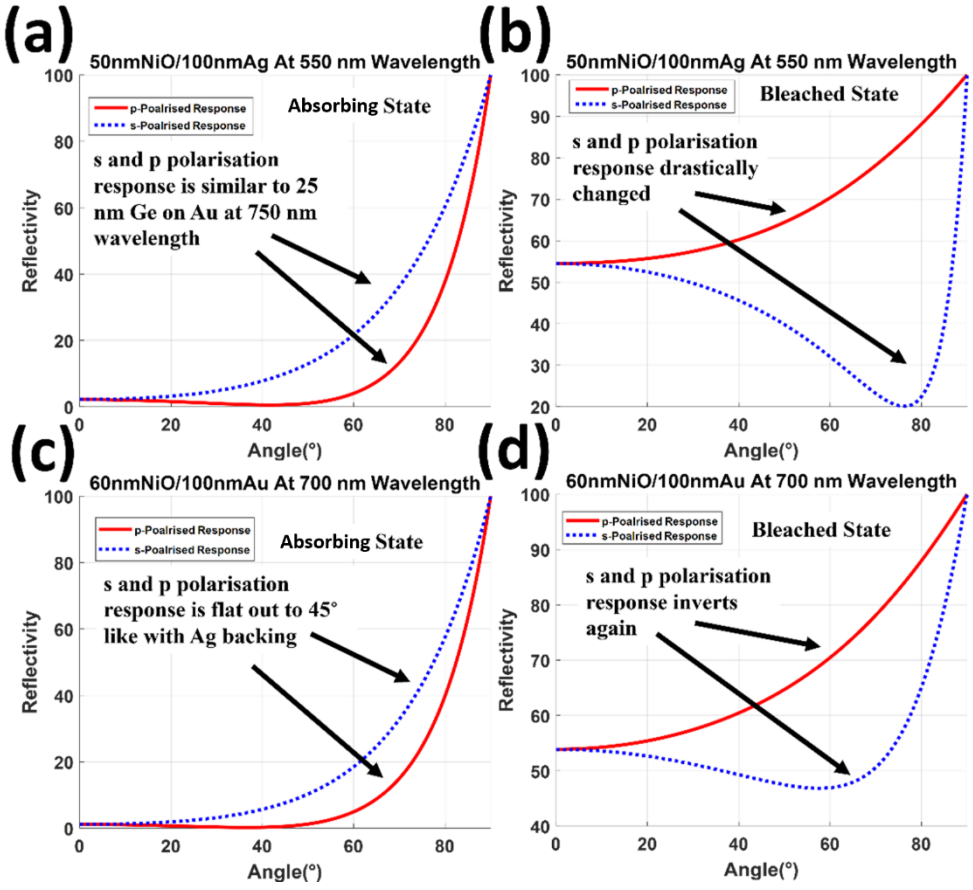


Figure 5.40. (a)-(b) Simulated angle and polarisation response of 50 nm NiO on Ag in the absorbing and bleached state. When NiO is lossy the stack has omnidirectionality comparable to the 25 nm Ge on Au discussed in the previous chapter. When bleached the NiO acts as a slightly lossy AR coating and the stack becomes iridescent. (c)-(d) simulated angle and polarisation response of 60 nm NiO on Au in the absorbing and bleached state. The absorbing and bleached state angular and polarisation response is similar to Ag backed NiO.

Both NiO/Ag and NiO/Au have an omnidirectional response analogous to Ge and Si on metal. However, when NiO is bleached the trend of the light orientation curves flip with s-polarisation reaching a minium at 60˚ for Au backing and 75˚ for Ag backing. Moreoever, the angle sensitvity is greatly increased in the bleached state, as the extianction coeffiient κ of NiO is considerably reduced. Naturaly the flat optical response is relagated to the ultrathin film regime only, due mostly to the low phase delay on propagation accumulated, so higher order modes will not benefit even if absorption is strong. See Fig.5.41 below clarifying this.

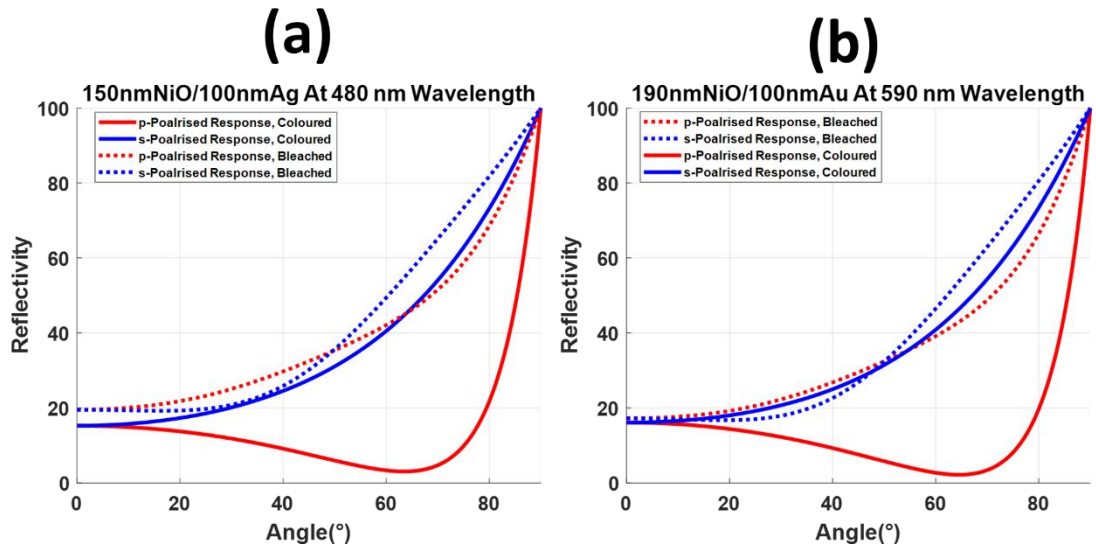


Figure 5.41. (a) Simulated reflectivity in a 1st FP mode strong absorption region in the NiO/Ag stack. (b) Simulated reflectivity in a 1st FP mode strong absorption region in the NiO/Au stack. The change in polarisation response when bleaching and extracting ions is only significant for the p-polarisation. The angle sensitivity is notably increased compared to the zeroth mode in Fig.5.40 for both orientations of light.

The remainder of this chapter will focus primarily on the relfection contrast capabilities of NiO on Ag in the ultrathin thickness range 20-100 nm as this regime remains relatively unexplored in the EC literature and worth further study and attention. Most importantly, being able to utlise the very strong broadband variance seen in this region is of the utmost relevance and interest for enabling future potential low energy fast EC display technology that may operate competeively with LCD and LED displays, or higer contrast large macroscopic dimmable smart windows as was discussed in section 5.1 on p.237-238 [24]. With this in mind, characterisation of EC parameters like the colouration efficiency, optical density and TMO film charge capacity becomes essential to quantifying the forte and limitiations of devices in this regime. To understand how the EC parameters can be found the following section will review the fundamanetal details of the electrochemical

measurement methods like cylic voltammetry (CV) in a 3-electrode cell system configuration and chronoamperometry (CA).

5.5 Explanation of CV & CA to Characterise the EC Parameters

5.5.1 Description of the Electrochemical Reduction Chemistry

Electron transfer processes lie at the heart of inorganic molecular electrochemistry, especially regarding the electrochromic materials covered in this work. Alongside this there are also great innovations in sustainable green energy like the revolutionary rechargeable lithium ion battery which is enabling the implementation of transformative technology like competitive fully electric cars and long-lasting powerful mobile devices [80]. In inorganic electrochemistry, chemical reactions, primarily reduction and oxidation, are driven electrically instead of chemically [81]. Using ferrocenium, $[Fe(Cp)_2]^+$, reduction as an example; the following chemical equations are used to describe the reversible reaction of Fc^+ to Fc.

$$Fc^+ + [Co(Cp^*)_2] \rightleftharpoons Fc + [Co(Cp^*)_2]^+ \quad (5.2)$$

$$Fc^+ + e^- \rightleftharpoons Fc \quad (5.3)$$

Where $[Fe(Cp)_2]$ is abbreviated as Fc , Cp is cyclopentadienyl, Cp^* is pentamethylcyclopentadienyl, e^- is an electron, Co is cobalt, and $[Co(Cp^*)_2]$ is a cobaltocene. In the chemically driven case, $[Co(Cp^*)_2]$ reduces Fc^+ by transfer of one of its electrons in the highest occupied molecular orbital (HOMO) to lowest unoccupied molecular orbital of the Fc^+. In the language of thermodynamics this reaction proceeds because the LUMO of the receiver sits lower in energy than the HOMO of the donor molecule as illustrated in Fig.5.42 below [81]. Therefore, the transformation is driven by a difference in the energy level of the chemically bound electron.

In contrast to this, the electrochemical reduction proceeds by applying an external potential to an electron using an electrode. This action drives heterogeneous electron transfer from

cathode to the Fc^+. The potential applied must be large enough to energise the electron into the LUMO of Fc^+. For chemical reduction the reaction occurs spontaneously but with the drawback being that a chemical reductant is needed. For the electrochemical reduction one must use an electrode to modulate the electron energy with no reductant molecule needed. The main advantage of electrochemistry thus lies in its ability to simplify the measuring of thermodynamic and kinetic factors while also eliminating the influence of an additional reductant in the reaction. Furthermore, the process of the electrons moving can be controlled tightly by adjusting the potential of the electrode while the chemical reductant will operate extemporaneously [81].

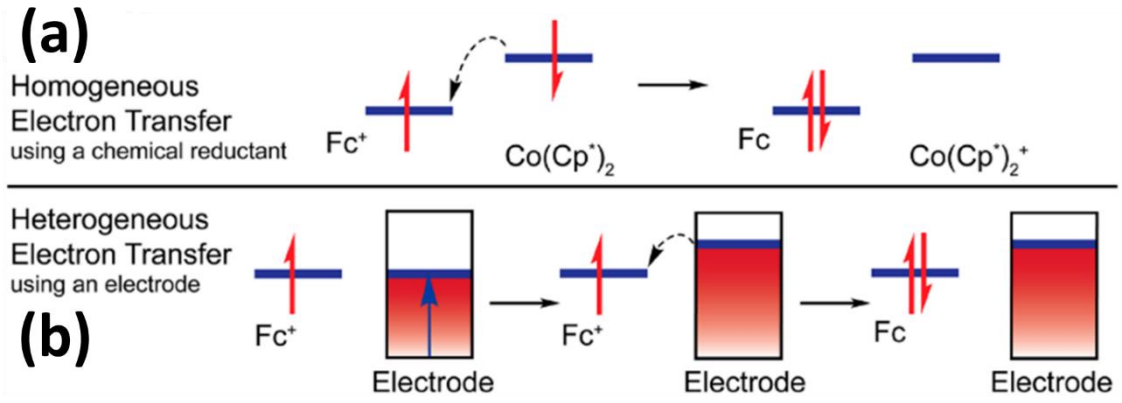


Figure 5.42. (a) Homogenous reduction of Fc^+ chemically driven by a molecular reductant. Total charge is conserved (b) heterogeneous transfer of electron from cathode to Fc^+ when the fermi level of the electrode is above the HOMO of Fc^+. In both cases the LUMO is fully occupied producing Fc. [81]

Cyclic voltammetry is an electrochemical technique that characterises the transfer of electrons to drive reductive and oxidative processes [81]. The data collected from CV cells will often be displayed as current versus voltage voltammograms. The traces in these graphs will likely take on the shape of a duck's bill due to the chemistry of electron transfer. See Fig.5.43 below for an outline of the US and IUPAC conventions on displaying CV data. In this work, the IUPAC convention is used.

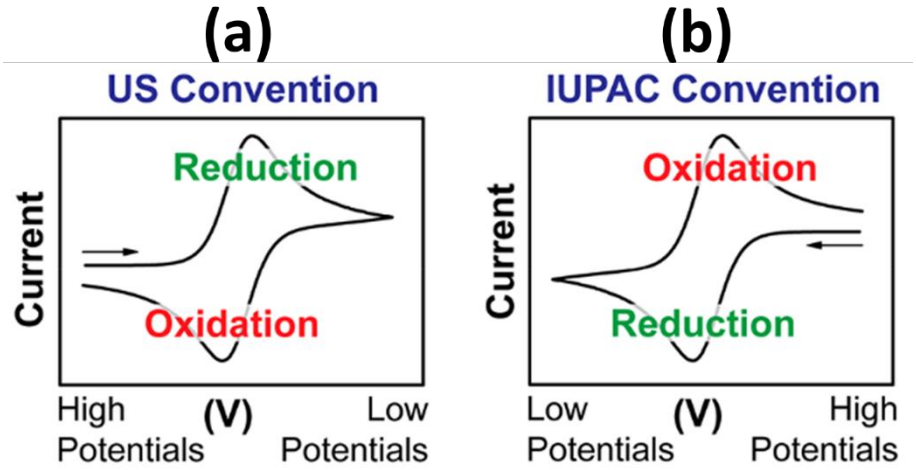


Figure 5.43. The US convention sweeps towards reduction first while the IUPAC does the opposite. Arrows indicate the direction. Current density may sometime be plotted instead of current on the y-axis.[81]

One of the most important parameters controlled in the CV setup is the scan rate which is the linear rate at which the voltage produced by the electrode is swept through [81]. Faster scan rates result in smaller diffusion layers forming in the electrochemically reduced material, increasing peak current observed in the CV diagram. The Randles−Sevcik equation, for simple reversible redox events, relates several key parameters together to predict the magnitude of peak current I_p, expressed below [81].

$$I_p = 0.4463n \cdot FAC\left(\frac{nFvD}{RT}\right)^{\frac{1}{2}} \qquad (5.4)$$

Where n is the number of electrons transferred in the reduction, typically $n = 1$ as is the case for bleaching and colouration of NiO. F is Faraday's constant, A is the area of the working electrode immersed in the CV cell, C is the concentration of the analyte, D is the diffusion coefficient of the analyte after oxidation, v is the scan rate, R is the gas constant from the ideal gas law in thermodynamics, and T is the temperature of the system. Higher values of v induce a larger concentration gradient at the electrode following directly form the Nernst equation [81].

A cathodic trace begins the CV experiment at a negative potential and scans up to the maximum positive voltage. Then the anodic trace begins to re-establish the starting

conditions. For an electrochromic material like NiO, the CV measurement would begin with bleaching the NiO with a negative voltage, followed by a scan up to positive potential maximum to enter the absorbing state. The reason this combined trace hysteresis is shaped like a duck bill is due to the previously mentioned Nernst equation which governs the equilibrium between the reduced and oxidised state concentrations. An equation relating the ratio of these two to the cell voltage and some additional thermodynamic parameters is expressed below [81].

$$V_{cell} = V_{cell}^{0} + \frac{RT}{nF} \cdot ln\left(\frac{C_{Reduced}}{C_{Oxidised}}\right) \quad (5.5)$$

Where V_{cell} is the potential applied to the CV cell, V_{cell}^{0} is the standard electromotive force (EMF) of a cell as it relates to the reducing power of the analyte being used, $C_{Reduced}$ is the concentration of the reduced chemical species, and $C_{Oxidised}$ is the same but for the oxygenated state. Again, n is normally taken to be unity for simple electrochemical reactions. V_{cell}^{0} can be estimated experimentally from the $E_{1/2}$ value which is the average potential between the top peak and bottom trough of the duck bill shaped hysteresis CV trace as shown below in Fig.5.44 for the ferrocenium reduction to ferrocene.

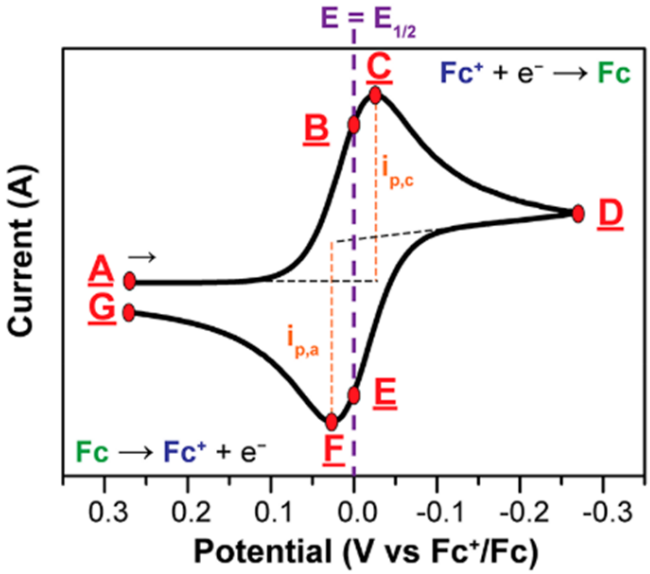


Figure 5.44. An overview of the CV trace. Starting with a cathodic voltage sweep from A to D and followed by an anodic sweep from D to G, Higher scan rates increase the peak current I_p. The separation between the current peak and trough is determined by the diffusion rate of the analyte. [81]

Given the form of the Nernst equation, the response of an electrochemical system to a change in analyte concentration or electrode potential can be formulated [81]. For CV, the sweeping of the voltage during the scan will change the concentration of the analyte around the electrode exactly in accordance with this expression if the system is Nernstian (electrochemically reversible) [81]. The evolution of the cyclic voltammogram trace for an Fc redox reaction is explained here: The voltage potential applied by the working electrode is scanned cathodically between points A and D and as a result the concentration of Fc^+ decreases here. The current peaks at point C with a value ultimately determined by the Randles−Sevcik equation above. After this point the growth of the diffusion layer starts to reduce the current (transport of Fc^+) to the cathode, lowering the rate of diffusion [81].

From points D to G the voltage scan is reversed towards the anodic direction re-oxidising the reduced analyte. Before reaching the current trough at point F, the concentration of Fc and Fc^+ will be equal at point E corresponding to the average potential between point C and F value $E_{1/2}$. The current peak and trough will always be separated in a diffusion limited electrochemical process [81]. If the analyte is stable and there is a low barrier to electron transfer in the cell, the Nernst equilibrium will form rapidly to any change in the working electrode potential. Irreversible reactions are often more sluggish such as those involving the chemical reductant homogenous electron transfer shown in Fig.5.42(a). For the purposes of this thesis, inorganic electrochromic materials follow Nernstian trends with some degradation that eventually plateaus over many repeated cycles.

5.5.2 Cyclic Voltammetry Cell Setup & Chronoamperometry

The usual layout of the CV electrochemical cell is illustrated in the schematic diagram below alongside the setup used in this thesis in Fig.5.45.

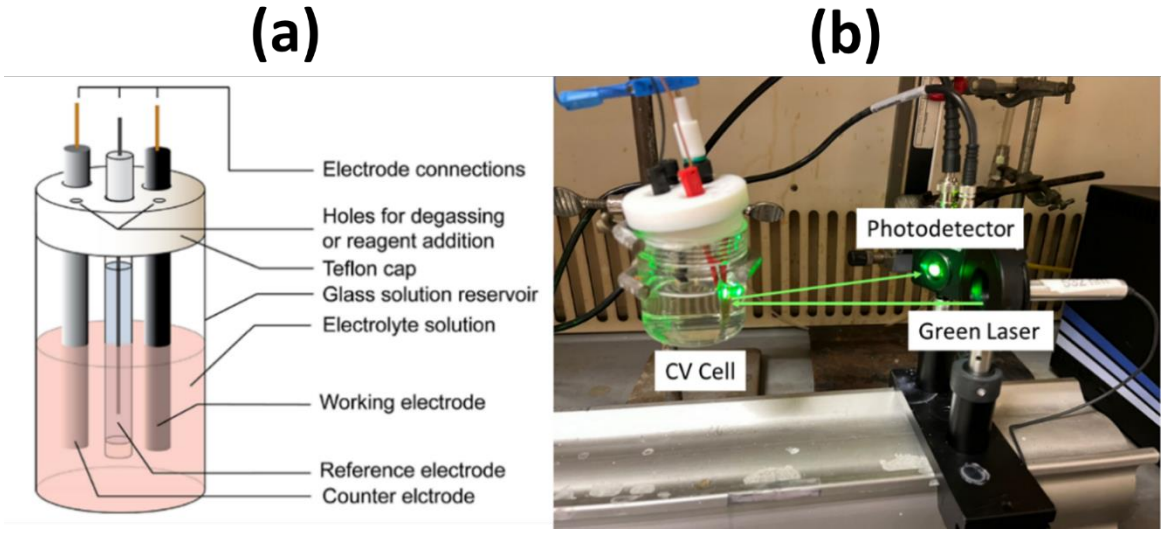


Figure 5.45. (a) The standard layout of a CV electrochemical cell with a anode electrode, reference electrode, working electrode, and degassing hole to maintain ambient pressure within the glass container.[81] *(b) The CV cell made by group member Dilkhush Khitcher was used to make CV measurements of ECMs like WO_3 and NiO. In this case the green laser system adjacent to the cell is designed for colourimetry measurements that are necessary to define the colouration efficiency.*

The main considerations of a practical CV cell are the analyte, the electrolyte solution, and the chosen electrode materials. In the context of EC CV sweeps, the analyte is the solid thin film ECM on the counter electrode (anode) electrode. Reduction and oxidation occur inside of the lattice bulk as outlined in section 5.2 of this chapter for NiO and WO_3. An electrolyte solution is a liquid containing the electrolyte used to neutralise charge as the electrons transfer from cathode to analyte. The ideal solution is liquid at operating temperatures, highly soluble to all chemical species involved, chemically reversible to ensure Nernstian behaviour, unreactive to key parts of the cell such as the electrode material, and optically transparent to allow additional non-contact techniques to be performed on the system [81].

Three electrodes are used in the CV technique. The working electrode (cathode) is connected to a potentiostat that varies the applied voltage. It is composed of material that is redox inert to prevent etching during the electrochemical process. Polishing of this electrode should be done in between measurements to remove adsorbed contaminants though this is not necessary for the setup in this work as disposable thin film electrodes were used. As the name suggests the reference electrode is used to reference the applied voltage on the working electrode. High quality references are commercially available with AgCl/Ag electrodes being very common. The configuration of a reference is shown below in Fig.5.46.

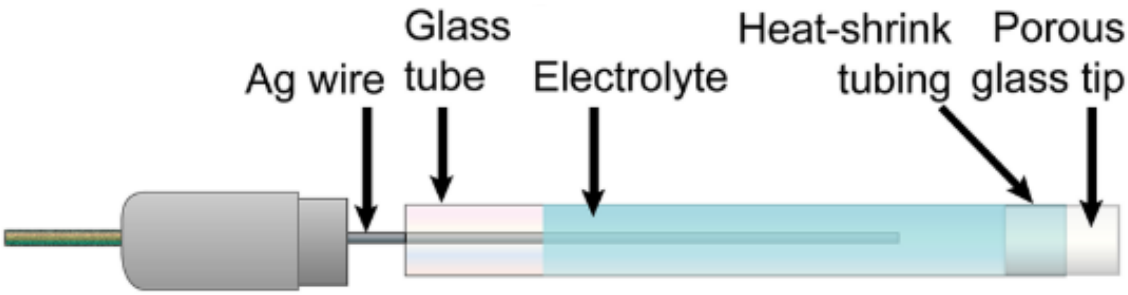


Figure 5.46. The reference is composed of a Ag wire immersed in an electrolyte in a glass tube. This tube has a porous glass tip to connect it to the cell solution when placed in the CV set up. [81]

Finally, the counter electrode (anode) is added to complete the circuit allowing electrons to flow. The counter electrode surface area is normally made bigger than the cathode to prevent reactions on the former inhibiting reactions on the latter [81]. In the CV system used during the thesis, the working electrode is typically thin film deposited Ag on glass or ITO on glass depending on the electrolyte being used. Furthermore, the counter electrode and the analyte are in direct physical contact with one another in a multilayer thin film configuration as well (NiO/Ag for example). The reference that is used is the industry standard AgCl/Ag electrode.

Certain unideal factors can work their way into the measurement, namely the ohmic drop phenomenon in which the voltage potential experienced by the analyte is not the same as the recorded potential. This effect is caused by the presence of uncompensated resistance in the electrochemical system [81]. Ohmic drop will produce unwanted artifacts in the CV measurement such as anomalous increased current peak to trough separation. Figure 5.47 below showcases a circuit model for this. Modern potentiostats will mitigate the intrinsic resistance of the solution R_{sol} with a compensation resistance between the reference and the counter electrode labelled R_c. What remains is the uncompensated amount R_u between the reference and working electrodes and several strategies exist to reduce its deleterious impact on the system. Namely, increasing conductivity by increasing electrolyte concentration (potentially problematic for ECM cycle stability), diminishing electrode dimensions to reduce the current, and decreasing the distance between the reference and working electrodes [81]. The latter is the most practical to implement, and if done correctly the ohmic drop effect can become negligible overall.

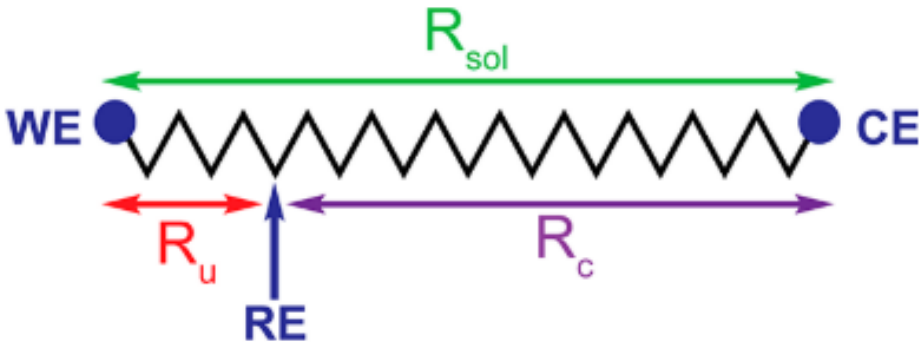


Figure 5.47. A circuit representation of the CV intrinsic solution resistance R_{sol} between the working electrode (WE) and counter electrode (CE). R_c can be accounted for on most systems while active measures must be taken to minimise R_u as much as possible. [81]

CA and colouration efficiency measurements were also carried out while doing CV on the ECMs studied. These auxiliary techniques were useful for ascertaining the kinematics and colour change aspects of the TMOs. Going over each briefly, the CA technique involves the stepping of the working potential voltage in the CV setup (positive to negative voltage switching and vice versa). When this is done a current from faradaic processes, electron transfer, occurs which typically exponentially decays w.r.t time [82]. This current starts out with a sharp peak that decays, and fitting this decay pattern can yield the time for reduction or oxidation depending on the polarity of the potential. When working with electrochromic materials the duration of the transient current peak curve determines bleaching time τ_B, colouration time τ_C, and ultimately the switching speed of the device structure. Faster switching between both states is clearly advantageous for display technology as discussed on p.237. The Cottrell equation, originally derived by physical chemist Frederick Gardner Cottrell in 1903, is a description of the time transient current when the planar working electrode potential is defined by a temporal step function; and is given by the expression below [83].

$$I = n \cdot FAC \left(\frac{D}{t\pi}\right)^{\frac{1}{2}} \qquad (5.6)$$

Where I is the current, n is the number of electrons transferred and is typically unity, and t is time. F, A, D, and C have their usual meanings as written above for eq.5.4. The

accumulative process of charge exchange during the decay of current, charge capacity, can be calculated from the integral of the current density curves w.r.t time as shown in Fig.5.48 below, taken from Fig.5.12(a) on p.248, for collected CA data. Increasing the potential applied clearly reveals that more charges will participate in the redox reaction and the current peaks will also narrow and become taller [21].

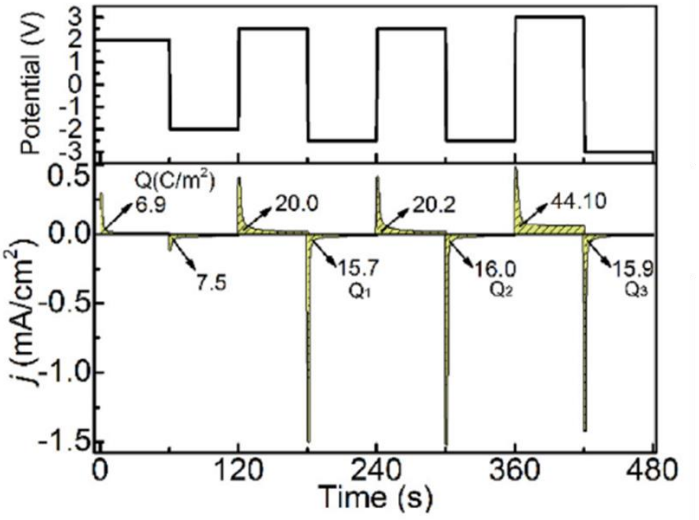


Figure 5.48. CA data using current density instead of current w.r.t time. The stepped voltage is shown across the same time domain. The charge capacity increases as step voltage grows larger. [21]

Colouration efficiency η is a necessary parameter to determine the efficiency of the EC colouration change, evaluated by the formula below [21].

$$\eta = \frac{log\left(\frac{T_B}{T_C}\right)}{Q} \qquad (5.7)$$

Where T_B is the optical transmission intensity of the ECM in the beached state, T_C is the optical transmission intensity of the ECM in the absorbing state, and Q is the charge capacity of the film. The sample area is the active area of the ATF EC device immersed in liquid electrolyte which is typically on the order of 5 cm^2. For reflective opaque samples, the reflectivity in bleached, R_B, and absorbing, R_C, state can be used instead. $log\left(\frac{T_B}{T_C}\right)$ is also known as the change of optical density parameter ΔOD [41]. The colouration efficiency is critical for comparing the performance of different ECMs to one another. It is optimum when

less charge is needed to produce a greater change in the UV-Vis spectra. Measured degradation in the charge capacity, CV trace, and colouration change w.r.t cycling can all be correlated together to show the electrochemical bistability of the ECM as shown in Fig.5.49 below for the CV trace graph. The larger the internal area of the CV trace, the easier it is for the charge transfer and diffusion of ions to take place [41]. Conversely, smaller area would be associated with poorer colouration change and reduced charge capacity Q. An ideal system would be 100 % reversible and stable over an infinite number of voltage sweep cycles, while in practice the real-world materials involved in the EC redox reaction are likely to be damaged somewhat over continued prolonged use. For ECMs this damage could be the dissolution of the active layer, the erosion of the working electrode [41], the loss or transformation of the electrolyte due to environmental factors like UV exposure or polluted air, and the addition of contaminants to the system that adsorb to the working surfaces.

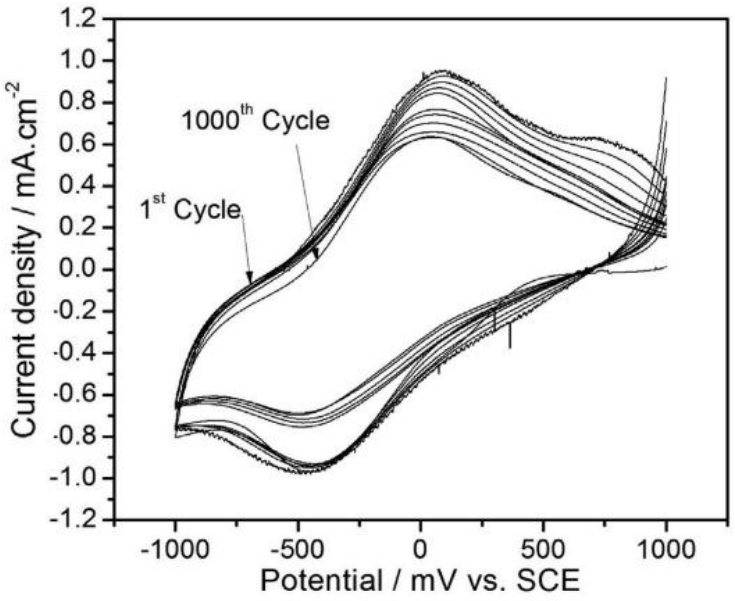


Figure 5.49. The electrochemical stability of a V_2O_5 thin film with 15 % WO_3 content. Sweep rate v = 100 mV/s. The electrolyte solution used is 0.5 M LiClO4 + PC electrolyte. After 1000 cycles the internal area of the voltammograms has noticeably shrunken, indicating the increased difficulty of the ion transport and diffusion. [41]

5.6 Study of the EC Response & Parameters of NiO on Ag

5.6.1 Electrochromic Parameter Results of Sputtered NiO on Ag

Below in Fig.5.50 are CV and CA diagrams based on some of the initial data collected from EC measurements done with 10, 20, 50, and 100 nm NiO on Ag, using a liquid electrolyte

KOH (supplying a H^+ ion for lattice intercalation in the redox reaction [42]). In general, the results showcase the trend that thicker NiO films can hold more charge than their thinner counterparts, with better diffusion rates, strongly corroborating the fact stipulated by Dongmei Dong *et al.* that EC ion intercalation is not just a shallow surface effect but also a bulk driven process as well [21].

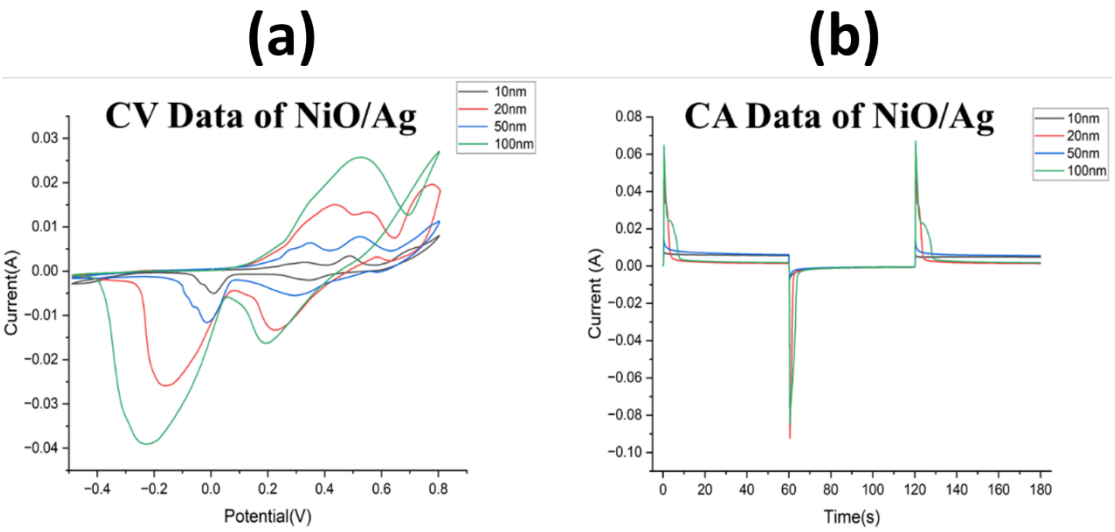


Figure 5.50. (a) CV voltage sweep for NiO/Ag anode immersed in a KOH electrolyte solution, and a planar working electrode made from thin film Ag. With 50 nm being the outlier, thicker NiO has better EC performance. The same story can be seen for the CA data in (b) where sharper peaks are seen for thicker NiO.

The charge capacity Q is equal to 267.48 C/m^2 for the 100 nm NiO as opposed to a value of 1.26 C/m^2 for the 10 nm NiO. The 50 nm NiO on Ag did not follow the trend as this sample failed due to lift-off of the thin film, later understood during the write up of this thesis to be cause by inadequate adhesion of the Ag and NiO. This problem can be fixed by the inclusion of sub-nanometer thin Ti adhesion and capping layers in manner similar to the way in which ultrathin Ag produced by the NPVD system was stabilised against dewetting on heated glass [75], [76]. To prove reproducibility, the experiment was repeated for 17, 25, 42, and 85 nm NiO and in this instance the near 50 nm NiO sample followed the increased charge capacity Q trend while the 85 nm sample did not (again due to stability issues due to poor adhesion), as shown in Fig.5.51. The improvement in ECM film cycle stability will be highlighted in chapter 7 as it enables the creation of viable Fano-resonant electrochromic devices (ECDs). These devices could not be made during the project due to stability issues again related to poor adhesion, as the results in chapter 6 will demonstrate. A filling factor γ ratio of 0.2633

was measured for 42 nm $H_\gamma NiO$, 0.2297 for 17 nm $H_\gamma NiO$, and 0.1798 for 25 nm $H_\gamma NiO$ giving an average of 0.2242 for ultrathin NiO.

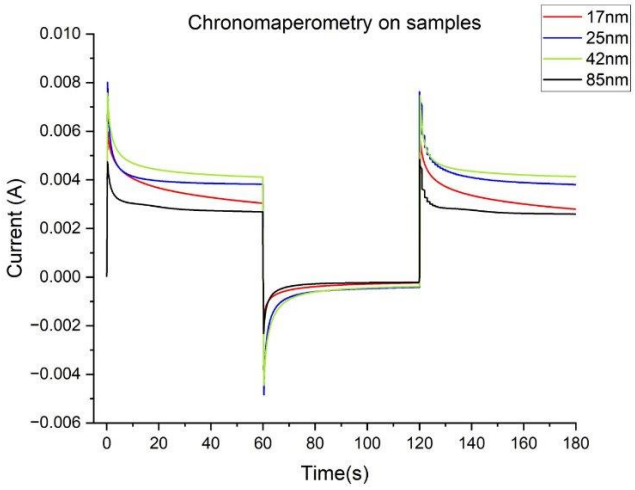


Figure 5.51. A chronoamperometry graph showing colouration and bleaching of NiO with current plotted against time. Except for the 85 nm sample, the trend seen is for bulkier NiO to have a greater charge capacity Q and peak current. The decay of this current can inform one of the bleaching and colouration time.

The cyclic bistability of ultrathin film NiO also has much more room for improvement compared to thicker TMOs in the literature which can withstand many hundreds to thousands of cycles before degrading considerably [6]. Fig.5.52 below diplays the rapid decline in pefromance of 43 nm NiO when scanned or switched between -0.5 V and +0.8 V.

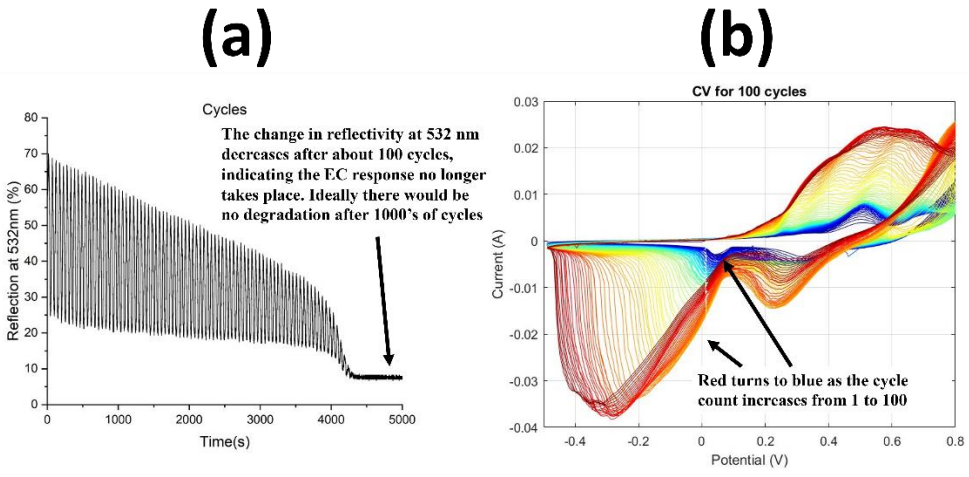


Figure 5.52. (a) The reflectance of a green laser off a 43 nm NiO films is monitored. As the applied voltage is flipped between positive and negative the change in reflection begins to degrade. After about 100 cycles the EC response is effectively terminated. (b) Instead of switching, the voltage is instead scanned across in steps of 100 mV on a CV trace plot. The Nernstian current peaks are observable for the initial cycles but after 80-100 traces the NiO no longer change state.

The higher value of γ for the ultrathin bleached NiO compared to the 400 nm NiO produced by Dongmei Dong *et al.* (0.224 versus 0.0046) indicates that a large amount of the NiO bulk becomes occupied by H^+ compared to Li^+, which may further exacerbate the ECM film stability issue. The time reponse of the EC process shortens rapidly for thinner NiO and grows larger for thicker films in a manner consisntent with the thickness-squarred dependence discussed on p.237. A fast reponse time for bleaching and colouration is very advantageous for display technology, and with further sample optimisation, such as minituisation of the sample area into the micron and nanometer regime, it could certainly be possible to reduce this time to well under 2s for both τ_B and τ_C. Further study is warranted in this regard. A practical pixel display device would need response times down in the milliseconds to compete with LCDs and LED displays [7].

Given the zeroth order FP large contrast achieved for 42 nm NiO on Ag (see Fig.5.54(b) below), this directly showcase that an active ECM layer, with area of $5cm^2$, can change its reflective state very quickly on time scales comparable or slightly better than current bulkier (hundreds of nanometres with many layers in the stack) electrochromic dimmable mirror technology that operate between several to many dozens of seconds [24]. Future work could certainly decrease the response time down closer to a second or under for ultrathin ECMs if steps are taken to optimise the surface conditions for ion intercalation (increase porosity for quicker ion diffusion [47]) and alternative electrolytes are considered for use, i.e., $LiClO_4$ which in the literature showcases very high η with a small Li^+ filling factor for Nio [21].

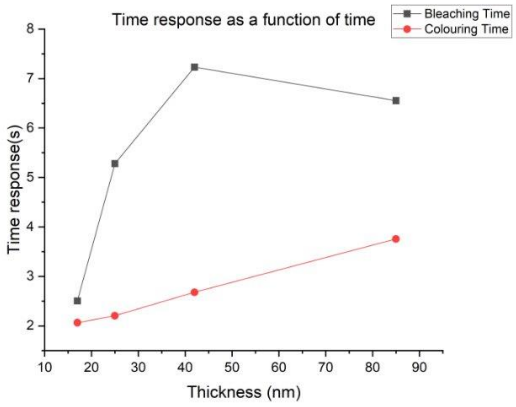


Figure 5.53. The time response for bleaching time τ_B and colouration time τ_C, as inferred from the CA peak current decay in Fig.5.51, is much less for ultrathin NiO films. The time to bleach is dramatically improved meaning the ions themselves diffuse much faster into the NiO lattice. For 17 nm NiO the colouration and bleaching are approximately equal under 2.5 seconds.

5.6.2 Colourimetry Results of Sputtered NiO on Ag

The reflectance spetcra of this batch of NiO/Ag is displayed below in Fig.5.54. As expected the 42 nm NiO, near the optimum position of the zeroth FP mode, has a very flat spectral reponse, high reflectviity, and large change in reflectance averaging 45-50 % across the visisble when biased. The change in reflection drops off for NiO thinner and thicker than this 42 nm film outside the zeroth FP mode absorption band region. The dispersion of the optical reflectviity is also much higher for these thin films outside (below and above) the band making them more colourful in appearnce as can be observed in Fig.5.55(b). As an example, samples A (17 nm) and B (25 nm) in Fig.5.55(a) and (b) have higher colouration efficiency than zeroth order FP sample C. The colouration efficiency of 25 nm (sample B) NiO at 541 nm wavelength is seen to be 205 cm^2/C which is very high even compared to values quoted in the literature ranging between 50-150 cm^2/C [6]. Meanwhile, the colouration efficiency of 42 nm (sample C) NiO is quarter of this value at the same wavelength. The colouration efficiency of all sample become comparable in the deep red and into the NIR spectral region.

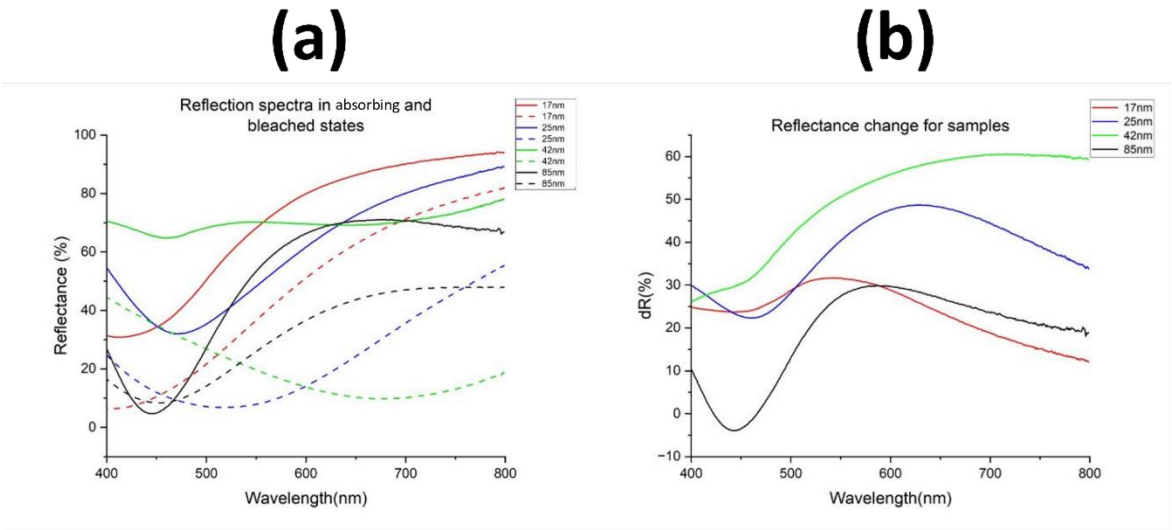


Figure 5.54. (a) The reflectivity response is flat as expected for 42 nm NiO on Ag. Solids lines indicate bleached samples while dashed lines indicate samples in the absorbing state (b) The change in reflectivity is also very large for the 42 nm NiO with an average change in reflection of around 50 % across the visible regime, comparable to the results seen in the TMM simulation of the NiO/Ag stack EC response.

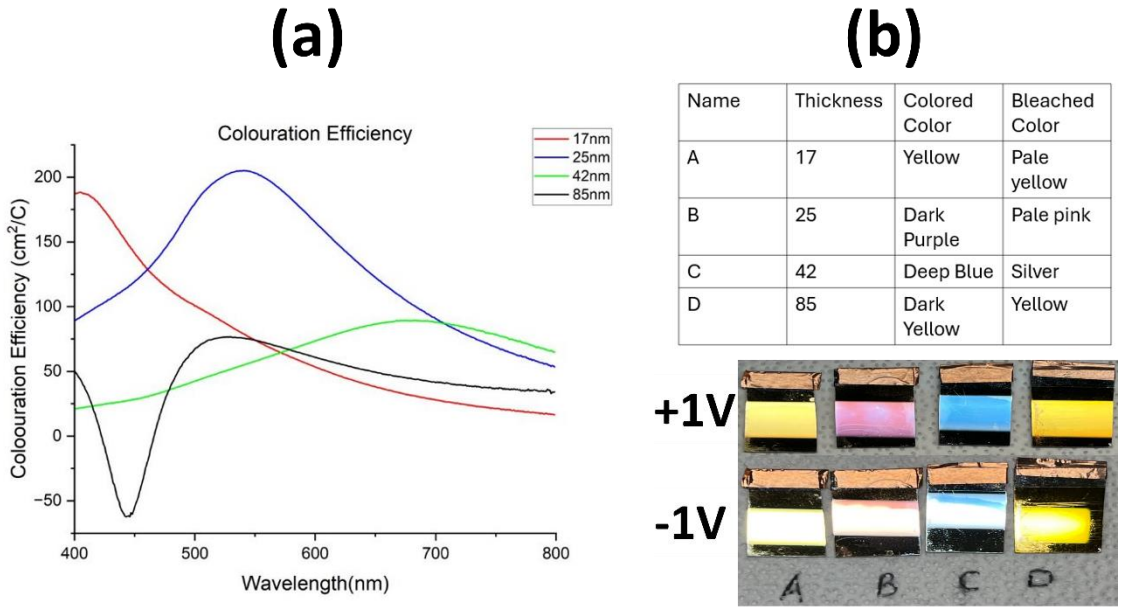


Figure 5.55. (a) The wavelength resolved colouration efficiency describes how well an intercalated ion changes the light-matter interaction across the spectrum regarding dynamic structural colouring. The higher the number the more efficient the colouration is meaning less electric charge is needed to modify the stack hue. (b) A descriptive table and corresponding photographic images of the 17, 25, 42, and 85 nm NiO on Ag in the absorbing state and reflective bleached state.

Another study with NiO films at 33, 66, 99, and 132 nm on Ag was done to compare the colouration of even thicker NiO to ultrathin NiO experimentally. The colouration chart in Fig.5.56 below shows the significant difference that exists in the EC colouration response of an ultrathin NiO near the zeroth mode and thicker films outside this resonance band. After bleaching the 33 nm NiO remains mostly the same drab grey in appearance while in the absorbing state the 66, 99, and 132 nm NiO have moved considerably closer towards the edges of the chromaticity chart, indicating the increase in structural colour saturation and purity (number of hues present).

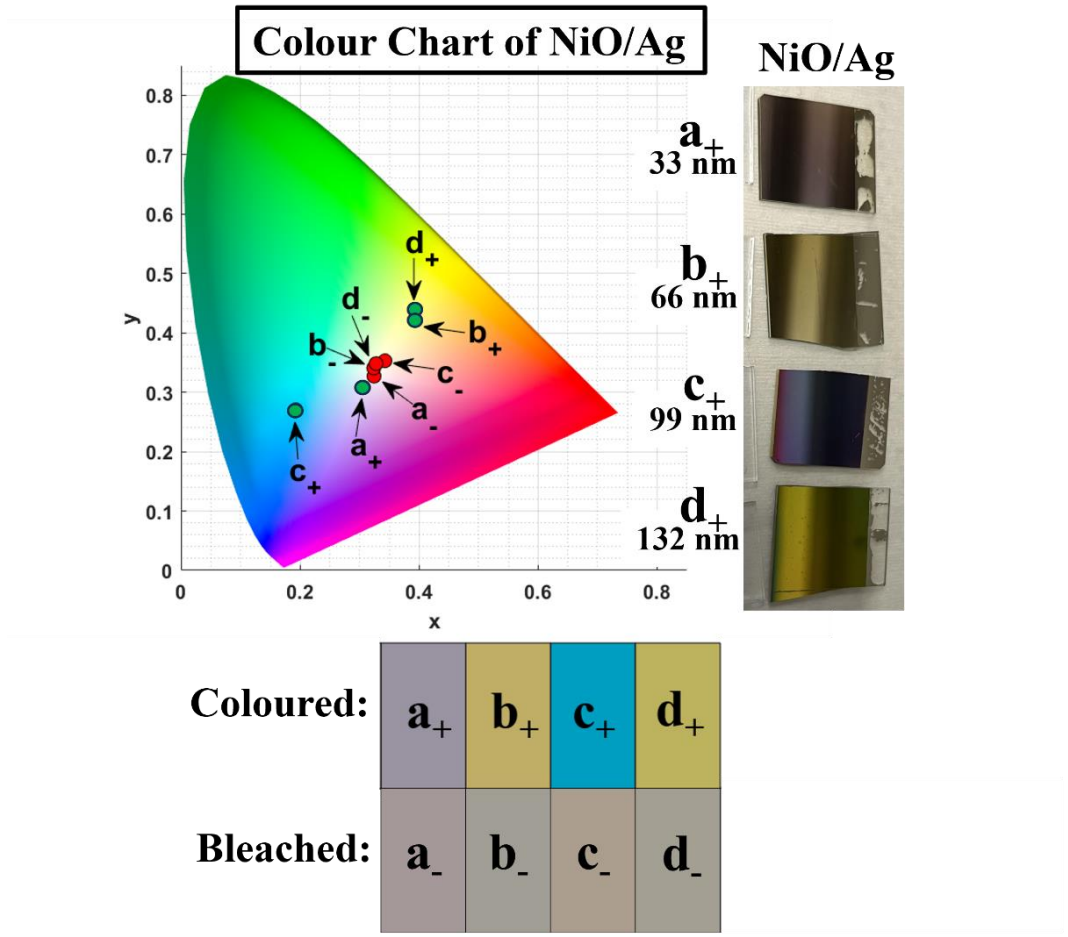


Figure 5.56. The superior dynamic colouration of thicker NiO thin films is apparent. 33 nm NiO, near the zeroth mode band, has poor colour change when intercalated. Meanwhile the much thicker 66, 99, and 132 nm NiO have significant changes in their colour coordinate position on the CIE chart between bleached and absorbing EC state.

The colour and state contrast reponse for NiO on ITO/Glass is much poorer than for NiO/Ag. The change in colouration is almost imperceptable and as photographic imagery shows, the colouration of these samples is grey to dark grey in appearnce compared with the blue and yellows of the metal backed NiO in a similar thickness range. With the absence of a strong zeroth FP mode absorption band the change in reflectvity no longer has a non-trivial deeply subwavelength solution. Instead, the magnitude of the optical reponse (in this case transmission) change becomes proportional to NiO film thickness. See Fig.5.57 below.

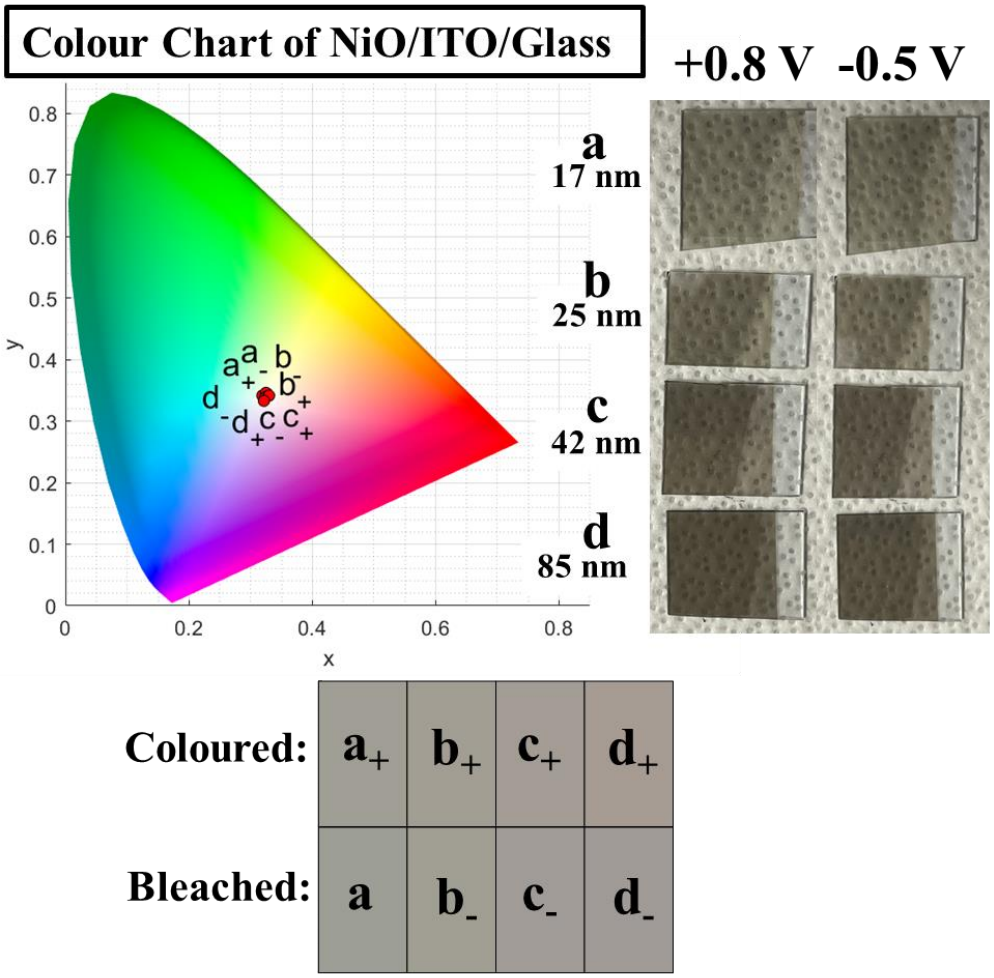


Figure 5.57. The passive and dynamic transmission colouration are terrible compared with the NiO on reflective Ag above. Even by eye it is difficult to distinguish the bleached from the absorbing samples due to the tiny colour gamut, though the increased iridescence in the bleached state does make it easier to ascertain which is which when handling them.

For future work the possibility of creating solid-state EC devices based on ultrathin NiO can also be explored wherein WO_3, NiO, and porous dielectrics, such as Ta_2O_5, are combined to form a solid state EC device that reversibly changes colour and reflectivity without the need for immersion in a concentrated acid liquid solution, as shown in the work of Zhang *et al.* (2020) [84]. This solid-state configuration is considered the most ideal implementation of EC technology because of the absence of the cumbersome liquid electrolyte which greatly bulks out the required size scale of the multilayer layer assembly, due to the needed addition of complementary layers to encapsulate the solution in [85]. These other layers will inevitably decrease the maximum contrast obtainable when utilizing the zeroth order FP mode with ultrathin NiO as shown previously in the ΔR line graphs of Fig.5.24 and Fig.5.25(b) on p.259-260.

5.7 Summary

In summary, throughout the course of this chapter inorganic electrochromic TMOs like WO_3 and NiO have been extensively reviewed, with particular emphasis put on understanding the EC response of anodic NiO due to its lossy nature enabling the zeroth order FP mode to be accessed for deeply sub wavelength non-trivial device stack structure solutions. The refractive index change of NiO using hydrogen ion intercalation with electrolyte KOH was found to be very large, changing NiO from a lossy TMO into a near transparent dielectric with nominal real index dispersion. It was also discovered that ultrathin NiO below 100 nm on reflective back metals like Ag had very large broadband contrast between the absorbing and bleached state, with 50 nm NiO on Ag being an optimum simulated stack configuration for nearly 60 % average change in the reflectivity across the visible regime. As was the case with Si, Ge, and MoS_2, NiO in its absorbing state showcased omnidirectionality and similarity in the angular response for both p and s polarisations. Moreover, it was shown that the angular insensitivity only pertained to the ultrathin film zeroth mode band region as the dispersion was much greater in the spectral and angular domain for higher order FP modes like the 1^{st} mode around 150 nm of NiO and thicker.

The passive and dynamic colouration response was far superior above 100 nm NiO thickness for all reflective back metals used. Furthermore, active colouration contrast for NiO/Au was greater than for NiO/Ag though the latter had a wider passive colour gamut. The response time of the EC bleaching, and extraction was shown to decrease w.r.t decreasing NiO film thickness, especially the bleaching time for ions to enter their position in the NiO lattice interstitial sites. With further miniaturisation of sample area into the micron pixel scale, it may be possible to create devices with response times on the order of milliseconds that can compete with LCDs and LED displays. Moreover, the highest contrast 42 nm NiO on Ag sample indicated that utilising the ultrathin film regime enabled both increased reflection contrast and on switching speeds on par the with contemporary dimmable mirror technology [24]. Further study on the pixel and large macroscopic surface size scales is certainly warranted for future work. Finally, there is much room for improvement in the bistability of the NiO films. The EC change dropped off to zero by the 100^{th} CV cycle compared to bulkier NiO in the literature retaining 80 % of its initial response after 1000 cycles. To overcome this, future devices could use other electrolytes such as Li^+ as perhaps the high γ ratio of 0.224 for H^+ intercalated ultrathin NiO (in contrast to 0.0046 for lithiated bulky NiO) put a

lot of stress on the NiO lattice structure. More careful control of the sample creation conditions could also be implemented to fine tune porosity, microscopic roughness, and crystalline grain size to help towards making more stable NiO films with faster response times.

5.8 References

[1] J. Chen, G. Song, S. Cong, and Z. Zhao, "Resonant-Cavity-Enhanced Electrochromic Materials and Devices," *Adv. Mater.*, vol. 35, no. 47, p. 2300179, 2023, doi: 10.1002/adma.202300179.

[2] D. Vaquero *et al.*, "Excitons, trions and Rydberg states in monolayer MoS2 revealed by low-temperature photocurrent spectroscopy," *Commun. Phys.*, vol. 3, no. 1, 2020, doi: 10.1038/s42005-020-00460-9.

[3] S. K. Deb, "A Novel Electrophotographic System," *Appl. Opt.*, vol. 8, no. S1, p. 192, 1969, doi: 10.1364/ao.8.s1.000192.

[4] Z. Wang, X. Wang, S. Cong, F. Geng, and Z. Zhao, "Fusing electrochromic technology with other advanced technologies: A new roadmap for future development," *Mater. Sci. Eng. R Reports*, vol. 140, p. 100524, 2020, doi: 10.1016/j.mser.2019.100524.

[5] Y. Yu, Y. Yu, L. Huang, H. Peng, L. Xiong, and L. Cao, "Giant Gating Tunability of Optical Refractive Index in Transition Metal Dichalcogenide Monolayers," *Nano Lett.*, vol. 17, no. 6, pp. 3613–3618, 2017, doi: 10.1021/acs.nanolett.7b00768.

[6] W. Wu, M. Wang, J. Ma, Y. Cao, and Y. Deng, "Electrochromic Metal Oxides: Recent Progress and Prospect," *Adv. Electron. Mater.*, vol. 4, no. 8, p. 1800185, 2018, doi: 10.1002/aelm.201800185.

[7] T. Xu *et al.*, "High-contrast and fast electrochromic switching enabled by plasmonics," *Nat. Commun.*, vol. 7, no. 10479, 2016, doi: 10.1038/ncomms10479.

[8] J. H. Ko, Y. J. Yoo, Y. Lee, H. Jeong, and Y. M. Song, "A review of tunable photonics : Optically active materials and applications from visible to terahertz,"

ISCIENCE, vol. 25, no. 8, 2022, doi: 10.1016/j.isci.2022.104727.

[9] Y. Lu, S. H. Lam, W. Lu, L. Shao, T. H. Chow, and J. Wang, "All-State Switching of the Mie Resonance of Conductive Polyaniline Nanospheres," *Nano Lett.*, vol. 22, no. 3, pp. 1406–1414, 2022, doi: https://doi.org/10.1021/acs.nanolett.1c04969.

[10] W. Zhang *et al.*, "Transparent inorganic multicolour displays enabled by zinc-based electrochromic devices," *Light Sci. Appl.*, vol. 9, no. 121, 2020, doi: 10.1038/s41377-020-00366-9.

[11] Y. Wang *et al.*, "A see-through electrochromic display via dynamic metal-ligand interactions," *Chem*, vol. 7, no. 5, pp. 1308–1320, 2021, doi: 10.1016/j.chempr.2021.02.005.

[12] J. W. Lu Yin, Samar S. Sandhu, Ruixiao Liu, Muhammad Inam Khan, Connor Wicker, Victor Garcia-Gradilla, Jiachi Zhou, An-Yi Chang, Shixuan Wu, Jong-Min Moon, Chuanrui Chen, Shichao Ding, "Wearable E-Skin Microgrid with Battery-Based, Self-Regulated Bioenergy Module for Epidermal Sweat Sensing," *Adv. Energy Mater.*, vol. 13, no. 4, p. 2203418, 2022, doi: 10.1002/aenm.202203418.

[13] J. Li *et al.*, "Ultrathin Smart Energy-Storage Devices for Skin-Interfaced Wearable Electronics," *ACS Energy Lett.*, vol. 8, no. 1, pp. 1–8, 2023, doi: 10.1021/acsenergylett.2c02029.

[14] F. Sun *et al.*, "Soft Fiber Electronics Based on Semiconducting Polymer," *Chem. Rev.*, vol. 123, no. 8, pp. 4693–4763, 2023, doi: 10.1021/acs.chemrev.2c00720.

[15] L. Li *et al.*, "Scalable fluid-spinning nanowire-based inorganic semiconductor yarns for electrochromic actuators," *Mater. Horizons*, vol. 8, no. 6, pp. 1711–1721, 2021, doi: 10.1039/d1mh00135c.

[16] H. Fan *et al.*, "Continuously Processed, Long Electrochromic Fibers with Multi-Environmental Stability," *ACS Appl. Mater. Interfaces*, vol. 12, no. 25, pp. 28451–28460, 2020, doi: 10.1021/acsami.0c09589.

[17] W. Cheng, J. He, K. E. Dettelbach, N. J. J. Johnson, R. S. Sherbo, and C. P.

Berlinguette, “Photodeposited Amorphous Oxide Films for Electrochromic Windows,” *Chem*, vol. 4, no. 4, pp. 821–832, 2018, doi: 10.1016/j.chempr.2017.12.030.

[18] L. Zheng *et al.*, “High reflectance tunable multi-color electrochromic films based on Fabry–Perot cavity,” *Ceram. Int.*, vol. 49, no. 9, pp. 13355–13362, 2023, doi: 10.1016/j.ceramint.2022.12.210.

[19] L. Komitov and G. Hegde, *Progress in Liquid Crystal Science and Technology: Chapter 22 - Fast Switching Liquid Crystal*. World Scientific, 2013.

[20] “Dimmable Glass: What You Need To Know,” *Smart Glass VIP*, 2021. https://smartglassvip.com/working-of-electronic-dimmable-glass-for-aircraft-windows/.

[21] D. Dong *et al.*, “Electrochromic and colorimetric properties of anodic NiO thin films: Uncovering electrochromic mechanism of NiO,” *Electrochim. Acta*, vol. 335, p. 135648, 2020, doi: 10.1016/j.electacta.2020.135648.

[22] “Dimmable Glass,” *Gentex Corporation*. https://www.gentex.com/products-technology/automotive/dimmable-glass/.

[23] D. Patrascu, “Dimming Mirrors Explained,” 2009. https://www.autoevolution.com/news/dimming-mirrors-explained-8414.html.

[24] K. Tajima, H. Hotta, Y. Yamada, M. Okada, and K. Yoshimura, “Electrochromic switchable mirror glass with controllable reflectance,” *Appl. Phys. Lett.*, vol. 100, no. 9, pp. 2012–2015, 2012, doi: 10.1063/1.3691256.

[25] K. Xu *et al.*, “Synergistic Effect and Electrochromic Mechanism of Nanoflake Li-doped NiO in LiOH Electrolyte,” *Energy Environ. Mater.*, vol. 6, no. 3, p. e12362, 2023, doi: 10.1002/eem2.12362.

[26] Z. Shao *et al.*, “All-solid-state proton-based tandem structures for fast-switching electrochromic devices,” *Nat. Electron.*, vol. 5, pp. 45–52, 2022, doi: 10.1038/s41928-021-00697-4.

[27] J. Jiang, L. Qin, J. Halim, P. O. Å. Persson, L. Hou, and J. Rosen, “Colorless-to-colorful switching of electrochromic MXene by reversible ion insertion,” *Nano Res.*, vol. 15, no. 4, pp. 3587–3593, 2022, doi: 10.1007/s12274-021-3913-y.

[28] J. Zhao *et al.*, “Trace H2O2-Assisted High-Capacity Tungsten Oxide Electrochromic Batteries with Ultrafast Charging in Seconds,” *Angew. Chemie - Int. Ed.*, vol. 55, no. 25, pp. 7161–7165, 2016, doi: 10.1002/anie.201602657.

[29] Z. Wang *et al.*, “Using Intrinsic Intracrystalline Tunnels for Near-Infrared and Visible-Light Selective Electrochromic Modulation,” *Adv. Opt. Mater.*, vol. 5, no. 11, p. 1700194, 2017, doi: 10.1002/adom.201700194.

[30] K. Madasamy, D. Velayutham, V. S. M. Kathiresan, and Kuo-Chuan Ho, “Viologen based Electrochromic Materials and Devices,” *J. Mater. Chem. C*, vol. 7, no. 16, pp. 4622–4637, 2019, doi: 10.1039/C9TC00416E.

[31] V. H. V. Quy *et al.*, “Tunable electrochromic behavior of biphenyl poly(viologen)-based ion gels in all-in-one devices,” *Org. Electron.*, vol. 100, p. 106395, 2022, doi: 10.1016/j.orgel.2021.106395.

[32] D. T. Gillaspie, R. C. Tenent, and A. C. Dillon, “Metal-oxide films for electrochromic applications : present technology and future directions,” *J. Mater. Chem.*, vol. 20, no. 43, pp. 9585–9592, 2010, doi: 10.1039/c0jm00604a.

[33] W. Zhang, H. Li, E. Hopmann, and A. Y. Elezzabi, “Nanostructured inorganic electrochromic materials for light applications,” *Nanophotonics*, vol. 10, no. 2, pp. 825–850, 2021, doi: 10.1515/nanoph-2020-0474.

[34] Y. Li, A. A. Talin, and M. L. Brongersma, “Dynamic Tuning of Gap Plasmon Resonances Using a Solid-State Electrochromic Device,” *Nano Lett.*, vol. 19, no. 11, pp. 7988–7995, 2019, doi: 10.1021/acs.nanolett.9b03143.

[35] T. Badloe, J. Kim, I. Kim, W. Kim, W. S. Kim, and Y. Kim, “Liquid crystal-powered Mie resonators for electrically tunable photorealistic color gradients and dark blacks,” *Light Sci. Appl.*, vol. 11, no. 118, 2022, doi: 10.1038/s41377-022-00806-8.

[36] J. Mlynarski *et al.*, “Electrochromic Bragg Mirror: ECBM,” *Adv. Mater.*, vol. 24, no. 35, pp. 265–269, 2012, doi: 10.1002/adma.201202484.

[37] L. Xiao *et al.*, “WO3 - Based Electrochromic Distributed Bragg Reflector : Toward Electrically Tunable Microcavity Luminescent Device,” *Adv. Opt. Mater.*, vol. 6, no. 1, p. 1700791, 2017, doi: 10.1002/adom.201700791.

[38] Z. Wang *et al.*, “Towards full-colour tunability of inorganic electrochromic devices using ultracompact fabry-perot nanocavities,” *Nat. Commun.*, vol. 11, no. 1, p. 302, 2020, doi: 10.1038/s41467-019-14194-y.

[39] J. Chen *et al.*, “Mimicking Nature’s Butterflies: Electrochromic Devices with Dual-Sided Differential Colorations,” *Adv. Mater.*, vol. 33, no. 14, p. 2007314, 2021, doi: 10.1002/adma.202007314.

[40] S. J. Kim *et al.*, “Color of Copper / Copper Oxide,” *Adv. Mater.*, vol. 33, no. 15, p. 2007345, 2021, doi: 10.1002/adma.202007345.

[41] C. E. Patil *et al.*, “Electrochromic performance of the mixed V2O5-WO3 thin films synthesized by pulsed spray pyrolysis technique,” *Curr. Appl. Phys.*, vol. 14, no. 3, pp. 389–395, 2014, doi: 10.1016/j.cap.2013.12.014.

[42] E. Pehlivan, C. G. Granqvist, and G. A. Niklasson, “Electrochromic nickel-oxide-based thin films in KOH electrolyte: Ionic and electronic effects elucidated by impedance spectroscopy,” *Sol. Energy Mater. Sol. Cells*, vol. 269, p. 112795, 2024, doi: 10.1016/j.solmat.2024.112795.

[43] M. Da Rocha, B. Dunn, and A. Rougier, “Faradaic and/or capacitive: Which contribution for electrochromism in NiO thin films cycled in various electrolytes?,” *Sol. Energy Mater. Sol. Cells*, vol. 201, no. August, 2019, doi: 10.1016/j.solmat.2019.110114.

[44] C. G. Granqvist, *Handbook of Inorganic Electrochromic Materials. (Elsevier, 1995).*, 1st ed. Elsevier Science Ltd 1995, 1995.

[45] H. Li *et al.*, “Solution-Processed Porous Tungsten Molybdenum Oxide Electrodes

for Energy Storage Smart Windows," *Adv. Mater. Technol.*, vol. 2, no. 8, p. 1700047, 2017, doi: 10.1002/admt.201700047.

[46] G. Cai, A. L. Eh, L. Ji, and P. S. Lee, "Recent Advances in Electrochromic Smart Fenestration," *Adv. Sustain. Syst.*, vol. 1, no. 12, p. 1700074, 2017, doi: 10.1002/adsu.201700074.

[47] G. Cai *et al.*, "Ultra-large optical modulation of electrochromic porous WO3 film and the local monitoring of redox activity," *Chem. Sci.*, vol. 7, no. 2, pp. 1373–1382, 2016, doi: 10.1039/c5sc03727a.

[48] H. Fang *et al.*, "Multifunctional hydrogel enables extremely simplified electrochromic devices for smart windows and ionic writing boards," *Mater. Horizons*, vol. 5, no. 5, pp. 1000–1007, 2018, doi: 10.1039/c8mh00856f.

[49] S. Cong, Y. Tian, Q. Li, Z. Zhao, and F. Geng, "Single-crystalline tungsten oxide quantum dots for fast pseudocapacitor and electrochromic applications," *Adv. Mater.*, vol. 26, no. 25, pp. 4260–4267, 2014, doi: 10.1002/adma.201400447.

[50] J. L. Wang, Y. R. Lu, H. H. Li, J. W. Liu, and S. H. Yu, "Large Area Co-Assembly of Nanowires for Flexible Transparent Smart Windows," *J. Am. Chem. Soc.*, vol. 139, no. 29, pp. 9921–9926, 2017, doi: 10.1021/jacs.7b03227.

[51] H. Li, C. J. Firby, and A. Y. Elezzabi, "Rechargeable Aqueous Hybrid Zn2+/Al3+ Electrochromic Batteries," *Joule*, vol. 3, no. 9, pp. 2268–2278, 2019, doi: 10.1016/j.joule.2019.06.021.

[52] J. Wu *et al.*, "Flexible Electrochromic V2O5 Thin Films with Ultrahigh Coloration Efficiency on Graphene Electrodes," *J. Electrochem. Soc.*, vol. 165, no. 5, pp. 183–189, 2018, doi: 10.1149/2.0481805jes.

[53] S. L. Kuai, G. Bader, and P. V. Ashrit, "Tunable electrochromic photonic crystals," *Appl. Phys. Lett.*, vol. 86, no. 22, p. 221110, 2005, doi: 10.1063/1.1929079.

[54] T. Kuno, Y. Matsumura, K. Nakabayashi, and M. Atobe, "Electroresponsive Structurally Colored Materials: A Combination of Structural and Electrochromic

Effects," *Angew. Chemie - Int. Ed.*, vol. 55, no. 7, pp. 2503–2506, 2016, doi: 10.1002/anie.201511191.

[55] J. Meng *et al.*, "Effects of pore size of reverse opal structured PEDOT films on their electrochromic performances," *Org. Electron.*, vol. 50, pp. 16–24, 2017, doi: 10.1016/j.orgel.2017.07.018.

[56] G. Cai *et al.*, "Diphylleia grayi-Inspired Stretchable Hydrochromics with Large Optical Modulation in the Visible-Near-Infrared Region," *ACS Appl. Mater. Interfaces*, vol. 10, no. 43, pp. 37685–37693, 2018, doi: 10.1021/acsami.8b12490.

[57] Y. Tang *et al.*, "Lattice Proton Intercalation to Regulate WO3-Based Solid-Contact Wearable pH Sensor for Sweat Analysis," *Adv. Funct. Mater.*, vol. 32, no. 4, p. 2107653, 2022, doi: 10.1002/adfm.202107653.

[58] Y. S. Zou *et al.*, "Structural and optical properties of WO3 films deposited by pulsed laser deposition," *J. Alloys Compd.*, vol. 583, pp. 465–470, 2014, doi: 10.1016/j.jallcom.2013.08.166.

[59] L. Pan *et al.*, "Reactively sputtered WO3 thin films for the application in all thin film electrochromic devices," *Electrochim. Acta*, vol. 328, 2019, doi: 10.1016/j.electacta.2019.135107.

[60] F. A. F. Lahiji *et al.*, "Growth and optical properties of NiO thin films deposited by pulsed dc reactive magnetron sputtering," *J. Vac. Sci. Technol. A*, vol. 41, no. 6, p. 063402, 2023, doi: 10.1116/6.0002914.

[61] A. Sawaby, M. S. Selim, S. Y. Marzouk, M. A. Mostafa, and A. Hosny, "Structure, optical and electrochromic properties of NiO thin films," *Phys. B Condens. Matter*, vol. 405, no. 16, pp. 3412–3420, 2010, doi: 10.1016/j.physb.2010.05.015.

[62] D. Khicher, "Study of Transition Metal Oxides Electrochromic Thin Films; Fabrication and Characterisation," no. August, 2023.

[63] E. Feigenbaum, K. Diest, and H. A. Atwater, "Unity-order index change in transparent conducting oxides at visible frequencies," *Nano Lett.*, vol. 10, no. 6, pp.

2111–2116, 2010, doi: 10.1021/nl1006307.

[64] Y.-W. W. Huang *et al.*, “Gate-Tunable Conducting Oxide Metasurfaces - Suplemental Material,” *Nano Lett.*, vol. 16, no. 9, pp. 5319–5325, 2016, [Online]. Available: http://pubs.acs.org/doi/abs/10.1021/acs.nanolett.6b00555.

[65] Z. Sun, A. Martinez, and F. Wang, “Optical modulators with 2D layered materials,” *Nat. Photonics*, vol. 10, no. 4, pp. 227–238, 2016, doi: 10.1038/nphoton.2016.15.

[66] Q. H. Wang, K. Kalantar-Zadeh, A. Kis, J. N. Coleman, and M. S. Strano, “Electronics and optoelectronics of two-dimensional transition metal dichalcogenides,” *Nat. Nanotechnol.*, vol. 7, no. 11, pp. 699–712, 2012, doi: 10.1038/nnano.2012.193.

[67] M. Sakurai, “Spectroscopic ellipsometry,” *Toraibarojisuto/Journal Japanese Soc. Tribol.*, vol. 57, no. 7, 2012.

[68] Y. Yu *et al.*, “Exciton-dominated Dielectric Function of Atomically Thin MoS2 Films,” *Sci. Rep.*, vol. 5, p. 16996, 2015, doi: 10.1038/srep16996.

[69] X. Li and H. Zhu, “Two-dimensional MoS2: Properties, preparation, and applications,” *J. Mater.*, vol. 1, no. 1, pp. 33–44, 2015, doi: 10.1016/j.jmat.2015.03.003.

[70] E. Complete, *CompleteEASE Software Manual Version 3.18*. J. A. Woollam Co., Inc., 2007.

[71] J. N. Hilfiker *et al.*, “Survey of methods to characterize thin absorbing films with Spectroscopic Ellipsometry,” vol. 516, pp. 7979–7989, 2008, doi: 10.1016/j.tsf.2008.04.060.

[72] R. Wang, L. Pan, Q. Han, H. Zhu, M. Wan, and Y. Mai, “Reactively sputtered Ta2O5 solid electrolyte layers in all thin film electrochromic devices,” *J. Alloys Compd.*, vol. 865, no. 158931, 2021, doi: 10.1016/j.jallcom.2021.158931.

[73] J. Eaves-Rathert, E. Kovalik, C. F. Ugwu, B. R. Rogers, C. L. Pint, and J. G. Valentine, “Dynamic Color Tuning with Electrochemically Actuated TiO2

Metasurfaces," *Nano Lett.*, vol. 22, no. 4, pp. 1626–1632, 2022, doi: 10.1021/acs.nanolett.1c04613.

[74] M. A. Kats and F. Capasso, "Optical absorbers based on strong interference in ultra-thin films," *Laser Photonics Rev.*, vol. 10, no. 5, pp. 735–749, 2016, doi: 10.1002/lpor.201600098.

[75] W. M. Abbott *et al.*, "Less is More: Improved Thermal Stability and Plasmonic Response in Au Films via the Use of SubNanometer Ti Adhesion Layers," *ACS Appl. Mater. Interfaces*, vol. 11, no. 7, pp. 7607–7614, 2019, doi: 10.1021/acsami.8b21193.

[76] A. L. Lynch, C. P. Murray, E. Roy, C. Downing, and D. Mccloskey, "Extreme Dewetting Resistance and Improved Visible Transmission of Ag Layers Using Sub-Nanometer Ti Capping Layers," *ACS Omega*, vol. 9, no. 8, pp. 9714–9719, 2024, doi: 10.1021/acsomega.3c09774.

[77] M. Fox, *Optical Properties of Solids*. 2010.

[78] "Potassium hydroxide." http://www.microkat.gr/msdspd90-99/Potassium hydroxide.html.

[79] K. R. Williams, K. Gupta, and M. Wasilik, "Etch Rates for Micromachining Processing—Part II," *J. Micromechanics Microengineering*, vol. 12, no. 6, pp. 761–778, 2003, doi: 10.1088/0960-1317/20/5/055033.

[80] A. Manthiram, "A reflection on lithium-ion battery cathode chemistry," *Nat. Commun.*, vol. 11, p. 1550, 2020, doi: 10.1038/s41467-020-15355-0.

[81] N. Elgrishi, K. J. Rountree, B. D. Mccarthy, E. S. Rountree, T. T. Eisenhart, and J. L. Dempsey, "A Practical Beginner's Guide to Cyclic Voltammetry," *J. Chem. Educ.*, vol. 95, no. 2, pp. 197–206, 2018, doi: 10.1021/acs.jchemed.7b00361.

[82] A. Peroff, "Chronoamperometry (CA)," 2023. https://pineresearch.com/shop/kb/software/methods-and-techniques/potentiostatic-methods/chronoamperometry-ca/.

[83] F. G. Cottrell, “Der Reststrom bei galvanischer Polarisation, betrachtet als ein Diffusionsproblem,” *Zeitschrift für Phys. Chemie*, vol. 42U, no. 1, pp. 385–431, 1903, doi: 10.1515/zpch-1903-4229.

[84] X. Zhang *et al.*, “Inorganic all-solid-state electrochromic devices with reversible color change between yellow-green and emerald green,” *Chem. Commun.*, vol. 56, no. 69, pp. 10062–10065, 2020, doi: 10.1039/d0cc04129g.

[85] B. W. Au and K. Chan, “Towards an All-Solid-State Electrochromic Device : A Review of Solid-State Electrolytes and the Way Forward,” *Polymers (Basel).*, vol. 14, no. 12, p. 2458, 2022, doi: 10.3390/polym14122458.

Chapter 6. Enhanced Structural Colouration & Broadband Absorption Using Ultrathin Lossy Dielectrics in Higher Order Fabry-Perot Resonators.

6.1 Introduction to Higher MIM Fabry-Perot Modes Modified by Strategically Placed Ultrathin Lossy Films

So far, the applications of lossy dielectric absorbers like NiO, MoS_2, WS_2, Si, and Ge on opaque metal backings have been looked at in detail. This asymmetric FP cavity setup allowed access to the zeroth order FP mode and all the advantages associated with said mode such as omnidirectionality, strong light-matter interaction, large reflection contrast, vivid colouration, and polarisation independence in the optical response. While covering the EC process for NiO, the use of higher order FP resonance modes of the 1st and potentially 2nd order ($m = 1$ and $m = 2$ in the FP phase condition), was also looked at to generate vibrant dynamic colouration that was difficult to achieve in the spectrally flat zeroth resonance mode of ultrathin lossy materials. Following directly on from this, new stack designs going beyond the simple absorber/metal configuration can also be shown to have strong light-matter interaction at resonance by targeting these higher order FP modes. Furthermore, in the following pages interesting stack structures, such as ultrathin central lossy absorber dielectric sandwiches and ATF Fano-resonant optical coatings (FROCs), will be investigated. These stacks use ultrathin lossy films to manipulate the higher order FP modes of an MIM that is coupled to it to gain some of the advantages associated with both the zeroth (omnidirectionality and polarisation independent optical response) and higher FP mode regime (sharper colour peaks).

6.2 Centrally Placed Lossy MIM Colour Filters

6.2.1 Lossy Ultrathin Absorber MIM Transmission Filters in Literature

An interesting idea is to add an ultrathin lossy layer to the middle of an opaque or semi-transparent MIM FP resonator for colour filtering purposes. Naturally, the filtering of colour with such a thin lossy layer implies strong absorption is occurring at certain wavelengths too. Some works exist in the literature exploring the concept of centrally placed ultrathin lossy layers, with the main idea being that this stack structure is designed to concentrate the oscillating electric field in the lossy absorber film to supress off-resonant frequencies. In this way undesirable FP resonance modes can be mitigated form the spectral profile as well. This removes unwanted colour peaks and in the right circumstances may also induce broadband strong absorption [1]–[3]. Focusing on the work done by Kyu-Tae Lee *et al*. (2019) as the first step, the transmission FP colour filter stack design they use incorporates many of the concepts previously outlined and also takes advantage of the non-trivial phase shift on reflection between metals and lossy dielectrics in the subwavelength ultrathin regime [4]. Figure 6.1 reveals the simplified MIM transmission filter before lossy layers are added.

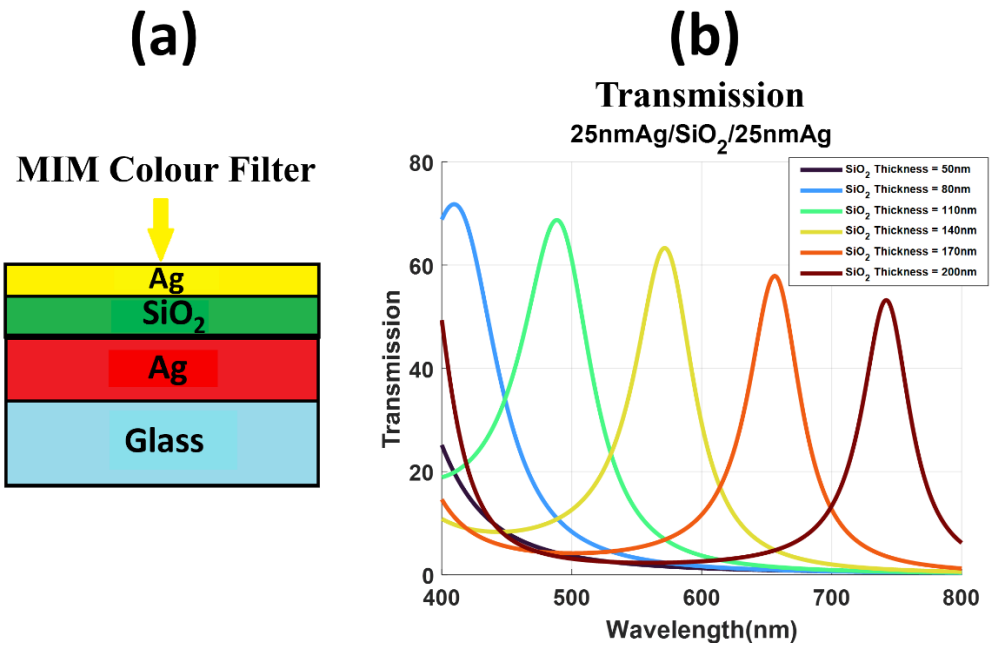


Figure 6.1. (a) The stack cross section of an Ag-SiO_2-Ag transmission colour filter. As this is a FP cavity structure, one can determine its optical behaviour from the phase shift conditions in the light. (b) A simulated array of different spacer thicknesses determining the dominant wavelength of the transmitted light. One can see that the tail end of the red filter peak trends up in the blue region. This mixes the colours.

Careful planning and design through simulation must be done to determine the optimum thicknesses and locations of each thin film for enhancing the purity, saturation, and brightness of the resultant structural colour. This difficulty is non-trivial because lossy dielectric materials can inevitably lead to issues with achieving high colour brightness and poor saturation due to their large absorption coefficient α. This can be compensated against to some degree by tuning the thickness of the metal layers in the MIM to optimise phase shift or performing even more exotic techniques such as mixing lossy layers to engineer ideal EMA refractive indices [3]. Eventually the issues compound to produce low transmission/reflection intensities and therefore dull colours. Only by operating the absorber in the ultrathin film regime can these drawbacks be mitigated to an extent.

Kyu-Tae Lee *et al.* carefully designed their stack such that they had multiple FP resonator cavities coupled to one another as shown in Fig.6.2(a). By doing this they could engineer the depth profile of the electric field in the stack to strongly suppress certain resonance modes more than others. In this case the 5th FP mode is supressed by the Ge while the 3rd mode remains unaffected as demonstrated in Fig.6.3(a).

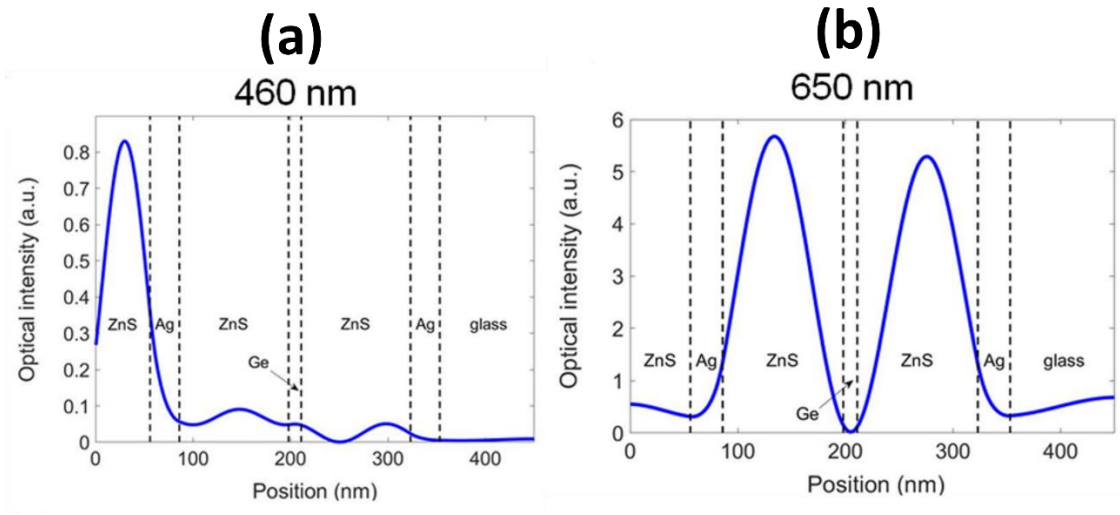


Figure 6.2. (a) The electric field of light w.r.t depth at a wavelength of 460 nm. The Ge efficiently suppresses the 5th order FP mode at this spectral position, eliminating it from the resultant transmission spectrum. (b) The intensity of the 3rd order mode remains completely unaffected, and the transmission peak is purer than a simpler MIM which cannot eliminate higher order adjacent FP mode peaks. [4]

This colour transmission filter stack also has some of the same advantages of the compact zeroth mode FP devices looked at such as a wide colour gamut, a certain degree of omnidirectionality, and even flexibility provided that the substrate is bendable [4]–[6], [7]. The robustness to bending makes this device design potentially useful in certain

technological applications such as the rapidly emerging e-paper and wearable electronics market worth 61.3 billion USD as of 2022 [8]. Moreover, this was all achieved with an ATF approach with no surface texturing, or gratings needed to modify the propagation and many reflections of light inside the stack. There is almost no loss in peak colour brightness intensity either as compared with the simple MIM stack in Fig.6.1(b) and the saturation is superior. Furthermore, with the refractive index and dispersion of ZnS being somewhat like TiO_2, one would preferentially want to use the latter in practical real-world devices as Ag in direct contact with any sulphide material is notoriously unstable and prone to being tarnished [9]. Some more results from the paper are displayed in Fig.6.3 [4].

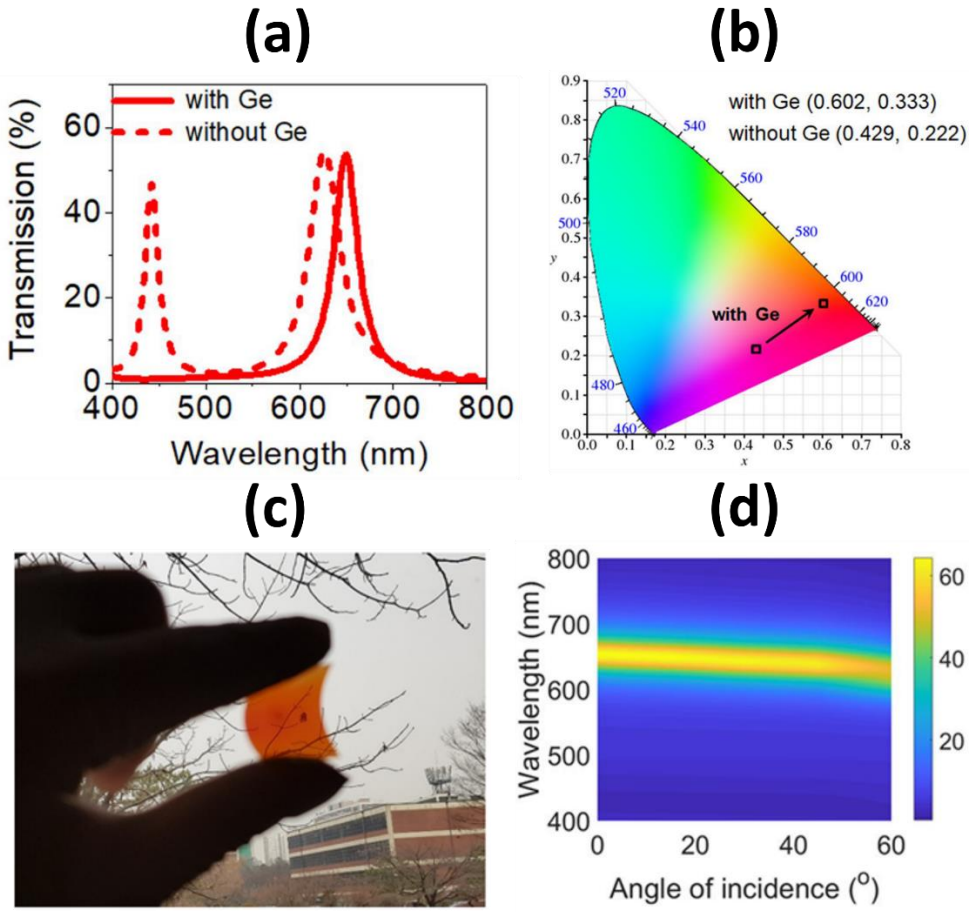


Figure 6.3. (a) The transmission spectra of the colour filter device made by Kyu-tae Lee et al. with and without the centrally placed lossy Ge. The disappearance of the resonance peak at 460 nm corresponds to suppression of the 5th FP mode. The presence of the Ge also redshifts the spectra slightly. (b) The colour map visualisation of (a). The colour transforms from purple to red. (c) An image of the sample deposited on a flexible transparent substrate. The colour remains unchanged even at somewhat steep angle. (d) A surface map of transmission w.r.t AOI. The flat response indicates omnidirectionality though only out to 60˚ which is slightly inferior to the 80˚ of the more compact two-layer FP resonators discussed above. [4]

The table below in Fig.6.4 displays the ideal layer thickness values of the materials used in the paper by Kyu-Tae Lee *et al*. [4]. Each column corresponds to one of the primary colours RGB. As the device becomes thicker the peak resonance position red shifts.

	Blue	Green	Red
Top ZnS	35 nm	45 nm	55 nm
Top Ag	35 nm	35 nm	30 nm
ZnS cavity	140 nm	185 nm	225 nm
Ge	5 nm	5 nm	13 nm
Bottom Ag	35 nm	35 nm	30 nm

Figure 6.4. Ideal layer thickness values when creating a central lossy absorber transmission filter stack with high index spacer materials. [4]

6.2.2 Lossy Ultrathin Absorber MIM Transmission Filters Based on MoS_2 & Cr

In lieu of the literature results shown for Ge, the central absorbing layer can be replaced with another high index lossy dielectric like MoS_2 and the ZnS dielectric spacer with TiO_2 which was made using the NPVD sputtering tool. As a matter of note, Ag cannot be in direct contact with ZnS (or MoS_2 either) due to sample stability issues when sulphides are placed in contact with Ag [9]. Despite this, Ag is a good mirror material in the context of these simulations to show how well these colour filter devices can perform, as silver is a very reflective material in the visible [10]. Al could also substitute in for Ag but with more optical losses occurring on average. See Fig.6.5 below for the resultant transmission spectrum using the red colour target film thickness list in Fig.6.4.

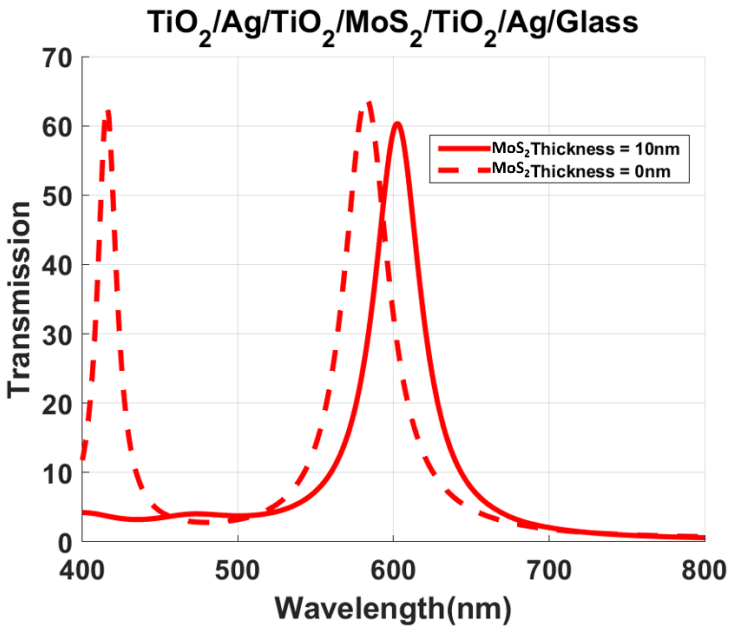


Figure 6.5. Similar behaviour is seen for the Ge transmission filter but with slightly higher peak transmission above 60 %. When MoS_2 is not centrally placed the 5th order FP peak just above 400 nm wavelength re-appears. The stack structure dimensions are the same as the red colour peak target from Fig.6.4, but with ZnS replaced with TiO_2 and a Ag thickness of 30 nm. The resultant transmission colour is yellow instead of red as can be seen on the chromaticity diagram in Fig.6.6. This data is simulated.

The MoS_2 eliminates the 5th order MIM FP mode almost completely from the transmission spectrum just like Ge, but with slightly less light attenuation. The change in colour is illustrated in Fig.6.6 below for this multilayer assembly in the blue, green, and orange colour filter target configurations.

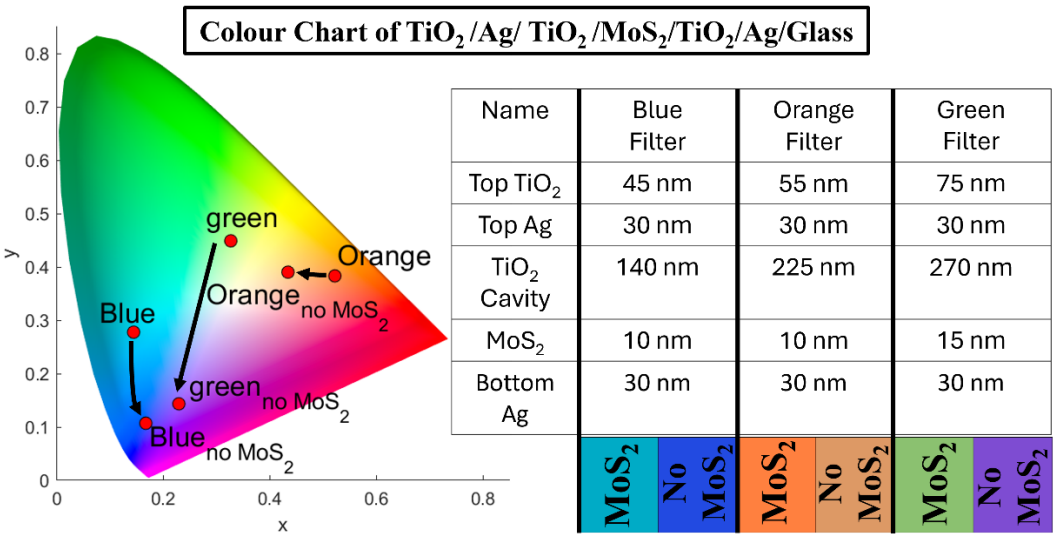


Figure 6.6. Simulated transmission chart of the central lossy absorber stack colour filter using MoS_2. Large colour changes are seen when the MoS_2 is removed going left to right on the colour bar. In the case of the blue colour its saturation is very high meaning the peak will be very narrow and sharp, higher wavelength peaks tend to be broader in terms of FWHM.

Instead of producing a red colour, the thicker spacer arrangement above the orange filter creates a green hue when MoS_2 is present as the central absorber. This is because additional higher FP modes that are not suppressed enter the visible spectrum. ZnS has higher index than TiO_2, so it can more easily avoid this issue due to a more compact stack configuration solution being possible (higher optical density). For the blue filter the spacing between adjacent odd modes is big enough to be larger than 400 nm, meaning even without the MoS_2 the colour is still pure. Therefore, the change in colouration for this blue configuration is due to the red shift caused by the central absorber.

It would be difficult to make such a sample however, as a temperature of 750 ˚C is required to convert oxidised Mo to MoS_2. This would most likely not bode well for the sample stability especially for the thin film 30-35 nm Ag at the bottom of the MIM structure. This metal layer is likely to dewet to a certain extent under the applied heat, even with the addition of the sub manometer Ti substrate adhesion layer shown to be capable of greatly increasing the stability of ultrathin Ag films against dewetting into nanoparticles (up to an annealing temperature in excess of 250 ˚C) [11].

Instead, Cr can be used as the central absorber. Cr has a similar real index and higher extinction coefficient than MoS_2 making it very optically dense and lossy. Its greater optical density allows for the use of a smaller thickness layer of Cr, around 5 nm, to get similar diminishment of the off-resonant transmission response. Furthermore, thinner central lossy layers will also reduce the transmission peak red shift caused by said layer in the stack (due to less phase shift on propagation), making comparison between the supressed state and no suppression state more unfeigned. If the electric field of the light is focused within a Cr thin film, then the light at the 5^{th} order mode can be attenuated very efficiently. The MATLAB simulated transmission spectra for a Cr based colour filter is shown in Fig.6.7, this time illustrating the blue and red colour response together, with and without a Cr absorber film.

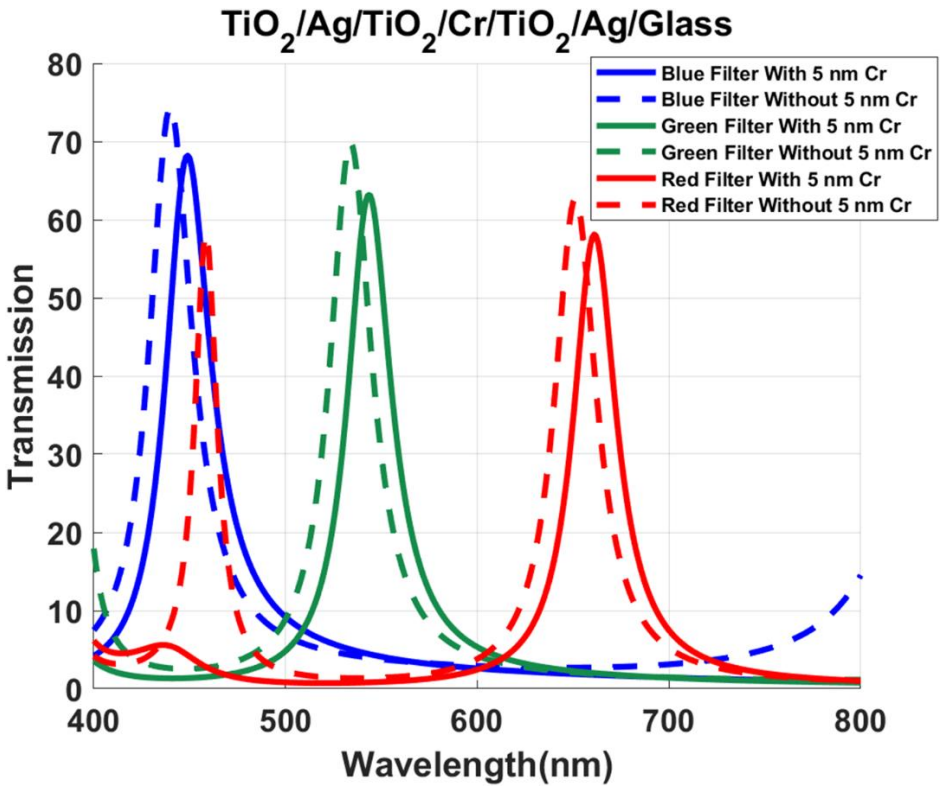


Figure 6.7. There is significant elimination of undesirable FP peaks especially for the red filter in which the light blue transmission peak is greatly attenuated. The central lossy absorber also seems to eliminate adjacent lower FP modes as seen for the blue filter beyond 700 nm wavelength. The addition of the AR layer not only increases peak brightness but also narrows the peak somewhat, elevating the saturation of the colour. Some degree of omnidirectionality is also conferred to the filter using a high index AR and inner spacer too. This data is simulated.

It is clear that lower FP modes can be attenuated such as in the case of the blue filter response at 700 nm wavelength dropping off to zero when the Cr is implemented into the stack assembly. Cr can be deposited using DC magnetron sputtering meaning the filter does not need to be put through a high temperature TAC process to be finalised. It is important to note however that the coating of Cr is incredibly thin. It may be difficult to create a continuous homogenous film of compact Cr at this incredibly ultrathin regime without it spontaneously dewetting. Adhesion layers are needed to counteract this tendency [11], [12]. The same sub nanometre Ti adhesion used for Ag could be used here too. For the sake of film quality a gentler atomic layer deposition (ALD) may be preferable for Cr synthesis at this step, as lots of progress has occurred over the last decade allowing thermal ALD of metals like Ti, Cr, and Co despite their high negative electrochemical potentials [13]. At the very least ALD has finer control over film quality because each layer is laid down one by one, which is why the semiconducting industry uses it for creating high quality copper interconnects on-chip.

The colourimetric response of these Cr transmission filters is given in Fig.6.8 below to picture the improvement that Cr confers to the elimination of off-target FP colour peaks. Although it is difficult to tell the difference in hue for the blue and green filter. The red filter (which came out pinker in appearance) changes colour coordinates by a lot as the 5th order FP mode stands out much sharper in this filter's optical response than for the other two. Even still because the 5th order is not completely supressed with 5 nm Cr, the colour becomes pink instead of red, and purple when no Cr is present. Additional Cr would redden the filter further at the cost of lower 3rd order FP mode peak reflectivity.

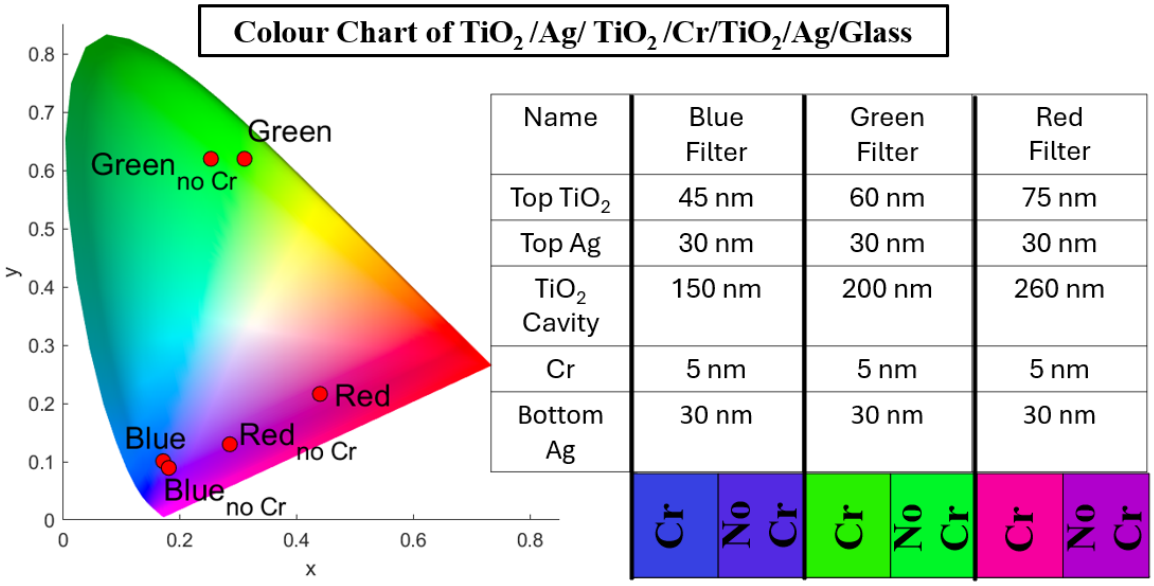


Figure 6.8. Simulated transmission chart of the central lossy absorber stack colour filter using Cr. Large colour changes are seen when the Cr is removed for the red filter going left to right on the colour bar. In the case of the blue and green filter the Cr supresses the 5th order mode and a lower order mode just outside the visible regime in the UV and NIR. These other mode peaks have a small influence on the transmission colour to begin with, so colour coordinate position does not change by a lot. However, the purity is still clearly increased by a small amount when the 5 nm Cr is added as the mixed purple colour become more pink-red.

The angle and polarisation response for these central lossy transmission filters using Cr and MoS_2 are given below at the peak resonant wavelength in Fig.6.9. Specifically in the thinnest and thickest layer arrangements, specified in their respective filter layer dimensions lists, to ascertain how much ultrathin optical response character is imparted onto the thicker higher FP order MIM structure shown to have greater dispersion both spectrally, and angularly in the literature [14], [15].

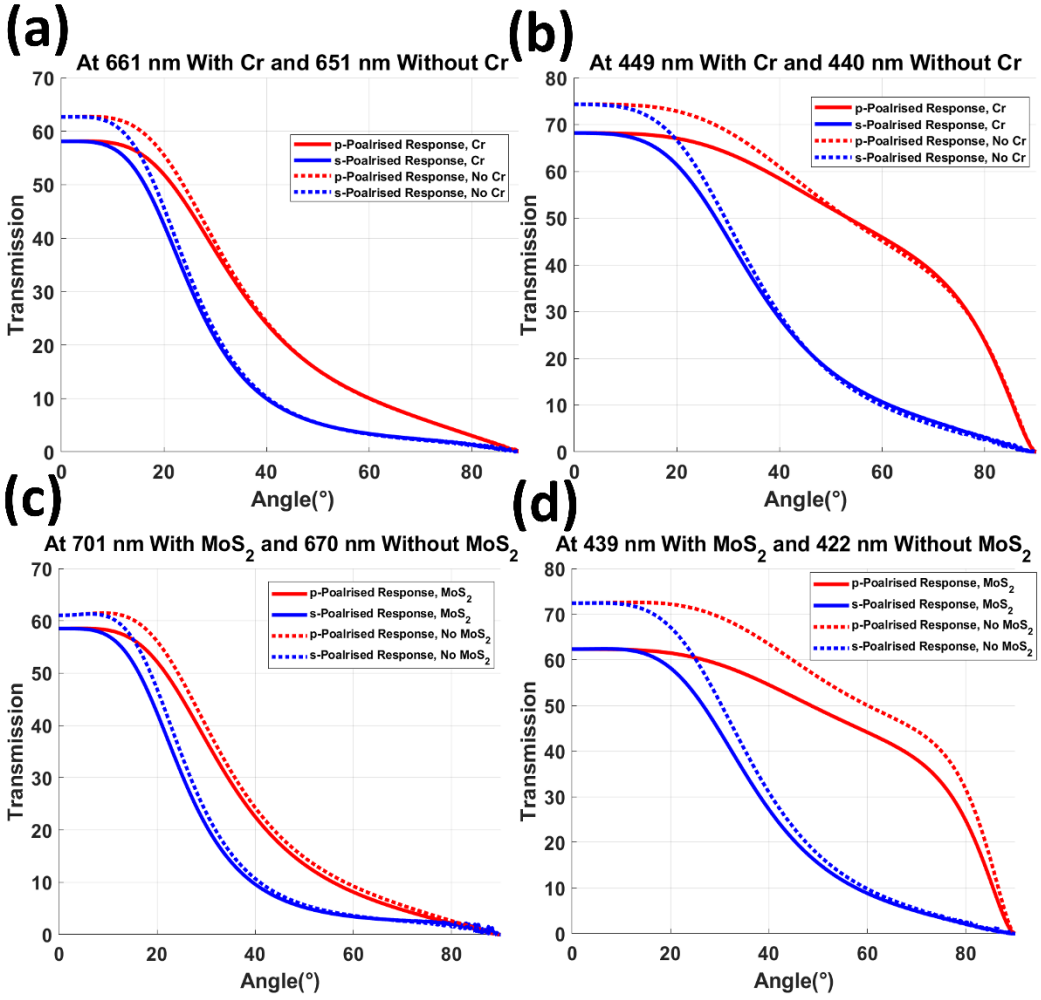


Figure 6.9. The simulated angle and polarisation response of Cr (a)-(b) and MoS_2 (c)-(d) for the thickest (a)-(c) and thinnest (b)-(d) stack configuration. It is clear that the thinner stacks have a flatter optical response especially for p polarisation. There is little difference between the absence and presence of the central ultrathin lossy absorber on the characteristic shape of the response curve. The dispersion is relatively flat out till 20 ˚, beyond which the transmission drops quickly in all cases.

The angle response is noticeably larger than was the case for the bi-layer asymmetric zeroth order FP cavity stack structures in ch.4 p.222. The polarisation response is similar for the thicker transmission filters (redder) while for thinner (bluer) there is a large difference between s and p orientations, with p being flatter in shape. The stack structures themselves are just too thick overall to maintain omnidirectionality out to high AOI. The transparent TiO_2 spacer within the MIM element is at minimum 140 nm, and when combined with the 50-80 nm AR coating and the two 30 nm Ag mirrors, this brings the device structure path length close to the order of the light's wavelength at the very least. Therefore, besides the increased vibrancy of the colouration due to the strong attenuation of light at undesirable resonant frequencies, these transmission filters do not display

noteworthy omnidirectionality in their optical response as compared to simpler ultrathin film lossy high index dielectrics on metal backings [6], [7], [16].

6.2.3 Lossy Ultrathin EMA Bilayer Absorber MIM Reflection Filters in Literature

Centrally placed lossy layers within an MIM FP cavity can also successfully generate vibrant structural colour in a reflecting setup such as the work carried out by Zhengmei Yang *et al.* (2019) [3]. Their stack design is unique in that they work backwards by calculating what the ideal indices of the central absorbing lossy dielectric layer would be to supress undesirable higher order FP modes. The only difference from the previous stack by Kyu-Tae Lee *et al.* [4] is the absence of the top metal layer which primarily controls saturation and brightness. Figure 6.10(a) is a cross section of the reflecting central absorbing FP resonator along with the ideal calculated index of the lossy layer w.r.t wavelength in Fig.6.10(b).

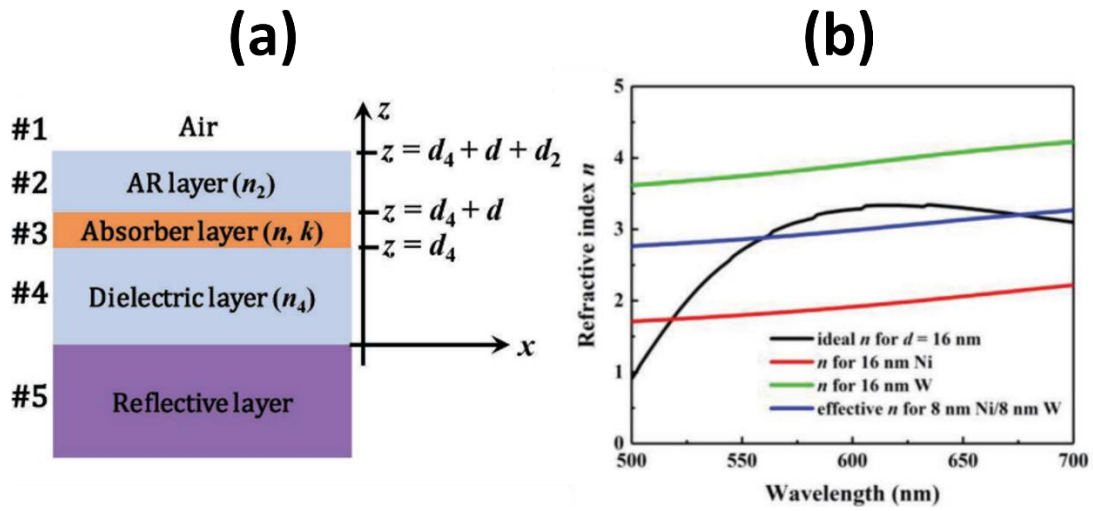


Figure 6.10. (a) Cross section of the FP device made by Zhengmei Yang et al. using an EMA absorbing bilayer to index match the ideal absorber. (b) A comparison between the indices of W, Ni, and their EMA combination with the optimum material to obtain the best colour purity, saturation, and brightness level. [3]

The EMA bilayer, which can also be thought of as an alloy, is optimised to be an ideal absorber for off-peak broadband absorption. Creating ultrathin alloys is a clever way of increasing the design freedom without abandoning the ATF approach. Going into greater detail on the justification behind each layer's position and dimension; The bottom back reflector should be as close to a perfect conductor as possible, meaning Ag would again be the most optimum material to use [10], minimizing any optical losses at the back of the stack. Moreover, the position of the central lossy absorber relative to the back reflector is controlled by the inner dielectric spacer layer dimensions as was the case for the

transmission filters [4]. The thickness of this spacer must be ideal to focus the electric field of light at the target frequencies, coupling it into the lossy strongly absorbing bilayer. When put into equation form, the following expressions can be obtained [3].

$$A(z,\lambda) = \frac{2\pi c \varepsilon_0 n \kappa}{\lambda} \cdot |E(z,\lambda)|^2$$

(6 . 1)

$$d_4 = \frac{\lambda_c}{2n_4}\ , E(\lambda_c)\ \approx 0$$

(6 . 2)

Where $A(z,\lambda)$ is the depth resolved absorption within the EMA bilayer, c is the speed of light, n and κ are the components of the refractive index with their usual meanings, λ is the wavelength, $E(z,\lambda)$ is the depth resolved Electric field, d_4 and n_4 are the thickness and refractive index of the inner dielectric spacer respectively, and λ_c is the peak reflection FP resonant wavelength. By choosing a specific colour one can work back through these equations to find the ideal dimensions to the bottom of the stack structure. Finally, the dimensions of the absorber EMA and the AR layer(s) must be optimised. To do this one can infer that since the electric field at λ_c in the optimum position z is both constant and zero [3],[4], and considering that an AR layer's thickness must satisfy the quarter wavelength condition [16], the following equations can be produced.

$$d \approx \frac{\lambda_c}{4\pi n}\ , d_2 = \frac{\lambda_0}{4n_2}$$

(6 . 3)

Where d is the approximate EMA bilayer thickness, d_2 and n_2 are the thickness and refractive index of the AR layer respectively, and λ_0 is the target wavelength that is supressed by the AR coating. Like with all the FP resonators samples explored so far, a large refractive index is ideal for angle insensitivity and device compactness [3], [16]–[19]. To calculate the optimum indices of the central bilayer absorber a range of thicknesses around

d is selected and from there the total reflection coefficient of the stack is set to zero to produce an array of best fit indices. This is easily done with the transfer matrix method (TMM) in MATLAB. In practice the EMA layer should be between 10 and 20 nm to maximise coupling of light into the stack while also ensuring efficient broadband absorption of the off-peak wavelengths. See Fig.6.11 below [3].

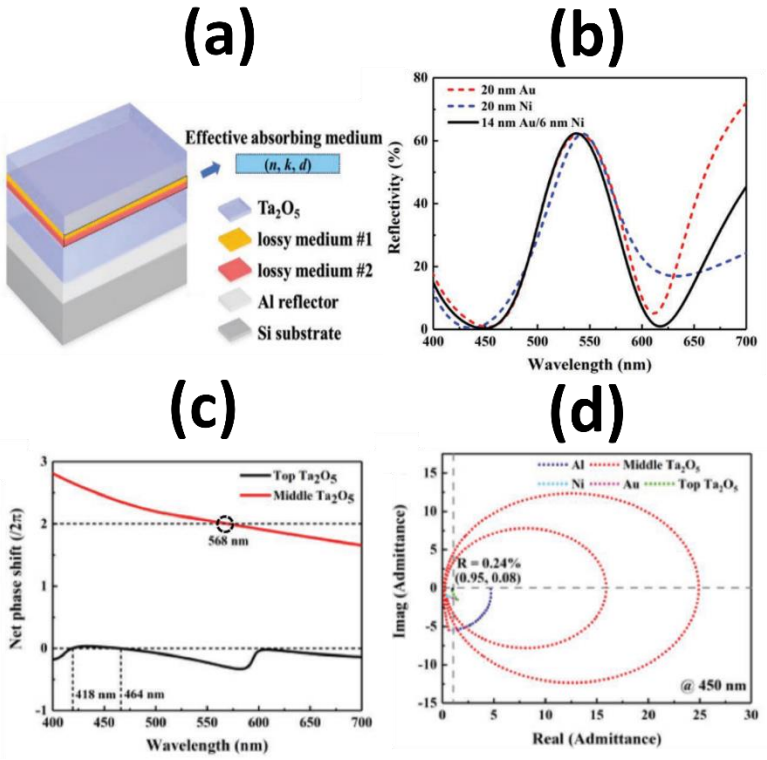


Figure 6.11. (a) Another cross section of the FP resonator made by Zhengmei Yang et al. The absorbing layer is an EMA bilayer lossy alloy. The combination of materials used is decided by best fit to the calculated ideal. (b) The reflectance spectrum of a green pixel device with and without the EMA bilayer. The alloy makes the green colour purer. (c) The phase shift of the light in the inner spacer and top AR layer are ideal for their respective roles in enhancing the green hue. In this case the second mode m = 2 is used. (d) An optical admittance diagram which swiftly informs one that the reflection of light in the blue is very low. [3]

Vivid green is the trickiest colour to generate using the ATF approach due to already mentioned limitations in design freedom. This is a common theme that is found among many of the resonators discussed so far. It is difficult to simultaneously supress the red and blue regions while enhancing the green without going to ever more complex high layer count bulkier stacks. The green colour seen in Fig.6.11(b) is more saturated due to it being the second mode $m = 2$. Higher modes are narrower with steeper dispersion, which is beneficial to saturation and purity, though unfortunately it requires thicker layers that have closely spaced successive resonance peaks. One can see this in the tail end of the green peak located in the red region, also in Fig.6.11(b). This reflectivity would ideally be 0 % or at

least symmetric with the low reflection response in the blue visible region. In this way the colour could be a purer (greener) peak.

The green pixel presented by Zhengmei Yang *et al.* [3] is quite good given the straightforward construction of the stack but there is clearly room for improvement in the red region response. To rectify this, additional AR layers can be added to target two wavelengths instead of one. This would add more complexity however and would further complicate the dynamics of the phase shifting within the stack. The added thickness could also negatively impact on other characteristics like omnidirectionality, a problem that is already present for their green filter in comparison to the red and blue which are at least 100 nm more compact as shown in Fig.6.12 below that lists the optimum layer dimensions for the RGB colourations.

	Top Ta_2O_5	Medium #1	Medium #2	Middle Ta_2O_5
Red	44 nm	8 nm W	8 nm Ge	130 nm
Green	26 nm	14 nm Au	6 nm Ni	228 nm
Blue	68 nm	8 nm Ni	8 nm W	80 nm

Figure 6.12. Idealised thickness parameters for different layer in the bilayer EMA reflector colour filter stack. [3]

To calculate the effective index of the EMA bilayer the equation below can be used [20].

$$\varepsilon_{eff} = \frac{t_1}{t_1 + t_2} \cdot \widetilde{\varepsilon_1} + \frac{t_2}{t_1 + t_2} \cdot \widetilde{\varepsilon_2}$$

(6 . 4)

Where ε_{eff} is the effective permittivity or square of the complex refractive index, $\widetilde{\varepsilon_1}$ is the complex permittivity of the first absorber, $\widetilde{\varepsilon_2}$ is the complex permittivity of the second absorber, and t_1 and t_2 are the respective thicknesses. $t_1 + t_2 = d$. There are alternative ways to add design freedom beside the mixing and matching of lossy layers. For example, a dynamic index material with an electrochromic, thermochromic, or electric bias tuneable response can be used. There exists a plethora of such materials such as NiO and WO_3 that were reviewed for their EC response previously. It would be difficult to incorporate EC

materials into such a stack structure however due to the need for complementary films like the ion storage layers to facilitate the ion intercalation process [21]. A solid-state EC system would utilise this to hold onto the ions without the need for a liquid electrolyte, but practical implementation can be quite difficult. A thermochromic material would be of interest as only a microheater array is required to change the state of the phase change material, without the need for extra unwanted layers to carry out electrochemistry. For VO_2, this crystal phase transition occurs well below the boiling point of water, at 68 ˚C [22], hence a heater array would have little effect on the other metal and oxide films in the stack with much higher melting points or thermodynamic stability (resistance against dewetting and diffusion). More on active index change material use will be discussed later in the chapter.

6.2.4 Lossy Ultrathin Cr/VO_2 EMA Bilayer Absorber MIM Reflection Filters

Using the equations outlined above to target specific resonant wavelengths for colour enhancement and background suppression, and EMA ultrathin absorber can be made using the NPVD system. Instead of using metal alloys, a material like MoS_2 or VO_2 in conjunction with a lossy metal like Cr, Ni, or Ti can be used. If the overall thickness is beneath 25 nm, that is it very deeply subwavelength, then the bilayer absorber effectively acts as one layer from the point of view of the incoming light even if not completely and thoroughly mixed like a metallic alloy would be [20]. Using the TMM, a program can be written to generate the EMA refractive indices of a composite of Cr and VO_2 using the effective medium equation above. A 16 nm bilayer EMA of 10 nm Cr and 6 nm VO_2 was found to meet the ideal indices condition for strong broadband absorption outside the resonant colour wavelength position λ_c. Essentially the ideal indices are on the order of 2-3 for both the real and imaginary component of the refractive index, increasing as one moves toward redder wavelengths [3]. Figure 6.13 below shows the indices of the EMA bilayer compared to its individual elements.

The stack structure used is a slight modification of what has been seen of the work done by Zhengmei Yang *et al*. [3]. Instead of one AR layer, two of them are used to eliminate two off-resonant positions for a flatter absorption response around the colouration peak. To achieve this a bilayer AR coating with variable thickness is wielded based on transparent zinc (ZnO) and TiO_2. Although the way in which two coupled AR coatings eliminate light is not strictly a linear addition of the independent response of both, a simple and useful view is to imagine each coating reducing the reflection at its target wavelength [23]. This

elimination will cause dips to form in the reflectivity intensity profile, and when two AR layers are used in tandem a characteristic W shape will appear with two minima instead of one. As can be seen in the Fig.6.14(c).

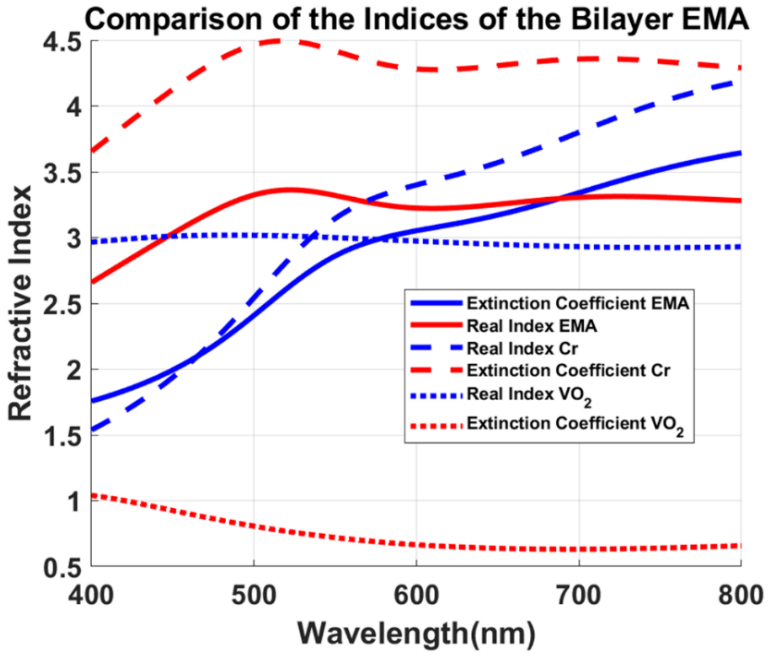


Figure 6.13. The 16 nm EMA absorber is three parts in eight VO_2 and five parts in eight Cr. The mixture of the two creates an effective medium with $n \approx \kappa$ across the visible but with a slight downward trend in the blue part of the spectrum. This matches the ideal dispersion curves seen in the work of Zhengmei Yang et al. [3] *for strong broadband absorption of off-resonance light.*

Compared with the transmission colour filters discussed on p308-314, the peak brightness of these reflection filters is higher around 90 % at the peak. There are big differences in the spectra produced by the EMA bilayer as compared to an equivalent layer made from only VO_2 or Cr only. By mixing the two lossy absorbers together, the elimination of wavelengths targeted by the anti-reflection coating layers is very efficient due to light being trapped. By changing the thickness of the internal TiO_2 spacer the resonant peak position can be blue or red shifted accordingly. Although a 16 nm EMA is used for each simulated RGB filter, further optimisation could be done likely with a thinner EMA being employed for the blue filter stack and a thicker near 20 nm EMA for the red filter.

More detail is given on the exact stack configuration for each filter colour in Fig.6.15. The most nontrivial aspect of the design is the AR coating layer thicknesses and arrangement wherein the TMM was used to optimise for minimisation of reflectivity at certain target wavelengths. To maintain the possibility of an angular independent response, also seen in the zeroth order FP devices, high index films are used throughout where $n > 2$. For the

blue filter both the ZnO and TiO_2 are placed at 45 nm and the light above 500 nm wavelength is greatly attenuated. The green filter has a 35 nm ZnO and 80 nm TiO_2 to trap light in the blue and red parts of the spectrum, respectively. The red filter uses very thin AR layer, 35 nm ZnO and 12 nm TiO_2, to lower the blue and green region reflectivity as much as possible.

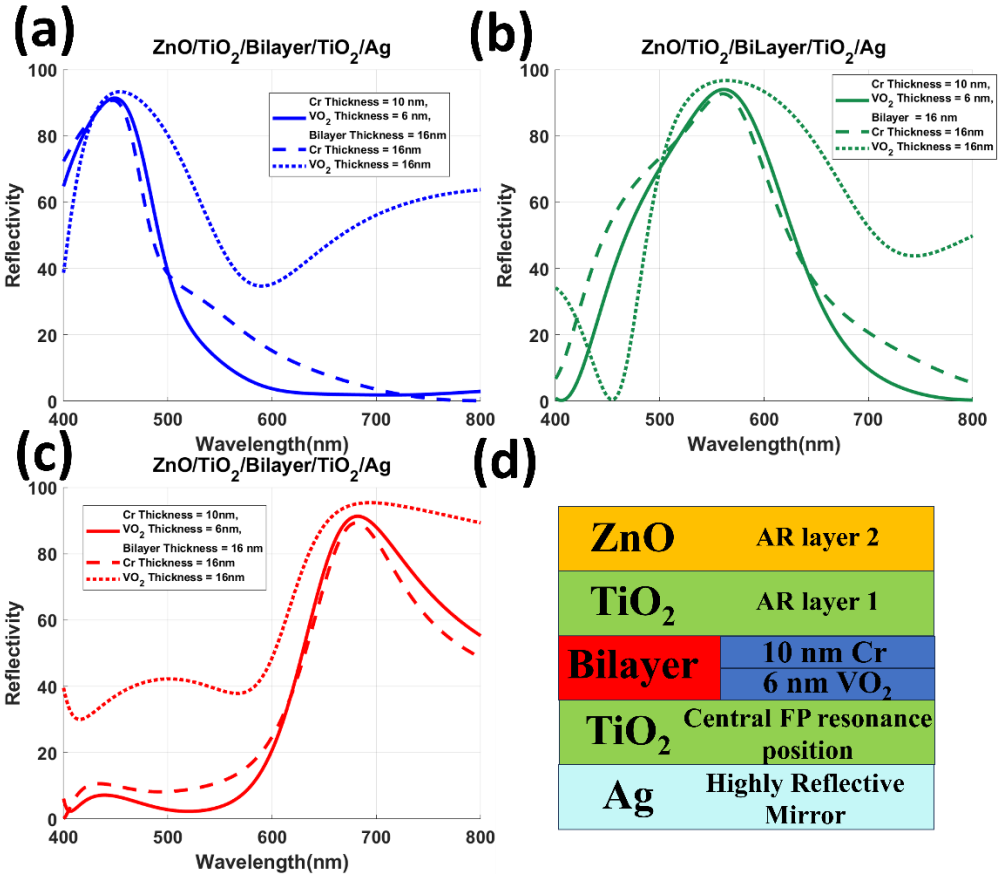


Figure 6.14. Different configurations of the EMA Cr/VO_2 bilayer absorbing stack (d) are shown producing (a) blue reflection, (b) green reflection, and (c) red reflection. The antireflection coatings ZnO and TiO_2 target different off-resonant wavelengths to lower the background spectrum away from the colour peak. The characteristic W reflection curve of a two-layer AR coating system can be seen in (c) between 400 and 550 nm. The brightness is high, but the saturation of the colours is not as large as for the Ge transmission filter sample given the resonant peak broadness of FWHM around 100-200 nm. This data is simulated.

Figure 6.15 presents the colourimetric response of these filters on the CIE chart. The blue and red filters, (a) and (c) respectively, are more vibrant in colouration as the colours produced at the edges of the visible spectrum benefit from the cut-off in sensitivity of the human eye. This allows effectively half of the breath of the resonant peak on either end to be ignored. The large FWHM of these peaks becomes apparent for the green filter, (b), causing its colour to become more pastel in appearance than vivid and saturated. In general, the colour of the filter is drabber for "Cr only" when used in place of the EMA bilayer, and even more dull when VO_2 is employed alone due to its flat index dispersion [1].

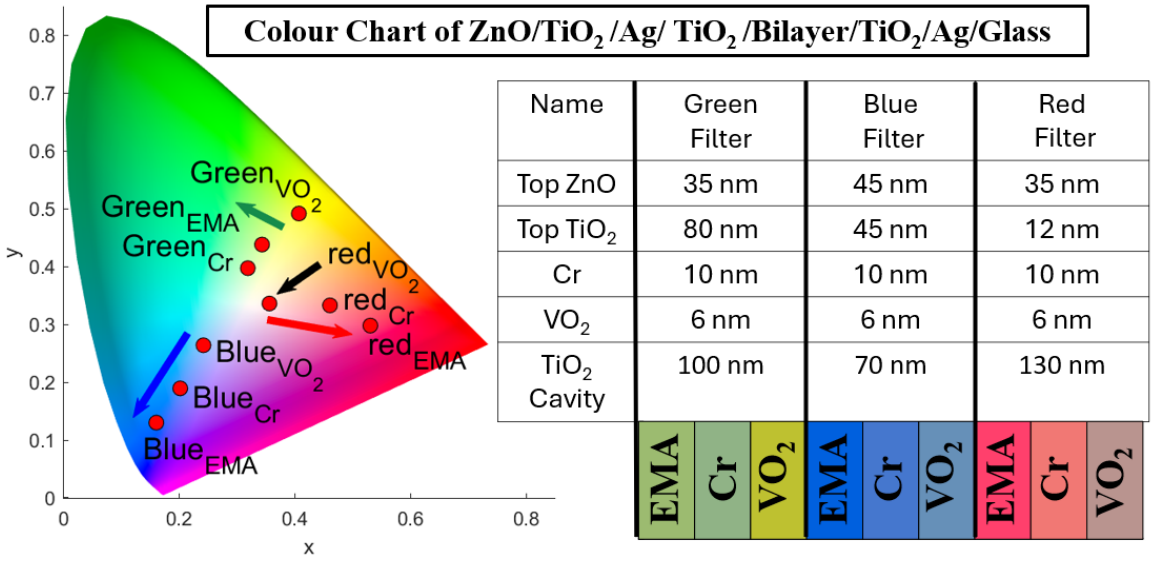


Figure 6.15. The simulated colouration of the reflection filter using a 16 nm EMA layer based on 10 nm Cr paired together with 6 nm VO_2. The stack configuration for each primary colour is given. Two AR coatings are used to eliminate off-resonant wavelengths more effectively and thoroughly. While red and blue are vibrant in appearance the cracks in the armour begin to show for this assembly in the green response which is duller than expected. This is due to low saturation caused by large colour peak FWHM, even with the two AR coatings helping to eliminate light on either side. To circumvent this issue a narrower FP mode must be utilised with an ultrathin absorber. Fano-resonant devices, discussed later, can possibly help in realising this.

For ideal colouration, the FP resonant peaks should be as sharp and narrow as possible, and this is not simple or practical to accomplish with this stack structure layout. To remedy the issue, Fano-resonance will be discussed later as a means of generating bright, saturated, and pure (one colour peak in the visible) colouration in an ATF approach [19], [24]. Before moving onto true broadband absorption without resonant FP reflection colour peaks, the angle and polarisation sensitivity response of these EMA ultrathin bilayer absorber filters will be characterised in a similar fashion to the transmission filters from p.308-314.

The angle and polarisation response for each reflection filter is much the same as seen in Fig.6.16. The reflectivity remains mostly unchanged out to 20° AOI after which there is a gradual drop off in reflectivity down to 60-70 % intensity around 70° AOI. This drop off in proportionate terms is only a reduction of a quarter in overall brightness compared to normal incidence. Furthermore, the colouration is stable even out to 70° demonstrating the large degree of omnidirectionality in the response of this stack structure. The change in colour depending on light's orientation is also shown in Fig.6.16(d) where the colour coordinate s-polarisation position is greater for the blue and green filter, while the opposite is true for the red filter.

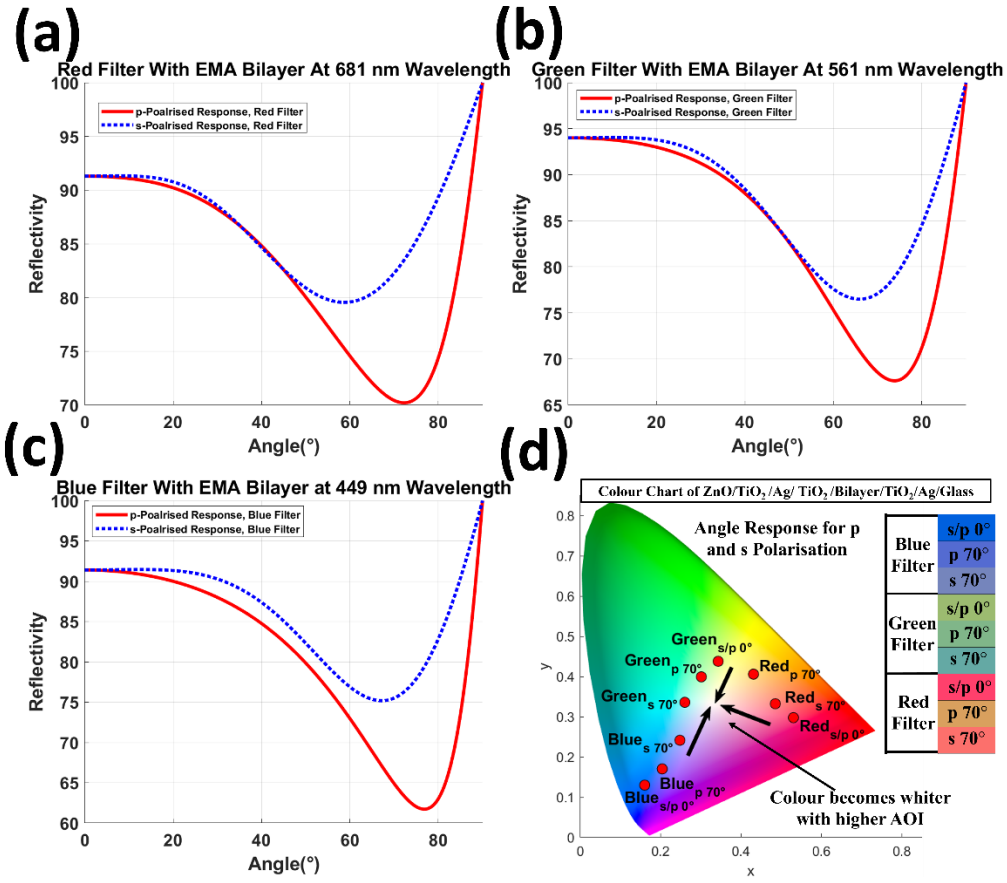


Figure 6.16. The simulated red (a), green (b), and (c) blue reflection filters have a similar angle and polarisation response. There is considerably less dispersion present in the optical response compared to the central lossy absorber transmission filter devices using Cr and MoS_2. The vivid structural colouration is maintained quiet well even out to 70° AOI. As the angle increases beyond 80° the sample colour coordinates converge on the middle white (0.33,0.33) x-y position for both polarisation states. The large FWHM on the order of 100-200 nm limits the purity of the colours in the middle of the visible spectrum like green, yellow, turquoise, orange, etc. Sharper more dispersive resonance peaks are needed to overcome this.

Thus, the main conclusion that can be drawn from this angle-resolved data is that the optical response of these absorbing EMA bilayer assemblies has many of the same advantages associated with the zeroth order FP resonators that use ultrathin lossy films, while concurrently also possessing the stronger colouration abilities inherent to thicker device structures that can access more spectrally dispersive higher order FP modes [25]. The amount of absorbing material present can also be considerably less in this arrangement than the ultracompact two-layer FP stacks as the additional high index transparent TiO_2 and ZnO layers help to focus the light into less material volume. The absorbing EMA layer never exceeds 20 nm while Si, Ge, and TMD samples on metal backings must be thicker over a larger range of the ultrathin film regime (10-50 nm) to realise a varied but inferior colouration gamut [7]. Thinner absorbing films almost always help to ensure the tallest possible intensity peaks in the output spectra compared to bulkier attenuators by minimizing

undesirable optical losses at the peak. In so doing it becomes feasible to picture an ultrathin few-layer lossy ATF device being able to approach the same kind of brightness level that much more bulky multi-layer broadband Bragg reflectors or complex all-dielectric nano ring-resonator meta surfaces can produce, i.e., near to unity intensity (100 % reflection) [26].

The layer resolved absorption data shown in Fig.6.17 below exhibits how the light trapped by the two AR films is preferentially attenuated by the EMA absorbing bilayer instead of the back Ag mirror. Meanwhile the MIM FP resonant peak is completely unaffected as the top absorber appears transparent to the light at that frequency. Moving on, an overview and analysis of strong broadband visible absorption using a centrally placed ultrathin high index lossy dielectric with low index spacer and capping layers will now be given.

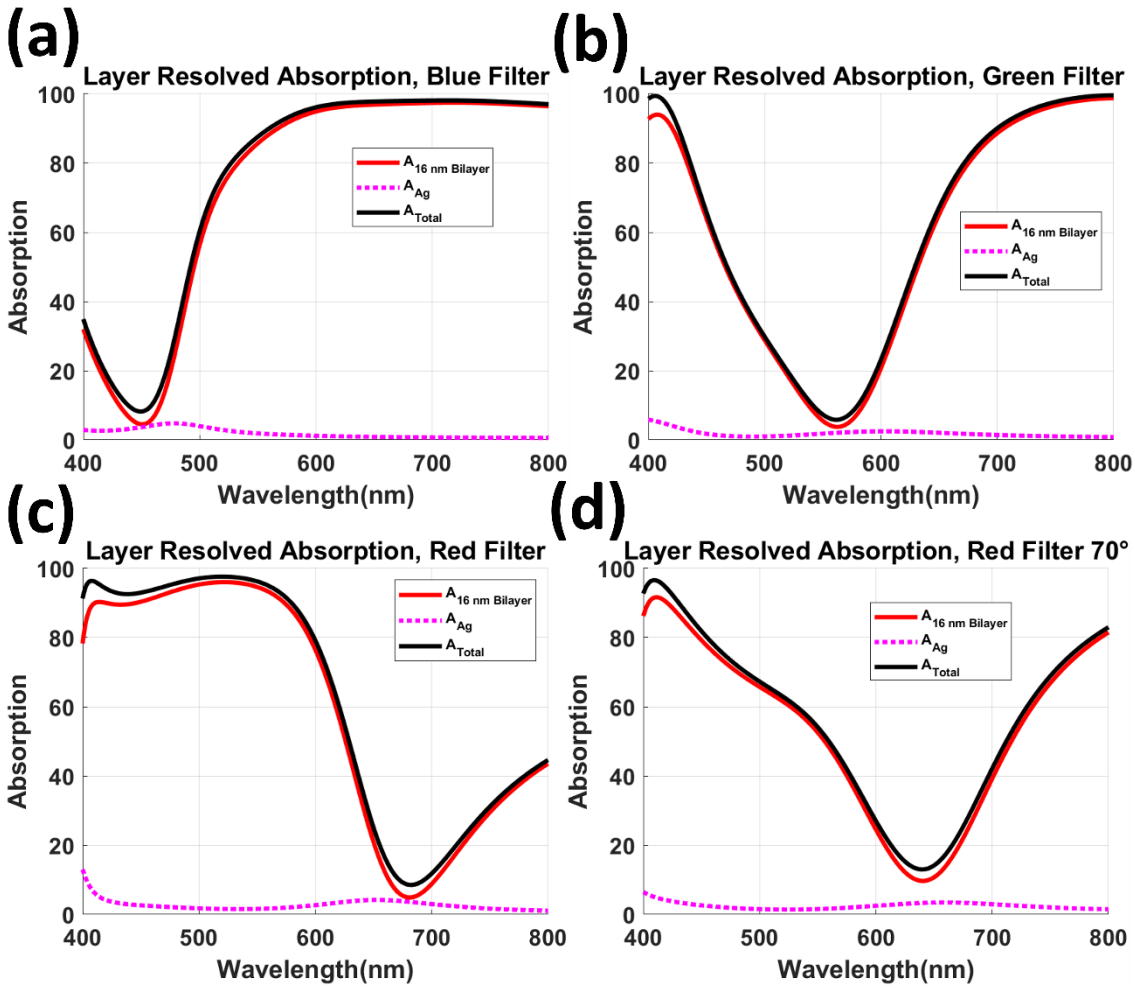


Figure 6.17. (A)-(c) The s and p polarisation response are identical at zero AOI. The light trapped at off-resonant wavelengths by the ZnO and TiO_2 AR coating layers is almost completely attenuated solely by the EMA bilayer. The silver layer absorption is very small and with no dispersion, acting like an ideal back mirror. (d) This strong absorption of light continues even at large AOI equal to 70°, demonstrating how well this stack structure focuses the incoming light into the 16 nm EMA absorber. This data is simulated.

6.3 Centrally Placed Lossy Ultrathin Broadband Absorber

6.3.1 Overview of Ultrathin Broadband Absorption Optics & the Ideal Stack Structure

Very interesting work done by Huixu Deng *et al*. (2015) [2] lays the groundwork for how the design of the base stack can be approached for the centrally placed lossy dielectric broadband absorber. Their design template, using 7 nm Cr films, presents several key advantages over contemporary broadband absorption devices such as being lithography-free, ultrathin, and highly temperature resistant. This last point is crucial in the case of solar thermal applications where the active layer can reach high temperatures [19]. Due to size effects at the nanoscales being dominant many metals will have lower metal melting points in the ultrathin regime, hence its preferable for light to be trapped and attenuated inside a refractory metal film than a noble metal like Au or Ag [27]. By using a metal such as Cr or W as the active absorbing layer, the operating temperature for solar thermal absorption can be greatly extended. The work by Huixu Deng *et al.* presents an analytical solution for an ideal absorbing layer based on the impedance matching method. This method, derived from wave optics, can be extended arbitrarily across the EM spectrum. The regime of greatest interest in this thesis is the visible spectral region given the fact that the sun gives off most of its radiated energy across that wavelength range [28].

The stack design at its simplest is a dielectric/thin-metal/dielectric/thick-metal structure, that is familiar from the EMA bilayer stack filter shown in Fig.6.14(d) p.320, shown below in Fig.6.18. Using impedance matching [29], and making certain assumptions about the nature of the materials involved (PECs back metals) one can derive the ideal permittivity of the active ultrathin absorbing film inside the multilayer assembly. Some of these assumptions include the active layer being extremely thin compared to the wavelength of light being absorbed (deeply subwavelength condition) wherein the phase propagation delay shift of the top metal absorber $\delta_m = k_0 d_m << 1$ [2]. The back metal must have a negligible real index n as well with a large κ to maximise the impedance mismatch, reflecting as much light as possible back into the active layer within the structure. Au and Ag are good choices.

The impedance matching equation is quiet unwieldy in size [2] but the important behaviour to note is that the resultant absorption bands are a function of wavelength and dielectric spacer thickness, as seen in Fig.6.19. By changing the thickness or indices of the dielectric

spacer one can modify the absorption characteristics of the stack. In place of Cr, other absorbers could be used such as Si, Ge, and MoS_2 all of which are more useful for photovoltaic applications as the absorbed energy will generate electron-hole pairs instead of excess heat [10]. The ultrathin film nature of the central absorbing layer could also be advantageous for recovering hot electrons before they thermalise, allowing the output voltage of the PV cell to operate beyond the bandgap limit though this would necessity the inclusion of a network of metal contact throughout to collect the excess charge [30]. Conversely ITO/FTO thin films may be used instead as both a transparent capping and inner spacer while also conducting charge out [31].

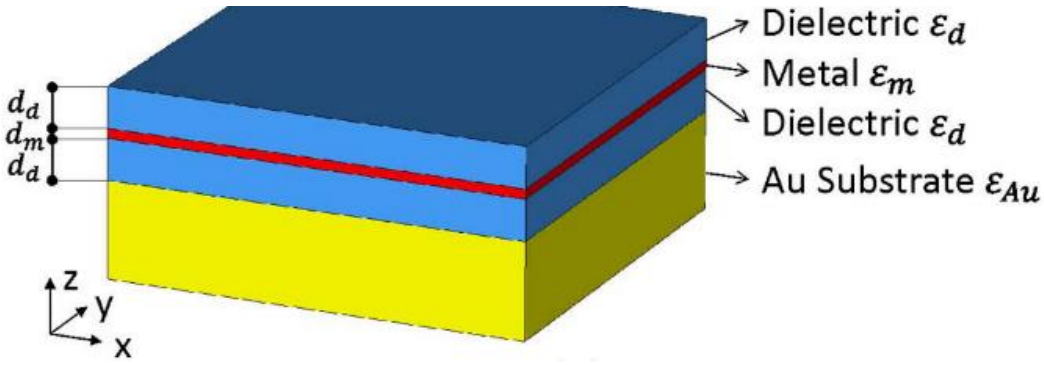


Figure 6.18. The stack structure of these low index dielectric sandwich broadband absorber devices. The centrally placed refractory top lossy metal is ultrathin while the back metal is optically thick and reflective. The ideal back metal mirror is a perfect electric conductor (PEC) with uniform broadband reflectivity. The electric field of light is focused within the ultrathin top lossy metal creating an overall black appearance to the stack. [2]

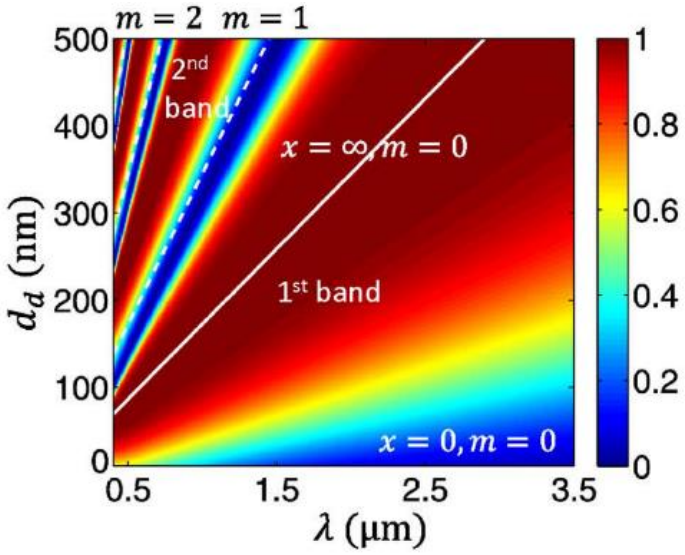


Figure 6.19. The absorption bands with an ideal ultrathin 7-8 nm top metal layer. These bands are a function of dielectric thickness and wavelength. The dashed and solid white line are the beginning and middle of the absorption bands respectively. [2]

The bandwidth of the absorption bands, $\delta\lambda$, is given by the ratio of wavelength to dielectric thickness. The refractive index of the dielectric will also affect the bandwidth as the optical path length will be changed. Relevant equations describing the bands are given below [2].

$$x = 0: d_d = \frac{m}{2n_d}\lambda_0, m = 0,1,2,\cdots; \quad (6.5)$$

$$x = \infty: d_d = \frac{(m+0.5)}{2n_d}\lambda_0, m = 0,1,2,\cdots; \quad (6.6)$$

Absorption at $x = 0$ will always be minimised near zero while at $x = \infty$, the middle of the band, the absorption will be maximised near to unity. In terms of the impedance Z, $Z = -i/\kappa_{Au}$ (where κ_{Au} is the extinction coefficient of gold) when $x = 0$, and $Z = 1$ when $x = \infty$. Which is to say light enters the stack easily in the middle of the absorption band and poorly in the dark blue narrow bands in between. It is clear that the lowest zeroth mode FP condition can be fulfilled for this stack structure as well in the first $x = \infty$ band [2]. Furthermore, this zeroth band is a little steeper like the dispersive higher order FP modes than the zeroth mode band previously seen in the ultracompact absorber/metal stacks in ch.4. The increased steepness is somewhat offset by the broadness of the zeroth absorption band; however, it can be readily seen that the increased dispersion in the band wr.t. wavelength makes it difficult to continue the broadband absorption response for a single stack out beyond 1000 nm wavelength as this places one in the $x = 0$ region where reflectivity is high. This higher reflectivity may be a blessing in disguise though as a multilayer thin film absorber structure can be designed around the idea of selectively rejecting thermal radiation while absorbing the visible to help keep them cooler since NIR frequencies lie below the bandgap energy of many semiconductors and only contribute to lattice thermal excitation [19].

The low index internal spacer and top AR coating form FP resonances that compensate each other, making it possible to maintain the zero-phase delay accumulation condition even for much bulkier stacks, across the visible and NIR regime provided that the top absorber metal

is kept high index and ultrathin [2]. This is the main differentiating point between the central lossy broadband absorber and the bright reflection colour filter EMA bilayer stacks discussed previously on p.314-320, which makes use of a thick inner spacer layers and two thinner sub 100 nm AR coatings to preserve the broad FP peak and selectively eliminate the rest of the light in the visible spectrum. See Fig.6.20 below for clarity on this point.

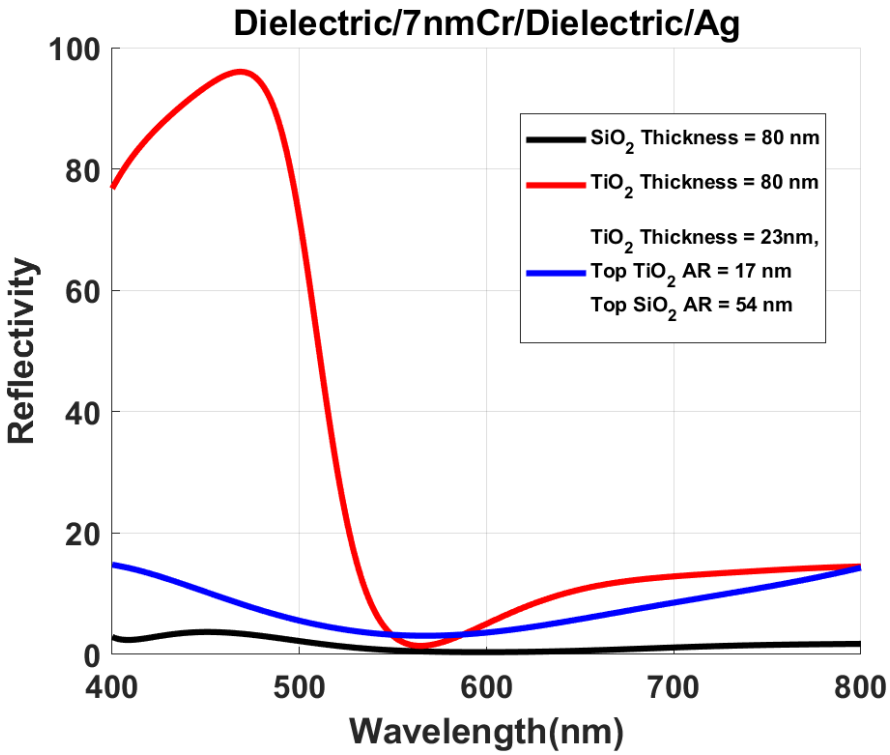


Figure 6.20. Using 80 nm SiO_2 as the top and bottom dielectric, broadband absorption can be achieved using a symmetric setup. Using 80 nm of TiO_2 for the top and bottom dielectric one can see a strong reflection peak instead indicating that a x = 0 strong reflection band has been crossed over. In practise, if one wants to create a broadband absorption response with a high index spacer, the thickness of the internal spacer must be driven down considerably to 20-30 nm and then make use of at least two AR layers to trap the light more effectively at left-over problematic reflective wavelength regions. The solution achieved with symmetric SiO_2 is much simpler and superior in its attenuation. This data is simulated.

If the thickness of the high index TiO_2 spacer in the EMA bilayer reflection filter is decreased, the reflection response can be flattened out due in part to the fundamental FP resonance being located outside the visible region, but it still will not be as broadband and flat as the symmetric stack shown by Huixu Deng *et al.* [2] The reflection response of the EMA absorber can be further flattened and lowered by using a very thin spacer around 23 nm and optimising a two-layer AR coating system on top of it, but again the absorption will not be as large. However, solutions do exist for higher index asymmetric broadband absorber setups like the configuration in Fig.6.21 below using 5.5 nm Ge as the top metal and 100 nm Ge as the bottom. In this stack the light is not trapped and preferentially focused onto the

top Ge layer. Instead, there is a 50/50 attenuation split between the top and bottom germanium in the optimum layer layout. Overall absorption across the visible (400-800 nm) is 99.27 % and because the top and bottom Ge are in direct contact with ITO one can envisage the improvement in external quantum efficiency as electrons and holes can escape the deeply subwavelength 5.5 nm Ge more easily before recombination or thermalization [32]–[34].

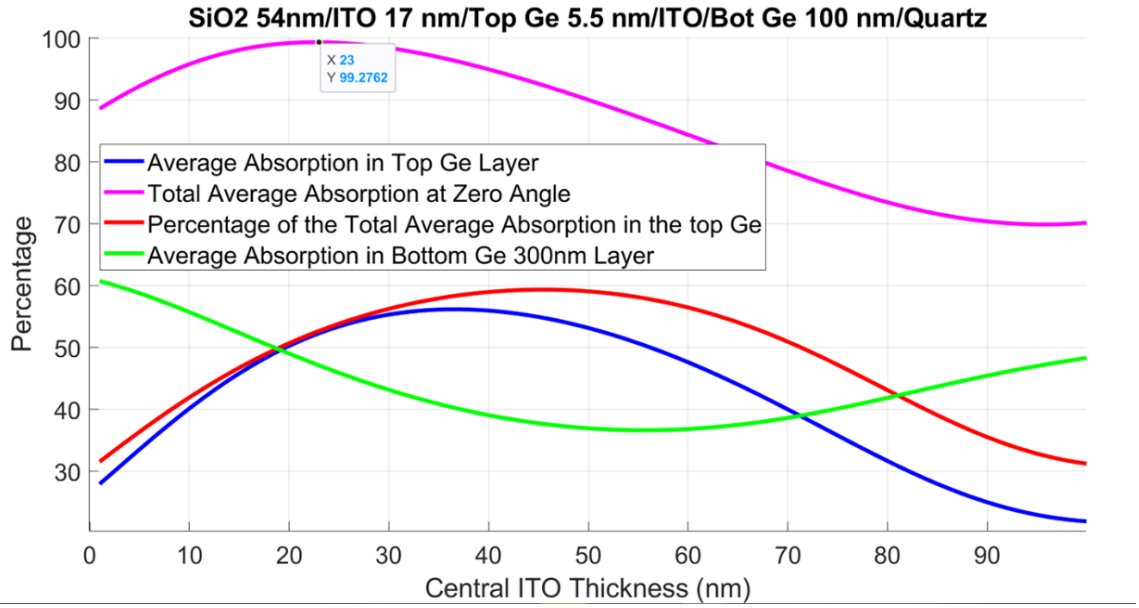


Figure 6.21. The average absorption across the visible is 99.27 % for the stack configuration shown. 50 % of the absorbed light is attenuated in the ultrathin 5.5 nm top Ge while the rest is extinguished in the bottom 100 nm Ge. The high index ITO dielectric layers are very thin to help flatten the reflection response. Finally, a lower index SiO_2 is added on top to improve impedance matching further. This data is simulated.

In the symmetric central ultrathin lossy absorber stack, the ideal dielectric spacer refractive index for broadening the absorption wavelength range as much as possible is as close to the index of air as one can get [2]. For this reason, SiO_2 makes a good choice as the index of SiO_2 is $n = 1.45$. Similarly, MgF_2 could be used as well due to its even lower index of $n = 1.38$ [35]. With all this information in hand the analytical equations for the ideal real, ε'_{dm}, and complex, ε''_{dm}, top metal absorber permittivity is given below [2].

$$\varepsilon'_{dm}(\lambda) = -\frac{\varepsilon_d}{\kappa_{bm}\delta_m} \tag{6.7}$$

$$\varepsilon''_{dm}(\lambda) = \frac{\varepsilon_d(\kappa_{bm} - \varepsilon_d\delta_m)}{\kappa_{bm}\delta_m}$$

(6 . 8)

Where ε_d is the permittivity of the dielectric, κ_{bm} is the extinction coefficient of the back metal, and δ_m is the phase shift of the top metal. When these are converted into indices n and κ and plotted against wavelength, the graph in Fig.6.22 below can be produced, provided all the materials in the stack have been well defined in the TMM. Cr is found to be the closest match of any metal to the ideal index dispersion w.r.t wavelength. This indexing match is consistent out until a wavelength of 1500 nm, after which the indices of Cr diverge too much away from the ideal [2].

Changing the thickness of the ultrathin layer will affect the ideal indices greatly. Extremely thin lossy films around 3 nm will require very high n and κ of 10 or higher to attenuate the light effectively. Such a material does not exist naturally. Too thick and the deeply subwavelength ultrathin condition will no longer hold. A top metal that is too thick will also decouple the top half of the stack from the bottom due to opacity. Therefore, in practice the sweet spot for the ultrathin central absorber thickness is 6-10 nm [2].

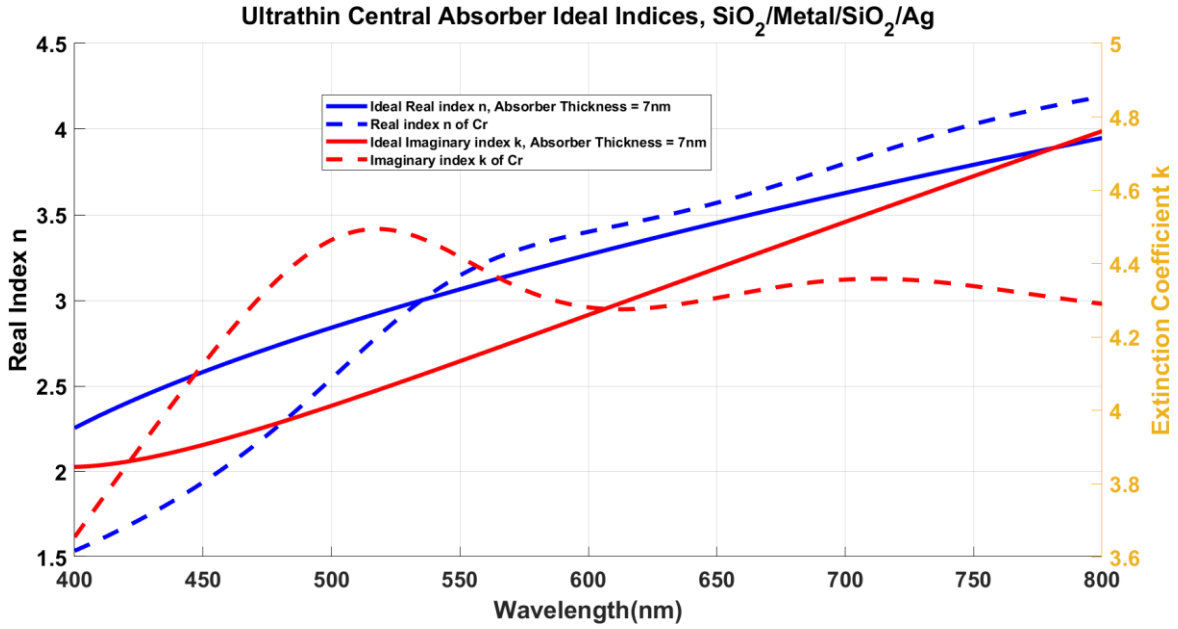


Figure 6.22. The ideal n and κ indices, for broadband absorption, of a 7 nm top absorbing metal layer in a symmetric low index dielectric sandwich on a highly reflective Ag back mirror substrate. This result is compared to ellipsometry measured Cr indices, showing a close match between 400-800 nm wavelength.

Huixu Deng *et al*. [2] also has data experimentally verifying how noble metals in place of Cr, W, or Ni will produce poor absorption profiles as Fig.6.23 demonstrates with UV-Vis-NIR spectroscopy data. The more reflective the top absorber material is the worse its performance will be due to the large impedance mismatch generated when $n << 1$ and $\kappa >> 1$. The top metal or absorbing ultrathin film must be lossy with high n and κ.

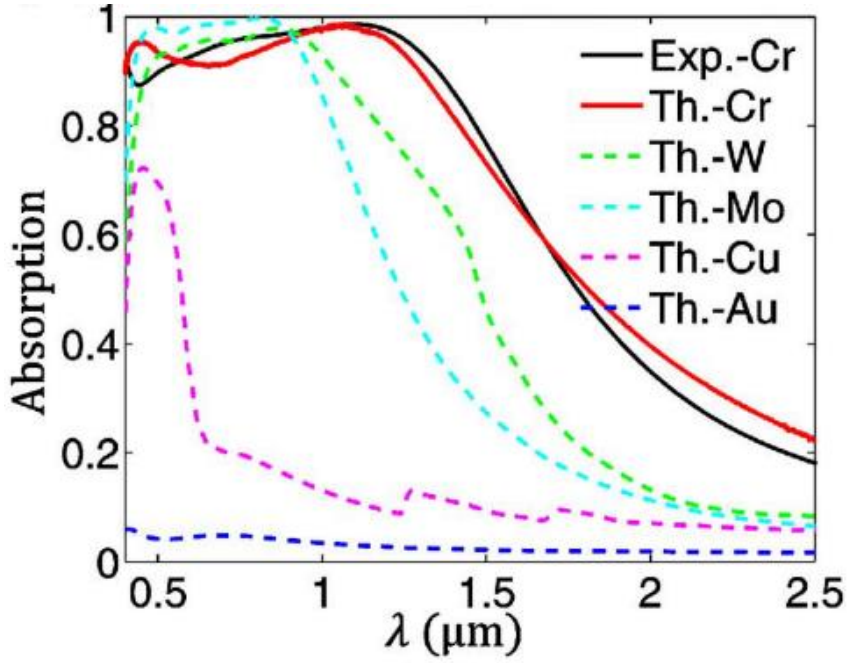


Figure 6.23. The absorption profile of many different top metals with Au backing and SiO_2 dielectric spacer and capping layer. The absorption response is large, broad, and flat for Cr, W, and Mo in the visible while in contrast to this the response of Au and Cu is very dispersive and narrow. [2]

In Fig.6.23, the drop-off in absorption beyond 1000 nm wavelength (in the NIR) can be mitigated to some extent by increasing the number of Cr-SiO_2 layer elements in the stack, one on top of the other, however this will increase sample complexity and thickness which may negatively affect angle response sensitivity as seen for the transmission colour filters on p.313. Furthermore, it is important for the Cr deposition to be as precisely controlled as possible to ensure a high quality and continuous film with n and k in the ideal range. A porous or discontinuous Cr layer will perform imperfectly due to lower effective index. Ideally a smooth and homogenous Cr film is most desirable as small variations in thickness can greatly affect the attenuation of the light [2].

Absorption is less sensitive to dielectric thickness, particularly the top dielectric, which is mostly acting as an AR layer, so deposition can be more aggressive and less controlled at this step of the sample creation process. To prove that the strong broadband absorption

occurs primarily within the ultrathin Cr layer a heat generation distribution Q is calculated by Huixu Deng *et al*. [2] from the propagation of the electric field inside the stack structure at 500 nm wavelength, shown below in Fig.6.24. MATLAB calculations using the transfer matrix method corroborate this in the layer resolved absorption graph found in Fig.6.25 showing localised absorption in an 80nmSiO_2/7nmCr/80nmSiO_2/Au stack. Over 90 % of light is absorbed within the Cr for wavelengths above 550 nm.

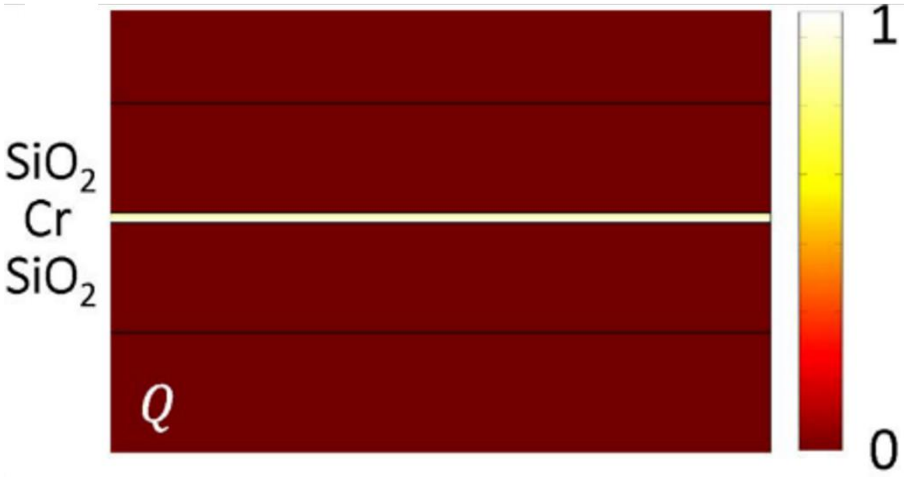


Figure 6.24. The time averaged energy density of the electric field is concentrated in the top ultrathin Cr layer. Most of the heat generation is occurring there. This simulation is performed at a wavelength of 500 nm [2].

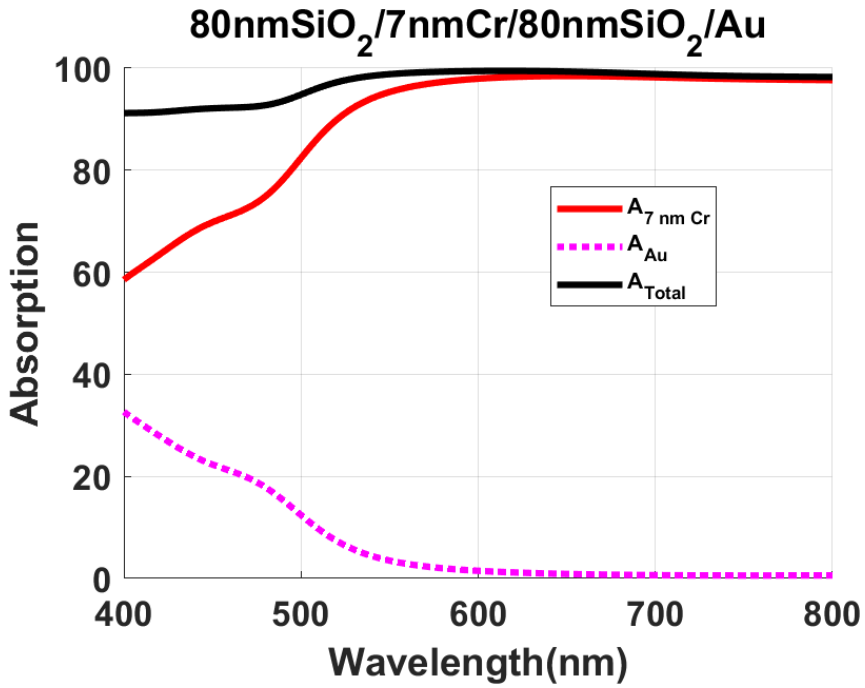


Figure 6.25. The simulated layer resolved absorption of a broadband absorbing stack with Cr, SiO_2 and Au. Almost all absorption occurs within the ultrathin Cr for wavelengths above 550 nm. Below 550 nm the absorption in the gold starts to creep upwards due to the low real index value condition being violated as gold's index rapidly increases back towards and overshooting unity.

6.3.2 Centrally Placed Ultrathin Cr Absorber in Dielectric Sandwich Backed with Ag

Gold clearly is not the most ideal backing metal though as its real refractive index rapidly approaches then overshoots unity below 600 nm wavelength [10]. On the other hand, the real index of Ag remains below 0.2 throughout the visible spectrum. This allows Ag to perform much better than gold at reflecting the light back into the Cr film in the blue part of the visible spectrum. Hence, Ag is used as the back mirror for most sample simulations. Figure 6.26 displays the refractive indices of both Ag and Au side by side for comparison alongside their optical penetration depths. The faster increase in penetration depth for Au coincides with the increase in real index that improves the impedance match to air.

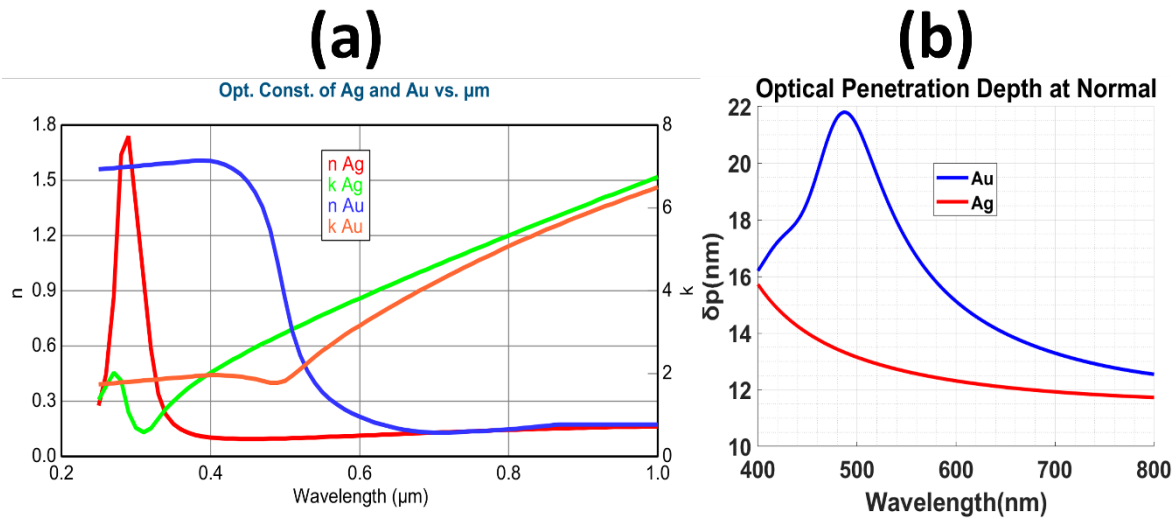


Figure 6.26. (a) The refractive indices of Ag and Au compared side-by-side. The extinction coefficient remains larger in Ag than Au across the visible regime, and the real index n remains flat below 0.2 down to 400 nm Wavelength for Ag. Meanwhile the index rapidly increases for Au below 600 nm causing its drop in κ to stop. (b) This results in increased penetration depth for light and less back reflection. The dispersion in silver's index below 400 nm is due to the presence of an interband transition [10].

The TMM can also be used to calculate the ideal top and bottom dielectric spacer thickness to maximise absorption across whichever wavelength range one requires. In Fig.6.27 such an optimisation was performed by averaging absorption across the visible range for various combinations of low index MgF_2 thicknesses with 7 nm ultrathin Cr absorber in a MgF_2/Cr/MgF_2/Ag stack. MgF_2 was chosen as it has an even lower ideal real index than SiO_2 of 1.38. MgF_2 is also very comparable to SiO_2 as both are transparent dielectrics with normal refractive index dispersion. An optimal stack using MgF_2 should theoretically have slightly superior broadband absorption results due to the lower index of refraction making solutions to eq.6.7-6.8 a closer match to lossy metal Cr. The ideal solution for an Ag backed

sample is for both the top and bottom MgF_2 dielectric to be approximately the same thickness at 94 nm. Different backing metals have different solutions. For example, Au has an ideal top and bottom dielectric thickness of 89 nm and 95 nm respectively shown in Fig.6.28. The optimum result will depend on the indices of one's backing metal choice, ultrathin absorber, and dielectric. There also appears to be a trend that less reflective back mirrors have more asymmetric ideal stack structure solutions for maximum absorption, as seen below for a SiO_2 and Ge based broadband absorber fabricated using the NPVD magnetron sputtering system. This is because in relative terms less light is absorbed by the top ultrathin layer when the bottom mirror is also lossy, a result that was seen for lossy metal backed zeroth FP samples in ch.4 Fig.4.32 p.220. Based on simulations, all reflective back mirror metals heavily trend towards a symmetric sandwich configuration for optimal broadband light attenuation.

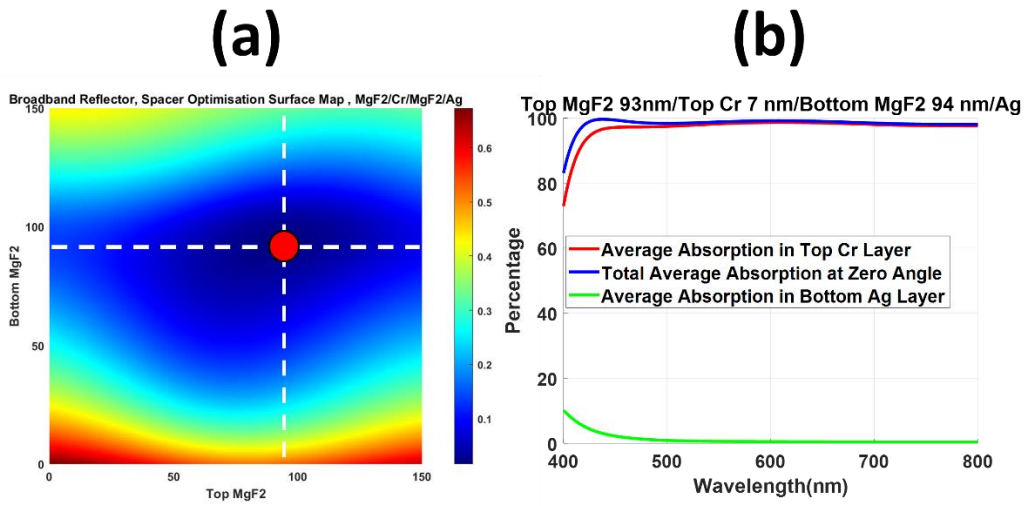


Figure 6.27. (a) A broadband optimization algorithm was written in MATLAB to find which combination of top and bottom dielectric spacer thickness minimised total stack reflection on Ag backing. Since the stack is opaque, near 0 reflection implies near unity absorption. (b) The layer resolved absorption spectrum of the ideal stack with an Ag back metal. Absorption in the Cr is high and consequently almost all light hitting the Ag layer is reflected back into the stack structure.

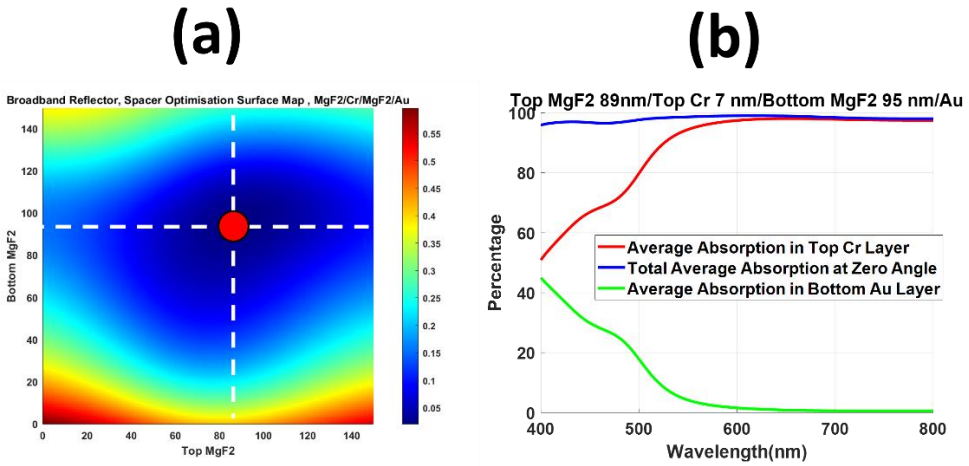


Figure 6.28. (a) The same broadband optimization algorithm used as before for the Ag backed sample, but this time using Au. Since the stack is also opaque, near 0 reflection implies near unity absorption. (b) The layer resolved absorption spectrum of the ideal stack with an Ag back metal. Absorption in the Cr is high and consequently almost all light hitting the Au layer is reflected back into the stack structure. There is a drop-off in light trapping in the Cr absorber associated with the rapid increase in real index of Au below 600 nm.

The angle and polarisation response across the visible spectrum is shown for the Ag and Au backed stacks with MgF_2 in Fig.6.29 below. The polarisation resolved response is nearly identical for both orientations except for very strong absorption around 70˚ for s-polarisation on both Ag and Au. The angle insensitivity of the reflection spectrum can be discerned from the dark blue low reflection band stretching across the spectrum. There is no appreciable drop off in absorption until around 40-45˚ which is quite impressive for a stack assembly using low index and thick dielectric spacer layers. The strongest absorption overall can be found in the 400-450 nm wavelength region where an increase in the Ag and Au absorption rises more rapidly than the decrease in Cr film absorption. These angle-resolved results fall in line with the data gathered by Huixu Deng *et al.* [2], corroborating the omnidirectional character of this symmetric dielectric sandwich broadband absorber stack system.

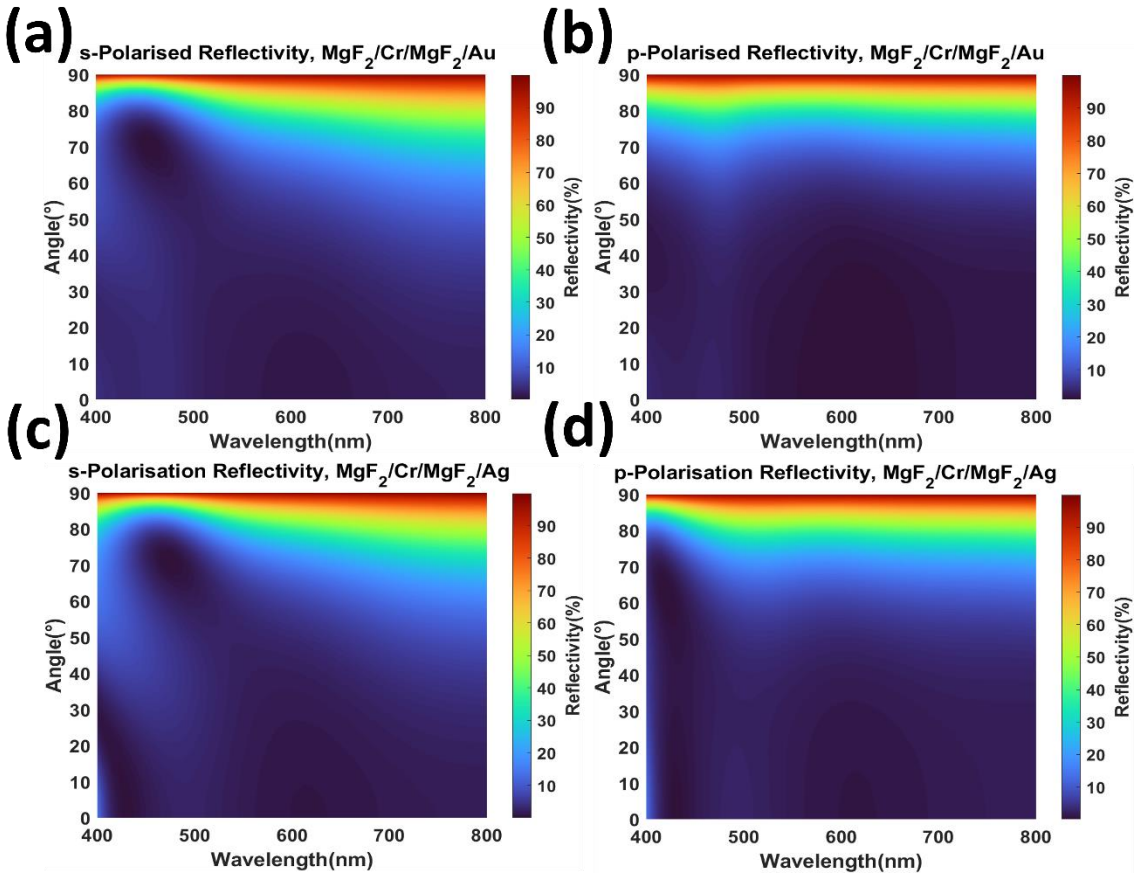


Figure 6.29. The simulated polarisation response w.r.t AOI for TE (a)-(c) and TM (b)-(d) light is displayed. Both orientations have a very low dispersion w.r.t angle and broadband absorption is maintained stably across the visible spectrum out to 40-45˚, after which the reflectivity starts to gradually increase and eventually hit unity for glancing angles above 80˚.

If a less reflective back mirror is used like Ge, the light will no longer be so strongly focused on the top Cr. Figure 6.30 illustrates this for an optimised stack structure where broadband absorption was again maximised. At 400 nm wavelength half of the absorption takes place in the top Cr layer while at 600 nm its 80 %. The optimum dielectric sandwich configuration is also no longer perfectly symmetric in thickness with the ideal top MgF_2 being 21 nm thinner than the bottom. Moreover, there is a slight increase in the reflectivity angle sensitivity, though the response is still quite flat out to 40-45 ˚.

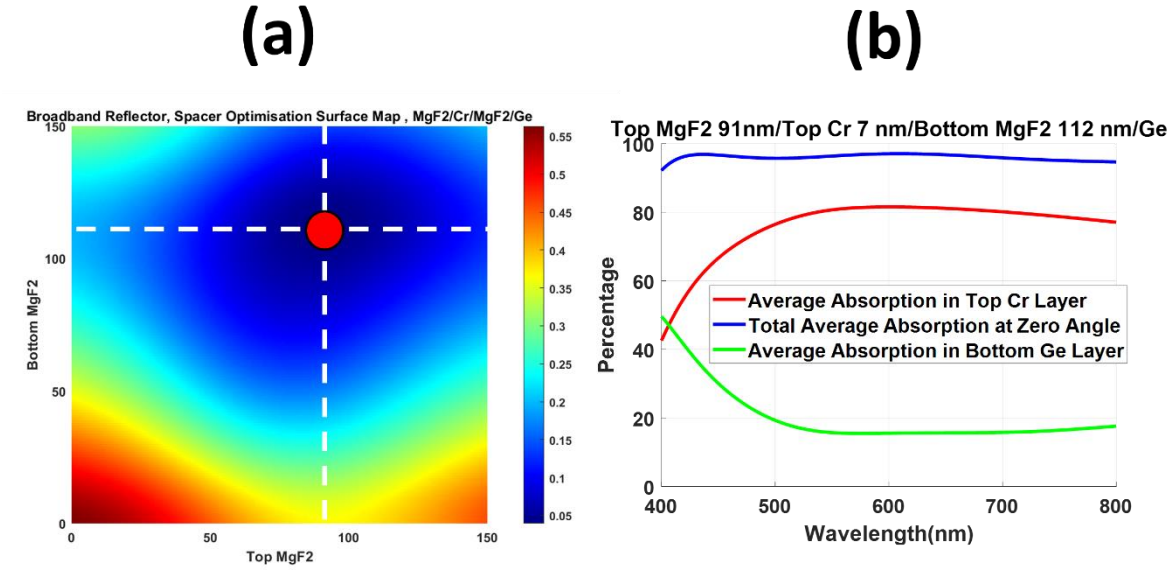


Figure 6.30. (a) The Ag back reflector has been replaced by Ge, changing the optimum absorber stack from a symmetric to a slightly more asymmetric layout. (b) The layer resolved absorption in the Cr is lower when compared to Au and Ag backing for all wavelengths, demonstrating that the internal oscillating electric field is no longer very strongly confined to the top lossy layer. This data is simulated.

6.3.3 Centrally Placed Ultrathin Ge Absorber in Dielectric Sandwich Backed with Ge

We can take this idea further and replace the top metal Cr with another ultrathin film of Ge, creating a stack similar to what was shown back in Fig.6.21 on p.328. See Fig.6.31 below.

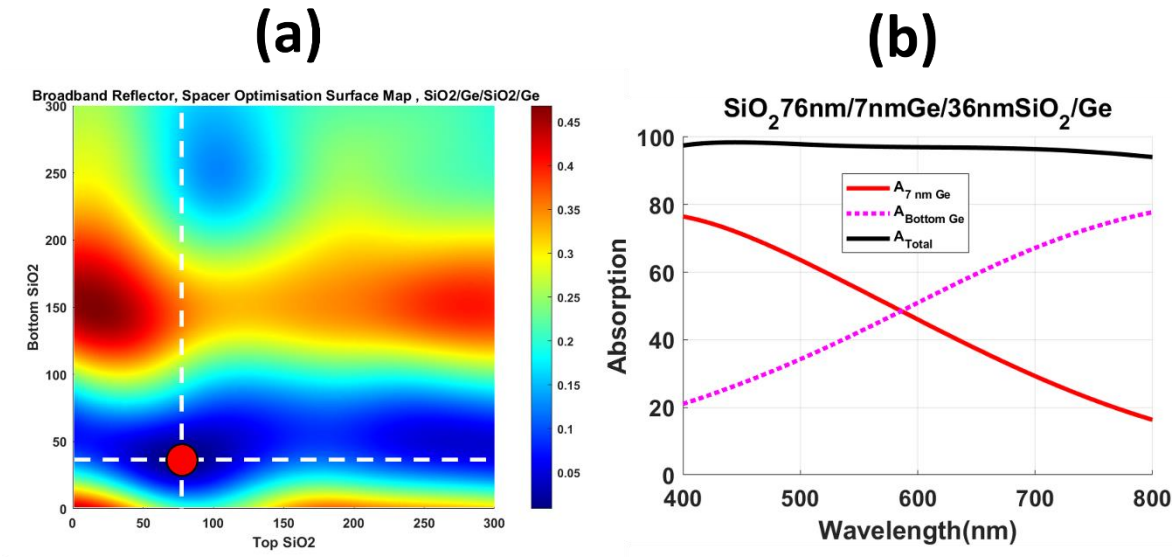


Figure 6.31. (a) Both the top and bottom metals have been replaced with semiconducting Ge. The ideal simulated stack solution for broadband absorption is now very asymmetric with the top dielectric being twice the thickness of the bottom. (b) The layer resolved absorption graph also reveals how on average across the visible spectrum each Ge layer contributes equally to the overall absorption response with the ultrathin film performing best in the blue and the thicker back mirror Ge in the red. This data is simulated.

Ge is chosen as a high index optically dense electro-absorber that was easily deposited by the NPVD sputtering system. By utilising ultrathin electro-absorption layers the ability to explore devices that could generate energy from hot electrons directly becomes possible. Taking advantage of this effect is a much more interesting and promising use of ultrathin films in modern nanophotonic research than relying solely on simpler thermal heating effects that would occur with most metals regardless of size [30], [36], [37]. The ideal top and bottom dielectric to maximise absorption are no longer equivalent in size. Instead, the inner spacer is on the order of half the thickness of the top capping layer. Using SiO_2, the ideal top AR layer thickness is found to be 76 nm and the inner spacer 36 nm with the TMM. SiO_2 is used instead of MgF2 as it is easier and quicker to deposit it thicker and make it stoichiometric on the NPVD system. Furthermore, the layer resolved absorption is strongest for the top Ge at 400 nm and weakest at 800 nm wavelength. The opposite is true for the opaque Ge back mirror. The contribution of both Ge films is identical at 585 nm wavelength. This trend continues even for higher AOI as seen in Fig.6.32 below due to the exceptionally omnidirectional and spectrally flat response.

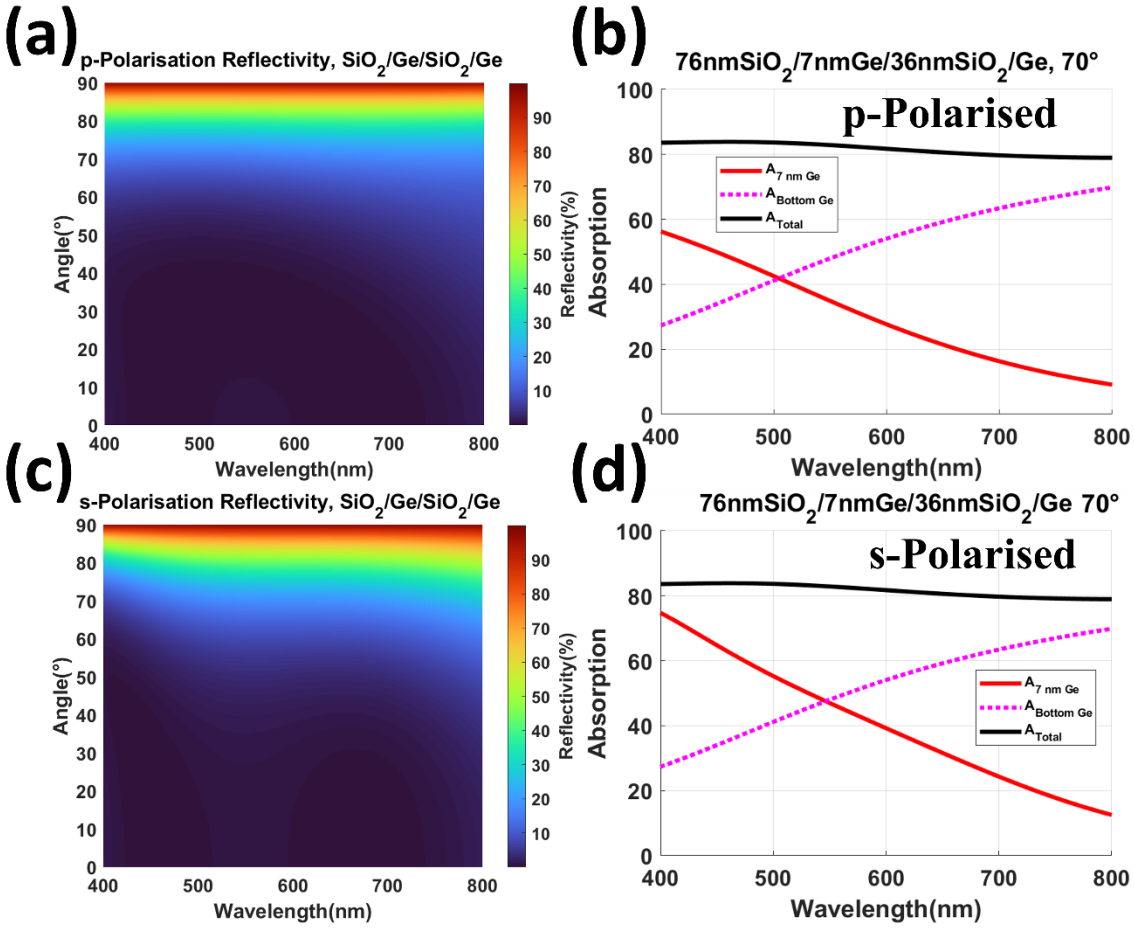


Figure 6.32. (a)-(c) The angle vs wavelength reflection surface map displays how spectrally broad and angularly independent the absorption is, even more so than the Chromium Ag stacks for the p-polarisation response which is incredibly flat below 1 % reflectivity out to 45˚. (b) – (d) The trend in the behaviour of the layer resolved absorption does not change all that much even for high AOI at 70˚, which explains why this stack maintains such strong absorption all the way out to grazing angles. This data is simulated.

Once this optimised broad absorbing sample was made its UV-Vis spectra was measured and compared with the TMM prediction. See Fig.6.33. The stack appears black to the naked eye even at angles of 40-45° reaffirming its angle insensitivity. There is good agreement between experiment and simulation for low wavelengths but poor for high. This discrepancy can be explained by the different thickness both Ge and SiO_2 may have compared to the intended target layout as shown by the blue dashed line. In the TMM correction the Ge is taken to be 4 nm in thickness and the SiO_2 is placed around 25-30 nm for both the capping and internal spacer layer. This inconsistency could have resulted from a calibration error due to a change in the known magnetron sputtering gun rates as at the time of sample creation the NPVD sputtering tool had been struggling to maintain vacuum and needed a thorough clean. It is also possible that back sputtering occurred causing the effective thicknesses of the deposited films to be reduced, with the most harshly affected coatings being those nearest

to the top. This could explain why the top dielectric layer was under half its excepted thickness, while the bottom SiO_2 was just a few nanometres under the intended thickness target, and the Ge was 2-3 nm thinner, possibly due to dewetting given it was not stabilised with sub nanometer Ti adhesion. A similar issue may also have transpired for the Fano-resonant reflection colour filter devices made, wherein the top lossy absorbing layer and the top semi-transparent Ag film did not stack well together during NPVD deposition.

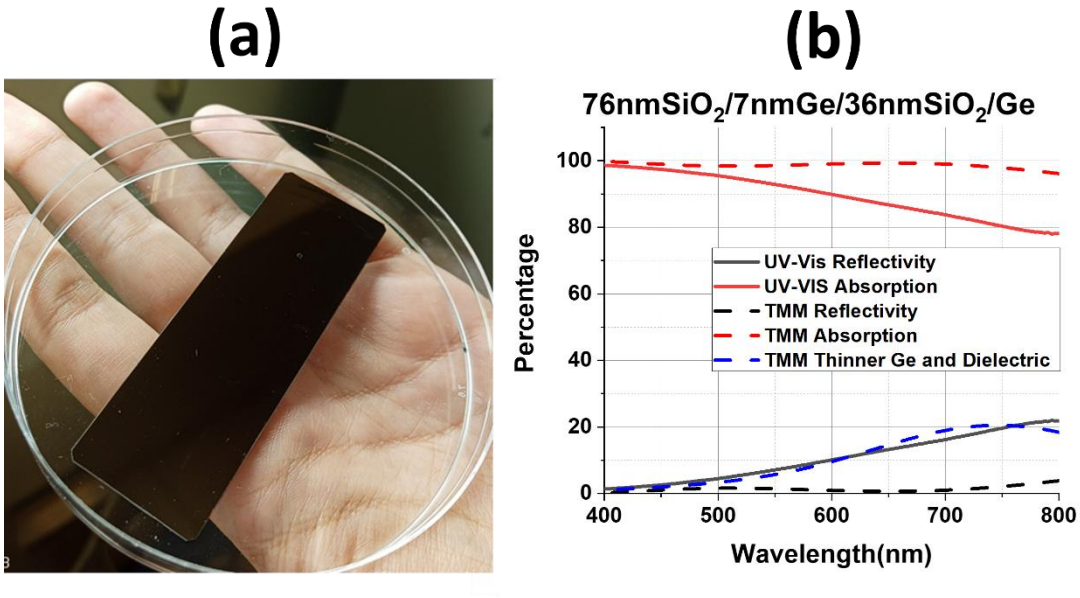


Figure 6.33. (a) The Ge based SiO_2 broadband absorber looks black-brownish depending on the angle of viewing. If the top Ge and SiO_2 had been a little bit thicker, very little dispersion would have been seen in the reflection response w.r.t wavelength and angle. (b) The thinner TMM model in the blue dotted line fits the true UV-Vis data better than the ideal stack dimension thicknesses in the black dotted line, which the NPVD magnetron sputtering tool failed to finalise properly.

6.4 Active Colour Change MIMs Using a Thermochromic VO_2 Spacer

In lieu of the passive engineered EMA layer index capabilities of Cr-VO_2 shown on p.320, active colouration devices utilising a thermochromic phase transition do exist in the literature such as the work carried out by Jiancun Zhao *et al*. (2021) [1] . The colouration of their VO_2 lossy cavity MIM asymmetric FP stack is also actively tuneable by applying temperature to the device with a heater array underneath the substrate. This heat will cause VO_2 to change from its monoclinic to rutile crystallographic form at 68˚C [1], markedly changing the real and imaginary components of the refractive index. In the work of Jiancun Zhao *et al*., an asymmetric MIM FP cavity is proposed with VO_2 placed centrally to function

as the spacer between an opaque Al back reflector and a semi-transparent Ag top metal with thickness in the range of about 20 nm, see Fig.6.34 below.

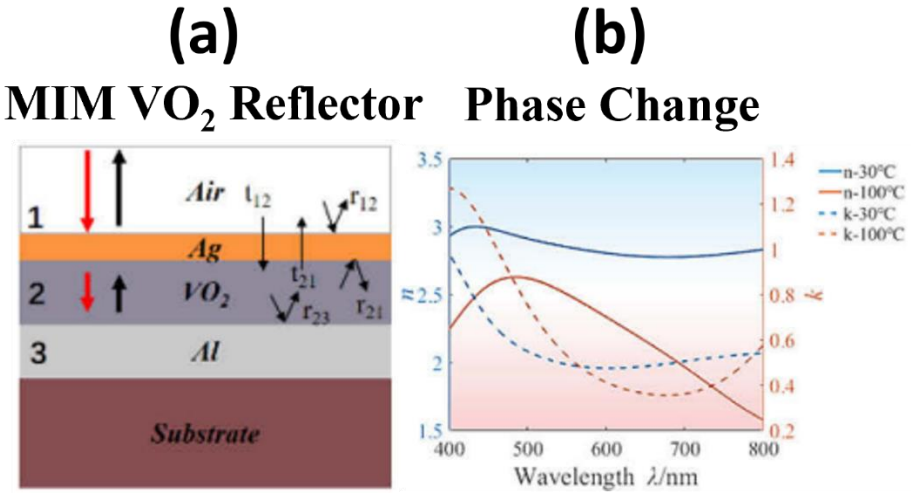


Figure 6.34. (a) A cross section of the ultrathin MIM reflector using a centrally placed VO_2 spacer for dynamic colour tuning. (b) The change in refractive index when VO_2 is heated above 68˚C, this phase change occurs much more rapidly on the scale of microseconds compared to electrochromic materials which change their colour over several seconds. [1]

Like all the other FP resonators discussed, the mathematics describing the resonance condition is given by a wave interference phase condition equation like that expressed here.

$$\lambda_0 = \frac{4\pi n_2 t_2 cos(\Theta_2)}{(2m\pi - \phi_{21} - \phi_{23})} \qquad (6.9)$$

Where λ_0 is the resonant wavelength, m is the order of the FP mode, ϕ_{21} and ϕ_{23} are the top and bottom interface phase delay factors for VO_2, Θ_2 is the refracted angle in VO_2, and n_2 and t_2 are the index and thickness of VO_2 respectively. The colouration of the samples is therefore controlled by tuning the thickness t_2 of the VO_2, the thickness t_1 of the Ag because this will control how much light enters the cavity and with what phase delay, and n_2 the actively changed index. As the oscillating electric field of the light is concentrated in the VO_2, modifying t_2 and n_2 will have the greatest dynamic shift in the colour. Changing t_1 will have a significant impact on the saturation and brightness of the resonant peak, like the central ultrathin Ge transmission filters discussed earlier. The general trend in

colouration shift when heated is a net blue shift in the reflection spectra. Figure 6.35 displays some of their results.

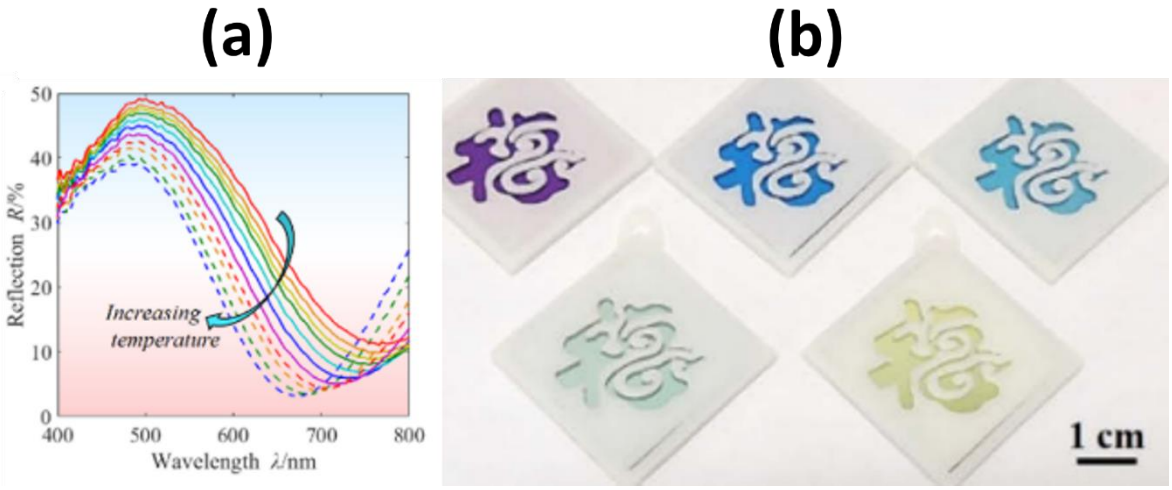


Figure 6.35. (a) The spectral blue shift caused by heating of the 70 nm VO_2 between 60˚C and 70˚C. (b) An example of the colour range produced while VO_2 is at room temperature. In this case the colours are pastel in appearance and have definite room for improvement in vibrancy. [1]

The ATF strategy they use is robust and scalable, and samples can be placed on flexible substrates as well. Omnidirectionality is also present for reasons similar to why the topical response of zeroth FP mode stacks are insensitive to AOI [6], [18]. Though the colours that are produced by Jiancun Zhao *et al*. are pastel due to the use of many lossy layers, they could be enhanced with additional transparent coatings such as the AR capping layers used to improve off-resonant peak absorption in the EMA bilayer reflection filters on p.320. Although thermal switching is much slower than electronics in the bulk, vibrant wide colour gamut thermochromic phase change device could be more competitive with much faster LCD and LED display technology due to the improved switching speeds possible with a scaled down ultrathin solid state pixel system if microheater arrays are used [38]. To help realise such a key result, the subject of active colouration in VO_2 alongside some other high index lossy dielectrics like NiO for their use in ATF Fano-resonant stack structures will be discussed. The Fano-resonator stacks have the premier advantage of a top placed absorbing film position making them easier to access than internally situated layers covered by transparent dielectrics. This is especially helpful for EC NiO as additional insulating capping films can act as a barrier to the ion intercalation process when immersed in the liquid electrolyte solution. A good ion conductor layer is necessary [21], [39].

6.5 Fano-Resonant MIM Reflection Filters

6.5.1 Explanation & Properties of Fano-Resonance in a Compact ATF Device

To make an FP resonator with more pure and saturated bright colouration one needs a way to create very sharp resonances such as with a patterned metasurface design like the all-dielectric split-ring resonator surface [26]. A nano/micro patterned surface like this has more design freedom owing to periodic conditions in the xy plane but the design, optimisation, and manufacturing is more complex and not a lithography free process. See Fig.6.36 below. Scalability in the engineering and economic sense have improved for patterned surfaces over the last few decades [40], [41], but for this thesis the ATF approach suited the objectives.

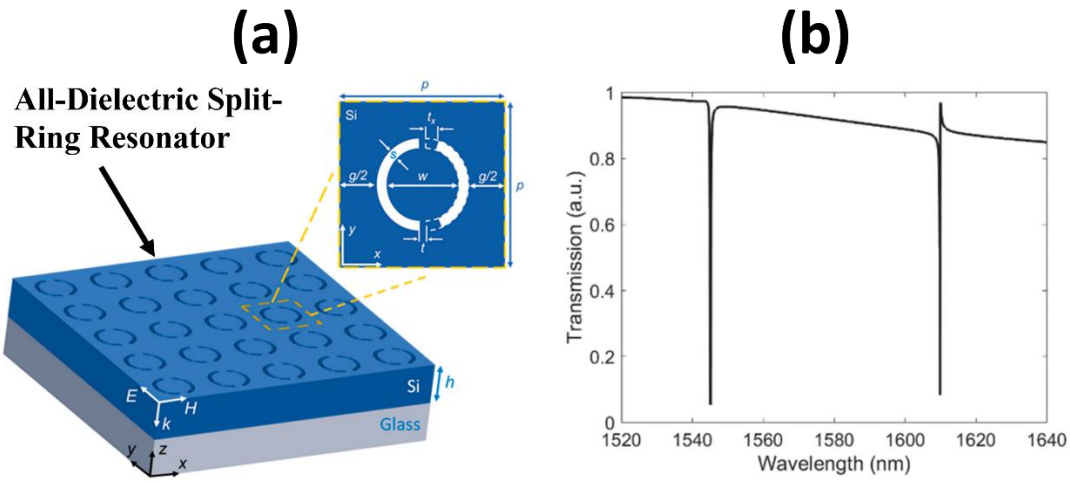


Figure 6.36. (a) A cross-section image of the metasurface with split-ring resonators etched into Si to create negative permeability. (b) The transmission spectra of this resonator device. There are incredible narrow peaks with bandwidths in the range of 1-2 nm.[26]

With the central lossy EMA bilayer absorber setup in the work of Zhengmei Yang *et al*. [3], it was seen how combining multiple resonators together could produce a purer more saturated colour with an ATF approach. With the same idea in mind, the layer configuration can be changed around so that this time the lossy layer is placed on top like with the zeroth FP mode ultrathin resonators [6], [7], [16], while also placing an MIM underneath. In so doing a system is created in which two oscillators can couple to one another in the weak limit [19], [24]. When one of the oscillators is weakly damped and the other is strongly damped, the weak coupling between the two causes a resonance peak in either the reflectivity or transmission depending on the opacity of the back metal [19]. Fano-resonant device have an inherent steep dispersion or put more succinctly the ability to have saturated

and pure colour with high brightness levels. This efficacious capability could have great use in various different applications such as; structural colouring, ultrasensitive spectroscopy, and image processing to name a few [24], [42], [43]. Mohamed ElKabbash *et al*. (2021) showed an ATF Fano-resonant device structure fabricated for both reflection and transmission purposes [19]. Shown below in Fig.6.37(a) is the reflector setup along with the fundamental stack resonator elements constituting it.

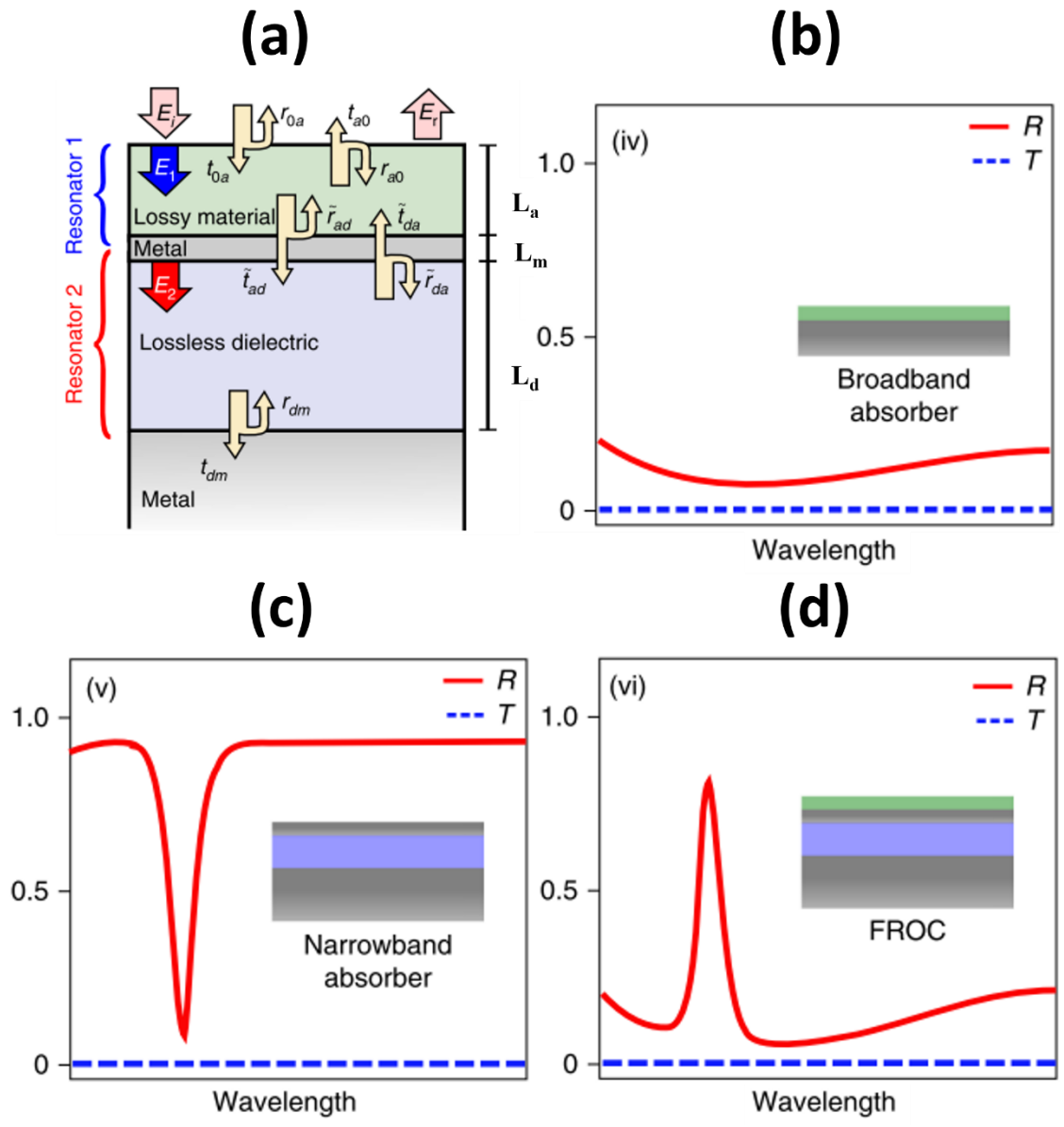


Figure 6.37. (a) A cross-sectional schematic of the Fano resonant optical coating (FROC) created by Mohamed ElKabbash et al. Provided that the top lossy later is thin enough, light will enter the stack and couple into the internal MIM structure wherein internal FP interference leads to a sharp resonant peak. (b)-(d) The individual units composing the FROC. The act of weakly coupling a broadband absorber like Ge or Si to a high quality MIM like Ag/TiO_2/Ag, causes a flip in the reflectance spectra. The result in (d) is the broadband suppression of all reflection off the resonant peak position, similar but narrower than the EMA bilayer FP cavity stack imaged in Fig.6.11(a) on p.316. [19]

Following the same trend as all the other FP reflectors, a highly reflective back mirror is ideal, so Ag is the chief go-to-choice of metal due to the very small real refractive index and large absorption coefficient, especially when paired adjacent with a high index spacer. To perfect the Fano device design, a coupled mechanical oscillator model is used to describe the role of each layer and resonator in the Fano stack. Starting from first principles a normalised electric field intensity ratio of A_k is utilised to go about describing the oscillator intensity of resonators 1 and 2, given for the conditions and in the equations below [19].

$$L_m \gg \frac{c}{\omega \kappa_m}$$

(6 . 10)

$$A_1(\omega) \approx \frac{1}{1 - |r_{a0} r_{am}| \cdot e^{(-2Im[\phi_a(\omega)])} \cdot e^{(i\{2Re[\phi_a(\omega)] + \phi_{a0} + \phi_{am}\})}}$$

(6 . 11)

$$A_2(\omega) \approx \frac{1}{1 - |r_{dm}|^2 \cdot e^{(2i[\phi_d(\omega) + \phi_{dm}])}}$$

(6 . 12)

Where r_{ij} and t_{ij} are the Fresnel coefficients between i^{th} and j^{th} layer, r_{a0} is the interface reflection coefficient between air and the lossy material, r_{am} is the interface reflection coefficient between the top metal and lossy layer, r_{dm} is the interface reflection coefficient between the bottom metal and the dielectric spacer, ϕ_a is the propagation phase delay of the lossy layer, ϕ_d is the propagation phase delay of the dielectric spacer, ϕ_{a0} is the interface phase delay at the air-lossy interface, ϕ_{am} is the interface phase delay at the lossy-metal interface, ϕ_{dm} is the interface phase delay at the spacer-back metal interface, n is the refractive index of i^{th} or j^{th} layer, and L_m and κ_m are the thickness and extinction coefficient of the top metal.

The thickness condition for L_m simply indicates that there is weak coupling between resonator 1 and 2 due to the thin metal in between them. For Ag, an ideal L_m is around 30

nm give or take 5 nm depending on the quality of the silver deposited. Figure 6.38(a) below shows the intensity profile of A_1 and A_2, as well as the overlap of the resonator 1 reflection and coupled Fano resonance reflection peak. The purity (very sharp peak alone in the visible), saturation, and brightness have all be drastically improved with the intensity rising as high as 80 %, as compared with 60 % seen in many other ATF FP resonators colour filters [19].

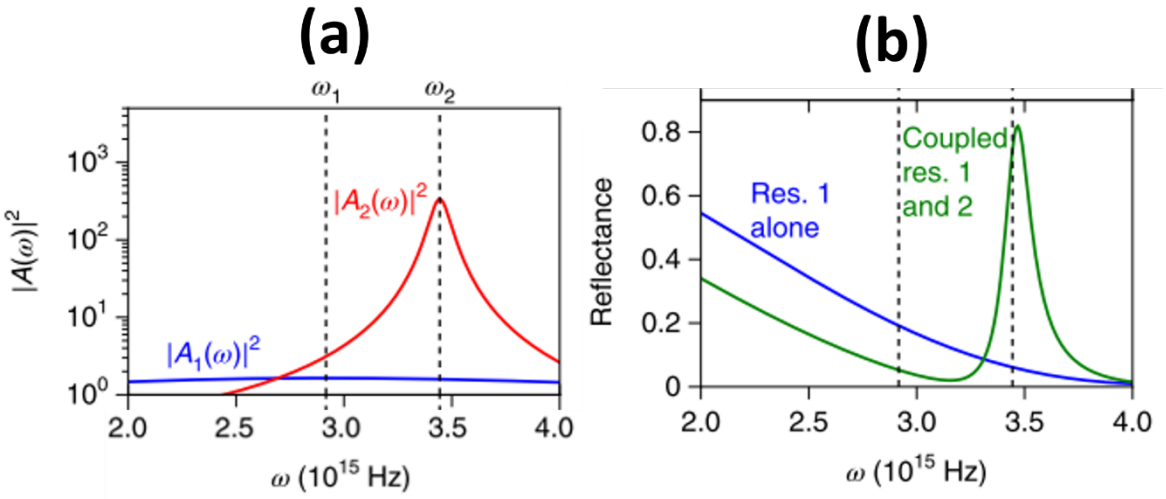


Figure 6.38. (a) The calculated oscillator intensity. A_1 is broader while A_2 is narrower. Both are centred somewhat closely to one another but just ever so slightly offset. This is necessary not only for the coupling to happen but also to generate the characteristic asymmetric peak. (b) The effect of weak coupling is to seemingly squeeze the spectra spectrally such that the colour becomes significantly purer, brighter, and more saturated; as if it were produced by a high FP mode in isolation. [19]

The electric field of the light incident into the FROC is $\overrightarrow{E_1}$ and the field incident to the inner MIM oscillator is $\overrightarrow{E_2}$. The matrix below represents the relationship between the incident and internal driving field and how they can couple as light transmits through the stack structure.

$$\begin{pmatrix} \frac{1}{A_1(\omega)} & -r_{dm}\tilde{t}_{da}r_{a0}\cdot e^{i([2\phi_d(\omega)+\phi_a(\omega)])} \\ -\tilde{t}_{ad}e^{ia(\omega)} & \frac{1}{A_2(\omega)} \end{pmatrix} \begin{pmatrix} \overrightarrow{E_1} \\ \overrightarrow{E_2} \end{pmatrix} = \begin{pmatrix} t_{0a}\overrightarrow{E_\iota} \\ 0 \end{pmatrix}$$

(6 . 13)

Where t_{ad} and t_{0a} are the Fresnel transmission coefficients across the top metal and air-lossy interfaces respectively, and $\overrightarrow{E_\iota}$ is the superstrate field. The coupling between $\overrightarrow{E_1}$ and $\overrightarrow{E_2}$ is via the off-diagonal terms going from the lower left to the upper right. One can clearly

see from this as well that making the top metal very thick will set the transmission coefficients to 0 and therefore the off-diagonal coupling will be 0. With this mathematical overview of the FROC's coupling behaviour, the equation below can be used to choose a resonant peak wavelength based on the MIM spacer dimensions [19].

$$L_d = \frac{\lambda}{2\pi n_d(\lambda)}\left\{m\pi - tan^{-1}\left[\frac{2n_d(\lambda)\kappa_m(\lambda)}{\kappa_m^2(\lambda) - n_d^2(\lambda)}\right]\right\}$$

(6 . 14)

Where L_d is the dielectric spacer thickness, n_d is spacer index, κ_m is the metal extinction coefficient, and m is the FP resonance mode integer number. This relation is very handy as the precise thickness of the top lossy layer is not a major concern. The important assumption is that the top layer and top metal are thin enough to drive the internal second oscillator in the weak coupling regime due to semi-transparency. Example reflectance spectra results from Mohamed ElKabbash *et al.* [19] are displayed in Fig.6.39(a) and (b) underneath.

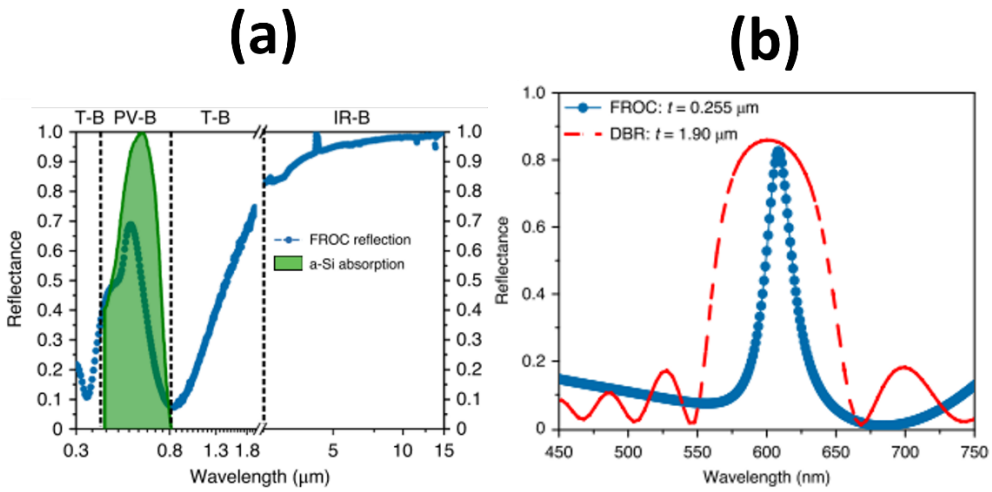


Figure 6.39. (a) The reflectance spectra of a Ge(15 nm)/Ni(5 nm)/TiO2(85 nm)/Ag(120 nm) FROC designed to send spectrally selective light in the green region of the visible spectrum onto an α-Si PV cell target, while simultaneously absorbing the unwanted below band gap thermal energy to keep the PV cell operating temperature cooler. (b) A comparison between a FROC and dielectric Bragg mirror (DBR). The Fano peak of the FROC is pure, highly saturated, and just as bright as the DBR. For the purpose of colour filtration, the FROC is superior.[19]

Depending on how large the refractive index of the lossy layer is, the thickness of this top lossy incident layer should be anywhere between 10-40 nm. In practice any less than that would weaken the ability for the FROC to supress off-peak reflection. Anymore and too

little light would make it into the second resonator inside the stack. 15 nm appears to be the sweet spot for Ge while lower index lossy materials like VO_2 and NiO would be closer to 35-40 nm. FROC's are also very compact compared to other thin film optical coatings that attempt to accomplish the same task such as DBRs [19]. The DBR in Fig.6.39(b) above is approximately 10 times thicker than the subwavelength compact FROC and produces an inferior colour saturation result.

Again, as has been discussed regarding the previously mentioned ATF FP resonators stacks, using high index dielectric spacers is very beneficial for structural colouring and can help to reduce iridescence in the optical response. The equation below is an analytical description of an ATF FROC reflection peak angle response [19]. The change in peak position w.r.t AOI is heavily dependent on the index properties of the dielectric spacer inside the MIM stack element.

$$\frac{1}{\lambda_{max}(\Theta)}\frac{d\lambda_{max}(\Theta)}{d\Theta} \sim H[\lambda_{max}(\Theta), \Theta, n_d]\frac{\cos(\Theta)\sin(\Theta)}{n_d^2 - \ sin^2(\Theta)}$$

(6 . 15)

Where λ_{max} is the peak wavelength, H is a dimensionless correction factor, Θ is the angle of incidence, and n_d is the spacer index. The rate of change of Fano peak position is inversely proportional to the square of n_d, hence a high index spacer will greatly mitigate shifting in the angular response as AOI increases. Figure 6.40(b) below exemplifies this with the comparison between $n = 2.2$ TiO_2 and $n = 1.38$ MgF_2.

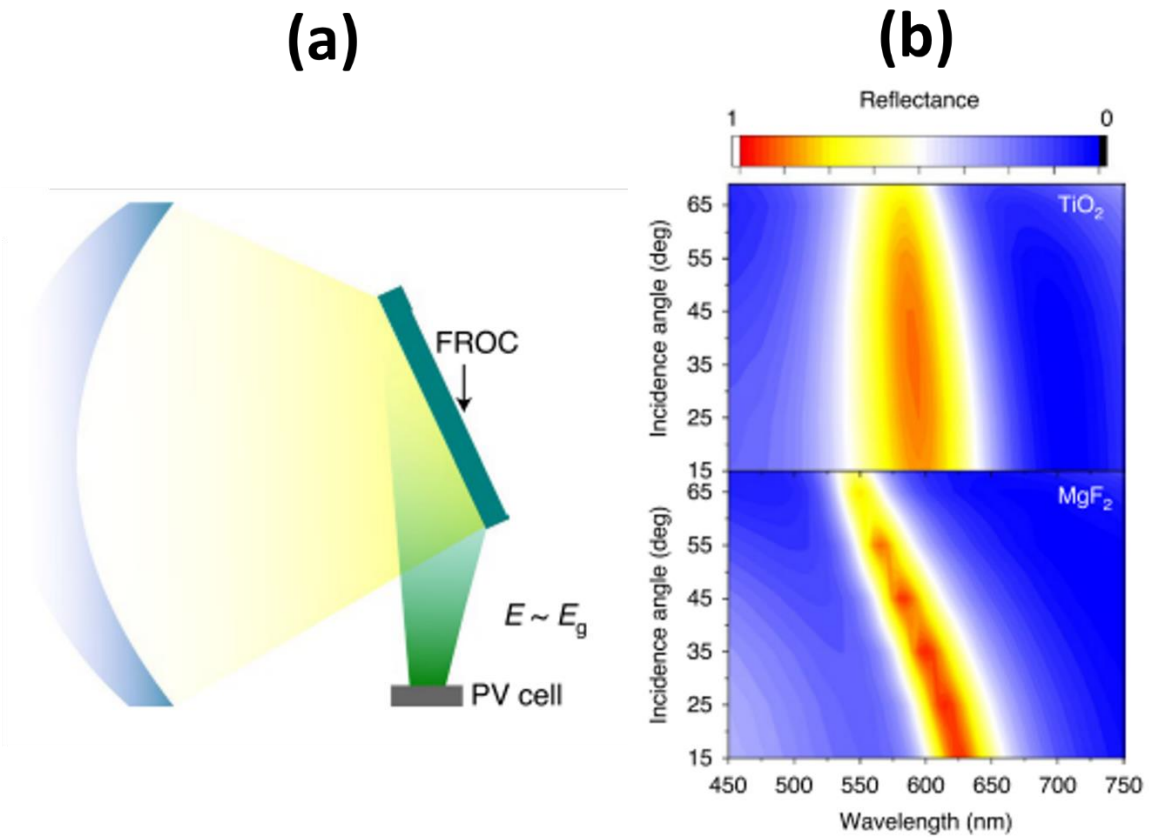


Figure 6.40. (a) A FROC Fano resonance is an excellent way to selectively reflect certain part of the solar spectrum onto a PV target cell while limiting the unwanted sub band gap thermal radiation falling incident onto that same cell. Mohamed ElKabbash et al. clearly outlines how this can increase PV cell efficiency and drastically improve the lifetime of the panel. (b) The rate of change of Fano peak position w.r.t angle. The higher the spacer index the better the response. [19]

The peak position shifts so much for the MgF_2 stack that a red FROC becomes green. Meanwhile the response for TiO_2 spacer remains flat and near uniform in value out to 45° AOI. Clearly this is ideal for structural colouring, but if one considers PV applications, it can be seen that an omnidirectional response in a concentrated solar selective setup, see Fig.6.40(a) above, could also greatly reduce the loss of photon energy that would otherwise be discarded through pernicious absorption or wasteful transmission by more iridescent reflectors. A major challenge with hybrid PV thermal systems is finding the best materials to efficiently divide the solar spectrum into the sub or above band gap photon groups [44]. Mohamed ElKabbash *et al*. [19] displays the ability of FROCs to greatly improve upon this as is laid out in Fig.6.41 below in terms of enhanced power output and reduced operating PV cell temperature using Fano resonance spectral filtering.

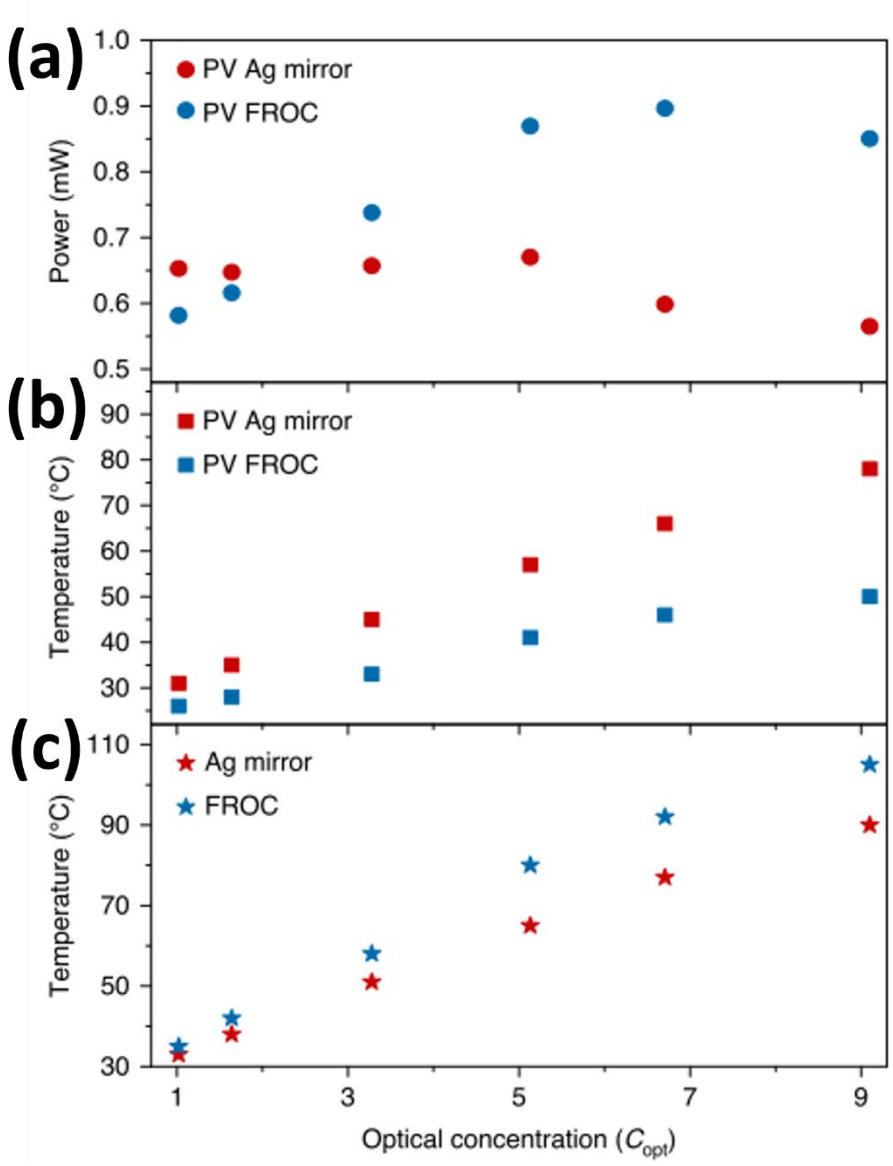


Figure 6.41. (a) The power generated by a PV cell illuminated by a FROC is on average is 50 % higher than an Ag mirror illuminated cell for high optical concentration, C_{opt} (b) The temperature of the PV cell follows an inverse trend to power as sub bandgap and UV light are being filtered out of the reflection spectrum by the FROC. Meanwhile the Ag mirror broadly reflects all wavelengths onto the cell causing it to heat up an additional 20˚C, and theoretically dropping efficiency by 10 %. (c) The filtered wavelengths are either absorbed or transmitted through the FROC causing it to heat up more than the Ag mirror by about 10˚C. A hotter thermal system will also run more efficiently based on the Carnot efficiency equation. [19]

It stands to reason that quantifying the bandwidth of the Fano peak is also important, given the overview that has been given thus far to describe the operation and optimisation of the FROC stack to generate saturated pure structural colouration. By considering that the weakly damped MIM cavity is the dominant factor in deciding the full-width half-maximum (FWHM) of the resonant peak, while also bearing in mind the line bandwidth, $\delta\lambda$, a concept that can be used to evaluate other FP resonator structures, one can utilise the generalised expression below to sharpen or broaden the resonance accordingly [19].

$$\delta\lambda = \frac{\lambda_0^2(1-R)}{2\pi\sqrt{R}n_d L_d cos(\Theta)}$$

(6 . 16)

Where λ_0 is the central peak position, R is the reflectivity of the MIM section of the stack, and all other variables have the same aforementioned meanings. This equation dictates that the Fano peak will broaden with decreasing n_d and R, and broaden with increasing AOI as the cosine factor will tend to zero for high angle [45]. To maximise R an ideal metal such as Ag or other broadband strong reflector mirror structures can be used. In the following, the results will be shown for VO_2, NiO, Ge, MoS_2 in the FROC layout on opaque Ag. Real UV-vis data will also be presented for colourful Ge FROC samples which encountered similar issues to the broadband SiO_2/Ge absorbers, wherein the top layers where not stacking stably.

6.5.2 Fano-Resonant MIM Reflection Filters Based on MoS_2 & Ge

Starting with MoS_2 and Ge film FROCs in Fig.6.42, it can be seen that the TMD is not lossy enough above 700 nm for the Fano peaks to be narrow. Therefore, for colouration purposes MoS_2 is not a good choice of top absorber. In contrast to this the Ge maintains a narrow reflection band out to 800 nm wavelength while off-resonant wavelengths have low reflectivity. The colour produced can vary from blue at 55-60 nm of TiO_2 to red at 110-120 nm TiO_2. Deeper reds beyond 700 nm wavelength will not be as pure in colour due to the appearance of the second order FP mode which starts around 130 nm TiO_2 for both MoS_2 and Ge. The similarity in the thickness versus wavelength reflection surface map of MoS_2 and Ge further affirms the mathematical description of the FROCs indicating that the internal spacer thickness L_d of the MIM resonator determines the FP resonant peak position [19]. The angle sensitivity of the FROC reflection peaks at 600 nm wavelength for both lossy dielectrics is very low with a relatively little change sustained out to 45-50 ° for p-polarised light. Indeed, the angle robust response is similar to the result seen for the low index symmetric broadband absorber devices discussed previously on p.324-339 [2], with the exception that the optical response is narrowband. One can also clearly see that the FANO peak broadens out beyond 80° AOI which is also as expected. Once grazing angles of incidence beyond 80° are reached its very difficult for any light to couple into the FROC due to the cosine factor of the Fresnel equations dominating the optical response [45], [46].

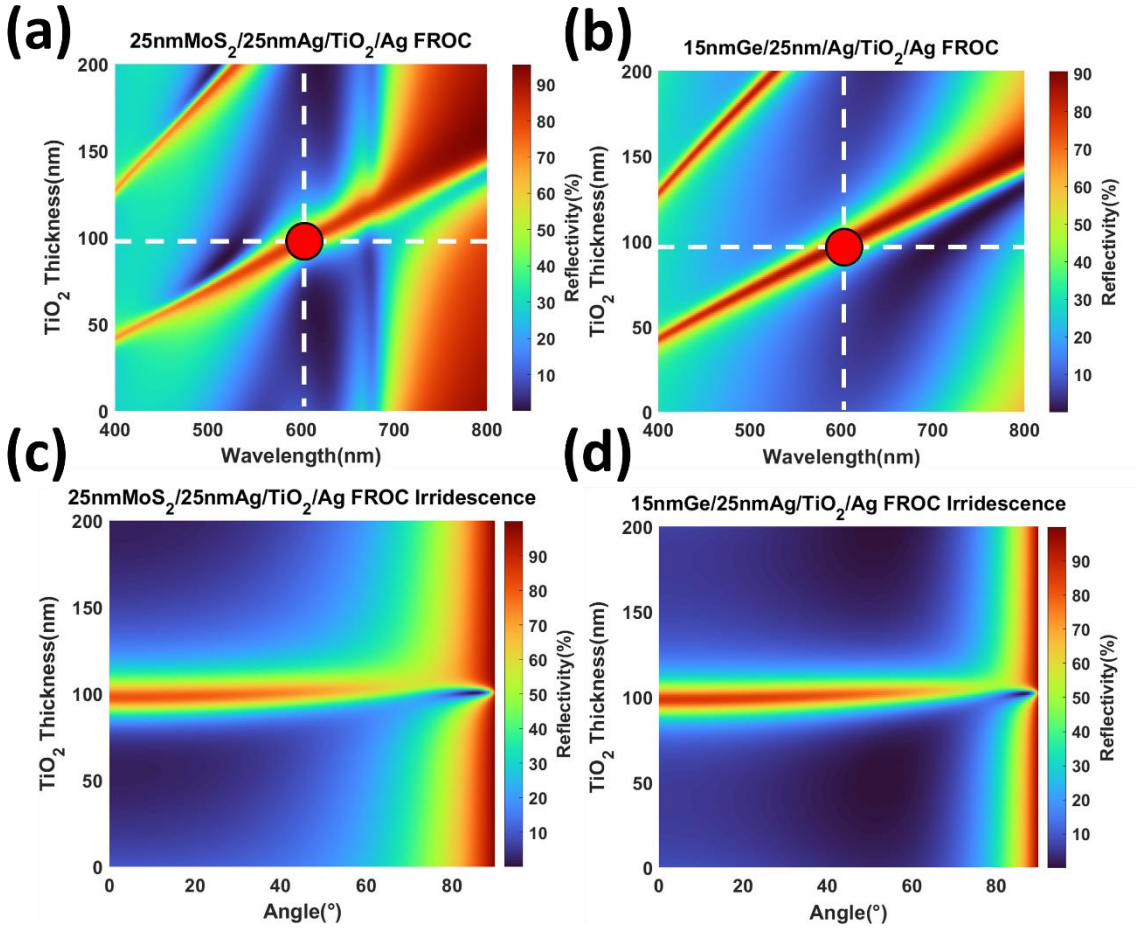


Figure 6.42. (a)-c) The simulated TiO_2 thickness versus wavelength and angle response of the FROC stack using MoS_2. (b)-(d) The TiO_2 thickness versus wavelength and angle response of the FROC stack using Ge. Narrow bands associated with m = 1 and m = 2 are seen in the spectral domain while in the angle domain for p-polarised light the Fano peak is maintained out to large AOI at 45° before a drop off in reflectivity starts to occur.

The colouration gamut of a 17 nm Ge FROC with TiO_2 spacer and Ag top and bottom metal is shown below in Fig.6.43 alongside a line plot of the reflection intensity profile at a TiO_2 thickness of 70 nm in the green region of the visible spectrum. The colour gamut is nearly circular as the Fano peak is narrow w.r.t thickness and wavelength, allowing for strong green structural colouring. Moreover, the dispersion of the colouration peaks is very steep rising rapidly on one side and descending even faster down to zero reflectivity on the other. For Ge, other FP resonant peaks do not appear until the TiO_2 spacer thickness exceeds around 135 nm, and by then all the primary colours have been swept through.

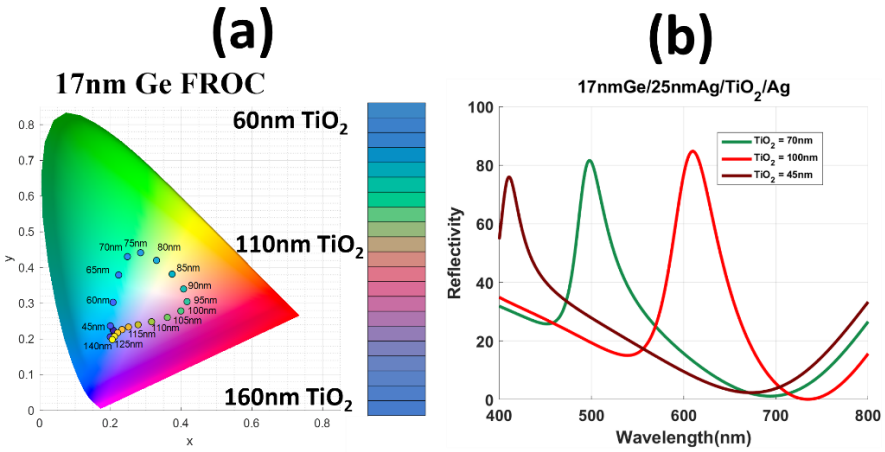


Figure 6.43. (a) The simulated colouration gamut is more circular than for Ge directly on a reflective metal backing. Due to the steep dispersion of the Fano peaks as well as the isolation of the first FP mode in the visible regime (large spacing between adjacent resonant peaks), greener hues are now accessible. The peak brightness is high at 80 %, Less dielectric material is needed to sweep across a broad range of hues compared to the transparent capped Ge-metal samples discussed in relation to the zeroth mode ultracompact resonators.

The colour purity and saturation can be enhanced a little bit further with the addition of a high index thin AR coating but at the cost of an increase in the sensitivity of the angle response. Figure 6.44 reveals this for the 17 nm Ge FROC from above. The 28 nm TiO_2 AR coating lowers the reflectivity in the blue but also elevates it a little in the red, so the overall colour does not become significantly purer. If even more AR layers are added to supress the off-resonant regions, then the angular sensitivity will become even more exacerbated.

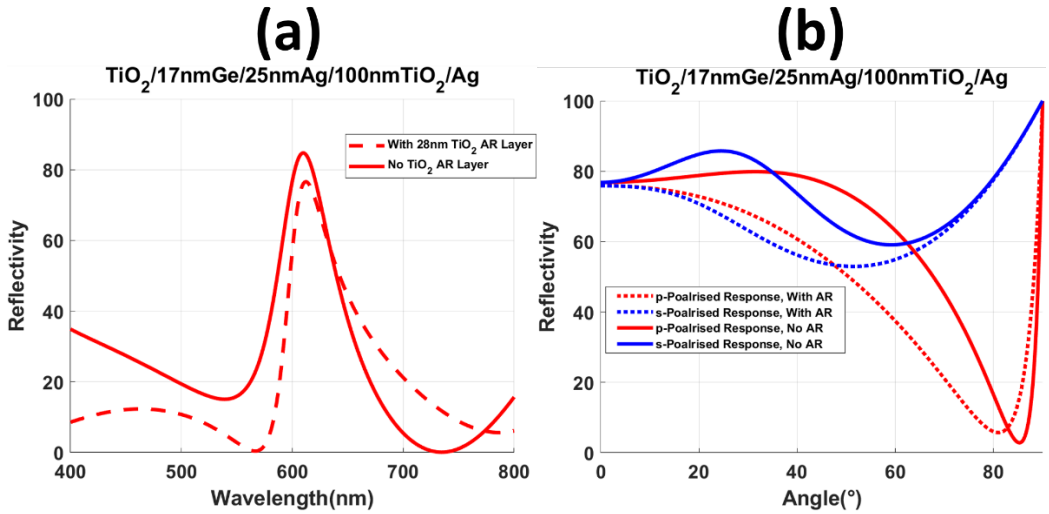


Figure 6.44. (a) If an antireflection coating is added on top of the Ge, the tail ends of the Fano peak can be lowered further. The difference is not that great though as its offset somewhat by an increase on the opposite side of the peak. (b) Even the inclusion of a thin AR layer of around 28 nm is enough to upset the omnidirectional response of the FROC. This data is simulated.

Using the NPVD magnetron sputtering tool, several different colourful 10 nm Ge FROC samples were created with Ag metal and a TiO_2 spacer as shown in Fig.6.45 below.

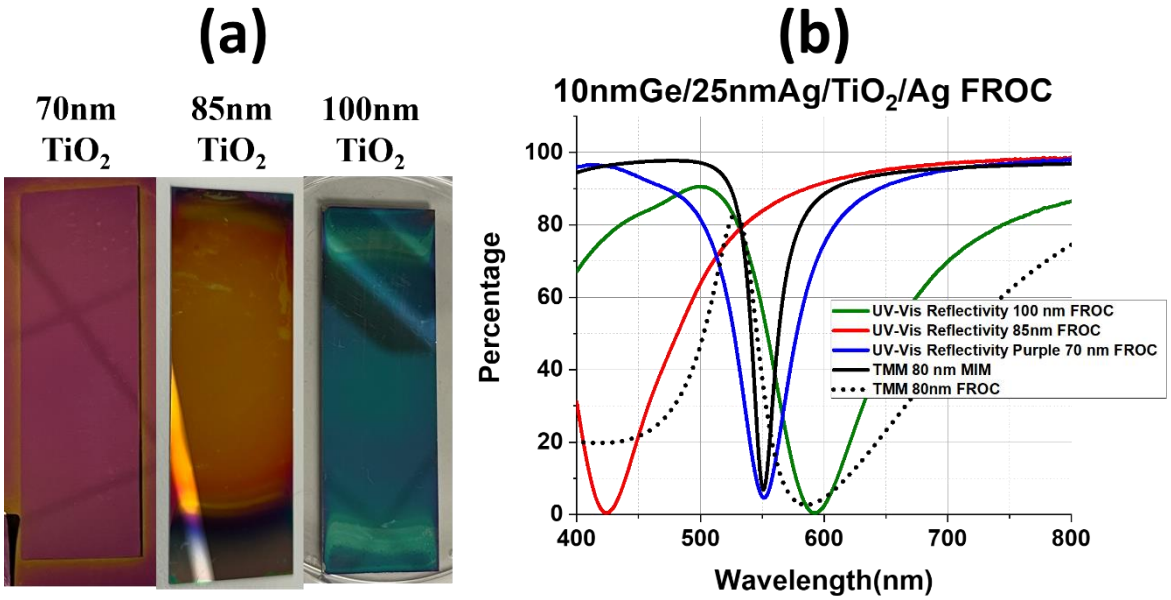


Figure 6.45. (a) Three of the samples made attempting to create a FROC device based on Ge. The colours do not match well to the chromaticity diagram as these samples are better fit by an MIM stack model (b) The MIM stack model is a better fit to the UV-Vis data than a FROC because the Ge has likely not formed a continuous layer above the top semi-transparent Ag film.

Unfortunately, there was large disagreement between observation and simulation. Modelling the stack as a silver based MIM instead of an ATF FROC yielded a much closer fit as seen for the blue and black line curves in Fig.6.45(b). This fit has slightly thinner Ag on top then expected but the internal TiO_2 spacer was unchanged. The difference in broadness is likely the result of Ge being present in some form on the top semi-transparent Ag. Therefore, it was surmised that the Ge had failed to form a continuous layer over the Ag, possibly undergoing back scattering or dewetting leaving small disconnected patches. There was also difficulty in finding a fit on the spectroscopic ellipsometer for these samples too due to a combination of uncertainty is the condition of the surface films as well as the overall increased complexity of the multilayer stack. Furthermore, for future work extra precautionary steps can be taken such as reducing the gun power to limit deposition rate (though that comes with issues regarding the striking and stability of the Ar plasma in the steady state) and using an adhesive sub-nanometre Ti layer for the top Ag on the TiO_2 spacer. Indeed, the most recent work as of this writing has indicated that the inclusion of sub-nanometer Ti adhesion and capping greatly improves upon thin film stability.

6.5.3 Fano-Resonant MIM Reflection Filters Based on NiO & VO_2

The potential active colouration abilities when using electrochromic NiO and solid-state thermochromic VO_2 in the FROC layout will be looked at. The FROC structure is well suited for these tuneable refractive index materials as they are quite lossy across the entire visible spectrum, and their position on top of the FROC MIM enables them to be more easily accessible when compared to the other higher order FP device designs seen earlier in the chapter in section 6.1-6.3, where the lossy ultrathin absorbers are placed internally deep in the stack assembly. The TiO_2 thickness versus wavelength reflectivity surface map response is shown for absorbing state NiO and monoclinic VO_2 below in Fig.6.46.

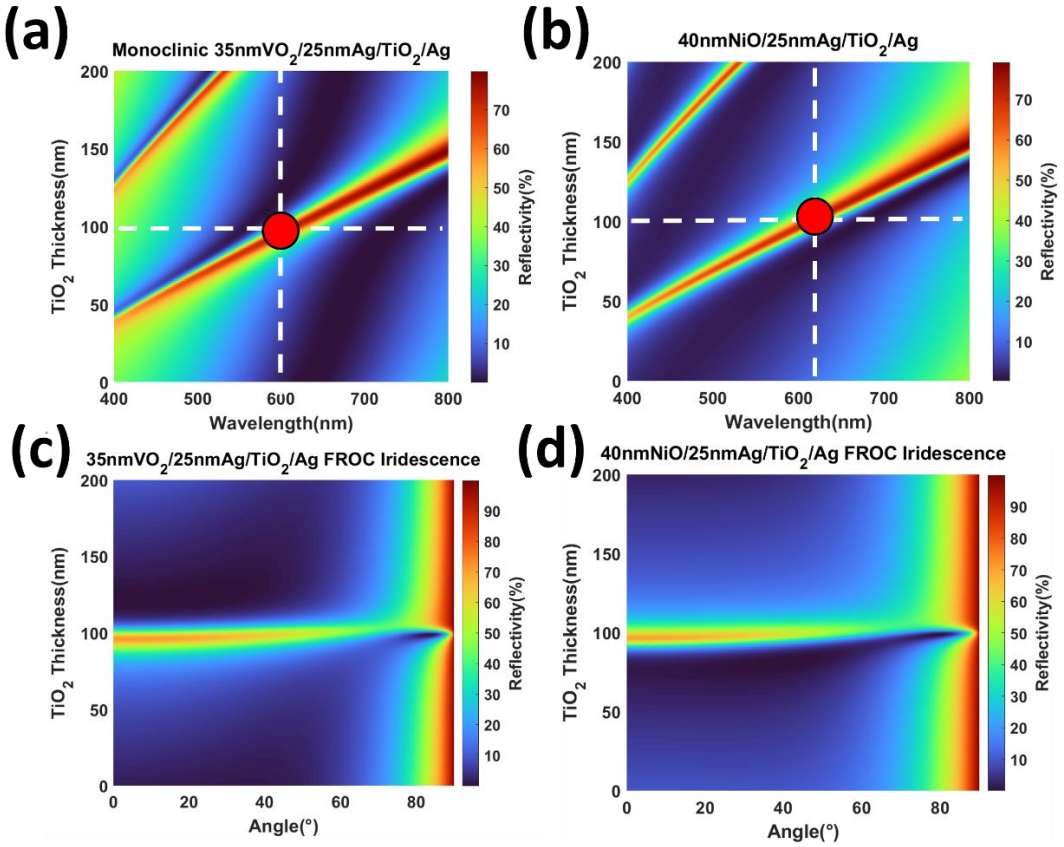


Figure 6.46. (a)-(c) The simulated TiO_2 thickness versus wavelength and angle response of the FROC stack using VO_2. (b)-(d) The TiO_2 thickness versus wavelength and angle response of the FROC stack using NiO. The Fano peak bands are even narrower than with the higher index lossy materials. Unlike MoS_2, NiO and VO_2 have a large extinction coefficient across the visible lowering the reflectivity of all wavelengths outside the resonant bands.

Strong Fano-resonant peaks in the reflectivity can be observed for NiO and VO_2 across the visible. The reflection bands are also noticeably thinner in the spectral and angular domains than the optical response for Ge and MoS_2, indicating that lower index lossy layers have a

narrower bandwidth too. The reduced extinction coefficient in NiO as wavelength decreases causes reflectivity to rise across the surface map floor for the blue spectral region in a similar but less extreme fashion as the high reflectivity for MoS_2 around and beneath its bandgap. The Fano peak for both remains omnidirectional, though with lower brightness than the Ge and MoS_2 FROCs. The most impressive dynamic behaviour seen for NiO and VO_2 in the FROC layout is the strong change in reflectivity seen when the EC or thermochromic response is carried out, see Fig.6.47 below. When NiO is KOH bleached at -1 V its colouration becomes very drab, grey, and reflective across the visible compared to its absorbing state. VO_2 heated into its rutile form will red shift towards a more orange hue.

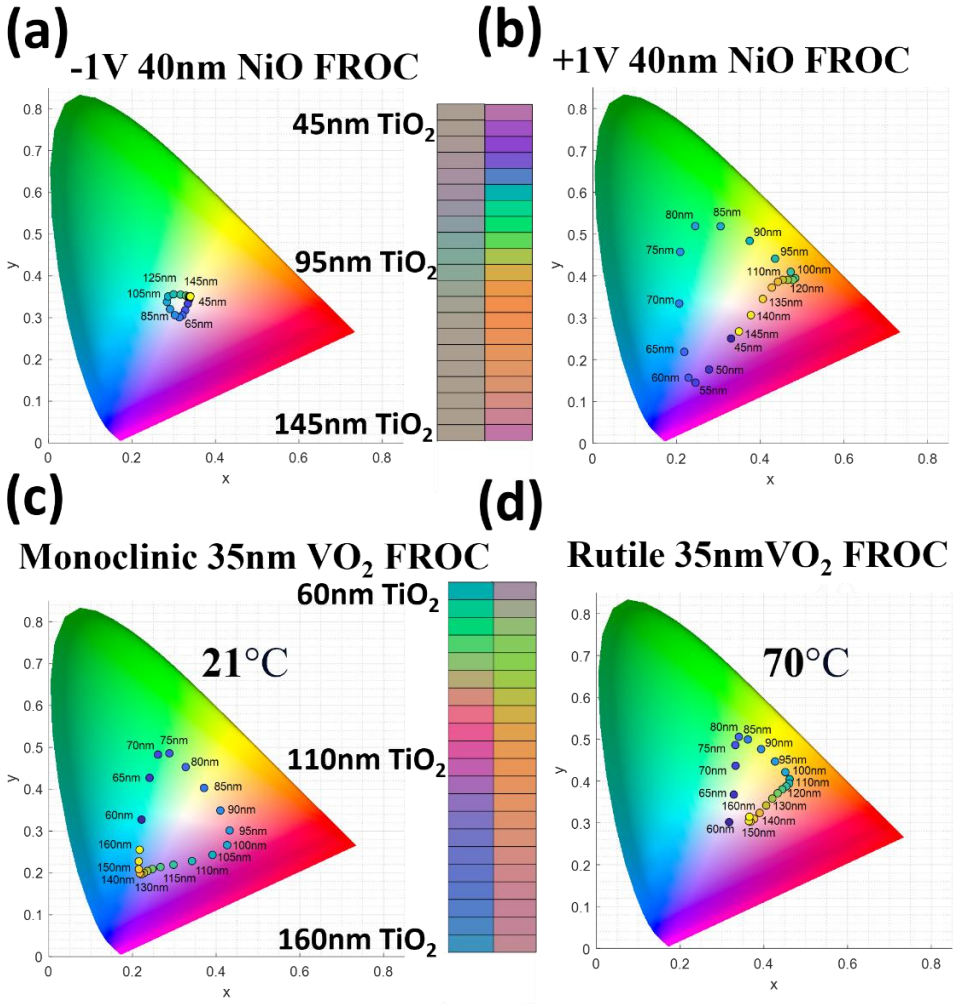


Figure 6.47.(a)-(d) The simulated dynamic colour gamut for NiO and VO_2 FROCs is considerable. There are many vibrant blues and greens to be seen. Deep red is a bit tricker to generate due to the presence of the second FP mode at the requisite TiO_2 thickness decreasing the colour purity and tuning red to a more purplish hue. The contrast in colouration between the bleached and coloured state for NiO is immense. However, due to the presence of the second mode the gamut is not perfectly circular as red 1st order and blue 2nd order Fano peaks are mixed in the spectral domain.

The colour change in NiO is particularly large due to its transition from a lossy to near transparent state, while the alteration of the colour coordinates of the VO_2 FROC is more subtle, preferentially moving to the greener, yellower, and more orange wavelengths when in rutile crystallographic form. The large expansion of the colour gamut of the NiO FROC in the absorbing state enables very vibrant green hues close to light emerald in appearance. This is a key result that has been hard to create with the other ATF colouration stacks, especially the ultrathin zeroth order mode stacks which have a very elliptical colour gamut stretching between blue and red wavelengths and skipping over green. Thus, using Fano resonance, an ultrathin film lossy absorber resonator can couple with a narrower higher FP mode MIM resonator to generate very vibrant structural colouration, while also simultaneously possessing many of the same qualities seen that make the zeroth order mode FP stacks attractive such as omnidirectionality and strong on/off state reflection contrast.

To achieve redder hues, one may think to replace the TiO_2 with SiO_2 such that the higher order modes are found at much thicker layers above the first mode, but in the process, the angle sensitivity is also increased. See Fig.6.48. Furthermore, the second mode will still affect the spectra when targeting a Fano peak above 700 nm. Only by proactively supressing the second FP mode can more vibrant red hues be created. Again, AR layers could possibly be employed to achieve this but with greater angle sensitivity again being a drawback.

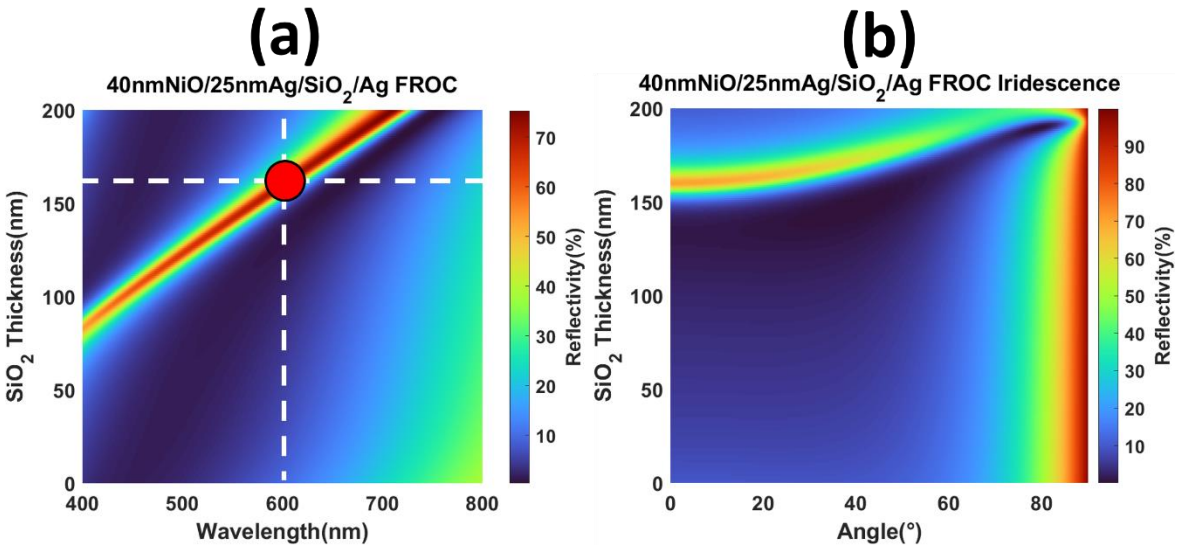


Figure 6.48. (a) When SiO_2 is utilised as the spacer the second order FP mode is only accessible at much thicker films amounts, but the Fano band also becomes steeper w.r.t wavelength, offsetting this beneficial mode isolation to a large degree. (b) Compared to TiO_2 the angle response is poor dropping to zero reflectivity at 45-50° for p-polarised light at 600 nm wavelength. This is simulated data.

Looking more closely at the reflection spectra for both NiO and VO_2, the change in reflectivity provides an intuitive outlook to explain why the NiO FROC colour change is so immense. See Fig.6.49 below for clarity. When NiO transitions from the absorbing state to the bleached state there is almost no change in the Fano peak bands in the spectral domain. Meanwhile the rest of the off-resonant wavelengths surge in reflectivity by 60 % on average. This result looks very similar to the zeroth order FP broadband large contrast seen for 50 nm NiO on Ag, see Fig.5.24 p.259. Indeed, the only major difference is that a select narrow bandwidth of wavelengths have now been isolated where no difference in reflection occurs. In this way the large on/off contrast seen in ultrathin NiO, that was previously concluded to be of no benefit to generating active vibrant structural colouration, can now be employed in the FROC layout to turn what would otherwise be a broadband tuneable mirror into a sharp colour filter that can also act as a broadband mirror when needed. The greatest change in the refractive index of VO_2 occurs above 600 nm in the NIR where the difference between monoclinic and rutile crystallographic forms is on the order of unity. This explain why rutile VO_2 favours much more orange hues, compared to the greener and bluer hues of monoclinic VO_2, when the thermochromic colouration change occurs.

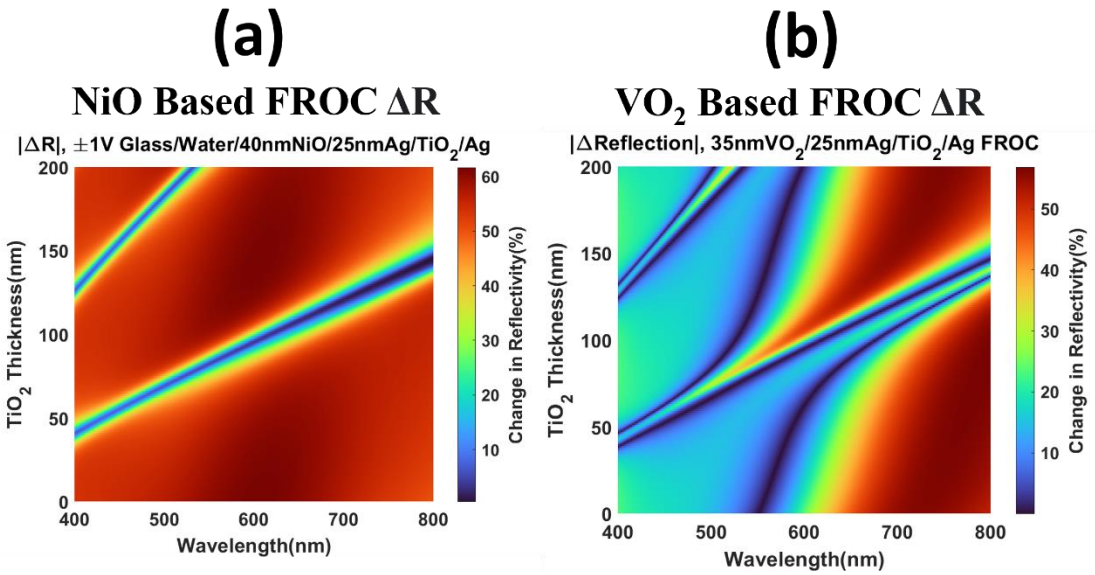


Figure 6.49. (a) The simulated large on/off broadband contrast observed for ultrathin NiO on an opaque Ag backing metal also occurs for the 40 nm NiO FROC as well for all frequencies of light that are off resonance, i.e., outside the Fano peak band regions. As a result, In the coloured state the NiO FROC produces a sharp Fano colour while in the beached state the off-resonant wavelength reflectivity is elevated by 60 % on average to match the Fano peak brightness, effectively turning the stack into a broadband mirror with a flat optical response. (b) A similar action happens for the VO_2 FROC though the change in refractive index is low in the blue part of the spectrum, excluding the possibility that it could transition from a broadband mirror into a sharp colour filter. Instead, the colouration of the stack become red shifted and orange-like when VO_2 coverts to rutile.

Like with other resonator stack structures, the layer resolved absorption of the FROCs can be examined to see how well the metal and the dielectric absorber films attenuate the incoming light. Figure 6.50 illustrates how the ultrathin top absorber still absorbs almost all the frequencies of light that is off-resonant. For both NiO and VO_2, the contribution of each absorbing film in the stack to the overall absorption is roughly equal at the Fano resonant peak wavelength, which in this case is 615 nm. At longer wavelengths than the Fano peak the amount of absorption in the top Ag is constant at around 5 %. Making the top Ag metal thinner can reduce this number but at the cost of broadening out the Fano absorption peak. The ideal is found to be somewhere between 25-35 nm to ensure the Fano peaks are sharp and narrow while also preventing the lower MIM resonators from being cut-off from the broad top resonator. The absorption of the bottom Ag is effectively zero for all wavelengths that are not at resonance.

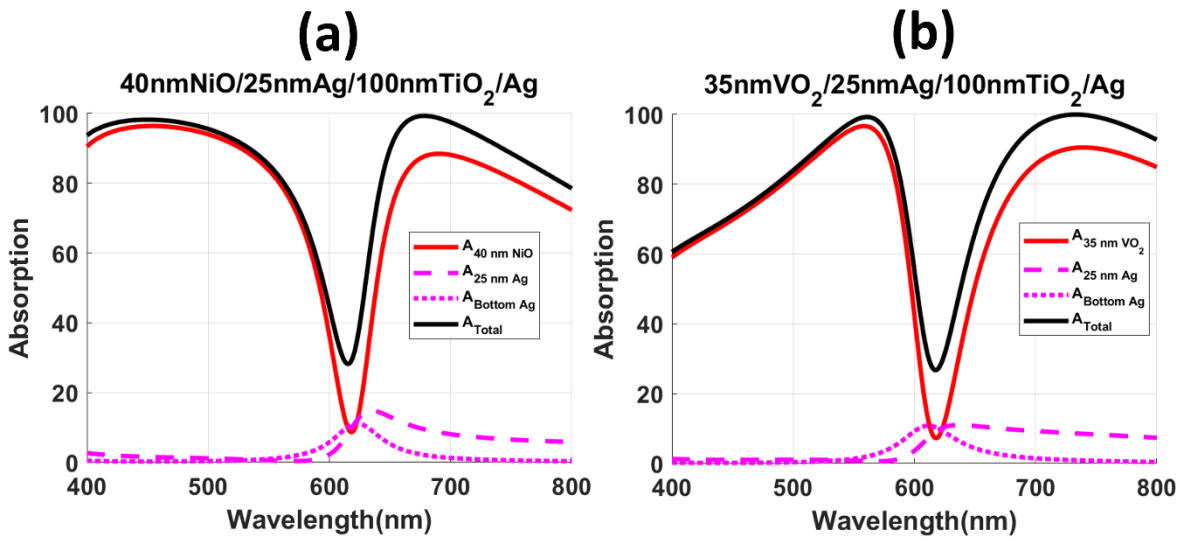


Figure 6.50. (a)-(b) The simulated layer resolved absorption of NiO and VO_2 on a TiO_2 and Ag based FROC. The NiO and VO_2 are by far the biggest contributor to absorption in the off-resonance wavelength region. The top 25 nm Ag metal also absorbs an amount equal to about 5 % of overall above the Fano peak position.

Like with Ge, lacklustre results were obtained for the NPVD fabricated NiO FROC samples deposited on the Ag-TiO_2-Ag stack base. The structures produced were not colourful in the absorbing state as expected, and instead they exhibited a drab grey silverish hue as shown in Fig.6.51 below.



Figure 6.51. A photographic image of a FROC sample with a sputtering target of 40 nm NiO on a 25 nm Ag on 80 nm TiO_2. Optical microscopic analysis reveals a seemingly smooth surface. The sample in question should be green/yellow as deposited and dull grey when bleached.

Going forward, fully solving the issue of lossy layer stability when deposited on the thin film semi-transparent Ag is definitely a major priority, as the capabilities of the FROC layout are next to none when it comes to ATF compact structural colouration. This too extends to all higher order FP stack structures that require the addition of delicate ultrathin films.

6.6 Summary

In summary many different types of higher order FP colour filters have been investigated. They utilise ultrathin lossy absorbing layers to attenuate off-resonant light while remaining transparent to the MIM FP peak. It has been shown that these thicker more complex stack structures can in some cases hold onto the advantages that their thinner more compact zeroth order FP mode stack counterparts possess, such as omnidirectionality. Optimising the index dispersion using an EMA bilayer material mixture, inspired by Zhengmei Yang *et al*. [3], was also shown to create a purer more saturated colour in reflection compared with the work done by Kyu-Tae Lee *et al*. in transmission [4] or indeed any reflection colour filters based on accessing the zeroth order FP mode in a simple asymmetric FP resonator stack configuration [1], [6], [7]. Contrary to the trend set of higher index dielectrics creating a more angle insensitive response, the broadband absorption across the visible of the symmetric dielectric sandwich ultrathin Cr central lossy absorber device was superior for lower index materials like SiO_2 and MgF_2 due to the phenomena of impedance matching

across the whole stack structure. Furthermore, it was shown that this broadband absorption could be extended to more useful absorbing materials like semiconducting Ge where electron-hole pair generation is possible for PV applications. This broadband absorption was far larger and broader than the attenuation of light achieved in simple zeroth order FP mode absorber/metal stacks shown in ch.4 or as compared to literature [6], [7], [47]. Finally, the coupling of an ultrathin lossy absorber film to a compact high index MIM underneath manifested an omnidirectional sharp and narrow bandwidth reflection peak known as a Fano peak which is ideal for structural colouration due to the steep dispersion in its optical response. Moreover, the colour gamut of electrochromic and thermochromic Fano devices using NiO and VO_2 were revealed to be large and circular in their response with the only missing hues being deep reds. This colour gamut was simultaneously wider and more bright than other ATF structural colour looked at in this study or seen in the literature [1], [16], [25], [48], [49].Given the promising results achieved with the Fano-resonator stacks in terms of both their colouration when NiO and VO_2 are absorbing, and large on/off contrast (very bright colour to very reflective broadband reflector) in comparison to other dynamic ATF colour filters found in the literature [14], [50], future work should mainly focus on creating FROCs that maintain layer stability and integrity throughout (and after) the magnetron sputtering process as the samples that were synthesised by the NPVD system appeared to undergo deleterious effects such as back scattering and/or dewetting of the top absorber and top semi-transport Ag film used to separate the weakly and strongly damped oscillators. From preliminary data gathered at the time of writing, the inclusion of sub nanometer Ti adhesion and capping layers appear to be the most promising avenue to achieve this goal.

6.7 References

[1] J. Zhao, Y. Zhou, Y. Huo, B. Gao, Y. Ma, and Y. Yu, “Flexible dynamic structural color based on an ultrathin asymmetric Fabry-Perot cavity with phase-change material for temperature perception,” *Opt. Express*, vol. 29, no. 15, p. 23273, 2021, doi: 10.1364/oe.431906.

[2] H. Deng, Z. Li, L. Stan, D. Rosenmann, and D. Czaplewski, “Broadband perfect absorber based on one ultrathin layer of refractory metal,” *Opt. Lett.*, vol. 40, no. 11, pp. 2592–2595, 2015, doi: 10.1364/OL.40.002592.

[3] Z. Yang, C. Ji, D. Liu, and L. J. Guo, “Enhancing the Purity of Reflective Structural

Colors with Ultrathin Bilayer Media as Effective Ideal Absorbers," *Adv. Opt. Mater.*, vol. 7, no. 21, p. 1900739, 2019, doi: 10.1002/adom.201900739.

[4] K. Lee, S. Y. Han, Z. Li, H. W. Baac, and H. J. Park, "Flexible High-Color-Purity Structural Color Filters Based on a Higher-Order Optical Resonance Suppression," *Sci. Rep.*, vol. 9, no. 14917, 2019, doi: 10.1038/s41598-019-51165-1.

[5] K. Lee, C. Ji, L. J. Guo, K. Lee, C. Ji, and L. J. Guo, "Wide-angle, polarization-independent ultrathin broadband visible absorbers," *Appl. Phys. Lett.*, vol. 108, no. 031107, 2016, doi: 10.1063/1.4939969.

[6] S. S. Mirshfieyan, T. S. Luk, and J. Guo, "Zeroth order Fabry-Perot resonance enabled ultra-thin perfect light absorber using percolation aluminum and silicon nanofilms," *Opt. Mater. Express*, vol. 6, no. 4, pp. 1032–1042, 2016, doi: 10.1364/OME.6.001032.

[7] S. S. Mirshafieyan, H. Guo, and J. Guo, "Zeroth Order Fabry – Perot Resonance Enabled Strong Light Absorption in Ultrathin Silicon Films on Different Metals and Its Application for Color Filters," *IEEE Photonics J.*, vol. 8, no. 5, pp. 1–12, 2016, doi: 10.1109/JPHOT.2016.2609143.

[8] "Wearable Technology Market Size, Share & Trends Analysis Report By Product (Head & Eyewear, Wristwear), By Application (Consumer Electronics, Healthcare), By Region (Asia Pacific, Europe), And Segment Forecasts, 2023 - 2030," *Grand View Research*, 2022. https://www.grandviewresearch.com/industry-analysis/wearable-technology-market#:~:text=The global wearable technology market,consumers is driving industry growth.

[9] K. R. Williams, K. Gupta, and M. Wasilik, "Etch Rates for Micromachining Processing—Part II," *J. Micromechanics Microengineering*, vol. 12, no. 6, pp. 761–778, 2003, doi: 10.1088/0960-1317/20/5/055033.

[10] M. Fox, *Optical Properties of Solids*. 2010.

[11] A. L. Lynch, C. P. Murray, E. Roy, C. Downing, and D. Mccloskey, "Extreme Dewetting Resistance and Improved Visible Transmission of Ag Layers Using Sub-

Nanometer Ti Capping Layers," *ACS Omega*, vol. 9, no. 8, pp. 9714–9719, 2024, doi: 10.1021/acsomega.3c09774.

[12] W. M. Abbott *et al.*, "Less is More: Improved Thermal Stability and Plasmonic Response in Au Films via the Use of SubNanometer Ti Adhesion Layers," *ACS Appl. Mater. Interfaces*, vol. 11, no. 7, pp. 7607–7614, 2019, doi: 10.1021/acsami.8b21193.

[13] L. C. Kalutarage, P. D. Martin, M. J. Heeg, and C. H. Winter, "Volatile and thermally stable mid to late transition metal complexes containing α-imino alkoxide ligands, a new strongly reducing coreagent, and thermal atomic layer deposition of Ni, Co, Fe, and Cr metal films," *J. Am. Chem. Soc.*, vol. 135, no. 34, pp. 12588–12591, 2013, doi: 10.1021/ja407014w.

[14] L. Xiao *et al.*, "WO3 - Based Electrochromic Distributed Bragg Reflector : Toward Electrically Tunable Microcavity Luminescent Device," *Adv. Opt. Mater.*, vol. 6, no. 1, p. 1700791, 2017, doi: 10.1002/adom.201700791.

[15] W. Wu, M. Wang, J. Ma, Y. Cao, and Y. Deng, "Electrochromic Metal Oxides: Recent Progress and Prospect," *Adv. Electron. Mater.*, vol. 4, no. 8, p. 1800185, 2018, doi: 10.1002/aelm.201800185.

[16] M. A. Kats and F. Capasso, "Optical absorbers based on strong interference in ultra-thin films," *Laser Photonics Rev.*, vol. 10, no. 5, pp. 735–749, 2016, doi: 10.1002/lpor.201600098.

[17] J. Park *et al.*, "Omnidirectional Near-Unity Absorption in an Ultrathin Planar Semiconductor Layer on a Metal Substrate," *ACS Photonics*, vol. 1, no. 9, pp. 812–821, 2014, doi: 10.1021/ph500093d.

[18] C. Park, V. R. Shrestha, S. Lee, E. Kim, and D. Choi, "Omnidirectional color filters capitalizing on a nano-resonator of Ag-TiO2-Ag integrated with a phase compensating dielectric overlay," *Sci. Rep.*, no. 8467, pp. 24–27, 2015, doi: 10.1038/srep08467.

[19] M. Elkabbash *et al.*, "Fano-resonant ultrathin film optical coatings," *Nat.*

Nanotechnol., vol. 16, pp. 440–446, 2021, doi: 10.1038/s41565-020-00841-9.

[20] M. Sakurai, “Spectroscopic ellipsometry,” *Toraibarojisuto/Journal Japanese Soc. Tribol.*, vol. 57, no. 7, 2012.

[21] Z. Shao *et al.*, “All-solid-state proton-based tandem structures for fast-switching electrochromic devices,” *Nat. Electron.*, vol. 5, pp. 45–52, 2022, doi: 10.1038/s41928-021-00697-4.

[22] M. Currie, M. A. Mastro, and V. D. Wheeler, “Characterizing the tunable refractive index of vanadium dioxide,” *Opt. Mater. Express*, vol. 7, no. 5, pp. 1697–1707, 2017, doi: 10.1364/ome.7.001697.

[23] A. M. Law, L. O. Jones, and J. M. Walls, “The performance and durability of Anti-reflection coatings for solar module cover glass – a review,” *Sol. Energy*, vol. 261, pp. 85–95, 2023, doi: 10.1016/j.solener.2023.06.009.

[24] Y. Shen, V. Rinnerbauer, I. Wang, V. Stelmakh, J. D. Joannopoulos, and M. Solja˘, “Structural Colors from Fano Resonances,” *ACS Photonics*, vol. 2, no. 1, pp. 27–32, 2015, doi: 10.1021/ph500400w.

[25] Z. Wang *et al.*, “Towards full-colour tunability of inorganic electrochromic devices using ultracompact fabry-perot nanocavities,” *Nat. Commun.*, vol. 11, no. 1, p. 302, 2020, doi: 10.1038/s41467-019-14194-y.

[26] M. Samadi, F. Abshari, J. F. Algorri, P. Rold, and F. D. Olio, “All-Dielectric Metasurface Based on Complementary Split-Ring Resonators for Refractive Index Sensing,” *Photonics*, vol. 9, no. 3, 2022, doi: 10.3390/photonics9030130.

[27] P. Buffat and J. P. Borel, “Size effect on the melting temperature of gold particles,” *Phys. Rev. A*, vol. 13, no. 6, pp. 2287–2298, 1976, doi: 10.1103/PhysRevA.13.2287.

[28] “The Solar Spectrum,” 2024. https://www.ossila.com/pages/the-solar-spectrum.

[29] H. A. Haus, *Waves and Fields in Optoelectronics (Prentice-Hall series in solid state physical electronics)*. Prentice Hall (1 Jan. 1984), 1984.

[30] W. A. Tisdale, K. J. Williams, B. A. Timp, D. J. Norris, E. S. Aydil, and X.-Y. Zhu, "Hot-electron transfer from semiconductor nanocrystals," *Science (80-.).*, vol. 328, no. 5985, pp. 1543–1547, 2010, doi: 10.1126/science.1185509.

[31] M. Shanmugam, T. Bansal, C. A. Durcan, and B. Yu, "Schottky-barrier solar cell based on layered semiconductor tungsten disulfide nanofilm," *Appl. Phys. Lett.*, vol. 101, no. 26, 2012, doi: 10.1063/1.4773525.

[32] K.-K. Kam, "Electrical properties of WSe2, WS2, MoSe2, MoS2, and their use as photoanodes in a semiconductor liquid junction solar cell," p. 119, 1982, [Online]. Available: https://lib.dr.iastate.edu/rtd/8356%0Ahttps://lib.dr.iastate.edu/rtd/8356/.

[33] F. Paquin, J. Rivnay, A. Salleo, N. Stingelin, and C. Silva, "Layered Semiconductor Molybdenum Disulfide Nanomembrane Based Schottky-Barrier Solar Cells," *J. Mater. Chem. C*, vol. 3, no. 207890, pp. 10715–10722, 2015, doi: 10.1039/b000000x.

[34] M. B. M. P. Maciej R. Molas, Karol Nogajewski, Artur O. Slobodeniuk, Johannes Binder, "Optical response of monolayer, few-layer and bulk tungsten disulfide," *J. Mater. Chem. C*, vol. 3, pp. 10715–10722, 2015, doi: 10.1039/b000000x.

[35] S. D. Rezaei, S. Shannigrahi, and S. Ramakrishna, "A review of conventional, advanced, and smart glazing technologies and materials for improving indoor environment," *Sol. Energy Mater. Sol. Cells*, vol. 159, pp. 26–51, 2017, doi: 10.1016/j.solmat.2016.08.026.

[36] K. Lee, J. Y. Lee, S. Seo, and L. J. Guo, "Colored ultrathin hybrid photovoltaics with high quantum efficiency," *Light Sci. Appl.*, vol. 3, p. e215, 2014, doi: 10.1038/lsa.2014.96.

[37] T. Mueller and E. Malic, "Exciton physics and device application of two-dimensional transition metal dichalcogenide semiconductors," *npj 2D Mater. Appl.*, vol. 2, no. 29, 2018, doi: 10.1038/s41699-018-0074-2.

[38] H. Ji, H. Tong, H. Qian, Y. Hui, N. Liu, and P. Yan, "Non-binary Colour Modulation for Display Device Based on Phase Change Materials," *Sci. Rep.*, vol.

6, p. 39206, 2016, doi: 10.1038/srep39206.

[39] X. Zhang *et al.*, “Inorganic all-solid-state electrochromic devices with reversible color change between yellow-green and emerald green,” *Chem. Commun.*, vol. 56, no. 69, pp. 10062–10065, 2020, doi: 10.1039/d0cc04129g.

[40] N. Yu and F. Capasso, “Flat optics with designer metasurfaces,” *Nat. Mater.*, vol. 13, no. 2, pp. 139–150, 2014, doi: 10.1038/nmat3839.

[41] S. E. Thompson and S. Parthasarathy, “Moore ’s law : the future of Si microelectronics,” *Mater. Today*, vol. 9, no. 6, pp. 20–25, 2006, doi: 10.1016/S1369-7021(06)71539-5.

[42] C. Wu *et al.*, “Fano-resonant asymmetric metamaterials for ultrasensitive spectroscopy and identification of molecular monolayers,” *Nat. Mater.*, vol. 11, no. 1, pp. 69–75, 2012, doi: 10.1038/nmat3161.

[43] A. Cordaro, H. Kwon, D. Sounas, A. F. Koenderink, A. Alu, and A. Polman, “High-Index Dielectric Metasurfaces Performing Mathematical Operations,” *Nano Lett.*, vol. 19, no. 12, pp. 8343–9174, 2019, doi: 10.1021/acs.nanolett.9b02477.

[44] A. Mojiri, R. Taylor, E. Thomsen, and G. Rosengarten, “Spectral beam splitting for efficient conversion of solar energy—A review,” *Renew. Sustain. Energy Rev.*, vol. 28, pp. 654–663, 2013, doi: 10.1016/j.rser.2013.08.026.

[45] C. C. Katsidis and D. I. Siapkas, “General transfer-matrix method for optical multilayer systems with coherent, partially coherent, and incoherent interference,” *Appl. Opt.*, vol. 41, no. 19, pp. 3978–3987, 2002.

[46] H. D. Young and R. A. Freedman, *University Physics with Modern Physics*, 14th ed. Pearson, 2016.

[47] C. Bueno-Blanco, S. A. Svatek, and E. Antolin, “High broadband light absorption in ultrathin MoS2 homojunction solar cells,” *Opt. Express*, vol. 30, no. 23, pp. 42678–42695, 2022, doi: 10.1364/OE.469931.

[48] S. J. Kim *et al.*, “Color of Copper / Copper Oxide,” *Adv. Mater.*, vol. 33, no. 15, p.

2007345, 2021, doi: 10.1002/adma.202007345.

[49] S. S. Mirshafieyan and J. Guo, “Silicon colors : spectral selective perfect light absorption in single layer silicon films on aluminum surface and its thermal tunability,” *Opt. Express*, vol. 22, no. 25, pp. 31545–31554, 2014, doi: 10.1364/OE.22.031545.

[50] L. Zheng *et al.*, “High reflectance tunable multi-color electrochromic films based on Fabry–Perot cavity,” *Ceram. Int.*, vol. 49, no. 9, pp. 13355–13362, 2023, doi: 10.1016/j.ceramint.2022.12.210.

Chapter 7. Conclusions & Future Work

7.1 Conclusions

To conclude this thesis, what has been achieved over the course of the work presented and what remains to be done for future work going forward will be covered. In the introduction chapter the core concept of colouration was introduced as it relates to human vision, and the explanation behind the history and workings of the CIE 1931 colour chart was explained in detail [1], [2]. It was here that the difference between pigmented and structural colouration was laid out. Focusing on the latter, many of its advantages were enumerated on such as its greater spatial resolution and stability as compared to chemical pigments which can degrade from UV or heat damage. Many examples of structural colour in nature were also given such as the appearance of the blue-sky during day and the vibrant hues of peacock tail feathers. Structural colour was divided into two categories: patterned and all-thin-film (ATF) structural colour. The advantages and disadvantages of both were listed with the discussion culminating in justifying why the ATF approach was the correct choice to focus on for the work in this thesis. Some of those reasons included design simplicity, less modelling complexity, and ease of scaling due to the sample creation process being lithography-free. Active colouration in nature and by artificial means was then briefly discussed, laying the groundwork for the electrochromic and thermochromic index change response as it applies to the ATF stack designs that were looked at closely in the results. Fabry-Perot (FP) optical resonators were described mathematically as they formed the heart of the design philosophy for all the thin film planar stacks analysed. The concept of combining lossy dielectric layers with FP resonators was explored in depth, with many different state-of-the-art multilayer assemblies given as examples to generate bright, pure, and saturated structural colour. Furthermore, some of these devices made use of ultrathin lossy absorber films to access non-trivial forbidden zeroth FP mode solutions that fully transparent thin film structures cannot. The various FP resonator structures covered formed the basis for what would be looked at in the result chapters.

A thorough overview was given on the theory of light matter interaction in chapter 2 wherein certain key topics such as light’s wave like characteristics, and matter’s quantum nature were highlighted to bring about a coherent and detailed explanation for how different kinds of solids interact with electromagnetic waves to produce their own unique optical response.

Specific attention was given to the description of how metal conductors, semiconductor absorbers, and insulating transparent dielectrics could be explained conceptually and mathematically using a semi-classical light-matter interaction theory approach, which considers light to be an oscillating electric wave and matter to be composed of oscillators that are either free or bound. With this knowledge in hand, it was shown how these models could be used to describe the refractive index dispersion response using the Kramers-Kronig integral relations. The transfer matrix method was then introduced to use this index data to predict the net outcome of how a thin film planar multilayer stack structure would interact with light because of the interference of internal optical fields that are superimposed one on top of another in the steady state. The transfer matrix method was elaborated on further to show how thick incoherent transparent layers could be accounted for in the stack simulation to eliminate coherent artefact fringes in the spectra. Moreover, an explanation was given on how layer resolved absorption was obtained by calculating the change in the Poynting vector inside the stack. Layer resolved absorption was illustrated to be an effective tool in categorising how strongly light is trapped and attenuated in different absorbing films within an FP resonator design.

Before cataloguing the results gathered, chapter 3 outlined the tools used for sample creation as well as sample characterisation. A comprehensive overview was given of the history and physics of magnetron sputtering using a DC and RF gun. Sputtering was the linchpin, vital for almost every sample made in this thesis. Brief mention was given of alternative sample synthesis methods like thermal assisted conversion (TAC) needed to sulphurise Mo into the TMD MoS_2. The details behind optical characterisation techniques such as spectroscopic ellipsometry and UV-Vis spectroscopy were intricately explained as these tools formed the core of results that were used to understand how the stack structures made interacted with light. Other ancillary techniques were reviewed like microscopy systems that can resolve the true structure of a thin film surface all the way down to the Angstrom scale. For example, when performing extremely sensitive atomic force microscopy analysis, the true morphology of a thin film's surface can be imaged through the deflection of a probe that raster scans across said surface. True microscopic surface roughness can be measured in this way. XRR was looked at as a technique to measure thin film thickness via first principles. XRR was most useful when ascertaining the agreement between different measurement methods on calibration samples, to amend any mistake that may be present in the SE derived optical model. The electrical characterisation method of 4PP was also elucidated on, with it

being very useful to characterise the integrity and thickness of thin metal films, as well as providing a way to determine the post anneal crystallographic structure of TCOs like ITO.

In chapter 4 a panoramic synopsis was given on the state-of-art research done with ultrathin lossy dielectrics like Si and Ge on metal backings in much more detail than outlined in the introduction, given that this stack layout formed the foundation of the results gathered in this thesis. It was shown that absorber films in this regime could access the normally forbidden zeroth FP interference mode by trapping and attenuating light very efficiently with complex reflection coefficients not constrained to the real number line, as is the case for transparent AR coatings. The spectral and angular response of this zeroth FP mode was revealed to be mostly flat, with enough dispersion existing to make blue or red colouration possible. Results were presented using NPVD Si, Ge, and TAC grown TMDs MoS_2 and WS_2. The strong absorption bands seen in the reflection versus lossy layer thickness surface map was shown to overlap exactly with the zero-phase delay band in phase space. Colouration chromaticity diagrams were produced for each absorber film on a whole host of different back metals like highly reflective Ag or very lossy Cr. The colour gamut was elliptical for the reflective Ag, Au, and Al backed samples while lossy metal backed dielectrics were drab due to their much broader absorption response. In the zeroth order mode stack configuration, all materials displayed an omnidirectional response in their total stack reflectivity. Furthermore, the reflectivity of s and p polarisation were effectively identical for MoS_2, a result that was not matched by any other lossy film used. MoS_2 also displayed the highest layer resolved absorption of any zeroth mode stack looked at with almost all the incoming light absorbed being attenuated in the TMD when backed with Nobel metal Ag or Au. The addition of a transparent oxide capping layer in the thickness regime of 100-300 nm was proven to greatly widen the colour gamut of Ge/metal stacks, offering insight into how the addition of an insulating spacer layer and/or AR coatings could enhance structural colouration or absorption at specific wavelengths, a topic that would be explored in full in chapter 6.

Chapter 5 carries on from chapter 4 in that the ultracompact zeroth order FP resonator stack layout is used again, this time to enhance the light-matter interaction of inorganic EC TMOs like WO_3 and NiO to make them more colourful and/or absorbing. ECMs are active index change materials which can transition between a near transparent bleached to a more absorbing state when intercalated with ions like Li^+ and H^+. The primary reason for their

introduction was to gather data on inorganic active index change after failing to do so for the TAC TMD samples. A detailed description of how ion intercalation occurs in WO_3 and NiO was established, showcasing how these ions are diffused into interstitial sites between the oxygen and transition metal atoms under the influence of an applied external electrical field that drives the heterogeneous electrochemical reduction. Great attention was paid to analysing NiO in the ultrathin film regime and the thicker film regime to ascertain the advantages/disadvantages of operating in both theatres. The results gathered indicated that NiO in the ultrathin regime around 50 nm in thickness had a very flat reflectivity response in both its bleached and as-deposited coloured state when backed with a reflective mirror. Moreover, this region directly overlapped with the zero-phase delay accumulation region in phase space, connecting the zeroth FP mode of NiO to this strong ultrathin film regime absorption that was much flatter than any other sample seen up until that point. More importantly, the on/off state contrast was revealed to be huge at an average of almost 60 % across the visible when backed with opaque Ag. Thus, ultrathin NiO demonstrated its capability to turn from a broadband absorber into a broadband reflector. Analysis of its angle response also disclosed results that were consistent with the observations of Si/metal and Ge/metal omnidirectionality. The attenuation of light within the ultrathin NiO in the absorbing-coloured state was also very high across the visible spectrum, with virtually all light absorption occurring in the top TMO film instead of Ag.

When thicker NiO films on metal backing were used, more vibrant structural colouration was generated as higher order FP modes like the 1^{st} and 2^{nd} mode were accessed. The colouration was better because these higher FP modes are more spectrally dispersive. They are also more sensitive to angle giving them an iridescent quality, which is generally undesirable. Au backed NiO had the greatest change in colour coordinates before and after H^+ ion intercalation, while for Ag and Al the colours produced as-deposited simply became more pastel after bleaching. It was also discovered that Al backing was incompatible with the KOH electrolyte due to chemical etching [3], though regardless some data was recorded using NiO/Al samples that were in good agreement with the TMM model. Likewise, a lot of data was collected for NiO/Ag samples in the ultrathin and thicker film regime to ascertain real EC data parameters like colouration efficiency, TMO lattice filling factor γ, device time response, cycle bistability, and charge capacity. To carry this out cyclic voltammetry (CV) and chronoamperometry (CA) were performed using a three-electrode electrochemical cell setup. Those results clearly demonstrated the superior contrast of NiO films on the order of

40-60 nm in thickness, while simultaneously proving that passive and active structural colouration outmatched the slimmer NiO layers. The bleaching and colouration time were also all greatly improved for ultrathin NiO as opposed to thicker 100 nm films. Thus the novel approach of implementing ultrathin NiO into the zeroth FP stack configuration was shown to be potentially useful in improving upon the response time and magnitude of change achievable in contemporary ultrathin film dimmable mirror technology [4].

However, the bistability of the NiO films left much to be desired. Almost immediate degradation was noticed in the on/off state contrast when the ECD was scanned and modulated. In comparison to lithiated bulkier NiO in the literature with 80 % of the initial response after 1000 cycles, the NPVD NiO samples failed after 100 cycles had elapsed. It is believed this may be due in part to both the poor Ag-NiO adhesion and the KOH electrolyte itself as the protonated filling factor was considerably higher than lithiated NiO by 50 times, potentially putting more stress on the NiO lattice structure when diffusing ions in and out. It could also be the case that ultrathin films are inherently more unstable than their bulkier counterparts as is the case with many ultrathin metal films [5], [6]. It is believed that further study is warranted to discern the issue more comprehensively, given the demonstrated improvements that accessing the zeroth FP mode in the ultrathin film regime can have for future ECD performance.

In chapter 6, several different higher order FP resonator stacks were looked at. Most of them were examined to improve upon the elliptical passive and active structural colouration gamut that was found to be somewhat lacking in the zeroth order FP mode devices discussed in chapter 4 and 5. The fundamental concept of many of these higher order stack resonators was the combination of a MIM, typically made from reflective Ag and a high index spacer like TiO_2, with a broad high index lossy absorber layer. Transmission filters that targeted the third FP mode for colouration were looked at using high index spacers and an ultrathin central lossy absorbing layer like Cr or MoS_2 to suppress the higher order FP modes adjacent to the target resonant wavelength. Suppression occurred primarily in the central absorber due to the stack design focusing off-resonant wavelengths of light into this layer. These multilayer assemblies could produce saturated pure colours in transmission, though peak brightness was not much more than 60-70 %. Reflection filters with a similar layer configuration to the transmission filter but with an opaque Ag metal backing, and no top Ag film, were also investigated. The centrally placed ultrathin film absorber in this instance was

composed of an EMA mixture of Cr and VO_2, engineering an effective medium with near-ideal indices to attenuate all off-resonant wavelengths. Multiple AR coatings were also used to target different off-resonant wavelengths to enhance this absorption by decreasing back reflections at the air-stack interface. The colouration performance of the EMA absorber was compared with an equivalent layer of just Cr or VO_2 and the results demonstrated that the EMA layer was indeed superior, improving colour saturation and purity. Comparing the transmission and reflection filter FP resonators, the former had purer and more saturated colour that was dimmer and less angle robust while the latter had considerably brighter and wider FWHM MIM resonant peaks that changed very little w.r.t AOI for both s and p polarisations below 45-50°.

By replacing the high index spacers seen in the filters above with low index SiO_2 and MgF_2, the light across the visible spectrum could be strongly absorbed for all wavelengths in a centrally placed ultrathin lossy dielectric. Analysis indicated that this strong broadband absorption stack could access the zeroth mode, though in this situation the zeroth mode was not as flat. Despite this fact, the absorption bandwidth was also revealed to be very large compensating for the higher dispersion. Ideal indices were calculated analytically for the ultrathin absorber layer and Cr was found to be the best match. Furthermore, the absorption was higher when backed with Ag as compared to Au, both overall and in terms of the layer resolved attenuation in the central absorber film. This was shown to be the result of the increase in the real index of Au below 600 nm (due to an interband transition), reducing its reflective capabilities relative to Ag. Using Cr and Ag the ideal thicknesses of the dielectric layers were found to be approximately the same at around 90 nm each. Using different lossy back metals like Ge, this ideal symmetric solution became more asymmetric. Replacing both Cr and Ag with Ge gave an ideal broadband absorption configuration wherein the top dielectric was twice as thick as the bottom internal spacer. Moreover, the angle response for all the broadband absorbers discussed for both TM and TE light was extremely flat out to 70-80° AOI. Using the NPVD system, a Ge-SiO_2 based broadband absorber was created and the TMM model fit quiet well to the final product, though the exact ideal structure that had been originally intended could not be made due to thin film stability issues.

To finish off chapter 6, the sharp dispersive peaks produced by Fano-resonance optical coatings (FROCs) were looked at in detail as a possible way to generate bright pure saturated colour with wide gamut. Sharp Fano-resonant peaks in an ATF FP resonator were produced

by placing an ultrathin lossy absorber on top of a MIM resonator. The weak coupling between these two resonators separated by a semi-transparent Ag film created a Fano optical response. All the results with Ge, NiO and VO_2, were consistent with the Fano-resonant peak phenomena, with each FROC displaying omnidirectional character and strong light attenuation off-resonance being focused almost entirely in the top lossy absorber film [7]. Furthermore, the dynamic colouration change, enabled by thermochromic phase transition and electrochromic ion intercalation in FROCs resulted in a large colouration and reflection contrast between the on/off state (colourful to grey for ECMs and a red shifted hue for TCMs), improving upon the results seen in the literature and this thesis work for the simpler zeroth mode samples. NiO FROCs, in particular, behave drastically different in the bleached and absorbing state due to the transition between the lossy and near transparent state across the entire visible. By utilising ultrathin film 40 nm NiO in the FROC layout, the strong contrast seen in the ultrathin zeroth mode samples can now be applied to the 1st MIM FP cavity mode with far better ATF structural colouration capabilities. There was an attempt to synthesise some Ge and NiO based FROCs using the NPVD magnetron sputtering tool but unfortunately this endeavour failed due to what is believed to be back sputtering occurring and or thin film lift off during the final deposition of the lossy layer on semi-transparent silver. Again, a stability issue in the adhesion between the different layers.

In conclusion, it has been demonstrated that the normally forbidden zeroth order FP mode can be accessed for a multitude of different lossy thin film dielectrics like Si, Ge, MoS_2, WS_2, NiO, and VO_2 to greatly increase the light-matter interaction therein, namely by enhancing deeply subwavelength absorption. Moreover, by utilising this zeroth mode, these ultrathin film resonator stacks can manifest an angle robust polarisation independent colour response. Furthermore, the advantageous qualities of this zeroth mode, such as omnidirectionality and greater on/off state contrast, can be superimposed onto higher FP modes when combining ultrathin lossy films in various stack positions with a narrow MIM resonator structure. In so doing, a substantial increase in the vibrancy and gamut of passive colouration produced can be achieved, such as the results seen using the FROC layout with NiO and VO_2. Future work should focus on fine tuning the FROC design for producing vivid angle robust colours, as current devices cannot preserve the top ultrathin absorber layer above the semi-transparent Ag. More work can be done as well on improving the EC results and ascertaining why the NPVD NiO bistability is low compared to literature results [8]. Steps should also be taken to bring the EC response into the solid-state regime [9], [10],

offering much greater potential to build constructs that are superior in compactness, robustness, and cycle stability compared to what has been seen from the liquid electrolyte results using KOH in this thesis. Finally, the manufacturing of VO_2 should be honed further to allow for synthesis of high-quality ultrathin film amounts in various stack positions, such as on top of FROC MIM resonators, in central EMA bilayer reflection filters, and possibly in temperature tuneable broadband central lossy absorber stacks that use a low index spacer and capping layer [11], [12].

7.2 Future Work

7.2.1 Future Work with Fano-Resonant Devices

The biggest problem encountered during the manufacturing of the NPVD FROC devices was in the final step when sputtering the ultrathin absorber on top of the thin semi-transparent Ag. When using NiO or Ge the sample would always fail to produce vibrant FROC colour in agreement with the optical model. Furthermore, spectroscopic ellipsometry could not fit the Ψ and Δ data recorded for them. Going forward a deeper investigation into whether the top absorber layer is being lifted off and/or back sputtered away should be conducted to gain further insight into the failure of the more complex higher order FP ATF stacks produced. There is good reason to believe this may be the case as the best TMM simulation fits to the UV-Vis data acquired for the Ge FROCs, use an MIM only stack without any lossy layer present. Moreover, this same discrepancy was noticed for the ultrathin broadband Ge-SiO_2 absorber samples synthesised, wherein the best TMM fit implicated reduced film thickness as the primary cause of the mismatch between observation and computed prediction.

To help carry out this investigation certain parameters should be controlled for during the sample creation process such as the magnetron sputtering gun power, the flow rate of reactive species in the vacuum chamber, and the addition or omission of adhesive metallic films like sub-nanometer Ti. In the case of the latter, it has already been shown how near monolayer deposits of Ti can help improve the stability of ultrathin 10 nm Ag against dewetting by an order of magnitude or more [6]. Up until now its inclusion for the top Ag film has been omitted, to speed up the sample creation time. Although the following would necessitate a new sputtering tool instrument, another factor which may be controlled for is

gun angle. In the NPVD system the gun is pointed at an angle to the substrate at around 30 degrees. To combat the irregularity this angle could produce on the thin film deposit, the substrate is rotated at a rate of around 1-2 Hz to increase homogeneity. Perhaps the angle of the gun is affecting the way in which a thin film coalesces on an equally thin semi-transparent or ultrathin film underneath.

Ultimately, if the issue could be overcome, and continuous stable absorber films could be created on top of a high-quality Ag-TiO_2 MIM, creating high contrast dynamic FROC devices would be the most significant goal to achieve. As far as I'm aware, there is no published work on ATF Fano-resonant devices using lossy dielectric NiO and VO_2 in the ultrathin film regime. Based on the results seen from the TMM, the gamut and vibrancy of the structural colouration is significantly improved with little increase in overall stack complexity. VO_2 would be the most practical to implement as only a microheater array would be necessary to add temperature control. See Fig.7.1 below of the microheater arrays that were built recently towards the end of this project. An SiO_2 layer would be needed to isolate the bottom Ag electrically from the Au microheater array channel underneath. By flowing increasing amounts of current into the heater array the temperature can increase in accordance with Joule's law [13].

Active colour EC NiO would be trickier to implement into the FROC as the electrochemical process requires direct contact to an electrolyte of some kind. With the liquid electrolyte approach taken in this thesis, the complementary layers like the electrolyte solution and electrode would all need to be included in a setup like the sample seen in Fig.7.2. The counter electrode (anode) would have to be the top Ag film as well in contact with the NiO. This would require supplementary steps to connect and complete the electrical circuit to carry out the reduction process.

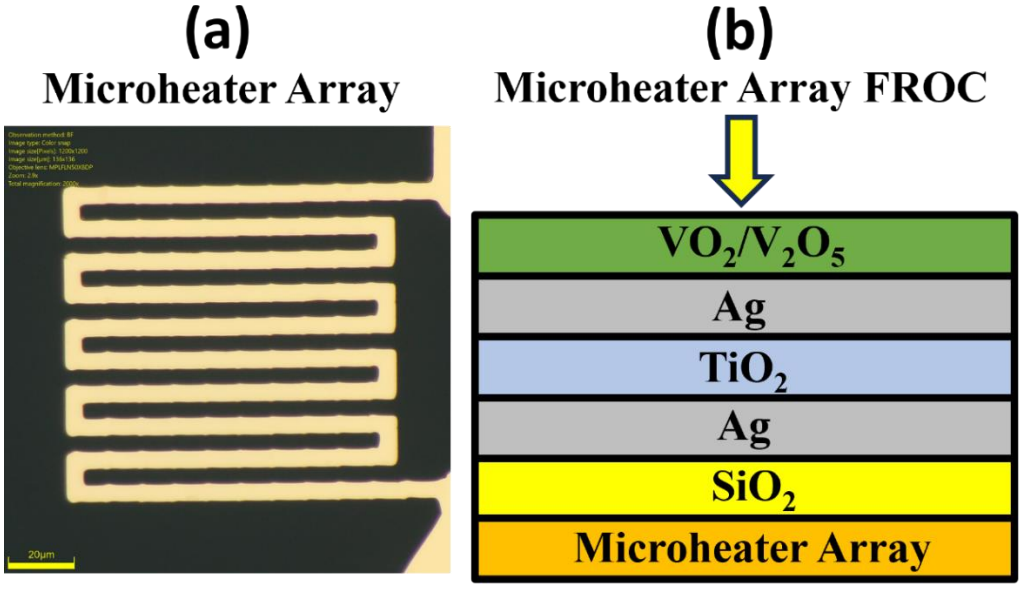


Figure 7.1. (a) An optical microscope image of a Au microheater array made using photo-lithography in the CRANN. (b) The position of the microheater array in the FROC stack layout. A SiO_2 layer acts as an insulating buffer isolating the Au form the bottom opaque Ag back reflector. Due to how thin the FROCs are the VO_2 could heat up very quickly, likely on the order of 1-100 microseconds, depending on the stack underneath.

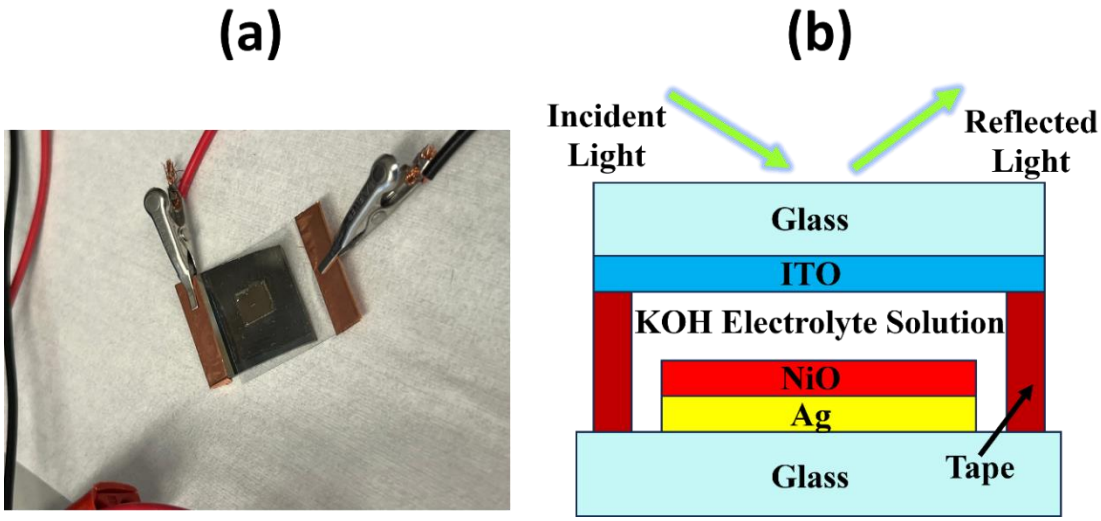


Figure 7.2. (a) An enclosed liquid electrolyte KOH zeroth order FP mode resonator based on NiO/Ag. The brown square in the middle is the resonator stack while the surroundings are the solution enclosed by glass on either side. Copper tape is then used to connect the ITO to the bottom Ag, electrically completing the circuit. (b) A cross-section layout of how this sample looks.

Additionally future work on FROCs should also explore their applications in spectrally selective solar absorption as Mohamed ElKabbash *et al*. (2021) [7] did. From the TMM simulated investigations of layer resolved absorption, the light matter interaction is very strong in the ultrathin top lossy absorber layer with effectively all the off-resonant light across the visible being attenuated in this layer. As monoclinic VO_2 is a semiconductor with

a low bandgap [14], and because its ultrathin in the FROC setup, the electron-hole pairs generated could potentially have an easier time exiting VO_2 into the thin Ag layer underneath if the physical dimensions are more constrained than the distance covered before recombination can occur. In this way the energy of incoming light can be absorbed more efficiently and harvested with higher external quantum efficiency than is possible using a conventional single pass amorphous-silicon absorber cell. The light reflected at peak resonant wavelengths on the other hand could then be sent to another PV cell unit with a bandgap ideal for attenuating the FP resonant wavelength Fano peak.

Incidentally, the versatile FROCs, as compared to other thin film coatings, can easily be modified for initially unforeseen uses. With very little change in the stack design and dimension, a FROC can also be re-purposed for use as a compact ATF beam splitter filter operating in both reflection and transmission mode. Unlike the typical FP resonator where the reflection and transmission will be the inverse of one another, the ATF FROC design of Mohamed ElKabbash *et al.* [7] instead produces near identical colour for both channels as seen below in Fig.7.3.

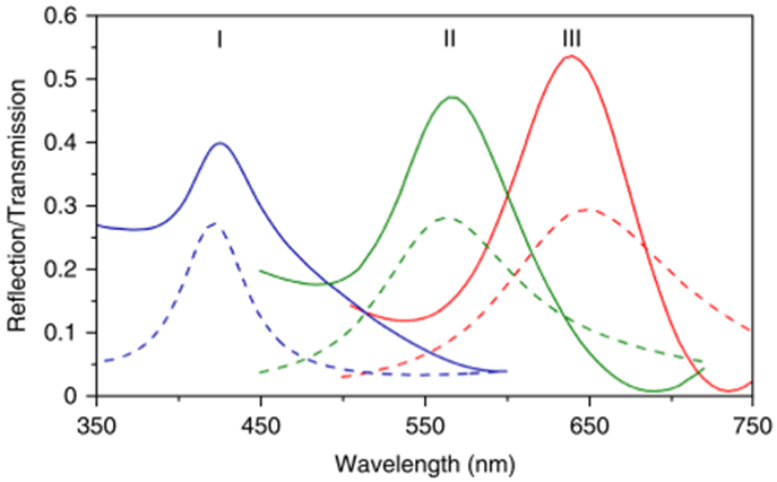


Figure 7.3. Solid lines denote reflection while dashed denotes transmission. Their colour is somewhat isomorphic demonstrating its potential use as a beam splitter device, though the brightness is inferior to the pure reflector FROCs. [7]

To bring about this transmission FROC device, the top and bottom metal must both be on the order of 20-30 nm in thickness if using Ag. In this way light can couple into and escape out of the FROC while still maintaining the weak coupling regime condition. These semi-transparent beam splitter filters (BSF) FROCs also have vibrant and varied colour as well though not as pure, saturated, and bright as with the reflector types since the resonance is

now no longer sharp (not as saturated). Figure 7.4 below shows an image of some of the possible BSF colours that are possible to achieve.



Figure 7.4. An array of BSF semi-transparent FROC samples with an incandescent light illuminating them, while also filtering fluorescent light from behind as well. The colours produced by both are near identical. Additionally, no iridescent effects are seen. Impressively, such a device can produce a reasonably pure green colour which is a challenge for most FP resonators that do not access higher modes above m = 2. [7]

A notable advantage of a BSF based on this stack design is the large range of acceptable working angles compared to lower index films. This could enable more freedom in range of working angles in different photonic setups on optics tables. Interesting experiments could be done in future work creating tuneable BSFs using electrochromic and thermochromic materials.

Figure 7.5 displays some preliminary data of a semi-transparent FROC using active EC NiO as the top lossy layer. In the coloured state the NiO acts like a beam splitter with high reflectivity above 700 nm wavelength. When bleached the transmission intensity increases significantly while all off-resonant wavelength reflectivity also elevates by 40-50 %. Thus, in the bleached state the NiO FROC acts like a high-quality transmission colour filter comparable in brightness to the lossy MIM transmission colour filter covered at the beginning of the chapter 6 p.305-314. The reflection colour was also inverted when transitioning between bleached and coloured state. These simulations do not include bulkier layers overhead like the electrolyte solution and glass, both of which would decrease maximum zeroth order FP reflection contrast anywhere form 5-10 % on average in the EC response. The characteristic result would remain unchanged though. Perhaps different thicknesses of NiO may be used here as well to optimise the transmission or reflection response accordingly. Deeper insight into the effect of film porosity (which was not controlled closely in this thesis study) may also be of interest for electrochromic NiO as

research in the literature indicates that increased porosity can improve upon the diffusion of ions into the lattice structure of an ECM [15], facilitating large optical modulation.

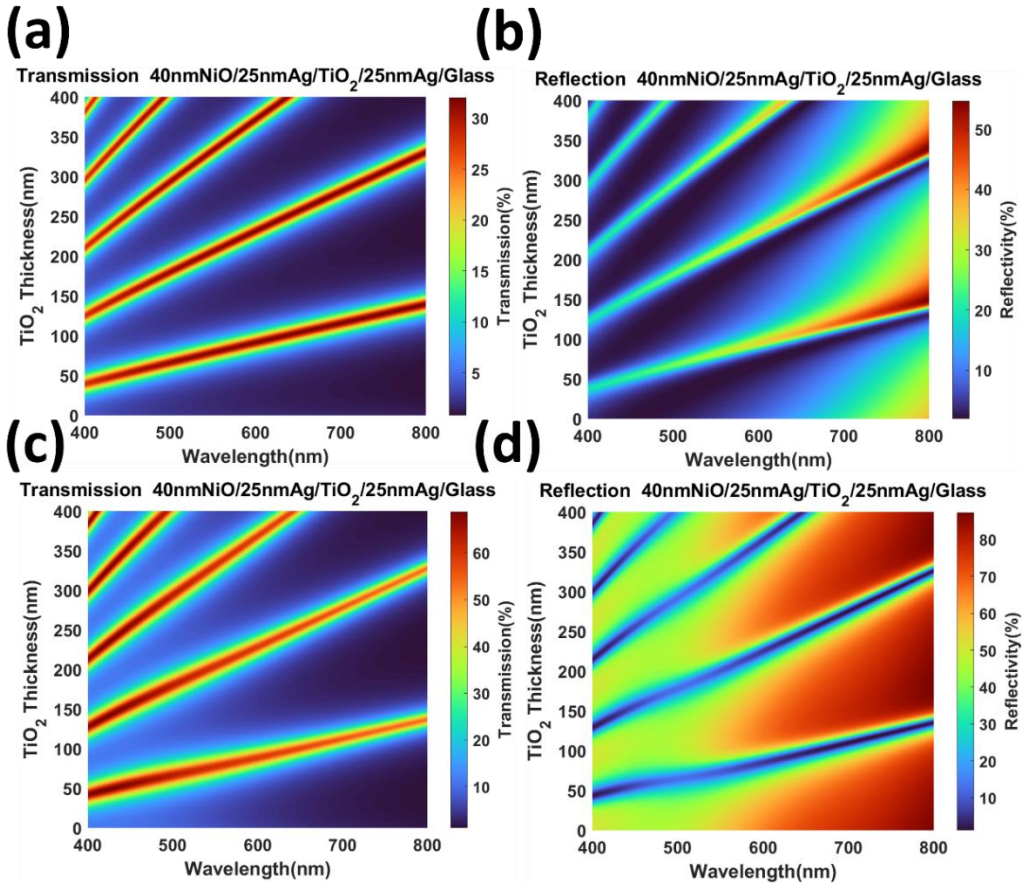


Figure 7.5. (a)-(b) The simulated reflection and transmission peaks for coloured state NiO overlap nearly exactly though the overall brightness is significantly reduced compared to the reflective FROCs, and there is large absorption at resonance wavelength. (c)-(d) The reflection and transmission peaks for bleached NiO overlap as well but the brightness of the transmission has significantly increased, and the reflection is now much higher off-resonance than it is on-resonance. Essentially the reflection spectrum has been inverted while the transmission spectrum is greatly enhanced by 100 %.

The response for thermochromic VO_2 in place of NiO would be much the same but with poor contrast in the blue region of the visible spectrum. A future study on the matter may focus on the NIR regime when investigating, as much larger changes can be found there using VO_2 [14], [16], [17]. Furthermore, many important technologies utilise this spectral region such as fibre optic laser communications [18]. Thus, there is certainly motivation to provide deeper insight, inquiry, and exploration into how these spectrally selective tuneable transmissive/reflective FROCs may be of use in those kinds of critical technological applications alongside other cutting edge optoelectronic device research that focuses on 2D materials like the TMDs and graphene [18], [19].

7.2.2 Future Work with EMA Lossy MIM FP Devices

To create bright saturated colours with central absorber lossy FP MIMs, a 16 nm thick EMA layer was designed based on placing 10 nm Cr on top of 6 nm VO_2. By creating deeply subwavelength material mixtures in this way, the degree of freedom in the design was greatly increased when it came to engineering an effective absorbing layer with an ideal refractive index dispersion w.r.t wavelength. Another layer could be added to the EMA effective medium equation to fine tune the index further towards the ideal. Future work could investigate this more deeply, and profile a list of material combinations that create even better index matching conditions that allow for sharper brighter colours in reflection. The same idea could also be applied to the broadband SiO_2 absorber to match the ideal indices for near unity absorption more closely in that situation too [12]. It would be trickier to work with though since the centrally placed ultrathin absorber in those circumstances is extremely thin at 7 nm. Combining two or more lossy layers together to form one effective medium may necessitate the use of nearly 2D thin films at certain points, whose dimensions are not accurately gauged in nanometres but instead by layer count. It would be quite troublesome to reliably reproduce such an ultrathin EMA layer homogenously at scale. Perhaps the use of materials like TMD MoS_2 are more useful in this regard due to size effects drastically increasing their excitonic absorption. The combination of MoS_2, VO_2, and Cr may make for interesting results going forward. The inclusion of sub-nanometer Ti adhesion and capping layers in between the different absorbing films by future researchers may also drastically improve the stability of such an EMA mixture in an easily scalable way, such that materials with different thermal expansion, lattice parameter mismatch, or surface energy may be grafted together quite without worry as much about destructive effects like sample lift-off (thin film detaching from the substrate), dewetting, and migration (diffusion of the one layer into another) [5], [20]

7.2.3 Future Work with Solid-State Electrolyte Electrochromic Devices.

Using a liquid electrolyte with ECDs is inherently a more messy process and bulkier, as seen in chapter 5. Significant problems were encountered with cycle stability using the KOH electrolyte solution, and it is also difficult to build a practical tuneable device without enclosing it completely with thick bulky glass to keep the solution encased and protected. Therefore, for future research using an ECM like NiO and WO_3, an all-solid-state approach

can be investigated to see how strong the refractive index change and optical response are when electrochemical reduction is carried out.

An all-thin film solid electrolyte EC device (ATF-ECD) at its most simple is composed of 5 stacked planar thin films comprising of two conductive layers, a solid electrolyte layer (SEL), an anodic EC layer or a cathodic EC layer. To make a functioning solid electrolyte EC device a buffer layer or SEL must be placed between an anodic/cathodic EC material and the electrode. State-of-the-art work by R. Wang *et al*. (2021) in the literature has used thin film Ta_2O_5 for this purpose [21]. See Fig.7.6 below.

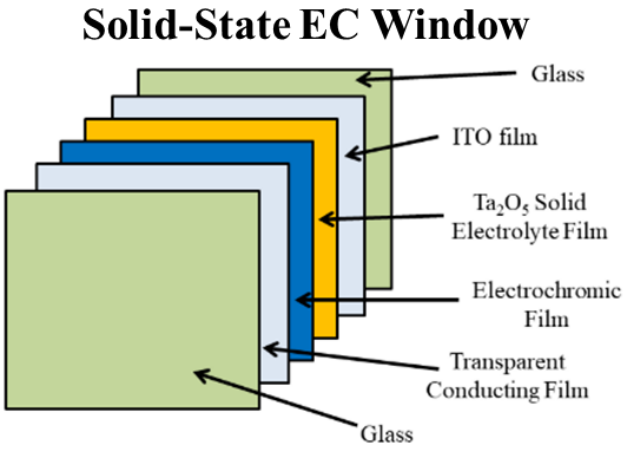


Figure 7.6. A solid state ECD in transmission mode. The Ta_2O_5 film acts like an ion storage layer or sponge when ions are not intercalated into the lattice. There is little to no change in Ta_2O_5 optical response when holding onto the ions.

Ta_2O_5 is an ideal material for this as its transparent. Initially, there was an attempt to make a working solid-state device with the protonated NPVD WO_3 samples by applying water to the Ta_2O_5 layer to introduce hydrogen into it during deposition, but unfortunately this research could not progress further due to the lack of a measurable EC response with UV-Vis or SE. It is unclear how this could be practically implemented into certain stack designs like FROCs as well since these resonator structure would be quiet sensitive to additional transparent films on top (AR layers would increase angle sensitivity in the optical response). TO gain deeper insight, work would have to be done to quantify how thin the Ta_2O_5 could be made relative to ultrathin NiO for complete EC bleaching to still be possible. It could be practical to utilise a solid state set up with the lossy EMA MIM FP reflection colour filter stack too. By replacing the internal FP MIM spacer with Ta_2O_5, the top spacer with ITO and TiO_2, and the bottom ITO with opaque Ag, a tuneable lossy MIM could be created. Figure

7.7 below showcases the active spectra response of solid-state EC NiO in this lossy MIM construct, assuming the change in the indices of NiO is like the response observed for the KOH H^+ ion intercalated samples.

Likewise, a similar substitution could happen for the broadband absorber discussed in chapter 6, though the index of ITO and Ta_2O_5 are too high for a symmetric ideal stack layout solution. Moreover, the NiO is not ideally lossy enough across the visible for strong attenuation to occur in an extremely thin 7 nm film, even if light is highly concentrated on it [12]. Instead, the Cr-VO_2 EMA bilayer could be placed centrally in the stack and a microheater array could phase transition the VO_2 reducing the effective index considerably above 600 nm into the NIR region.

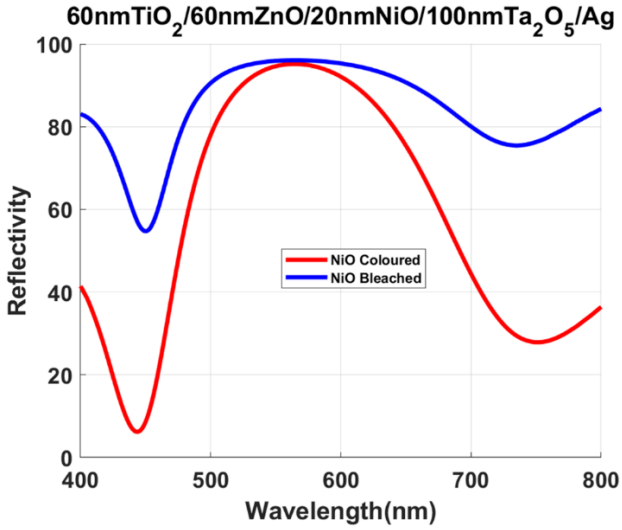


Figure 7.7. In the coloured state a broad green peak is observed with the top two dielectrics acting as antireflection coatings in the blue and red spectral regions. When NiO is bleached the overall response across the visible becomes much flatter on average and the colour produced will be drab and white in appearance. With more optimisation in future work the saturation and brightness on/off contrast can be improved with better design and more ideal layer dimensions.

Other electrolytes, like $LiClO_4$, should also be looked at in future work as the EC response in NiO may differ considerably depending on which ion is intercalated. In particular, both protonation and lithiation should be investigated further, thoroughly, to gauge ECD cycle stability w.r.t this variable. For the KOH H^+ intercalated NiO, the filling factor γ for how many available interstitial sites were occupied by potassium was large at 0.22, almost ¼. The superior stability found in literature for lithiated NiO could indeed be due to the much smaller filling factor of 0.0046 reported by Dongmei Dong *et al*. (2020) [8]. Likewise lithiated WO_3 is also stable even after many thousands of EC cycles [22]. Therefore, the

destruction of these KOH H^+ intercalated samples after 100 CV cycles could simply be the result of the electrolyte being non-optimal for the materials in use. Or perhaps ultrathin film EC materials really are inherently unstable at this size scale, hence why the inclusion of adhesion and capping layers is necessary to prevent it lifting off the substrate underneath. Answering this question definitively is of the upmost importance in characterising deeply subwavelength active ECMs as the research moves forward.

7.3 References

[1] D. Wang, Z. Liu, H. Wang, M. Li, L. J. Guo, and C. Zhang, "Structural color generation: From layered thin films to optical metasurfaces," *Nanophotonics*, vol. 12, no. 6, pp. 1019–1081, 2023, doi: 10.1515/nanoph-2022-0063.

[2] E. J. Gerl and M. R. Morris, "The Causes and Consequences of Color Vision," *Evol. Educ. Outreach*, vol. 1, no. 4, pp. 476–486, 2008, doi: 10.1007/s12052-008-0088-x.

[3] K. R. Williams, K. Gupta, and M. Wasilik, "Etch Rates for Micromachining Processing—Part II," *J. Micromechanics Microengineering*, vol. 12, no. 6, pp. 761–778, 2003, doi: 10.1088/0960-1317/20/5/055033.

[4] K. Tajima, H. Hotta, Y. Yamada, M. Okada, and K. Yoshimura, "Electrochromic switchable mirror glass with controllable reflectance," *Appl. Phys. Lett.*, vol. 100, no. 9, pp. 2012–2015, 2012, doi: 10.1063/1.3691256.

[5] W. M. Abbott *et al.*, "Less is More: Improved Thermal Stability and Plasmonic Response in Au Films via the Use of SubNanometer Ti Adhesion Layers," *ACS Appl. Mater. Interfaces*, vol. 11, no. 7, pp. 7607–7614, 2019, doi: 10.1021/acsami.8b21193.

[6] A. L. Lynch, C. P. Murray, E. Roy, C. Downing, and D. Mccloskey, "Extreme Dewetting Resistance and Improved Visible Transmission of Ag Layers Using Sub-Nanometer Ti Capping Layers," *ACS Omega*, vol. 9, no. 8, pp. 9714–9719, 2024, doi: 10.1021/acsomega.3c09774.

[7] M. Elkabbash *et al.*, "Fano-resonant ultrathin film optical coatings," *Nat. Nanotechnol.*, vol. 16, pp. 440–446, 2021, doi: 10.1038/s41565-020-00841-9.

[8] D. Dong *et al.*, “Electrochromic and colorimetric properties of anodic NiO thin films: Uncovering electrochromic mechanism of NiO,” *Electrochim. Acta*, vol. 335, p. 135648, 2020, doi: 10.1016/j.electacta.2020.135648.

[9] Z. Shao *et al.*, “All-solid-state proton-based tandem structures for fast-switching electrochromic devices,” *Nat. Electron.*, vol. 5, pp. 45–52, 2022, doi: 10.1038/s41928-021-00697-4.

[10] Y. Tang *et al.*, “Lattice Proton Intercalation to Regulate WO3-Based Solid-Contact Wearable pH Sensor for Sweat Analysis,” *Adv. Funct. Mater.*, vol. 32, no. 4, p. 2107653, 2022, doi: 10.1002/adfm.202107653.

[11] Z. Yang, C. Ji, D. Liu, and L. J. Guo, “Enhancing the Purity of Reflective Structural Colors with Ultrathin Bilayer Media as Effective Ideal Absorbers,” *Adv. Opt. Mater.*, vol. 7, no. 21, p. 1900739, 2019, doi: 10.1002/adom.201900739.

[12] H. Deng, Z. Li, L. Stan, D. Rosenmann, and D. Czaplewski, “Broadband perfect absorber based on one ultrathin layer of refractory metal,” *Opt. Lett.*, vol. 40, no. 11, pp. 2592–2595, 2015, doi: 10.1364/OL.40.002592.

[13] H. D. Young and R. A. Freedman, *University Physics with Modern Physics*, 14th ed. Pearson, 2016.

[14] M. Jiang *et al.*, “Room Temperature Optical Constants and Band Gap Evolutionof Phase Pure M1-VO2 Thin Films Deposited at Different OxygenPartial Pressures by Reactive Magnetron Sputtering,” *J. Nanomater.*, vol. 2014, no. 1, pp. 1–6, 2014, doi: 10.1155/2014/183954.

[15] G. Cai *et al.*, “Ultra-large optical modulation of electrochromic porous WO3 film and the local monitoring of redox activity,” *Chem. Sci.*, vol. 7, no. 2, pp. 1373–1382, 2016, doi: 10.1039/c5sc03727a.

[16] G. R. Khan, “Impact of ion irradiation , elemental doping and coating cycles on structural characteristic parameters of nanocrystalline VO2 thin films,” *Micro Nano Lett.*, vol. 15, no. 3, pp. 196–200, 2020, doi: 10.1049/mnl.2019.0186.

[17] V. I. P. Sergey S. Maklakov, A. D. M. Sergey A. Maklakov, and V. N. K. Ilya A. Ryzhikov, Alexander L. Trigub, Vadim A. Amelichev, Konstantin I. Maslakov, "Post-deposition annealing of thin RF magnetron sputter-deposited VO2 films above the melting point," *J. Alloys Compd.*, vol. 763, pp. 558–569, 2018, doi: 10.1016/j.jallcom.2018.06.014.

[18] Z. Sun, A. Martinez, and F. Wang, "Optical modulators with 2D layered materials," *Nat. Photonics*, vol. 10, no. 4, pp. 227–238, 2016, doi: 10.1038/nphoton.2016.15.

[19] F. J. Rodriguez, D. E. Aznakayeva, O. P. Marshall, V. G. Kravets, and A. N. Grigorenko, "Solid-State Electrolyte-Gated Graphene in Optical Modulators," *Adv. Mater.*, vol. 29, no. 19, p. 1606372, 2017, doi: 10.1002/adma.201606372.

[20] J. Chen, G. Song, S. Cong, and Z. Zhao, "Resonant-Cavity-Enhanced Electrochromic Materials and Devices," *Adv. Mater.*, vol. 35, no. 47, p. 2300179, 2023, doi: 10.1002/adma.202300179.

[21] R. Wang, L. Pan, Q. Han, H. Zhu, M. Wan, and Y. Mai, "Reactively sputtered Ta2O5 solid electrolyte layers in all thin film electrochromic devices," *J. Alloys Compd.*, vol. 865, no. 158931, 2021, doi: 10.1016/j.jallcom.2021.158931.

[22] L. Pan *et al.*, "Reactively sputtered WO3 thin films for the application in all thin film electrochromic devices," *Electrochim. Acta*, vol. 328, 2019, doi: 10.1016/j.electacta.2019.135107.

Appendix - Material Recipes

NPVD Sputtering tool: No heating unless specified. Rotation setting at 3-4. Maximum RF gun power is 150 W. Maximum DC gun power is 800 W.

Ag	DC gun at 2 % power with 5 sccm Ar flow. 6.9 nm/min
Al	DC gun at 5 % power with 5 sccm Ar flow. 3.1 nm/min
Al_2O_3	RF gun at 50 % power with 5 sccm Ar flow. 3.14 nm/min
Au	DC gun at 5 % power with 5 sccm Ar flow. 17.22 nm.min
Cr	DC gun at 5 % power with 5 sccm Ar flow. 3.88 nm/min
Ge	DC gun at 5 % power with 5 sccm Ar flow. 9.3 nm/min
ITO	RF gun at 50 % power with 5 sccm Ar flow. 8.5 nm/min
MgF_2	RF gun at 75% power with 5 sccm Ar flow. 0.6 nm/min
Mo	DC gun at 2 % power with 5 sccm Ar flow. 1.89 nm/min
Ni	DC gun at 5 % power with 5 sccm Ar flow. 5.2 nm/min
NiO	DC gun with Ni target at 10 % power with 5sccm Ar and O_2 flow. 1.72 nm/min
Si	RF gun at 50 % power with 5 sccm Ar flow. 4.26 nm/min
SiO_2	RF gun at 75 % power with 5 sccm Ar flow. 2.72 nm/min
Ta	RF gun at 15 % power with 5 sccm Ar flow. 1.05 nm/min
Ta_2O_5	RF gun at 75 % power with 10 sccm Ar flow. 1.5 nm/min
Ti	RF gun at 50 % power with 5 sccm Ar flow. 3.36 nm/min
TiO_2	RF gun at 75 % power with 5 sccm Ar flow. 0.38 nm/min
V_2O_5	RF gun at 75 % power with 5 sccm Ar flow. 2 nm/min
W	DC gun at 10 % power with 5 sccm Ar flow. 5.94 nm/min
WO_3	DC gun with W target at 5-10 % power with 5sccm Ar and 2 sccm O_2 flow. 12.16 nm/min

Thermal Assisted Conversion:

MoS_2/WS_2	20-30 minute TAC sulphurisation at 750 ˚C of 10 % power DC gun sputtered Mo or W on quartz substrate. Factor of 2.6 expansion in precursor film thickness when sulphurised.